Transactions of the ASME®

Transactions of the ASME, Journal of Heat Transfer (ISSN 0022-1481) is published quarterly (Feb., May, Aug., Nov.) for $155 per year by The American Society of Mechanical Engineers, 345 East 47th Street, New York, NY 10017. Second class postage paid at New York, NY and additional mailing offices. POSTMASTER: Send address changes to Transactions of the ASME, Journal of Heat Transfer, c/o THE AMERICAN SOCIETY OF MECHANICAL ENGINEERS, 22 Law Drive, Box 2300, Fairfield, NJ 07007-2300.

CHANGES OF ADDRESS must be received at Society headquarters seven weeks before they are to be effective. Please send old label and new address.

PRICES: To members, $29.00, annually; to nonmembers, $155.00. Add $15.00 for postage to countries outside the United States and Canada.

INDEXED by Applied Mechanics Reviews and Engineering Information, Inc.

Journal of Heat Transfer

Published Quarterly by The American Society of Mechanical Engineers

VOLUME 111 • NUMBER 3 • AUGUST 1989

ANNOUNCEMENTS

648 Errata on a previously published paper by S. Chellaiah and R. Viskanta

674 Change of address form for subscribers

820 Announcement: Fourth International Topical Meeting on Nuclear Reactor Thermal-Hydraulics

820 Call for Papers: International Symposium on Gas-Liquid Two-Phase Flows

882 Information for authors

TECHNICAL PAPERS

592 Temperature Response of a Heated Cylinder Subject to Side Cooling: Asymptotic and Numerical Solutions
K. Ramakrishna, I. M. Cohen, and P. S. Ayyaswamy

598 Numerical and Analytical Solutions for Two-Dimensional Gas Distribution in Gas-Loaded Heat Pipes
P. F. Peterson and C. L. Tien

605 Suppression of the Sonic Heat Transfer Limit in High-Temperature Heat Pipes
Flavio Dobran

611 Heat Transfer Characteristics in Two-Phase Closed Conventional and Concentric Annular Thermosyphons
A. Faghri, M.-M. Chen, and M. Morgan

619 Approximate Solution—One-Dimensional Energy Equation for Transient, Compressible, Low Mach Number Turbulent Boundary Layer Flows
J. Yang and J. K. Martin

625 Flow and Heat Transfer in the Space Between Two Corotating Disks in an Axisymmetric Enclosure
C. J. Chang, C. A. Schuler, J. A. C. Humphrey, and R. Greif

633 Finite Analytic Solution of Convective Heat Transfer for Tube Arrays in Crossflow: Part I—Flow Field Analysis
Tzong-Shyan Wung and Ching Jen Chen

641 Finite Analytic Solution of Convective Heat Transfer for Tube Arrays in Crossflow: Part II—Heat Transfer Analysis
Ching Jen Chen and Tzong-Shyan Wung

649 High Rayleigh Number Laminar Natural Convection in an Asymmetrically Heated Vertical Channel
B. W. Webb and D. P. Hill

657 Natural Convection Flows Due to the Combined Buoyancy of Heat and Mass Diffusion in a Thermally Stratified Medium
D. Angirasa and J. Srinivasan

664 Induction Electrohydrodynamic Pump in a Vertical Configuration: Part I—Theory
J. Seyed-Yagoobi, J. C. Chato, J. M. Crowley, and P. T. Krein

670 Induction Electrohydrodynamic Pump in a Vertical Configuration: Part 2—Experimental Study
J. Seyed-Yagoobi, J. C. Chato, J. M. Crowley, and P. T. Krein

675 Combined Forced and Free Upward-Flow Convection in the Entrance Region Between Inclined Parallel Plates
E. Naito and Y. Nagano

683 Mixed Convection in an Annulus of Large Aspect Ratio
L. S. Yao and B. B. Rogers

690 Prediction of Conjugate Heat Transfer in a Solid-Liquid System: Inclusion of Buoyancy and Surface Tension Forces in the Liquid Phase
J. R. Keller and T. L. Bergman

699 A Heat Transfer Analysis for Solidification of Slabs, Cylinders, and Spheres
M. Pruh'homme, T. Hung Nguyen, and D. Long Nguyen

706 An Experimental Investigation of Binary Solidification in a Vertical Channel With Thermal and Solutal Mixed Convection
W. D. Bennon and F. P. Incropera

713 Transient Radiative Heat Transfer From a Sphere Surrounded by a Participating Medium
Y. Bayazitoglu and P. V. R. Suryanarayana

(Contents continued)

719 Heat and Mass Transfer During Piloted Ignition of Cellulosic Solids
A. Atreya and I. S. Wichman

726 Energy Storage in a Fluidized Bed
N. Merry and B. Rubinsky

731 Void Fraction Measurements During Saturated Pool Boiling of Water on Partially Wetted Vertical Surfaces
S. P. Liaw and V. K. Dhir

739 Framework for a Unified Model for Nucleate and Transition Pool Boiling
V. K. Dhir and S. P. Liaw

747 The Influence of Subcooling on the Frequency of Bubble Emission in Nucleate Boiling
R. L. Judd

752 Microelectronic Cooling by Enhanced Pool Boiling of a Dielectric Fluorocarbon Liquid
T. M. Anderson and I. Mudawar

760 The Effect of Surface Motion on Forced Convection Film Boiling Heat Transfer (87-WA/HT-5)
D. A. Zumbrunnen, R. Viskanta, and F. P. Incropera

767 *Stability of a Direct-Contact Spray Column Heat Exchanger*
M. Golafshani and H. R. Jacobs

773 A Heuristic Evaluation of the Governing Mode of Heat Transfer in a Liquid-Liquid Spray Column
H. R. Jacobs and M. Golafshani

780 Direct Contact Evaporation Between Two Immiscible Liquids in a Spray Column
K. N. Seetharamu and P. Battya

786 Modeling the Thermally Governed Transient Flow Surges in Multitube Condensing Flow Systems With Thermal and Flow Distribution Asymmetry
G. L. Wedekind and B. L. Bhatt

792 Forced Convection Condensation on a Horizontal Tube—Experiments With Vertical Downflow of Steam
A. G. Michael, J. W. Rose and L. C. Daniels

798 The Measurement of Surface Heat Flux Using the Peltier Effect
E. C. Shewen, K. G. T. Hollands, and G. D. Raithby

TECHNICAL NOTES

804 On the Nondimensionalization of Constriction Resistance for Semi-infinite Heat Flux Tubes
K. J. Negus, M. M. Yovanovich, and J. V. Beck

807 Similarity Solution for Non-Darcy Free Convection From a Nonisothermal Curved Surface in a Fluid-Saturated Porous Medium
A. Nakayama, H. Koyama, and F. Kuwahara

811 Geometric Mean Beam Lengths for the Space Between Two Coaxial Cylinders
K. M. Andersen and S. Hadvig

813 A Dimensionless Number for the Contact Line Evaporative Heat Sink
P. C. Wayner, Jr.

815 An Upper Bound for the Critical Boiling Heat Flux
W. R. Gambill and J. H. Lienhard

818 A New Interpolation Formula for Forced-Convection Condensation on a Horizontal Surface
J. W. Rose

K. Ramakrishna
Mem. ASME
Technology Laboratory,
IBM Corporation,
Endicott, NY 13760

I. M. Cohen
Mem. ASME

P. S. Ayyaswamy
Mem. ASME

Department of Mechanical Engineering
and Applied Mechanics,
School of Engineering and Applied Science,
University of Pennsylvania,
Philadelphia, PA 19104-6315

Temperature Response of a Heated Cylinder Subject to Side Cooling: Asymptotic and Numerical Solutions

The temperature response of a cylinder, subject to heat input at one end and heat loss from its side by radiation and natural convection, is studied analytically and numerically. A singular perturbation expansion gives the limiting case of large heat flux. The governing equations for arbitrary heat flux are solved numerically. The results of this investigation are useful for application to the microelectronic interconnection process using the ball bonding technique.

1 Introduction

Many problems of practical interest deal with a solid body, subject to a heat flux input at one end and heat loss through natural convection and radiation from the surface. For example, microelectronic interconnection by the ball bonding process involves ball formation by heating a thin wire on its bottom face using a heat source, usually an electrical discharge (Onuki et al., 1984). During heating, the temperature of the material increases from an initial value to the melting temperature. The transfer process in this situation is nonlinear.

For a summary of many steady and transient problems dealing with the combined modes of heat transfer that arise in similar situations, Siegel and Howell (1981) may be consulted. The temperature response of one-dimensional solid bodies has received considerable attention. Most often, two types of base temperature boundary conditions have been considered, viz., a constant temperature and a periodic variation. Several numerical solutions have also been found. Duffy (1985) obtained analytical and numerical solutions to the problem of the temperature response of a sphere with a directed heat flux. The temperature response of a two-dimensional circular fin, subject to a constant heat transfer coefficient on the sides, was analyzed by Chu et al. (1983). The finite element solution of heat conduction with the radiative boundary condition was treated through a simple iteration and the Gauss-Seidel method by Reddy and Sharan (1985), through a mixed explicit/implicit time integration technique by Zhang et al. (1986), and for temperature-dependent thermal conductivity by Reddy and Sharan (1986).

In this paper, we are concerned with the temperature response of a cylinder, subject to heat input at one end and heat loss from its side by radiation and natural convection. The role of natural convection and radiation at the surface, the aspect ratio (the ratio of wire radius to its length), and the variation of heat input are investigated. The time taken to reach melting temperature has been determined as a function of these parameters. Temperature response curves are presented for some representative cases; asymptotic solutions are presented for the limiting case of large heat flux. For large heat flux, the solutions are independent of aspect ratio.

The equations for the full formulation have also been solved numerically. Comparisons are made with the asymptotic solutions to outline their range of validity and as a check on the numerical solution. The lack of relevant experimental data precludes comparison.

2 Model

2.1 Governing Equations and Initial and Boundary Conditions. Consider a homogeneous solid circular cylinder, initially at a uniform, constant temperature equal to that of the ambient (see Fig. 1). At time $t' = 0$, a uniform and constant heat flux q_o'' is applied to its bottom face. The cylinder loses heat from its side through natural convection and radiation. The radiative cooling process is nonlinear. In the calculations, the thermophysical properties of the cylinder have been evaluated at a reference temperature, which is the average of the ambient and the melting temperature.

2.2 Small Aspect Ratio Problem. When the cylinder radius is much smaller than its length, conduction is mainly due to the temperature gradient along the axial direction (see Fig. 1). The heat conduction equation and initial and boundary conditions are

$$\frac{\partial^2 T}{\partial z'^2} - \frac{2\,h_c}{k\,r_o}(T - T_\infty) - \frac{2\epsilon\sigma}{k\,r_o}(T^4 - T_\infty^4) = \frac{1}{\alpha}\frac{\partial T}{\partial t'} \quad (1)$$

with

$$T(z', 0) = T_\infty;\quad \left.\frac{\partial T}{\partial z'}\right|_{(0,t')} = 0;\quad \left.\frac{\partial T}{\partial z'}\right|_{(L,t')} = \frac{q_o''}{k} \quad (2)$$

where T is the cross-sectionally averaged temperature and the cylinder is assumed to radiate as a gray body.

These equations are rendered dimensionless using the following definitions: $\theta = (T - T_\infty)/T_R$, $T_R = (T_m - T_\infty)$, $z = z'/L$, $t = \alpha t'/L^2$, so that equations (1) and (2) become

$$\frac{\partial^2\theta}{\partial z^2} - \left[C_1\,\mathrm{Nu} + C_2\,N_R(\theta)\right]\theta = \frac{\partial\theta}{\partial t} \quad (3)$$

with

$$\theta(z, 0) = 0;\quad \left.\frac{\partial\theta}{\partial z}\right|_{(0,t)} = 0;\quad \left.\frac{\partial\theta}{\partial z}\right|_{(1,t)} = q$$

where

$$A = \frac{r_o}{L};\quad q = \frac{q_o''\,L}{k\,T_R};\quad \beta = \frac{T_\infty}{T_R}$$

$$C_1 = \frac{2\,k_a}{k\,A^2};\quad C_2 = C_1\left(\frac{\epsilon\sigma\,r_o\,T_R^3}{k_a}\right) \quad (5)$$

$$N_R = [4\beta^3 + 6\beta^2\,\theta + 4\beta\,\theta^2 + \theta^3];\quad \mathrm{Nu} = \frac{h_c\,r_o}{k_a}$$

Contributed by the Heat Transfer Division for publication in the JOURNAL OF HEAT TRANSFER. Manuscript received by the Heat Transfer Division February 25, 1988. Keywords: Conduction, Materials Processing and Manufacturing Processes, Transient and Unsteady Heat Transfer.

From a formal dimensional analysis, it can be shown that θ, z, t, A, q, Nu, k/k_a, β, and $\epsilon\sigma r_o T_R^3/k_a$ are the pertinent dimensionless quantities for the problem

2.3 Finite Aspect Ratio Problem. When the radius of the cylinder is of the same order of magnitude as its length, the aspect ratio is finite and the temperature field in the cylinder is two dimensional. The nondimensional conduction equation, initial and boundary conditions are

$$\frac{1}{r}\frac{\partial}{\partial r}\left[r\frac{\partial\theta}{\partial r}\right] + A^2\frac{\partial^2\theta}{\partial z^2} = \frac{\partial\theta}{\partial \bar{t}} \tag{6}$$

with

$$\theta(r, z, 0) = 0 \tag{7a}$$

$$|\theta(r, z, \bar{t})| < \infty \tag{7b}$$

$$-\left.\frac{\partial\theta}{\partial r}\right|_{(1,z,\bar{t})} = [D_1\,\mathrm{Nu} + D_2 N_R(\theta)]\,\theta\Big|_{(1,z,\bar{t})} \tag{7c}$$

$$\left.\frac{\partial\theta}{\partial z}\right|_{(r,0,\bar{t})} = 0 \tag{7d}$$

$$\left.\frac{\partial\theta}{\partial z}\right|_{(r,\,1,\,\bar{t})} = q \tag{7e}$$

where

$$D_1 = (k_a/k) \tag{8a}$$

$$r = r'/r_o \tag{8b}$$

$$D_2 = \epsilon\sigma\, r_o\, T_R^3/k \tag{8c}$$

$$\bar{t} = \alpha t'/r_o^2 \tag{8d}$$

3 Asymptotic Solution at the Large Heat Flux

In the limiting case of large heat flux, the one and two-dimensional problems, given by equations (3), (4) and (6), (7), respectively, admit asymptotic solutions. For the sake of generality, we consider the two-dimensional formulation in this limit.

As $q \to \infty$, equation (7*e*) cannot be satisfied and the problem becomes singular. We divide the solution domain into an outer region, in which the solution does not satisfy the boundary condition at $z = 1$, and an inner region, where the boundary condition at $z = 1$ is satisfied upon a rescaling of the variables. Such regions also exist at $r = 1$, as can be demonstrated by scaling arguments. The solutions in these regions are matched in an intermediate region to the same order in the small parameter $(1/q)$.

Let u and v denote inner and outer solutions, respectively. The outer region temperature v satisfies equation (6) and the boundary condition at $z = 0$. For the sake of convenience, x is introduced as

$$x = 1 - z \tag{9}$$

Outer Region. The outer region temperature field is described by

$$\frac{1}{r}\frac{\partial}{\partial r}\left[r\frac{\partial v}{\partial r}\right] + A^2\frac{\partial^2 v}{\partial x^2} = \frac{\partial v}{\partial \bar{t}} \tag{10}$$

with

$$v(r, x, 0) = 0 \tag{11a}$$

$$|v(r, x, \bar{t})| < \infty \tag{11b}$$

$$-\left.\frac{\partial v}{\partial r}\right|_{(1,x,\bar{t})} = [D_1\,\mathrm{Nu} + D_2 N_R(v)]\,v\Big|_{(1,x,\bar{t})} \tag{11c}$$

and

$$\left.\frac{\partial v}{\partial x}\right|_{(r,1,\bar{t})} = 0 \tag{11d}$$

Inner Region. To derive equations for the inner region, the variables in equations (6) and (7) have to be rescaled in such a way that the resulting equations for the inner region can satisfy at least the "lost" boundary condition at $z = 1$. The formal process of scaling has been carried out near both $r = 0$ and $r = 1$ and near $z = 1$. Using the principle of maximal balance by Kruskal (1963), we arrive at the following scaling for the inner region:

$$\xi = x\,q \quad \text{and} \quad \bar{\tau} = \bar{t}\,q^2 \tag{12}$$

We note that time is scaled as the square of the heat flux while temperature is not scaled. In developing equation (12), it may be demonstrated that, to the leading order, the temperature in the inner region does not depend on the radial coordinate and therefore the radial variation of temperature is a higher-order effect. The details of the derivation of equation (12) are provided in Appendix A.

In terms of the rescaled variables u, the inner region temperature variable must be O(1). Therefore, the inner expansion for temperature, in terms of $1/q$, can be written as

$$u(\xi, \bar{\tau}; q) = u_o(\xi, \bar{\tau}) + \mathrm{O}(1/q) \tag{13}$$

Nomenclature

A = aspect ratio = r_o/L
C_1, C_2 = nondimensional quantities, see equation (5)
D_1, D_2 = nondimensional quantities, see equation (8)
h_c = convective heat transfer coefficient
k = thermal conductivity
L = length of the cylindrical wire
N_R = a function, see equation (5)
N = number of grid points in the finite difference solution
Nu = Nusselt number based on cylinder radius = $h_c r_o/k_a$
q_o'' = prescribed heat flux at the bottom face of the cylinder
q = nondimensional heat flux = $q_o'' L/(k T_R)$
r_o = radius of the cylinder
r' = dimensional radial coordinate
r = nondimensional radial coordinate = r'/r_o
t' = dimensional time
t = nondimensional time in one-dimensional problem = $\alpha t'/L^2$
T = temperature
T_R = normalization temperature = $T_m - T_\infty$
u = inner variable for temperature in high heat flux problem
v = outer variable for temperature in high heat flux problem
x = $1 - z$
z' = dimensional axial coordinate
z = nondimensional axial coordinate = z'/L
α = thermal diffusivity
β = ratio of ambient to reference temperature = T_∞/T_R
ϵ = hemispherical total emissivity
θ = nondimensional temperature = $(T - T_\infty)/T_R$
τ = rescaled $t = t\,q^2$
σ = Stefan–Boltzmann constant
ξ = rescaled $x = x\,q$

Subscripts

∞ = ambient
a = properties of ambient gas
m = at melting temperature
o = leading order solution

Superscripts

$'$ = dimensional quantities
n = current time level in the numerical integration

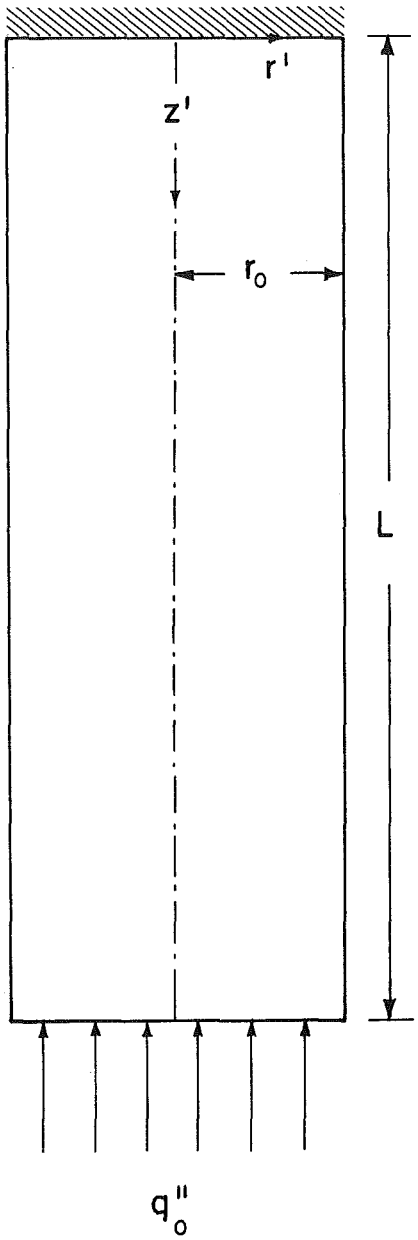

Fig. 1 Schematic diagram of the cylinder

The temperature response in the inner region is given by the substitution of equations (9), (12), and (13) in equations (6) and (7):

$$\frac{\partial^2 u_o}{\partial \xi^2} - \frac{\partial u_o}{\partial \tau} = O(q^{-1}) \tag{14}$$

where $\tau = \bar{\tau} A^2$.

To the leading order, in the high heat flux limit, the right-hand side of equation (14) is suppressed; the boundary conditions are

$$u_o(\xi, 0) = 0 \tag{15a}$$

$$\left.\frac{\partial u_o}{\partial \xi}\right]_{(0,\tau)} = -1 \tag{15b}$$

Equations (14) and (15) state that for large heat fluxes, the temperature in the inner region behaves similarly to the heat conduction within a semi-infinite region that is initially at zero temperature and then is suddenly subjected to a constant heat input at its surface.

When a cylinder is heated on its bottom face and loses heat from the side by natural convection and radiation, the depth of penetration of the heating effect is small and the associated heat loss is negligible for high values of heat input. Because of this, the heatup of the cylinder at high heat fluxes closely follows that of a semi-infinite medium. This is formally demonstrated from an asymptotic analysis presented above without an *a priori* assumption about the amount of side heat loss and the depth of penetration of the heating on the bottom face.

Upon finding u_o and v_o, both solutions have an arbitrary constant that may be determined by matching u and v in their overlap. From equations (14) and (15), the inner solution is given by the error function, which decays exponentially as its argument $\xi/(2\sqrt{\tau})$ tends to infinity. Therefore, the outer solution for temperature must also tend to zero as x tends to zero.

The solution to equations (14) and (15) is

$$u_o(\xi, \tau) = 2\sqrt{\tau/\pi}\, e^{-\xi^2/4\tau} - \xi \operatorname{erfc}(\xi/2\sqrt{\tau}) \tag{16}$$

where erfc $\{\xi/(2\sqrt{\tau})\}$ is the complementary error function. As the bottom face has the highest temperature, melting begins at $\xi = 0$ when $\theta = 1$. Thus we obtain the nondimensional time τ_m as

$$\tau_m = \pi/4 \tag{17}$$

This simple and useful result shows that the time taken to reach melting temperature, τ_m, is a constant to the leading order. The corresponding dimensional time taken to reach melting temperature, t'_m, is derived from equation (17) for high heat flux q''_o, as

$$t'_m = \frac{\pi\, k\, \rho\, c\, (T_m - T_\infty)^2}{4\, q''^2_o} \tag{18}$$

The temperature on the bottom face of the cylinder is derived from equation (16) and equals $u_o(0, t) = 2q\sqrt{(t/\pi)}$.

Since the above solutions have been derived for a two-dimensional problem, they also describe qualitatively the small aspect ratio case. Thus in the large heat flux limit, the time taken to reach melting temperature is also constant independent of the aspect ratio. A rigorous analysis of the small aspect ratio problem confirms this finding.

4 Numerical Solutions

The asymptotic solutions are valid in the limit of large heat flux where they give leading order solutions to the problem. However, for moderate heat fluxes, equations (3) and (4) for the one-dimensional cases and equations (6) and (7) for the two-dimensional cases must be solved numerically.

4.1 Small Aspect Ratio Problem. Equations (3) and (4) are solved by using central differences (second-order accurate) for the spatial derivatives and an implicit time differencing scheme. The resulting nonlinear, simultaneous, algebraic equations are

$$\frac{\theta_{i-1}}{\Delta z^2} + \frac{\theta_{i+1}}{\Delta z^2} + \frac{\theta_i^{n-1}}{\Delta t} - \left[\frac{2}{\Delta z^2} + \frac{1}{\Delta t} + C_1\,\mathrm{Nu} + C_2\, N_R\,(\theta_i)\right]\theta_i = 0 \quad \text{for } 1 < i < N \tag{19a}$$

$$-\left[\frac{2}{\Delta z^2} + \frac{1}{\Delta t} + C_1\,\mathrm{Nu} + C_2\, N_R\,(\theta_1)\right]\theta_1 + \frac{2\theta_2}{\Delta z^2} + \frac{\theta_1^{n-1}}{\Delta t} = 0 \quad \text{for } i = 1 \tag{19b}$$

$$\frac{2\theta_{N-1}}{\Delta z^2} + \frac{\theta_N^{n-1}}{\Delta t} - \left[\frac{2}{\Delta z^2} + \frac{1}{\Delta t} + C_1\,\mathrm{Nu} + C_2\,N_R\,(\theta_N)\right]\theta_N + \frac{2\,q}{\Delta z} = 0 \quad \text{for } i = N \tag{19c}$$

In equations (19) the superscript $(n-1)$ denotes values at the previous (already solved) time level while n denotes the solution at the next time step. Equations (19) have been solved using the Newton–Raphson method and Thomas algorithm (see, for example, Carnahan et al., 1969).

4.2 Finite Aspect Ratio Problem. Equations (6) and (7), which describe the two-dimensional problem, are solved using central differences for spatial derivatives and an implicit time integration scheme. The discretization involves five spatial points and the resulting coefficient matrix is no longer tridiagonal. Furthermore, discretization at the $r = 1$ boundary gives rise to nonlinear equations. The algebraic equations are cumbersome and will not be reproduced here. This system of algebraic equations is solved using a line-by-line method, along with the Newton–Raphson scheme and Thomas algorithm. Appendix B provides details of the method of solution.

5 Results and Discussion

Numerical computations have been carried out for aspect ratios A from 0.001 to 10 and for nondimensional heat flux values q in the range from 0.5 to 1500. For ball formation in the microelectronic interconnection processes, aspect ratios of 0.001–0.05 and heat flux values in the range from 7 to 700 are typical. For an aluminum wire 2 mils in diameter ($r_o = 2.54 \times 10^{-5}$ m), this range of heat input would correspond to 0.02–2 milli-Joules with corresponding heat flux values of 10^7–10^9 W/m^2. In all the numerical computations, steady-state natural convection heat transfer correlations from Hama et al. (1959) and Churchill and Usagi (1972) have been employed at each instant of time during the integration. At large heat fluxes, the heat loss from the side is a higher-order effect, while at intermediate heat fluxes the transient lasts long enough to justify the use of steady-state correlations. The ambient fluid is taken to be air at 300 K. Total hemispherical emissivity values for gold, aluminum (polished and oxidized), and stainless steel (AISI 304) are from Touloukian and Ho (1972). In the numerical solutions, grid size and time steps were varied until two successive calculations agreed within a prescribed accuracy. Typically 501 to 8001 grid points are used for the small aspect ratio formulation (one-dimensional—along the axis of the cylinder). For the two-dimensional formulation the grid size is 51×51 when $A = 2$ and $q = 1$. In general the grid size is increased with increase in q for both the formulations. The nonlinear algebraic equations and the two-dimensional finite difference equations were iteratively solved until the difference between two successive iterations agreed within a prescribed limit. This accuracy is set at 10^{-6} during the earlier part of the transient and is never allowed to exceed 0.01. The number of iterations required to obtain a converged solution varied from 10 to approximately 40 depending upon the q value.

Figure 2(*a*) shows the dependence of time taken for melting to start, t_m, on q for various aspect ratios. The solid line is the leading order asymptotic solution (equation (17)). For the high q limit the agreement between the numerical and analytical results is excellent. It can be concluded in this limit that t_m varies inversely as the square of nondimensional heat flux q, independent of the aspect ratio, and is given by $\pi/(4\,q^2)$. For smaller values of q, t_m becomes dependent upon the aspect ratio.

Figure 2(*b*) shows a comparison between the numerical and analytical results for τ_m $(= t_m\,q^2)$ as a function of q, for an intermediate range of values of q, i.e., $q = \mathrm{O}(1)$. The asymptotic solution (solid line) shows that τ_m is constant, and this is valid at high values of q. Below a certain heat flux, denoted by q^*, τ_m becomes a function of q, and q^* is a function of A in addition to other parameters, such as emissivity, the nature of the ambient gas (convection effects), etc. This is evident from Fig. 2(*b*) for $A = 0.5$ and 2.0, and $q < 5$.

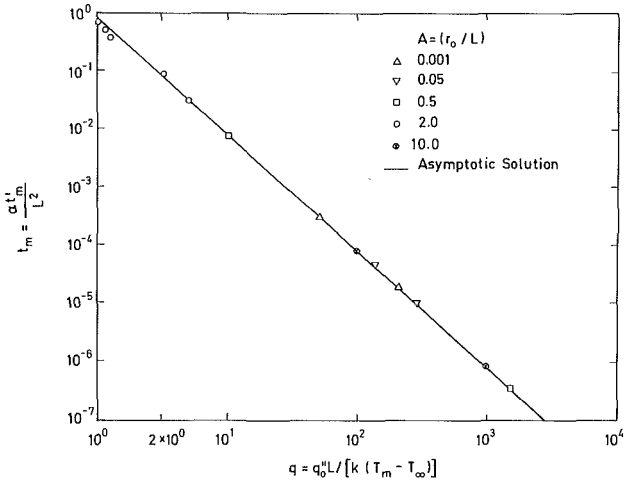

Fig. 2(*a*) Nondimensional time taken to reach the melting temperature, t_m, versus nondimensional heat flux q for varous aspect ratios

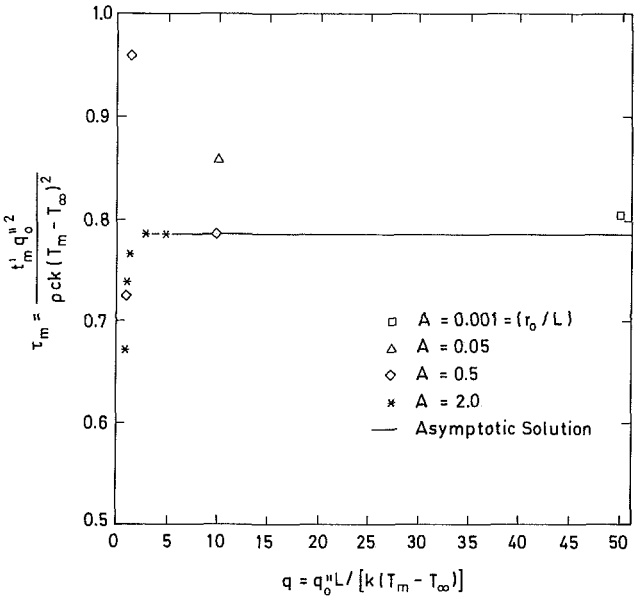

Fig. 2(*b*) Rescaled nondimensional time taken to reach melting temperature, τ_m, versus nondimensional heat flux q for various aspect ratios

Radial temperature profiles on the bottom face (where the heating is occurring) are shown as a function of the heat flux in Fig. 3. The instant of time is such that melting has just been initiated at the center of the bottom face ($t = t_m$ and $\theta = 1$). Note that for smaller q values, the variations in the radial direction may not be ignored in calculating the melt times. Clearly, for large q values, the solution becomes independent of the radial coordinate and coincides with the asymptotic limit.

To assess the role played by the radiative loss mechanism, we now consider the effect of the emissivity on the temporal variation of the temperature at the center of the base of the cylinder (where melting may be initiated) for fixed q, aspect ratio A, and ambient conditions (i.e., fixed effect of natural convection). Figure 4 shows that for a larger emissivity, $\epsilon = 0.5$ (typical of oxidized metal surfaces), the radiative heat loss

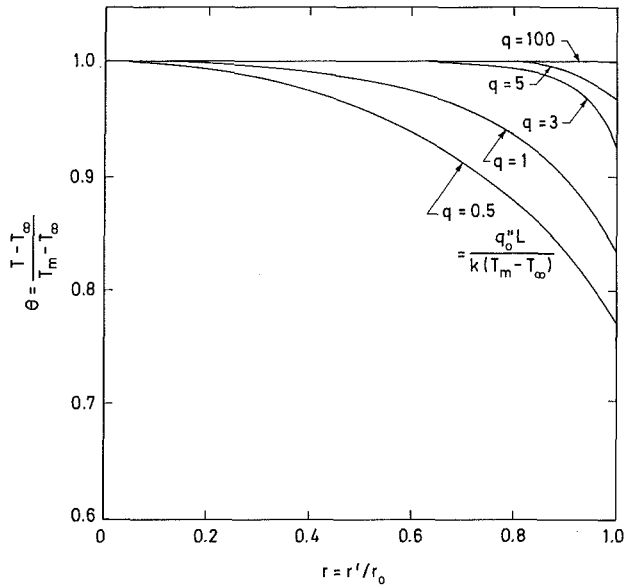

Fig. 3 Temperature variation along the base of the cylinder at the beginning of melting for $q = 0.5, 1, 3, 5, 100$; $A = 2$ and $\epsilon = 0.5$

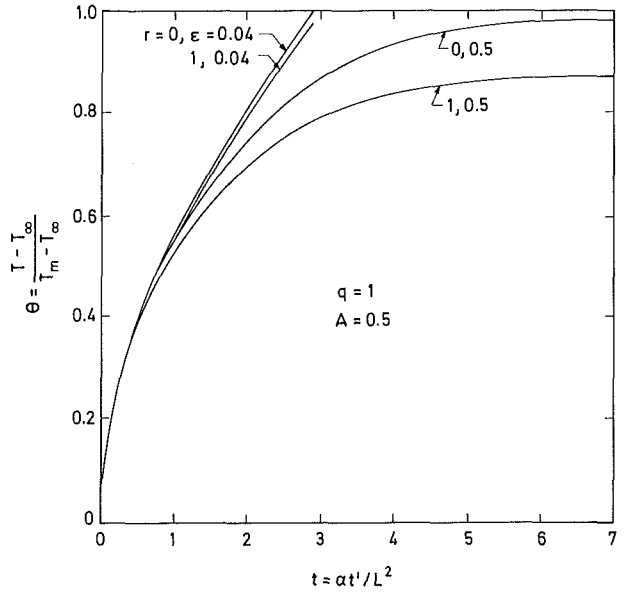

Fig. 4 Effect of surface emissivity on the temperature response at the center of the bottom face at $q = 1$, $A = 0.5$, and $\epsilon = 0.04, 0.5$

is sufficiently large that heat conduction removes enough heat so that no melting is possible. With decreasing emissivity (for example, $\epsilon = 0.04$ for a polished aluminum surface), the wire begins to melt at $t = t_m$ ($= 2.886$).

The effects of variation in aspect ratio on the temporal variation of the temperature at the center of the base of the rod for a given q, ϵ, and ambient conditions are shown in Fig. 5. At a small enough aspect ratio ($A = r_o/L$), conduction may be dominant and a steady-state situation may be attained ($A = 0.5$). Alternatively, at a higher aspect ratio ($A = 2$—thick cylinder with a larger base), the heat input may be sufficient to cause melting eventually.

The effect of the variation in the natural convection heat transfer coefficient has not been investigated separately because it is expected to be negligible for the ambient gases (air and argon, and for that matter for all substances that could be treated as ideal gases) used in the ball bonding process.

The quantitative results obtained in this study are useful to the industry. More information in this regard is available in the doctoral dissertation by Ramakrishna (1989).

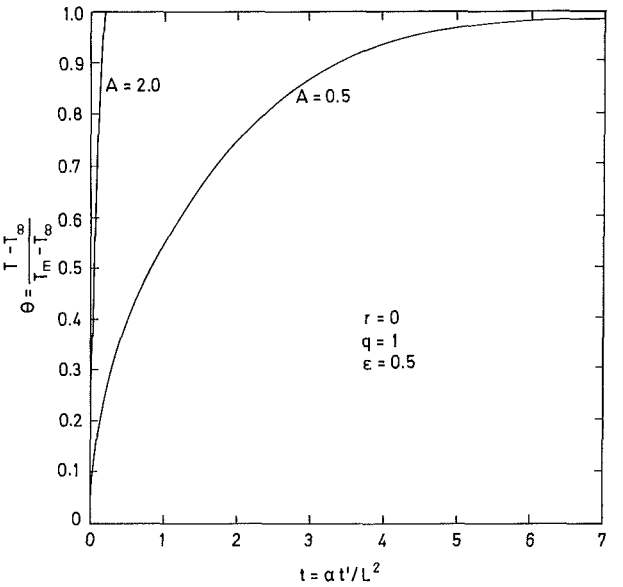

Fig. 5 Effect of aspect ratio on the temperature response at the center of the bottom face at $q = 1$, $\epsilon = 0.5$, and $A = 0.5, 2$

6 Conclusions

For a solid cylinder subject to a high heat flux at the bottom, which loses heat by radiation and natural convection from its sides, the dimensionless scaled time taken to reach melting temperature, τ_m, is constant and equals $\pi/4$. At lower values of the input heat flux the wire may reach steady state depending on the surface loss characteristics and aspect ratio r_o/L. The time taken to reach melting in these latter cases has to be ascertained by numerically solving the resulting nonlinear conduction problem. In this paper the time required to initiate melting has been found to depend upon certain nondimensional quantities. Manufacturing industries, and in particular microelectronic interconnection using ball bonding, will benefit from this study. The results of the study are also of interest to the general field of nonlinear heat conduction.

Acknowledgments

This paper is based upon work supported by the National Science Foundation under Grant No. DMC 8513128. Numerical computations are made possible under the NSF Supercomputer grant No. DMC 0000000/8513128. The authors thank Prof. Y. K. Joshi of the Naval Post Graduate School, Monterey, CA, and Prof. M. W. Nansteel of University of Pennsylvania, Philadelphia, PA, for many helpful discussions.

References

Carnahan, B., Luther, H. A., and Wilkes, J. O., 1969, *Applied Numerical Methods*, Wiley, New York, pp. 319 and 441–442.

Chu, H. S., Chen, C. K., and Weng, C. I., 1983, "Transient Response of Circular Pins," ASME JOURNAL OF HEAT TRANSFER, Vol. 105, No. 1, pp. 205–208.

Churchill, S. W., and Usagi, R., 1972, "A General Expression for the Correlation of Rates of Transfer and Other Phenomena," *AIChE J.*, Vol. 18, pp. 1121–1128.

Duffy, D., 1985, "The Temperature Distribution Within a Sphere Placed in a Directed Uniform Heat Flux and Allowed to Radiatively Cool," ASME JOURNAL OF HEAT TRANSFER, Vol. 107, No. 1, pp. 28–32.

Hama, F. R., Recesso, J. V., and Christiaens, J., 1959, "The Axisymmetric Free-Convection Temperature Field Along a Vertical Thin Cylinder," *J. of the Aero/Space Sciences*, Vol. 26, pp. 335–342.

Kruskal, M. D., 1963, "Asymptotology," in: *Mathematical Models in Physical Sciences*, S. Drobot, ed., Prentice-Hall, Engelwood Cliffs, NJ, pp. 17–48.

Onuki, J., Suwa, M., Iizuka, T., and Okikawa, S., 1984, "Study of Aluminum Ball Bonding for Semiconductors," *Proceedings, 34th Electronic Components Conference*, IEEE CHMT Division, New Orleans, LA, pp. 7–12.

Ramakrishna, K., 1989, "Study of Electrical Breakdown Phenomena and Wire Heating for Ball Formation in Ball Bonding," Ph.D dissertation, Dept. of Mechanical Engineering and Applied Mechanics, University of Pennsylvania, Philadelphia, PA.

Reddy, B. S., and Sharan, A. M., 1985, "The Transient Heat Transfer Analysis of Solids With Radiative Boundary Condition Using Finite Element Analysis," *Letters in Heat and Mass Transfer*, Vol. 12, No. 2, pp. 169-178.

Reddy, B. S., and Sharan, A. M., 1986, "The Method of Nonlinear Finite Element Modelled Heat Transfer Problems," in: *Current Researches in Heat and Mass Transfer: A Compendium and a Festschrift for Professor Arcot Ramachandran*, M. V. Krishna Murthy et al., eds., Indian Society for Heat and Mass Transfer, Madras, India, pp. 211-217.

Siegel, R., and Howell, J. R., 1981, *Thermal Radiation Heat Transfer*, 2nd ed., Hemisphere Publ. Co., Washington, DC, Chap. 12, pp. 384-411.

Touloukian, Y. S., and Ho, C. Y., eds., 1972, *Thermophysical Properties of Matter*, Plenum Press, New York, Vol. 7.

Zhang, Y. F., Yao, G. F., and Wei, Z., 1986, "Mixed Time Integration Methods for Transient Heat Conduction With Radiation Boundary Condition," in: *Numerical Methods in Heat Transfer*, J. L. S. Chen and K. Vafai, eds., ASME HTD-Vol. 162, New York, pp. 57-61.

APPENDIX A

Derivation of Scaling for the Finite Aspect Ratio Problem in the Large Heat Flux Limit

In this Appendix, the scaling for the transient heat conduction equation (6) is derived. First we will consider a region near $r = 0$ and $x = 0$, and then near $r = 1$ and $x = 0$.

1 Near r = 0. Let

$$\xi = xq^{\alpha_1}; \quad \rho_i = rq^{\alpha_2}; \quad \bar{\tau} = \bar{t}q^{\alpha_3}; \quad \psi = uq^{\alpha_4} \tag{A1}$$

Substituting equations (A1) and (9) into equation (6) we have

$$q^{(2\alpha_2-\alpha_4)}\frac{1}{\rho_i}\frac{\partial}{\partial\rho_i}\left(\rho_i\frac{\partial\psi}{\partial\rho_i}\right) + A^2 q^{(2\alpha_1-\alpha_4)}\frac{\partial^2\psi}{\partial\xi^2} = q^{(\alpha_3-\alpha_4)}\frac{\partial\psi}{\partial\bar{\tau}} \tag{A2}$$

In order to retain the maximum number of terms in equation (A2), with a minimum of the term(s) representing the boundary condition(s) following Kruskal (1963), we obtain

$$2\alpha_2 - \alpha_4 = 2\alpha_1 - \alpha_4 = \alpha_3 - \alpha_4 \tag{A3}$$

From the initial condition, we arrive at $\alpha_4 = 0$, from equation (7*e*) $\alpha_1 = 1$, from equation (A3) $\alpha_2 = 1$, $\alpha_3 = 2$, and $\partial\psi/\partial\rho_i = 0$ at $\rho_i = 0$. The solution in this region, near $r = 0$, should match with the outer region solution as $\rho_i \to \infty$ and it *cannot* satisfy the boundary condition at $r = 1$.

2. Near r = 1. An analysis similar to that above is carried out by defining

$$\bar{\xi} = xq^{\beta_1}; \quad \rho_o = (1-r)q^{\beta_2}; \quad \bar{\bar{\tau}} = \bar{\bar{t}}q^{\beta_3}; \quad \bar{\psi} = u \tag{A4}$$

Substitution of these relationships into the governing equation for the inner region results in:

$$q^{2\beta_2}\frac{\partial^2\bar{\psi}}{\partial\rho_o^2} - [q^{\beta_2} + \rho_o + o(1)]\frac{\partial\bar{\psi}}{\partial\bar{\rho}_o} + A^2 q^{2\beta_1}\frac{\partial^2\bar{\psi}}{\partial\bar{\xi}^2} = q^{\beta_3}\frac{\partial\bar{\psi}}{\partial\bar{\bar{\tau}}} \tag{A5}$$

We can retain the maximum number of terms in equation (A5) by choosing:

$$2\beta_2 = 2\beta_1 = \beta_3 \tag{A6}$$

From the heat input condition at $x = 0$, we have $\beta_1 = 1$ and, then, from equation (A6) we obtain $\beta_2 = 1$ and $\beta_3 = 2$. Equation (A5) becomes:

$$\left[\frac{\partial^2\bar{\psi}}{\partial\rho_o^2} + A^2\frac{\partial^2\bar{\psi}}{\partial\bar{\xi}^2} - \frac{\partial\bar{\psi}}{\partial\bar{\bar{\tau}}}\right] = \left[q^{-1} + \bar{\rho}_o q^{-2} + o(q^{-2})\right]\frac{\partial\bar{\psi}}{\partial\bar{\rho}_o} \tag{A7}$$

and the radial heat loss condition is

$$\left.\frac{\partial\bar{\psi}}{\partial\bar{\rho}_o}\right|_{\bar{\rho}_o=0} = \frac{1}{q}\left[\left[D_1\,\mathrm{Nu} + D_2 N_R(\bar{\psi})\right]\bar{\psi}\right]_{\bar{\rho}_o=0} \tag{A8}$$

As seen from equation (A8), the radial heat loss from the side of the wire does not appear as a leading order term as $q \to \infty$. We also note that the initial condition does not give rise to any radial dependence. For these reasons, we can conclude that the radial dependence near $r = 1$ is also a higher-order effect and the leading order temperature response near the base of the cylinder is governed by equations (12) and (14). These equations can also be derived beginning with the one-dimensional formulation, equations (3) and (4).

APPENDIX B

Details of Finite Difference Solution of the Nonlinear Conduction Equation

1 Two-Dimensional Problem: The finite difference form of equations (6) and (7) can be arranged in the form

$$a_{i,j-1}\theta_{i,j-1} + a_{i,j}\theta_{i,j} + a_{i,j+1}\theta_{i,j+1} + a_{i-1,j}\theta_{i-1,j} + a_{i+1,j}\theta_{i+1,j} = -\frac{\theta_{i,j,n}}{\Delta t}$$
$$\text{for } 2 \le i < M-1 \text{ and } 1 \le j \le N \tag{B1}$$

At $r = 1$, i.e., $i = M$

$$f_j(\underline{\theta}) \equiv a_{M,j-1}\theta_{M,j-1} + a_{M,j}\theta_{M,j} + a_{M,j+1}\theta_{M,j+1} + a_{M-1,j}\theta_{M-1,j} + \frac{\theta_{M,j,n}}{\Delta t} = 0 \tag{B2}$$

The Newton-Raphson form of equation (B2) is

$$F_{j-1}\Delta\theta_{M,j-1} + F_j\Delta\theta_{M,j} + F_{j+1}\Delta\theta_{M,j+1} = f_j(\underline{\theta}^{(k)}) \tag{B3}$$

where

$$\underline{\theta} \equiv \{\theta_{M,1}, \theta_{M,2}, \ldots, \theta_{M,j}, \ldots, \theta_{M,N}\}^T \tag{B4}$$

k = most recent known iteration level

$$\underline{\theta}^{(k+1)} = \underline{\theta}^{(k)} - \underline{\Delta\theta} \tag{B5}$$

$$F_{j-1}(\underline{\theta}) = \frac{\partial f_j}{\partial\theta_{M,j-1}} \tag{B6}$$

$$F_j(\underline{\theta}) = \frac{\partial f_j}{\partial\theta_{M,j}} \tag{B7}$$

and

$$F_{j+1}(\underline{\theta}) = \frac{\partial f_{j+1}}{\partial\theta_{M,j+1}} \tag{B8}$$

In the above equations the subscript i is along the radial direction and j is along the axial direction. For the purpose of sweeping the line-by-line method in the radial direction, equation (B1) is rewritten as

$$a_{i,j-1}\theta_{i,j-1} + a_{i,j}\theta_{i,j} + a_{i,j+1}\theta_{i,j+1} = -\frac{\theta_{i,j,n}}{\Delta t} - a_{i-1,j}\theta_{i-1,j}^{(\ell+1)} - a_{i+1,j}\theta_{i+1,j}^{(\ell)} \tag{B9}$$

where the superscript ℓ refers to the current (known) level in the line-by-line method for interior radial locations.

2 One-Dimensional Problem. For the one-dimensional problem the finite difference form of equations (3) and (4) is

$$f_j(\underline{\theta}) \equiv b_{j-1}\theta_{j-1} + b_j\theta_j + b_{j+1}\theta_{j+1} + \frac{\theta_j^{(n-1)}}{\Delta t} = 0 \tag{B10}$$

These equations have the same form as equations (B2) and are solved by the Newton-Raphson and Thomas algorithms.

Numerical and Analytical Solutions for Two-Dimensional Gas Distribution in Gas-Loaded Heat Pipes

P. F. Peterson
Assoc. Mem. ASME

C. L. Tien
A. Martin Berlin Professor.

Department of Mechanical Engineering,
University of California,
Berkeley, CA 94720

This work presents a two-dimensional axisymmetric diffusion model for the noncondensable gas distribution in gas-loaded heat pipes and thermosyphons. The new model, based on an integral analysis, has major advantages over existing, computationally time consuming, two-dimensional models. It has equal accuracy while using only the computational effort required for the cruder one-dimensional model, and also includes the effects of wall conduction and spatial variation of the condenser heat transfer coefficient. To simplify design calculations further an analytic two-dimensional solution is established, which gives excellent results over a wide range of parameters.

Introduction

Properly designed gas-loaded heat pipes and thermosyphons can remove heat at varying rates and yet maintain the cooled equipment at a virtually constant temperature. These devices control the cooling rate by using a noncondensable gas to shut off a varying portion of the condenser (Fig. 1). Increased evaporator power raises the system pressure, which compresses the gas plug. This exposes more condenser surface, moderating the evaporator temperature change. The design and performance evaluation of these devices can be approached at three levels of sophistication and accuracy, ranging from complex numerical models to analytic approximations to the simple flat-front model. This paper makes improvements at each of these levels, in addition to investigating the potentially substantial changes in the shutoff length that occur when radiation or natural convection is the condenser cooling mechanism.

At the lowest level the flat-front model assumes a sharp interface between the gas and vapor regions. Since it provides a simple means for calculating the evaporator temperature and heat load, this model is commonly applied in initial design calculations and in dynamic models (Dunn and Reay, 1982). In practice deviations from this ideal "flat front" occur due to diffusion, natural convection, and axial conduction through the wall. In many cases the flat-front assumption results in gross errors. To determine how real devices deviate from flat-front behavior, this analysis derives four simple parameters that characterize diffusive transport, axial wall conduction, the condenser/evaporator temperature difference, and the working fluid saturation pressure. It then presents a parametric study showing when and by how much the flat-front model errs.

At the highest level numerical models account for diffusive transport in the gas/vapor interface region. They neglect natural convection, which can distort the gas distribution (Peterson and Tien, 1988). The widely used model developed by Edwards and Marcus (1972) assumes a one-dimensional (1-D) distribution of gas and is relatively simple, but since it neglects the multidimensional distribution and radial diffusion of the noncondensable gas, it can underpredict the length shut off to condensation and the evaporator temperature, especially when axial wall conduction is small. Hijikata et al. (1984) and Rohani and Tien (1973) allowed for two-dimensional (2-D) axisymmetric gas distribution, but both models are computationally time consuming and cannot be applied to devices where axial wall conduction is important. None of the works investigate the effects of the temperature dependence of the condenser heat transfer coefficient when radiation or natural convection is the cooling mechanism. To remedy these difficulties, this paper combines the best features of the existing 1-D and 2-D axisymmetric models by using the integral technique to reduce the 2-D governing equations. This numerical integral model agrees excellently with both exact 2-D numerical results and experimental gas-concentration measurements.

At an intermediate level of accuracy, many applications, such as multinode calculations for satellites, require an analytical formulation since numerical models are too time consuming. Bobco (1987) developed a simplified analytic formulation that replaces the condensation rate with an arbitrary heat flux, requiring the introduction of empirical constants.

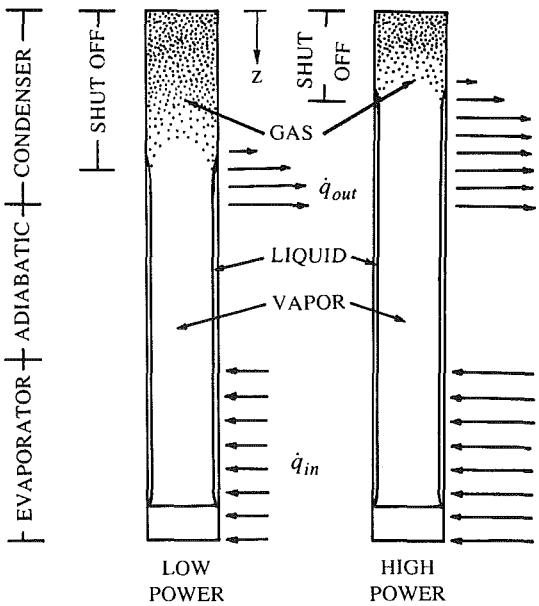

Fig. 1 Schematic of gas-loaded thermosyphon

Contributed by the Heat Transfer Division for publication in the JOURNAL OF HEAT TRANSFER. Manuscript received by the Heat Transfer Division January 29, 1988. Keywords: Condensation, Heat Pipes and Thermosyphons, Mass Transfer, Multiphase Flows.

This paper derives a new analytic solution for the temperature profile that requires no empirical constants and yet is accurate over a wide range of parameters.

Two-Dimensional Formulation

This two-dimensional axisymmetric diffusion model is based on work by Hijikata et al. (1984). Use of the integral technique both simplifies the equations and allows the inclusion of axial wall conduction. Since the gas and vapor molecular weights can be different, the molar density is assumed constant in the species conservation equation, instead of their assumption of constant mass density. Additional assumptions used are steady-state diffusion with no natural convection inside the device, and negligible energy transport due to vapor temperature gradients. Because energy transport in the vapor phase by conduction and convection of sensible heat is neglected, overall energy conservation requires the use of constant latent heat. The analysis is simplified by evaluating the diffusion coefficient at the average of the condenser and evaporator temperatures.

Application of Fick's law of diffusion to the gas molar flow vector $\dot{\mathbf{c}}_g$ yields

$$\dot{\mathbf{c}}_g = cx_g\mathbf{V} - cD\nabla x_g \tag{1}$$

where $\mathbf{V}$ is the average molar velocity vector, x_g the gas molar fraction, c the molar density, and D the mass diffusivity. If the gas remains stationary (i.e., no natural convection), $\dot{\mathbf{c}}_g = 0$ and equation (1) becomes

$$\mathbf{V} = D\nabla(\ln x_g) \tag{2}$$

For steady state and constant molar density, $\nabla\cdot\mathbf{V} = 0$, there follows

$$\nabla^2(\ln x_g) = 0 \tag{3}$$

Energy conservation requires that the heat gained from condensation equal the heat lost via convection, radiation, and axial conduction along the pipe wall

$$h_{fg}M_v c_e D\left(\frac{\partial(\ln x_g)}{\partial r}\right)_{r=r_i} = h_i(T_i^s - T_c) - \frac{\overline{kA}}{2\pi r_i}\frac{d^2T_i^s}{dz^2} \tag{4}$$

where T_i^s is the interface temperature, T_c the cooling-medium temperature, M_v the vapor molecular weight, h_{fg} the latent heat of evaporation, r the radial coordinate, and z the axial coordinate measured from the top of the condenser. This expression implicitly incorporates the assumption of Edwards and Marcus (1972) that the second derivative of the wall temperature equals that of the interface temperature. The heat transfer coefficient h_i is based on the liquid/vapor surface area, not the outside tube area, and includes radiation, external convection, wick/wall structure, and internal film thermal resistances. When radiation or natural convection provides cooling, the temperature dependence of the heat transfer coefficient becomes important, since h_i may vary by more than an order of magnitude over the length of the condenser. The total axial conductance $\overline{kA} = \Sigma k_j A_j$ includes the wall, liquid, and wick conductances.

The associated boundary conditions, in addition to equation (4), are

$$\text{at } z = 0\text{: } v = 0 \text{ or } \partial(\ln x_g)/\partial z = 0;\ dT_i^s/dz = 0 \tag{5}$$

$$\text{as } z\to\infty\text{: } x_g \to 0;\ dT_i^s/dz \to 0 \tag{6}$$

$$\text{at } r = 0\text{: } u = 0 \text{ or } \partial(\ln x_g)/\partial r = 0 \tag{7}$$

In practice the $z\to\infty$ boundary condition is met at finite z, and thus imposes no restrictions on analysis of finite devices. The interface temperature and composition are related by the Clausius–Clapeyron equation,

$$\text{at } r = r_i\text{:} \qquad x_g = 1 - \exp(T_*(1 - T_e^s/T_i^s)) \tag{8}$$

where T_e^s is the saturation temperature of the pure vapor. Use of $T_* = (1 - T_e^s/T_c)^{-1}\ln(P_c^s/P_e^s)$, rather than an expression based on h_{fg}, provides the best fit between T_e^s and T_c for the saturation pressure P^s and thus for the mole fraction. The quantity of noncondensable gas in the heat pipe is

$$N_g = \int_0^\infty\int_0^{r_i} c_g 2\pi r\,dr\,dz \tag{9}$$

where c_g is the local molar density of the gas. Division by $c_c\pi r_i^2$ provides a relation between the gas inventory and the condenser geometry

$$L_g = 2\int_0^\infty\int_0^{r_i}(c_i/c_c)(x_g)(r/r_i)d(r/r_i)dz \tag{10}$$

where L_g is the length the gas would occupy if all the gas were restricted to the top of the condenser at the cooling-medium temperature. The function c_i/c_c is the ratio of the molar density at the local interface temperature T_i^s to the total molar den-

Nomenclature

A = function defined by equation (23)
B = nondimensional condensation rate, equation (23)
c = molar density, kmol/m^3
$\dot{\mathbf{c}}$ = net-molar-flux vector, kmol/m^{2}s
D = mass diffusivity, m^2/s
E = diffusion parameter $= (c_e M_v D h_{fg})/(h(T_e^s - T_c)r_i)$
F = transformed mole fraction $= E \ln x_g$
h = heat transfer coefficient, W/m^{2}K
h_{fg} = latent heat of vaporization, J/kg
H = heat transfer correction function, equations (14) and (15)
$\overline{kA}$ = sum of axial conductances $= \Sigma k_j A_j$, Wm/K
L_g = gas-inventory length, equation (10), m
M = molecular weight, kg/kmol
N_g = moles of noncondensable gas, kmol
P = absolute pressure, Pa
r = radial coordinate, m
q = evaporator power input, W
Q_g^* = length shut off to condensation, equation (21)
T = absolute temperature, K
T_* = constant $= (1 - T_e^s/T_c)^{-1}\ln(P_c^s/P_e^s)$
u = radial molar velocity, m/s
v = axial molar velocity, m/s
$\mathbf{V}$ = molar average velocity vector, m/s
W = wall conduction parameter $= \overline{kA}/2\pi r_i^3 h$
x = mole fraction
z = axial coordinate, m
θ = dimensionless wall temperature $= (T_i^s - T_c)/(T_e^s - T_c)$
θ_c = dimensionless temperature $= T_c/(T_e^s - T_c)$
ξ = natural-convection constant, equation (15)
$\phi = A - 2W\theta$

Subscripts

ad = condenser/adiabatic transition point
c = cooling-medium temperature
e = evaporator
ff = flat front
g = noncondensable gas
i = interface between vapor and liquid/wick structure
L = position where $\theta = 1$
max = maximum
v = vapor

Superscripts

s = saturation
$*$ = nondimensional quantity

sity at the cooling-medium temperature T_c. For an ideal gas $c_i/c_c = T_c/T_i^s$, while Edwards and Marcus (1972) recommended a polynomial in T_i^s.

The equations are nondimensionalized as follows:

$$r^* = r/r_i \qquad \theta = (T_i^s - T_c)/(T_e^s - T_c)$$
$$E = (c_e M_v D h_{fg})/(h(T_e^s - T_c) r_i)$$
$$z^* = z/r_i \qquad \theta_c = T_c = T_c/(T_e^s - T_c) \qquad F = E \ln x_g \tag{11}$$
$$Q_g^* = z_{ad}/r_i - q/2\pi r_i^2 h(T_e^s - T_c) \qquad H = h_i/h$$
$$L_g^* = L_g/r_i = N_g/c_c \pi r_i^3 \qquad W = \widetilde{kA}/2\pi r_i^3 h$$

where z_{ad} is the distance to the end of the condenser. In nondimensional form and axisymmetric cylindrical coordinates, the governing equation, equation (3), becomes

$$\frac{1}{r^*}\frac{\partial}{\partial r^*}\left(r^* \frac{\partial F}{\partial r^*}\right) + \frac{\partial^2 F}{\partial z^{*2}} = 0 \tag{12}$$

where F is the transformed mole fraction and r^* and z^* are the nondimensional radial and axial coordinates. The energy balance, equation (4), becomes

$$\left(\frac{\partial F}{\partial r^*}\right)_{r^*=1} = H\theta - W\frac{d^2\theta}{dz^{*2}} \tag{13}$$

where θ is the nondimensional interface temperature and W the wall-conduction parameter. The heat-transfer function, $H = h_i/h$, is the ratio of the local heat transfer coefficient to the coefficient in the region where $\theta = 1$. For forced convection, $H = 1$. For radiation,

$$H = \frac{(\theta + 2\theta_c)(\theta^2 + 2\theta\theta_c + 2\theta_c^2)}{(1 + 2\theta_c)(1 + 2\theta_c + 2\theta_c^2)} \tag{14}$$

since the heat flux is proportional to the difference of the fourth powers of the wall and ambient temperatures. For natural convection in the horizontal orientation the heat transfer function takes the form

$$H = (1 + \xi\theta^{1/4})/(1 + \xi) \tag{15}$$

where ξ can be evaluated from standard natural-convection correlations (Churchill and Chu, 1975).

The boundary conditions, in addition to equation (13), are

$$\text{at } z^* = 0: \qquad \frac{\partial F}{\partial z^*} = 0; \quad d\theta/dz^* = 0 \tag{16}$$

$$\text{as } z^* \to \infty: \qquad F \to -\infty; \quad d\theta/dz^* \to 0 \tag{17}$$

$$\text{at } r^* = 0: \qquad \frac{\partial F}{\partial r^*} = 0 \tag{18}$$

with the constraint

$$\text{at } r^* = 1: \qquad \exp(F/E) = 1 - \exp\left(T_* \frac{(\theta - 1)}{(\theta + \theta_c)}\right) \tag{19}$$

where E is the diffusion parameter.

Since the first boundary condition given by equation (17) is indeterminate, the above equations possess infinitely many solutions. Only one of them will satisfy the total gas inventory. The gas-inventory length, equation (10), becomes

$$L_g^* = 2\int_0^\infty \int_0^1 (1 + \theta/\theta_c)^{-1} \exp(F/E) r^* dr^* dz^* \tag{20}$$

using the nondimensional ideal-gas relation for c_i/c_c. The length effectively shut off to condensation by this quantity of gas is

$$Q_g^* = \int_0^\infty (1 - H\theta) dz^* \tag{21}$$

Figure 2 illustrates the significance of L_g^* and Q_g^*. The length

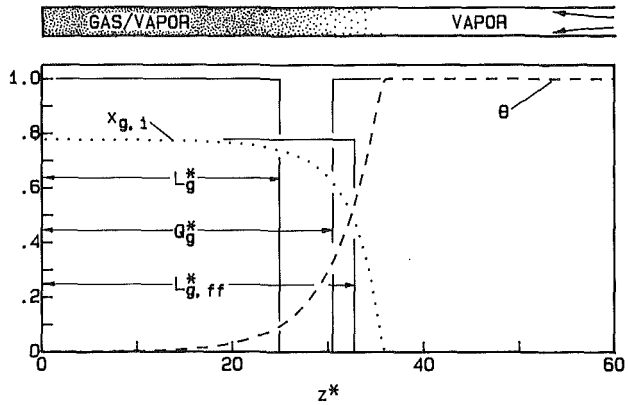

Fig. 2 Illustration of relationship of L_g^*, $L_{g,ff}^*$, and Q_g^* with the temperature and interface mole fraction profiles

that would be shut off if there were a flat front, $L_{g,ff}^* = L_g^*/x_{g,max}$, is also shown. The maximum concentration of gas present, $x_{g,max}$, can be found by setting $T_i^s = T_c$ in equation (8).

When the axial wall conduction is negligible, $W \approx 0$, the problem can be solved numerically. Using the iterative method of Hijikata et al. (1984), a central-finite-difference scheme can be applied to solve the governing equation. Their method converges quickly for smaller values of E, but as E increases progressively coarser grids are required to achieve convergence. Coarser grids decrease the accuracy of the solution, and thus limit the range of E for which solutions can be found.

The numerical difficulty of the unbounded boundary condition is handled by the same method used for the unmodified model of Hijikata et al. (1984). They discuss how the temperature θ becomes constant and equal to one when z^* is large, resulting in a parabolic distribution of F in the radial direction,

$$F = 1/2\ r^{*2} + C(z^*) \tag{22}$$

where a value of $C(z^*)$ is picked at a sufficiently large z^* so as to give the desired value of L_g^*.

Integral Formulation

The above exact 2-D numerical solution scheme has three primary difficulties. It is computationally very tedious; it becomes unstable for large values of E; and it is only successful for cases with negligible axial wall conduction. However the exact numerical solution is valuable for confirming the accuracy of solutions using the integral technique. To apply the integral technique, the parabolic distribution found for large z^*, equation (22), is assumed to exist over the entire range of integration, so that

$$F = A(z^*) + B(z^*)(r^{*2} - 1/2) \tag{23}$$

where A and B are functions of z^* only. The variable B is a nondimensional condensation rate, which approaches a constant value $B \to 1/2$ as $z^* \to \infty$. The governing equation, equation (12), the energy balance, equation (13), and the equilibrium constraint, equation (19), then reduce to

$$\frac{d^2 A}{dz^{*2}} = -4B \tag{24}$$

$$H\theta - W\frac{d^2\theta}{dz^{*2}} = 2B \tag{25}$$

$$A + 1/2\ B = E \ln\left[1 - \exp\left(T_* \frac{(\theta - 1)}{(\theta + \theta_c)}\right)\right] \tag{26}$$

The derivation of the 1 – D model assumes $F = A(z^*)$, where A is a function of z^* only, so the concentration profiles are flat rather than parabolic. Thus the function $B(z)$ is eliminated and the resulting 1-D formulation is

$$\frac{d^2A}{dz^{*2}} = -2H\theta + 2W\frac{d^2\theta}{dz^{*2}} \tag{27}$$

$$A = E\ln\left[1-\exp\left(T_*\frac{(\theta-1)}{(\theta+\theta_c)}\right)\right] \tag{28}$$

Numerical Solution. Substituting $\phi = A - 2W\theta$ both eases the numerical solution and facilitates the comparison of the 2-D integral and 1-D models, by reducing equations (24–28) to the working equations for the numerical solution

$$\text{(2-D, 1-D)} \qquad \frac{d^2\phi}{dz^{*2}} = -2H\theta \tag{29}$$

$$\text{(2-D)} \quad \phi + 2W\theta - E\ln\left[1\text{-}\exp\left(T_*\left(\frac{\theta-1}{\theta+\theta_c}\right)\right)\right] = \frac{1}{4}\left(W\frac{d^2\theta}{dz^{*2}} - H\theta\right) \tag{30}$$

$$\text{(1-D)} \qquad \phi + 2W\theta - E\ln\left[1-\exp\left(T_*\left(\frac{\theta-1}{\theta+\theta_c}\right)\right)\right] = 0 \tag{31}$$

There are two limiting conditions for which the second derivative on the right of equation (30) can be neglected. When axial wall conduction W is small, the second derivative term is negligibly small compared to the other terms, and the 1-D and 2-D equations differ by the $\theta/4$ term. When W is large most of the axial energy transport in the interface region is by wall conduction rather than diffusion, so $B \to 0$, the right-hand side is zero, and thus equations (30) and (31) become identical.

The appropriate boundary conditions for the working equations are

$$\text{(2-D, 1-D)} \qquad \text{at } z^* = 0: \quad \frac{d\phi}{dz^*} = 0; \quad \phi = \phi_{int} \tag{32}$$

$$\text{(2-D)} \qquad \text{at } z^* = 0: \quad \frac{d\theta}{dz^*} = 0 \tag{34}$$

$$\text{(2-D)} \qquad \text{as } z^* \to \infty: \quad \theta \to 1 \tag{34}$$

where ϕ_{int} is an initial value of ϕ chosen iteratively to give the desired L_g^*. The shut-off length becomes

$$\text{(2-D)} \quad L_g^* = \int_0^\infty (1+\theta/\theta_c)^{-1}\frac{E}{B}\left[1-\exp\left(-\frac{B}{E}\right)\right]\left[1-\exp\left(T_*\left(\frac{\theta-1}{\theta+\theta_c}\right)\right)\right]dz^* \tag{35}$$

$$\text{(1-D)} \quad L_g^* = \int_0^\infty (1+\theta/\theta_c)^{-1}\left[1-\exp\left(T_*\left(\frac{\theta-1}{\theta+\theta_c}\right)\right)\right]dz^* \tag{36}$$

Equations (35) and (36) show that the 2-D distribution of the gas decreases the effective gas inventory, L_g^*, by a factor $(1-\exp(B/E))E/B$.

At least two of the terms on the left-hand side of equation (30) are of much larger magnitude than the second derivative on the right. This makes equation (30) stiff and difficult to integrate numerically. However, in the limits of W being small or large the right-hand side can be set equal to the limiting values of $\theta/4$ or 0, repectively. This reduces the order of the equations to two and allows them to be solved with the same fourth-order Runge-Kutta routine used to solve the one-dimensional problem. Elimination of the second derivative also automatically satisfies two of the boundary conditions, equations (33) and (34), so only two boundary conditions remain. The value of B used for calculating L_g^* in equation (35) is then obtained from equation (25).

Equations (30) and (31) are not explicit in θ, but a Newton–Raphson routine using θ from the previous step as an initial guess converges to within 10^{-8} in an average of under 1.1 iterations. This two-equation implicit formulation has clear computational advantages over the five-equation explicit formulation given by Edwards and Marcus (1972).

Analytic Solution. As noted by Bobco (1987), the lack of a simple analytic model creates perhaps the most serious impediment to the widespread use of variable-conductance heat pipes. For this reason Bobco developed a closed-form, implicit relation between the heat load, evaporator temperature, and condensation-front location. The condensation heat flux was replaced with an arbitrary heat flux and the gas inventory was evaluated at an average temperature. Unfortunately, this method required the determination of two empirical parameters, which must be calculated by fitting experimental data or numerical results.

A useful characteristic of the equilibrium constraint, equation (26), permits a simple analytic solution. When E is relatively small, the right-hand term of equation (26) is very small except when θ approaches one, at which point the term suddenly grows to infinity. This sudden increase causes the sharp, almost discontinuous change of slope near $\theta = 1$ that is characteristic of analytic and experimentally measured temperature profiles. For most of the range of integration, it is valid to set the right-hand term equal to zero. Then, for the constant heat transfer coefficient case, $H = 1$, equations (24)–(26) become linear and simple to integrate. The appropriate boundary conditions are

$$\text{at } z^* = 0: \quad \frac{dA}{dz^*} = 0; \quad \frac{d\theta}{dz^*} = 0 \tag{37}$$

$$\text{at } z^* \geq z_L^*: \quad \theta = 1; \quad B = 0.5 \tag{38}$$

where z_L^* is the position of the end of the gas-loaded zone, which can be adjusted to give the desired L_g^* or Q_g^*. Equation (38) arises from equation (25), since in the region $z^* \geq z_L^*$ the wall temperature θ is unity. The resulting temperature and condensation-rate expressions for the region $0 \leq z^* \leq z_L^*$ are

$$\theta = \frac{1}{8W-1}\left[8W\frac{\cosh(W^{-1/2}z^*)}{\cosh(W^{-1/2}z_L^*)} - \frac{\cosh(8^{1/2}z^*}{\cosh(8^{1/2}z_L^*)}\right] \tag{39}$$

$$B = -2A = 1/2\cosh(8^{1/2}z^*)/\cosh(8^{1/2}z_L^*) \tag{40}$$

while for $z^* \geq z_L^*$, θ and B constants are given by equation (38). The effective length lost to heat transfer and the shutoff length are, respectively,

$$Q_g^* = z_L^* - \frac{1}{(8W-1)}\left[8W^{3/2}\frac{\sinh(W^{-1/2}z_L^*)}{\cosh(W^{-1/2}z_L^*)} - 8^{-1/2}\frac{\sinh(8^{1/2}z_L^*)}{\cosh(8^{1/2}z_L^*)}\right] \tag{41}$$

$$L_g^* = \int_0^{z_L^*}\frac{E}{B}\left[1-\exp\left(-\frac{B}{E}\right)\right](1+\theta+\theta_c)^{-1}\left[1-\exp\left(T_*\left(\frac{\theta-1}{\theta+\theta_c}\right)\right)\right]dz^* \tag{42}$$

For larger z^* equation (41) can be reduced by setting the ratios of the hyperbolic sines and cosines equal to one. One disadvantage is that equation (42) for L_g^* cannot be solved analytically. However, equation (42) integrates numerically in a straightforward and rapid manner to any desired level of accuracy. For first-order calculations, the numerical procedure could consist of discretization and evaluation at average temperatures as Bobco (1987) does.

Integral Method Validation. As equation (22) indicates, the parabolic profile for F assumed for the integral analysis is exact at large z^*, since the wall temperature θ is constant. Thus the largest deviation from the parabolic profile occurs in regions where the slope of θ is large. Since the greatest slopes occur when diffusion and axial wall conduction are small, comparison with the exact 2-D numerical model with $W = 0$ and smaller values of E provides the most stringent test. The

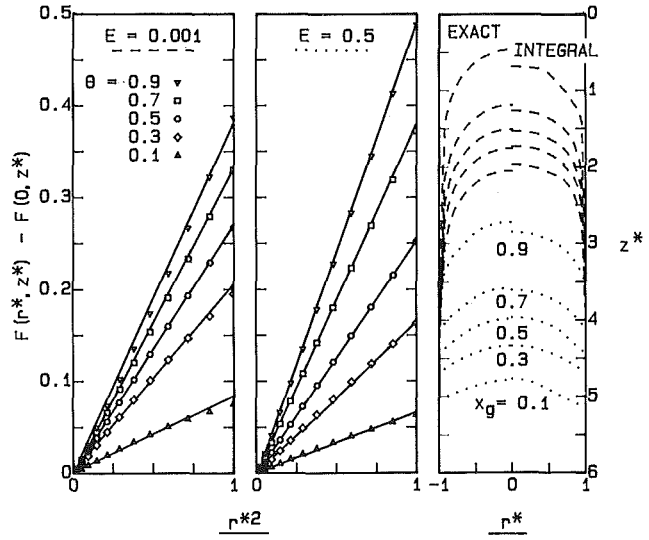

Fig. 3 Variation of F with radius squared for two values of E (left) and corresponding comparison isoconcentration profiles (right)

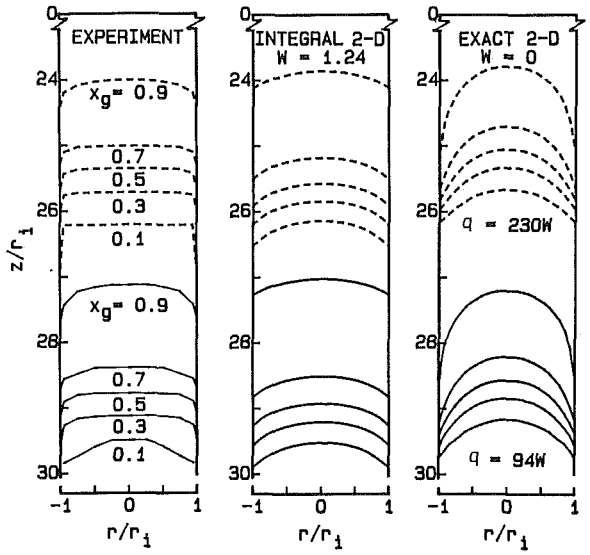

Fig. 4 Comparison of integral 2-D model isoconcentration profiles with experimental and exact 2-D numerical results

left side of Fig. 3 shows numerical results for the variation of F with the square of the radius. The fact that the points form virtually straight lines validates the parabolic profile assumption. The right side of the figure compares the isoconcentration profiles for the exact numerical and integral solutions. The integral solution deviates more for the smallest diffusion parameter, which corresponds to the steepest temperature slope.

To illustrate the importance of axial wall conduction and to demonstrate further the validity of the 2-D integral model, Fig. 4 reproduces experimental and analytic results reported previously by Peterson and Tien (1987). They used a miniature wet-bulb/dry-bulb probe to make point gas-concentration measurements in a gas-loaded thermosyphon. The figure shows the gas-isoconcentration profiles interpolated from experimental measurements. Compared with the results of the exact 2-D numerical model with zero wall conduction, the 2-D integral model with the proper, though relatively small, wall-conduction parameter W matches the experimental measurements much better.

Parametric Study

The parametric study answers three primary questions, namely how much does the flat-front model err, when are 2-D effects important, and when must the temperature dependence of the heat transfer coefficient be considered. Most practical applications of gas-loaded devices will fall in the middle of the parameter range studied here, but the extreme values illustrate trends. For reference Table 1 gives parameter values for some actual gas-loaded devices. The relative simplicity of the integral formulation allowed this parametric study, since over 500 integral cases can be solved with the amount of computation required for one exact 2-D numerical case.

The 2-D and 1-D models predict that a length Q_g^*, given by equation (21), will be shut off to condensation, while the flat-front model predicts a length $L_{g,ff}^*$. The difference is then

$$Q_g^* - L_{g,ff}^* = Q_g^* - L_g^*/x_{g,max} \tag{43}$$

where $x_{g,max} = (1 - \exp(-T_*/T_c))$ is the maximum gas concentration. Figure 2 graphically illustrates the meaning of these parameters. The quantity $Q_g^* - L_{g,ff}^*$ is independent of the location of the interface region, as long as the region is sufficiently removed from the end of the condenser. This difference is directly related to the evaporator temperature and evaporator power input through the definition of Q_g^*, equation (11), and is plotted in Figs. 5–7. The following paragraphs summarize the significance of these results.

Exact 2-D. The largest value of E for which Fig. 5 gives exact 2-D numerical model results is 0.5, at which point doubling the number of nodes to the minimum spacing allowing convergence caused a 18.0 percent change in the calculated value of $Q_g^* - L_{g,ff}^*$. For $E = 0.1$, the change decreases to 0.31 percent. Both the integral 2-D and analytic models match the exact numerical results very well.

2-D Effects. The upper and lower solid curves in Fig. 5 represent the small and large W limits, respectively, of the 2-D integral solution. The results of the two limiting relations are identical for larger E, and they diverge for small E where the calculation of L_g^* becomes very sensitive to small errors in B. The 1-D and 2-D models give essentially identical results for $E > 1$. For smaller values of E and W two-dimensional effects become increasingly important. Since E is the ratio of the rate of energy transport by diffusion, $c_e M_v D h_{fg}/r_i$, to energy transport by convection, $h(T_e^s - T_c)$, 2-D effects can be expected to be important in devices with low diffusivity, low latent heat fluid combinations, and higher-heat-flux, low-wall-conductivity condensers.

Analytic Model. Figure 5 shows that the simple analytic 2-D model does a good job of matching the numerical integral 2-D model over a relatively wide range of parameters. The analytic model deviates at high values of E, where the assumption of small E breaks down, and at small values of E, where the approximate function for B is not sufficiently accurate.

Variable Heat-Transfer Coefficient. When natural convection or radiation cools the condenser, Fig. 6 shows that the length shutoff to condensation, Q^*, can increase substantially. In the shutoff region the decreased heat transfer coefficient value increases the condenser temperature required to remove the heat transported through the wall from the interface region. Though, as Edwards and Marcus (1972) note, this only modifies the temperature profile slightly; for larger W or E it increases the vapor pressure in the shutoff region and thus substantially changes Q^*. This has important implications for space applications, since often the wall-conduction parameter is quite large (Table 1, Eninger et al., 1976), even though great efforts may be made to minimize it by grooving the condenser tube and segmenting the radiator panel.

Figure 7 contains a considerable amount of information,

Table 1 Typical parameter values

Case	E	θ_c	T_*	W	ξ
Edwards and Marcus (1972)[1]	7.4–2.4	5.9–2.6	14.8–12.3	20.6–16.0	10.2–11.2
Eninger et al. (1976)[2]	22.4	5.0	25.5	160	-
Peterson and Tien (1987b)[3]	0.49–0.52	5.9–5.6	15.2–15.1	1.24	-

[1]Stainless steel, air/water, natural-convection/radiation cooled, 1.4 cm o.d. heat pipe, 2–73 W.
[2]Stainless steel with segmented aluminum radiator, nitrogen/methanol, 1.1 cm o.d. heat pipe, 24 W.
[3]Glass, helium/water, vertical, forced-convection cooled, 5.1 cm o.d. thermosyphon, 94–230 W.

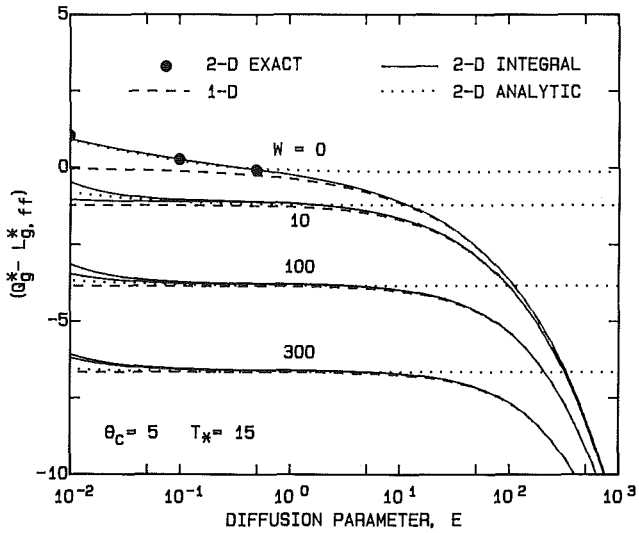

Fig. 5 Deviation of the 1-D and the numerical and analytic 2-D models from flat-front predictions

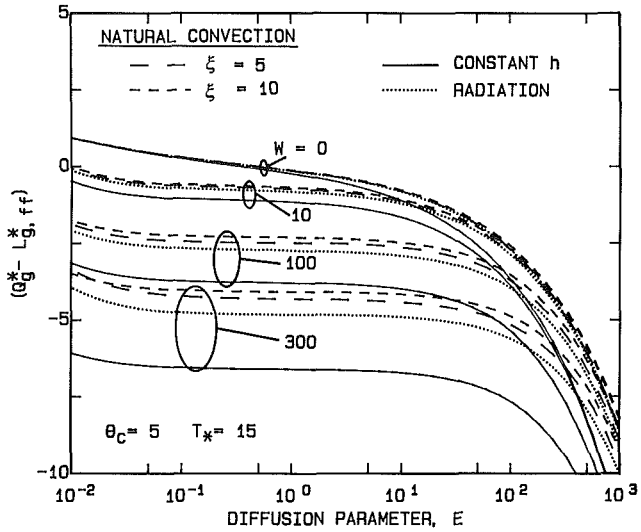

Fig. 6 Effects of radiation and natural-convection as condenser cooling mechanisms

which helps to extend the results of Figs. 5 and 6 to include the effect of θ_c. The largest deviations from the flat-front model occur at $\theta_c \approx 3$. Since $E=1$, the 1-D and analytic and numerical 2-D solutions all give similar results. When radiation or natural convection is the cooling mechanism the results change substantially.

Conclusions

Both experimental measurements and exact numerical solutions show that the integral approximation predicts the gas distribution very well. Application of the integral technique allows significant improvements at each of the three levels of analysis sophistication and complexity. At the complex level of numerical modeling, it allows the inclusion of both axial wall conduction and 2-D gas distribution in a formulation that can be solved with the same routine used for the 1-D model. At an intermediate level of complexity, the implicit formulation of equations (29)–(31) suggests an approximation that allows a simple analytic solution, providing excellent results over a wide range of parameters. For work at the simplest level of analysis, this study gives users of the flat-front model a quantitative measure of the error involved in the flat-front assumption. The use of all of these methods is illustrated by an example in Appendix B, while Appendix A shows how to treat an adiabatic section.

The parametric study illustrates the difference between the 2-D and 1-D models, showing that 2-D effects become important when wall conduction W is less than ten and when the diffusion parameter E is less than one. When natural convection or radiation cools the condenser, the temperature dependence of the heat transfer coefficient can substantially increase the length shut off to condensation. This effect is largest when wall conduction is high, as is commonly the case for space radiators.

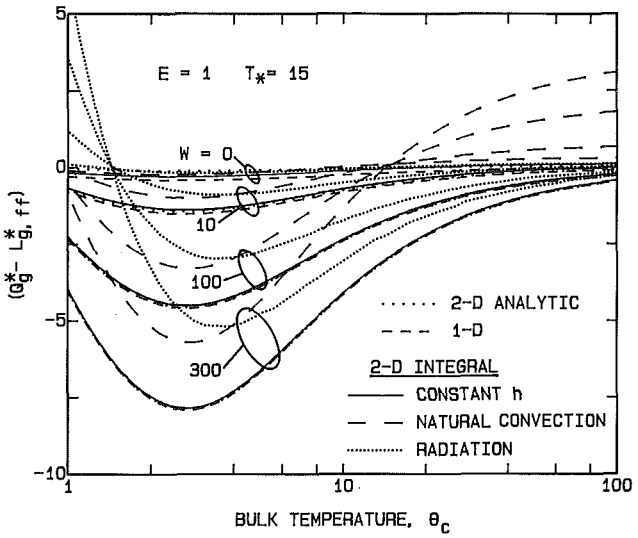

Fig. 7 Deviation of various models from flat-front predictions as a function of $\theta_c = T_c/(T_e^s - T_c)$

References

Bobco, R. P., 1987, "Variable Conductance Heat Pipes: A First Order Model," *Journal of Thermophysics and Heat Transfer*, Vol. 1, pp. 35–42.

Churchill, S. W., and Chu, H. H. S., 1975, "Correlating Equations for Laminar and Turbulent Free Convection From a Horizontal Cylinder," *International Journal of Heat and Mass Transfer*, Vol. 18, pp. 1049–1053.

Dunn, P. D., and Reay, D. A., 1982, *Heat Pipes*, 3rd ed., Pergamon Press, Oxford, pp. 201–234.

Edwards, D. K., and Marcus, B. D., 1972, "Heat and Mass Transfer in the Vicinity of the Vapor-Gas Front in a Gas-Loaded Heat Pipe," ASME JOURNAL OF HEAT TRANSFER, Vol. 94, pp. 155–162.

Eninger, J. E., Luedke, E. E., and Wanous, D. J., 1976, "Flight Data Analysis and Further Development of Variable-Conductance Heat Pipes," NASA CR-137782.

Hijikata, K., Chen, S. J., and Tien, C. L., 1984, "Non-condensable Gas Effect on Condensation in a Two-Phase Closed Thermosyphon," *International Journal of Heat and Mass Transfer*, Vol. 27, pp. 1319–1325.

Peterson, P. F., and Tien, C. L., 1987, "A Miniature Wet-Bulb Technique for Measuring Gas Concentrations in Condensing or Evaporating Systems," *Experimental Heat Transfer*, Vol. 1, pp. 1–15.

Peterson, P. F., and Tien, C. L., 1988, "Gas-Concentration Measurements and Analysis for Gas-Loaded Thermosyphons," ASME JOURNAL OF HEAT TRANSFER, Vol. 110, pp. 743–747.

Rohani, A. R., and Tien, C. L., 1973, "Steady Two-Dimensional Heat and Mass Transfer in the Vapor-Gas Region of a Gas-Loaded Heat Pipe," ASME JOURNAL OF HEAT TRANSFER, Vol. 95, pp. 377–382.

APPENDIX A

Adiabatic Section

In the adiabatic section the 2-D equations reduce to a particularly simple form. Since no external convection occurs, the θ term is eliminated from the energy balance, equation (25). Then the substitution $\phi = A - 2W\theta$ shows that the second derivative of ϕ equals zero, so an analytic solution is possible. Mass and energy conservation require that ϕ and its slope match at the transition point between the adiabatic and condensing systems, z^*_{ad}. The results for the adiabatic section are then

$$\phi = \phi'_{ad}(z^* - z^*_{ad}) + \phi_{ad} \tag{A1}$$

$$\phi + 2W\theta - E\ln\left[1 - \exp\left(T_*\left(\frac{\theta - 1}{\theta + \theta_c}\right)\right)\right] = \frac{1}{4}W\frac{d^2\theta}{dz^{*2}} \tag{A2}$$

where ϕ_{ad} and ϕ'_{ad} are the matching values at the transition point of ϕ and its slope, respectively.

For the analytic solution the expression for the condensation rate B, equation (40) remains the same. The temperature profile, equation (39), is modified. Noting the boundary conditions that θ and its derivative must match at z^*_{ad}, the temperature profile becomes

$0 < z^* < z^*_{ad}$:

$$\theta = \frac{1}{8W-1}\left[\Phi_1(\Phi_2 + \Phi_3)\frac{\cosh(W^{-1/2}z^*)}{\cosh(W^{-1/2}z^*_{ad})} - \frac{\cosh(8^{1/2}z^*)}{\cosh(8^{1/2}z^*_L)}\right] \tag{A3}$$

$z^*_{ad} < z^* < z^*_L$:

$$\theta = 1 + \frac{1}{8W}\left[1 - \frac{\cosh(8^{1/2}z^*)}{\cosh(8^{1/2}z^*_L)}\right] + \frac{\Phi_1(\Phi_2 + \Phi_3) - \Phi_2}{(8W-1)}\frac{(z^*_L - z^*)}{(z^*_L - z^*_{ad})} \tag{A4}$$

and

$$Q^*_g = z^*_{ad} - \frac{1}{(8W-1)}\left[\Phi_1(\Phi_2 + \Phi_3)W^{1/2}\frac{\sinh(W^{-1/2}z^*_{ad})}{\cosh(W^{-1/2}z^*_{ad})} - 8^{-1/2}\frac{\sinh(8^{1/2}z^*_{ad})}{\cosh(8^{1/2}z^*_L)}\right] \tag{A5}$$

where

$$\Phi_1 = \left[1 + \frac{(z^*_L - z^*_{ad})}{W^{1/2}}\frac{\sinh(W^{-1/2}z^*_{ad})}{\cosh(W^{-1/2}z^*_{ad})}\right]^{-1} \tag{A6}$$

$$\Phi_2 = 8W - \frac{1}{8W}\left[1 - \frac{\cosh(8^{1/2}z^*_{ad})}{\cosh(8^{1/2}z^*_L)}\right] \tag{A7}$$

$$\Phi_3 = \frac{(z^*_L - z^*_{ad})}{8^{1/2}W}\frac{\sinh(8^{1/2}z^*_{ad})}{\cosh(8^{1/2}z^*_L)} \tag{A8}$$

APPENDIX B

Sample Calculation

As an example of the application of the techniques developed in this paper, this section calculates the quantity of noncondensable gas present in the heat-pipe experiment of Edwards and Marcus (1972). At one of the intermediate power levels they examined, $q = 26.3$ W, with a horizontal, natural-convection-cooled stainless-steel heat pipe, the evaporator temperature was $T^s_e = 370.6$ K. The following information from their paper is used for the calculation:

$$T_c = 298.7\text{ K}, \quad \overline{kA} = 4.02 \times 10^{-4}\text{ Wm/K}, \quad r_i = 0.578\text{ cm}$$
$$h = 22.6\text{ W/m}^2\text{K}, \quad \xi = 11.0, \quad D = 0.343\text{ cm}^2/\text{s},$$
$$z_{ad} = 76.2\text{ cm}$$

From the steam tables,

$$P^s_c = 3.30\text{ kPa}, \quad P^s_e = 92.6\text{ kPa},$$
$$c_{v,e} = 0.0304\text{ kmol/m}^3, \quad h_{fg} = 2263\text{ kJ/kg}$$

With these values, the following nondimensional parameters are determined:

$$\theta_c = 4.15, \quad T_* = 14.8, \quad E = 4.53,$$
$$W = 1.82, \quad x_{g,max} = 0.964$$

The length shut off to condensation is the difference between the condenser length z^*_{ad} and the active length

$$Q^*_g = z_{ad}/r_i - q/2\pi r_i^2 h(T^s_e - T_c) = 54.73$$

The flat-front model predicts a gas inventory of

$$L^*_g = L^*_{g,ff}x_{g,max} = Q^*_g x_{g,max} = 52.6$$
$$N_g = L^*_g P^s_e \pi r_i^3/RT_c = \underline{1.13 \times 10^{-6}\text{ kmol}}$$

With the flat-front correction from Figs. 5 and 6, $Q^*_g - L^*_{g,ff} \approx -1.0$, so

$$L^*_g = 53.7, \quad N_g = \underline{1.15 \times 10^{-6}\text{ kmol}}$$

To use the analytic model, equation (41) is solved for z^*_L noting that for larger z^*_L the ratios of the hyperbolic sines and cosines equal one. Then equation (42) is integrated numerically to find L^*_g,

$$z^*_L = 59.0 \quad L^*_g = 54.5, \quad N_g = \underline{1.17 \times 10^{-6}\text{ kmol}}$$

To use the numerical model, equation (29) is integrated numerically as described previously, using an initial guess for ϕ_{int}. The solution procedure is iterated using different ϕ_{int} until the desired value of Q^*_g is obtained. The results are

$$L^*_g = 54.0, \quad N_g = \underline{1.16 \times 10^{-6}\text{ kmol}}$$

The results of the four different methods can be compared to the experimentally measured mole inventory, $N_g = 1.21 \times 10^{-6}$ kmol.

Suppression of the Sonic Heat Transfer Limit in High-Temperature Heat Pipes

Flavio Dobran
Applied Science Department,
New York University,
New York, NY 10003

The design of high-performance heat pipes requires optimization of heat transfer surfaces and liquid and vapor flow channels to suppress the heat transfer operating limits. In the paper an analytical model of the vapor flow in high-temperature heat pipes is presented, showing that the axial heat transport capacity limited by the sonic heat transfer limit depends on the working fluid, vapor flow area, manner of liquid evaporation into the vapor core of the evaporator, and lengths of the evaporator and adiabatic regions. Limited comparisons of the model predictions with data of the sonic heat transfer limits are shown to be very reasonable, giving credibility to the proposed analytical approach to determine the effect of various parameters on the axial heat transport capacity. Large axial heat transfer rates can be achieved with large vapor flow cross-sectional areas, small lengths of evaporator and adiabatic regions or a vapor flow area increase in these regions, and liquid evaporation in the evaporator normal to the main flow.

1 Introduction

Heat pipes are very useful heat transfer devices in terrestrial and space-based systems. The specific application determines the heat pipe's operating temperature, working fluid, and material of construction, whereas the nature of the application determines the heat pipe's detailed design characteristics such as the internal liquid and vapor flow geometry and external shape. The heat pipe application temperatures may range from the liquid helium temperature at a few degrees Kelvin (for maintaining low temperatures of infrared detectors) to a thousand or more degrees as in the cooling of rocket combustion chambers and envisioned space nuclear reactors.

Dobran (1987a) reviewed the heat pipe technology for terrestrial and space systems applications and found that most of the current heat pipe research and development efforts pertain to the applications to space-based systems (Vanlandingham, 1986; Barthelemy et al., 1986; Desanctis et al., 1986; Sadunas and Lehtinen, 1985). High-temperature heat pipes are envisioned to be used in the space nuclear reactor of about 300 kW_e (Vanlandingham, 1986) with a very compact design and its core operating at about 1000°C (Merrigan et al., 1984; Merrigan, 1986). Because of this requirement, Merrigan et al. (1983) discuss the typical heat transfer conditions of a space nuclear reactor as: (1) 100–200 W/cm^2 radial power density, (2) 10 kW/cm^2 axial power density, (3) long adiabatic sections to provide separation between the nuclear core and conversion system, and (4) an operation close to the material limits. To cool such a nuclear reactor use can be made of high-temperature heat pipes with the working fluids potassium, sodium, or lithium, since they offer several favorable characteristics (self-regulation and startup, decay heat removal after reactor shutdown, and a high reliability), provided also that many operating limits, such as the sonic heat transfer limit, can be suppressed or eliminated.

The basic heat pipe configuration is illustrated in Fig. 1. It consists of a container such as a pipe whose interior wall is lined with a porous wick structure saturated with a working fluid. Heat transfer in the evaporator region of the heat pipe causes the liquid in the wick to evaporate and flow into the condenser zone where it is condensed. The return of liquid from the condenser to the evaporator occurs due to the capillary forces in the wick that create a surface tension pressure difference required to overcome the vapor and liquid pressure drops, including that due to gravitation or other externally imposed body forces. For a given geometry pipe and working fluid, the thermohydrodynamic flow aspects in a heat pipe determine its heat transport limits (Dobran, 1987a). The depletion of liquid on the surface of the evaporator produces the *boiling heat transfer limit*, whereas the porous wick structure is endowed with the *capillary heat transfer limit* where an effective liquid supply (pumping) from the condenser to the evaporator ceases. At high axial heat fluxes and in long heat pipes, the countercurrent flow of liquid and vapor produces the *entrainment heat transfer limit* where any further increase in the vapor flow by heat addition, for example, cannot sustain any more increase in the liquid condensate flow. When the design of a heat pipe overcomes the liquid flow limitations, the vapor flow can produce sonic and viscous flow limiting operations. The *sonic or choked flow heat transfer limit* is produced under the control of the inertial forces in the vapor. Heat addition or mass injection in the evaporator accelerates the vapor and can produce choking at the evaporator exit where the Mach number reaches unity, if the downstream condenser temperature is sufficiently low, as may occur during the startup of a heat pipe. Figure 2 illlustrates the experimental data of Kemme (1969) taken in a sodium heat pipe with no adiabatic region. Curve A in this figure corresponds to the subsonic flow in the evaporator and condenser, whereas curve B corresponds to the sonic flow condition at the evaporator exit. Curves C and D correspond to the situations of supersonic flow in the condenser region close to the evaporator and vapor flow deceleration through shocks. The mass withdrawal in the condenser has the tendency to produce large nonunifor-

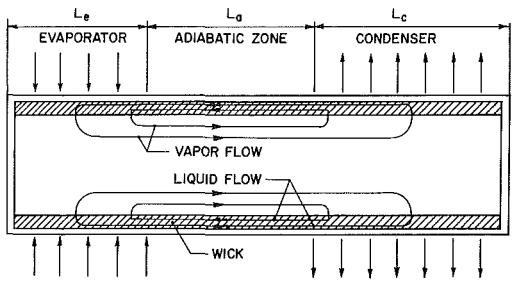

Fig. 1 Basic heat pipe configuration

Contributed by the Heat Transfer Division for publication in the JOURNAL OF HEAT TRANSFER. Manuscript received by the Heat Transfer Division January 5, 1988. Keywords: Heat Pipes and Thermosyphons, High-Temperature Phenomena, Liquid Metals.

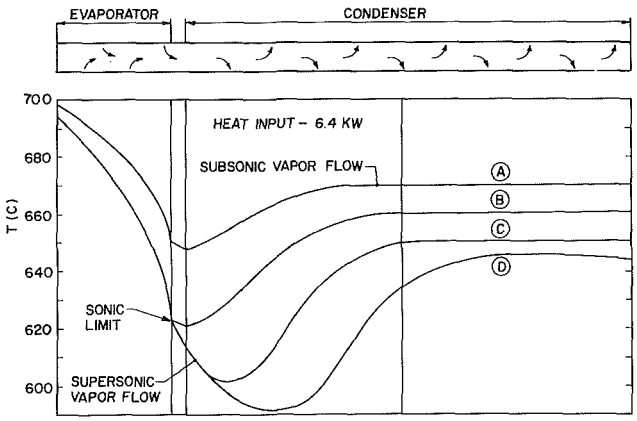

Fig. 2 Temperature distribution in a sodium heat pipe (Kemme, 1969)

mities in flow properties in the radial direction and may yield flow reversals (Busse, 1986). For this reason, the shock regions in the condenser are poorly defined (see Fig. 2). Near the working fluid's freezing point the vapor density is low and a heat pipe is more prone to choking than at higher temperatures. Fluids such as sodium and lithium have low vapor densities and are, therefore, more influenced by the sonic heat transfer limit than other high-vapor-density fluids. A heat pipe operation beyond the sonic heat transfer limit will produce an operation at a higher temperature that may adversely affect the performance of the device transferring the heat to the heat pipe and possibly destroy the heat transfer surfaces. For this reason, a high-temperature heat pipe should not be operated beyond the design temperature and sonic heat transfer limit. When the inertia and viscous forces of vapor are of the same order of magnitude, choking occurs at the condenser inlet, since the subsonic flow in an adiabatic region with friction can only produce a Mach number increase (Shapiro, 1953; Levy and Chou, 1973). With negligible inertia forces, however, choking does not occur (Busse, 1973); the heat transfer increases steadily with decreasing pressure at the evaporator exit and becomes limited by the zero vapor pressure or the *viscous heat transfer limit*.

The objective of this paper is to present an analytical model that may be used to determine the effects of working fluid, vapor flow area, lengths of evaporator and adiabatic regions, and the manner of liquid evaporation into the vapor core of the evaporator on the sonic heat transfer limit in high-temperature heat pipes. The presented analysis is an extension of previous works (Levy, 1968; Levy and Chou, 1973), which did not systematically and analytically investigate the effects of most of the parameters noted above on the sonic limit heat transfer of high-temperature heat pipes. The methods of suppression of the boiling and wicking heat transfer limits in heat pipes have been discussed by Dobran (1987b).

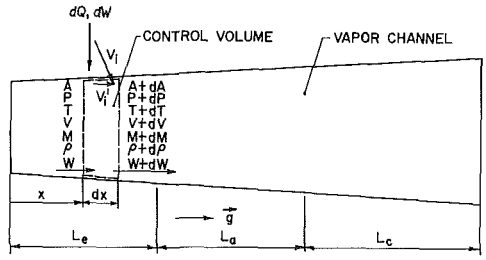

Fig. 3 Definition of the vapor flow variables and control volume for compressible flow analysis

2 Analysis of the Vapor Flow

The vapor flow thermohydrodynamics in a heat pipe determines the sonic heat transfer limit. For the purpose of determining the first-order effects of vapor flow in a heat pipe, use will be made of one-dimensional, steady-state compressible flow analysis. Figure 3 illustrates the vapor core region and defines the flow variables and a control volume that will be used to derive a set of equations for the analysis. For simplicity, and with a good approximation, the vapor will be assumed to obey a perfect gas equation of state, i.e.

$$P = \rho RT \tag{1}$$

The speed of sound is thus

$$c = (kRT)^{1/2} \tag{2}$$

and the Mach number is defined as

$$\mathrm{M} = V/c \tag{3}$$

The conservation of mass and liquid–vapor interface energy balance at an axial position x of the heat pipe give

$$w = \rho VA \tag{4}$$

$$dw = \frac{q}{h_{lv}}\,dx \tag{5}$$

where dw is positive for the injected mass in the evaporator

Nomenclature

a = factor defined by equation (35)
A = flow cross-sectional area
b = factor defined by equation (27)
c = speed of sound defined by equation (2)
C = factor defined by equation (34)
Cp = specific heat at constant pressure
D = hydraulic diameter
f = friction coefficient defined by equation (12)
g = body force per unit mass
h = enthalpy
h_{lv} = enthalpy of evaporation
H = energy term defined by equation (9)
k = ratio of specific heats
L = heat pipe length
m = coefficient in equation (18)
M = Mach number = V/c
n = coefficient in equation (18)
P = pressure
P_{er} = perimeter
q = heat transfer rate per unit length
q_s = sonic limit heat transfer rate per unit length
Q = heat transfer rate
R = gas constant
Re = Reynolds number $= wD(1-y_i)/\mu A$
T = temperature
V = velocity
V_i' = axial component of injection velocity, Fig. 3
w = mass flow rate
x = axial coordinate along the heat pipe
y_i = V_i'/V
μ = viscosity
ρ = density
τ = shear stress

Subscripts

a = adiabatic region of heat pipe
c = condenser region of heat pipe
e = evaporator region of heat pipe
eff = effective
i = vapor injection or withdrawal
l = pertains to the liquid phase
o = stagnation condition at the evaporator inlet
s = sonic condition
v = vapor
w = wall

and negative for the withdrawn mass in the condenser, and q is the heat transfer rate per unit length of evaporator (positive) or condenser (negative) and represents the heat transfer capability of the working fluid.

Applying the first law of thermodynamics to the control volume in Fig. 3 yields

$$\frac{dQ}{w} = dh + d\left(\frac{V^2}{2}\right) + \left[h - h_i + \frac{1}{2}(V^2 - V_i^2)\right]\frac{dw}{w} \tag{6}$$

where the potential energy terms have been neglected. For an ideal gas, the enthalpy is given as

$$dh = CpdT \tag{7}$$

so that substituting into equation (6) and using equation (2) we obtain

$$\frac{dQ + dH}{wCpT} = \frac{dT}{T} + \frac{k-1}{2}\mathrm{M}^2\frac{dV^2}{V^2} \tag{8}$$

where

$$dH = -\left(h - h_i + \frac{1}{2}(V^2 - V_i^2)\right)dw \tag{9}$$

represents the effect of injection or nonequilibrium between the liquid–vapor interface and mean vapor core parameters.

The momentum equation gives

$$-AdP - \tau_w P_{er}dx + g\rho Adx = d(wV) - Vy_i dw \tag{10}$$

where

$$y_i = \frac{V_i'}{V} \tag{11}$$

represents the directional effect of the injected or withdrawn mass (see Fig. 3). Using the definition of the friction factor and hydraulic diameter, i.e.

$$f = \frac{\tau_w}{\frac{1}{2}\rho V^2}, \quad D = \frac{4A}{P_{er}} \tag{12}$$

the momentum equation (10) can be written as follows:

$$\frac{dP}{P} + \frac{k\mathrm{M}^2}{2}\frac{dV^2}{V^2} + \frac{k\mathrm{M}^2}{2}4f\frac{dx}{D} - \mathrm{M}^2 gk\frac{dx}{V^2} + k\mathrm{M}^2(1 - y_i)\frac{dw}{w} = 0 \tag{13}$$

where use was made of equations (1) and (3).

From the definition of stagnation temperature, speed of sound, and Mach number we have

$$T_o = T + \frac{V^2}{2Cp} = T\left(1 + \frac{k-1}{2}\mathrm{M}^2\right) \tag{14}$$

so that equation (8) can also be written as

$$\frac{dQ + dH}{wCpT} = \left(1 + \frac{k-1}{2}\mathrm{M}^2\right)\frac{dT_o}{T_o} \tag{15}$$

Equations (1)–(4) and (13)–(15) give 7 equations with 11 variables P, ρ, T, c, M, V, T_o, w, A, $(dQ + dH)/wCpT$, and

$$4f\frac{dx}{D} - 2g\frac{dx}{V^2} - 2y_i\frac{dw}{w}$$

where four may be chosen as independent. Choosing the last four in this list as independent variables it is then possible to manipulate the above equations and solve for the remaining seven dependent variables. For example, the solutions for the Mach number and pressure distributions are

$$\frac{d\mathrm{M}^2}{\mathrm{M}^2} = \frac{1 + k\mathrm{M}^2}{1 - \mathrm{M}^2}\frac{dQ + dH}{wCpT} + \frac{k\mathrm{M}^2\left(1 + \frac{k-1}{2}\mathrm{M}^2\right)}{1 - \mathrm{M}^2}\left[4f\frac{dx}{D} - 2g\frac{dx}{V^2} - 2y_i\frac{dw}{w}\right] + \frac{2(1 + k\mathrm{M}^2)\left(1 + \frac{k-1}{2}\mathrm{M}^2\right)}{1 - \mathrm{M}^2}\frac{dw}{w} - \frac{2\left(1 + \frac{k-1}{2}\mathrm{M}^2\right)}{1 - \mathrm{M}^2}\frac{dA}{A} \tag{16}$$

$$\frac{dP}{P} = -\frac{k\mathrm{M}^2}{1 - \mathrm{M}^2}\frac{dQ + dH}{wCpT} - \frac{k\mathrm{M}^2(1 + (k-1)\mathrm{M}^2)}{2(1 - \mathrm{M}^2)}\left[4f\frac{dx}{D} - 2g\frac{dx}{V^2} - 2y_i\frac{dw}{w}\right] - \frac{2k\mathrm{M}^2\left(1 + \frac{k-1}{2}\mathrm{M}^2\right)}{1 - \mathrm{M}^2}\frac{dw}{w} + \frac{k\mathrm{M}^2}{1 - \mathrm{M}^2}\frac{dA}{A} \tag{17}$$

Equations (16) and (17) are similar to the results of Shapiro (1953), where the influence coefficients multiply the independent variables. In these equations dw can be replaced by the evaporation or condensation heat flux (equation (5)) and the friction coefficient by

$$f = m\mathrm{Re}^{-n} \tag{18}$$

$$\mathrm{Re} = \frac{\rho(V - V_i')D}{\mu} = \frac{wD(1 - y_i)}{\mu A} \tag{19}$$

where the coefficients m and n depend on whether the flow is laminar or turbulent and with or without the mass injection or withdrawal. For the vapor flow in the adiabatic region of a heat pipe, $y_i = 0$ and m and n may be taken as

$$\begin{aligned} &m = 16, \quad n = 1; \text{ laminar flow } (\mathrm{Re} < 2000) \\ &m = 0.079, \quad n = 0.25; \text{ turbulent flow } (\mathrm{Re} \geq 2000) \end{aligned} \tag{20}$$

The velocity profile of a laminar incompressible flow in the evaporator has a cosine rather than a parabolic distribution (Busse, 1973; Bankston and Smith, 1971) with

$$m = 2\pi^2, \quad n = 1 \tag{21}$$

In the condenser with high heat transfer rates it is dangerous to use the above analysis and laminar flow expressions for the friction factor owing to the possibility of flow reversals (secondary flow) in this region as discussed previously. High heat fluxes produce high radial Reynolds numbers of the vapor in the evaporator and condenser and yield a turbulent flow in cylindrical condensers even if the axial Reynolds number is below 2000 (Quaile and Levy, 1975).

Equations (16) and (17) can be used to study the effects of the external heat transfer Q, vapor injection and suction y_i, the degree of vapor nonequilibrium $h - h_i$, gravity g, and vapor flow area A, on the limiting heat transfer rates in heat pipes. Thus Levy (1968) neglected the frictional effects, area change, and gravitational effect, and assumed that $dQ + dH = 0$ and $y_i = 0$. From equation (16) it then follows that

$$\frac{d\mathrm{M}^2}{\mathrm{M}^2} = \frac{2(1 + k\mathrm{M}^2)\left(1 + \frac{k-1}{2}\mathrm{M}^2\right)}{1 - \mathrm{M}^2}\frac{dw}{w} \tag{22}$$

The combination of equation (22) with equation (5) can be integrated from $M(x=0)=0$ and $w(x=0)=0$ to $M(x=L_e)=1$ and $w(x=L_e)=qL_e/h_{lv}$ to obtain an expression for the commonly utilized sonic heat flux limit q_s, i.e.

$$q_s L_e = \frac{\rho_o c_o h_{lv} A}{(2(k+1))^{1/2}} \tag{23}$$

where ρ_o and c_o are the (stagnation) density and speed of sound at the evaporator inlet. When account is also taken of the frictional effects in the above analysis and choking assumed at the condenser inlet, it was found numerically (Levy and Chou, 1973) that the computed heat transfer limits agree better with data than the predictions using equation (23).

To investigate the more general solution of equation (16) we may take $dQ+dH=0$, $g=0$, and assume that the flow is laminar. Thus

(i) Evaporator or Condenser Regions

$$\frac{1-M^2}{M^2(2+(k-1)M^2)}\,dM^2 = (1+aM^2)\frac{dw}{w} - \frac{dA}{A} \tag{24}$$

where

$$a = k(1-y_i) + \frac{2mk\mu A h_{lv}}{(1-y_i)D^2 q} \tag{25}$$

(ii) Adiabatic Region

$$\frac{1-M^2}{M^2(2+(k-1)M^2)}\,dM^2 = bM^2 dx - \frac{dA}{A} \tag{26}$$

where

$$b = \frac{2mk\mu A h_{lv}}{D^2 q L_e} \tag{27}$$

Moreover, by taking A, y_i, and q constant, the solutions of equations (24) and (26) between any two sections 1 and 2 of the corresponding regions are given by

(i) Evaporator and Condenser Regions

$$\frac{M_2}{M_1}\left[\frac{1+\frac{k-1}{2}M_1^2}{1+\frac{k-1}{2}M_2^2}\right]^{1/2} \times \left[\frac{1+\frac{k-1}{2}M_2^2}{1+\frac{k-1}{2}M_1^2}\,\frac{1+aM_1^2}{1+aM_2^2}\right]^{\frac{1+a}{1+2a-k}} = \frac{w_2}{w_1} \tag{28}$$

(ii) Adiabatic Region

$$\frac{1}{2}\left[\frac{1}{M_1^2}-\frac{1}{M_2^2}\right] + \ln\left[\frac{M_1^2}{M_2^2}\,\frac{1+\frac{k-1}{2}M_2^2}{1+\frac{k-1}{2}M_1^2}\right]^{(k+1)/4} = b(x_2-x_1) \tag{29}$$

In particular, the solution represented by equation (23) is a special case of the solution expressed by equation (28). This may be proved by taking in the latter equation $y_i=0$, $\mu=0$ $(a=k)$, $w_1=\rho_1 c_1 M_1 A$, $M_1(x=0)=0$, $M_2(x=L_e)=1$, and $w_2=qL_e/h_{lv}$.

The more useful forms of equations (28) and (29) are obtained by solving these equations for the maximum heat transfer rate q, which occurs when the flow chokes at the exit of the adiabatic region of a heat pipe. Setting in equation (28) $w_1=\rho_o c_o M_1 A$, $M_1(x=0)=0$, $w_2=qL_e/h_{lv}$ and $M_2=M_e$ (exit of evaporator), and in equation (29) $M_1(x=L_e)=M_e$, $M_2(x=L_e+L_a)=1$ and $x_2-x_1=L_a$, we obtain the following results

$$\frac{qL_e}{h_{lv}\rho_o c_o A} = \frac{M_e}{\left(1+\frac{k-1}{2}M_e^2\right)^{1/2}}\left[\frac{1+\frac{k-1}{2}M_e^2}{1+aM_e^2}\right]^{\frac{1+a}{1+2a-k}} \tag{30}$$

$$\frac{1}{2}\left[\frac{1}{M_e^2}-1\right] + \ln\left[\frac{k+1}{2}\,\frac{M_e^2}{1+\frac{k-1}{2}M_e^2}\right]^{(k+1)/4} = bL_a \tag{31}$$

and after normalizing by the sonic heat flux limit q_s (equation (23)), it follows that

$$\frac{q}{q_s} = M_e\left[\frac{2(k+1)}{1+\frac{k-1}{2}M_e^2}\right]^{1/2}\left[\frac{1+\frac{k-1}{2}M_e^2}{1+aM_e^2}\right]^{\frac{1+a}{1+2a-k}} \tag{32}$$

$$\frac{1}{2}\left[\frac{1}{M_e^2}-1\right] + \ln\left[\frac{k+1}{2}\,\frac{M_e^2}{1+\frac{k-1}{2}M_e^2}\right]^{(k+1)/4} = Ck\left(\frac{L_a}{L_e}\right)\left(\frac{q_s}{q}\right) \tag{33}$$

$$C = 2m\left(\frac{\mu}{\rho_o c_o D}\right)\frac{L_e}{D}\,(2(k+1))^{1/2} \tag{34}$$

$$a = k\left[(1-y_i) + \frac{C}{(1-y_i)}\left(\frac{q_s}{q}\right)\right] \tag{35}$$

In particular, when $L_a=0$ and $M_e=1$ (choking at the evaporator exit), equation (32) is reduced to the form

$$\frac{q}{q_s} = 2\left[\frac{k+1}{2(1+a)}\right]^{\frac{1+a}{1+2a-k}} \tag{36}$$

Equations (32) and (33) can now be solved for q/q_s in terms of the independent parameters C, k, L_a/L_e, and y_i, or since μ, ρ_o, c_o, and k can be evaluated at the saturation temperature at the evaporator inlet, the independent variables may also be taken as T_{sat}, D, L_a/D, L_a/L_e, and y_i.

3 Discussion of Results

Using equations (32) and (33), Figs. 4 and 5 illustrate the predicted heat transfer rates with the sonic flow at the evaporator and adiabatic section exits, respectively, and a comparison with the sodium, potassium, and cesium data (Kemme, 1966, 1969; Levy and Chou, 1973; Dzakowic et al., 1969). The analytical results in these figures were generated by assuming that $y_i=0$ (normal-to-the-main-flow vapor injection in the evaporator) and using the perfect gas equation of state for the calculation of density and speed of sound at the saturation temperature at the evaporator inlet. As can be seen from these figures, the inclusion of frictional effects into the model produces a superior comparison of analysis with data and reduces the axial heat transport capacities of heat pipes. At high temperatures, some sodium data (Kemme, 1966; Dzakowic et al., 1969) show a deviation from the sonic heat transfer limit behavior and may be associated with the attainment of the wicking heat transfer limit in heat pipes as dis-

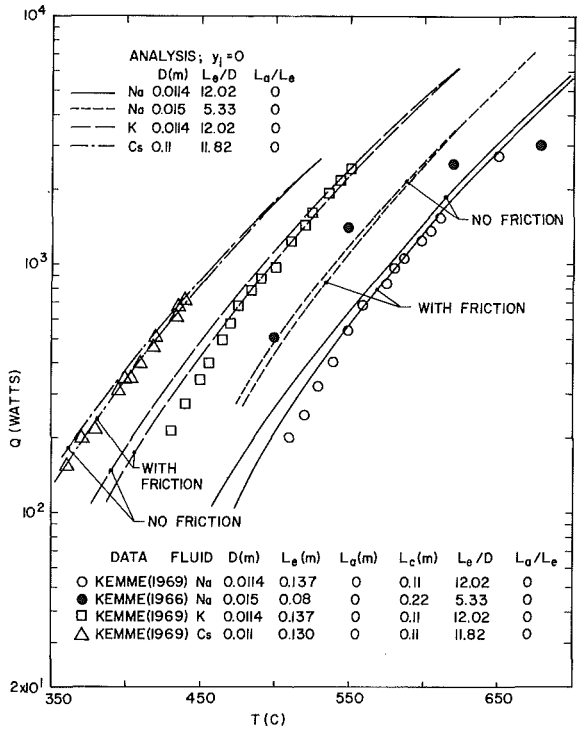

Fig. 4 Comparison of analytic results, with and without friction and choking at the evaporator exit, with data

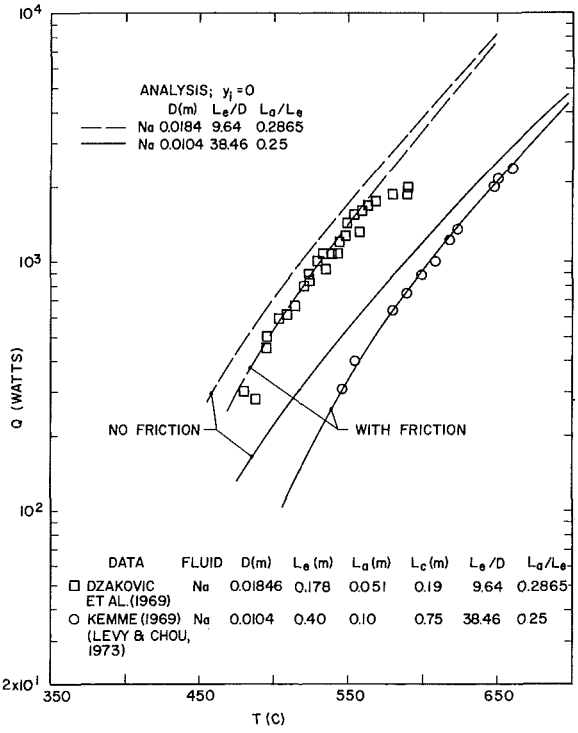

Fig. 5 Comparison of analytic results, with choking at the adiabatic section exit and with and without friction, with data

cussed earlier. At lower temperatures, the heat pipe performance becomes sensitive to the frictional effects, and the axial heat transfer capacity can be considerably reduced as illustrated in Fig. 5, which shows a good comparison of analysis with data with a finite length of the adiabatic region. The data in Fig. 5 are also predicted with the numerical model of Levy and Chou (1973) when they accounted for the frictional effects in evaporator and condenser.

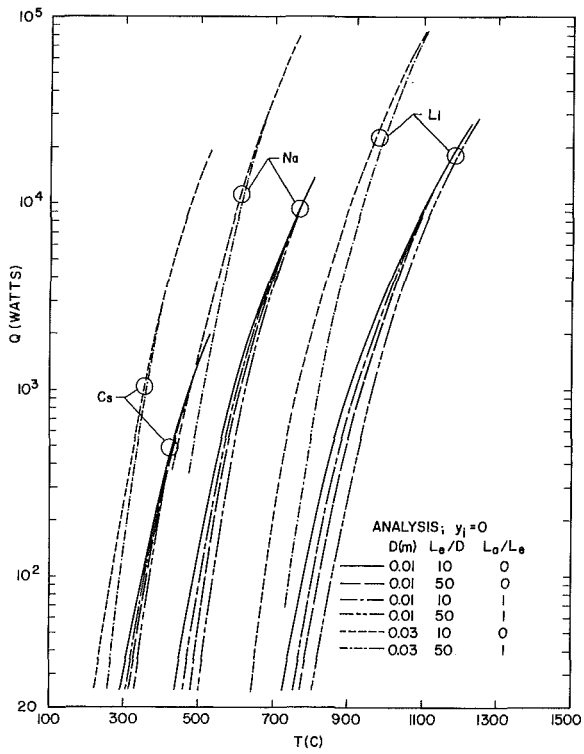

Fig. 6 The effect of vapor diameter, evaporator, and adiabatic lengths on the sonic heat flux limit for Li, Na, and Cs

The effects of the vapor diameter D, evaporator length to diameter ratio L_e/D, and adiabatic length to evaporator length ratio L_a/L_e, on the sonic heat transfer limits for lithium, sodium, and cesium are illustrated in Fig. 6. At constant D, an increase of the evaporator and adiabatic lengths has the effect of reducing the heat pipe's axial heat transport capacity; this reduction is considerable for long heat pipes and at lower temperatures where the frictional effects become more important. With the temperature and evaporator and adiabatic lengths fixed, a heat pipe with a larger vapor flow area can transport larger axial heat fluxes for all fluids in Fig. 6. The axial heat transport capacities of Li are also more sensitive to the frictional effects (and, therefore, on L_a and L_e) than those of Na, K, and Cs.

Figure 7 shows the effect of the non-normal-to-the-main-flow vapor injection in the evaporator ($y_i > 0$). Large values of y_i are seen to produce a considerable decrease of the sonic heat transfer limits for Li and Na at lower temperatures and a slight increase beyond the frictionless sonic heat transfer limit at very high temperatures. The physical explanation of these results is that at lower temperatures the frictional effects are important, whereas at higher temperatures the inertial effects dominate and require higher axial heat fluxes for $y_i > 0$ than for $y_i = 0$ for attainment of the sonic limit (see equation (24)). The non-normal-to-the-main-flow vapor injection has not been previously investigated and may be present in some systems where heat pipes are integrally built into the systems' structures.

Equation (24) also shows that an area increase for the vapor flow in the evaporation and adiabatic regions of a heat pipe can produce larger sonic heat transfer limits than in a uniform area pipe. This implies that heat pipes with long evaporator and adiabatic sections may require nonuniform cross-sectional areas for vapor flow ($dA/dx > 0$) in order to compensate for the reduction of sonic heat transfer limits brought about by the frictional effects. For applications to nuclear reactors in space, a super heat pipe system may be envisioned with a heat source supplying heat to variable cross-sectional areas of heat

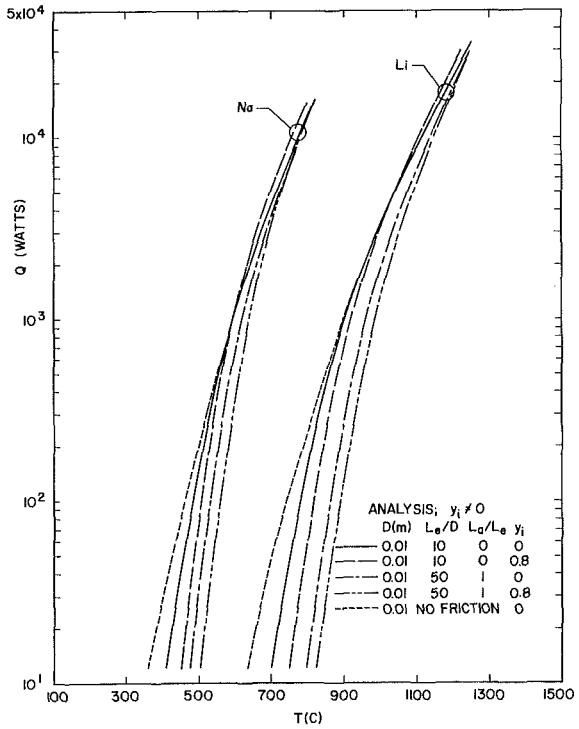

Fig. 7 The effect of variable y_i on the sonic heat flux limits for L_i and N_a

pipe evaporators that in turn transfer this heat to the power conversion system that may be removed by a considerable distance from the power source. In this manner a more compact reactor design can be achieved than by utilizing constant and large-diameter heat pipes.

4 Summary and Conclusions

The current designs of terrestrial and space-based systems use heat pipes for a variety of tasks. These applications require optimum heat pipe performance over a large range of system and environmental conditions. For these reasons, the heat pipe design has strived toward the development of super heat pipes that transfer optimum heat transfer rates without exceeding the heat transfer operating limits. Many of these limits may be suppressed and some may be eliminated through a judicious optimization of heat pipe geometry and selection of working fluids.

In the paper an analytical model has been presented for the design of high-temperature heat pipes with the sonic flow limiting the axial heat transport capacity. It was shown that the sonic heat transfer limit is affected by the working fluid, vapor flow area, manner of vapor introduction into the vapor core region of the evaporator, and lengths of the evaporator and adiabatic regions. Achieving high rates of heat transfer requires large vapor flow cross-sectional areas, small lengths of the evaporator and adiabatic regions or a vapor flow area increase in these regions, and normal-to-the-main-flow liquid evaporation in the evaporator. A comparison of the analytical results with data of high-temperature heat pipes operating with sonic heat transfer limits is shown to be reasonable. The presented model can be readily adopted for the optimization of high-temperature heat pipe design.

References

Bankston, C. A., and Smith, H. J., 1971, "Incompressible Laminar Vapor Flow in Cylindrical Heat Pipes," ASME Paper No. 71-WA/HT-15.

Barthelemy, R. R., Massie, L. D., and Borger, W. U., 1986, "Military Space Power Systems Technology for the Twenty-First Century," *Intersociety Energy Conversion Engineering Conference*, Vol. 3, pp. 1401-1404.

Busse, C. A., 1973, "Theory of the Ultimate Heat Transfer Limit of Cylindrical Heat Pipes," *Int. J. Heat Mass Transfer*, Vol. 16, pp. 169-186.

Busse, C. A., 1986, Personal Communications.

Desanctis, C., Priest, C., and Wood, W., 1986, "Space Station Overview," Paper No. AIAA-86-0315.

Dobran, F., 1987a, "Heat Pipe Research and Development in the Americas," *Proc. 6th International Heat Pipe Conference*, May 25-28, Grenoble, France; also in *Heat Recovery Systems & CHP*, Vol. 9, 1989, pp. 67-100.

Dobran, F., 1987b, "Super Heat Pipe Design Considerations for Applicatoins to Space-Based Systems," *Int. Symp. on Thermal Problems in Space-Based Systems*, F. Dobran and M. Imber, eds., ASME, New York, pp. 1-12.

Dzakowic, G., Tang, Y., and Arcella, F., 1969, "Experimental Study of Vapor Velocity Limit in a Sodium Heat Pipe," ASME Paper No. 69-HT-21.

Kemme, J. E., 1966, "Heat Pipe Capability Experiments," *IEEE Thermionic Conversion Conference*, pp. 159-168.

Kemme, J. E., 1969, "Ultimate Heat Pipe Performance," *IEEE Transactions on Electron Devices*, Vol. ED-16, pp. 717-723.

Levy, E. K., 1968, "Theoretical Investigation of Heat Pipes Operating at Low Vapor Pressures," ASME *Journal of Engineering for Industry*, Vol. 90, pp. 547-522.

Levy, E. K., and Chou, S. F., 1973, "The Sonic Limit in Sodium Heat Pipes," ASME JOURNAL OF HEAT TRANSFER, Vol. 95, pp. 218-223.

Merrigan, M. A., Martinez, E. H., Keddy, E. S., Runyan, J. E., and Kemme, J. E., 1983, "Performance Demonstration of a High Power Space Reactor Heat Pipe Design," *Intersociety Energy Conversion Engineering Conference*, Vol. 4, pp. 1874-1879.

Merrigan, M. A., Keddy, E. S., Sena, J. T., and Elder, M. G., 1984, "Heat Pipe Technology Development for High Temperature Space Radiator Applications," *Intersociety Energy Conversion Engineering Conference*, Vol. 1, pp. 592-597.

Merrigan, M. A., 1986, "Heat Pipe Design for Space Power Heat Rejection Applications," *Intersociety Energy Conversion Engineering Conference*, Vol. 3, pp. 1993-1998.

Quaile, J. P., and Levy, E. K., 1975, "Laminar Flow in a Porous Tube With Suction," ASME JOURNAL OF HEAT TRANSFER, Vol. 97, pp. 66-71.

Sadunas, J. A., and Lehtinen, A., 1985, "Thermal Management Systems Options for the High Power Space Platforms," Paper No. AIAA-85-1047.

Shapiro, A. H., 1953, *Compressible Fluid Flow*, Vol. 1, Ronald, New York.

Vanlandingham, E. E., 1986, "The NASA Space Power Technology Program," *Intersociety Energy Conversion Engineering Conference*, Vol. 3, pp. 1405-1410.

Heat Transfer Characteristics in Two-Phase Closed Conventional and Concentric Annular Thermosyphons

A. Faghri
Professor

M.-M. Chen
Graduate Research Assistant.

M. Morgan
Research Student.

Department of Mechanical Systems Engineering,
Wright State University,
Dayton, OH 45435

The heat transfer in the condenser sections of conventional and annular two-phase closed thermosyphon tubes has been studied experimentally and analytically. In addition, the results of a series of experiments on the flooding phenomena of the same thermosyphons are reported. Freon 113 and acetone were used as working fluids. An improved correlation was developed to predict the performance limits of conventional thermosyphons using the present and previously existing experimental data for flooding with different working fluids. The prediction of the theoretical Nusselt number for the situations associated with measured heat transfer coefficients in the condenser section indicated that the effect of interfacial shear on the film flow is small. The increase of the experimental reflux condensation heat transfer coefficients over theoretical predictions is attributed to waves at the vapor–liquid interface.

1 Introduction

The two-phase closed thermosyphon is a simple but effective heat transfer device. It is nothing more than a wickless heat pipe with a liquid reservoir at the bottom. The thermosyphon is best described by dividing it into three sections. Heat is input through the evaporator section, turning the working fluid into vapor. The vapor rises and passes through the adiabatic section to the condenser section. In the condenser section the vapor condenses and gives up its latent heat. Gravity then forces the condensate back to the evaporator section as a liquid film.

Due to their high efficiency, reliability, and cost effectiveness, thermosyphons have been used in many different applications. These applications include preservation of permafrost (Long, 1963; Vasiliev et al., 1981), de-icing of roadways (Hurich et al., 1980; Tanaka et al., 1981), turbine blade cooling (Cohen and Bayley, 1955; Bayley and Bell, 1957), and applications in heat exchangers (Lee and Bedrossian, 1978; Larking, 1981).

The present paper examines the operation of a different type of thermosyphon. The concentric annular two-phase closed thermosyphon is depicted in Fig. 1 The concentric annular thermosyphon is constructed of two pipes of unequal diameter placed one inside the other and sealed at the ends by end caps to create an annular vapor space. The advantage of this type of thermosyphon over the conventional thermosyphon is the increased surface area for heat transfer into and out of the pipe without necessarily increasing the outside pipe diameter.

The heat transfer characteristics of conventional thermosyphons are usually described by heat transfer coefficients for the condenser section and by the flooding limit. In the case of vertical thermosyphons, the measured condensation heat transfer coefficients are usually compared with Nusselt's theory (Onosovskii et al., 1972; Larkin, 1971, 1981; Andros and Florchuetz, 1978) or extended theories (Seban and Faghri, 1984; Chen et al., 1984).

For the flooding limit, a number of empirical correlations have been obtained by Wallis (1969), Kutateladze (1972), and Tien and Chung (1978). The flooding limit is the most common concern for long thermosyphons with large liquid fill ratios, large axial heat fluxes, and small radial heat fluxes. This limit occurs due to the instability of the liquid film generated by a high value of interfacial shear. This high value of interfacial shear comes from the large vapor velocities induced by high heat fluxes. The vapor shear "holdup" prevents the condensate from returning to the evaporator and leads to a flooding condition in the condenser section. This causes a partial dryout of the evaporator, which results in wall temperature excursions or in limiting the operation of the system.

In this paper the condensate heat transfer coefficient for the conventional thermosyphon as well as the condensate heat transfer coefficients for the inner and outer walls of the annular thermosyphon were obtained experimentally. These experimental values were compared to analytical values that were calculated by using Nusselt's solution and by extending Nusselt's theory to include the variation of the shear at the vapor–liquid film interfaces for the inner and outer walls.

In addition, the experimental flooding phenomenon of a concentric annular thermosyphon was compared to that of a

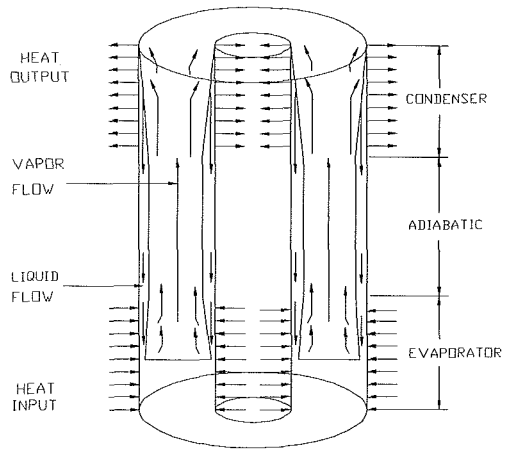

Fig. 1 Concentric annular two-phase closed thermosyphon

Contributed by the Heat Transfer Division and presented at the National Heat Transfer Conference, Houston, Texas, July 24-27, 1988. Manuscript received by the Heat Transfer Division May 4, 1988. Keywords: Condensation, Heat Pipes and Thermosyphons, Thin Film Flow.

conventional thermosyphon. An improved correlation was obtained that predicts the flooding limit for conventional thermosyphons using present and previously existing experimental data for different working fluids.

2 Experimental Apparatus and Procedures

To accomplish the objectives of this experiment, a conventional thermosyphon and a concentric annular thermosyphon were designed and built. A summary of the design parameters for both thermosyphons is given in Table 1.

A schematic of the test setup for the annular thermosyphon is shown in Fig. 2. The setup for the conventional thermosyphon is similar. Figure 2 also illustrates the thermocouple locations used for recording temperature values throughout the concentric annular thermosyphon and at the coolant inlet and outet of the heat sinks. The wall temperature of the adiabatic section of the concentric annular thermosyphon was measured by thermocouples mounted on a rod of insulating material (Aremcolox 502-600) that was press fitted into the adiabatic section of the inner pipe. The thermocouple labeling for the conventional thermosyphon is similar to the outer wall of the concentric annular thermosyphon. Separate a-c power supplies were used to supply power to the inner and outer evaporator section heaters. Two electric heaters of 2.4 kW each were double-helically wrapped around a ceramic rod and covered with a thermally conductive cement. This heater assembly was then covered with a thermally conductive grease and press fitted into the inner pipe. Two electric heaters rated at 4.8 kW were coiled around the outer pipe and cemented into place. Three helically coiled 2.4 kW electric heaters were used to supply heat to the conventional thermosyphon. All of the heaters used were covered with a heat conductive cement to hold them in place and to distribute the heat flux evenly throughout the heater sections. Wattmeters were used to measure the power input to the heaters.

The heat sink used in the inner pipe of the annular thermosyphon has a center baffle running its entire length. This baffle has a hole in the bottom of it that allows the inlet water to run the full length of the heat sink before crossing to the outlet side. This configuration ensures even cooling of the inner pipe condenser section. The outer heat sink is a cooling jacket designed to envelop the condenser section of the outer pipe. This cooling jacket design is also used for the heat sink of the conventional therosyphon. All of the heat sinks were provided with cooling water from a constant head tank. Coolant flow was measured and recorded at frequent intervals throughout the experiments.

The thermosyphons were cleaned using standard procedures and then evacuated to 10E-5 torr. After evacuation the thermosyphons were filled with working fluid using an apparatus specifically designed for filling heat pipes.

During testing, steady-state operation was attained before increasing the power input through the heaters. The power was increased in small increments to allow for the careful observance of the operating parameters. When the flooding limit was reached, testing was terminated before damage to the thermocouples or degradation of the working fluid occurred.

The mean heat transfer coefficient for the condenser zone is calculated by

$$\bar{h} = \frac{\dot{Q}/A_c}{\bar{T}_c - T_a} \tag{1}$$

where $\dot{Q}$ is the heat flow rate, A_c represents the surface area of the condenser section, $\bar{T}_c$ is the mean temperature in the cooling zone, and T_a is the temperature in the middle of the adiabatic section where thermocouple C28 is located. The location of T_a was selected to avoid measuring the temperature of the superheated boiling liquid or the subcooled condensate.

Energy balances between the heat input by the heaters and the heat removed by the sinks were monitored, and the flow rates through the heat sinks were maintained to ensure an energy balance of at least 90 percent. An error analysis using the standard square root technique was performed to determine the accuracy of $\bar{h}$ calculated from the experimental data. This calculation was based on a temperature reading with an accuracy of $\pm 0.5\,^{\circ}C$ and resulted in $\bar{h}$ being accurate to within ± 7.4 percent.

Nomenclature

A = cross-sectional area of the vapor space
Bo = Bond number $= D\,[g(\rho_L - \rho_v)/\sigma]^{1/2}$
C_f = friction coefficient $= 2\tau/\rho_v u_v^2$
C_k = coefficient in equation (10)
C_w = coefficient in equation (9)
D = diameter
D_h = hydraulic diameter $= D_O - D_I$
g = acceleration due to gravity
h = heat transfer coefficient
h_{fg} = latent heat of vaporization
j = volumetric flux
j^* = dimensionless volumetric flow rate, $j_i^* = j_i \rho_i^{1/2} [gL(\rho_L - \rho_v)]^{-1/2}$
K = modified Kutateladze number $= \dot{Q}/[Ah_{fg}[\sigma g(\rho_L - \rho_v)]^{1/4}(\rho_L^{-1/4} + \rho_v^{-1/4})^{-2}]$
K^* = ratio of inner diameter to outer diameter
k = thermal conductivity
L = length
m = coefficient in Wallis' correlation
N = modified Jakob number $= k_L(T_s - T_w)/\mu_L h_{fg}$
P = pressure
$\dot{Q}$ = heat transfer rate
R = coefficient in terms of the ratio of liquid to vapor density $= (\rho_L/\rho_v)^{0.14}$
Re = Reynolds number
S = dimensionless interfacial shear stress $= (\tau_\delta/\rho_L g)(g/\nu_L^2)^{1/3}$
T = temperature
ΔT_I = $T_s - T_{w,I}$
ΔT_O = $T_s - T_{w,O}$
u = axial component of velocity
x = axial coordinate
y = radial coordinate
Γ = mass flow rate per unit width
δ = liquid film thickness
μ = absolute viscosity
ν = kinematic viscosity
ρ = fluid density
σ = liquid surface tension
τ = shear stress

Subscripts

a = adiabatic section
c = condenser section
e = evaporator section
E = experimental results
h = based on the hydraulic diameter
i = liquid or vapor
I = inner wall
L = liquid phase
N = Nusselt's solution
O = outer wall
P = present analysis
s = saturation condition
v = vapor phase
w = wall
x = at any x location
δ = liquid-vapor interface

Superscripts

$-$ = mean value
$+$ = nondimensional variable

Table 1 Summary of thermosyphon specifications

	Dimensions	
	Annular	Conventional
Total length	1000.0 mm	1000.0 mm
Evaporator length	457.2 mm	389.1 mm
Adiabatic length	323.6 mm	178.7 mm
Condenser length	219.2 mm	432.2 mm
Outer pipe (o.d.)	53.3 mm	19.1 mm
Outer pipe (i.d.)	44.5 mm	15.9 mm
Inner pipe (o.d.)	29.4 mm	N/A
Inner pipe (i.d.)	25.4 mm	N/A

	Fluid Inventory	
	Annular	Conventional
Acetone	171.1 cc	39.1 cc
Freon 113	171.1 cc	39.1 cc

	Heater Elements		
	Annular		Conventional
	outer	inner	
Length	2387.6 mm	2108.2 mm	838.2 mm
Diameter	4.8 mm	3.2 mm	3.2 mm
Voltage	230 V	230 V	230 V
Maximum power	4.8 kW (ea)	2.4 kW (ea)	2.4 kW (ea)

3 Analysis

3.1 Reflux Condensation Heat Transfer Analysis. In the present section, the Nusselt analysis for laminar film condensation is extended for countercurrent vapor flow inside a concentric annular thermosyphon. The inner and outer walls of the annulus can be held at the same temperature or at different temperatures; the former is symmetric cooling and the latter is asymmetric cooling. The solution procedures are somewhat similar to those used in the paper by Seban and Faghri (1984) for conventional thermosyphons and in the paper by Faghri and Chow (1987) for an open annulus in a microgravitational environment.

The liquid Reynolds numbers for the inner and outer walls for the laminar flow case are given as follows:

$$\mathrm{Re}_{L,I} = -S_I \frac{\delta_I^{+2}}{2} - \left(\frac{dP^+}{dx^+} - 1\right)\frac{\delta_I^{+3}}{3} \tag{2a}$$

$$\mathrm{Re}_{L,O} = -S_O \frac{\delta_O^{+2}}{2} - \left(\frac{dP^+}{dx^+} - 1\right)\frac{\delta_O^{+3}}{3} \tag{2b}$$

These and subsequent equations involve the nondimensional variables

$$\delta_I^+ = \delta_I\left(\frac{g}{\nu_L^2}\right)^{1/3}, \quad \delta_O^+ = \delta_O\left(\frac{g}{\nu_L^2}\right)^{1/3},$$

$$D^+ = D\left(\frac{g}{\nu_L^2}\right)^{1/3}, \quad x^+ = x\left(\frac{g}{\nu_L^2}\right)^{1/3},$$

$$u^+ = \frac{u}{(\nu_L g)^{1/3}}, \quad P^+ = \frac{P}{\rho_L g}\left(\frac{g}{\nu_L^2}\right)^{1/3},$$

$$N_I = \frac{k_L(T_S - T_{w,I})}{\mu_L h_{fg}}, \quad N_O = \frac{k_L(T_S - T_{w,O})}{\mu_L h_{fg}}$$

$$S_I = \frac{\tau_{\delta,I}}{\rho_L g}\left(\frac{g}{\nu_L^2}\right)^{1/3}, \quad S_O = \frac{\tau_{\delta,O}}{\rho_L g}\left(\frac{g}{\nu_L^2}\right)^{1/3}$$

A momentum balance for the annular vapor region yields

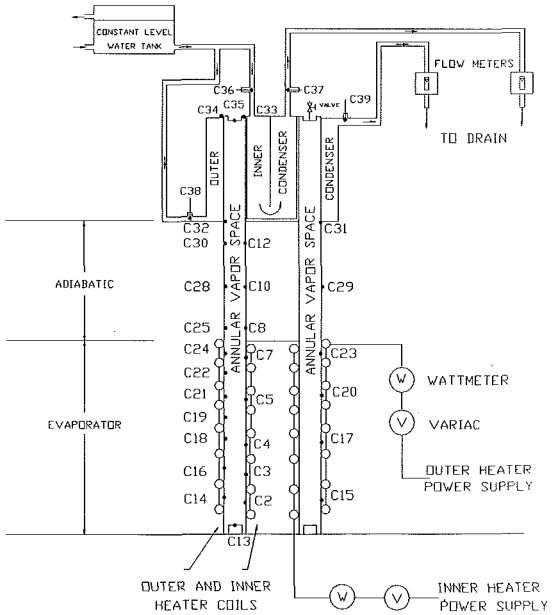

Fig. 2 Schematic of test setup

$$\frac{dP^+}{dx^+} = \frac{4}{(1+K^*)D_h^+}(S_O + K^* S_I) + \frac{\rho_v}{\rho_L} \tag{3}$$

Neglecting the convective terms in the energy equation, the following energy balances can be made for the liquid flow on the inner and outer walls:

$$\frac{d\mathrm{Re}_{L,I}}{dx^+} = \frac{N_I}{\delta_I^+} \tag{4a}$$

$$\frac{d\mathrm{Re}_{L,O}}{dx^+} = \frac{N_O}{\delta_O^+} \tag{4b}$$

The functions $\tau_{\delta,I}$ and $\tau_{\delta,O}$ contained in the quantities S_I and S_O are specified the same as for vapor flow in a smooth tube annulus, with an augmentation factor due to the two-phase nature of the flow as in the papers by Seban and Faghri (1984)

and Faghri and Chow (1987). The shear stress is assumed to be the sum of the shear stress due to friction (with no mass transfer) and the shear stress due to the faster-moving vapor condensing onto the slower-moving liquid. This method accounts for the change of the interfacial shear along the condenser due to the mass flow of vapor.

$$S_I = \frac{C_{f,I}}{2}\frac{\rho_v}{\rho_L}(u_v^+ + u_{L,I,\delta}^+)^2 + \frac{N_I}{\delta_I^+}(u_v^+ + u_{L,I,\delta}^+) \quad (5a)$$

$$S_O = \frac{C_{f,O}}{2}\frac{\rho_v}{\rho_L}(u_v^+ + u_{L,O,\delta}^+)^2 + \frac{N_O}{\delta_O^+}(u_v^+ + u_{L,O,\delta}^+) \quad (5b)$$

In addition, a mass balance between the vapor and the liquid films yields the following relation in terms of the Reynolds numbers:

$$\mathrm{Re}_{v,h} = 4\frac{\mu_L}{\mu_v}\frac{K^*}{1+K^*}\mathrm{Re}_{L,I} + 4\frac{\mu_L}{\mu_v}\frac{1}{1+K^*}\mathrm{Re}_{L,O} \quad (6)$$

The positive direction of the calculation domain for x^+ and the liquid velocity u_L^+ is from the top to the bottom of the pipe. For the vapor velocity u_v^+, the positive direction is from the bottom to the top of the pipe. It should be emphasized that the above analysis was developed for the condenser section and is not applicable to the evaporator section.

The local and average Nusselt numbers are obtained from the following relations:

$$h_{x,I}^+ = \frac{h_{x,I}}{k_L}\left(\frac{\nu_L^2}{g}\right)^{1/3} = \frac{1}{\delta_I^+},$$

$$h_{x,O}^+ = \frac{h_{x,O}}{k_L}\left(\frac{\nu_L^2}{g}\right)^{1/3} = \frac{1}{\delta_O^+} \quad (7)$$

$$\bar{h}_I^+ = \int_0^1 h_{x,I}^+ d\left(\frac{x^+}{L_c^+}\right), \quad \bar{h}_O^+ = \int_0^1 h_{x,O}^+ d\left(\frac{x^+}{L_c^+}\right)$$

Equations (2)–(6) can be solved numerically to find δ_I^+, δ_O^+, $\mathrm{Re}_{L,I}$, $\mathrm{Re}_{L,O}$, and $\mathrm{Re}_{v,h}$ as functions of the dimensionless distance along the condenser section. The numerical procedure starts from the top of the condenser section of the annular thermosyphon and proceeds downward. This problem is governed by five dimensionless parameters: ρ_L/ρ_v, μ_L/μ_v, N_I, N_O, and K^*. The accuracy of the numerical solution was checked by systematically varying the grid size uniformly and nonuniformly (power-law) and the results for different grid sizes were compared to the extrapolated results of an infinitesimal grid spacing. The final results are obtained by using power-law grid spacings so that a smaller grid spacing is set in the region with a sharp change of the condensate film thickness. A total of 50 grids were used for the presentation of the final results.

3.2 Empirical Correlation for the Flooding Limit of Closed Two-Phase Conventional Thermosyphons. There are two major fundamental correlations for predicting the flooding limit of closed two-phase thermosyphons. The first one is Wallis' correlation (1969), which is characterized by a balance of the inertial and hydrostatic forces. The second is the Kutateladze two-phase flow stability criterion (1972). Wallis' empirical correlation is based on results from open channel water–gas experiments. Two coefficients in Wallis' correlation must be determined by experiment because they are dependent upon the design of the pipe. In Kutateladze's correlation, the effect of the diameter of the pipe is not included. For small tubes, the diameter of the vapor flow passage plays an important role in the flooding characteristics. It was shown by Wallis and Makkenchery (1974) that the Kutateladze criterion produces a good correlation of the results for pipes with large diameters, but for small-diameter pipes the effect of the diameter should be considered.

Based on the stability analysis at the liquid–vapor interface, Prenger (1984) proposed a correlation for flooding in dimensionless form. This is basically the same as the Kutateladze correlation with $K = 3.2$ being replaced by $K = \sqrt{2\pi}$ in the Prenger correlation. In fact, these two numbers are the square root of the coefficients of the upper and lower limits in the Taylor instability criterion for the critical wavelength.

The shortcoming of Wallis' correlation is that the effect of surface tension is not taken into account. The effect of surface tension is important to the hydrodynamic and heat transfer characteristics of gas–liquid systems. Physically, increasing the surface tension means that a higher pressure difference can be sustained across a film surface without forming waves. Tien and Chung (1978) combined Kutateladze's correlation for cases with $j_L = 0$ by an analogy to the Wallis correlation in order to account for the diameter of the pipe and surface tension effects. This correlation resulted in a good agreement with experimental data for certain working fluids, but large deviations were found when water was used as the working fluid.

Bezrodnyi (1978) proposed a correlation similar to Kutateladze's with the Kutateladze number being determined by the vapor pressure and other properties. Imura et al. (1983) compared a number of existing empirical correlations with a large number of experimental data. The results showed that Sakhuja's correlation (1973), Katto's correlation (1978), and the correlation developed by Imura et al. (1977) underpredicted most of the results when water was used as the working fluid, while Bezrodnyi's correlation overpredicted most of the experimental data no matter what working fluid was used. The results from all of these correlations deviated significantly from the experimental results. Imura et al. (1983) also proposed a new empirical correlation that is similar to Kutateladze's correlation, with the Kutateladze number being determined by the ratio of the density of the liquid to that of the vapor. In that correlation the effect of diameter was not included.

The objective of this section is to improve the existing correlation, which predicts the flooding limit for different types of working fluids. Starting with the Wallis correlation (1969), we have

$$(j_v^*)^{1/2} + (j_L^*)^{1/2} = C_w \quad (9)$$

where

$$j_i^* = j_i \rho_i^{1/2}[gL(\rho_L - \rho_v)]^{-1/2} \quad (i = L, v)$$

$$C_w = 0.7 \sim 1.0$$

Wallis suggested that the liquid film would always flow upward if $j_v^* > 1$ and would flow downward wetting a dry wall below it if $j_v^* < 0.5$. In the present study, $C_w = 1.0$ was chosen. Thus, $j_v^* = 1$ is considered to be the case of total flooding ($j_L^* = 0$). Tien and Chung (1978) extended Kutateladze's correlation for cases with $j_L = 0$ by an analogy to the Wallis correlation

$$(K_v)^{1/2} + (K_L)^{1/2} = C_k \quad (10)$$

where

$$K_i = j_i \rho_i^{1/2}[g\sigma(\rho_L - \rho_v)]^{-1/4} \quad (i = L, v)$$

Comparing equation (10) with Wallis' correlation equation (9) gives

$$L = \left(\frac{C_k}{C_w}\right)^4 \left(\frac{\sigma}{g(\rho_L - \rho_v)}\right)^{1/2} \quad (11)$$

The critical wavelength of the Taylor instability is

$$L_{\mathrm{crit}} = (2\pi \sim 2\pi\sqrt{3})\sqrt{\frac{\sigma}{g(\rho_L - \rho_v)}} \quad (12)$$

Setting equation (11) equal to equation (12) and choosing the upper limit in equation (12) results in

$$\left(\frac{C_k}{C_w}\right)^4 = 3.2^2, \quad \frac{C_k}{C_w} = \sqrt{3.2}$$

If we let $C_w = 1.0$, the previous equation gives $C_k = \sqrt{3.2}$. $K = C_k^2 = 3.2$ is really the Kutateladze number for flooding, which does not consider the effect of diameter as mentioned previously in this section. According to the experimental results of Wallis and Makkenchery (1974), the Kutateladze number decreases as the dimensionless diameter, or Bond number, decreases.

If the characteristic length is set equal to the diameter, equation (11) gives

$$\left(\frac{C_k}{C_w}\right)^4 = D\left(\frac{g(\rho_L - \rho_v)}{\sigma}\right)^{1/2} = \text{Bo}$$

or

$$\frac{C_k}{C_w} = \text{Bo}^{1/4} \tag{13}$$

This indicates that C_k is a function of the Bond number. With reference to the variation of the Kutateladze number versus the Bond number in the paper by Wallis and Makkenchery (1974) with $j_v^* = 1.0$, the function $y = \tanh x$ is introduced to account for the effect of the diameter on the flooding limit. If we let $x = \text{Bo}^{1/4}$, equation (13) results in

$$\frac{C_k}{C_w} = \sqrt{3.2}\ \tanh\ \text{Bo}^{1/4} \text{ with } C_w = 1.0$$

or

$$(K_v)^{1/2} + (K_L)^{1/2} = \sqrt{3.2}\ \tanh\ \text{Bo}^{1/4} = C_k \tag{14}$$

This correlation was found to be highly accurate in predicting the flooding limit with water as the working fluid. The experimental deviations from this correlation are within 15 percent. For other fluids the deviations are more significant. It is noticed that for different working fluids, the variation of the ratio of the density of the liquid to that of the vapor is quite different within the same temperature range. Using the experimental results for different working fluids, the following correlation is proposed:

$$K = C_k^2 = \left(\frac{\rho_L}{\rho_v}\right)^{0.14} \tanh^2\ \text{Bo}^{1/4} = R\ \tanh^2\ \text{Bo}^{1/4} \tag{15}$$

or for the maximum heat transfer rate

$$\dot{Q}_{\max} = Kh_{fg}A\,[g\sigma(\rho_L - \rho_v)]^{1/4} [\rho_v^{-1/4} + \rho_L^{-1/4}]^{-2} \tag{16}$$

Equation (15) is a combination of the correlations developed by Tien and Chung (1978) and Imura et al. (1983). It should be noted that in Tien and Chung's correlation (1978), the argument of the hyperbolic tangent in equation (14) is $1/2\ \text{Bo}^{1/4}$ rather than $\text{Bo}^{1/4}$.

Figure 3 shows the variation of the modified Kutateladze number with respect to the Bond number for $R = 3.2$ and 2.0. The experimental data corresponding to the parameters in Table 2 are also plotted in Fig. 3. For the case of $R = 3.2$, the varition of K is similar to Wallis' experimental data (1974) of water with $j_v^* = 1.0$, which is the criterion for the present derivation. Figure 3 shows that for most of the experimental data of water with $R = 2.81 \sim 4.34$ are around the curve $R = 3.2$, and the data of Freon 113, ethanol, and methanol with $R = 1.62 \sim 2.43$ are around the $R = 2.0$ curve. For the experimental data of Freon 113, ethanol, and methanol, the

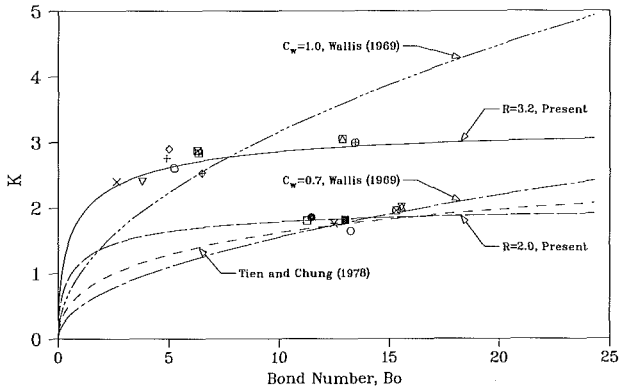

Fig. 3 Variation of the modified Kutataladze number versus the Bond number

Table 2 Range of experimental parameters and specifications for the flooding limit of two-phase closed thermosyphons

1	2	3	4	5	6	7	8
Test liquid	Investigator	Inside diameter D, mm	Working temperature, °C	Bond number Bo	$\frac{\rho_L}{\rho_v}$	$R = \left(\frac{\rho_L}{\rho_v}\right)^{0.14}$	Symbols in Fig. 3
Water	H. Nguyen-Chi et al. (1979)	7.0	50	2.64	11,929	3.72	×
		10.0	50	3.78	11,929	3.72	▽
	H. Imura et al. (1983)	13.1	40	4.90	19,846	4.0	+
		13.1	60	5.0	7562	3.49	◇
		13.1	100	5.23	1597	2.81	○
	Nguyen-Chi and Groll (1981)	17.0	30	6.29	34,268	4.31	⊠
		17.0	40	6.35	19,846	4.0	⊞
		17.0	60	6.49	7562	3.49	⊕
	M. Groll and Spendel (1984)	34.0	50	12.84	11,929	3.72	⊠
		34.0	90	13.42	2297	2.96	⊕
Freon 113	Present (conventional)	15.9	56.5	15.54	135	2.01	⊠
		15.9	53.4	15.30	151	1.96	⊗
	H. Imura et al. (1983)	13.1	50	12.46	171	2.05	✳
		13.1	65	12.96	108	1.93	■
Ethanol	H. Imura et al. (1983)	19.4	70	11.23	184	2.43	□
		19.4	90	11.43	280	2.20	●
Methanol	T. Fukano et al. (1983)	20.9	77	13.23	364	1.62	○

results are also close to Tien and Chung's prediction as well as Wallis' correlation with $C_w = 0.7$, but a large deviation occurs with water as the working fluid. Choosing the upper or lower limit for C_w will make a significant difference in the prediction of the critical heat flux. Figure 3 illustrates a good agreement of the results of the present correlation with the experimental data of the conventional thermosyphon for different working fluids. For annular thermosyphons it is recommended to modify equation (15) to predict the maximum heat transfer rate with the diameter D being replaced by the hydraulic diameter. However, more experimental results, other than those reported in Section 4.1, are needed to modify this equation with different working fluids and diameters for concentric annular thermosyphons.

4 Results and Discussion

4.1 Flooding Limit and Oscillation Phenomenon

(A) Annular Thermosyphon. In Fig. 4, the transient phenomenon of the flooding limit is illustrated. The working fluid used in this thermosyphon was Freon 113. The liquid charge was 171 cc, which brought the height of the liquid pool to 20 percent of the total length of the pipe. As shown by Fig. 2, this brings the pool surface to just below thermocouple C19. The outer wall thermocouples C14–C18 and the inner wall thermocouples C2–C4 are all within the liquid pool region. Thermocouple C28 is located in the middle of the adiabatic section and was used to measure the vapor temperature.

Constant low temperatures at the evaporator wall were observed up to a total heat input of 2730 W. The heat input was gradually increased until the readings at thermocouple C28 started to fluctuate. This critical point was reached at a total heat input of 2950 W. This temperature fluctuation appears to be the onset of liquid entrainment. The entrainment of the liquid is a result of liquid being caught up in the vapor flow due to shear forces at the liquid–vapor interface. The vapor velocity is not high enough to maintain all of the entrained droplets in its flow, so some of the droplets fall back through the adiabatic section, rewetting the area of thermocouple C28. This results in small temperature fluctuations at thermocouple C28. As more heat was input to the thermosyphon, the temperature fluctuation at C28 became more pronounced, as shown in Fig. 4(*a*). When the total heat input reached 3050 W ($\dot{Q}_I = 750$ W, $\dot{Q}_O = 2300$ W), it was noted that the temperature fluctuations at C28 had a longer period than before. At the same time, dryout in the evaporator section began. This is demonstrated by the temperature variations with time at thermocouples C3, C16, C19, and C24 shown in Fig. 4(*b*). In this case, dryout of the pipe surface occurred first near the liquid-pool surface, i.e., near thermocouple C19.

Using the Reynolds number calculated for the liquid film, there are waves present on the liquid film. According to Negishi's observations (1984), the condensing liquid film is in the form of a rivulet. Weber-Carstanjen and Busse (1984) observed and concluded that with the formation of waves on the surface of the rivulets, a dynamic pressure drop at the wave fronts can be produced by the vapor. This pressure drop adds to the pressure drop caused by the liquid flow resistance at the wall. These combined pressure drops must be overcome by the hydrostatic pressure for the condensate to flow back to the evaporator. When the vapor velocity increases to the point where the hydrostatic pressure drop cannot overcome the combined pressures, the liquid condensate does not reach the evaporator. This phenomenon completely stops the flow of condensate to the evaporator, resulting in local dryout at the surface of the liquid pool first. This is demonstrated by the initial temperature increase at thermocouple C19 followed by a temperature increase at thermocouple C24, as shown in Fig. 4(*b*). With the liquid not returning to the evaporator, the

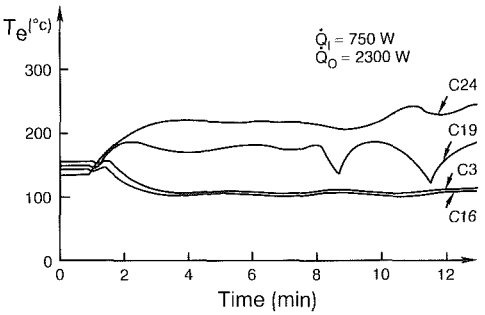

Fig. 4(*a*) Adiabatic temperature variation at the flooding limit of the annular thermosyphon

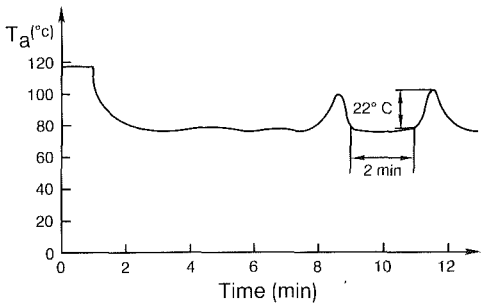

Fig. 4(*b*) Evaporator temperature variation at the flooding limit of the annular thermosyphon

vapor flow decreases and the dynamic pressure drop at the wave fronts diminishes along with a system pressure drop. This system pressure drop is shown in Fig. 4(*a*). By comparing Fig. 4(*a*) to Fig. 4(*b*), it can be seen that as the system pressure changes, the temperatures at thermocouples C19 and C24 change in the opposite direction compared to the temperature at thermocouple C28. Along with the decrease in the dynamic pressure drop, the large flow area now allows the hydrostatic pressure drop to force the liquid condensate into the adiabatic section. This causes the temperature decrease at thermocouples C19 and C24 and the corresponding temperature increase at thermocouple C28 as shown in Figs. 4(*a*) and 4(*b*). It is believed that the temperature increases at thermocouples C19 and C24 are not very pronounced due to their close proximity to the heater coils. The wall surfaces at the lower end of the evaporator were then rewetted and the corresponding wall temperatures dropped off abruptly as shown in Fig. 4(*b*).

With two exceptions, the phenomena observed for the annular thermosyphon were very similar to what Fukano et al. (1983) observed for conventional thermosyphons. The first exception is that the oscillation of the temperatures in the evaporator section is not as pronounced as Fukano et al. (1983) observed. This is probably due to the thermocouple location being too close to the heater coils in the present experiment. It is also believed that the heater cement leveled out the wall temperature in the evaporator section and reduced the magnitude of the oscillations compared to Fukano et al. (1983). The second exception is the lack of periodicity in the temperature oscillations in the evaporator section of this experiment compared to the experiment of Fukano et al. (1983) where the oscillations were periodic.

The flooding limit for this experiment was defined as the point where the adiabatic temperature oscillation became significant and large temperature excursions occurred at the heated wall. This condition is assumed to be the "total flooding" used to derive the existing flooding correlation. The experimental data for $\dot{Q}$ have an accuracy of ± 25 W.

(B) Conventional Thermosyphon. The experiment for the flooding limit was also performed for the conventional

thermosyphon. Phenomena similar to what were observed for the annular thermosyphon were also observed in the conventional thermosyphon. The one exception to this is the small oscillation of the adiabatic temperature. In addition, a temperature increase followed by an abrupt temperature drop at thermocouple C16 in the liquid pool region was noticed.

4.2 Reflux Heat Transfer Coefficients. The theoretical results and Nusselt predictions for the dimensionless condensate heat transfer coefficients are listed with the corresponding experimental results in Table 3 for the annular thermosyphon. In Table 3 the subscripts P and E denote the predicted and experimental average Nusselt numbers, $\bar{h}(\nu_L^2/g)^{1/3}/k_L$. The subscript N denotes the average Nusselt numbers found using Nusselt's solution for a vertical plate with stagnant vapor. For all of the cases the predicted mean Nusselt numbers were averaged over the length of the condenser section. The influence of interfacial shear is not significant for the cases involving the concentric annular thermosyphon with Freon 113 and acetone as the working fluids. This is generally in agreement with the previous results (Seban and Faghri, 1984; Chen et al., 1984) for conventional thermosyphons. The small decrease in the Nusselt number is due to the countercurrent vapor flow. On the other hand, the experimental coefficients for heat transfer in general were higher than the predicted ones and increased as the liquid Reynolds number increased. This increase in the heat transfer coefficients was attributed mainly to the waviness of the film, which enhances heat transfer. The experimental data at low Reynolds numbers agree closely with the values predicted by including the effect of interfacial shear. This general trend was observed by Faghri and Seban (1985) in the analysis of evaporation in wavy falling liquid films. Although the analysis given by Faghri and Seban (1985) was for evaporation where the average film thickness over a wavelength did not vary significantly with distance, the analysis can be applied to the case of condensation where the average thickness varies more significantly. In this wavy analysis, the increase in heat transfer was due to the contribution of convection because of mixing as well as the two-dimensional nature of the conduction that exists because of the variation of the liquid layer thickness. In the paper by Faghri and Seban (1985), the convection made the largest contribution to the increase in heat transfer. Unfortunately, a direct comparison of the present experimental results with the analysis for wavy flow given by Faghri and Seban (1985) is impossible due to the lack of the properties of the waves for the cases presented in Table 3. However, the trend and the order of magnitude for the increase is very close to the cases with the same liquid Reynolds number as given by Faghri and Seban (1985).

Figure 5 shows the variation of the condensate film thickness along the length of the condenser section with three different ΔT's corresponding to cases 5, 9, 16 as listed in Table 3. These values of the condensate film thickness were calculated using the analysis presented in Section 3.1 as well as Nusselt's solution. Since the results for both the inner and outer walls were so close to each other, only the outer wall results are plotted here. It is clearly seen that the present results including the effects of interfacial shear are greater than Nusselt's predictions along the condenser with an increasing trend toward the adiabatic section. This is because the interfacial shear stress reduces the velocity of the falling liquid film and thus results in a thicker liquid film. Figure 5 also shows that as ΔT increases, the deviation increases between Nusselt's solution and the results that include the effect of interfacial shear. The higher values of ΔT correspond to larger mass flow rates, which increase the effect of the vapor shear when the vapor temperature remains the same. For the present experiment, the vapor temperature T_v increased as ΔT increased, so the effect of the vapor shear was less pronounced

Table 3 Reflux condensation heat transfer coefficients for the concentric annular thermosyphon

1	2	3	4	5	6	7	8	9	10	11	12	13
Case No.	Working fluid	$T_v - T_{w,I}$, °C	$T_v - T_{w,O}$, °C	$\left.\frac{\Gamma}{\mu}\right\|_{L,I}$	$\left.\frac{\Gamma}{\mu}\right\|_{L,O}$	$\mathrm{Re}_{v,h}$	$\frac{\bar{h}_I}{k_L}\left(\frac{\nu_L^2}{g}\right)^{1/3}_{P,I}$	$\frac{\bar{h}_I}{k_L}\left(\frac{\nu_L^2}{g}\right)^{1/3}_{N,I}$	$\frac{\bar{h}_I}{k_L}\left(\frac{\nu_L^2}{g}\right)^{1/3}_{E,I}$	$\frac{\bar{h}_O}{k_L}\left(\frac{\nu_L^2}{g}\right)^{1/3}_{P,O}$	$\frac{\bar{h}_O}{k_L}\left(\frac{\nu_L^2}{g}\right)^{1/3}_{N,O}$	$\frac{\bar{h}_O}{k_L}\left(\frac{\nu_L^2}{g}\right)^{1/3}_{E,O}$
1	Acetone	7.20	6.62	21.6	20.3	2865.2	0.3165	0.3335	0.2940	0.3238	0.3204	0.3490
2	Acetone	12.00	9.60	29.4	28.6	3686.5	0.2827	0.3000	0.2930	0.2859	0.303	0.3340
3	Acetone	14.90	14.60	43.4	41.5	4947.5	0.2456	0.2629	0.2497	0.2470	0.2643	0.3182
4	Acetone	18.50	18.50	53.9	53.9	5793.6	0.2270	0.2441	0.2436	0.2270	0.2441	0.3031
5	Acetone	23.80	23.70	69.2	69.0	6858.9	0.2067	0.2239	0.2139	0.2070	0.2242	0.2858
6	Acetone	30.60	29.80	88.6	87.0	8030.6	0.1879	0.2055	0.2008	0.1894	0.2069	0.2749
7	Acetone	37.83	36.43	110.7	107.8	9198.6	0.1725	0.1905	0.2170	0.1744	0.1923	0.2617
8	Freon 113	13.69	13.20	37.6	36.6	7511.3	0.2674	0.2791	0.2751	0.2699	0.2817	0.3144
9	Freon 113	17.50	18.75	48.4	50.9	9431.8	0.2440	0.2560	0.2447	0.2397	0.2517	0.2783
10	Freon 113	20.73	19.58	50.7	48.6	9931.3	0.2373	0.2505	0.2493	0.2409	0.2541	0.3178
11	Freon 113	30.20	29.30	78.1	76.4	13448.1	0.2033	0.2170	0.2116	0.2050	0.2186	0.2733
12	Freon 113	30.85	29.30	80.1	77.2	13433.6	0.2010	0.2144	0.2247	0.2039	0.2172	0.2775
13	Freon 113	30.40	32.77	111.8	118.1	14323.2	0.1801	0.1925	0.2087	0.1764	0.1889	0.2232
14	Freon 113	39.40	38.05	130.6	127.3	16295.9	0.1681	0.1817	0.1885	0.1698	0.1833	0.2289
15	Freon 113	39.60	38.10	130.7	127.0	16325.4	0.1680	0.1817	0.1811	0.1699	0.1835	0.2365
16	Freon 113	40.05	40.90	169.7	172.3	16889.7	0.1522	0.1658	0.1790	0.1513	0.1649	0.2093

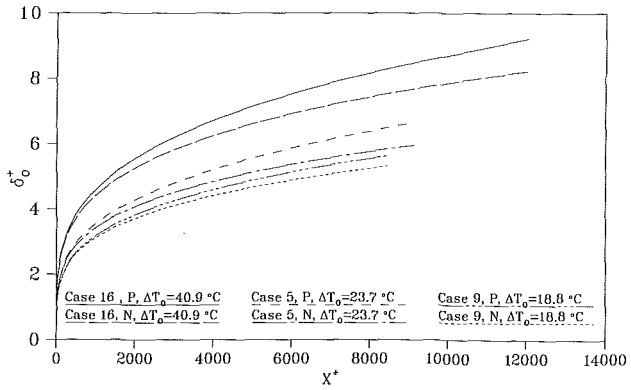

Fig. 5 Variation of the outer wall condensate film thickness of the annular thermosyphon along the condenser

than if the vapor temperature was held constant. Since the film thickness is inversely proportional to the heat transfer coefficient, smaller values of heat transfer are predicted by the analysis including the effect of interfacial shear than by Nusselt's theory.

5 Conclusions

Flooding and reflux heat transfer coefficients determine the performance characteristics of two-phase thermosyphons. A series of experiments were performed to examine the flooding limitation and the reflux heat transfer coefficients for a conventional and a concentric annular thermosyphon. The experimental results for the heat transfer coefficient were compared with values calculated by extending Nusselt's theory to include the variation of the interfacial shear along the length of the condenser section. It was found that for conventional and annular thermosyphons at low liquid Reynolds numbers, the experimental data for the heat transfer coefficients agreed with the predicted values, but at higher liquid Reynolds numbers the predicted values fell below the experimental data. This significant increase in the heat transfer coefficient was attributed to the increase in the liquid film surface area as well as the mixing action due to waves at the vapor–liquid interface. An improved correlation was obtained to predict the flooding limit for conventional thermosyphons using present and previous experimental data for different working fluids. To propose a valid correlation for predicting the flooding limit of concentric annular thermosyphons, many more experimental data using different working fluids and annular sizes are required.

References

Andros, F. E., and Florchuetz, L. W., 1978, "The Two-Phase Closed Thermosyphon: An Experimental Study With Flow Visualization," *Two-Phase Transfer and Reactor Safety*, T. N. Verziroglu, ed., Hemisphere, Washington, DC, pp. 1231–1267.

Bayley, F. J. and Bell, N., 1957, "Cooling Turbine Blades," *Engineering*, Vol. 183, pp. 300–302.

Bezrodnyi, M. K., 1978, "The Upper Limit of Maximum Heat Transfer Capacity of Evaporative Thermosyphons," *Teploenergetika*, Vol. 25, pp. 63–66.

Chen, S. J., Reed, J. G., and Tien, C. L., 1984, "Reflux Condensation in a Two-Phase Closed Thermosyphon," *Int. J. Heat Mass Transfer*, Vol. 27, No. 9, pp. 1587–1594.

Cohen, H., and Bayley, F. J., 1955, "Heat Transfer Problems of Liquid-Cooled Gas-Turbine Blades," *Proc. Instn. Mech. Engrs.*, Vol. 169, pp. 1063–1080.

Faghri, A., and Chow, L. C., 1987, "Annular Condensation Heat Transfer in a Microgravity Environment," *Proceedings of AIAA 22nd Thermophysics Conference*, Hawaii, AIAA paper No. 87-1533.

Faghri, A., and Seban, R. A., 1985, "Heat Transfer in Wavy Liquid Films," *Int. J. Heat Mass Transfer*, Vol. 28, No. 2, pp. 506–508.

Fukano, T., Chen, S. J., and Tien, C. L., 1983, "Operating Limits of the Closed Two-Phased Thermosyphon," *ASME-JSME Thermal Engineering Joint Conference*, pp. 95–101.

Groll, M., and Spendel, Th., 1984, "Thermal Behavior of High-Performance Closed Two-Phase Thermosyphons," *Proc. of 5th Int. Heat Pipe Conf.*, pp. 30–35.

Hurich, W., 1980, "Fahrbahnheizung mittels Warmerohren," Diploma thesis, Institut fur Thermodynamik und Warmetechnik, Universitat Stuttgart, Federal Republic of Germany.

Imura, H., Sasaguchi, K., and Kozai, H., 1983, "Critical Heat Flux in a Closed Two-Phase Thermosyphon," *Int. J. Heat Mass Transfer*, Vol. 26, No. 8, pp. 1181–1188.

Imura, H., Kusuda, H., and Funatsu, S., 1977, "Flooding Velocity in a Countercurrent Annular Two-Phase Flow," *Chem. Engng Sci.*, Vol. 32, pp. 79–87.

Katto, Y., 1978, "Generalized Correlation for Critical Heat Flux of the Natural Convection Boiling in Confined Channels," *Trans. Japan. Soc. Mech. Engrs.*, Vol. 44, pp. 3908–3911.

Kutateladze, S. S., 1972, "Elements of Hydrodynamics of Gas-Liquid Systems," *Fluid Mechanics—Soviet Research*, Vol. 1, pp. 29–50.

Larkin, B. S., 1981, "An Experimental Study of the Temperature Profiles and Heat Transfer Coefficients in a Heat Pipe for a Heat Exchanger," *Advances in Heat Pipe Technology*, D. A. Reay, ed., Pergamon Press, Oxford, pp. 177–191.

Larkin, B. S., 1971, "An Experimental Study of the Two-Phase Thermosyphon Tube," *Trans. C.S.M.E.*, Vol. 14, pp. I–VIII.

Lee, A., and Bedrossian, A., 1978, "The Characteristics of Heat Exchangers Using Heat Pipes or Thermosyphons," *Int. J. Heat Mass Transfer*, Vol. 21, pp. 221–229.

Liu, J. S. K., Collier, R. P., and Cudnik, R. A., 1978, "Flooding Countercurrent Steam-Water Flow in an Annulus," *Topics in Two-Phase Heat Transfer and Flow*, ASME, New York, pp. 107–113.

Long, E. L., 1963, "The Long Thermopile," *Proceedings of the Permafrost International Conference*, pp. 487–491.

Naff, S. A., and Whitebeck, J. F., 1973, "Steady State Investigation of Entrainment and Countercurrent Flow in Small Vessels," Topical Meeting on Water Reactor Safety, Conference paper No. F30304, p. 212.

Negishi, K., 1984, "Thermo-Fluid Dynamics of Two-Phase Thermosyphons," *Proc. of 5th Int. Heat Pipe Conf.*, Part IV, pp. 193–200.

Nguyen-Chi, H., Groll, M., and Dang-Van, Th., 1979, "Experimental Investigation of Closed Two-Phase Thermosyphons," *AIAA 14th Thermophysics Conf.*, pp. 1079–1106.

Nguyen-Chi, H., and Groll, M., 1981, "Entrainment or Flooding Limit in a Closed Two-Phase Thermosyphon," *Advances in Heat Pipe Technology*, Pergamon Press, Oxford, 147–162.

Onosovskii, V. V., Sokolow, V. S., Buchko, N. A., and Obraztsov, Yu. N., 1972, "Investigation of Thermopiles Filled With a Low-Boiling Liquid," *Heat Transfer—Soviet Res.*, Vol. 4, pp. 49–55.

Prenger, F. C., 1984, "Performance Limits of Gravity-Assisted Heat Pipes," *Proc. of 5th Int. Heat Pipe Conference*, Part 1, pp. 1–5.

Sakhuja, R. K., 1973, "Flooding Constraint in Wickless Heat Pipes," ASME Paper No. 73-WA/HT-7.

Seban, R. A., and Faghri, A., 1984, "Film Condensation in a Vertical Tube With a Closed Top," *Int. J. Heat Mass Transfer*, Vol. 27, No. 6, pp. 944–948.

Tanaka, O., Yamakaga, H., Ogushi, T., Murakami, M., and Tanaka, Y., 1981, "Snow Melting Using Heat Pipes," *Advances in Heat Pipe Technology*, D. A. Reay, ed., Pergamon Press, Oxford, pp. 11–23.

Tien, C. L., and Chung, K. S., 1978, "Entrainment Limits in Heat Pipes," *Proceedings of 3rd Int. Heat Pipe Conference*, Palo Alto, CA, pp. 36–40.

Vasiliev, L. L., Vaaz, S. L., Grakovich, L. P., and Sedelkin, V. M., 1981, "Heat Transfer Studies for Heat Pipe Cooling and Freezing of Ground," *Advances in Heat Pipe Technology*, D. A. Reay, ed., Pergamon Press, Oxford, pp. 63–71.

Wallis, G. B., 1969, *One-Dimensional Two-Phase Flow*, McGraw-Hill, New York.

Wallis, G. B., and Makkenchery, S., 1974, "The Hanging Film Phenomenon in Vertical Annular Two-Phase Flow," ASME *Journal of Fluids Engineering*, No. 3, pp. 297–298.

Weber-Carstanjen, C. T., and Busse, C. A., 1984, "Liquid-Vapor Interaction in Vertical Gravity-Assisted Heat Pipes," *Proc. of 5th Int. Heat Pipe Conf.*, Part II, pp. 7–12.

Approximate Solution—One-Dimensional Energy Equation for Transient, Compressible, Low Mach Number Turbulent Boundary Layer Flows

J. Yang

J. K. Martin

Engine Research Center,
Department of Mechanical Engineering,
University of Wisconsin–Madison,
Madison, WI 53706

Unsteady surface heat-flux and temperature profiles in the transient, compressible, low Mach number, turbulent boundary layer typically found in internal combustion engines have been determined by numerically integrating a linearized form of the one-dimensional energy equation. An empirical relation for μ_t/μ has been used to consider turbulent conductivity. Approximate solutions have been acquired by multiparameter fits to the numerical solutions. Comparisons of the approximate solutions with motored engine experiments show good agreement.

1 Introduction

Transient, low Mach number, compressible boundary layers exist in the combustion chamber of internal combustion engines where boundary movement by the piston and combustion cause significant transient pressure variations. The time-dependent three-dimensional turbulent flow, significant pressure change, and combustion make it necessary to model in-cylinder processes with multidimensional models. Because the boundary layer is, in general, thin relative to the grid size of normal three-dimensional calculations, and because typical turbulence models are not applicable in the viscous sublayer, some relationship describing the boundary layer must be employed to determine temperatures and velocities at the computational nodes adjacent to the wall. For example, the three-dimensional hydrodynamic computer program KIVA (Amsden et al., 1985) uses the law of the wall to calculate surface friction and heat flux. However, application of the law of the wall to calculate heat flux may produce errors since the analogy between velocity and temperature no longer exists when the pressure change becomes significant. A different relationship for this type of turbulent boundary layer is necessary, even if only the pressure change is considered.

Heat transfer in engines is a very complicated phenomenon (Borman and Nishiwaki, 1987). Although in-cylinder heat transfer is essentially three dimensional, it is difficult to study the three-dimensional turbulent boundary layer either analytically or numerically. A one-dimensional study has been done here. In addition, the analysis here considers only the effect of the pressure change on the boundary layer, which corresponds to the actual engine condition during compression and the case of a motored engine. The effects of combustion on the boundary layer remain to be considered.

In the current study, a linearized and normalized partial differential equation for the transient compressible turbulent boundary layer has been formulated. Its response to a unit step function, which corresponds to a step pressure increase, is unique. By applying multiparameter curve fitting to the numerical solution of the step function response, simple functions have been found that can also be seen as an approximate solution. Then, by employing Duhamel's theory, the instantaneous surface heat flux or the temperature distribution in the boundary layer for an arbitrary pressure history can be determined.

2 Previous Studies

Efforts to solve the one-dimensional energy equation analytically have been pursued for some time (Dao et al., 1973; Elser, 1955; Greif et al., 1978; Isshiki and Nishiwaki, 1970; Nikanjam and Greif, 1978; Oguri, 1960; Pfriem, 1940). In general, the energy equation is linearized by the elimination of nonlinear terms. First, a Lagrangian coordinate is used to eliminate the convective term. Then, a dependent variable $\phi = T/T_\infty$ is introduced to eliminate the pressure term. For laminar flow, it is not difficult to solve the linearized PDE (Greif et al., 1978; Isshiki and Nishiwaki, 1970; Nikanjam and Greif, 1978; Pfriem, 1940). However, for the compressible turbulent boundary layer, determining the turbulent conductivity k_t correctly and solving the equation becomes more difficult. Elser (1955) and Oguri (1960) introduced an effective conductivity for turbulent flow

$$\frac{k}{k_1} = \frac{T}{T_1}\left[1 + \left(\frac{P}{P_1}\right)^{-1/2}\frac{y}{y_1}\right]$$

This relation neglects the influence of local flow, the pressure term incorrectly predicts that increasing pressure will decrease the conductivity in the same Lagrangian coordinate, and the linear increase with y means the viscous-dominated layer is neglected. Dao et al. (1973) have also modeled the turbulent conductivity according to

$$\frac{k_t}{k} = 0.00156\left(\frac{P_0}{P_1}\right.$$

$$\left.\cdot\frac{c^2\omega}{\nu_w}\frac{T_w}{T_0}\frac{r}{c}SR\cdot CR\right)^{0.75}\left(\frac{S}{c}\right)^{0.14}\left(\frac{T_w}{T_b}\right)^{0.58}$$

They also added a term to the energy equation to include effects from large-scale turbulence. Hence the effects of turbulence were considered by both turbulent conductivity and a new term in the energy equation. Because the turbulent conductivity is related only to global flow information rather than local flow information, the local heat flux cannot be modeled correctly if the air flow in the central core is not well behaved. Furthermore, it is necessary to determine constants that depend on specific experimental data for application of this model.

Contributed by the Heat Transfer Division for publication in the JOURNAL OF HEAT TRANSFER. Manuscript received by the Heat Transfer Division January 26, 1988. Keywords: Modeling and Scaling, Transient and Unsteady Heat Transfer, Turbulence.

In the studies mentioned, the initial conditions were very simple; initial gas temperature was uniform and equal to the wall temperature. However, in IC engines, the wall temperature is typically higher than the gas temperature during the intake process and the initial boundary layer is probably formed during the intake process. At some point during the compression process $T_\infty = T_w$; however, this does not mean that the gas temperature is uniform, and the heat flux is zero.

3 Linearized and Normalized Energy Equation

The following assumptions and restrictions were used in the derivation of the linearized energy equation:

1 Derivatives parallel to the wall are assumed to be zero, i.e., the phenomenon is assumed to be uniform parallel to the wall. This is probably a reasonable assumption for engine flows that are dominated by swirl motion. However for engine flows that are not swirl-dominated, it is likely that this assumption would not be valid.

2 The mechanisms for momentum and heat transfer are similar to those occurring in boundary layers of turbulent, steady-state, incompressible flows. Thus relationships relating the turbulent viscosity to the absolute viscosity from incompressible flow are assumed to be acceptable. In addition, the turbulent viscosity is assumed to be proportional to the turbulent conductivity. Again these assumptions are most likely to be valid in engines with swirl-dominated flows. In any environment, large-scale transport of momentum from interactions of the boundary layer and the free stream or core turbulence would invalidate these assumptions.

3 The pressure is assumed to be uniform in space, i.e., $P = P(t)$ only. This is typically true in engines in the absence of knock, as the time to achieve pressure equilibrium is very short relative to other phenomena in the combustion chamber.

4 The gas conductivity is proportional to the absolute gas temperature.

5 The gas in the chamber is assumed to be ideal.

The one-dimensional energy equation for a pure ideal gas

$$\rho C_p \frac{\partial T}{\partial t} + \rho v C_p \frac{\partial T}{\partial y} = \frac{\partial}{\partial y}\left((k + k_t)\frac{\partial T}{\partial y}\right) + \frac{dP}{dt} \tag{1}$$

can be expressed in Lagrangian coordinates

$$\rho C_p \frac{\partial T}{\partial t} = \frac{\rho}{\rho_0}\frac{\partial}{\partial y'}\left(\frac{\rho}{\rho_0} k\left(1 + \frac{k_t}{k}\right)\frac{\partial T}{\partial y'}\right) + \frac{dP}{dt} \tag{2}$$

The relation between Lagrangian coordinates and Eulerian coordinates is

$$y' = \int_0^y \frac{\rho}{\rho_0}\, dy \tag{3}$$

Since $\rho = P/RT$, $R = C_p - C_v$, and $\lambda = C_p/C_v$, equation (2) can be expressed as

$$\frac{\partial T}{\partial t} = \frac{k_0}{\rho_0 C_p}\frac{\partial}{\partial y'}\left(\frac{k\rho}{k_0\rho_0}\left(1 + \frac{k_t}{k}\right)\frac{\partial T}{\partial y'}\right) + \frac{\lambda - 1}{\lambda}\frac{T}{P}\frac{dP}{dt} \tag{4}$$

The following relations can be used to simplify equation (4). Far away from the wall, the gas is assumed to be compressed isentropically

$$\frac{P}{P_0} = \left(\frac{T_\infty}{T_0}\right)^{\frac{\lambda}{\lambda - 1}} \tag{5}$$

The assumption that gas conductivity is proportional to absolute temperature, following Isshiki and Nishiwaki (1970), gives

$$\frac{k\rho}{k_0\rho_0} = \frac{P}{P_0} \tag{6}$$

The relation between k and μ can be described by

$$\frac{k_t}{k} = \frac{\mathrm{Pr}}{\mathrm{Pr}_t}\frac{\mu_t}{\mu} \tag{7}$$

Finally, following Isshiki and Nishiwaki (1970), the dependent variable

$$\phi(y', t) = \frac{T(y', t)}{T(\infty, t)} - 1 \tag{8}$$

Equation (4) becomes

$$\frac{\partial \phi}{\partial t} = \alpha_0 \frac{P}{P_0}\frac{\partial^2 \phi}{\partial y'^2} + \alpha_0 \frac{P}{P_0}\frac{\partial}{\partial y'}\left(\frac{\mathrm{Pr}}{\mathrm{Pr}_t}\frac{\mu_t}{\mu}\frac{\partial \phi}{\partial y'}\right) \tag{9}$$

Nomenclature

a = constant = 0.06
B = wall roughness constant
C = empirical constant
c = engine clearance height at TDC
C_p = specific heat at constant pressure
C_v = specific heat at constant volume
CR = engine compression ratio
k = gas conductivity
l = characteristic length $= \mu_w/(\kappa\rho_0 u^*)$
n = engine speed, rpm
P = gas pressure
Pr = Prandtl number
q = heat flux
R = gas constant
r = radius from cylinder centerline
S = instantaneous distance between cylinder head and piston of engine
SR = engine swirl ratio
T = gas temperature
t = time
U = dimensionless variable as part of ϕ
$\bar{U}$ = unit-step-function response of U
u^* = friction velocity $= (\tau_w/\rho)^{1/2}$
V = dimensionless variable as part of ϕ
y = coordinate normal to wall
y' = Lagrangian transform coordinate
y^+ = dimensionless distance $= \dfrac{u^*}{\mu_w}\int_0^y \rho dy$
α = thermal diffusivity
ϵ = $\mathrm{Pr}/\mathrm{Pr}_t$
η = dimensionless distance $= y'/l$
θ = dimensionless time
κ = Kärmän constant = 0.41
λ = specific heat ratio $= C_p/C_v$
μ = viscosity
ν = kinematic viscosity
ρ = density
τ = transformed time $= \int_0^t \dfrac{P}{P_0}\dfrac{\alpha_0}{l^2}\, dt$
ϕ = dimensionless temperature $= (T/T_\infty - 1)$
ω = engine speed, rpm $\cdot 2\pi/60$

Subscripts

0 = initial conditions
1 = standard conditions
b = bulk
t = turbulent
tank = intake tank
max = maximum in cylinder
min = minimum in cylinder
w = wall
∞ = outside boundary layer

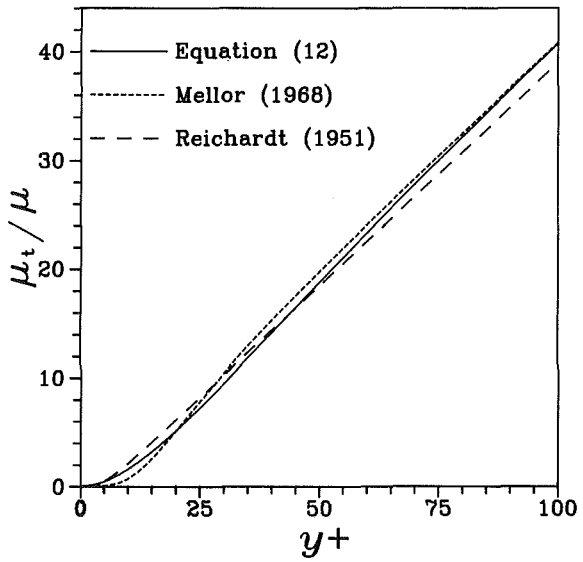

Fig. 1 Ratio of turbulent viscosity to molecular viscosity

where $\alpha_0 = k_0/\rho_0 C_p$. The boundary conditions and initial condition of equation (9) are

$$\phi(0, t) = \frac{T(0, t)}{T(\infty, t)} - 1 = f(t)$$
$$\phi(\infty, t) = 0 \tag{10}$$
$$\phi(y', 0) = \frac{T(y', 0)}{T(\infty, 0)} - 1 = f(0)g(y')$$

where $g(y')$ is a function of y', corresponding to the initial boundary layer existing at the beginning of the compression process.

The derivation up to this point has followed the work by Isshiki and Nishiwaki (1970), with exception of the turbulent diffusion term and the initial condition, which is nonzero. Isshiki and Nishiwaki made the transformation $d\tau = (P/P_0)dt$ and solved the equation. When the turbulent diffusion term is considered, it is more difficult to solve equation (9). First, a relation for μ_t/μ must be considered. Empirical expressions of μ_t/μ for incompressible turbulent flow include:

Reichardt (1951):

$$\mu_t/\mu = \kappa(y^+ - 5\tanh(y^+/5)) \tag{11a}$$

Mellor (1968):

$$\mu_t/\mu = (\kappa y^+)^4/[(\kappa y^+)^3 + 328.5)] \tag{11b}$$

Both relations are plotted in Fig 1. To make the energy equation easier to solve, a new relation was formed to fit the Reichardt and Mellor relations. This new relation is

$$\mu_t/\mu = \kappa y^+[1 - \exp(-2a\kappa y^+)] \tag{12}$$

where $a = 0.06$. This equation is compared with the other two in Fig. 1. As shown, results are very similar for three relations.

Next, a characteristic length was chosen to normalize the energy equation. Because the one-dimensional model describes local phenomena, the characteristic length l should contain only local properties. An appropriate characteristic length is given by

$$l = \mu_w/(\kappa\rho_0 u^*) \tag{13}$$

The nondimensional length will be

$$\eta = y'/l \tag{14}$$

The advantage of such a choice of l can be seen below. Since

$$\kappa y^+ = \frac{\kappa\rho_0 u^*}{\mu_w}\int_0^y \frac{\rho}{\rho_0}\,dy = \eta \tag{15}$$

the relation (12) can be expressed as

$$\mu_t/\mu = \eta[1 - \exp(-2a\eta)] \tag{16}$$

Instead of the transformation $d\tau = (P/P_0)dt$, the transformation

$$d\tau = \frac{P}{P_0}\frac{\alpha_0}{l^2}\,dt \tag{17}$$

is used to define the nondimensional time. Substituting equations (14)–(17) into equations (9) and (10), and letting $\epsilon = \mathrm{Pr}/\mathrm{Pr}_t = \text{const}$, the linearized and normalized energy equation is given by

$$\frac{\partial\phi}{\partial\tau} = \frac{\partial^2\phi}{\partial\eta^2} + \epsilon\frac{\partial}{\partial\eta}\left[\eta(1 - \exp(-2a\eta))\frac{\partial\phi}{\partial\eta}\right] \tag{18}$$

with initial and boundary conditions given by

$$\phi(0, \tau) = f(\tau)$$
$$\phi(\infty, \tau) = 0 \tag{19}$$
$$\phi(\eta, 0) = f(0)g(\eta).$$

The function $\phi(\eta, \tau)$ can be defined as the sum of the two functions to deal with the two nonhomogeneous conditions

$$\phi(\eta, \tau) = U(\eta, \tau) + V(\eta, \tau) \tag{20}$$

Since equation (18) itself is a linear equation, the problem can be divided into time-dependent (U) and (V) problems

$$\frac{\partial U}{\partial\tau} = \frac{\partial^2 U}{\partial\eta^2} + \epsilon\frac{\partial}{\partial\eta}\left[\eta(1 - \exp(-2a\eta))\frac{\partial U}{\partial\eta}\right]$$
$$U(0, \tau) = f(\tau) - f(0) \tag{21}$$
$$U(\infty, \tau) = 0$$
$$U(\eta, 0) = 0$$

and

$$\frac{\partial V}{\partial\tau} = \frac{\partial^2 V}{\partial\eta^2} + \epsilon\frac{\partial}{\partial\eta}\left[\eta(1 - \exp(-2a\eta))\frac{\partial V}{\partial\eta}\right]$$
$$V(0, \tau) = f(0) \tag{22}$$
$$V(\infty, \tau) = 0$$
$$V(\eta, 0) = f(0)g(\eta)$$

Duhamel's theory can be employed in solving equation (21). Once the unit-step-function response $\bar{U}$ of equation (21) is found through

$$\frac{\partial\bar{U}}{\partial\tau} = \frac{\partial^2\bar{U}}{\partial\eta^2} + \epsilon\frac{\partial}{\partial\eta}\left[\eta(1 - \exp(-2a\eta))\frac{\partial\bar{U}}{\partial\eta}\right]$$
$$\bar{U}(0, \tau) = 1$$
$$\bar{U}(\infty, \tau) = 0 \tag{23}$$
$$\bar{U}(\eta, 0) = 0$$

the solution of equation (21) can be acquired by Duhamel's integral

$$U(\eta, \tau) = \int_{\theta=0}^{\tau}\bar{U}(\eta, \tau - \theta)\frac{df(\theta)}{d\theta}\,d\theta \tag{24a}$$

and

$$\frac{\partial U(\eta, \tau)}{\partial\eta}\bigg|_{\eta=0} = \int_{\theta=0}^{\tau}\frac{\partial\bar{U}(\eta, \tau - \theta)}{\partial\eta}\bigg|_{\eta=0}\frac{df(\theta)}{d\theta}\,d\theta \tag{24b}$$

The solution of equation (22) can be acquired from the solutions of equation (23). The function $f(0)g(\eta)$ in equation (22) describes the initial boundary layer formed before compres-

sion in a period of time τ_0. If θ represents a different dimensionless time variable starting at $\tau = -\tau_0$, the thickness of the initial boundary layer at $\theta = 0$ will be zero, and equation (22) can be rewritten as

$$\frac{\partial V}{\partial \theta} = \frac{\partial^2 V}{\partial \eta^2} + \epsilon \frac{\partial}{\partial \eta}\left[\eta(1-\exp(-2a\eta))\frac{\partial V}{\partial \eta}\right]$$
$$V(0,\theta) = f(0) \tag{25}$$
$$V(\infty,\theta) = 0$$
$$V(\eta,0) = 0$$

Because equation (25) is of the same form as equation (23), with similar initial and boundary conditions, the solution will be similar, that is,

$$V(\eta,\theta) = f(0)\bar{U}(\eta,\tau)$$
$$\left.\frac{\partial V(\eta,\theta)}{\partial \eta}\right|_{\eta=0} = f(0)\left.\frac{\partial \bar{U}(\eta,\tau)}{\partial \eta}\right|_{\eta=0} \tag{26}$$

Rewriting in terms of τ, equations (26) become

$$V(\eta,\tau) = f(0)\bar{U}(\eta,\tau+\tau_0)$$
$$\left.\frac{\partial V(\eta,\tau)}{\partial \eta}\right|_{\eta=0} = f(0)\left.\frac{\partial \bar{U}(\eta,\tau+\tau_0)}{\partial \eta}\right|_{\eta=0} \tag{27}$$

4 Approximate Solutions of Equation (23)

Analytical solutions to equation (23) have been acquired by employing a regular perturbation method. Here, however, are described the approximate solutions found by fitting numerical solutions of these equations.

The numerical solutions of equation (23) were acquired using a finite difference procedure, similar to that suggested by Patankar (1980). In this procedure, the region of interest is subdivided into N control volumes, and the finite difference form of the equations is integrated over each of these control volumes. The Crank–Nicolson scheme was used in the discretization process, and the acquired algebraic equations were then solved directly. In computing the numerical solutions, N was as large as 10,000 with node spacing $\Delta\eta$ as small as 0.005. Typical time steps $\Delta\tau$ were 3.125×10^{-5}. The constant ϵ in equation (23) was taken as 0.72.

After determining the numerical solutions, a set of functions was fit to the numerical results. This was done to produce simple approximate relations that could be used to replace the empirical relations currently used in multidimensional calculations. The fitted function to the numerical solution of equation (23) is

$$\bar{U}(\eta,\tau) = \exp\left[-\left(\frac{1}{\sqrt{\tau}}+0.06\right)\Big/\left(\frac{1}{\eta}+0.06\right)\right] \tag{28}$$

Comparisons with the numerical solution are shown in Fig. 2. The curve fits match the numerical solution well up to the dimensionless time τ of 2560, which corresponds to the length of time of the compression process for an ordinary IC engine.

Although the derivative of $\bar{U}$ at $\eta = 0$ can be acquired by derivation of equation (28), the result is not very precise. This is because the fit was done considering the whole range of dimensionless distance η(0 to ∞), rather than only considering the range where η approaches zero. To get a more precise derivative of $\bar{U}$ at $\eta = 0$, curve fitting was performed to the numerical value of $\Delta\partial\bar{U}/\partial\eta$ at $\eta = 0$, which is the difference between the numerical solution of equation (23) and the numerical solution of equation (23) with $\epsilon = 0$, i.e., no turbulent diffusion. The reason for not fitting the numerical results of equation (23) directly was to avoid fitting a curve

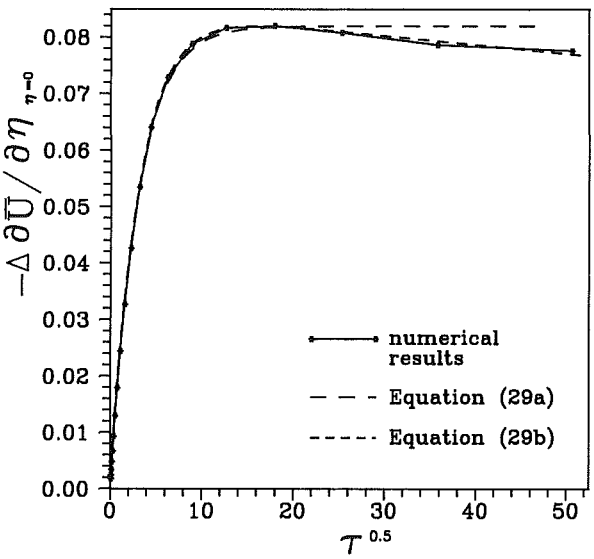

Fig. 3 Difference of derivatives of $\bar{U}$ at the wall surface

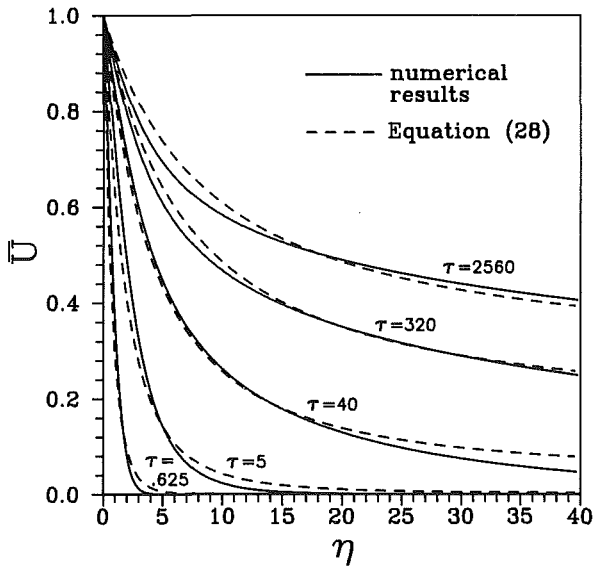

Fig. 2 Dimensionless variable $\bar{U}$ versus dimensionless distance at different dimensionless times

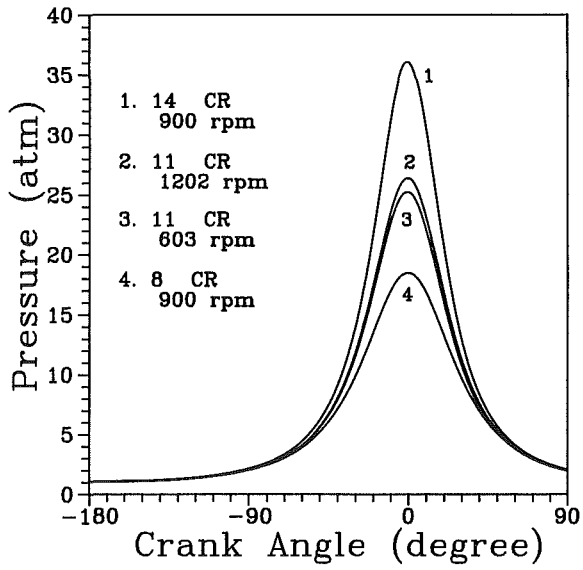

Fig. 4 Engine pressure data from Dao (1972)

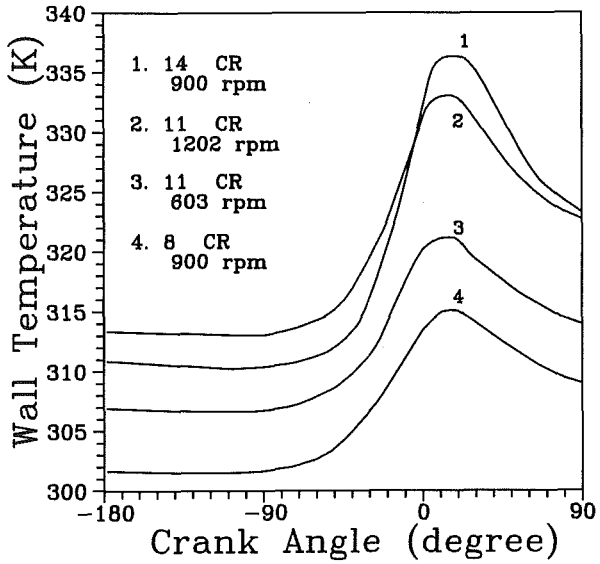

Fig. 5 Wall temperature data from Dao (1972)

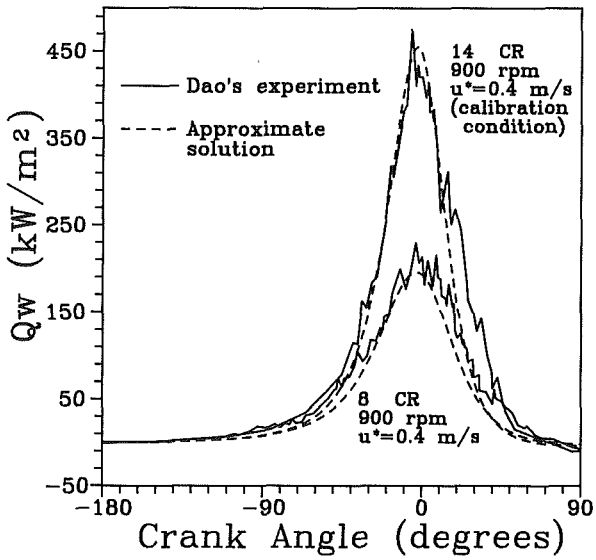

Fig. 7 Surface heat flux for different compression ratios

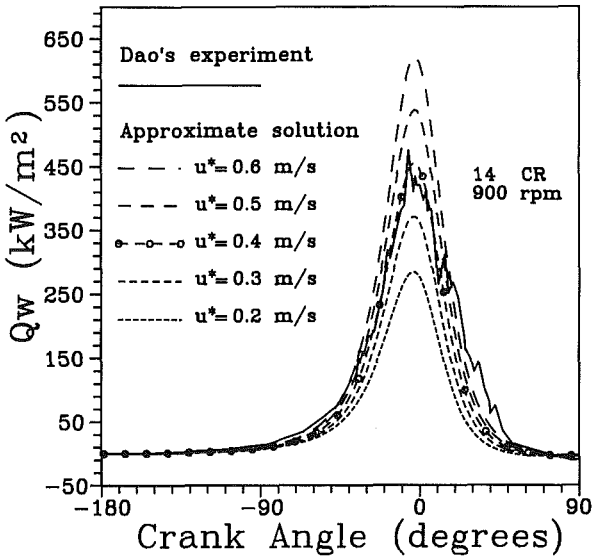

Fig. 6 Comparison of measured heat flux from Dao and sensitivity of model predictions to choice of u^*

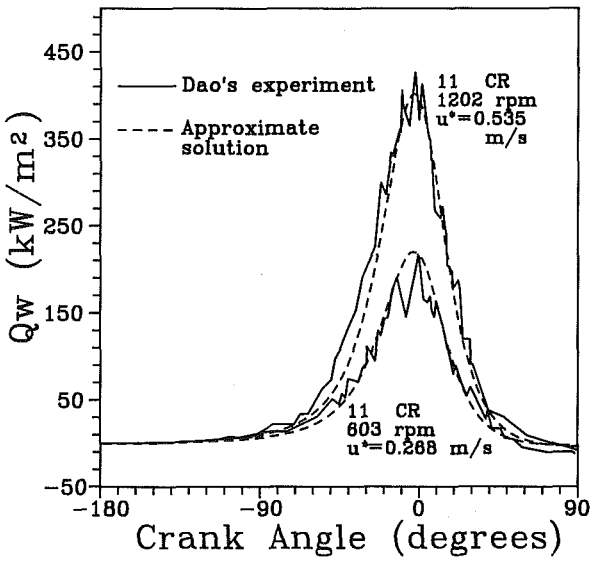

Fig. 8 Surface heat flux for different engine speeds

that approaches infinity when dimensionless time approaches zero. The acquired function from curve fitting is

$$\Delta \left.\frac{\partial \bar{U}}{\partial \eta}\right|_{\eta=0} = -0.082\,(1-\exp(-\sqrt{\tau}/3)) \qquad (29a)$$

or

$$\Delta \left.\frac{\partial \bar{U}}{\partial \eta}\right|_{\eta=0} = -0.085(1-\exp(-\sqrt{\tau}/3.1)) + 0.00016\sqrt{\tau} \qquad (29b)$$

The derivatives calculated from equations (29*a*) and (29*b*) are compared to the results from the numerical solution in Fig. 3. Equation (29*b*) is a better fit at larger τ, while equation (29*a*) is adequate for $\sqrt{\tau}$ less than 16, and is a simpler relation. Finally, since the derivative of $\bar{U}$ for laminar flow is known, the derivative of $\bar{U}$ at $\eta = 0$ can be expressed as

$$\left.\frac{\partial \bar{U}}{\partial \eta}\right|_{\eta=0} = -\frac{1}{\sqrt{\pi\tau}} + \Delta \left.\frac{\partial \bar{U}}{\partial \eta}\right|_{\eta=0} \qquad (30)$$

5 Comparisons With Experimental Data

The estimated surface heat fluxes were compared with experimental data from Dao (1972). The measurement was performed on a modified Fairbanks–Morse diesel engine, having a cylinder bore and stroke of 79.4 and 101.6 mm, respectively. The intake valve was shrouded to induce swirl in the cylinder, which could be varied by a change in the shroud position. Steady-state measurements of swirl ratio produced a maximum value of 7.15. The cylinder head and piston were both modified to produce a pancake-shaped combustion chamber. The piston-to-head clearance was variable, for compression ratios from 8:1 to 14:1. The surface temperatures were measured by thermistors, one of which was located on each side of a thin pyrex disk, which was flush-mounted to the cylinder head. An analog R-C network was used to determine the heat flux through the pyrex disk. In all tests the engine was operated in a motored condition.

Four specific sets of data from the measurements were chosen to be compared with the approximate solution. Table 1

Table 1 Measurement conditions

Speed, rpm	CR	T_{in}, °C	P_{tank}, kPa	$P_{max} - P_{min}$, kPa
900	8	24.4	137.8	1764.
900	14	24.4	137.8	3550.
603	11	23.9	137.8	2450.
1202	11	23.9	137.8	2570.

shows the measurement conditions. Two of the tests were at the same speed, but different compression ratios, and two of the test were at the same compression ratio but different engine speeds. For all the tests the intake valve was in the same position; hence it is assumed that the swirl ratio SR did not change for these test conditions. Figure 4 shows the pressure histories reduced from the data for each of the run conditions. Peak pressure and rates-of-pressure change are functions of engine speed and compression ratio, as indicated.

The ensemble-averaged wall temperatures for each of the operating conditions are shown in Fig. 5. Wall temperature swings were between 13 and 23 K. Both compression ratio and engine speed affect the average wall temperature and temperature swing.

Because the velocity was not determined in the engine experiments by Dao, it was necessary to estimate the friction velocity for one operating condition, and determine a relation between friction velocity and engine speed so comparison could be made between the experiments and calculation at other operating conditions. There are two steps in determining this relation. First, the relation between the engine speed and in-cylinder mean flow needs to be determined. Second, a relation between the in-cylinder mean flow and the friction velocity is necessary. Many experimental studies of engine flows have shown that the mean swirl velocity is proportional to engine speed (for example, Bopp et al., 1986). Thus we have assumed that the in-cylinder mean flow for this set of experiments is directly proportional to engine speed. Relating the friction velocity to the mean flow, consider the logarithmic overlap layer equation

$$\frac{u}{u^*}=\frac{1}{\kappa}\ln y^+ + B \tag{31}$$

At the outer edge of the boundary layer, y^+ is large and the right-hand side of equation (31) is essentially constant. Hence we have assumed that the friction velocity is proportional to the free-stream or in-cylinder swirl flow. Using these two observations, the relation between u^* and engine speed n can be written

$$u^* = C \cdot n \tag{32}$$

The calculated heat flux is very sensitive to the magnitude of u^*, as shown in Fig. 6. For this case, heat flux at any crank angle varies linearly with friction velocity. This is the particular operating condition for which the friction velocity was determined by best fit to the experimental heat flux. As shown in Fig. 6, $u^*=0.4$ m/s was chosen, giving a value of $C=4.4\times10^{-4}$ m/s•rpm.

Shown in Figs. 7 and 8 are the comparison between the calculated surface heat flux and that measured by Dao, using the estimated value of u^* from equation (32). In general, it appears that the measured and calculated heat flux are in good agreement. The fluctuations observed in the experiment are not present in the approximate solution, as would be expected. Dao attributed these variations to the effects of turbulent eddies on the local heat flux. The measured heat flux appears to increase more rapidly than that predicted by the approximate solutions early in the compression process. This may be due in part to several factors. First, because of shear, the friction velocity will tend to decrease during the compression and expansion strokes. A constant value was used in the calculation. Second, three-dimensional effects may be important during the initial stage of compression, which also were not accounted for. In addition, there are small discrepancies in the peak heat flux, although these are less than 5 percent in every case.

6 Summary

1 The one-dimensional energy equation for the transient, compressible, low Mach number, turbulent boundary layer has been linearized and normalized, utilizing the empirical relation of μ_t/μ from incompressible turbulent boundary layer analysis.

2 Simple approximation solutions of the linearized and normalized energy equations were acquired by multiparameter fits to the numerical solutions.

3 The calculated surface heat flux shows good agreement with measurements from a motored engine.

Acknowledgments

This work was funded by the U.S. Army TACOM, and also in part by the U.S. Army Research Office through the Award for the Center of Excellence in Advanced Propulsion Systems.

References

Amsden, A. A., Ramshaw, J. D., O'Rourke, P. J., and Dukowicz, J. K., 1985, "KIVA: A Computer Program for Two- and Three-Dimensional Fluid Flows With Chemical Reactions and Fuel Sprays," Los Alamos National Lab., LA-10245-MS.

Bopp, S., Vafidis, C., and Whitelaw, J. H., 1986, "The Effect of Engine Speed on the TDC Flow Field in a Motored Reciprocating Engine," SAE Paper No. 860023.

Borman, G. L., and Nishiwaki, K., 1987, "Internal-Combustion Engine Heat Transfer," *Prog. Energy Combust. Sci.*, Vol. 13, pp. 1–46.

Dao, K., 1972, "Heat Transfer With Cyclic Pressure Variations (in Piston Engines)," Ph.D. Thesis, University of Wisconsin–Madison.

Dao, K., Uyehara, O. A., and Myers, P. S., 1973, "Heat Transfer Rates at Gas–Wall Interfaces in Motored Piston Engine," SAE Paper No. 730632.

Elser, K., 1955, "Instationäre Wärmeübertragung bei periodisch, adiabatischer Verdichtung turbulenter Gase," *VDI Forsch.*, Vol. 21, No. 3, pp. 65–74.

Greif, R., Namba, T., and Nikanjam, M., 1978, "Heat Transfer During Piston Compression Including Side Wall and Convection Effects," *Int. J. Heat Mass Transfer*, Vol. 22, pp. 901–907.

Isshiki, N., and Nishiwaki, N., 1970, "Study on Laminar Heat Transfer of Inside Gas With Cyclic Pressure Change on an Inner Wall of a Cylinder Head," *Proc. 4th Int. Heat Transfer Conference*, FC3.5, Paris–Versailles, pp. 1–10.

Mellor, G. L., 1968, *Proc. Symp. Fluidics Internal Flow*, Pennsylvania State University, Pa.

Nikanjam, M., and Greif, R., 1978, "Heat Transfer During Piston Compression," ASME JOURNAL OF HEAT TRANSFER, Vol. 100, pp. 527–530.

Oguri, T., 1960, "Theory of Heat Transfer in the Working Gases of Internal Combustion Engines," *Bulletin of JSME*, Vol. 3, No. 11, pp. 370–377.

Patankar, S. V., 1980, *Numerical Heat Transfer and Fluid Flow*, Hemisphere, Washington, DC.

Pfriem, H., 1940, "Probleme der periodischen Wärmeübertragung mit Bezug auf Kolbenmaschinen," *VDI Forsch.*, Vol. 10, No. 1, pp. 27–40.

Reichardt, H., 1951, *Ann Angew. Math. Mech.*, Vol. 31, p. 7.

Flow and Heat Transfer in the Space Between Two Corotating Disks in an Axisymmetric Enclosure

C. J. Chang

C. A. Schuler

J. A. C. Humphrey

R. Greif

Department of Mechanical Engineering,
The University of California at Berkeley,
Berkeley, CA 94720

A numerical investigation was undertaken to characterize the laminar flow and heat transfer in axisymmetric coaxial corotating shrouded disk configurations. Attention was focused on calculation conditions favoring steady, stable, symmetric solutions of the conservation equations. The justification for this is based on velocity measurements obtained in a test section that matches the numerical configuration. Calculations were performed to investigate the dependence of the flow characteristics on disk angular velocity, disk spacing, and the disk–shroud gap width. Conditions involving a radial throughflow (blowing) and/or an axially directed disk–shroud gap flow were also predicted. In the region of the shroud the results show a strong sensitivity of the flow and heat transfer to variations in the flow Reynolds number (rotation) and Rossby number (blowing). By contrast, the flow was found to be less dependent on the disk spacing and the disk–shroud gap width for the conditions investigated. The introduction of an axially directed disk–shroud gap flow significantly alters the flow and heat transfer characteristics in the region between two disks. This finding is important for the improved design and control of corotating disk systems.

1 Introduction

1.1 The Problem of Interest. Rotating disks give rise to complex unsteady three-dimensional flows that are relevant to geophysical and biochemical systems, and that also have many engineering applications. We are concerned here with the elemental configuration illustrated in Fig. 1, corresponding to magnetic disk storage systems, which are pertinent to the computer industry. In this idealized configuration, several disks are concentrically and equidistantly fixed along a rotatable spindle or hub, and placed in an enclosure where they are made to corotate at high speed. Enclosure asymmetries and the presence of objects between the disks contribute to the highly complex flow patterns that arise in the spaces between and about the disks. These flows affect the transport of heat and particulates that may be present in the enclosure. At high speeds they induce eddy shedding from obstacles, such as magnetic heads and their supporting arms. Such flow and thermal nonuniformities can affect disk rotational stability and the location of a magnetic head relative to the disk. As a result, the read/write characteristics of the head may be drastically affected. Particulates suspended in the flow may lodge in the narrow space between a head and a disk, thus causing severe system failure problems. An improved understanding of the complex flows that arise in real disk storage devices is essential for the proper operation of these systems. In addition, the basic phenomena are also of broad fundamental interest. A study is underway at our institution that has focused on measuring and predicting the flow between a pair of coaxial corotating parallel disks in an axisymmetric enclosure. In this paper we report on the numerical component of this effort pertaining to the laminar flow regime.

Although perhaps less important from the practical point of view, the flow configuration in the laminar regime displays interesting features and its numerical simulation is free from turbulence model uncertainties. Therefore, it also provides the necessary framework for developing and testing a numerical calculation procedure for subsequent turbulent flow calculations. Even this problem is quite formidable and, to render it numerically tractable, attention has been restricted initially to the axisymmetric geometry illustrated in Fig. 1. Two sets of boundary conditions have been investigated, according to the type of throughflow allowed, and both assume steady circumferentially symmetric (axisymmetric) flows. In the first case, corresponding to the boundary conditions shown in Fig. 2(*a*), the possibility of a radially directed throughflow is allowed. This case is possessed of an additional plane of symmetry located halfway between the corotating disks. In the second case, corresponding to the boundary conditions shown in Fig. 2(*b*), various combinations of radially and axially directed

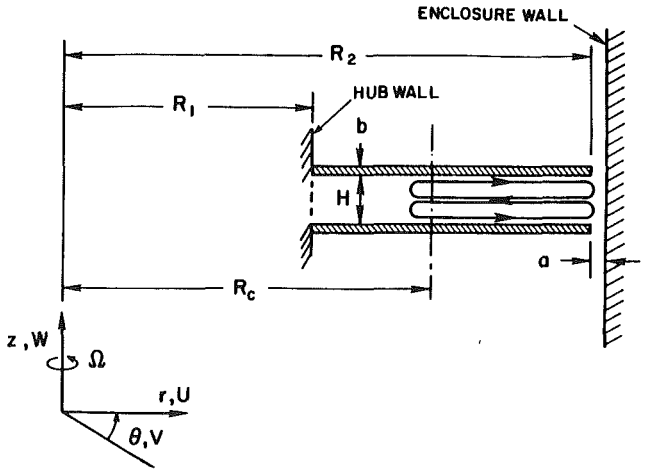

Fig. 1 The elemental flow configuration of interest, with relevant length scales, coordinate system, and velocity components defined

Contributed by the Heat Transfer Division and presented at the National Heat Transfer Conference, Houston, Texas, July 24–27, 1988. Manuscript received by the Heat Transfer Division March 31, 1988. Keywords: Enclosure Flows, Forced Convection, Numerical Methods.

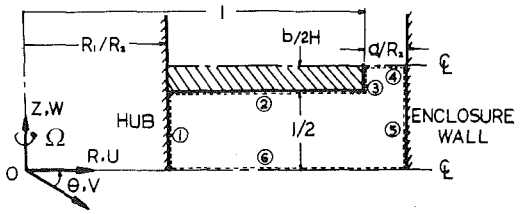

Fig. 2(*b*) Schematic defining the planes where flow calculation boundary conditions are imposed for case of combined radial and axial disk-shroud gap flow

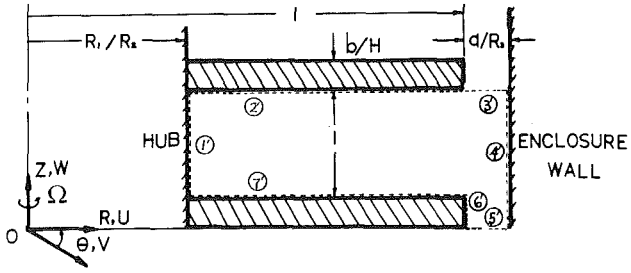

Fig. 2(*a*) Schematic defining the planes where flow calculation boundary conditions are imposed for the case with radial throughflow only

throughflow are examined. Since the axially directed throughflow removes the extra degree of axial symmetry present in the first case, in the second case it is necessary to calculate the flow over the entire region between a pair of corotating disks.

1.2 Related Work. Rotating disk configurations have been investigated extensively and even the literature on highly idealized systems is extensive as a result of the large number of possible geometric arrangements and flow conditions. Of particular interest to this study are the investigations performed in corotating, centrally supported configurations of two or more disks in axisymmetric enclosures with and without a radially directed throughflow in the space between the disks. The basic element of interest is illustrated schematically in Fig. 1, which shows the side view of a pair of centrally clamped coaxial disks corotating at an angular velocity Ω. Due to the imbalance that results from the outward-directed centrifugal force and the associated (weaker) inward-directed radial pressure gradient, fluid in the boundary layer on the disk surface is accelerated radially outward, toward the enclosure or shroud side wall, while the bulk of the fluid core moves radially inward at lower speed toward the hub. The figure also suggests that the two main recirculation cells anticipated in the r–z plane do not significantly penetrate the space between the hub at R_1 and a critical radius Rc that depends on the value of Ω. This is due to the nature of the flow near the hub that, at steady state and in the absence of a source (or sink) throughflow, will approach solid body rotation. Thus, at very small values of Ω one anticipates a steady or quasi-steady streamlined motion between the disks. As Ω increases, the relative motion between the rotating disks and the fixed shroud wall also increases and it is reasonable to expect radial and circumferential flow instabilities to arise, and eventually for a transition to turbulent motion to occur in the region where $r > Rc$.

The flow visualization experiments of Lennemann (1974) for a pair of corotating disks in an axisymmetric enclosure support the above expectations. They reveal two types of instabilities: the first in the form of equi-angular spirals embedded in the disk boundary layer; the second in the form of ruptures of these spirals by large-scale, circumferentially periodic, radially directed inflows and outflows in the space between the disks. The first instability is of the type observed in Ekman boundary layers and has been the subject of considerable research (see Humphrey, 1986). The second is associated with axially directed vortical structures shed from the enclosure side wall, which were observed to rotate at about 8/10 of the rotational speed of the disks. As a result of the latter structures, the bulk of the flow in the space between the disks was observed to be periodically indented to yield the shape of a regular polygon whose number of sides (equivalent to the number of axially aligned vortices) was found to increase with decreasing a/R_2. In particular, for $a/R_2 = \infty$ Lennemann observed a two-lobed polygon structure, while for $a/R_2 = 0.045$ he observed a hexagonal structure. A more recent flow visualization study by Abrahamson et al. (1988) shows that the number of axially aligned vortices increases with increasing values of R_2/H. We have assumed that these trends, which were respectively observed for turbulent flow, also apply to the laminar flow regime.

In Lennemann's experiment, the equi-angular boundary layer spirals were observed for Re $> 3.44 \times 10^4$ approximately, where Re is the Reynolds number defined further below. However, there is no indication in his paper, or in that of Abrahamson et al. (1988), concerning the Re at which the axially aligned flow structures first appear. All observations were made for Re $> 4.30 \times 10^3$.

Kaneko et al. (1977) visualized the flow between corotating disks in a disk pack. At low rotational speeds they observed that the indentations in the core flow could be made to vanish by imposing a radial outflow in the space between the disks.

Detailed measurements of the velocity field in the space between a pair of rotating coaxial finite disks were made by Szeri et al. (1983), primarily in the laminar flow regime, and by Bakke et al. (1973) in the turbulent regime. Both studies investigated the effects of an imposed radial throughflow, but neither examined the influence of the gap width a. Using water as the working fluid, Szeri et al. measured the radial and circumferential components of velocity with a laser-Doppler velocimeter. In their experiment the values of the disk space aspect ratio were $(R_2 - R_1)/H = 74.7$ and 18.8. The disk angular velocity ratios ($\gamma = \Omega_2/\Omega_1$) explored were $\gamma = -1$, 0, and 1. Measurements were also made for the case $\Omega_1 = \Omega_2 = 0$, with radial throughflow. For all the conditions investigated the flows were observed to be unique, and at midradius showed an insensitivity to the boundary conditions in r. For corotating disk flow ($\gamma = 1$) at Re = 965 and without radial throughflow, the authors were unable to detect the radial velocity component. Measurements of the circumferential velocity component revealed that the fluid at the midradius location was essentially in solid body rotation.

Most of the corotating disks flow studies are for configurations with $(R_2 - R_1)/H \gg 1$. Also the effect of radial blowing on the flow in shrouded systems with $(R_2 - R_1)/H \leq 10$ is not well documented. Theoretical analyses (see, for example, Holodniok et al., 1981) predict the existence of multiple steady states in flows with $(R_2 - R_1)/H \gg 1$ in the absence of a surrounding wall. While the number of predicted states increases with increasing angular velocity Ω, the limited experimental information available points to unique and repeatable flows.

1.3 Additional Experimental Evidence. This study is of a computational nature, the calculation procedure having been used to conduct numerical explorations of the parameters of interest. Confidence in the calculations was rigorously established through self-consistent testing of the numerical procedure, and by comparisons with several carefully documented steady flow fields. In this regard the measurements of Szeri et al. have been important for validation purposes. However, at some critical value of Re, the flow of interest is known to develop circumferentially periodic structures whose rotational speed is not necessarily in phase with the rotational speed of the corotating disks. Thus, it is necessary to consider how

restrictive are the calculation assumptions of (*i*) steady, and (*ii*) axisymmetric flow. These considerations are the subject of a separate experimental investigation by Schuler et al. (1988) and two observations that are relevant to the present study are summarized here in order to substantiate assumptions (*i*) and (*ii*).

Laser-Doppler velocimetry measurements of the circumferential velocity component V have been obtained in the space between a pair of corotating disks in an axisymmetric enclosure. The geometric characteristics of the experimental corotating disks are identical to the ones modeled numerically. In both the experiments and the calculations, $R_1 = 0.0564$ m, $R_2 = 0.105$ m, $a = 2.946 \times 10^{-3}$ m, $b = 2.032 \times 10^{-3}$ m, and $H = 9.525 \times 10^{-3}$ m. From these values it follows that $R_1/R_2 = 0.537$, $R_2/H = 11.024$, and $a/R_2 = 0.028$.

Radial profiles of the V velocity component were measured at the midplane location ($Z = 1/2 + b/2H$) between the two disks for 100, 200, and 300 rpm, corresponding to Re = 635, 1270, and 1905, respectively. At each radial position both the time history and time average of V were obtained. The time-averaged results are shown in Fig. 4(*b*) and are discussed below. The total uncertainty in the V component measurements was estimated to be better than about ± 2 percent at any of the radial locations except those nearest the shroud where velocity gradient broadening increases the uncertainty to ± 10 percent.

Detailed time histories of V at various radial locations along the midplane reveal a transition from steady to unsteady flow at about 62 ± 2 rpm (corresponding to Re = 394 ± 13). Between 62 and 300 rpm the V component varies sinusoidally almost everywhere along the midplane, the amplitude of the wave depending on the particular radial location but increasing with disk rotational speed at any radial location. Nevertheless, blow 300 rpm, Schuler et al. show that the structures producing the sinusoidal oscillations are relatively weak and rotate essentially at the disk rotational speed.

The conclusion of this section is that: (*i*) From the point of view of a frame of reference fixed on one of the two corotating disks, the flow is essentially steady; and (*ii*) although structured circumferentially as of 62 ± 2 rpm, the small amplitude sinusoidal character of the oscillations is expected to yield time-averaged V velocities that will not differ markedly from corresponding predictions that assume steady flow. That this is the case for the conditions of interest to this study is shown below.

2 Numerical Calculation Procedure

2.1 Conservation Equations and Boundary Conditions. For steady, axisymmetric, laminar flow conditions, the dimensionless equations describing the transport of momentum and heat of a constant property fluid (air) in the space between a pair of corotating disks are:

Continuity

$$\frac{1}{R}\frac{\partial}{\partial R}(RU) + \frac{\partial W}{\partial Z} = 0 \tag{1}$$

R-Momentum

$$U\frac{\partial U}{\partial R} - \frac{V^2}{R} + W\frac{\partial U}{\partial Z} = -\frac{\partial P}{\partial R} + \frac{1}{\mathrm{Re}}\left[\frac{1}{s}\frac{\partial}{\partial R}\left(\frac{1}{R}\frac{\partial}{\partial R}(RU)\right) + s\frac{\partial^2 U}{\partial Z^2}\right] \tag{2}$$

Θ-Momentum

$$U\frac{\partial V}{\partial R} + \frac{UV}{R} + W\frac{\partial V}{\partial Z} = \frac{1}{\mathrm{Re}}\left[\frac{1}{s}\frac{\partial}{\partial R}\left(\frac{1}{R}\frac{\partial}{\partial R}(RV)\right) + s\frac{\partial^2 V}{\partial Z^2}\right] \tag{3}$$

Z-Momentum

$$U\frac{\partial W}{\partial R} + W\frac{\partial W}{\partial Z} = -s^2\frac{\partial P}{\partial Z} + \frac{1}{\mathrm{Re}}\left[\frac{1}{s}\frac{1}{R}\frac{\partial}{\partial R}\left(R\frac{\partial W}{\partial R}\right) + s\frac{\partial^2 W}{\partial Z^2}\right] \tag{4}$$

Energy

$$U\frac{\partial \Theta}{\partial R} + W\frac{\partial \Theta}{\partial Z} = \frac{1}{\mathrm{Re}\cdot\mathrm{Pr}}\left[\frac{1}{s}\frac{1}{R}\frac{\partial}{\partial R}\left(R\frac{\partial \Theta}{\partial R}\right) + s\frac{\partial^2 \Theta}{\partial Z^2}\right] + \frac{1}{s}\frac{\mathrm{Ec}}{\mathrm{Re}}\Phi \tag{5}$$

where

$$\Phi = 2\left[\left(\frac{\partial U}{\partial R}\right)^2 + \left(\frac{U}{R}\right)^2 + \left(\frac{\partial W}{\partial z}\right)^2\right] + \left[R\frac{\partial}{\partial R}\left(\frac{V}{R}\right)\right]^2 + s^2\left(\frac{\partial V}{\partial Z}\right)^2 + \left[s\frac{\partial U}{\partial Z} + \frac{1}{s}\frac{\partial W}{\partial R}\right]^2 \tag{6}$$

In these equations the following definitions apply, where T_s and T_H are the shroud and hub temperatures, respectively

$$U = \frac{u}{\Omega R_2},\quad V = \frac{v}{\Omega R_2},\quad W = \frac{w}{\Omega H},\quad \Theta = \frac{T - T_s}{T_H - T_s}$$

$$P = \frac{p}{\rho(\Omega R_2)^2},\quad R = \frac{r}{R_2},\quad Z = \frac{z}{H},\quad s = \frac{R_2}{H}$$

$$\mathrm{Re} = \frac{H\Omega R_2}{\nu},\quad \mathrm{Pr} = \frac{\mu c_p}{\kappa},\quad \mathrm{Ec} = \frac{(\Omega R_2)^2}{c_p(T_H - T_s)},\quad \mathrm{Ro} = \frac{u_b}{\Omega R_2} \tag{7}$$

where Pr, Ec, and Ro are the Prandtl, Eckert, and Rossby numbers, respectively.

The length scale H used in the definition of the Reynolds number is preferred to the length scale R_2. This is because the region of the flow where inertial effects are largest arises near the shroud, where shearing is most intense, and the size of this region, as illustrated by the streamline plots discussed below, scales with H.

While Φ, representing the viscous dissipation, was retained in the problem formulation, for the low rotational speeds investigated its effect on the calculated temperature fields was very small.

With reference to Fig. 2(*a*), the dimensionless boundary conditions for the case of an imposed purely radial throughflow are:

Plane 1: $R = R_1/R_2$, $0 < Z < 1/2$ (rotating porous hub)
$U = \mathrm{Ro}$, $V = R_1/R_2$, $W = 0$

Plane 2: $R_1/R_2 < R < 1$, $Z = 1/2$ (rotating disk surface)
$U = 0$, $V = R$, $W = 0$

Plane 3: $R = 1$, $1/2 < Z < 1/2 + b/2H$ (rotating disk rim)
$U = 0$, $V = 1$, $W = 0$

Plane 4: $1 < R < 1 + a/R_2$, $Z = 1/2 + b/2H$ (symmetry plane through disk)
$\partial U/\partial Z = 0$, $\partial V/\partial Z = 0$, $W = 0$

Plane 5: $R = 1 + a/R_2$, $0 < Z < 1/2 + b/2H$ (fixed porous shroud wall)
$U = (A_1/A_5)\,\mathrm{Ro}$, $V = 0$, $W = 0$

Plane 6: $R_1/R_2 < R < 1 + a/R_2$, $Z = 0$ (symmetry plane between disks)
$\partial U/\partial Z = 0$, $\partial V/\partial Z = 0$, $W = 0$

It is important to note that in this work planes "4" and "6" in Fig. 2(*a*) are taken as symmetry planes, while the hub and shroud wall are treated as uniformly porous surfaces through which air flows when the radial blowing boundary

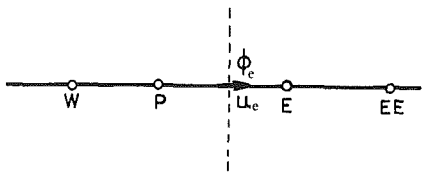

Fig. 3 One-dimensional grid point layout illustrating the QUICK scheme

condition (Ro > 0) is invoked. A more realistic blowing situation, which could arise in a disk pack, requires specifying an axially directed component of motion across both planes "4" and "6" as shown below. These planes then no longer represent symmetry planes for the flow. This first choice of radial flow boundary conditions yields important results and also allows an unambiguous and rigorous evaluation of the numerical calculation procedure.

The hub and shroud wall are taken to be at uniform constant temperatures $\Theta = 1$ and $\Theta = 0$, respectively. The domain for calculating the thermal field encompasses the entire symmetric half-space between the disks; i.e., from $Z = 0$ to $Z = 1/2 + b/2H$ in Fig. 2(*a*). In the portion of this field corresponding to the disk, i.e., from $Z = 1/2$ to $Z = 1/2 + b/2H$ for $R_1/R_2 < R < 1$, the energy equation reduces to the conduction equation. Over the remaining region the complete energy equation and momentum equations are solved. In this way, the conjugate heat transfer problem is readily dealt with; see Patankar (1980).

With reference to Fig. 2(*b*), the dimensionless boundary conditions for the case of combined radial and axial throughflows are the same as above except for:

Plane 3′: $1 < R < 1 + a/R_2$, $Z = 1 + b/H$ (upper disk–shroud gap)

$$U = 0, \quad V = 1 - (R-1)R_2/a, \quad W = W_3'$$

Plane 4′: $R = 1 + a/R_2$, $0 < Z < 1 + b/H$ (fixed impermeable shroud wall)

$$U = 0, \quad V = 0, \quad W = 0 \qquad (8\text{-}b)$$

Plane 5′: $1 < R < 1 + a/R_2$, $Z = 0$ (lower disk–shroud gap)

$$U = 0 \quad V = 1 - (R-1)\,R_2/a, \quad W = W_5'$$

For this case the shroud wall is taken as impermeable. The temperatures of the two disks are specified as $\Theta = 1$ and that of plane 5′ is fixed to $\Theta = 0.5$. The temperature at plane 3′ is assumed to be uniform and is obtained by first using $\partial T/\partial Z = 0$ and then calculating the bulk temperature at this plane.

2.2 Finite Difference Approximations and Solution Algorithm. The momentum and energy equations can be recast in the general form

$$\frac{\partial}{\partial t}(\rho\Phi) + \frac{1}{r}\frac{\partial}{\partial r}(\rho r u\Phi) + \frac{\partial}{\partial z}(\rho w\Phi) = \frac{1}{r}\frac{\partial}{\partial r}\left(r\Gamma\frac{\partial\Phi}{\partial r}\right) + \frac{\partial}{\partial z}\left(\Gamma\frac{\partial\Phi}{\partial z}\right) + S_\Phi \qquad (9)$$

where Γ is the diffusion coefficient for the general variable Φ ($\equiv u, v, w, T$) and S_Φ represents all terms that are not included in the convection and diffusion terms shown. In the calculations the time variations of Φ are not explicitly computed. Instead, this time-dependent term is used as a "false transient" to stabilize the calculation procedure in converging to a steady state solution.

A general finite difference expression for equation (9) is obtained by volume integration over a discrete control volume or cell on a staggered grid configuration (refer to Patankar, 1980). The result is

$$\Phi_P = \frac{\Sigma A_i \Phi_i + S_a}{\Sigma A_i + S_b} \qquad (10)$$

where the A_i coefficients account for the combined effects of diffusion and convection and the S_a and S_b source terms include numerically stabilizing contributions proportional to $\Phi_P/\Delta t$ and $1/\Delta t$, respectively, such that $\Delta\Phi_P/\Delta t \to 0$ as the converged solution is achieved.

Leonard's (1977) QUICK interpolation scheme is used to represent the convection terms in equation (9) in finite difference form. This method combines global second-order accuracy with the numerical stability typical of the first-order accurate upwind scheme. In order to resolve the flow near boundaries and not waste grid points in the interior of the calculation domain, a nonuniform grid version of QUICK was employed. QUICK uses a quadratic curve-fit to interpolate for a value at the desired spatial location. With reference to Fig. 3, we take, for example,

$$u_c > 0 : \Phi_e = C_1\Phi_P + C_2\Phi_E + C_3\Phi_W + \mathbf{a}\Phi_E \text{ (source)}$$

$$u_e < 0 : \Phi_e = C_4\Phi_P + C_4\Phi_E + \mathbf{C}_6\Phi_{EE} \text{ (source)} \qquad (11)$$

where the C_i's are found using a Lagrangian interpolation procedure. The coefficient **a** above is adjusted to ensure positive values of the A_i coefficients in equation (10).

The algorithm for solving the system of equations obtained by applying equation (10) to each variable on each cell of the calculation grid is based on the repeated use of the tridiagonal-matrix algorithm. This is applied line-by-line throughout the calculation domain to obtain values of the variables at the appropriate grid nodes. The dynamic component of pressure is calculated using the SIMPLE procedure of Patankar (1980). The actual code used was REBUFFS, which has been extensively discussed and tested by LeQuere et al. (1981). Briefly, this iterative calculation procedure seeks to establish a velocity field that simultaneously satisfies the momentum and continuity conservation equations. Intermediate corrections are obtained for the pressure field, which are then used to correct the velocities. Once the flow field is determined to within an accepted residual imbalance, the temperature field is solved.

2.3 Testing and Miscellaneous Matters. The REBUFFS code has been extensively used and tested. Additional tests were performed in the present study to validate the assumptions of steady axisymmetric flow and grid independence. Figure 4(*a*) shows a comparison between the present calculations and the measurements and calculations of the radial velocity component from the study by Szeri et al. The comparison suggests that the present calculations, obtained on a 27×44 ($Z \times R$) nonuniform grid, are more accurate than the thick-film approximation results predicted by Szeri et al.

Figure 4(*b*) shows a comparison between the present calculations and the time-averaged measurements of the circumferential velocity component obtained by Schuler et al. (1988). This comparison shows that in spite of the unsteady nature of the flow for rotational frequencies exceeding 62 rpm, approximately, very good agreement is obtained with the steady-state calculation approach. In addition, the figure shows virtually indistinguishable results for the two nonuniform grids used. As a consequence, the coarser of the two grids was used for the numerical study.

A remark is in order concerning the boundary condition used at plane 4 in Fig. 2(*a*) to predict the results in Fig. 4(*b*). Because of end effects at the top and bottom of any finite stack of disks, plane 4 is not a true symmetry plane. To perform the comparison with the measurements, it was considered more appropriate to let dependent variables at this plane "float" by setting $\partial/\partial z(u, v, w, T) = 0$ as the boundary condition. This approach yielded better agreement between the measurements and the calculations than did the imposition of the symmetry plane condition.

Typical calculations on a 27×44 grid required 2000 iterations to achieve convergence. This required about 212 cpu seconds on a CRAY X-MP machine. The convergence criterion was

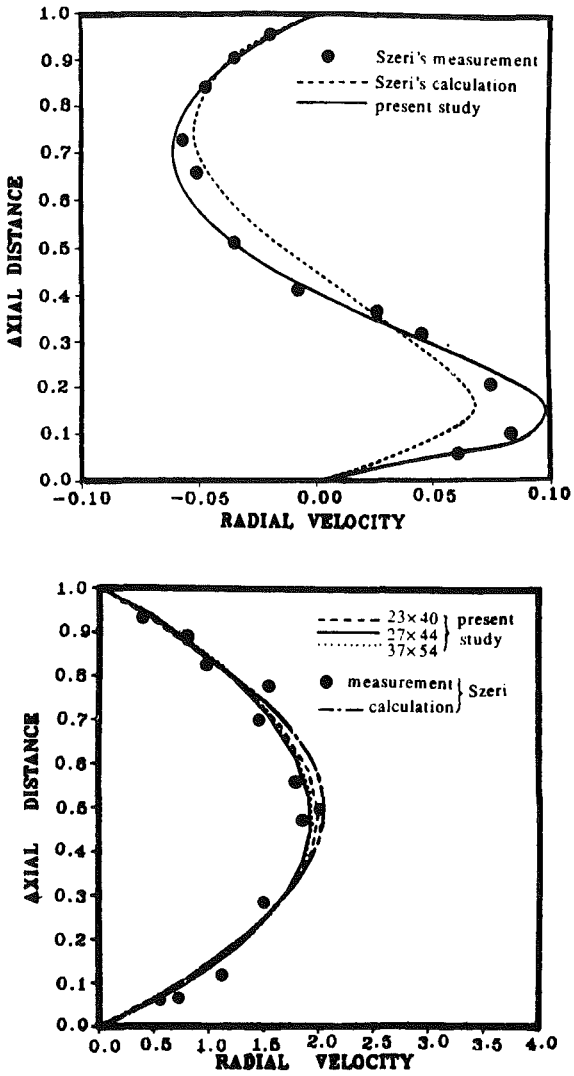

Fig. 4(*a*) Comparison between measurements and calculations of the disk flow configuration with $\gamma = 0$ investigated by Szeri et al. (1983); present calculations are for the grid refinements shown; top: Ro = 0, Re = 187; bottom: Ro = 3.5, Re = 15

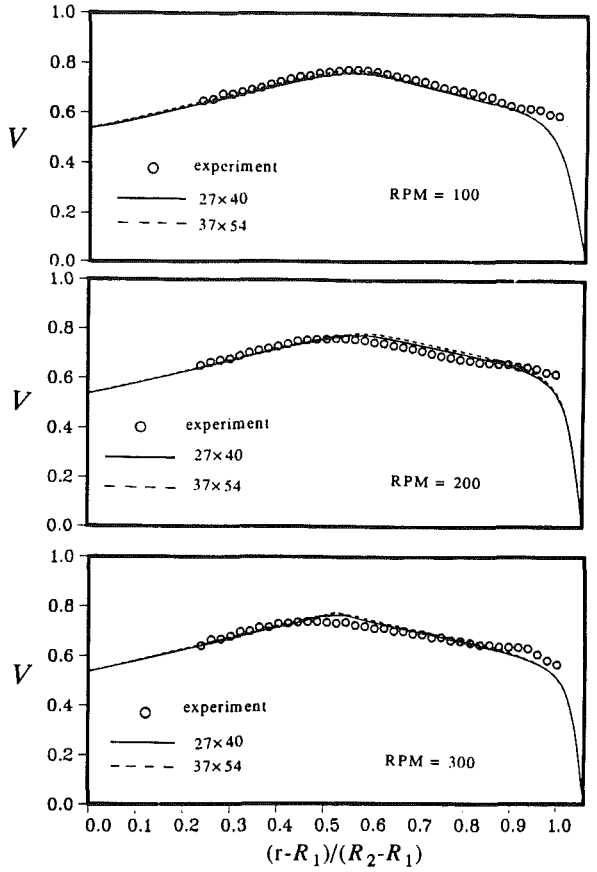

Fig. 4(*b*) Comparison between time-averaged measurements and predictions of the circumferential velocity along the midplane between two corotating disks in an axisymmetric enclosure; experimental data from Schuler et al. (1988)

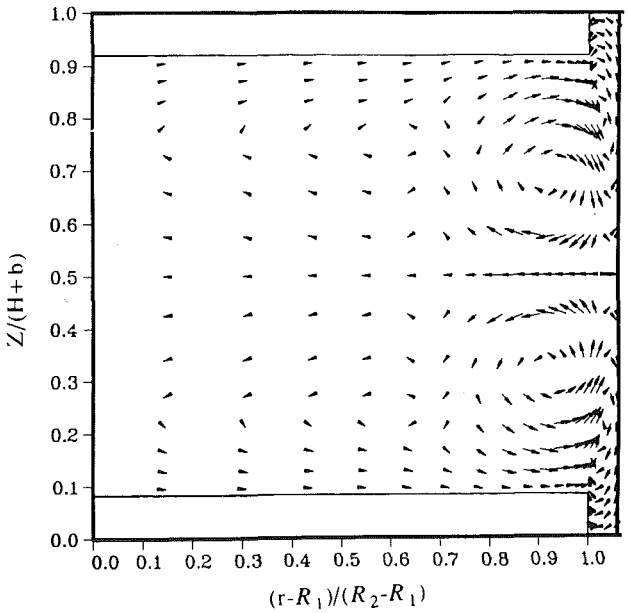

Fig. 5 Cross-stream vector velocity field (compressed in radial direction) for rpm = 300 and Ro = 0

that the largest of the residual sources due to mass, energy, or momentum imbalance should be less than 10^{-5}. In addition to the false transient terms, underrelaxation factors were used to stabilize the calculation sequence. Values of 0.5, 0.5, 0.5, 0.6, and 0.8 were used in the radial, angular, and axial momentum, pressure correction, and energy equations, respectively.

3 Results and Discussion

This section presents a discussion of the numerical results obtained for the flow of air between the two corotating disks of Fig. 1. For the case of an imposed purely radial throughflow, the variables are the Reynolds number Re, the Rossby number Ro, the disk radius to spacing ratio (R_2/H), and the disk-shroud gap width to disk radius ratio (a/R_2). For the case of combined radial and axial throughflows, the ratio of the mass flow rate through the gap to that through the hub, $M = (\rho A w)_5'/(\rho A W)_1'$, is an additional parameter. All the calculations were performed for a fixed value of the radius ratio, $R_1/R_2 = 0.537$. The results shown in Figs. 5–8 are for $R_2/H = 11.024$ and $a/R_2 = 0.028$.

Figure 5 shows the vector velocity field in the r–z plane for 300 rpm in the absence of radial or axial throughflow. Two large eddies recirculate on either side of the symmetry plane in the region $(r-R_1)/(R_2-R_1) > 0.7$. Two smaller counter-rotating eddies are present near the shroud in the gaps between the disk tips and the shroud. This flow pattern is also illustrated in Fig. 6, which shows the calculated streamline contours for 100, 200, and 300 rpm corresponding to values of Re equal to

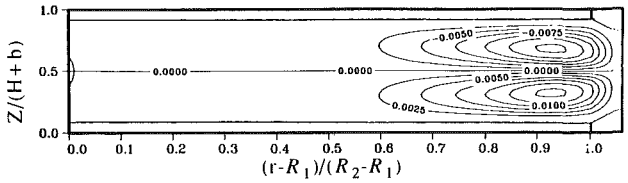

Fig. 6(*a*) Streamline contours for rpm = 100 and Ro = 0

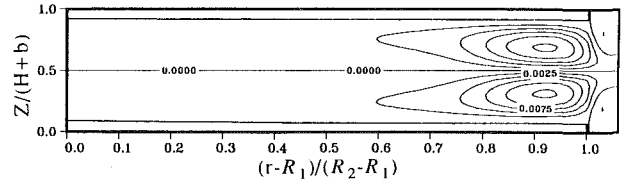

Fig. 6(*b*) Streamline contours for rpm = 200 and Ro = 0

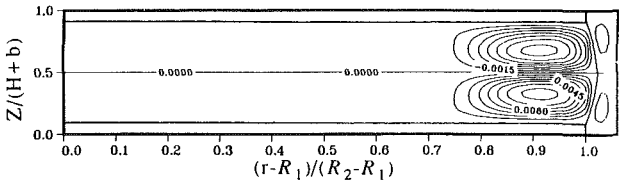

Fig. 6(*c*) Streamline contours for rpm = 300 and Ro = 0

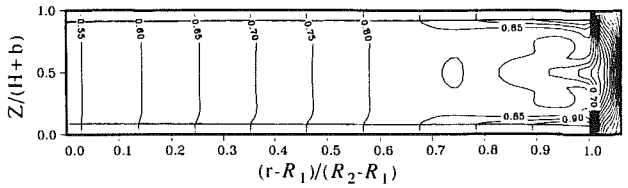

Fig. 7(*a*) Circumferential velocity contours for rpm = 300 and Ro = 0

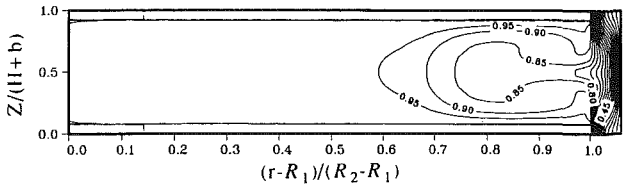

Fig. 7(*b*) Temperature contours for rpm = 300 and Ro = 0

635, 1270, and 1905 for the no-blowing condition. The two small eddies near the shroud grow in size with increasing values of Re. The streamline plots also show that the radial penetration of the larger pair of eddies decreases with increasing values of Re. This is attributed to the viscous action of the growing pair of smaller eddies adjacent to the shroud, which act as a sink for the momentum that is eventually lost by shearing on the shroud.

Circumferential velocity and temperature contours at 300 rpm are shown in Figs. 7(*a*, *b*) for the no-blowing condition (Ro = 0), which may be compared with corresponding results with purely radial blowing (Ro = 0.061) shown in Figs. 8(*a–c*). Physical properties of aluminum were used to calculate the temperature distribution in the disk, which was found to be very uniform (cf. Figs. 7(*b*) and 8(*c*)). A comparison between Figs. 7 and 8 shows the dramatic effect that blowing has on the streamline, velocity, and temperature profiles. The radial component of motion results in steep velocity and temperature profiles along the shroud wall, which significantly increase the shear stress and heat transfer in this region. It is noteworthy that in spite of the uniform blowing and suction boundary

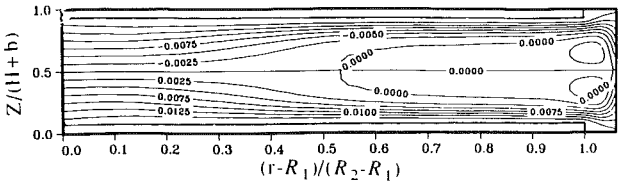

Fig. 8(*a*) Streamline contours for rpm = 300 and Ro = 0.061

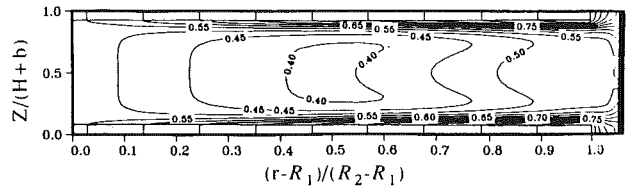

Fig. 8(*b*) Circumferential velocity contours for rpm = 300 and Ro = 0.061

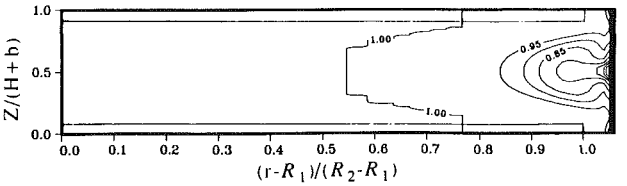

Fig. 8(*c*) Temperature contours for rpm = 300 and Ro = 0.061

conditions imposed on the hub and the shroud walls respectively, the outward radial flow gradually channels into two small regions (the Ekman layers) adjacent to the disk surfaces. As a result, the condition of solid body rotation that is so prominent in Fig. 7(*a*) for $(r-R_1)/(R_2-R_1) < 0.6$ is altered considerably, as shown in Fig. 8(*b*).

Values of the dimensionless shear stress F and the Nusselt number Nu were determined by evaluating the following expressions:

$$F = -\frac{1}{t}\int_0^t \frac{\partial V}{\partial R}\Big|_{\text{wall}} dZ \tag{12}$$

and

$$\text{Nu} = -\frac{1}{t}\int_0^t \frac{\partial \Theta}{\partial R}\Big|_{\text{wall}} dZ \tag{13}$$

where

$$t = 1/2 + b/H$$

The results are shown in Figs. 9 and 10 where the Rossby number Ro, the spacing to disk radius ratio H/R_2, and the disk–shroud gap width to disk radius ratio a/R_2 have been varied. While purely radial blowing results in a considerable increase in the conduction heat transfer through the shroud wall, it is accompanied by a substantial increase in the shear stress. Figure 10 shows a pronounced minimum for F at Re = 1270, which corresponds to 200 rpm, when Ro = 0.061. Variations in the geometric factors H/R_2 and a/R_2 show a small but significant influence on the shear stress and the Nusselt number.

Axially directed gap flow calculations were performed for three values of the mass flow ratio $M = m_5'/m_1'$ with the boundary conditions as discussed in section 2.1, where m_5' and m_1' are the mass flow rate at plane 5′ and plane 1′, respectively. A sample of the results obtained is shown in Fig.

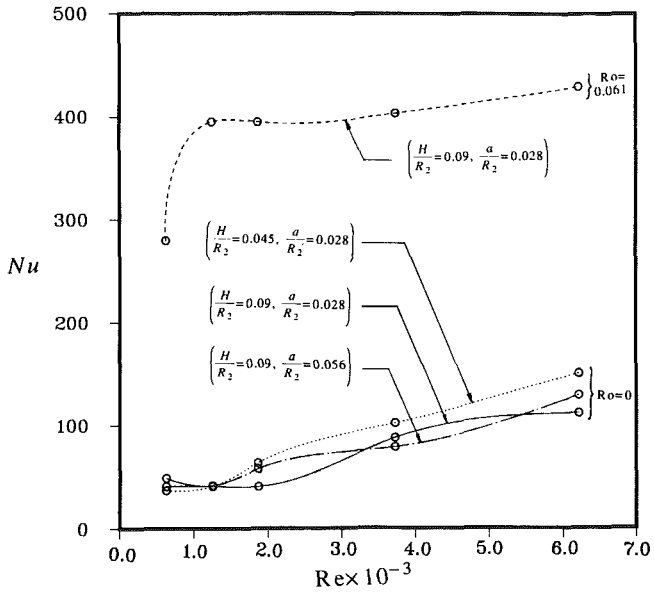

Fig. 9 Variation of Nusselt number with Reynolds number for different values of Ro, H/R_2, a/R_2 in corotating disk flow

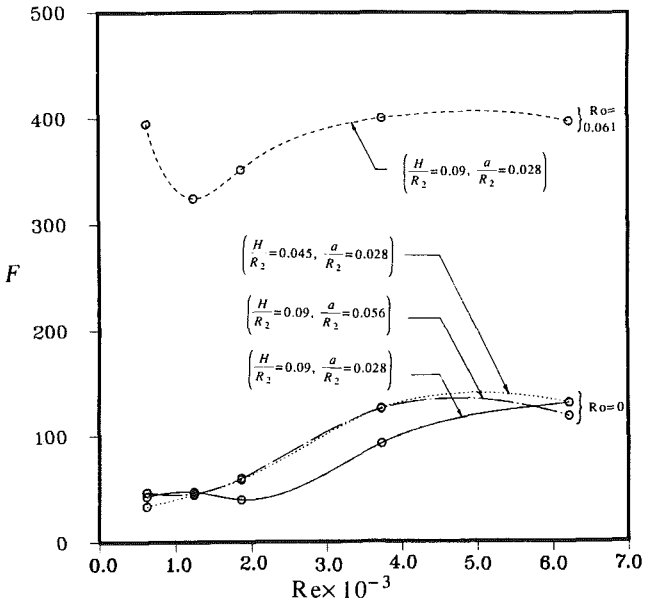

Fig. 10 Variation of dimensionless shear stress with Reynolds number for different values of Ro, H/R_2, a/R_2 in corotating disk flow

11 for rpm = 100 and Ro = 0.009. Contrast these with the results shown in Fig. 12 for which the boundary conditions are identical except that $M = 0$ and a porous shroud exists instead. The streamline contours show that for $M = 0.1$ there is already a substantial asymmetric influence of the axially directed disk–shroud gap flow upon the cross-stream secondary flow cell patterns generated in the space between the disks, especially in the vicinity of the shroud.

The secondary flow cell in the bottom half of the space between the disks is strongly reinforced by the axial component of motion in the gap. In turn, the secondary flow cell in the top half of this space appears to be influenced by the cell in the bottom half. However, the closed-cell character of the top cross-stream flow disappears for M less than 10 as a result of the opposing sense of axially directed motions in the top half of the gap region.

The axial component of motion through the gap results in an air barrier that obstructs the transfer of heat (and momentum) from fluid in the space between the disks to the shroud. This, combined with the intensified cross-stream flow, results in a higher value, but much more uniform distribution, of temperature in the space between the disks than is obtained with purely radial blowing only. Figure 11(*d*) illustrates the point for the case of $M = 0.1$ when contrasted with Fig. 12(*b*).

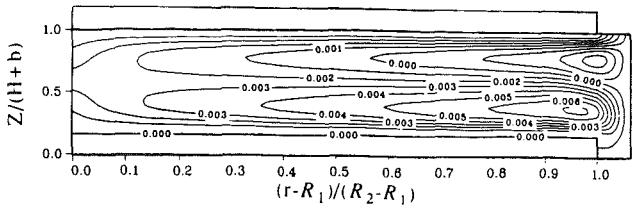

Fig. 11(*a*) Streamline contours for rpm = 100, Ro = 0.009, and M = 0.1

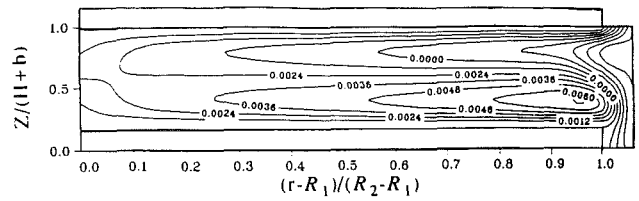

Fig. 11(*b*) Streamline contours for rpm = 100, Ro = 0.009, and M = 1.0

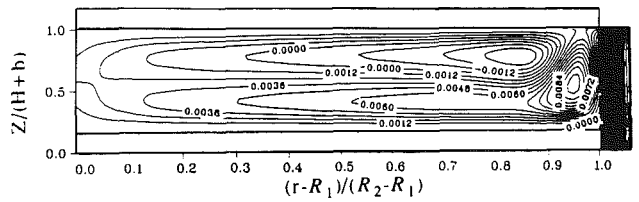

Fig. 11(*c*) Streamline contours for rpm = 100, Ro = 0.009, and M = 10.0

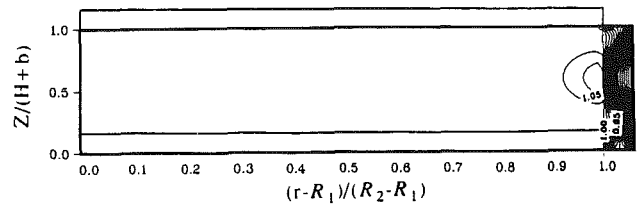

Fig. 11(*d*) Temperature contours for rpm = 100, Ro = 0.009, and M = 0.1

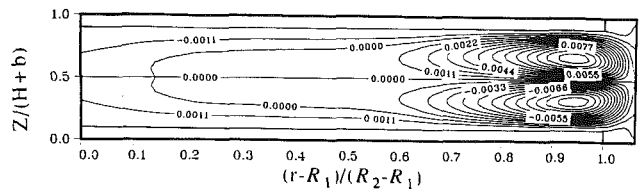

Fig. 12(*a*) Streamline contours for rpm = 100, Ro = 0.009, and M = 0

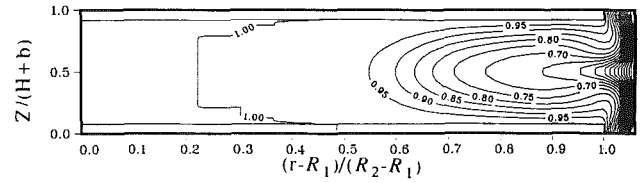

Fig. 12(*b*) Circumferential velocity contours for rpm = 100, Ro = 0.009, and M = 0

Very similar temperature distributions were predicted for $M = 1$ and 10 with the result that over the range of M explored (0.1–10) the Nusselt number for the shroud only varied between 48.2 and 52.5. Similarly, the protective air barrier resulted in a wall shear stress variation ranging from 28.1 to 29.8 only.

The main conclusion of the numerical explorations involving combined axial and radial throughflows is that with relatively small values of the mass flow ratio M, an axially aligned air barrier can be induced in the disk–shroud gap region that effectively insulates the shroud from recirculating fluid in the space between the disks. The result is for a higher but more uniform distribution of temperature to arise in the space between the disks. For equal values of the radial mass throughflow, the imposition of an axial gap flow results in a substantial decrease in the heat transfer between the fluid in the space between the disks and the shroud. This finding may have important applications for the design and control of the thermal characteristics of disk pack systems.

4 Summary and Conclusions

A numerical investigation was performed for the laminar flow and heat transfer in the space between a pair of coaxial corotating disks in an axisymmetric enclosure. The assumptions of steady and axisymmetric flow were examined in the light of new experimental results. Although the present flow goes unsteady at 62 ± 2 rpm, the small-amplitude sinusoidal character of the motion for rpm < 300 yields long-time average results that are accurately predicted assuming steady axisymmetric flow. Purely radial and combined radial–axial throughflow configurations were investigated numerically. In the absence of throughflows, the results show that the structure of the flow varies from solid body rotation near the hub to a strongly sheared flow in the vicinity of the shroud wall. In the presence of purely radial throughflow, the structure of the flow and its thermal characteristics, especially near the shroud, are found to be very sensitive to variations in the Reynolds number Re, and Rossby number Ro, and less sensitive to variations in the disk spacing to disk radius ratio H/R_2, and the disk–shroud gap width to disk radius ratio a/R_2. A purely radial throughflow (as imposed through the boundary conditions analyzed here) results in threefold increases in both the dimensionless shear stress and the Nusselt number at the shroud wall. By contrast, the imposition of an axial gap flow adjacent to the shroud results in a substantial decrease in heat transfer, which may have important applications in disk storage configurations.

Acknowledgments

This work was supported by a contract with the IBM Almaden Research Center in San Jose, CA. The authors are pleased to express their appreciation for this support and the encouragement received from IBM in the course of performing the investigation. Support from the Computer Center of The University of California at Berkeley is also appreciated.

References

Abrahamson, S. D., Koga, D. J., and Eaton, J. K., 1988, "An Experimental Investigation of the Flow Between Shrouded Corotating Disks," Report MD-50, Thermoscience Division, Department of Mechanical Engineering, Stanford University, CA.

Bakke, E., Kreider, J. F., and Kreith, F., 1973, "Turbulent Source Flow Between Parallel Stationary and Co-rotating Disks," *J. Fluid Mech.*, Vol. 58, pp. 209–231.

Holodniok, M., Kubicek, M., and Hlavacek, V., 1981, "Computation of the Flow Between Two Rotating Coaxial Disks: Multiplicity of Steady-State Solutions," *J. Fluid Mech.*, Vol. 108, pp. 227–240.

Humphrey, J. A. C., 1986, "Summary Literature Review on Rotating Disk Flows," The University of California at Berkeley, Report No. FM-86-2.

Kaneko, R., Oguchi, S., and Hoshiya, K., 1977, "Hydrodynamic Characteristics in Disk Packs for Magnetic Storage," *Rev. Elec. Comm. Lab.*, Vol. 25, No. 11–12, pp. 1325–1336.

Lennemann, E., 1974, "Aerodynamic Aspects of Disk Files," *IBM J. Res. Devel.*, Vol. 18, No. 6, pp. 480–488.

Leonard, B. P., 1979, "A Stable and Accurate Convective Modelling Procedure Based on Quadratic Upstream Interpolation," *Comp. Method Appl. Mech. Engng.*, Vol. 19, pp. 59–98.

LeQuere, P., Humphrey, J. A. C., and Sherman, F. S., 1981, "Numerical Calculation of Thermally Driven Two-Dimensional Unsteady Laminar Flow in Cavities of Rectangular Cross Section," *Num. Heat Trans.*, Vol. 4, pp. 249–283.

Patankar, S. V., 1980, *Numerical Heat Transfer and Fluid Flow*, Hemisphere/McGraw-Hill, New York.

Schuler, C. A., Usry, W., Weber, B., Humphrey, J. A. C., and Greif, R., 1989, "Experimental Investigation of Unsteady Flow Between Corotating Disks in an Axisymmetric Enclosure," in preparation.

Szeri, A. Z., Schneider, S. J., Labbe, F., and Kaufman, H. N., 1983, "Flow Between Rotating Disks (Part 1, Basic Flow)," *J. Fluid Mech.*, Vol. 134, pp. 103–132.

Finite Analytic Solution of Convective Heat Transfer for Tube Arrays in Crossflow: Part I—Flow Field Analysis

Tzong-Shyan Wung[1]

Ching Jen Chen
Professor and Chairman.

Department of Mechanical Engineering,
Iowa Institute of
Hydraulic Research,
College of Engineering,
The University of Iowa
Iowa City, IA 52242

The convective motion in two types of tube array is solved numerically by the Finite Analytic Method. The Finite Analytic Method utilizes the local analytic solution of governing differential equations in obtaining its discretized algebraic representation. Both in-line tube arrays and staggered tube arrays with longitudinal and transverse pitches of 2 are studied. The geometries are expressed in boundary-fitted coordinates on which the Navier–Stokes equations and energy equation are solved. Solutions for Reynolds numbers of 40, 120, 400, and 800 are obtained. Differences in stream function, vorticity function, and location of separation and reattachment for flow past in-line tube arrays and staggered tube array are predicted and compared. The zone of separation for both arrays tends to increase with increasing Reynolds number. The predicted results on flow field and heat transfer are shown to agree with available experimental measurements.

1 Introduction

There are numerous designs of industrial heat exchangers involving a bank of tubes in a fluid crossflow. Depending on applications and design criteria, the layouts of tubes in an array have many possible arrangements. A heat exchanger designer, therefore, needs to have a large data base available in order to choose the optimal one among the different design options. The most reliable performance information often comes from actual measurements. However, this approach is not only expensive but also time consuming. For each new tube pattern, a new model has to be constructed and the experiments run. The other approach to obtaining heat transfer data of a given tube bank is the theoretical study, provided that the phenomena can be properly simulated by a mathematical model. Changes of the geometric parameters and fluid flow conditions can be easily accomplished by changing the values of parameters in the simulation. Unfortunately, there is only a handful of exact solutions of the governing equations that simulate the fluid flow problems. The difficulties arise in the nonlinearity of the Navier–Stokes equations, the coupling of variables through continuity, momentum, and energy equations, and the complexity of the heat exchanger geometry. Due to rapid development in computer architecture, the computational speed and capacity of memory have increased drastically. Consequently, the numerical solution becomes a good alternative during design of engineering devices. The numerical predictions usually give reasonable results, especially for cases that do not differ much from the baseline case that has been confirmed with the experimental results.

The numerical study of the fluid flow past tube bundles can be traced back to Thom and Apelt (1961). One of the obstacles in using the numerical methods to study the tube-bank problem is the complex geometry. The pioneering work of Thom and Apelt (1961) used the conformal mapping technique to transform the boundaries of the staggered tubes to coincide with equivalued surfaces of one of the independent variables. Later work by Le Feuvre (1973) employed nonuniform Cartesian grid lines in which the spacing between nodes was adjusted so that all the near-wall nodes fall on surfaces of tubes. In his study dense grid lines are produced in the regions far from the cylinder where they are not necessary. By realizing the fact that the steepest gradients of flow properties occur in the radial direction close to each cylinder, Launder and Massey (1978) incorporated a cylindrical network of nodes in the vicinity of the tubes with a Cartesian mesh covering the remainder of the flow domain. In order to provide a connection between the cylindrical and Cartesian coordinates in the region of overlap, a false row of nodes was introduced to both coordinate systems, and the interpolation scheme was used for the intersections between cylindrical and Cartesian grids.

Recently, the boundary-fitted coordinate system was introduced by Thompson et al. (1974, 1977) to solve fluid dynamic problems. The boundary-fitted coordinate transformation can generate a general curvilinear coordinate system numerically by solving Poisson's equations with proper control of grid densities. Ho and Chen (1983) and Antonopoulos (1985) employed the boundary-fitted coordinate system to solve the flow and heat transfer in tube banks successfully. Although the governing differential equations expressed in terms of the new coordinates are more complex than in Cartesian or cylindrical coordinates, the boundary-fitted coordinate system has proven to be a powerful and flexible tool to solve the flow fields associated with complex geometries. This two-part paper presents the finite analytic numerical solutions of laminar flow (Part I) and heat transfer (Part II) in tube bundles of in-line and staggered arrangements with both longitudinal and transverse pitches of 2. The numerical solutions are obtained by solving the Navier–Stokes equations, written in the form of stream function-vorticity formulation, and the energy equation, via the finite analytic numerical method (Chen, 1987; Chen and Chen, 1984).

2 Problem Description

In the present study attention is focused on the convective heat transfer from a heated tube in the fully developed region of fluid flow past tube bundles, as shown in Fig. 1. The fluid is considered incompressible with constant properties and the flow is assumed to be steady and two dimensional. Therefore, the flow pattern is assumed exactly repeated from one row to

[1]Present address: Associate Professor, Institute of Applied Mechanics, National Taiwan University, Taipei, Taiwan.

Contributed by the Heat Transfer Division and presented at the National Heat Transfer Conference, Houston, Texas, July 24–27, 1988. Manuscript received by the Heat Transfer Division November 11, 1987. Keywords: Forced Convection, Heat Exchangers.

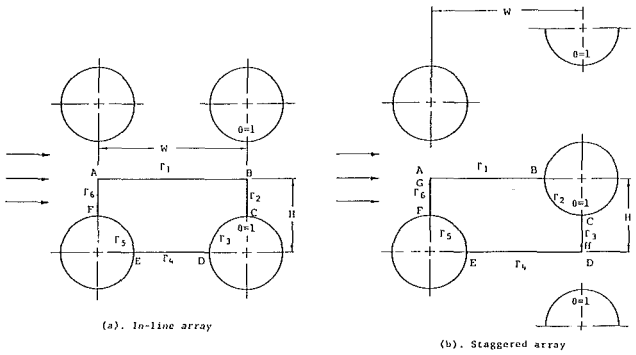

Fig. 1 Computational domain for staggered and in-line tube

the next and is symmetric from one column to the other column for both in-line and staggered arrays. Based on the above assumptions, only one period of arrays is needed for the solution of flow field, as shown in Fig. 1(*a*) for an in-line array and Fig. 1(*b*) for a staggered array. However, three periods of arrays are considered for the solution of temperature field because temperature boundary conditions are not periodic. Part I of this paper gives the finite analytic solution of flow field in both in-line and staggered tube arrays. Part II of the paper gives the heat transfer analysis for a heated tube in in-line and staggered tube arrays.

2.1 Governing Equations. The stream function-vorticity formulation of the flow past tube bank, written in dimensionless form, is given as follows:

$$\mathrm{Re}(\zeta_t + \varphi_y \zeta_x - \varphi_x \zeta_y) = \zeta_{xx} + \zeta_{yy} \tag{1}$$

$$\varphi_{xx} + \varphi_{yy} = -\zeta \tag{2}$$

and the energy equation with no heat generation, no radiation, and negligible viscous dissipation is

$$\mathrm{Pe}(\theta_t + \varphi_y \theta_x - \varphi_x \theta_y) = \theta_{xx} + \theta_{yy} \tag{3}$$

where φ, ζ, and θ are dimensionless parameters and are the stream function, vorticity, and temperature, respectively. They are made dimensionless by scaling vorticity ζ by V/d, the stream function φ by Vd, the temperature by $T_w - T_0$, the space dimensions x and y by d, and time t by d/V. $\mathrm{Re} = Vd/\nu$ is the Reynolds number based on the cylinder diameter d and the average velocity V in the minimum free flow area between tubes, and Pe is the Peclet number $\mathrm{Pe} = \mathrm{Pr}\ \mathrm{Re}$, where Pr is the Prandtl number. T_w is the isothermal temperature of the heated tube and T_0 is the constant inlet temperature of the fluid or the temperature of the unheated tubes. The vorticity ζ is defined by

$$\zeta = v_x - u_y = -\nabla^2 \varphi \tag{4}$$

and velocity components

$$u = \varphi_y, \quad v = -\varphi_x \tag{5}$$

The transient terms in the vorticity equation (1) and energy equation (3) are retained because the time-marching method will be used in the numerical calculation of the steady flow and heat transfer problem.

2.2 Initial and Boundary Conditions. The boundary conditions are required for all boundaries of a computational domain since the governing equations are elliptic in spatial coordinates. In general, along the boundaries of the lower and upper symmetric planes the stream function is respectively set equal to zero and to a constant value, which is equivalent to one half of the mean mass flow rate through the channel as shown in Fig. 1. The vorticity and the normal gradients of temperature are zero along the planes of symmetry. Around the surface of the cylinders, the value of the stream function is uniform, corresponding to an impermeable wall, and is the same as the value of the adjacent symmetric plane. The value of vorticity on the cylinder is unknown and must be solved as a part of solution. However, it can be approximated from the

Nomenclature

a, b, c = FA coefficients defined in equation (21)
A, B = convective coefficients in transport equation (19)
C_n = FA coefficient
d = diameter of tube
D_x, D_y = transformation coefficients defined in equation (15)
E = coefficient of unsteady term, equation (16)
E_2 = series summation in finite analytic solution, equation (22)
g = inhomogeneous source term in PDE
h, k = grid spacing in a stretched element, equation (20)
H = height of the computational domain
J = Jacobian of the coordinate transformation, equation (9*d*)
k = thermal conductivity of the fluid
P = pressure
P, Q = grid contraction functions, equation (11)
P_A, P_B = coefficients defined in equation (23)
Pe = Peclet number
Pr = Prandtl number
Re = Reynolds number $= Vd/\nu$
s = vector in streamwise direction
S = source term in PDE, equation (16)
t = time
t = tangential vector
T = temperature
v_i, u, v, w = velocity components
V = averaged velocity in the minimum flow area
W = width of computational domain
x, y = Cartesian coordinates
α, β, γ = transformation coefficients defined in equation (9)
Γ = boundary contour
ζ = vorticity
θ = dimensionless temperature
$\lambda_m h$ = $(m - 1/2)\pi$
ν = kinematic viscosity
ρ = density
σ, τ = transformation coefficients defined in equation (15)
ϕ = generalized dependent variable
φ = stream function
∇^2 = Laplacian

Subscripts

0 = initial value
C = center
d = downstream
E = east
N = north
P = central point
S = south
u = upstream
w = wall
W = west

Superscripts

$n, n-1$ = nth and $n-1$st time step
$k, k-1$ = kth and $k-1$st iteration
$*$ = in transformed plane
$\bar{}$ = averaged value

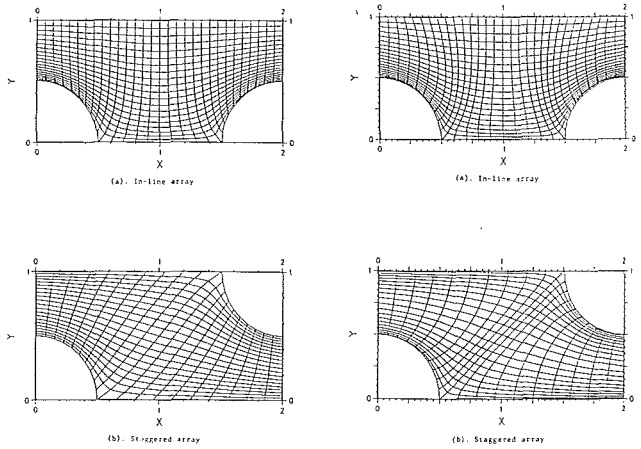

(1) Thompson and et al contraction function (2) Chen and Obasih contraction function

Fig. 2 Boundary-fitted coordinate system

stream function in the immediate vicinity of the surface according to the impermeable condition. The temperature boundary condition for the inlet fluid and unheated tubes are at isothermal temperature T_0 while the heated tubes are at another isothermal temperature T_w. Details of the outlet temperature condition are discussed in Part II of the present study. The initial condition is taken to be uniform velocity V and temperature T_0.

3 Methods of Numerical Solution

3.1 The Boundary-Fitted Curvilinear Coordinate System. The boundary-fitted coordinate in which grid line coincides with the body contour in the flow region can provide an accurate representation of boundary conditions in the region of greatest sensitivity. Thompson et al. (1974, 1977) introduced a method for numerical generation of curvilinear coordinate systems with coordinate lines conformal with all boundaries of arbitrarily shaped bodies in a two-dimensional flow region. In the method, the Cartesian coordinates (x, y) of the boundary-fitted grid points in complex physical space are computed as solutions of an elliptic system of partial differential equations with Dirichlet boundary conditions. In this study, two different sets of partial differential equations are used in generating boundary-fitted coordinates (ζ, η). The first one was proposed by Thompson et al. (1974) and the other by Chen and Obasih (1987).

Thompson et al. (1974) proposed Poisson equations as the coordinate generating system. They are

$$\xi_{xx}+\xi_{yy}=P(\xi,\eta) \tag{7a}$$

$$\eta_{xx}+\eta_{yy}=Q(\xi,\eta) \tag{7b}$$

Since it is desired to execute all numerical computations in the uniform rectangular transformed plane, the roles of the dependent and independent variable must be interchanged in equation (7). This yields an elliptic system of quasilinear equations in the transformed plane

$$\alpha x_{\xi\xi}-2\beta x_{\xi\eta}+\gamma x_{\eta\eta}=-J^2(Px_\xi+Qx_\eta) \tag{8a}$$

$$\alpha y_{\xi x}-2\beta y_{\xi\eta}+\gamma y_{\eta\eta}=-J^2(Py_\xi+Qy_\eta) \tag{8b}$$

where α, β, and γ are transformation coefficients

$$\alpha=x_\eta^2+y_\eta^2 \tag{9a}$$

$$\beta=x_\xi x_\eta+y_\xi y_\eta \tag{9b}$$

$$\gamma=x_\xi^2+y_\xi^2 \tag{9c}$$

and J denotes the Jacobian of the transformation

$$\mathrm{J}=\frac{\partial(x,y)}{\partial(\xi,\eta)}=x_\xi y_\eta-x_\eta x_\xi \tag{9d}$$

The constant ξ lines and constant η lines can be spaced as desired around the boundaries in the physical domain, since the assignment of the (ξ, η) values to (x, y) boundary points via x_i and y_j functions are arbitrary if the shapes of the boundaries Γ_i shown in Fig. 1 are prescribed.

Control of the coordinate line spacing in the field, and on the boundary if Neumann boundary conditions are imposed, can be accomplished through the control functions P and Q. Two methods of specifying the control functions are used in the present study. The first one is that of Thompson et al. (1977). They utilized the exponential functions to achieve the attraction of coordinate lines to other coordinate lines and/or points in the following forms:

$$P(\xi,\eta)=-\sum_{i=1}^{n}a_i\,\mathrm{sign}(\xi-\xi_i)\exp(-c\,|\xi-\xi_i|)$$

$$-\sum_{j=1}^{m}b_i\,\mathrm{sign}(\xi-\xi_j)\exp\{-d_j[(\xi-\xi_j)^2+(\eta-\eta_j)^2]^{1/2}\} \tag{10a}$$

$$Q(\xi,\eta)=-\sum_{i=1}^{n}a_i\,\mathrm{sign}(\eta-\eta_i)\exp(-c_i\,|\eta-\eta_i|)$$

$$-\sum_{j=1}^{m}b_i\,\mathrm{sign}(\eta-\eta_j)\exp\{-d_j[(\xi-\xi_j)^2+(\eta-\eta_j)^2]^{1/2}\} \tag{10b}$$

where $\mathrm{sign}(x)$ is simply the sign of x, and the positive amplitudes, a_i, b_j, and decay factor, c_i, d_j, are not necessarily the same in the two equations.

The second method is suggested by Chen and Obasih (1986). They attempt to create a nearly orthogonal boundary-fitted coordinate by setting the cross-derivative transformation coefficient β in equation (8) to zero and choosing the direct control functions P and Q as

$$P(\xi,\eta)=\frac{\sqrt{\alpha\gamma}}{\mathrm{J}^2}\left(\sqrt{\frac{\alpha}{\gamma}}\right) \tag{11a}$$

$$Q(\xi,\eta)=\frac{\gamma}{\mathrm{J}^2}[(y\xi_{x_{\eta\eta}}-x_\xi y_{\eta\eta})/\mathrm{J}]_{\Gamma_i} \tag{11b}$$

The term in brackets in equation (11b) is evaluated at a boundary Γ_i with a user specified grid distribution in the η direction in which clustering is desired. Figure 2 shows respectively the coordinate systems generated by control function given by equations (10) and (11). The above two grid systems are used to examine their influences on the flow and temperature fields.

3.2 Governing Equations in Boundary-Fitted Coordinate Systems. The transport equations governing unsteady two-dimensional flow and heat transfer must be transformed into the boundary-fitted coordinates, ξ and η. The governing equations (1), (2), and (3) in the Cartesian coordinates (x, y) may be written in the transformed coordinates (ξ, η) in the following:

$$\mathrm{J}^2\mathrm{Re}\zeta_t+(\mathrm{JRe}\varphi_\eta-\tau)\zeta_\xi+(-\mathrm{JRe}\varphi_\xi-\sigma)\zeta_\eta$$

$$=\alpha\zeta_{\xi\xi}+\gamma\zeta_{\eta\eta}-2\beta\zeta_{\xi\eta} \tag{12}$$

$$-\tau\varphi_\xi-\sigma\varphi_\eta=\alpha\varphi_{\xi\xi}+\gamma\varphi_{\eta\eta}-(2\beta\varphi_{\xi\eta}-\mathrm{J}^2\zeta) \tag{13}$$

$$\mathrm{J}^2\mathrm{Pe}\theta_t+(\mathrm{JPe}\Psi_\eta-\tau)\theta_\xi+(-\mathrm{JPe}\Psi_\xi-\sigma)\theta_\eta$$

$$=\alpha\theta_{\xi\xi}+\gamma\theta_{\eta\eta}-2\beta\theta_{\xi\eta} \tag{14}$$

where σ and τ are respectively defined as

$$\sigma=\frac{1}{\mathrm{J}}(y_\xi D_x-x_\xi D_y) \tag{15a}$$

$$\tau = \frac{1}{J}(x_\eta D_y - y_\eta D_x) \tag{15b}$$

with

$$D_x = \alpha x_{\xi\xi} - 2\beta x_{\xi\eta} + \gamma x_{\eta\eta} \tag{15c}$$

$$D_y = \alpha y_{\xi\xi} - 2\beta y_{\xi\eta} + \gamma y_{\eta\eta} \tag{15d}$$

It is noted that the transformation coefficients α, β, γ, σ, τ, and J at each node of computational domain are merely geometric functions of the physical plane. Once the boundary-fitted coordinates are generated, the coefficients of coordinate transformation can be calculated and stored once for all for use in the solutions of equations (12), (13), and (14).

In general, equations (12), (13), and (14) can be cast into a suitable generic form that is convenient to implement in the finite analytic method (Chen, 1987; Chen and Chen, 1984) as

$$\alpha\phi_{\xi\xi} + \gamma\phi_{\eta\eta} = 2A\phi_\xi + 2B\phi_\eta + E\phi_t + S \tag{16}$$

when ϕ is the vorticity ξ in equation (12)

$$A = \frac{1}{2}(\mathrm{JRe}\varphi_\eta - \tau); \qquad E = \mathrm{J}^2\mathrm{Re}$$

$$B = \frac{1}{2}(-\mathrm{JRe}\varphi_\xi - \sigma); \qquad S = 2\beta\zeta_{\xi\eta}$$

and when ϕ is the stream function ϕ in equation (13)

$$A = -\frac{\tau}{2}; \qquad E = 0$$

$$B = -\frac{\sigma}{2}; \qquad S = -\mathrm{J}^2 + 2\beta\varphi_{\xi\eta}$$

and when ϕ is the temperature θ in equation (14)

$$A = \frac{1}{2}(\mathrm{JPe}\varphi_\eta - \tau); \qquad E = \mathrm{J}^2\mathrm{Pe}$$

$$B = \frac{1}{2}(-\mathrm{JPe}\varphi_\xi - \sigma); \qquad S = 2\beta\theta_{\xi\eta}$$

3.3 Finite Analytic Numerical Method. The finite analytic (FA) method (Chen, 1987) was developed recently to remedy the difficulties experienced in the numerical solutions of fluid flow and heat transfer problems. The basic idea of the finite analytic numerical method is to utilize the local analytic solutions in an element to obtain the algebraic representations of the governing partial differential equations, thus eliminating the truncation error in the finite difference approximation and the use of approximation function in the finite element method. Although the finite analytic solution needs approximation boundary functions and local linearization, it exhibits a special feature that can shift automatically and analytically the upwind influence of the adjacent nodal values according to direction and magnitude of convection. The FA solutions have been shown (Zeng and Li, 1987) to be stable and accurate and to converge rapidly in many problems (Chen et al., 1985, 1987).

In the FA method, like many other numerical methods, the computational domain of the problem is divided into many small elements. The analytic solution is then solved for the governing equation in the local elements. A set of algebraic equations that approximates the governing equation in the whole domain can be obtained for numerical solution.

Consider an elliptic partial differential equation (16) in a transformed region D with a rectangular numerical element shown in Fig. 3. The element has uniform grid spacing $\Delta\xi = \Delta\eta = 1$. Equation (16) is locally linearized as

$$\alpha_P\phi_{\xi\xi} + \gamma_P\phi_{\eta\eta} = 2A_P\phi_\xi + 2B_P\phi_\eta + g_p \tag{17}$$

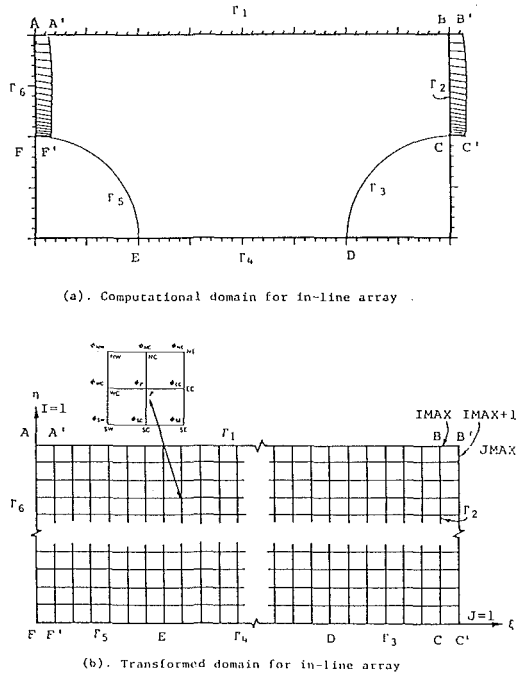

Fig. 3 Finite analytic element and domain of computation

with

$$g_p = E_P(\phi_P - \phi_P^{n-1})/\Delta t + S_P$$

where the subscript P signifies that the term is evaluated at the central node P of a local element and the superscript $n-1$ denotes the value at the previous time step (the superscript n for current value is omitted) and Δt is the time increment. It is noted that the transient term is approximated by the backward difference. The coefficients of second-order derivatives in equation (17) can be eliminated by utilizing the coordinate stretching functions

$$\xi' = \frac{\xi}{\sqrt{\alpha_P}}, \qquad \eta' = \frac{\eta}{\sqrt{\gamma_P}} \tag{18}$$

and equation (17) reduces to the standard convenient form of two-dimensional convective transport equation described in Chen and Chen (1984) as

$$\phi_{\xi'\xi'} + \phi_{\eta'\eta'} = 2A\phi_{\xi'} + 2B\phi_{\eta'} + g_p \tag{19}$$

where

$$A = \frac{A_P}{\sqrt{\alpha_P}}, \qquad B = \frac{B_P}{\sqrt{\gamma_P}}$$

Note that the local element, after being stretched by equation (18), has the dimensions of

$$\xi' = h = \frac{1}{\sqrt{\alpha_P}}, \qquad \eta' = k = \frac{1}{\sqrt{\gamma_P}} \tag{20}$$

In seeking the analytic solution in a local element, shown in Fig. 3, four boundary conditions on the east, west, north, and south sides are required because of the ellipticity of equation (19). Various functions can be used to approximate the boundary conditions where three nodes are located on each boundary. Chen and Chen (1984) proposed a combination of a linear and exponential function for the boundary function. The choice of a linear and exponential function is made because they are derived from the natural solution of the governing equation (19). For example, the boundary function on the eastern boundary $\xi' = h$ of a local element is

$$\phi(h, \eta') = a_E(e^{2B\eta'} - 1) + b_E\eta' + c_E \tag{21}$$

where a, b, and c are constant and can be determined by the three nodal values on the boundary considered.

$$a_E = \frac{\phi_{NE} + \phi_{SE} - 2\phi_{EC}}{4\sinh^2 Bk} \tag{21a}$$

$$b_E = \frac{1}{2k}[\phi_{NE} - \phi_{SE} - \coth(Bk)\,(\phi_{NE} + \phi_{SE} - 2\phi_{EC})] \tag{21b}$$

$$c_E = \phi_{EC} \tag{21c}$$

With the boundary functions of equation (21), an analytic solution of equation (19) can be obtained for each element by the method of separation of variables or any other analytic technique. Details of the solution procedures are documented in Chen and Chen (1984). Evaluation of the local analytic solution at the central node P of the rectangular element results in the following nine-point FA algebraic equation:

$$\begin{aligned}\phi_P &= \sum_{n=1}^{8} C_n\phi_n - C_P g_P \\ &= C_{NE}\phi_{NE} + C_{NW}\phi_{NW} + C_{SE}\phi_{SE} + C_{SW}\phi_{SW} \\ &\quad + C_{EC}\phi_{EC} + C_{WC}\phi_{WC} + C_{NC}\phi_{NC} + C_{SC}\phi_{SC} - C_P g_P\end{aligned} \tag{22}$$

where

$$\begin{aligned}C_{SC} &= \left(\frac{e^{Bk}}{2\cosh Bk}\right)P_A \\ C_{WC} &= \left(\frac{e^{Ah}}{2\cosh Ah}\right)P_B \\ C_{NC} &= e^{-2Bk}C_{SC} \\ C_{EC} &= e^{-2Ah}C_{WC} \\ C_{SW} &= \left(\frac{e^{Ah+Bk}}{4\cosh Ah\cosh Bk}\right)(1 - P_A - P_B) \\ C_{SE} &= e^{-2Ah}C_{SW} \\ C_{SE} &= e^{-2Ah}C_{SW} \\ C_{NE} &= e^{-2Ah-2Bk}C_{SW} \\ C_P &= \frac{h\tanh Ah}{2A}(1 - P_A) = \frac{k\tanh Bk}{2B}(1 - P_B) \\ P_A &= 4E_2 Ah\cosh Ah\cosh Bk\coth Ah \\ P_B &= 1 + \frac{Bh\coth Bk}{Ak\coth Ah}(P_A - 1)\end{aligned} \tag{23}$$

and

$$E_2 = \sum_{m-1}^{\infty} \frac{(-1)^{m+1}(\lambda_m h)}{[(Ah)^2 + (\lambda_m h)^2]^2\cosh(\sqrt{A^2 + B^2 + \lambda_m^2})k}$$

$$\lambda_m h = \left(m - \frac{1}{2}\right)\pi$$

The above FA coefficients are always positive (Zeng and Li, 1987) because of the positive values of P_A and P_B and $(P_A + P_B) \le 1$. The ellipticity of the flow equation (19) is then represented accurately. In addition, the FA coefficients can provide a gradual upwind bias since the cell Reynolds number $|2Ah|$ and $|2Bk|$ are contained in the exponents. Hence, the characteristics of the convective-diffusion equation is properly preserved in the FA coefficients. Moreover, the local analytic solution for the interior point P includes all corner points that can minimize false numerical diffusion.

For the unsteady convective transport equation (19) with source term g, the local analytic solution can be obtained by substituting g from equation (17a) into equation (22)

$$\begin{aligned}\phi_P &= \frac{1}{1 + C_P E_P/\Delta t}\left[\sum_{n=1}^{8} C_n\phi_n + \frac{E_P C_P}{\Delta t}\phi_P^{n-1} - C_P S_P\right] \\ &= \frac{1}{1 + C_P E_P/\Delta t}\left[C_{NE}\phi_{NE} + C_{NW}\phi_{NW} + C_{SE}\phi_{SE} + C_{SW}\phi_{SW}\right. \\ &\quad + C_{EC}\phi_{EC} + C_{WC}\phi_{WC} + C_{NC}\phi_{NC} + C_{SC}\phi_{SC} \\ &\quad \left. + \frac{E_P C_P}{\Delta t}\phi_P^{n-1} - C_P S_P\right]\end{aligned} \tag{24}$$

It is seen that ϕ_P depends upon all eight nodal values at the current time step as well as the value at the previous $(n-1)$ time step. In evaluation of the source term S_P, Chen and Chen (1984) suggested it be treated as a known value either from the previous time step or the previous iteration.

The local finite-analytic solutions can be assembled for all elements in the computational domain resulting in a set of linear algebraic equations. The simultaneous equations are solved by proper numerical procedures such as the Gauss-Seidel iterative method, or by the line-by-line tridiagonal matrix algorithm.

4 Discussion of Numerical Solutions

This section discusses the numerical aspects of the solutions for laminar flow and heat transfer across tube bundles with in-line and staggered arrangements. The computations were performed on a PRIME 850 computer system, which has a speed approximately 400 times slower than that of the CRAY 1 system.

4.1 Numerical Sweeping Direction. In obtaining the finite analytic solutions, the line-by-line iteration test was carried out to compare the computing time required in iteration for different directions of sweeping on the flow across staggered array at Re = 40. When the problem was solved iteratively by sweeping along the ξ direction (the flow direction) of a 21×21 grid node, as shown in Fig. 3, it took 168 global iterations to achieve the convergent criteria of $|\Delta\varphi/\varphi_{\max}| < 1 \times 10^{-4}$ and $|\Delta\zeta/\zeta_{\max}| < 1 \times 10^{-4}$ with 1167 second CPU on the PRIME 850. In other words, it took an average of 6.9 second CPU for each iteration. When the problem was selected to march in the η direction (normal to the flow direction), it took 174 iterations and 1347 second CPU for the initial conditions and convergent criteria. The CPU required for each iteration in this case is 7.7 seconds. The alternating direction implicit (ADI) method consumed 1750 second CPU on 163 iterations, averaging 10.7 second CPU per iteration. It is seen that the ADI method incorporated with the FA method does not have much benefit over the other single-direction marching methods; rather, it consumes 30 to 50 percent more CPU time in changing the computation routine alternatively. The reason that simple line-by-line iteration works well for the FA method is that the FA equation (22) already incorporates all corner points in the solution and properly represents the characteristics of the elliptic partial differential equation. Therefore, the FA solution converges well without invoking alternative direction iteration. Similar results have been found in solving the energy equation. Hence in the present investigation a simple marching of iteration in the ξ direction is adopted for the rest of the computations.

4.2 Influence of the Boundary-Fitted Coordinate Systems. The effect of the grid control functions and number of nodal points on the solutions of fluid flow and temperature distribution is presented in Fig. 4 for a Reynolds number of 400. The solid line and dotted line contours in the plots are the solutions employing the boundary-fitted coordinate respectively with 31×21 and 21×21 grid nodes based on the Thompson et al. (1977) control function specified by equation (10), while the broken line contours utilize 21×21 grid nodes with grid control functions of equation (11) based on Chen and Obasih (1986). It can be seen that the solutions for the stream function with an interval increment of 0.0625 are very close to each other in the main stream. It should be noted that the gradients of the stream function, which is related to the velocity, inside the recirculation zone are relatively low. For instance, the values of the three closed contours of stream function inside the recirculation zone, from the outer to the inner, are -0.0063, -0.0125, and -0.025, respectively. Hence, the differences in velocity are not evident as indicated by the stream line plots. Also shown in Fig. 4, the solutions of the vorticity on three different coordinate systems coincide closely in the main stream, but differ somewhat inside the separation zone. The predicted vorticity in the vicinity of the stagnation points of the tube shows that the differences between solutions obtained from three different coordinate systems are not as severe as those at the other parts. Hence, due to the lower velocity in the recirculation region, whether the coordinate is attracted toward the stagnation point or not, the flow solution is not sensitive in the range of low Reynolds numbers investigated.

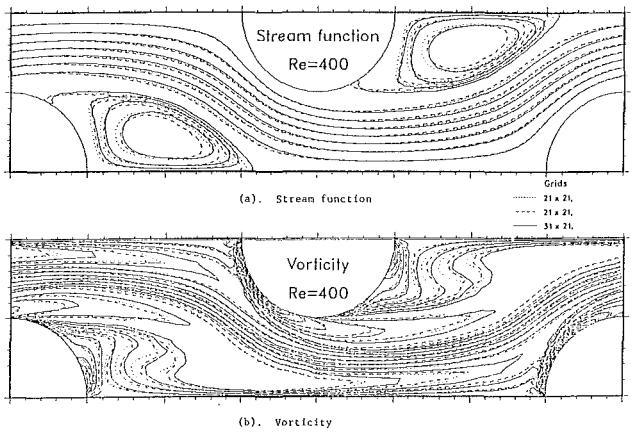

Fig. 4 Effect of the grid system on numerical solutions

It is concluded that the numerical solutions using both boundary-fitted coordinate systems with 21×21 are acceptable for the present study.

5 Flow Field Analysis. Since it is assumed that the flow is symmetric with respect to the top and bottom boundaries of the computational domain and is periodic or reverse periodic with respect to the inlet and outlet portions, the unsteady, asymmetric vortex shedding phenomenon behind a tube, if it exists, is not considered in the present investigation. However, even when the flow is assumed to be symmetric with respect to the top and bottom boundaries, the flow separation may be predicted during the computation if the Reynolds number is high. The flow pattern is best represented in stream line and vorticity distribution. The combined resistance from skin friction and form drag is tabulated in pressure drop per row of tube bundles, which is presented in Part II of the present paper.

5.1 In-line Array. The distributions of stream function across the in-line array are presented in Fig. 5 for Reynolds numbers of 40, 120, 400, and 800. A general view of the stream function in the range of Reynolds number investigated shows that the main stream of the flow is mostly confined in the open channel between columns of tubes in the array. The flow separates at the rear portion of a tube and reattaches at the front portion of the following tube in the array to form a stationary recirculation region between the two adjacent tubes. In the present study the angle of separation is measured clockwise from the rear stagnation point to the point of separation, which the angle of reattachment is measured counterclockwise from the forward stagnation point to the point of reattachment. Both angles increase with increase in the Reynolds number, as shown in Table 1. In Fig. 5 the stream function that marks the separation zone on the lower tube wall is set equal to zero and that on the top boundary is set equal to 0.5. At low Reynolds number of 40 the contours of stream lines exhibit slight wavy form, while for the Reynolds number of 400 and 800, the stream lines are com-

Table 1 Angles of separation and reattachment for tube banks

	In-line array				Staggered array			
Re	40	120	400	800	40	120	400	800
Separation	39°	48°	55°	58°	38°	54°	66°	73°
Reattachment	23°	39°	49°	52°				

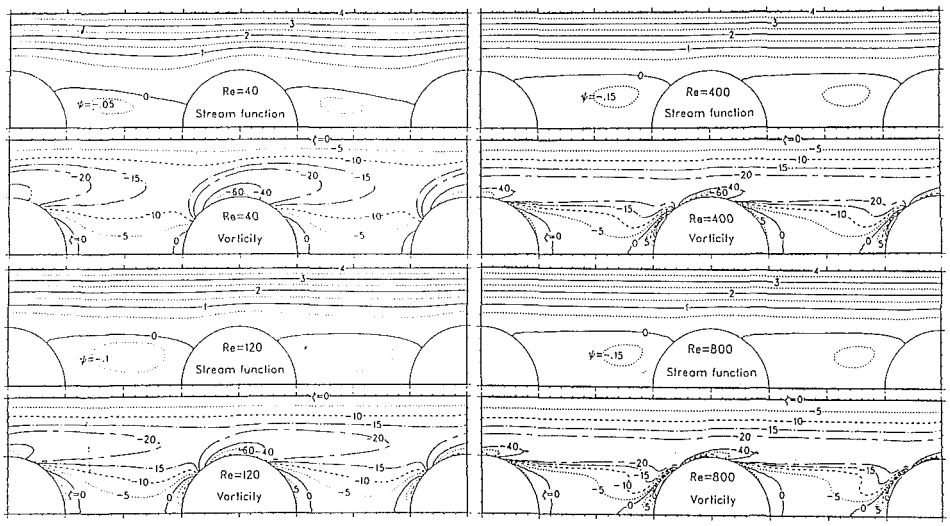

Fig. 5 Stream function and vorticity for in-line array

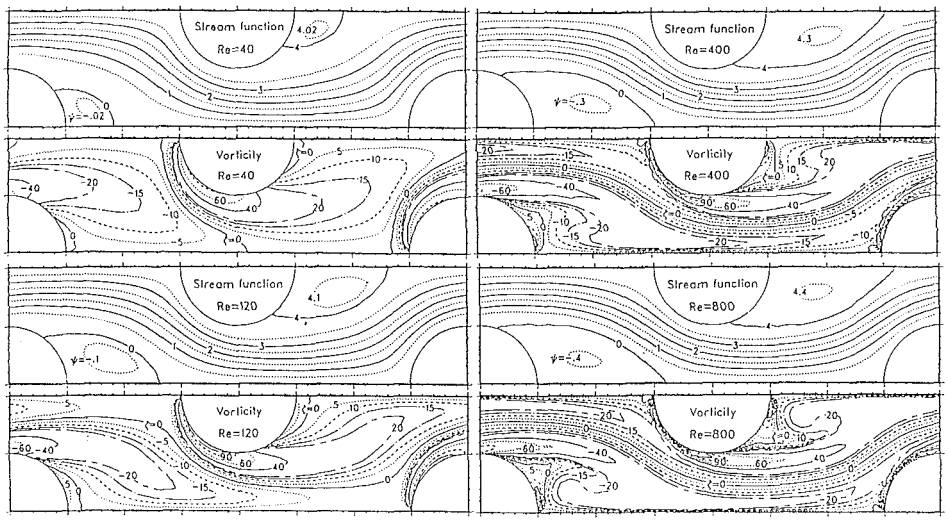

Fig. 6 Stream function and vorticity for staggered array

parable with that in a straight channel. The strength of the recirculation inside the eddy increases with increasing Reynolds number. The center of the recirculation at low Reynolds numbers is located close to the rear of the preceding tube and moves toward the middle of the separation region as the Reynolds number is increased. It then shifts farther downstream near the reattachment point on the following tube when the Reynolds number is further increased.

The general trend of the vorticity reveals that in the region of throughflow the vorticity is convected along the stream line. Close to the wall the vorticity is relatively high, particularly near the separation and reattachment points. As the Reynolds number is increased, the contours of constant vorticity begin to lean downstream, enveloped in the thin boundary layer.

Figure 5 shows that at low Reynolds number of $Re = 40$, the viscous diffusion tends to cover a large fluid region between the tubes after the main flow passed the top of a tube. The recirculation zone is small behind the tube with small value of vorticity. However, unlike the flow past a single cylinder at low Reynolds number where the vortex is small and attached to the rear of the cylinder, the vortex in the in-line array is elongated and reattaches to the following tube. The center of recirculation is still closer to the upstream tube. The flow is separated at 39 deg when measured counterclockwise from the rear stagnation point of the tube and reattached at 23 deg when measured clockwise from the front stagnation point of the following tube. Because diffusion is still significant at $Re = 40$ the contours of the vorticity that penetrate into the main stream elongate downstream as shown in Fig. 5. The local maximum gradients of the vorticity in the ξ direction that is tangent to the tube surface occur near the separation and reattachment points, while the largest gradient in the η direction that is normal to the surface is located near the top of the tube slightly upstream. It should be noted that the contour of zero vorticity exists not only along the symmetric planes of the bottom and top boundaries but also inside the vortex at the rear and front of tubes. The changing sign of the vorticity in the separation zone is due to the change of velocity gradient in the zone.

At Reynolds number of 120, the inertial force is large and the stream lines in the main flow, when compared with those at $Re = 40$, are much more straight. The value of the stream function in the separation zone becomes larger because of a higher recirculation velocity in the vortex. The flow separates at 48 deg and reattaches at 39 deg. The center of the recirculation now is located near the middle of the separation zone because of a larger driven velocity and a larger vortex. With increase of the inertial force in the main stream, the vorticity in the throughflow increases as shown in Fig. 5. The trend of vorticity distribution near the wall is similar to that at the Reynolds number of 40, except that the value of vorticity is larger.

As the Reynolds number is further increased to 400 and 800, the stream lines are further straightened, like a flow in a straight channel, and the size of the separation zone grows bigger. The center of the vortex is shifted downstream, which is also observed in a driven cavity flow. The separation angles are respectively 55 and 58 deg for the Reynolds numbers of 400 and 800, while the reattachment angles are 49 and 52, respectively. It is seen that the high value of vorticity at the top of the tubes is confined to the thin boundary layer. The vorticity distributions in the separation zone are similar for the Reynolds numbers of 400 and 800; however, the contours of the vorticity are distorted near the center of the recirculation because of the higher vorticity at the Reynolds number of 800.

5.2 Staggered Array. Figure 6 presents the distribution of the stream function for the two-dimensional incompressible flow across the staggered array. Unlike flow passed through an in-line array, which has an open-channel path, the flow in a staggered array has to alter its flow direction of the through stream because of the repeated blockage of the staggered tubes in a bank, resulting in quite different flow patterns in tube bundles. In general, the stream lines in a staggered array approach the front of a tube like a stagnation flow, and then are deflected away and moved downstream along the front curvature of the tube. Due to the inertial force of the main stream, the flow tends to move straight forward after passing the extrusion of the cylinder in the flow field until it encounters an obstruction of the staggered tube in the downstream. A pair of symmetric eddies normally forms behind the cylinder. As the Reynolds number is increased, the stream lines tend to move closer to the front portion of a cylinder before being deflected sideways. This results in forming a thin boundary layer on the tube. The size and the length of the separation zone increase with the increase of the Reynolds number. In general the flow in a staggered array resembles the flow in a curved channel with periodically converging and diverging cross section. Vortices behind a cylinder can be diminished at low Reynolds number by reducing the longitudinal pitch.

The distribution of the vorticity near the top of a tube is similar to that of an in-line array; however, the overall distributions differ for both geometries. They are discussed separately for each Reynolds number below.

At the Reynolds number of 40, the stream lines in the throughflow have nearly equal distance across the minimum cross-sectional area, and have a larger distance when the stream changes direction because of an obstacle in the downstream. The roles of stream lines near the wall and on the symmetry plane are exchanged for each row of tubes in the bank. The attached eddies behind a tube are small at the Reynolds number of 40 because of strong viscous diffusion. The separation angle for this case is 38 deg when measured counterclockwise from the symmetric plane. Note that the intensity of the recirculation region for the staggered array is lower than that for the in-line array for the same given Reynolds number and geometric pitches. Reduction in the longitudinal pitch can reduce the area between two adjacent tubes in the longitudinal direction; therefore, the size of the attached eddy can be reduced or even totally vanished. The vorticity distribution of the staggered array at low Reynolds number shown in Fig. 6 is divided by the zero contour of vorticity for each tube. The vorticity is generated densely at the upstream facing surface of the cylinder where the velocity gradient is large, and is diffused into the main flow. Due to the existence of the throughflow, the vorticity is convected and elongated into the downstream area. Unlike the vorticity in the in-line array, the zero contour of vorticity exists only in the rear surface of the tube where the separation zone attached.

As the Reynolds number increases to 120, the increased inertial force delays the deflection of the stream lines near the front part of the tube resulting in a thin boundary layer on the upstream surface and a larger separation zone on the downstream surface. Because of the higher velocity in the throughflow the recirculation strength is increased in the separation zone. A feature of vorticity distribution is characterized by the contour of zero vorticity contours for each row in the tube banks as shown in Fig. 6. The other contour lines are similar to that for the Reynolds number of 40, except with higher strength and convection farther downstream.

At higher Reynolds numebrs of 400 and 800, the contours of the stream functions shown in Fig. 6 are similar to those for the Reynolds number of 40 with stronger recirculation in the separation zone. The stream lines in the throughflow are nearly parallel to each other negotiating through staggered tubes. It should be remarked that in the case of $Re = 800$, the eddy behind the cylinder may be no longer steady since it was observed that if a large time step is employed in the computation the numerical solution and hence the flow physically may be on the verge of becoming unsteady flow. The steady flow solution is obtained after additional underrelaxation factors and physically smaller disturbance are introduced in the time-marching method. The steady-state solution is shown in Fig. 6. The distribution of vorticity at this higher Reynolds number shows that the high vorticity region is confined in the region near the tube. The constant contour lines of vorticity are not only carried farther downstream by the higher convective velocity but also rolled up near the center of the recirculation due to the stronger vortical motion in the separation zone.

6 Conclusions

The flow and heat transfer from arrays of tubes in crossflow are complex phenomena because of its complex geometry, and are important in many engineering applications. In the present study, the boundary-fitted coordinate system is incorporated with the FA numerical method to predict laminar flow and heat transfer in the standard layouts of tube banks. The FA solutions were obtained for the two-dimensional Navier–Stokes equations written in the stream-function and vorticity formulation and the energy equation in the transformed plane. The present numerical procedure worked successfully for both in-line and staggered arrays. It is shown that the boundary-fitted coordinate transformation can be utilized successfully with the FA method to solve flow problems with complex geometries because one of the boundary-fitted coordinates coincides with irregular boundaries. Where the boundary conditions can be imposed precisely, accurate solutions can be obtained. Furthermore, the FA solutions obtained are shown to be stable and converge rapidly. This is mainly because the FA solution contains the automatic upwinding influence of neighboring nodes, hence the characteristics of the convection-diffusion equations are preserved properly in the FA algebraic equations.

References

Antonopoulos, K. A., 1985, "Heat Transfer in Tube Banks Under Conditions of Turbulent Inclined Flow," *Int. J. Heat and Mass Transfer*, Vol. 28, No. 9, pp. 1645–1656.

Chen, C. J., 1987, "Finite Analytic Method," in: *Handbook of Numerical Heat Transfer*, W. J. Minkowycz, E. M. Sparrow, R. H. Pletcher, and G. E. Schneider, eds., Wiley, New York, Chap. 17.

Chen, C. J., and Chen, H. C., 1984, "Development of Finite Analytic Numerical Method for Unsteady Two-Dimensional Navier–Stokes Equations," *J. Computational Physics*, Vol. 53, No. 2, pp. 209–226.

Chen, C. J., and Obasih, K. M., 1986, "Numerical Generation of Nearly Orthogonal Boundary-Fitted Coordinate System," *Proceeding, The Symposium on Advancement in Aerodynamics, Fluid Mechanics and Hydraulics*, ASCE, Minneapolis, MN, June 3–5, pp. 585–592.

Chen, C. J., and Cheng, W. S., 1985, "Finite Analytic Prediction of Turbulent Flow Past an Inclined Cylinder," *Third Symposium on Numerical and Physical Aspects of Aerodynamic Flows*, California State Univ., Long Beach, CA, pp. 3.27–3.41.

Chen, C. J., Yu, C. H., and Chandran, K. B., 1987, "Finite Analytic Numerical Solution of Unsteady Laminar Flow Past Disc-Valves," *J. Engineering Mechanics*, Vol. 113, No. 8, Aug., pp. 1147–1162.

Ho, K. S., and Chen, C. J., 1983, "Finite Analytic Solution of Laminar Convective Heat Transfer in Tube Bundles," ASME Paper No. 83-WA/HT-23.

Launder, B. E., and Massey, T. H., 1978, "The Numerical Prediction of Viscous Flow and Heat Transfer in Tube Banks," ASME JOURNAL OF HEAT TRANSFER, Vol. 100, pp. 565–571.

Le Feuvre, R. F., 1973, "Laminar and Turbulent Forced Convection Processes Through In-Line Tube Banks," Imperial College London, Mechanical Engineering Dept., HTS/74/5.

Thom, A., and Apelt, C. J., 1961, *Field Computations in Engineering and Physics*, Van Nostrand, London.

Thompson, J. F., Thames, F. C., and Mastin, C. W., 1974, "Automatic Numerical Generation of Body-Fitted Curvilinear Coordinate System for Fields Containing Any Number of Arbitrary Two-Dimensional Bodies," *J. Computational Physics*, Vol. 15, pp. 299–319.

Thompson, J. F., Thames, F. C., and Mastin, C. W., 1977, "TOMMCAT—A Code for Numerical Generation of Body-Fitted Curvilinear Coordinate System on Fields Containing Any Number of Arbitrary Two-Dimensional Bodies," *J. Computational Physics*, Vol. 24, pp. 274–302.

Zeng, X. J., and Li, W., 1987, "The Stability and Convergence of Finite Analytic Method for Unsteady Two-Dimensional Convective Transport Equations," in: *Turbulence Measurements and Flow Modeling*, C. J. Chen, L. D. Chen, and F. M. Holly, eds., Hemisphere Publishing Co., pp. 427–433.

Finite Analytic Solution of Convective Heat Transfer for Tube Arrays in Crossflow: Part II—Heat Transfer Analysis

Ching Jen Chen
Professor and Chairman.

Tzong-Shyan Wung[1]

Department of Mechanical Engineering,
Iowa Institute of
Hydraulic Research,
College of Engineering,
The University of Iowa,
Iowa City, IA 52242

The convective heat transfer and pressure drop in flow past two types of tube array are solved numerically by the Finite Analytic Method in this investigation. The tube arrays considered are an in-line tube array and a staggered tube array with longitudinal and transverse pitch of two. The flow field solution is obtained and analyzed in Part I of the study. In the present Part II, the temperature field, heat transfer characteristics, and pressure drop are investigated. The fluid and tubes are considered to be at the same temperature, except for the array tube, which is heated or cooled. The solution domain covers three pitches of tube arrays in order to simulate accurately the non-periodic behavior of the temperature field downstream of the heated tube. In general, the heat transfer in a staggered array of tubes is found to be higher than that in an in-lined array of tubes. However, the pressure drop in a staggered array arrangement is also higher. Local heat transfer varies between in-line and staggered tube arrays and depends on Reynolds number and Prandtl number. At high Reynolds number, the local heat transfer tends to peak at the upstream surface of the heated tube but away from the stagnation point and becomes minimum at the separation point. Heat transfer in recirculation zones are, in general, small.

I Introduction

This study is the second part of a two-part investigation on convective heat transfer for tube arrays in a crossflow. The tube arrangements selected for the study are an in-line array and a staggered array, both with longitudinal and transverse pitch of two. These two tube arrays are perhaps the most typical tube arrangements in the design of industrial heat exchangers. In this study, it is demonstrated that the flow and heat transfer in these complex geometries can be numerically simulated. In Part I (Wung and Chen, 1989) of the present investigation, the flow field is analyzed for Reynolds numbers of 40, 120, 400, and 800. The numerical solutions are obtained by solving the Navier–Stokes equations, written in the form of stream function-vorticity formulation via the finite analytic numerical method. Boundary-fitted coordinates were used to obtain accurate numerical solutions. In this part, the numerical solutions for a temperature field are obtained from energy equations in a larger domain of computation. Hence, an accurate temperature field and details of heat transfer characteristics are predicted.

In the present study, attention is focused on the convective heat transfer from a heated tube in the fully developed region of tube arrays in a crossflow, as shown in Fig. 1. The fluid is considered incompressible with constant properties and the flow is assumed to be steady and two dimensional. The flow pattern is assumed exactly repeated from one row to the next and is symmetric from one column to the other column for both in-line and staggered arrays. It should be remarked that although only one period of arrays is needed for the solution of flow field in in-line or staggered arrays, three periods of arrays, as shown in Fig. 1, are considered for the solution of the temperature field because temperature boundary conditions are not periodic.

2 Analysis

2.1 Governing Equations. The stream function-vorticity formulation of the flow past a tube bank, written in dimensionless form, is given as follows:

$$\mathrm{Re}(\zeta_t + \varphi_y \zeta_x - \varphi_x \zeta_y) = \zeta_{xx} + \zeta_{yy} \tag{1}$$

$$\varphi_{xx} + \varphi_{yy} = -\zeta \tag{2}$$

and the energy equation with no heat generation, no radiation, and negligible viscous dissipation is

$$\mathrm{Pe}(\theta_t + \varphi_y \theta_x - \varphi_x \theta_y) = \theta_{xx} + \theta_{yy} \tag{3}$$

where φ, ζ, and θ are dimensionless parameters and are the stream function, vorticity, and temperature, respectively. They are made dimensionless by scaling vorticity ζ by V/d, the stream function φ by Vd, the temperature θ by $T_w - T_0$, the space dimensions x and y by d, and time t by d/V. $\mathrm{Re} = Vd/\nu$ is the Reynolds number based on the cylinder diameter d and the average velocity V in the minimum free flow area between tubes, and the Pe is the Peclet number $\mathrm{Pe} = \mathrm{Pr}\,\mathrm{Re}$, where Pr is the Prandtl number. T_w is the isothermal temperature of the heated tube and T_0 is the constant inlet temperature of the fluid and the unheated tubes. The vorticity ζ is defined by

$$\zeta = v_x - u_y = -\nabla^2 \varphi \tag{4}$$

and velocity components

$$u = \varphi_y, \qquad v = -\varphi_x \tag{5}$$

The transient terms in the vorticity equation (1) and energy equation (3) are retained because the time-marching method will be used in the numerical calculation of the steady flow and heat transfer problem. Equations (1) and (2) with pertinent body conditions are solved first and given in Part I of the pres-

[1] Present address: Associate Professor, Institute of Applied Mechanics, National Taiwan University, Taipei, Taiwan.

Contributed by the Heat Transfer Division and presented at the National Heat Transfer Conference, Houston, Texas, July 24–27, 1988. Manuscript received by the Heat Transfer Division November 11, 1987. Keywords: Forced Convection, Heat Exchangers.

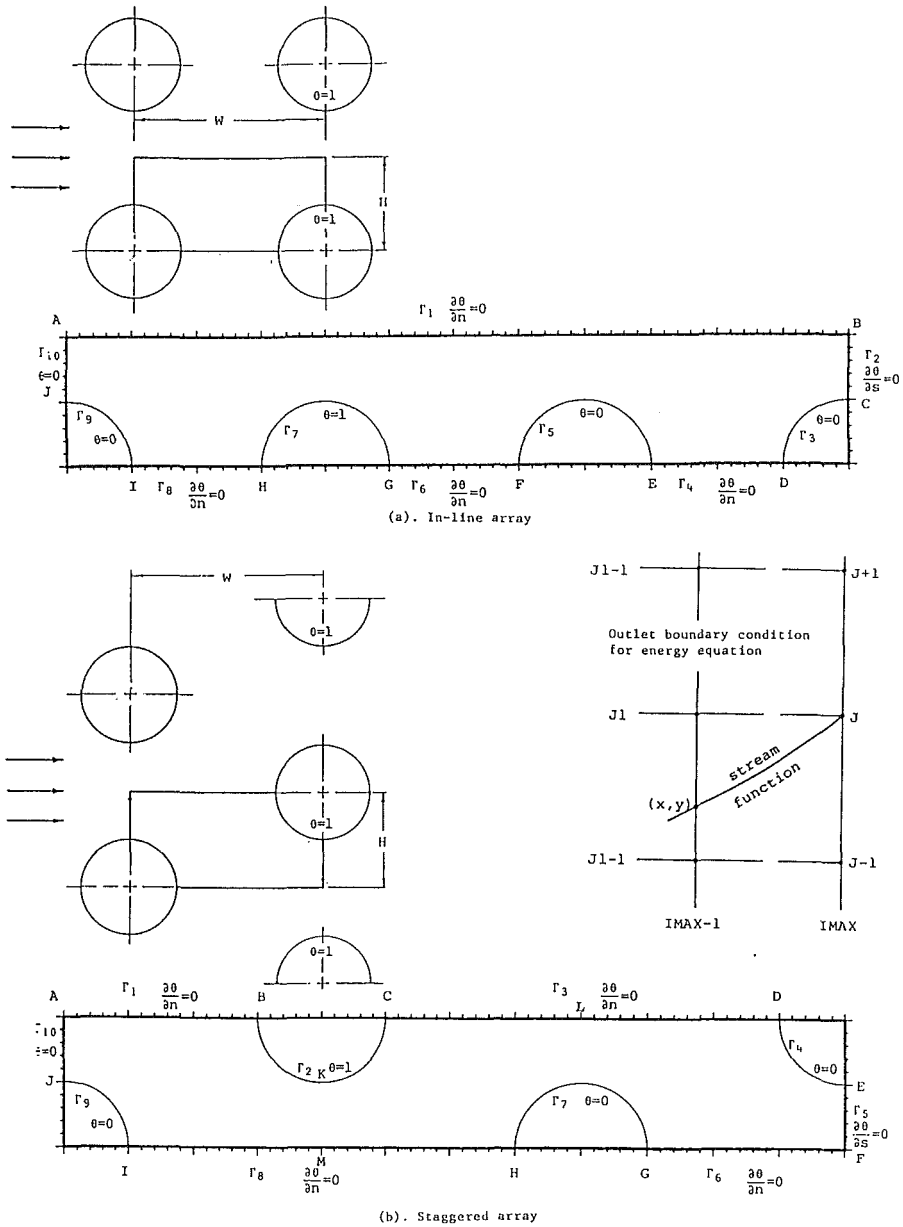

Fig. 1 Computational domain for in-line and staggered tube

Nomenclature

d = diameter of tube
$h, \bar{h}$ = local and average convection heat transfer coefficient
H = height of computational domain or one half transverse pitch height
k = thermal conductivity of the fluid
n = direction normal to the wall
Nu, $\overline{\text{Nu}}$ = local and average Nusselt number
P = pressure
Pe = Peclet number
Pr = Prandtl number
Re = Reynolds number = Vd/ν
s = vector in streamwise direction
t = time
t = tangential vector
T = temperature
u, v = velocity components
V = averaged velocity in the minimum flow area
W = width of computational domain or longitudinal pitch width
x, y = Cartesian coordinates
Γ = boundary contour
ζ = vorticity
θ = dimensionless temperature
ν = kinematic viscosity
ρ = density
φ = stream function
∇^2 = Laplacian

Subscripts

0 = initial value
w = wall

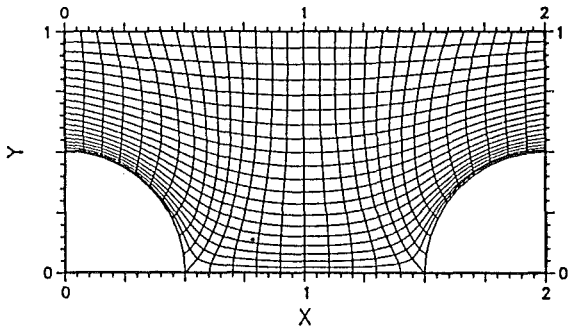

(a). In-line array

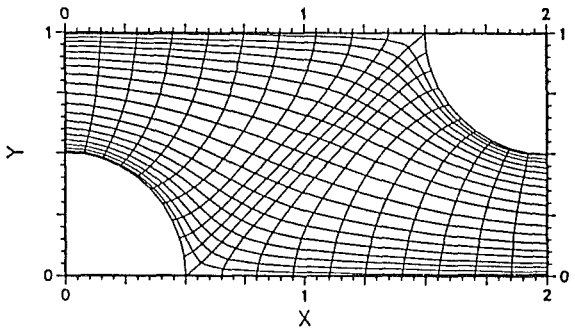

(b). Staggered array

Fig. 2 Boundary-fitted coordinate system with Chen and Obasih contraction function

ent study (Wung and Chen, 1989). In this study, equation (3) is solved in a larger computational domain as shown in Fig. 1.

2.2 Initial and Boundary Conditions. The boundary conditions are required for all boundaries of a computational domain since the governing equations are elliptic in spatial coordinates. In general, along the boundaries of the lower and upper symmetric planes, the stream function is respectively set equal to zero and to a constant value, which is equivalent to one half the value of the mean mass flow rate through the channel. The vorticity and the normal gradients of temperature are zero along the planes of symmetry. Around the surface of the cylinders, the value of the stream function is uniform, corresponding to an impermeable wall, and is the same as the value of the adjacent symmetric plane. The value of vorticity on the cylinder is unknown and must be solved as a part of solution. However, it can be approximated from the stream function in the immediate vicinity of the surface according to the impermeable condition. In order to investigate the temperature distribution around a heated tube, the computational domain is extended three periods for both in-line and staggered arrays as shown in Fig. 1. The temperature of one cylinder is kept at a higher uniform value of one, while the others are kept at zero. The boundary conditions for the flow variables along the inlet and outlet plane are chosen to be periodic in the in-line array, or to be reversely periodic in the staggered array. The temperature of the inlet flow is assumed to be zero, while the outlet temperature at the boundary, which is located three periods downstream, is imposed to be the same in the streamwise direction, or

$$\partial\theta(x, y, t)/\partial s = 0 \tag{6}$$

where s denotes the unit vector along the streamwise direction, as shown in Fig. 1, passing through the nodal point on the outlet boundary. The physical meaning of this outlet boundary condition is that the temperature field along the outlet contour is dominated by the streamwise convection. The detailed computational procedures are documented by Wung (1986).

3 Analysis

3.1 Numerical Solution. The boundary-fitted coordinates are numerically generated based on the transformation and the contraction function suggested by Chen and Obasih (1986). The boundary fitted coordinates for in-line arrays and staggered arrays are shown in Fig. 2. The finite analytic solutions for both velocity and temperature field are then obtained on the boundary-fitted coordinates before they are converted into the physical coordinates. The velocity field is solved in a computational domain with one period of the array arrangement since the flow field is periodic for every pitch of tube array. The temperature field, however, is solved in an expended computational domain of three periods since the temperature field is not periodic when a tube is heated in the arrays. Details of solution procedure are described in Part I of this investigation by Wung and Chen (1989) and Wung (1986).

3.2 Heat Transfer Coefficient. In many practical applications, engineers are also interested in the heat transfer rate from tubes in addition to the temperature distribution between tubes. The heat transfer coefficient h can be expressed in the dimensionless form by the local and mean Nusselt numbers Nu and $\overline{\text{Nu}}$, defined as

$$\text{Nu} = \frac{hd}{k} = -\frac{\partial\theta}{\partial n}\bigg|_{\Gamma} \tag{6}$$

and

$$\overline{\text{Nu}} = \frac{\bar{h}d}{k} = \left(\int_{\Gamma} \text{Nu}\, ds\right)\Big/\left(\int_{\Gamma} ds\right) \tag{7}$$

respectively, where h and $\bar{h}$ are the local and mean heat transfer coefficients and ds is the infinitesimal distance on the contour Γ of the tube wall.

3.3 Recovery of Surface Pressure and Pressure Drop. In the stream function–vorticity formulation of the fluid flow problem, the pressure field is eliminated in obtaining the solution. The pressure field can be recovered from the converged stream function and vorticity fields. The distribution of surface pressure and pressure drop across the tube bank can be easily computed by integrating the pressure gradients along the solid boundaries and symmetry planes of the flow. These pressure gradients are derived from the momentum equations along with the constant values of stream function and vorticity on the symmetric planes and the impermeable conditions around the wall. For the surface of the cylinder, the pressure gradient is conveniently expressed in terms of the local normal and tangential coordinates (n, t) as

$$\frac{\partial p}{\partial t} = -\frac{1}{\text{Re}}\frac{\partial\zeta}{\partial n} \tag{8}$$

while along the symmetry planes of the flow

$$\frac{\partial p}{\partial x} = -\frac{1}{2}\frac{\partial}{\partial x}\left[\left(\frac{\partial\varphi}{\partial y}\right)^2\right] - \frac{1}{\text{Re}}\frac{\partial\zeta}{\partial y} \tag{9}$$

Integration of equation (8) along the surface of the cylinders will provide the detailed pressure distribution on the tube surface. In order to obtain the pressure drop across the tube banks, one needs to select an appropriate integrating path that has the end point located at the same position in the following period as the starting point. For the in-line array shown in Fig. 1, the pressure drop for three pitches can be obtained by

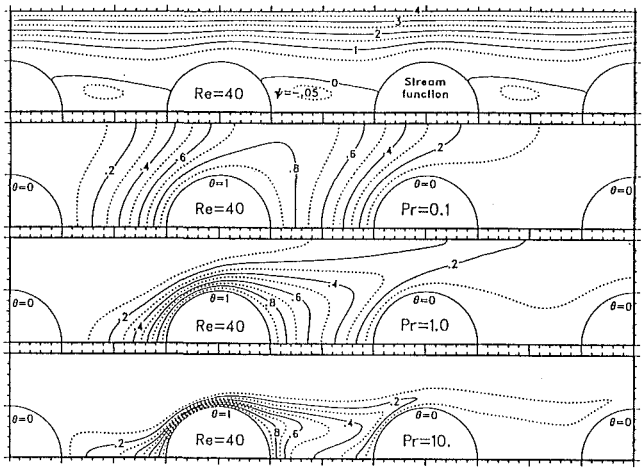

Fig. 3 Temperature distribution for in-line array at Re = 40

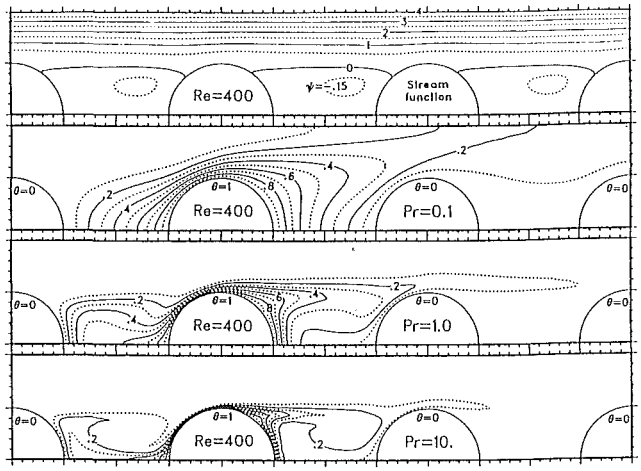

Fig. 5 Temperature distribution for in-line array at Re = 400

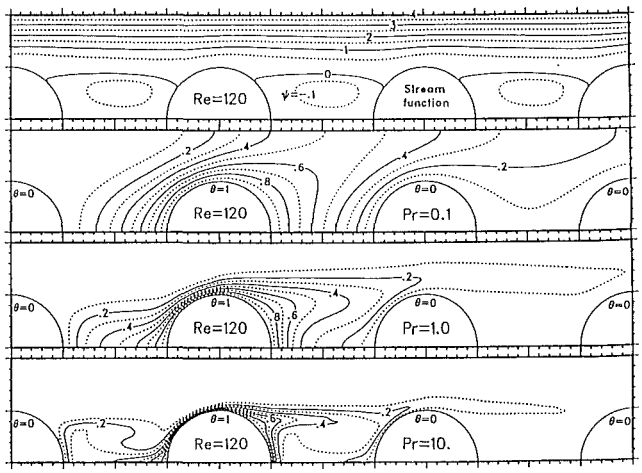

Fig. 4 Temperature distribution for in-line array at Re = 120

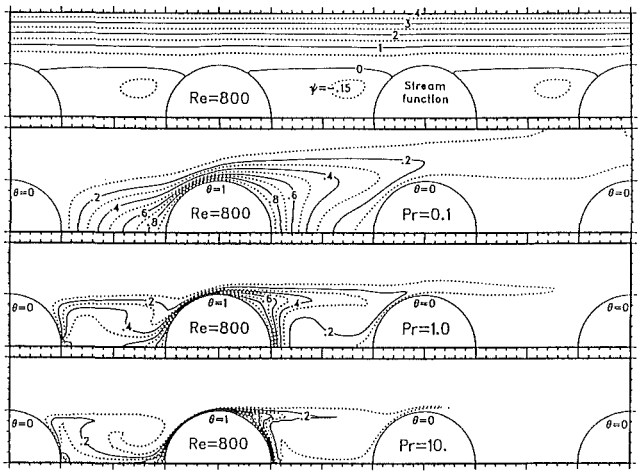

Fig. 6 Temperature distribution for in-line array at Re = 800

$$p_A - p_B = \int_B^A \frac{\partial p}{\partial x}\, dx \tag{10}$$

or for one pitch

$$P_F - p_D = \int_E^F \frac{\partial p}{\partial t}\, dt + \int_D^E \frac{\partial p}{\partial x}\, dx \tag{11}$$

For the staggered array of tubes, since there are two rows in a period, as illustrated in Fig. 1, the integrating path may be selected as

$$P_B - p_D = \int_C^B \frac{\partial p}{\partial t}\, dt + \int_D^C \frac{\partial p}{\partial x}\, dx \tag{12}$$

It is noted that the pressure drop in equation (12) is a result of the flow past two rows of a staggered array.

4 Results and Discussion

This section presents the numerical solutions of convective heat transfer across tube bundles with in-line and staggered arrays at four Reynolds numbers, 40, 120, 400, and 800. The computations were performed by a PRIME 850 computer system.

4.1 Distribution of Temperature. The temperature fields are solved in the expanded domains of three periods with 91×21 and 61×21 grid nodes for the in-line array and staggered array, respectively. Since it is assumed that the fluid flow is incompressible with constant transport properties, the solution for the energy equation (3) is obtained via the FA numerical method with velocity fields expressed in terms of the stream function (Wung and Chen, 1989). In this study, three Prandtl numbers of 0.1, 1, and 10 are considered in the flow fields of Re = 40, 120, 400, and 800. The heat transfer problems thus correspond to a Peclet number in the range of 4 to 8000.

Before presenting the results of the temperature solutions, the validity of the outlet thermal boundary condition is examined by comparing the solutions of the temperature fields in the two different computational domains, namely two and three periods of tube arrays, with the same outlet thermal boundary condition described in equation (6). The maximum difference of the temperature between solutions of two and three periods of tubes was found to be within 0.014, which occurred at the low Peclet number along the lines near the outlet boundary. The maximum difference of the heat transfer of the heat transfer from heated tubes was found to be less than 0.5 percent, which occurred in the separation zone. Hence, the assumption of the predominant convection along the outlet boundary is excellent. Although only two periods are needed to compute the temperature field around a heated tube, solutions presented below are obtained for the three-period domain since they provide a detailed temperature distribution for the downstream area without significantly increasing the computational time. This is because the flow fields are already solved and an overrelaxation factor of 1.0 to 1.8 can be used for the computation of the temperature.

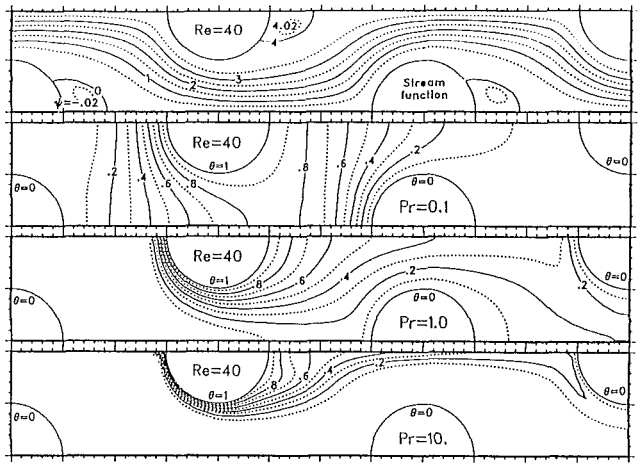

Fig. 7 Temperature distribution for staggered array at Re = 40

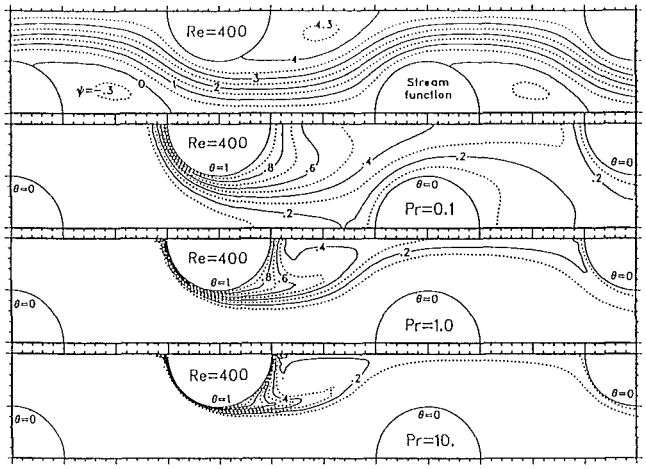

Fig. 9 Temperature distribution for staggered array at Re = 400

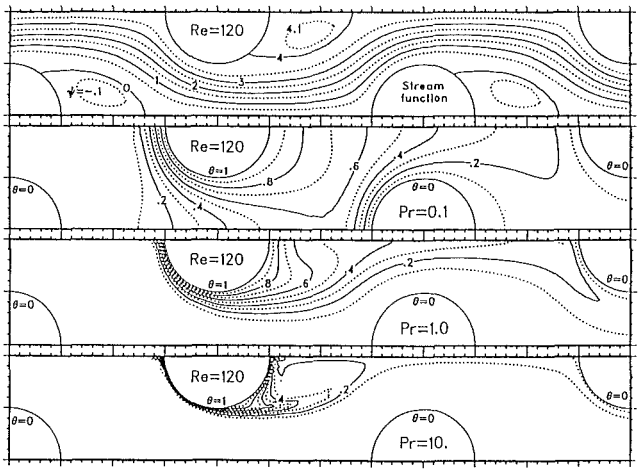

Fig. 8 Temperature distribution for staggered array at Re = 120

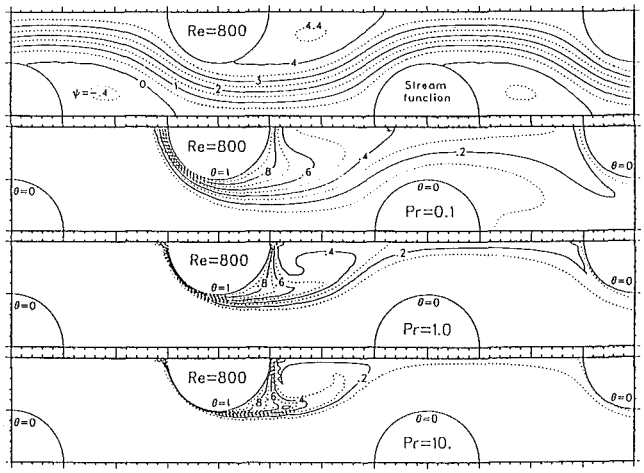

Fig. 10 Temperature distribution for staggered array at Re = 800

A In-Line Array. The temperature distributions, around a heated cylinder in the in-line array are plotted in Figs. 3–6. For each figure, the stream function is presented at the top followed by the temperature plots for three Prandtl numbers of 0.1, 1, and 10.

In general, the temperature distribution in the tube array is a strong function of Reynolds number and Prandtl number, and consequently the Peclet number. At a low Peclet number, the temperature distribution is mainly dominated by thermal diffusion, while for the higher Peclet number, the convection heat transfer plays an important role.

For the same Peclet number, the influence of the flow field on the temperature distribution can be readily realized by comparing the isotherms of Fig. 3 to Fig. 6. For instance, at Pe = 40, the temperature distribution for Re = 40 and Pr = 1 shown in Fig. 3 is very similar to that in Fig. 5 with Re = 400 and Pr = 0.1, except in the vortex region where the latter case has stronger recirculation strength. The difference is more evident at the Peclet number of 400. The front separation zone of the heated tube is filled with the isothermal lines for Re = 400 and Pr = 1, due to the larger and strengthened vortex, while for the case of Re = 400 and Pr = 10, the isotherms are confined near the bottom symmetric plane because of the small and weak recirculation. It can be observed that the area affected by the heat transfer is smaller for the higher Prandtl number in the same flow field since the thermal diffusivity is lower.

B Staggered Array. The temperature distributions for a staggered array are presented in Figs. 7–10 for four Reynolds numbers and three Prandtl numbers. A general view of the plots indicates that the temperature fields are quite different from those for the in-line array because of the wavy motion of the through stream in the staggered array and the isolation of the separation zone behind the cylinder. For the medium to high Peclet number, the temperature contours are packed along the upstream facing surface and diffused into the downstream. In the separation zone, the thermal layer is relatively thick, particularly near the separation point. Again, the similarity of temperature profiles between different Reynolds numbers but with similar Peclet numbers is observed.

4.2 Heat Transfer From a Heated Tube. The temperature distribution of a heat transfer configuration can provide detailed information about a temperature field such that one can determine the existence of hot spots or other phenomena related to the temperature. Many engineering applications are also concerned with the rate of the heat transfer from or to a surface. The heat transfer rate is conveniently expressed in the dimensionless form, the Nusselt number, defined by equation (6).

A Heat Transfer From In-Line Arrays. The local heat transfer coefficient from a heated cylinder in the in-line array is shown in Fig. 11 for the four Reynolds numbers in-

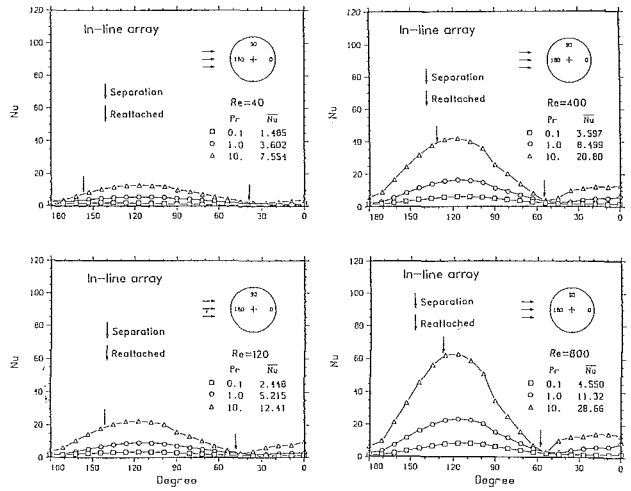

Fig. 11 Local Nusselt number of a heated tube in the in-line array

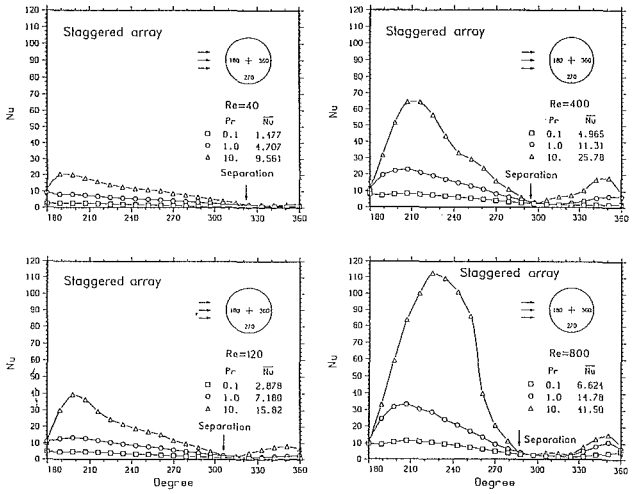

Fig. 12 Local Nusselt number of a heated tube in the staggered array

vestigated. The averaged Nusselt numbers are also inscribed in the plot. It is seen that the local Nusselt number Nu is a strong function of both Reynolds number and Prandtl number. In general, the heat transfer coefficient is increased with increase of Reynolds number and Prandtl number. Unlike the case of a single cylinder in a crossflow (Zukauskas and Ziugsda, 1985), where the maximum local heat transfer is around the front stagnation point, the maximum local heat transfer rate for an in-line array is located near 120 deg from the rear stagnation point where the cold fluid makes its first contact with the tube, while the minimum local heat transfer rate is located near the separation point where the heated fluid departs the surface. In the front surface of the heated tube, although it is immersed in the separation zone, the oncoming cold flow creates a thin thermal boundary layer, resulting in higher heat transfer rate. As the fluid convected along the heated wall to the top of the tube, the fluid is heated and the thermal boundary layer is thickened, hence, the heat transfer rate is decreased drastically to reach the minimum near the separation point where the heated fluid is carried away. Because of the slow circulating motion inside the separation zone behind the heated tube, the heat transfer rate in this region is relatively low.

B Heat Transfer From Staggered Arrays. Figure 12 presents the local heat transfer coefficient from a heated tube in the staggered array. The plots show that the local Nusselt number is also a strong function of the Reynolds number and

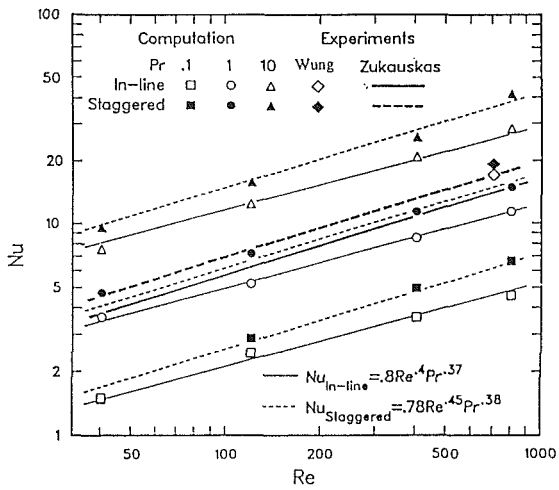

Fig. 13 Variations of averaged Nusselt number versus Re and Pr for the heated tubes in the array

Prandtl number. The position of the maximum local Nusselt number is not fixed around 120 deg as that for the in-line array; rather, it moves with flow condition or the Reynolds and the Prandtl number. At a low Prandtl number of 0.1, the profile of the local Nusselt number is very similar to that of a single cylinder (Zukauskas and Ziugsda, 1985). In this case, the local heat transfer rate is high near the region of the front stagnation point, and then as the fluid moves past the stagnation point, the heat transfer rate becomes smaller due to the growth of the thermal boundary layer, as shown in Figs. 7–10. Low Nusselt numbers in the separation zone are also seen in the staggered array.

The profile of the local Nusselt number changes with the Reynolds number. At a low Reynolds number, the position of the maximum heat transfer rate is located close to the front stagnation point. As the Reynolds number is increased, this peak shifts toward the top of the cylinder since the thermal boundary layer is very thin at high Peclet numbers.

For a medium Prandtl number of 1, the tendency of the local heat transfer rate at the low Reynolds number is similar to that of a low Prandtl number of 0.1, while at a high Reynolds number it is closer to the performance of a high Prandtl number of 10.

4.3 Correlation of the Nusselt Number. The averaged Nusselt numbers for the in-line and staggered array at three Prandtl numbers and four Reynolds numbers are summarized in Fig. 13. In general, the averaged heat transfer coefficient for the staggered array is higher than that for the in-line array. This is mainly because the flow must negotiate through the staggered array in a meandering fashion, which prevents the formation of a large separation zone in the arrays.

Computed data for a given type of tube array are used to correlate the relationship between the Nusselt number and the Reynolds number and Prandtl number. For the in-line array, the correlation equation is

$$\overline{Nu} = 0.8\ Re^{0.4} Pr^{0.37} \tag{13}$$

while for the staggered array the equation is

$$\overline{Nu} = 0.78\ Re^{0.45} Pr^{0.38} \tag{14}$$

In Fig. 13, the empirical correlations of Zukauskas et al. (1978) and measured data for Wung (1986) for air flow ($Pr \cong 1$) in in-line and staggered arrays are also presented for comparison. It is seen that the present numerical predictions are slightly lower than the experimental data, especially in the

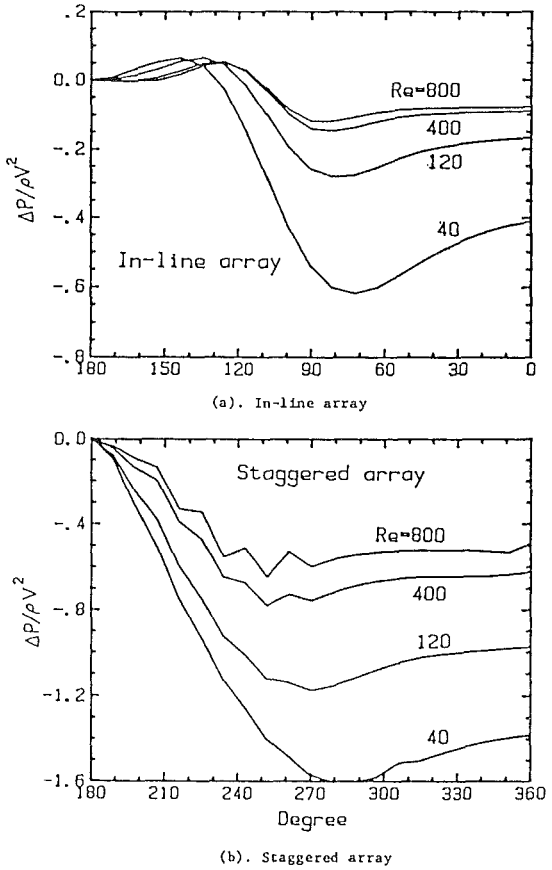

(a). In-line array

(b). Staggered array

Fig. 14 Distribution of surface pressure along tubes in bundles

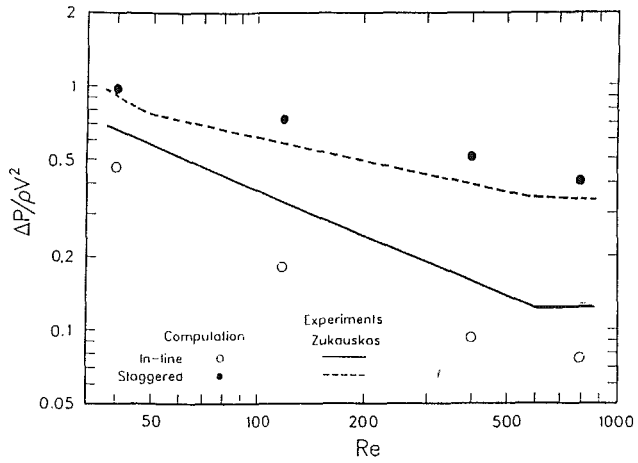

Fig. 15 Pressure drop across tube banks

higher Reynolds numbers investigated. This may be because shedding in the flow is not considered in the computation while in the experiment the shedding may appear at high Reynold numbers. The shedding behind a cylinder, in general, will promote the heat transfer rate since it sweeps the heated fluid downstream.

4.4 Surface Pressure and Pressure Drop Across Tube Banks. The distributions of the surface pressure along the cylinder surfaces are shown in Fig. 14 for both in-line array and staggered arrays. In general, there is a difference in distribution of the pressure coefficient around the tube surface between in-line arrays and staggered arrays. There are no experimental data available for comparison of the surface pressure in the range of the Reynolds number investigated. However, the general trends of the surface pressure coefficients are in agreement with those shown in Zukauskas et al. (1978).

For the in-line array, Fig. 14 shows some increase of the pressure on the tube surface in the upstream side between the front stagnation point and the reattachment point. The reattachment points are a function of Reynolds number and are provided in Part I of this study by Wung and Chen (1989). There is a large pressure drop between the reattachment point and the top of the tube where the throughflow swept over. The pressure is gradually recovered in the rear recirculation zone. The pressure distribution around a tube surface in a staggered array is more or less similar to that of a single cylinder in a crossflow (Zukauskas and Ziugsda, 1985). The magnitude of the pressure drop along the tube surface in a staggered array is higher than that in an in-line array because the throughflow changes its direction near the upstream facing surface. For high Reynolds number of 400 and 800, the computed pressure distributions are not smooth in the upstream facing surface. This is mainly due to the fact that the distributions of vorticity in this region have severe gradients, as shown in Figs. 5 and 6 of Part I in this investigation (Wung and Chen, 1989). Therefore, their derivatives show some zigzag shapes in the upstream facing surface.

Figure 15 gives the computed pressure drop across one period of tube banks and its comparison with the empirical correlations suggested by Zukauskas et al. (1978). The predicted pressure drop for staggered tubes is slightly above the experimental data while that for the in-line tubes is lower than the experimental correlation. Further study is needed in analyzing the difference. However, the comparison shows that the predicted trend of pressure drop agrees with the observation of Zukauskas et al.

5 Conclusions

The flow and heat transfer from arrays of tubes in crossflow are important in many engineering applications. In the present study, the boundary-fitted coordinate system is incorporated with the FA numerical method to predict characteristics of convective heat transfer in the two standard layouts of tube banks. The finite analytic (FA) solutions were obtained for the two-dimensional Navier–Stokes equations and the energy equation in the transformed plane. Some findings are explained as follows:

1 The boundary-fitted coordinate transformation can be utilized successfully with the FA method to solve flow and heat transfer problems with complex geometries. Because one of the boundary-fitted coordinates coincides with irregular boundaries where the boundary conditions can be imposed precisely, accurate solutions can be obtained.

2 The FA solutions obtained are shown to be stable and converge rapidly. This is mainly because the FA solution contains the automatic upwinding influence of neighboring nodes; hence, the characteristics of the convection-diffusion equations are preserved properly in the FA algebraic equations.

3 The flow pattern and temperature distribution are strongly affected by the arrangements of the tubes and flow parameters such as the Reynolds number and Prandtl number. The heat transfer coefficients are correlated with these two parameters.

4 Because of the shading created by the preceding tube in the in-line array, the recirculation regions are formed in the front and rear of a tube in the range of Reynolds numbers

studied. In general, the heat transfer rates are relatively low in the recirculation zone. However, due to the direction of recirculation, the heat transfer rate near the front surface of a heated tube is higher than that near the rear surface. The location of the maximum local heat transfer rate in the in-line array is almost stationary at 60 deg when measured from the front stagnation point.

5 Flow and heat transfer around a heated tube in the staggered array at low Peclet numbers are somewhat similar to that of a single cylinder. In this case, the local heat transfer displays a high value near the front stagnation point and then decreases to the minimum value around the separation point near the rear part of the cylinder. The profile of the local heat transfer coefficient is influenced by the Reynolds number.

References

Chen, C. J., and Obasih, K. M., 1986, "Numerical Generation of Nearly Orthogonal Boundary-Fitted Coordinate System," ASCE *Symposium on Advancement in Aerodynamics, Fluid Mechanics and Hydraulics*, Minneapolis, MN, June 3-5, pp. 586-592.

Wung, T. S., and Chen, C. J., 1989, "Finite Analytic Solution of Convective Heat Transfer for Tube Arrays in Crossflow: Part I—Flow Field Analysis," ASME JOURNAL OF HEAT TRANSFER, Vol. 111, pp. 633-640.

Wung, T. S., 1986, "Experimental and Numerical Study of Flow and Heat Transfer for Arrays of Tubes in Crossflow," Ph.D. Dissertation, Department of Mechanical Engineering, The University of Iowa, Iowa City, IA.

Zukauskas, A. A., Ulinskas, R. V., and Bubelis, E. S., 1978, "Average Heat Transfer and Pressure Drop in Cross Flow of Viscous Fluid Over a Tube Bundle at Low Re," *Heat Transfer—Soviet Research*, Vol. 10, No. 6, pp. 90-101.

Zukauskas, A. A., and Ziugsda, J., 1985, *Heat Transfer of a Cylinder in Crossflow*, Hemisphere Publishing Corp., Washington, DC.

ERRATA

Errata for "Freezing of Water-Saturated Porous Media in the Presence of Natural Convection: Experiments and Analysis," by S. Chellaiah and R. Viskanta, published in the May 1989 issue of the ASME JOURNAL OF HEAT TRANSFER, Vol. 111, pp. 425–432.

Table 1 referred to on p. 427 should be added to the paper.

The following corrections should be made in equation (8):

Error

$$\overline{\rho c} = [\phi\rho_l c_l + (1-\phi)\rho_s c_s] + (1-\phi)\rho_p c_p \tag{8}$$

Corrected Version

$$\overline{\rho c} = \phi\,[\gamma\rho_l c_l + (1-\gamma)\rho_s c_s] + (1-\phi)\rho_p c_p \tag{8}$$

and in equation (9):

Error

$$K = \frac{d^2\phi^3}{175(1-d)^2} \tag{9}$$

Corrected Version

$$K = \frac{d^2\phi^3}{175(1-\phi)^2} \tag{9}$$

Table 1 Summary of experimental conditions, $A = 0.75$

Exp.No.	d(mm)	T_h(°C)	T_c(°C)	ϕ	K×10^9(m^2)	S	Ste	Ra*
1	12.5	6.1	-6.2	0.412	180.6	0.077	0.04	441.0
2	12.5	12.4	-15.8	0.412	180.6	0.157	0.110	1691.1
3	12.5	18.1	-10.3	0.412	180.6	0.230	0.066	3462.6
4	6.0	6.6	-7.2	0.396	35.0	0.084	0.046	99.2
5	6.0	12.5	-13.4	0.396	35.0	0.159	0.085	332.7
6	6.0	18.5	-11.9	0.396	35.0	0.235	0.076	699.4
7	2.85	6.3	-6.9	0.377	6.4	0.080	0.044	16.6
8	2.85	12.9	-13.9	0.377	6.4	0.164	0.089	64.6
9	2.85	17.9	-13.8	0.377	6.4	0.227	0.088	120.2
10	2.85	0.2	-7.1	0.377	6.4	0.000	0.045	0.0

High Rayleigh Number Laminar Natural Convection in an Asymmetrically Heated Vertical Channel

B. W. Webb
Assoc. Mem. ASME

D. P. Hill

Department of Mechanical Engineering,
Brigham Young University,
Provo, UT 84602

Experiments have been performed to determine local heat transfer data for the natural convective flow of air between vertical parallel plates heated asymmetrically. A uniform heat flux was imposed along one heated wall, with the opposing wall of the channel being thermally insulated. Local temperature data along both walls were collected for a wide range of heating rates and channel wall spacings corresponding to the high modified Rayleigh number natural convection regime. Laminar flow prevailed in all experiments. Correlations are presented for the local Nusselt number as a function of local Grashof number along the channel. The dependence of both average Nusselt number and the maximum heated wall temperature on the modified Rayleigh number is also explored. Results are compared to previous analytical and experimental work with good agreement.

Introduction

The heat transfer characteristics of laminar natural convection flow of air between vertical parallel plates is receiving renewed interest in the heat transfer research community. This comes primarily in response to the problem of thermal control of microelectronic equipment. Passive (natural convective) cooling of communications and other microelectronic equipment continues to play a prominent role in thermal management of such systems because of its characteristically low operating noise level, low cost, ease of maintenance, and simplicity. However, basic understanding of the fundamental mechanisms for natural convective heat transfer is lacking (Incropera, 1986). This paper reports on an experimental study focusing on local heat transfer phenomena in an asymmetrically heated, vertical parallel plate channel with laminar air flow in the high Rayleigh number regime.

Natural convective heat transfer along vertical plates has been studied previously by several investigators. The pioneering experimental work of Elenbaas (1942) laid the foundation for the study of natural convection in isothermal parallel plate channels. A subsequent analytical study by Bodoia and Osterle (1962) served to confirm Elenbaas' experiments. More recently, Sparrow and Bahrami (1980) studied experimentally the analogous isothermal plate boundary condition using the naphthalene sublimation technique, examining the effect of open edges at the plate lateral extremities.

Investigations of heat transfer in vertical plates with the uniform heat flux thermal boundary condition are fewer in number. Sparrow and Gregg (1956) developed a similarity solution for natural convection along an isolated vertical, uniform heat flux surface. The governing equations have been solved for a parallel plate geometry in the developing flow region (Aung et al., 1972) and the fully developed limit (Aung, 1972) for both symmetrically and asymmetrically heated isothermal and isoflux plates. Limits bounding three possible flow regimes (fully developed, developing, and single plate) were proposed as a function solely of the modified Grashof number, defined by

$$\mathrm{Gr}^* = \frac{g\beta q b^4}{k\nu^2}\,\frac{b}{H} \tag{1}$$

Note that the modified Grashof number as defined for use in the study of heat transfer in vertical parallel plate channels includes the channel aspect ratio b/H. Raithby and Hollands (1975) developed a simplified analysis for the prediction of the local heat transfer coefficient in a vertical parallel plate channel with arbitrary wall temperature distribution. Their results compared favorably with the experimental and analytical work of previous investigators. Miyatake et al. (1973) performed both analysis and experiment for natural convection between vertical parallel plates with the same thermal boundary conditions as this study. Experiments were performed with water as the working fluid, and results were compared to the theoretical predictions with good agreement.

Experimental data on natural convection flow of air between vertical parallel plates with uniform heat flux are nearly nonexistent. Wirtz and Stutzman (1982) reported measurements of local heat transfer in a symmetrically heated channel. Correlations were developed for the local heat transfer along the channel and the maximum wall temperature as a function of relevant problem parameters. Their experiments spanned the range of modified Rayleigh number from 17.7 to 2414.

More recently, an investigation of the optimum spacing of vertical parallel plates with a variety of thermal boundary conditions was undertaken by Bar-Cohen and Rohsenow (1984). Their paper reviews thoroughly the available data and describes the recommended correlations.

This paper reports on laboratory experiments designed to determine local heat transfer characteristics for natural convective flow in a vertical parallel plate channel, one wall heated with uniform heat flux and the other thermally insulated. In many practical applications the imposed heat flux at the boundary and characteristic dimensions of the system dictate moderate to high Rayleigh number natural convection, while still in the laminar regime. Additionally, the asymmetric heating boundary condition studied is a limiting case prototypical of the arrays of heat-dissipating devices used in the electronics industry. The experiments reported here were designed to characterize the local and average heat transfer of such systems. To this end, the heating rates and channel wall spacings were selected such that the Rayleigh numbers were in the range $503 \le \mathrm{Ra}^* \le 1.75 \times 10^7$. The results reported herein present much-needed local heat transfer correlations for the asymmetric heating case, complementing the symmetric

Contributed by the Heat Transfer Division for publication in the JOURNAL OF HEAT TRANSFER. Manuscript received by the Heat Transfer Division January 26, 1988. Keywords: Electronic Equipment, Natural Convection.

heating data of Wirtz and Stutzman (1982). A comparison of experimental results obtained in this study with the analytical work of Aung et al. (1972) is also performed in the Rayleigh number range where overlap of the two studies exists.

Experimental Apparatus

A schematic diagram of the experimental apparatus used in the experiments is shown in Fig. 1. A vertical parallel plate channel is formed by two walls, one heated and the other adiabatic. The heated section consists of a 15.2-cm-high (in the flow direction) sheet of 0.0051-cm-thick 316 stainless steel shim stock positioned in the vertical center on one side of a 30.5-cm-high channel. The unheated 7.62-cm entry and exit lengths were imposed to minimize radiation losses near the channel entrance and exit, which would otherwise have been radiatively exposed to a relatively cold ambient environment. The presence of the unheated entry region has the effect of reducing the local heat transfer slightly, since the flow is somewhat more developed hydrodynamically upon reaching the heated surface. This phenomenon has been treated in a recent analytical investigation, which explored the influence of hydrodynamic development on local heat transfer in buoyancy-driven flow. The effect of inlet velocity distribution on local and average heat transfer in natural convection from heated vertical parallel plates was studied numerically (Chappidi and Eno, 1988). Uniform and fully developed velocity profiles were imposed at the channel inlet, and the resulting heat transfer characteristics were examined. It was concluded that, except at very large Grashof numbers, the influence of fully developed flow conditions at the inlet is negligible. It is unlikely that the 7.62-cm unheated entry length used in this study would result in fully developed flow conditions at the start of the heated section, and asymptotic results to be presented in sections to follow bear this out. Additionally, the presence of the unheated exit length has been shown to exhibit negligible influence on the local heat transfer in the channel except for very large adiabatic sections above the heated surface (Oosthuizen, 1984).

The spanwise channel dimension depth (normal to the plane of the figure) is 45.7 cm. With the wall spacings used in this study the channel cross-sectional aspect ratio (ratio of channel spanwise depth to wall spacing) ranged from 44.9 to 6.0. The relatively high aspect ratio was selected to insure that the flow and heat transfer in the channel were two dimensional, which will be quantified in a section to follow. The stainless steel foil was polished using successively finer grit polishing wheels to minimize its radiative emissivity. The emissivity was subsequently measured using an infrared radiometer to be 0.1 ± 0.03. The results were found to be relatively insensitive to the 30 percent uncertainty in emissivity, modifying the correlations to be presented by no more than 3 percent. The heated foil was instrumented with 31 copper-constantan thermocouples epoxied to its back surface at equal 0.508-cm inter-

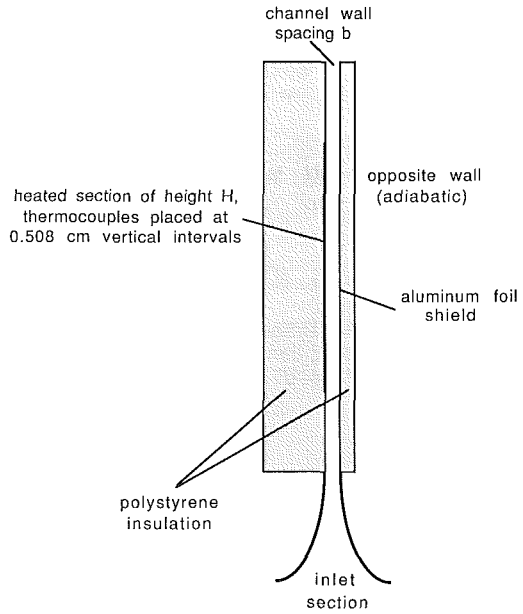

Fig. 1 Schematic of experimental apparatus

Nomenclature

A = correlation constant, equation (5)
b = channel wall spacing, Fig. 1
Gr_b = Grashof number based on channel wall spacing $= g\beta q b^4/k\nu^2$
Gr_H = Grashof number based on channel height, $g\beta q H^4/k\nu^2$
Gr^* = modified Grashof number, equation (1)
Gr_x = local Grashof number $= g\beta q x^4/k\nu^2$
h_x = local heat transfer coefficient, equation (3)
$\bar{h}$ = average heat transfer coefficient, equation (11)
H = channel height, Fig. 1
m = correlation exponent, equation (5)
Nu_x = local Nusselt number $= h_x x/k$
Nu_H = Nusselt number at the top of the heated surface $= h_H H/k$
$\overline{\mathrm{Nu}}_b$ = average Nusselt number, equation (10)
$\mathrm{Nu}_{1/2}$ = average Nusselt number at channel midheight as defined by Aung et al. (1972), equation (13)
p, q = correlation parameters, equation (7)
Pr = fluid Prandtl number $= \nu/\alpha$
q = heat flux
q_{cond} = conduction loss through the insulating substrate, equation (4)
q_{conv} = local convective heat flux $= q_{\mathrm{Ohm}} - q_{\mathrm{rad}} - q_{\mathrm{cond}}$
q_{Ohm} = Ohmic dissipation in the heated foil
q_{rad} = radiation loss from the heated foil
$\bar{q}$ = spatial average of heat flux corrected for radiation and conduction losses
Ra = Rayleigh number $= \mathrm{GrPr}$
Ra^* = modified Rayleigh number $= (b/H)\mathrm{Ra}$
T_0 = channel inlet air temperature
$T_{s,x}$ = local heated surface temperature
$T_{2,x}$ = local insulated wall temperature
$\overline{T_b}$ = estimate of the average bulk temperature in the channel, equation (6)
x = coordinate direction along axis of channel
θ_2 = dimensionless temperature of adiabatic wall $= (T_{2,x} - T_0)/(\bar{q}b/k)$

vals along a vertical line midway between the horizontal extremities of the channel. Small diameter wire (0.0127 cm dia.) was used in the fabrication of the thermocouples to minimize the thermal disturbance at the back surface of the heated foil.

Additional thermocouples were positioned 11.4 cm to either side of the primary centerline instrumentation to monitor the horizontal variations in the heated surface temperature. One can characterize these horizontal variations by defining a parameter

$$\Delta h = \left| \frac{T_{s,x} - T_{\Delta,x}}{T_{s,x} - T_0} \right| \tag{2}$$

where $T_{\Delta,x}$ is the measured surface temperature at the same axial location, and to either side of the local centerline temperature $T_{s,x}$. The parameter Δh indicates the possible error in the calculated local heat transfer coefficient due to three-dimensional effects in the system. The maximum variation of the horizontal temperatures as quantified by the parameter Δh of equation (2) was 3 percent, with the average deviation being 1.5 percent. Hence, the flow and heat transfer in the channel may be assumed to be two dimensional for all channel configurations and heating rates studied.

The heated foil was mounted to a 21.6-cm-thick slab of closed-pore extruded polystyrene insulation to minimize conduction losses. Thermocouples were also placed at the rear surface of this insulation in order to estimate and correct for the conduction losses. In all experiments these losses never exceeded 1.8 percent of the Ohmic heating in the foil. The opposite wall forming the channel was a 1.27-cm-thick sheet of polystyrene insulation similar to that used as backing for the heating plate. This wall was covered with aluminum foil to minimize the radiation interaction of the two walls. The surface temperature of this wall was measured at three vertical locations by inserting thermocouples through small holes in the back of the polystyrene sheet and pressing them snugly against the aluminum foil.

The two remaining vertical channel walls were a pair of masonite strips that had been precision-milled to give the desired wall spacing b. Several sets of these strips were machined to give a range of six wall spacings from 1.02 cm to 7.62 cm, with an expected accuracy of ± 0.25 mm. The channel was designed such that experiments could be performed with no opposing channel wall as well, corresponding to free convection from a single vertical plate. A smooth channel entrance was fabricated by forming Mylar sheets around blocks of contoured polystyrene insulation. The temperature of the air entering the channel was also measured with a thermocouple positioned directly below the entrance.

The thermocouples used in the temperature measurement were calibrated prior to performing the experiments. These thermocouple voltages were read to an accuracy of 1 μV and were software-compensated to yield temperatures in °C directly. Expected accuracy of the measured absolute temperatures is ± 0.5°C. However, the maximum uncertainty in temperature differences is expected to be ± 0.1°C. Power was supplied to the foil heater from a d-c source with voltage and current regulation stable to 0.01 percent. The current was displayed directly by the power supply, while the voltage drop across the heated surface was measured with small voltage taps attached electrically to the foil. The data submitted in the original version of this study were based on measurements of the voltage drop across the aluminum busbars. However, a nearly 13 percent drop in voltage was subsequently measured due to electrical contact resistance from the busbars to the heated foil. The authors gratefully acknowledge the reviewer's comments that triggered the discovery of this error. The Ohmic dissipation rate was measured with an expected accuracy of 1 percent. However, considerably more uncertainty is expected in the determination of the local convective heat flux along the heated surface due to radiation losses and two-dimensional conjugate effects in the insulating substrate. It is estimated that the maximum uncertainty in q_{conv} is less than 5 percent of the Ohmic dissipation in the foil, q_{Ohm}. A period of approximately 24 h was required for the foil surface and insulation temperatures to cease changing appreciably. After steady state was reached, all temperatures were read and stored for later data reduction.

The experiments were performed in a room within a room in a basement laboratory. The room was isolated completely from ventilation equipment, eliminating convection currents in the ambient air. The room had adequate thermal mass so that the ambient temperature strayed less than 0.2°C over the course of a typical 24-h experiment. Since the emphasis of this work was on heat transfer, no measurements of the velocity field were made, nor was visualization of the flow performed. There is some question as to the ability of standard flow visualization techniques to track a buoyancy-driven air flow without significantly perturbing the flow field itself.

Three different power levels were used in the experiments, corresponding to nominal wall heat fluxes of $\bar{q} = 215$, 275, and 345 W/m^2. These heating rates are spatial averages of the values corrected for radiation and conduction losses. The corresponding Ohmic dissipation heat fluxes were 235, 300, and 375 W/m^2, respectively. The heating rates employed are considerably higher than those studied by Wirtz and Stutzman (1982), and correspond to typical heating rates found in many applications.

Aung et al. (1972) have characterized the flow between parallel plates using the modified Grashof number such that $\text{Gr}^* < 0.2$ represents a fully developed temperature profile, $0.2 < \text{Gr}^* < 1000$ corresponds to developing flow, and $\text{Gr}^* > 1000$ corresponds to the single plate limit. Local and average heat transfer characteristics are functionally different in each regime. Values of Gr* used in this study spanned the range $709 \le \text{Gr}^* \le 2.47 \times 10^7$. Hence, nearly all 17 data sets reported here lie above the single plate limit proposed by Aung. The largest values of Gr* studied here were used to approach the asymptotic behavior whose results were established analytically by Sparrow and Gregg (1956).

Heat transfer coefficients for natural convection with air are typically quite low. Consequently, it was expected that radiation might be an important mode of heat transfer in the heated channel described in the foregoing, despite the low surface emissivities and relatively low surface temperatures. Since correlations were to be developed for the convective heat transfer coefficient, the heat transfer results were corrected for radiation loss from the heated surface. The channel was treated as a diffuse-gray enclosure with known (measured) temperatures. Thirty-one spatial intervals were used along the heated plate, and corresponding intervals were used on the opposing adiabatic wall. Temperatures along the adiabatic wall were interpolated between the measured temperatures there. The local radiation heat flux was determined by solving the coupled simultaneous equations describing the radiation exchange in the two-dimensional enclosure whose sides were comprised of the vertical heated and adiabatic walls, and the "surfaces" formed by the openings at the channel top and bottom (Siegel and Howell, 1981). The Ohmic dissipation rate was then reduced by the calculated local radiation loss. Corrected heat transfer results were used in all correlations presented in the following.

The temperature rise between the top and bottom of the heated wall was of order 30 to 40°C in the experiments. The corresponding variation in thermophysical properties of air over such a temperature range is significant; the thermophysical property grouping $g\beta/k\nu^2$, which appears in the Grashof number, varies by nearly 30 percent between 20°C and 40°C. Accordingly, the local heat transfer data were correlated with properties based on the local wall temperature, rather than an estimate of the average bulk temperature of the

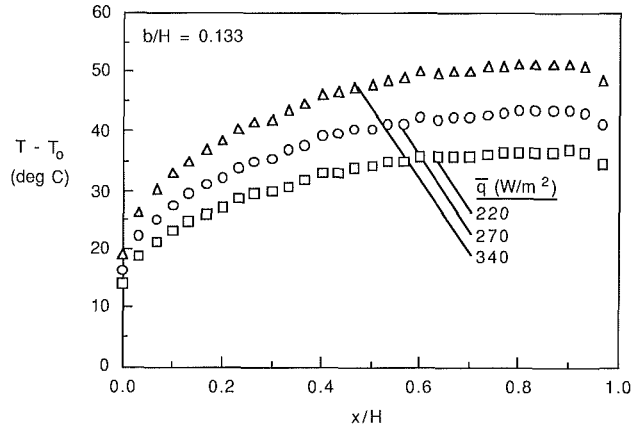

Fig. 2 Variation of the heated wall temperature with height for the three heating rates studied, wall spacing $b = 2.03$ cm

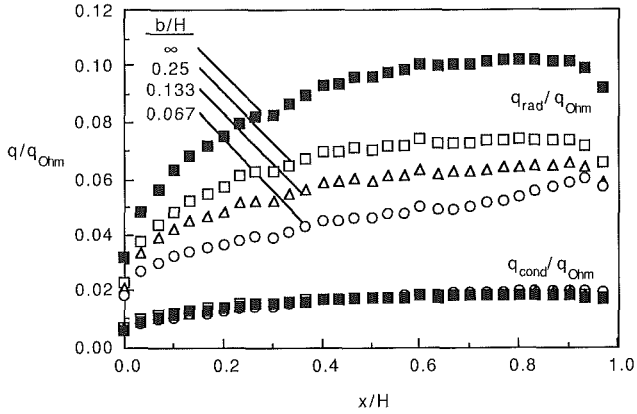

Fig. 3 Ratio of the local radiative and conductive heat flux to the imposed Ohmic dissipation as a function of wall spacing for $q_{Ohm} = 300$ W/m^2

air. Justification for this lies in the fact that the local convective heat transfer occurs at the wall, where temperature continuity requires that the air be in thermal equilibrium with the heated wall. The effect of using local temperatures in correlating the experimental data will be discussed in a later section.

The uncertainty in the experimental measurements was determined following the procedure recommended by Kline and McClintock (1953). The propagation of the uncertainties into the relevant dimensionless parameters was then determined. The uncertainty in local Nusselt number Nu_x is estimated at 6 percent, while the uncertainties in local Grashof number Gr_x and modified Rayleigh number Ra* are estimated at 10 and 12 percent, respectively.

Experimental Results and Discussion

General Observations. Profiles of the local heated wall temperature were recorded for each experimental heating rate and channel spacing. Figure 2 illustrates typical measured temperature profiles for the three heating rates employed and wall spacing of $b = 2.03$ cm. The heat fluxes shown are spatial averages of the local heat flux corrected for conduction and radiation losses. Note that T_0 is the air temperature at the channel inlet. In general, the profiles are smooth with little scatter. Very fine spatial resolution of the wall temperature was achieved with the thermocouple intervals chosen. As expected, the wall temperatures are higher for higher heating rates; the convective driving potential must increase in order to dissipate the Ohmic generation. Local temperatures are relatively low near the channel entrance where the thermal boundary layer is thin. The wall temperatures climb quickly as the boundary layer thickens. There was no indication of transition to turbulent flow in any of the experiments.

One also notices a slight decrease in the heated wall temperature near $x/H = 1$. A flow reversal near the top of the heated section, as observed by Sparrow et al. (1984) in an asymmetrically heated buoyancy-driven channel flow, might account for this lower temperature. However, the flow reversals in the aforementioned study were confined to the unheated wall, and were observed to exercise no influence on the heat transfer at the heated wall. The slight decrease in the wall temperature near $x/H = 1$ is more likely a result of conduction to the polystyrene insulation in the unheated section above, effectively reducing the thermal resistance at the top of the heated section. This last temperature data point was discarded for each experiment in the development of heat transfer correlations and their analysis.

Having measured the local wall temperatures, and knowing the Ohmic dissipation rate, the local heat transfer coefficient was determined using the relation

$$h_x = (q_{\text{Ohm}} - q_{\text{rad}} - q_{\text{cond}})/(T_{s,x} - T_0) \tag{3}$$

where q_{rad} is the local radiative heat flux calculated using the procedure outlined in the foregoing. The term q_{cond} is the local correction for conduction losses and is calculated assuming one-dimensional conduction in the polystyrene substrate on which the foil heater was mounted. The conduction loss was determined using the relation

$$q_{\text{cond}} = k_{\text{ins}}(T_{s,x} - T_0)/L_{\text{ins}} \tag{4}$$

where k_{ins} and L_{ins} are, respectively, the thermal conductivity and thickness of the insulation substrate on which the heated foil is mounted. It should be noted that the foregoing correction for conduction loss is unable to account for the redistribution of convective heat flux due to two-dimensional conjugate effects. This effect is present particularly near the leading and trailing edges of the heated foil, where the energy dissipated Ohmically in the foil is able to diffuse through the substrate to the insulation surfaces exposed to the convective flow in the unheated entrance and exit lengths. As stated previously, the effect of this redistribution is estimated to be less than 5 percent of q_{Ohm}.

It was anticipated that radiation might play a nonnegligible role in the heat transfer from the heater despite the low surface emissivities and temperatures. Figure 3 illustrates the calculated ratio of radiative and conductive heat fluxes to the Ohmic heat flux dissipated electrically in the foil for the Ohmic heating rate of 300 W/m^2. The conduction losses are very nearly uniform over the heated channel length and amount to about 1.5 percent of the Ohmic dissipation. The radiation losses, on the other hand, are quite nonuniform over the channel height owing to the strong variation in heated surface temperature. Radiation losses are observed to increase as the wall spacing b increases. The reasons for this are twofold: (1) The opposite adiabatic wall temperatures are lower for higher wall spacing (as will be shown subsequently), and (2) the heated surface "sees" more of the relatively cold, black environment through the channel entrance and exit at higher channel wall spacings. The radiation correction is highest for the case of free convection with no opposing wall, since under these conditions the entire heated surface is exposed to the environment. The ratio of radiative to Ohmic heat flux for the vertical channels studied here ranges from about 2 to 10 percent. Results of the heat loss corrections may then be summarized by stating that the actual heat flux convected from the heated foil was not uniform in reality, but varied by nearly 4 percent from channel bottom to top. The conduction and radiation corrections combined varied between 6 and 10 percent of the Ohmic dissipation. These corrections are significant and underline the fact that radiation in particular should not be neglected in natural convection situations in gases even

with very low surface emissivities. As stated previously, all of the local and average heat transfer correlations developed and analyzed in the sections to follow were based on locally corrected heat transfer.

Correlation of Local Nusselt Number. Having determined the local heat transfer coefficient, the local Nusselt number can be calculated. Sparrow and Gregg (1956) determined analytically the local heat transfer characteristics of a vertical plate heated with a uniform heat flux. The local Nusselt number was found to vary with the local Grashof number according to the relation

$$\mathrm{Nu}_x = A\,(\mathrm{Gr}_x)^m \tag{5}$$

where the constant A was determined to be 0.52 for air ($\mathrm{Pr} = 0.71$), and the exponent m was found to be 0.2. One might argue that as a wall is placed opposite the heated surface and is brought closer, the temperature distribution along the heated wall would continue to behave in a power-law fashion. This was shown for symmetrically heated channels by Wirtz and Stutzman (1982). The local Nusselt number for heat transfer in an asymmetrically heated channel may then be correlated as a function of the local Grashof number using equation (5). Figure 4 presents such a correlation for the two Rayleigh number extremes of this study, $\mathrm{Ra}^* = 5.03 \times 10^2$ and 1.75×10^7. It should be underlined that the local Grashof number was based on thermophysical properties evaluated at the local wall temperature. The correlation of the form of equation (5) represents very well the heat transfer data for the two Rayleigh numbers shown. Using a least-squares regression the two data sets were fit with a correlation coefficient of unity to three significant figures. A similar regression was performed for each data set with equally good fit.

All data sets were correlated using a least-squares regression with equation (5). The dependence of the constant term A and the exponent m on the modified Rayleigh number is shown in Fig. 5. The modified Rayleigh number used in the abscissa is based on the estimated average of the bulk temperature in the channel, given by

$$\overline{T_b} = T_0 + \frac{T_{s,H} - T_{s,0}}{2} \tag{6}$$

Figure 5 shows that both correlation parameters vary quite strongly with the modified Rayleigh number until a critical number, $\mathrm{Ra}^*_{\mathrm{crit}}$, after which they become independent of Ra^*. The experimental data show that $\mathrm{Ra}^*_{\mathrm{crit}}$ has an approximate value of 10^5. This critical modified Rayleigh number will subsequently be shown to relate to the interaction between the thermal boundary layer growing along the heated wall and the adiabatic opposite wall.

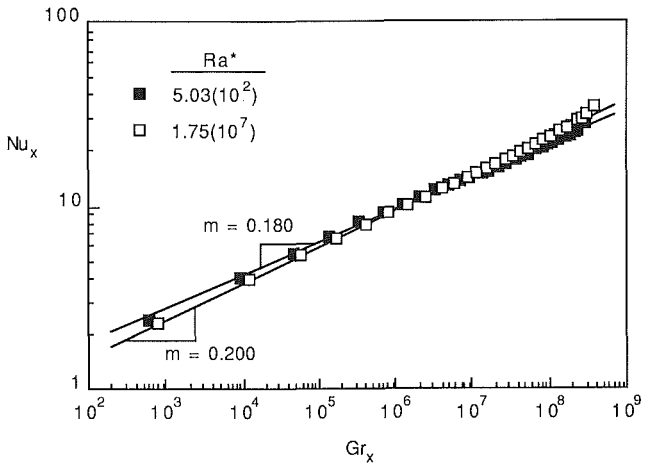

Fig. 4 Correlation of local Nusselt number with local Grashof number for the two modified Rayleigh number extremes studied

Using the correlation parameters A and m plotted in Fig. 5 in the correlation equation (5), one can predict the variation of the local heat transfer coefficient along the heated surface, and hence, the local surface temperature. Obviously, the correlation given by equation (5) used in conjunction with Fig. 5 may be used accurately for the Rayleigh number range studied here, $503 \le \mathrm{Ra}^* \le 1.75 \times 10^7$. Attempts to incorporate an aspect ratio dependence into the local Nusselt number correlation (5) were unsuccessful. The experimental findings reveal that, for a given heating rate, the local heat transfer coefficient increases as the channel wall spacing b decreases. The result is higher local surface temperatures as the channel becomes wider. This is due to the so-called chimney effect; the presence of the adiabatic opposite wall effectively reduces the thickness of the thermal boundary layer growing along the heated wall. This phenomenon is expected to be more pronounced for narrow channels where the influence of the shrouding wall is felt more strongly. This decrease in local heat transfer coefficient (with increasing b) ceases, however, when the walls are sufficiently far apart, reaching $\mathrm{Ra}^*_{\mathrm{crit}}$. The value $\mathrm{Ra}^* \approx 10^5$ may thus be perceived as the lower Rayleigh number bound for the attainment of the single-plate asymptote proposed by Aung et al. (1972), and represented by the isolated plate analysis of Sparrow and Gregg (1956).

Figure 5 shows that A and m asymptote to a constant value at high modified Rayleigh numbers, the asymptotic values being determined to be approximately $A = 0.58$ and $m = 0.20$. As the channel wall spacing increases, the heat transfer characteristics are expected to approach the value proposed by Sparrow and Gregg (1956) for laminar natural convection from a single vertical plate. The correlated asymptotic value of the exponent from this study, $m = 0.20$, corresponds exactly to that determined analytically by Sparrow and Gregg. Note that the exponent correlating data from this study was arrived at by using local thermophysical properties in the definition of the local Nusselt and Grashof numbers. Correlations were also attempted with all properties evaluated at an estimated value of the average bulk temperature, equation (6). Using this reference temperature in correlating the local heat transfer

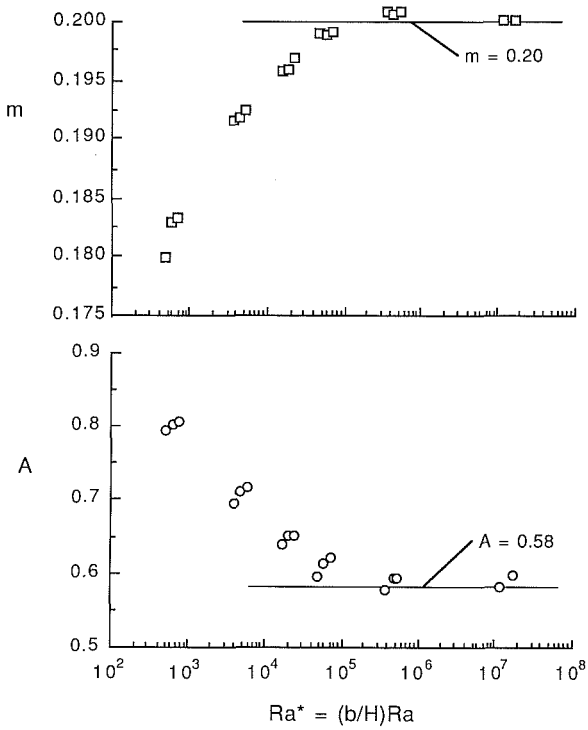

Fig. 5 Variation of correlation parameters of equation (5) with modified Rayleigh number

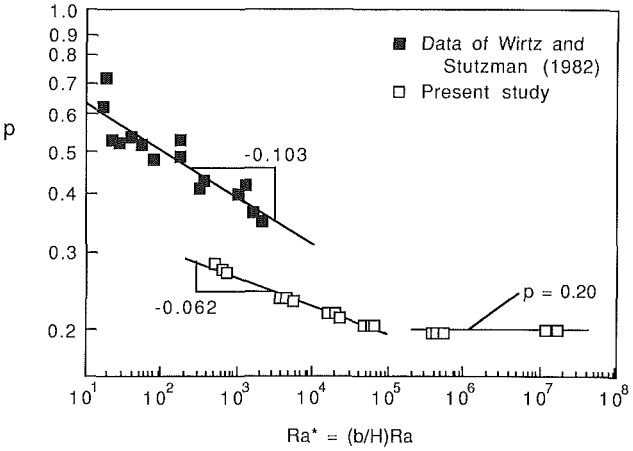

Fig. 6 Comparison of the correlation exponent p of equation (7) with the symmetric heating data of Wirtz and Stutzman (1982)

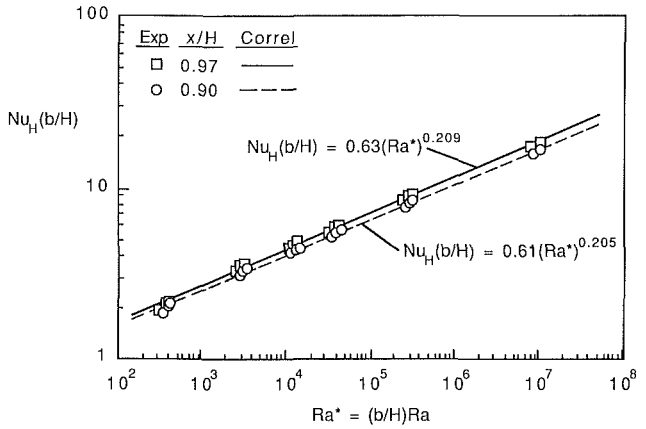

Fig. 7 Local Nusselt number near the top of the heated surface as a function of modified Rayleigh number

data, the asymptotic value of the exponent m was found to be 0.196 (compared to 0.20 when local properties were used). Indeed, the value of m was consistently 2–4 percent lower for all data sets when thermophysical properties evaluated at the reference temperature proposed by equation (6) were used in the definition of the local Grashof number. Corresponding values of the constant term A were 2–3 percent higher when the approximate average bulk temperature given by equation (6) was used for determining the properties. This suggests that the use of local properties may be more appropriate in the correlation of local heat transfer data for natural convection in air, where relatively strong temperature variations and the corresponding variations in thermophysical properties can occur. However, such correlations may be more difficult to apply in a thermal design setting.

The asymptotic value of the constant coefficient A in the correlation equation (5) has an approximate numerical value of 0.58. The corresponding value of the large channel spacing limit given from the isolated vertical plate analysis of Sparrow and Gregg (1956) is $A=0.52$ for air ($\mathrm{Pr}=0.71$). The experimentally determined correlation parameter found in this study is about 11 percent higher than the $A=0.52$ single plate limit. The difference in the experiment and analysis may be explained by one or more of the following phenomena. Two-dimensional conjugate heat transfer in the insulating substrate results in higher apparent heat transfer coefficients, which would increase the experimentally observed value of A. Radiation losses become more prominent as the channel aspect ratio increases, and substantially alter the uniformity of the imposed heat flux. The resulting nonuniformity undoubtedly affects the local heat transfer behavior. It is also certain that the aforementioned substantial bulk temperature rise and associated change in thermophysical properties would affect the analytical results, which have been stated here only for constant property flow and heat transfer. Wirtz and Stutzman (1982) determined the asymptotic value of the coefficient A exhibited by the predictions of Aung et al. (1972) to be 0.577, and concluded that this may be due to the presence of a residual pressure gradient in the channel even at large channel aspect ratios. The analysis of free convection from a single vertical plate assumes everywhere a hydrostatic pressure gradient. It was suggested that the acceleration of fluid in the channel case due to the induced axial pressure gradient will increase the local heat transfer coefficient, which is in agreement qualitatively with the experimental observation made here.

The value of $A=0.58$ from the correlated data of this study agrees very well with the value of $A=0.577$ found in the analytical study of Aung et al. (1972) for natural convection between vertical parallel plates. Their numerical predictions were limited to a maximum modified Rayleigh number Ra* of approximately 4000 for the thermal boundary conditions of this study.

Wirtz and Stuzman (1982) proposed a correlation for the local Nusselt number of the form

$$\mathrm{Nu}_x = C\frac{x}{b}\left(\frac{H}{x}\right)^p (\mathrm{Ra}^*)^q \tag{7}$$

where Nu_x is as defined in the present study. Correlating the data of the present study in the form of equation (7) gives the results of Fig. 6, where the exponent p is plotted as a function of Ra*. Results of this study are seen to extend the Rayleigh number range of available experimental data. The symmetric heating data of Wirtz and Stutzman have been reproduced in the figure to contrast with the asymmetric results of this study. Note that the dependence of p on the Rayleigh number is higher for the symmetric heating case, the slope being -0.103. The $p-\mathrm{Ra}^*$ slope for the asymmetric heating boundary condition (-0.062) is slightly more than half that of the symmetric heating data. This may be indicative of the dual-sided versus single-sided heating in the channel. The asymptotic value of p at high Ra* in Fig. 6 is $p=0.20$, agreeing very well with the expected value of 0.20 corresponding to the single-plate limit.

Maximum Plate Temperature. Of interest to thermal designers particularly in the electronics industry is the maximum temperature along the heated surface. The maximum heated surface temperature is expected to occur at the top, since the fluid is continually heated as it flows upward. The reciprocal of the local Nusselt number at the heated surface top is then an indication of the maximum temperature there. Figure 7 illustrates the correlated Nusselt number at two definitions of the channel top, $x/H=0.90$ and 0.97, as a function of the modified Rayleigh number. Both x/H locations are shown in order to illustrate the influence of lateral conduction on the maximum temperature near the exit of the heated section. The thermophysical properties used in the modified Rayleigh number presented in Fig. 7 were based on the local wall temperature at the channel top. Hence, the correlation parameters shown in Fig. 7 and those of Fig. 5 are slightly different. The parameter $\mathrm{Nu}_H(b/H)$ was used on the abscissa because it corresponds to $h_H b/k$, the definition of Nusselt number at $x=H$ used in previous studies.

The data of Fig. 7 correlate very well with the equations

$$\mathrm{Nu}_H(b/H) = 0.63(\mathrm{Ra}^*)^{0.209} \tag{8}$$

at $x/H=0.97$ and

$$\mathrm{Nu}_H(b/H) = 0.61(\mathrm{Ra}^*)^{0.205} \tag{9}$$

at $x/H=0.90$. As with the correlation of local Nusselt number data, the high Rayleigh number limit is seen to depend very nearly on $(\mathrm{Ra}^*)^{0.2}$. The experimentally determined value of

$A = 0.63$ at $x/H = 0.97$ for this study appears somewhat high when compared to the single-plate limiting value of $A = 0.577$ found by Aung et al. (1972), and used by Wirtz and Stutzman (1982) in the development of a composite correlation valid over the entire Rayleigh number range (fully developed, developing, and single-plate limit regimes). However, the correlation for the $x/H = 0.90$ data is considerably closer to the aforementioned previous work, and substantiates the suggestion that conjugate effects are present near the trailing edge of the heated surface. Again, is should be noted that the maximum modified Rayleigh number investigated by these previous investigators was about 4000, making it difficult to draw definitive conclusions about the asymptotic behavior at high Ra*.

Average Nusselt Number. The average Nusselt number for the asymmetrically heated channel studied may be defined as

$$\overline{\mathrm{Nu}}_b = \frac{\bar{h}b}{k} \tag{10}$$

where $\bar{h}$ is the average heat transfer coefficient over the channel height and is calculated according to the relation

$$\bar{h} = \frac{1}{H}\int_0^H h_x dx \tag{11}$$

The average heat transfer coefficient was calculated from the local temperature measurements for all experiments by numerically approximating the integral in equation (11). The results of the integration are shown in Fig. 8. The modified Rayleigh number is based on properties evaluated at the estimated mean bulk temperature, equation (6). The average Nusselt is correlated by the equation

$$\overline{\mathrm{Nu}}_b = 0.82(\mathrm{Ra}^*)^{0.194} \tag{12}$$

Raithby and Hollands (1975) and Bar-Cohen and Rohsenow (1984) have shown that transition from the fully developed limit (low Ra*) to the single-plate limit (high Ra*) occurs near $\mathrm{Ra}^* = 20$ with deviations from the single-plate limit as the Rayleigh number is decreased occurring first at $\mathrm{Ra}^* = 400$. The data from this study are all well above this limit, and hence, show little deviation from the expected single-plate limiting relationship $\overline{\mathrm{Nu}}_b$ depending functionally on $(\mathrm{Ra}^*)^{0.2}$.

Aung et al. (1972) have defined an average Nusselt number at the channel midheight as

$$\overline{\mathrm{Nu}}_{1/2} = qb/(\bar{T}_{1/2} - T_0)k \tag{13}$$

where $\bar{T}_{1/2}$ is the average of the two wall temperatures at $x/H = 1/2$. Figure 8 also compares $\overline{\mathrm{Nu}}_{1/2}$ determined experimentally from this study with Aung's analytical work. The solid line indicates numerical predictions and the dashed line extension is the extrapolation of model predictions further into the Ra* range studied here. The agreement between predictions and data is very good. Aung's numerical predictions show a functional relationship

$$\overline{\mathrm{Nu}}_{1/2} = 0.60(\mathrm{Ra}^*)^{0.2} \tag{14}$$

whereas the experimental work of this study is represented more closely by

$$\overline{\mathrm{Nu}}_{1/2} = 0.58(\mathrm{Ra}^*)^{0.206} \tag{15}$$

However, the difference in predicted and experimentally determined midheight Nusselt numbers given by equations (14) and (15), respectively, is only about 5 percent.

Opposite Wall Temperature. The surface temperature along the adiabatic wall was measured at three locations corresponding to $x/H = 0$, 0.5, and 1.0 with x/H being measured from the leading edge of the heated surface. The dimensionless temperature along the insulated wall θ_2 is plotted as a function of the modified Rayleigh number in Fig. 9 for the three vertical locations stated previously. The figure shows that the insulated wall temperature increases with axial distance x/H for each Rayleigh number. Also of note is the trend toward dimensionless temperatures near zero at all locations for high Ra*. This indicates that the opposite wall remains at or near the ambient temperature at all vertical locations for high Rayleigh numbers. As the Rayleigh number decreases, the opposite wall temperature rises dramatically, deviating from $\theta_2 = 0$ near $\mathrm{Ra}^* = 10^5$. Not coincidentally, this corresponds to the critical Rayleigh number $\mathrm{Ra}^*_{\mathrm{crit}}$, identified in Fig. 5, where the correlation constants for equation (5) also began to show dependence on the Rayleigh number. If the radiation transfer between the two vertical plates is minimized, the insulated wall temperature will rise only when it is influenced by the thermal boundary layer growing along the heated surface. It would seem that this begins to occur near $\mathrm{Ra}^* = 10^5$. The thermal boundary layer appears to interact strongly with the adiabatic opposite wall for $\mathrm{Ra}^* = 10^3$, especially at $x/H = 1.0$. The data for $\mathrm{Ra}^* \approx 10^3$ correspond to a dimensional channel wall spacing of $b = 1.02$ cm. Interaction of the thermal boundary layer with the adiabatic wall at this wall spacing is in close agreement with the thermal boundary layer thickness of approximately $\delta_t \approx 0.9$ cm predicted by the analytical solution of Ostrach (1953) for free convection from an isolated vertical plate.

Also shown in Fig. 9 are numerical predictions for the maximum insulated wall temperature $\theta_{\max,2}$ (which occurs at $x/H = 1.0$), made by Aung et al. (1972) for the asymmetric

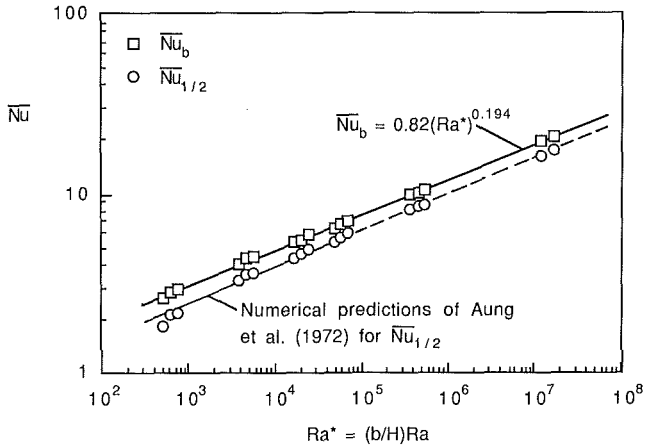

Fig. 8 Variation of the average Nusselt number and midheight Nusselt number as defined by equations (10) and (13), respectively, with modified Rayleigh number

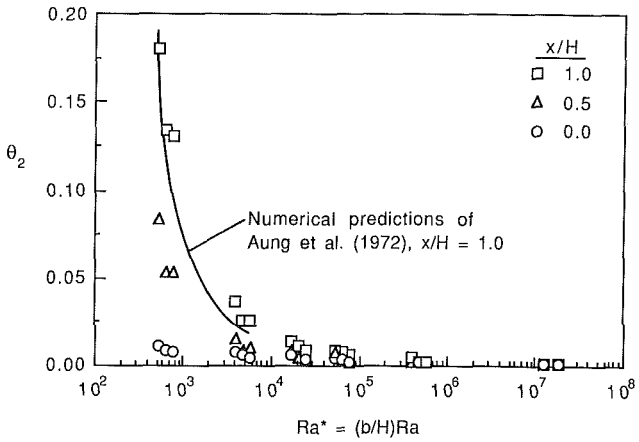

Fig. 9 Temperature of the adiabatic wall at dimensionless axial locations $x/H = 0.0$, 0.5, and 1.0 as a function of modified Rayleigh number

thermal boundary conditions studied here. The predicted variation matches quite closely the experimental data in the region of overlapping Rayleigh numbers for the two studies. The experimentally measured temperatures for this study are slightly higher than the analytical results, but this could be the result of the minor radiation transfer to the adiabatic wall from the heated surface.

Also of note is the reduced radiation transfer from the heated surface at smaller channel wall spacings (smaller Ra*). As was seen in Fig. 3, the correction for radiation loss from the heated wall was reduced for smaller channel wall spacings. As explained previously, one reason for this is that the opposite wall is at a higher temperature due to its interaction with the thermal boundary layer, as seen in Fig. 9. The higher temperature, θ_2, increases the resistance to thermal radiation heat transfer from the heated to the adiabatic channel.

Conclusions

Experiments have been performed to investigate high Rayleigh number laminar natural convecton in an asymmetrically heated parallel plate channel. Heat transfer coefficients were determined from local temperatures along the heated wall while correcting for radiation and conduction losses. Correlations for the local and average Nusselt number, as well as the Nusselt number at the channel top, were presented for the modified Rayleigh number range studied, $503 \le Ra^* \le 1.75 \times 10^7$. The local Nusselt number correlated very well as a function of local Grashof number. The parameters of the correlating equation (5) were found to be functionally dependent on the modified Rayleigh number, Ra^* below $Ra^* \approx 10^5$. At higher modified Rayleigh numbers the correlating constant and exponent were found to be independent of Ra^*.

As the channel wall spacing increases (characterized by higher modified Rayleigh number) the heat transfer behavior approaches that characteristic of free convection from an isolated vertical plate heated uniformly (Sparrow and Gregg, 1956). The asymptotic value of the constant coefficient A in the correlating equation (5) was found to be 11 percent higher than that predicted by the isolated vertical plate analysis. This was explained by the uncertain influence of radiation loss, two-dimensional conjugate effects, variation of the thermophysical properties with temperature, and possibly a residual pressure gradient in the channel flow even for high channel aspect ratios.

Results of the present study compare favorably with experimental and analytical data from other investigations as far as the previous work extends into the high Rayleigh number regime. Additionally, the importance of corrections for radiation and conduction losses, and the appropriate use of local thermophysical properties in correlating the data, were underlined.

Acknowledgments

The financial support of this work by the National Science Foundation under Grant No. CBT-8552493 is gratefully acknowledged.

References

Aung, W., 1972, "Fully Developed Laminar Free Convection Between Vertical Plates Heated Asymmetrically," *International Journal of Heat and Mass Transfer*, Vol. 15, pp. 1577–1580.

Aung, W., Fletcher, L. S., and Sernas, V., 1972, "Developing Laminar Free Convection Between Vertical Plates With Asymmetric Heating," *International Journal of Heat and Mass Transfer*, Vol. 16, pp. 2293–2308.

Bar-Cohen, A., and Rohsenow, W. M., 1984, "Thermally Optimum Spacing of Vertical, Natural Convection Cooled, Parallel Plates," ASME JOURNAL OF HEAT TRANSFER, Vol. 106, pp. 116–123.

Bodoia, J. R., and Osterle, J. F., 1962, "The Development of Free Convection Between Heated Vertical Plates," ASME JOURNAL OF HEAT TRANSFER, Vol. 84, pp. 40–44.

Chappidi, P. R., and Eno, B. E., 1988, "Natural Convection in a Heated Parallel Plate Vertical Channel: Influence of Inlet Conditions," *Proceedings of the 1988 National Heat Transfer Conference*, H. R. Jacobs, ed., ASME, New York, Vol. 2, pp. 135–143.

Elenbaas, W., 1942, "Heat Dissipation of Parallel Plates by Free Convection," *Physica*, Vol. 9, pp. 1–23.

Incropera, F. P., ed., 1986, "Research Needs in Electronic Cooling," Proceedings of a workship sponsored by the National Science Foundation and Purdue University, Andover, MA.

Kline, S. J., and McClintock, F. A., 1953, "Describing Uncertainties in Single-Sample Experiments," *Mechanical Engineering*, Jan., pp. 3–12.

Miyatake, O., Fukii, T., Fujii, M., and Tanaka, H., 1973, "Natural Convective Heat Transfer Between Vertical Parallel Plates—One Plate With a Uniform Heat Flux and the Other Thermally Insulated," *Heat Transfer—Japanese Research*, Vol. 4, pp. 25–33.

Oosthuizen, P. H., 1984, "A Numerical Study of Laminar Free Convective Flow Through a Vertical Open Partially Heated Plane Duct," in: *Fundamentals of Natural Convection—Electronic Equipment Cooling*, L.C. Witte and L. S. Saxena, eds., ASME, New York, pp. 41–47.

Ostrach, S., 1953, "An Analysis of Laminar Free Convection Flow and Heat Transfer About a Flat Plate Parallel to the Direction of the Generating Body Force," National Advisory Committee for Aeronautics Report No. 1111.

Raithby, G. D., and Hollands, K. G. T., 1975, "A General Method of Obtaining Approximate Solutions to Laminar and Turbulent Free Convection Problems," in: *Advances in Heat Transfer*, T. F. Irvine, Jr. and J. P. Hartnett, eds., Vol. 11, pp. 265–315.

Siegel, R., and Howell, J. R., 1981, *Thermal Radiation Heat Transfer*, 2nd ed., Hemisphere, Washington, DC.

Sparrow, E. M., and Bahrami, P. A., 1980, "Experiments on Natural Convection From Vertical Parallel Plates With Either Open or Closed Edges," ASME JOURNAL OF HEAT TRANSFER, Vol. 102, pp. 221–227.

Sparrow, E. M., Chrysler, G. M., and Azevedo, L. F., 1984, "Observed Flow Reversals and Measured-Predicted Nusselt Numbers for Natural Convection in a One-Sided Heated Vertical Channel," ASME JOURNAL OF HEAT TRANSFER, Vol. 106, pp. 325–332.

Sparrow, E. M., and Gregg, J. L., 1956, "Laminar Free Convection From a Vertical Plate With Uniform Surface Heat Flux," *Trans. ASME*, Vol. 78, pp. 435–440.

Wirtz, R. A., and Stutzman, R. J., 1982, "Experiments on Free Convection Between Vertical Plates With Symmetric Heating," ASME JOURNAL OF HEAT TRANSFER, Vol. 104, pp. 501–507.

Natural Convection Flows Due to the Combined Buoyancy of Heat and Mass Diffusion in a Thermally Stratified Medium

D. Angirasa

J. Srinivasan

Department of Mechanical Engineering,
Indian Institute of Science,
Bangalore—560 012, India

This paper presents a numerical study of laminar doubly diffusive free convection flows adjacent to a vertical surface in a stable thermally stratified medium. The two buoyant mechanisms are thermal diffusion and species diffusion. The species concentration is assumed to be small. Boussinesq approximations are incorporated and the governing conservation equations of mass, momentum, energy, and species are nondimensionalized. These equations are solved using a finite-difference method. The results are explained in terms of the basic physical mechanisms that govern these flows. It is observed that the ambient thermal stratification has a profound influence on the transport characteristics. The results show many interesting aspects of the complex interaction of the two buoyant mechanisms.

Introduction

Natural convection flows driven by temperature differences have been studied extensively; see, for example, Gebhart (1971), Jaluria (1980), and Raithby and Hollands (1985). In many natural and technological processes, temperature and concentration differences occur simultaneously. Such processes occur in cleaning operations, drying, crystal growth, solar ponds, and photosynthesis. A clear understanding of the nature of interaction between thermal and concentration buoyancies is necessary to control these processes.

In oceanography, convection processes involving thermal and salinity gradients are referred to as thermohaline convection. The term doubly diffusive convection is now widely accepted for all the processes involving simultaneous thermal and concentration gradients. In a recent survey, Ostrach (1980) classified doubly diffusive convection based on the orientation of thermal and concentration gradients with respect to gravity vector. Turner (1985) reviewed certain classes of multicomponent convection with a number of applications.

Gebhart and Pera (1971) studied laminar natural convection flows driven by thermal and concentration buoyancy adjacent to flat vertical surfaces. They presented similarity solutions, and investigated, in addition, the laminar stability of such flows. They also presented an excellent summary of this class of doubly diffusive natural convection. Pera and Gebhart (1972) extended their previous work to flows from horizontal surfaces. In the above studies the effect of stable ambient stratification on heat and mass transfer was not considered. In many natural convection flows, a stable thermal stratification in the ambient is usually present. This occurs, for example, in cooling ponds, lakes, solar ponds, and in the atmosphere. Natural convection flows are extremely sensitive to the configuration and the ambient conditions, as emphasized by Ostrach (1980). In the case of multicomponent convection, the interaction can be quite complex. An analytical solution using the local nonsimilarity method for natural convection heat transfer from a vertical surface to a thermally stratified fluid was obtained by Chen and Eichhorn (1976). They also present experimental results and a summary of related work by other investigators.

In this paper we present a numerical study of the double-diffusive natural convection flow adjacent to a vertical surface in a thermally stratified ambient. We have considered situations where the two buoyant mechanisms aid as well as oppose each other. We have studied the role of ambient thermal stratification by considering the simple case of linear temperature variation. In the present paper we have used the boundary layer approximation. This assumption makes it easier to interpret the interaction between the two buoyant mechanisms. We expect that the physical insight gained in this work will enable us to understand better the more complex flow situations where boundary layer approximations cannot be made. In addition, boundary layer flows have a number of practical applications like vaporization cooling of equipment (Somers, 1956), and others (Gebhart and Pera, 1971). We have used an explicit finite-difference scheme to solve the conservative equations of mass, momentum, energy, and species. We have considered the case of gaseous double-diffusive flows with Prandtl number equal to 0.7 and Schmidt number varying between 0.5 and 5. We have also considered aqueous double-diffusive flows by assuming Prandtl number equal to 7.0 and a representative value of 100 for Schmidt number.

Analysis

The physical configuration of the problem and the ambient temperature variation are given in Fig. 1. Consider a vertical surface that is at a temperature t_w. The concentration of the diffusing species is c_w at the surface. In the ambient, the temperature increases linearly with height, $t_{\infty,o}$ being its value

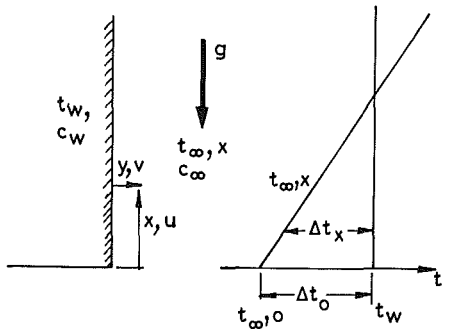

Fig. 1 Coordinate system and boundary conditions

Contributed by the Heat Transfer Division for publication in the JOURNAL OF HEAT TRANSFER. Manuscript received by the Heat Transfer Division January 13, 1987. Keywords: Double Diffusion Systems, Natural Convection.

at $x=0$. The concentration of the diffusing species in the ambient is c_∞, which is constant.

The governing equations for double-diffusive natural convection flows are well known and given by Gebhart (1971) and Jaluria (1980). Using Boussinesq, boundary layer, and dilute solution approximations, we obtain the following mass, momentum, energy, and species conservation equations for laminar flow adjacent to a flat vertical surface:

$$\frac{\partial u}{\partial x}+\frac{\partial v}{\partial y}=0 \tag{1}$$

$$\frac{\partial u}{\partial \tau}+u\frac{\partial u}{\partial x}+v\frac{\partial u}{\partial y}=\nu\frac{\partial^2 u}{\partial y^2}+g\beta(t-t_{\infty,x})-g\beta^*(c-c_\infty) \tag{2}$$

$$\frac{\partial t}{\partial \tau}+u\frac{\partial t}{\partial x}+v\frac{\partial t}{\partial y}=\alpha\frac{\partial^2 t}{\partial y^2} \tag{3}$$

$$\frac{\partial c}{\partial \tau}+u\frac{\partial c}{\partial x}+v\frac{\partial c}{\partial y}=D\frac{\partial^2 c}{\partial y^2} \tag{4}$$

where β^*, the volumetric coefficient due to concentration, is defined as $1/\rho\,(\partial\rho/\partial c)_{t,p}$ (see Turner, 1979). While β is almost always positive, β^* may have either sign. If the molecular weight of the species is higher than the solution, β^* is positive, and vice versa. Hence, we observe from the momentum equation (2) that the two buoyant mechanisms aid each other when the quantities $\beta(t_w-t_\infty)$ and $\beta^*(c_w-c_\infty)$ have opposite signs and oppose each other when they have the same sign.

To make the velocity components dimensionless, a convective velocity based on the temperature difference at $x=0$, $(t_w-t_{\infty,o})$ is employed. The nondimensional variables can be written as follows:

$$X=x\left(\frac{g\beta\Delta t_o}{\nu^2}\right)^{1/3},\quad Y=y\left(\frac{g\beta\Delta t_o}{\nu^2}\right)^{1/3}$$

$$U=\frac{u}{(\nu g\beta\Delta t_o)^{1/3}},\quad V=\frac{v}{(\nu g\beta\Delta t_o)^{1/3}}$$

$$T=\frac{t-t_{\infty,x}}{t_w-t_{\infty,o}},\quad C=\frac{c-c_\infty}{c_w-c_\infty} \tag{5}$$

and

$$\tau^*=\frac{\tau}{\nu^{1/3}}\,(g\beta\Delta t_o)^{2/3}$$

where $\Delta t_o=t_w-t_{\infty,o}$.

The nondimensional conservative equations are then obtained as

$$\frac{\partial U}{\partial X}+\frac{\partial V}{\partial Y}=0 \tag{6}$$

$$\frac{\partial U}{\partial \tau^*}+U\frac{\partial U}{\partial X}+V\frac{\partial U}{\partial Y}=\frac{\partial^2 U}{\partial Y^2}+T-BC \tag{7}$$

$$\frac{\partial T}{\partial \tau^*}+U\frac{\partial T}{\partial X}+V\frac{\partial T}{\partial Y}+SU=\frac{1}{\mathrm{Pr}}\frac{\partial^2 T}{\partial Y^2} \tag{8}$$

$$\frac{\partial C}{\partial \tau^*}+U\frac{\partial C}{\partial X}+V\frac{\partial C}{\partial Y}=\frac{1}{\mathrm{Sc}}\frac{\partial^2 C}{\partial Y^2} \tag{9}$$

where $B=\beta^*(c_w-c_\infty)/\beta(t_w-t_{\infty,o})$ is defined as the buoyancy ratio and $S=1/\Delta t_o\; dt_{\infty,x}/dX$ as the thermal stratification parameter.

The following boundary and initial conditions are prescribed.

$\tau^*>0$

$$Y=0,\ U=V=0,\ T=1-SX$$

$$Y\to\infty,\ U=T=C=0$$

$\tau^*=0$

$$U=V=T=C=0 \text{ for all } X \text{ and } Y$$

We obtain the boundary condition for temperature at the wall in nondimensional form as follows:

$$T_w=\frac{t_w-t_{\infty,x}}{t_w-t_{\infty,o}}=1-\left(\frac{t_{\infty,x}-t_{\infty,o}}{t_w-t_{\infty,o}}\right)$$

Since $t_{\infty,x}$ is a linear function

$$T_w=1-\frac{1}{\Delta t_o}\frac{dt_{\infty,x}}{dX}X$$

By definition of S

$$T_w=1-SX$$

For linear thermal stratification S is a constant, and for other variations it can be represented as a function of X. The value of the buoyancy ratio B indicates the relative strengths of the two buoyant mechanisms, and its sign determines whether they aid or oppose each other. The value of B is approximately equal to 2 for a temperature level of 20°C with a difference of about 15°C, and with the difference in the concentration of water vapor in air associated with saturated conditions for these temperature levels. For a salinity difference

Nomenclature

B = buoyancy ratio = $\beta^*(c_w-c_\infty)/\beta(t_w-t_{\infty,o})$
c = concentration of diffusing species
C = concentration difference ratio = $(c-c_\infty)/(c_w-c_\infty)$
D = diffusion coefficient
g = acceleration due to gravity
Gr = Grashof number
h_m = local mass transfer coefficient
h_x = local heat transfer coefficient
$\bar{h}$, $\bar{h}_m$ = average heat and mass transfer coefficients, respectively
L = dimensional height of the surface
$\overline{\mathrm{Nu}}$ = average Nusselt number
Pr = Prandtl number
S = thermal stratification parameter $=\frac{1}{\Delta t_o}\frac{dt_{\infty,x}}{dx}$
Sc = Schmidt number
$\overline{\mathrm{Sh}}$ = average Sherwood number
t = temperature
T = temperature excess ratio = $(t-t_{\infty,x})/(t_w-t_{\infty,o})$
u, v = velocity components
U, V = nondimensional velocity components
w = subscript for surface
x, y = space coordinates
X, Y = nondimensional space coordinates
$X_{\max}$ = nondimensional height of the surface
α = thermal diffusivity
β = volumetric coefficient of thermal expansion $=-\frac{1}{\rho}\left(\frac{\partial\rho}{\partial t}\right)_{p,c}$
β^* = volumetric coefficient of expansion with concentration $=\frac{1}{\rho}\left(\frac{\partial\rho}{\partial c}\right)_{t,p}$
ν = kinematic viscosity
τ = time
τ^* = nondimensional time
∞ = subscript denoting location at large distance from surface

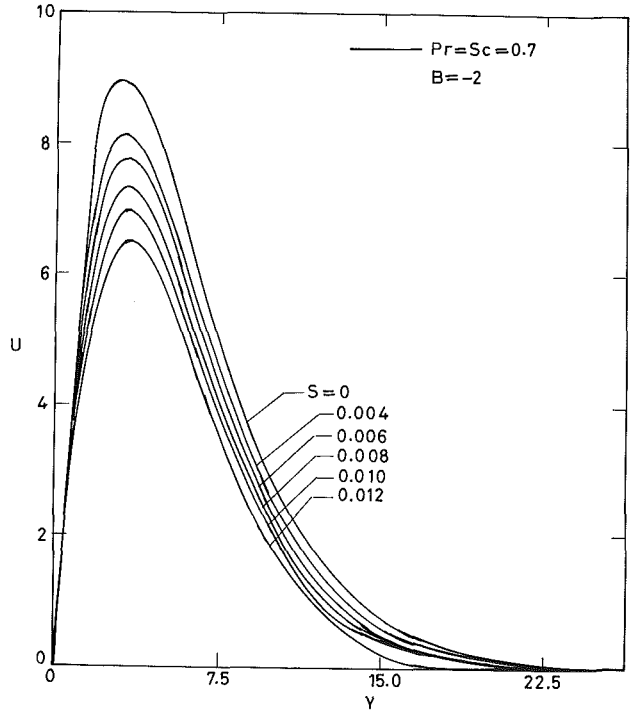

Fig. 2 Velocity profiles at $X=100$ for $Pr=Sc=0.7$ and for various values of the stratification parameter S

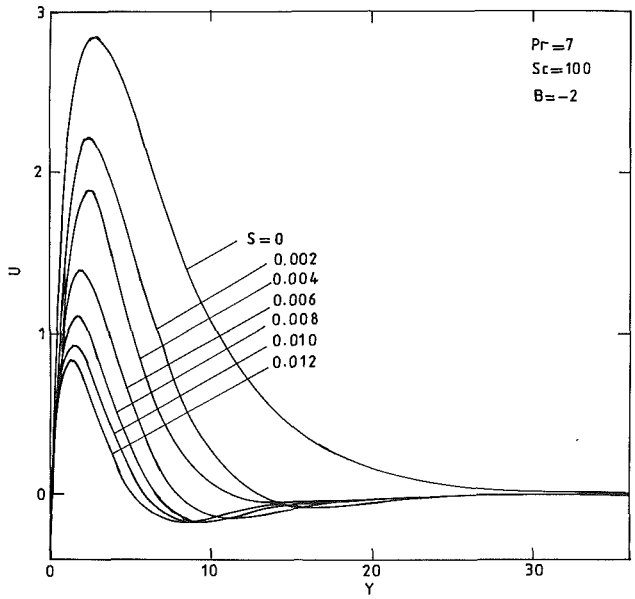

Fig. 3 Velocity profiles at $X=100$ for $Pr=7$ and $Sc=100$, and for various values of stratification parameter S

of 100 ppm in sea water with a temperature difference of 1°C the value of B is about 0.2 (see Gebhart and Pera, 1971).[1] When B is negative the two buoyant forces aid, and when positive, oppose each other.

The energy and species concentration equations are coupled through the momentum equation; hence the set of four equations (6)–(9) is to be solved simultaneously. Yang et al. (1972) have shown that a similarity solution is not possible for flows in stably stratified media. Similarity transformation is possible only for the case of temperature decreasing with height, which is physically unstable. So we have employed a finite-difference technique to solve the governing partial differential equations.

Numerical Procedure

The unsteady nondimensional governing equations have been written in finite-difference form and time marched by employing a uniform grid in each direction. The converged solutions then represent steady flow conditions.

For convenience, we have used an explicit scheme, forward in time. We have employed upwind-differencing for convective terms, and central-differencing for diffusion terms. We observe that the cell Reynolds number, Re_c, defined as $|U\Delta X/(1/Pr)|$ or $(1/Sc)$, is higher than 2. Hence, upwind-differencing is required for stability (see Roache, 1982).

An explicit scheme has restrictions on the time step due to stability considerations, as discussed by Roache (1982). We varied the grid size from 10×10 to 50×50. For a grid size finer than 30×30, numerical values changed only in the fourth decimal place. This corresponds to an error of less than 0.5 percent. We have chosen a grid size of 40×40 for the results presented. This ensures that there are at least four grid points between the surface and the point where the U velocity reaches its maximum.

The convergence criterion employed is of the form $|\theta_i^{n+1}{}_j - \theta_{ij}^n|_{max} \le \epsilon$ where n refers to time level, and i and j to space. The value of ϵ was chosen to be 10^{-4}.

[1] An exhaustive catalog of gaseous and aqueous systems is given by Gebhart et al. (1988).

Results and Discussion

The maximum value of X chosen is 100. At higher values of X, laminar flow assumption may not be valid. From the definition of S, we observe that for $S=0.01$ the temperature in the ambient equals the surface temperature at $X=100$, and for a value of $S>0.01$, a portion at the top of the surface will have a temperature less than the ambient.

In Figs. 2 and 3, velocity profiles at $X=100$ have been shown for $Pr=Sc=0.7$, and $Pr=7$ and $Sc=100$, respectively, for the values of the stratification parameter S varying between zero and 0.012. $S=0$ refers to the unstratified environment. With the value of B chosen as -2, the two buoyancies aid each other. An increase in ambient thermal stratification invariably decreases the thermal buoyancy. Hence we observe a reduction in velocity. The stratification effects are quite significant. For instance, for $Pr=Sc=0.7$ and $S=0.01$ the decrease in peak U velocity is about 20 percent. For the same stratification level, and for $Pr=7$ and $Sc=100$, it is as much as 65 percent. For $Pr=Sc=0.7$ no negative velocities are indicated (Fig. 2), but for $Pr=7$ and $Sc=100$, we observe flow reversal in the outer part of the boundary layer (Fig. 3). Since the numerical value of B is 2, the buoyancy created by the concentration difference outweighs the thermal buoyancy by a factor of 2 at $X=0$. As the flow proceeds downstream, the former contributes the major driving force because of the progressive decrease in thermal buoyancy. For $S=0.01$, the temperature potential at $X=100$ is zero. In the absence of the concentration difference causing buoyancy, a horizontal plume would result at this location, as demonstrated by Chen and Eichhorn (1976). For $S=0.012$ the temperature potential at $X=100$ is negative. If the other buoyant mechanism is not present, flow reversal will take place here, and at a location of X less than 100 there will be a horizontal plume. Since a dominant positive buoyant mechanism through mass diffusion is present, the boundary layer flow upward is sustained in both cases. The small flow reversal in the outer region of the boundary layer in the case of $Pr=7$ and $Sc=100$ (Fig. 3) is due to the adverse thermal buoyancy, which as explained above is not sufficient to cause the total flow to reverse.

Figure 4 represents the temperature profiles at $X=100$ for $Pr=Sr=0.7$ and for the same values of S as above. If thermal stratification is not present, the temperature and concentration profiles will be identical when $Pr=Sc$. As can be ex-

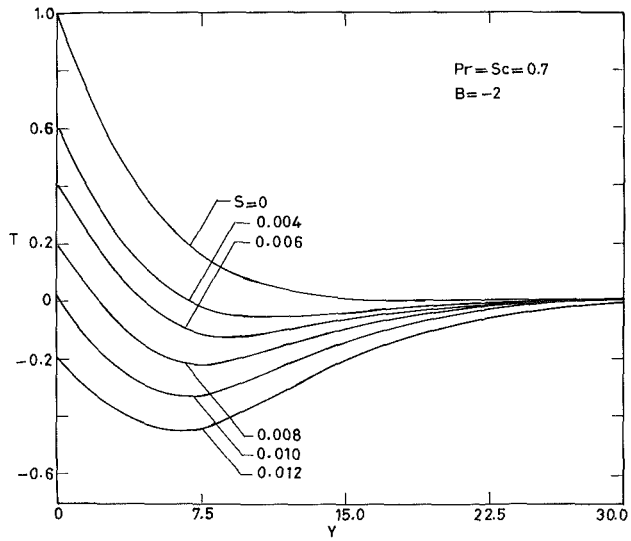

Fig. 4 Temperature profiles at $X = 100$ $Pr = Sc = 0.7$, and for various values of the stratification parameter S

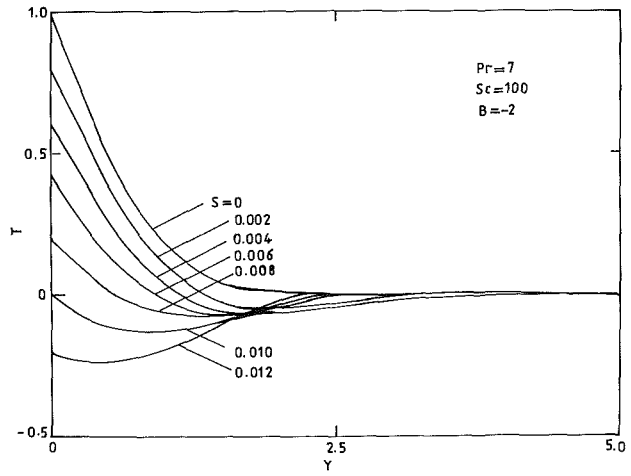

Fig. 5 Temperature profiles at $X = 100$ for $Pr = 7$ and $Sc = 100$ and for various values of stratification parameter S

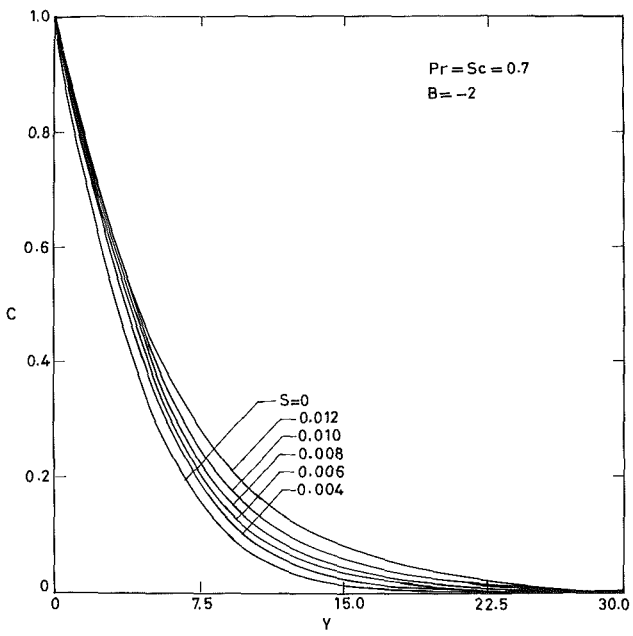

Fig. 6 Concentration profiles at $X = 100$ for $Pr = Sc = 0.7$, and for various values of the stratification parameter S

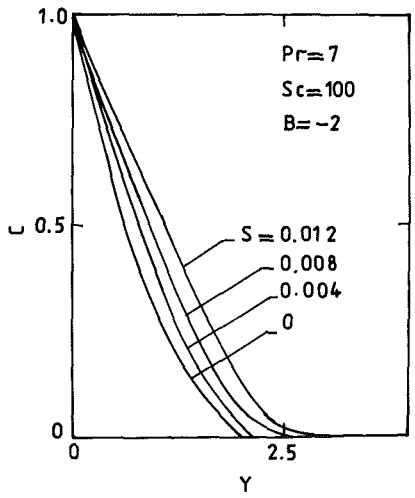

Fig. 7 Concentration profiles at $X = 100$ for $Pr = 7$ and $Sc = 100$, and for various values of the stratification parameter S

pected, a stable ambient thermal stratification affects the thermal and concentration boundary layers in different ways. In Fig. 4, it is observed that the values of nondimensional temperature are negative within the boundary layer for $S = 0.01$ and 0.012. This phenomenon can be explained as follows. In the case of $S = 0.01$, the temperature difference between the surface and the ambient at $X = 100$ is zero. But fluid coming up from below with the flow sustained by the other buoyant force will have a temperature that is markedly less than that of the surface or the ambient. Hence the nondimensional temperature starts with a value of zero at the surface, dips to significant negative values and finally reaches zero again at the edge of the boundary layer. The same explanation holds for the case of $S = 0.012$, except that the nondimensional temperature at the surface is -0.2, and it drops further before asymptotically reaching zero.

For values of $S < 0.01$, there is positive thermal buoyancy at $X = 100$, but negative nondimensional temperatures are still observed in the outer regions. For higher values of S, the temperature in the ambient increases so rapidly with height that the fluid coming up will be much cooler in the outer region of the boundary layer. Hence negative values of nondimensional temperature appear in the "wings" of the profile. This occurrence is often referred to as "temperature defect" in the flow and it is also observed in thermal buoyant convection flows in thermally stratified media, as described by Yang et al. (1972) and Jaluria and Gebhart (1974). However, in the case of natural convection flows with combined heat and mass transfer the temperature defect is more pronounced, as has been explained above. When the Prandtl number is higher, thermal diffusivity is lower. So, for a higher value of Prandtl number, the thermal boundary layers are thinner, as shown in Fig. 5.

In Figs. 6 and 7, we present the effect of thermal stratification on concentration boundary layers. Since thermal stratification suppresses the thermal buoyancy with the resultant decrease in velocities, local concentration levels increase. This causes diffusion to be more dominant and the concentration boundary layers to thicken. For $S = 0.012$, the increase in concentration boundary layer thickness is almost double that of $S = 0$, for $Pr = Sc = 0.7$, thus indicating strong influence of thermal stratification on species diffusion. A fluid with higher Schmidt number has a smaller value of the species diffusion coefficient; consequently, its concentration boundary layers are thinner and the profiles steeper as clearly seen in Fig. 7.

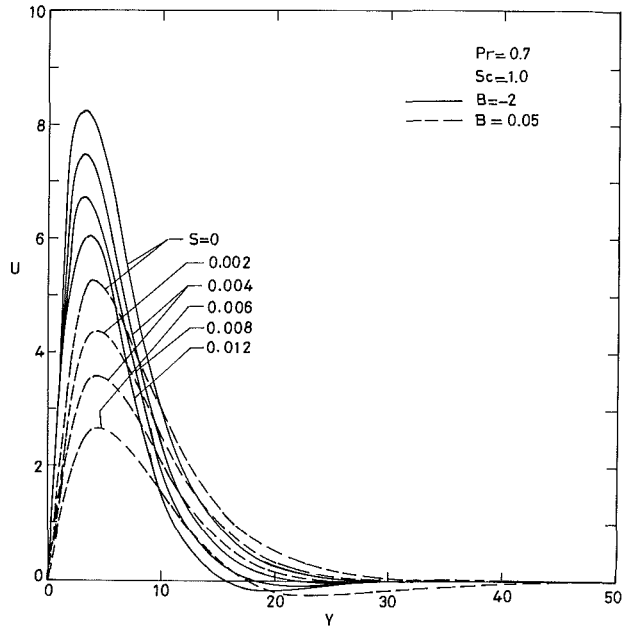

Fig. 8 Velocity profiles at $X=100$ for $B=-2$ and 0.05 for various values of the stratification parameter S

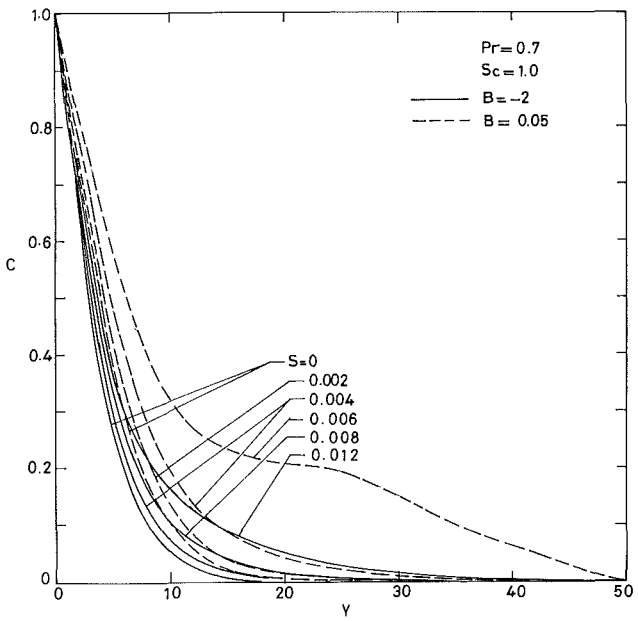

Fig. 10 Concentration profiles at $X=100$ and $B=-2$ and 0.05 for various values of the stratification parameter S

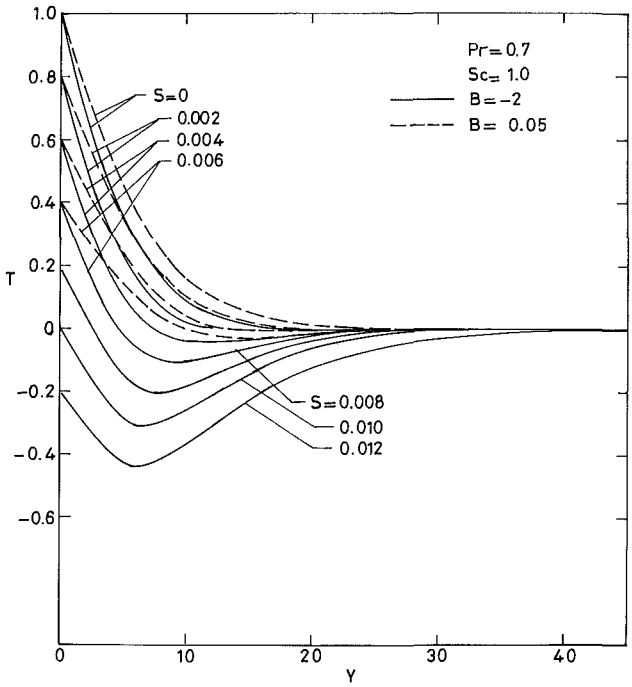

Fig. 9 Temperature profiles at $X=100$ for $B=-2$ and 0.05 for various values of the stratification parameter S

Figures 8–10 compare the effect of thermal stratification on velocity, temperature, and concentration profiles when the two buoyant mechanisms aid and oppose each other. In Fig. 8, the velocity profiles are given for $Pr=0.7$ and $Sc=1.0$, for aiding ($B=-2$) and opposing ($B=0.05$) flows for various values of the stratification parameter S. The decrease in velocity levels with increase in thermal stratification is fairly obvious. The fact that the opposing flows considerably reduce the velocities is also quite apparent. The reason for the appearance of negative velocities has been discussed already. In the case of opposing flows, more than half of the boundary layer away from the surface undergoes mild flow reversal, for $S=0.006$. The increase in the region of boundary layer where there is flow reversal is due to the opposing nature of one buoyant mechanism to the other. We observe that the boundary layer thickness is significantly higher in the case of opposing flows. In such flows, convection is reduced, which allows diffusion to play a dominant role. For values of S higher than 0.006, the opposing flow became unstable. It is questionable that the boundary layer analysis is valid for opposing flows at such high stratification levels.

In Fig. 9, we present the temperature profiles for aiding and opposing flows for various values of S. The nature of temperature defect has been discussed before. In contrast to aiding flows, there is no discernible temperature defect for opposing flows. The opposing buoyancies counteract the effect produced by the cooler fluid coming up from below to a warmer ambient.

In Fig. 10, concentration profiles are shown for aiding and opposing flows for different values of S. An interesting profile is observed for opposing flows when the value of S is 0.006 The unusual nature of this profile can be explained as follows. Referring to the velocity profile for this case (Fig. 8), it is observed that a significant part of the boundary layer has negative velocities that are small in magnitude. This increase in the portion of the boundary layer undergoing flow reversal is due to the opposing buoyant mechanism in the flow. In the region of the boundary layer where flow reversal takes place, concentration levels increase.

Figures 11–13 consider the effect of Schmidt number on flow, heat, and mass transfer characteristics of aiding flow under thermal stratification. Two levels of thermal stratification are considered, $S=0.006$ and 0.01. The former gives a positive thermal buoyancy at $X=100$, and the latter zero thermal buoyancy at the same location. A fluid with a higher Schmidt number has a lower species diffusion coefficient. This reduces the mass diffusion rate, and hence concentration-driven buoyancy. The velocities consequently fall with increasing value of Schmidt number. High thermal stratification in the ambient further suppresses the thermal buoyant mechanism and hence the velocities drop even further. These are clearly indicated in Fig. 11. Higher Schmidt number fluids have thinner concentration boundary layers because of low species diffusion as indicated in Fig. 13. However, it is interesting to note that an increase in ambient thermal stratifica-

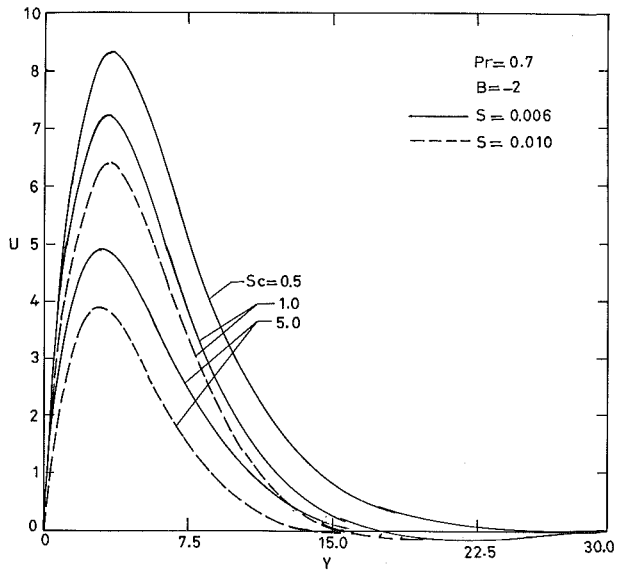

Fig. 11 Velocity profiles at $X = 100$ for $S = 0.006$ and 0.01 for various values of Schmidt number Sc

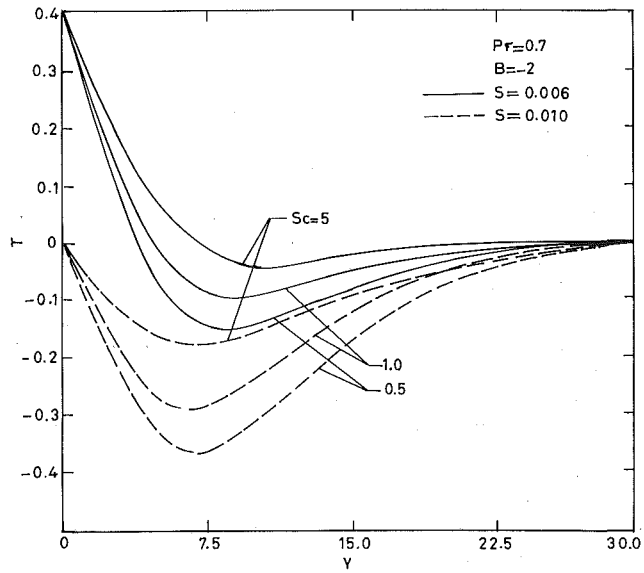

Fig. 12 Temperature profiles at $X = 100$ for $S = 0.006$ and 0.01 for various values of Schmidt number Sc

tion thickens the concentration boundary layer for the same value of Sc. This can be attributed to the suppression of convection by thermal stratification, allowing diffusion to have a more dominant role. We find in Fig. 12 that, for the same Prandtl number, the temperature defect is less for fluids with higher values of Schmidt number. Since the velocities drop considerably with increasing Schmidt number, there is a smaller quantity of cold fluid coming up from below to a warmer ambient. Hence the fluid in the boundary layer is warmer with a higher Schmidt number, which lessens the temperature defect.

Calculation of Nusselt and Sherwood Number

We may define a local heat transfer coefficient based on the local temperature potential as

$$h_x(t_w - t_{\infty,x}) = -k \left.\frac{\partial t}{\partial y}\right|_0$$

which may be integrated over the height of the surface to obtain the average heat transfer coefficient. This results, in non-dimensional form, in

$$\overline{\mathrm{Nu}} = \frac{\bar{h}L}{k} = \int \frac{1}{T_w}\left(-\left.\frac{\partial T}{\partial Y}\right|_0\right) dX$$

In the above expression L is the dimensional height of the plate. We may rewrite

$$X = (\mathrm{Gr}_x)^{1/3}$$

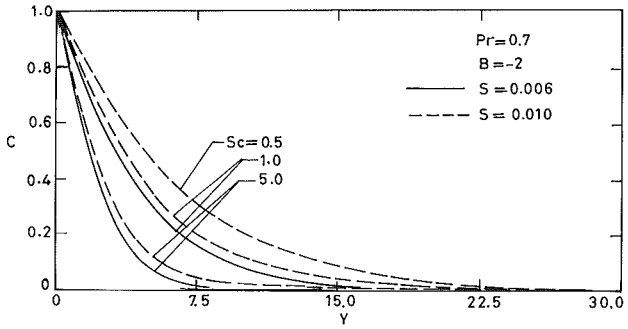

Fig. 13 Concentration profiles at $X = 100$ for $S = 0.006$ and 0.01 for various values of Schmidt number Sc

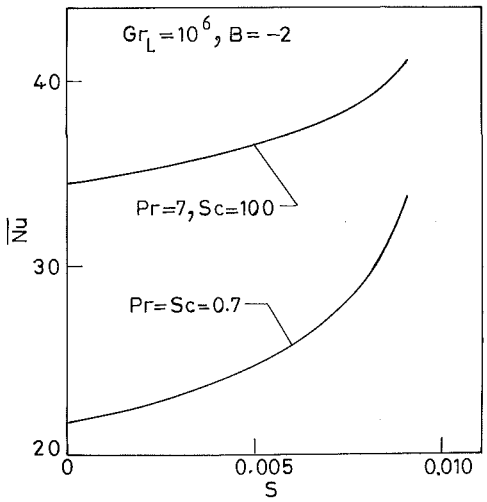

Fig. 14 Variation of $\overline{\mathrm{Nu}}$ with the thermal stratification parameter S

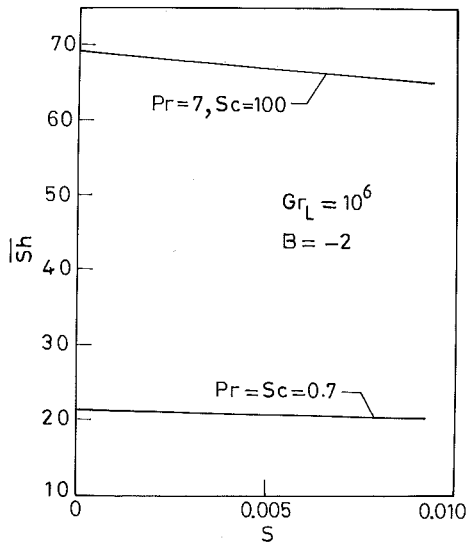

Fig. 15 Variation of $\overline{\mathrm{Sh}}$ with S

Table 1 Comparison of the average Nusselt number without mass transfer

$Gr_L Pr$	McAdams (1954)	Churchill and Chu (1975)	Present
0.7×10^6	17.066	15.531	16.923
7×10^6	30.348	32.175	30.623

where Gr_x is defined as $g\beta(t_w-t_{\infty,o})x^3/\nu^2$. Hence, X_{max} indicates the value of $(Gr_L)^{1/3}$.

Similar to the calculation of the average Nusselt number, the average mass transfer coefficient may be obtained to yield the average Sherwood number as

$$\overline{Sh} = \frac{\bar{h}_m L}{D} = \int \left(-\frac{\partial C}{\partial Y}\right)_0 dX$$

By setting B and S equal to zero in equations (7) and (8), respectively, and ignoring the species conservation equation (9), we arrive at the classical problem of natural convection heat transfer from a vertical surface. Table 1 gives a comparison of the $\overline{Nu}$ from the present computation with the available literature.

In Fig. 14 $\overline{Nu}$ data are presented as a function of S. Since the local heat transfer coefficient is based on the local temperature difference, $(t_w-t_{\infty,x})$, $\overline{Nu}$ is dependent on the mean temperature difference over the entire surface. Since the mean temperature difference decreases with increasing value of S, $\overline{Nu}$ increases with S. This trend is similar to the $\overline{Nu}$ data of Chen and Eichhorn (1976). Figure 15 presents data for the average Sherwood number.

Conclusions

The present numerical study highlights the complex interaction between the two buoyant mechanisms in a laminar doubly diffusive free convection flow. Ambient thermal stratification is found to decrease the local buoyancy levels significantly, which reduce the velocities and increase the concentrations. The temperature defect, which has been observed in thermal buoyant convection flows in thermally stratified media, is more pronounced in doubly diffusive free convection flow. For fluids with higher values of Schmidt number, the temperature defect is found to be less. When the two buoyant mechanisms oppose each other, the opposing nature, in conjunction with ambient stratification, destabilizes the flow.

References

Chen, C. C., and Eichhorn, R., 1976, "Natural Convection From a Vertical Surface to a Thermally Stratified Fluid," ASME JOURNAL OF HEAT TRANSFER, Vol. 98, pp. 446–451.

Churchill, S. W., and Chu, H. H. S., 1975, "Correlating Equations for Laminar and Turbulent Free Convection From a Vertical Plate," *Int. J. Heat Mass Transfer*, Vol. 18, pp. 1323–1329.

Gebhart, B., 1971, *Heat Transfer*, 2nd ed., McGraw-Hill, New York.

Gebhart, B., Jaluria, Y., Mahajan, R. L., and Sammakia, B., 1988, *Buoyancy Induced Flows and Transport*, Ch. 6, Hemisphere, Washington/Springer-Verlag, Berlin.

Gebhart, B., and Pera, L., 1971, "The Nature of Vertical Natural Convection Flows Resulting From the Combined Buoyancy Effects of Thermal and Mass Diffusion," *Int. J. Heat Mass Transfer*, Vol. 14, pp. 2025–2050.

Jaluria, Y., 1980, *Natural Convection Heat and Mass Transfer*, Pergamon, Oxford.

Jaluria, Y., and Gebhart, B., 1974, "Stability and Transition of Buoyancy-Induced Flows in a Stratified Medium," *J. Fluid Mech.*, Vol. 66, Part 3, pp. 593–612.

McAdams, W. H., 1954, *Heat Transmission*, 3rd ed., McGraw-Hill, New York.

Ostrach, S., 1980, "Natural Convection With Combined Driving Forces," *Physico-Chemical Hydrodynamics*, Vol. 1, pp. 233–247.

Pera, L., and Gebhart, B., 1972, "Natural Convection Flows Adjacent to Horizontal Surfaces Resulting From the Combined Buoyancy Effects of Thermal and Mass Diffusion," *Int. J. Heat Mass Transfer*, Vol. 15, pp. 269–278.

Raithby, G. D., and Hollands, K. G. T., 1985, "Natural Convection," in: *Handbook of Heat Transfer Fundamentals*, W. M. Rohsenow et al., eds., 2nd ed., McGraw-Hill, New York.

Roache, P. J., 1982, *Computational Fluid Dynamics*, Hermosa, Albuquerque.

Somers, E. V., 1956, "Theoretical Considerations of Combined Thermal and Mass Transfer From a Vertical Flat Plate," ASME *J. Applied Mechanics*, Vol. 23, pp. 295–301.

Turner, J. S., 1979, *Buoyancy Effects in Fluids*, Cambridge University Press, Cambridge.

Turner, J. S., 1985, "Multicomponent Convection," *Ann. Rev. Fluid Mech.*, Vol. 17.

Yang, K. T., Novotny, J. L., and Cheng, Y. S., 1972, "Laminar Free Convection From a Non-isothermal Plate Immersed in a Temperature Stratified Medium," *Int. J. Heat Mass Transfer*, Vol. 15, pp. 1097–1109.

Induction Electrohydrodynamic Pump in a Vertical Configuration: Part 1—Theory

J. Seyed-Yagoobi
Texas A&M University,
College Station, TX 77843

J. C. Chato

J. M. Crowley

P. T. Krein

University of Illinois,
Urbana, IL 61801

An induction electrohydrodynamic (EHD) pump in an axisymmetric, vertical configuration is studied theoretically. The model includes the effect of entrance conditions, buoyancy effects, secondary flow, and Joule heating. Primarily the forward (cooled wall) and to a lesser extent the backward (heated wall) modes are investigated. A finite difference technique is used to obtain the numerical solutions. A set of these solutions is presented to show the influence of the controlling factors of operating an induction EHD pump. The results indicate that the entrance temperature profile plays an important role in the operation of the pump because steeper profiles produce higher velocities. The pump must be operated at an optimum frequency, wavelength, and electric conductivity level.

Introduction

Electrohydrodynamic (EHD) pumping is achieved when traveling electric fields are generated that attract or repel the charges in a given direction. One way of establishing the free charges is establishment of a conductivity gradient perpendicular to the desired direction of fluid motion, giving an EHD induction punp. The electrical conductivity of fluids is often a strong function of temperature. Thus, if there is a temperature gradient, there is also a conductivity gradient. In an electric field, this results in a net charge inside the medium.

In the induction EHD pump, the charges in the fluid come from dissociation of molecules into positive and negative ions. As a result, the net electrical charge is zero when averaged over the entire pump; there are local regions of positive or negative charge, however, that tend to return to equilibrium in an amount of time on the order of the electrical relaxation time of the liquid (Melcher, 1981). This differs from the ion drag pump, which has a net charge imbalance caused by injection of carriers from an electrode.

The charged regions in the induction pump are formed by a combination of thermal gradients and applied electric fields. For forward pumping the tube walls that carry the electrodes are cooled, giving the charge distribution shown as a simplified two-fluid model in Fig. 1 (in our experiments the electrodes were in contact with the fluid, but this is not necessary). The central core of liquid is hotter, which promotes the dissociative formation of charge carriers there. Equal numbers of carriers are formed, but they are free to move individually and tend to congregate at the edge of the hot core facing the oppositely charged electrodes. Further progress toward the electrodes is much slower, because the cooler shell of fluid has a higher viscosity, which slows the progress of the ions.

While the charges are delayed at the thermal gradient, the voltage distribution on the electrodes moves along the wall, creating a traveling wave. The ions opposite the electrodes are attracted to the new voltage location, so that they tend to follow the wave, dragging the surrounding fluid with them. This is the basis of the attraction type of EHD induction pump in which the fluid and the electric wave travel in the same direction.

If the walls are heated, the more conductive hot fluid near the wall causes the charges with opposite polarities to collect on the electrodes, while the charges with like polarities are repelled to and along the interface of the hot and cold fluids. This is the basis of the repulsion type of EHD induction pump in which the fluid and the electrical wave travel in opposite directions.

A possible application in the power industry is the pumping of oil to cool underground power cables. This has been the subject of research at the University of Illinois since 1976 (Chato et al., 1977, 1981; Crowley et al., 1983). EHD pumping could also be a feasible alternative to mechanical pumps in high-voltage electrical equipment such as transformers (Seyed-Yagoobi, 1984; Shaurbaugh and Walker, 1983). EHD pumping has neither moving mechanical parts nor the need of external pressure drop for operation.

Melcher (1966) developed the basic theory for thermal induction pumping and demonstrated a small working model. Kuo et al. (1984) developed a theoretical model for induction EHD pumping in horizontal configuration. Their results showed that effective pumping can be achieved without grounding electrode along the axis of the tube.

Part 1 presents a theoretical model of an induction EHD pump in the vertical, axisymmetric configuration. A finite difference technique is used to obtained the numerical solutions. In Part 2, the theoretical model is compared to the experimental results.

Theoretical Analysis

Consider the electrohydrodynamically pumped fluid in a vertical pipe shown in Fig. 2 where the flow is assumed to be in the positive z direction. The pipe is either being cooled or heated uniformly at the wall. The primary assumptions are as follows:

(1) The fluid is Newtonian;
(2) the flow is steady and laminar;
(3) the flow is neither thermally nor hydrodynamically quasi-fully developed, i.e., entrance effects are considered;
(4) the flow and the electric field are axisymmetric;
(5) properties of the working fluid are temperature depen-

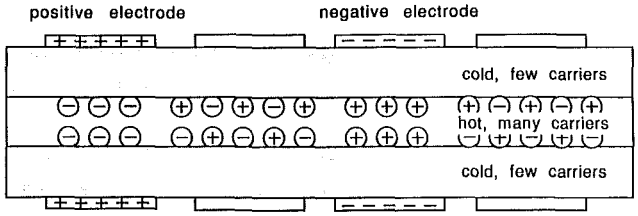

Fig. 1 Charge distribution in the forward mode

Contributed by the Heat Transfer Division for publication in the JOURNAL OF HEAT TRANSFER. Manuscript received by the Heat Transfer Division December 1, 1987. Keywords: Forced Convection, Heat Exchangers, Mixed Convection.

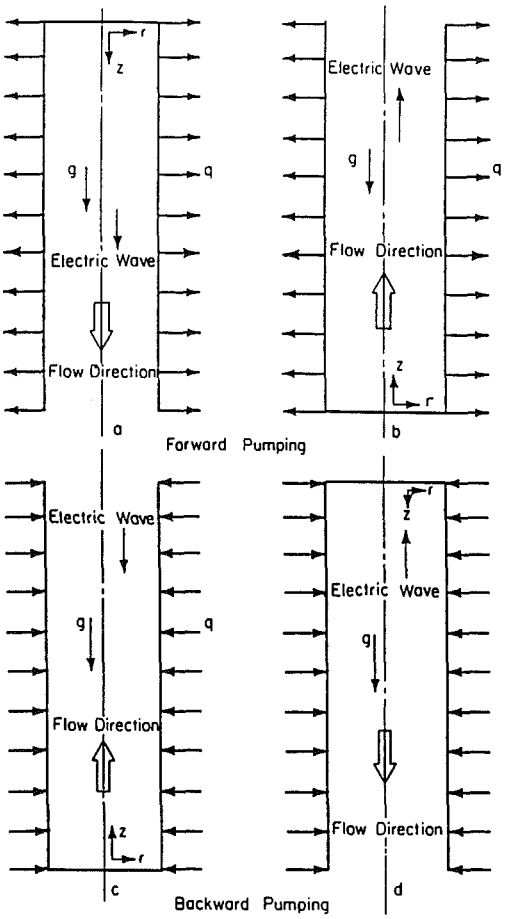

Fig. 2 The vertical EHD pump

dent with the exception of constant thermal conductivity and electric permittivity.

The detailed derivation of the theoretical model is in Seyed-Yagoobi (1984).

The momentum equations in the axial and radial directions and the energy equation can be expressed as follows:

$$\rho\left(u\frac{\partial w}{\partial r}+w\frac{\partial w}{\partial z}\right)=\left(-\frac{dP}{dz}-\rho_b g+\rho g\right)+\frac{1}{r}\frac{\partial}{\partial r}\left(\mu r\frac{\partial w}{\partial r}\right)+\frac{1}{r}\frac{\partial}{\partial r}\langle r\tau_{e,rz}\rangle \tag{1}$$

$$\rho\left(u\frac{\partial u}{\partial r}+w\frac{\partial u}{\partial z}\right)=-\left\{\frac{1}{r}\frac{\partial}{\partial r}\left(-2\mu r\frac{\partial u}{\partial r}\right)+2\mu\frac{u}{r^2}-\frac{\partial}{\partial z}\left[\mu\left(\frac{\partial w}{\partial r}+\frac{\partial u}{\partial z}\right)\right]\right\} \tag{2}$$

$$u\frac{\partial T}{\partial r}+w\frac{\partial T}{\partial z}=\frac{k}{\rho c_p}\frac{1}{r}\frac{\partial}{\partial r}\left(r\frac{\partial T}{\partial r}\right)+\frac{\sigma E^2}{\rho c_p} \tag{3}$$

In equation (1) the last term is the time average of electric shear stress in the r–z plane. In the axial momentum equation it is assumed that the changes of u and $\langle\tau_{e,zz}\rangle$ in the flow direction are negligible. The electrical force and pressure drop in the r direction are ignored in the radial momentum equation because they are negligible.

The effect of Joule heat is the last term in the energy equation (3). The viscous dissipation is not included in the energy equation. As indicated by Test (1968), including the viscous dissipation term for laminar flow yielded no more than a one percent change in the value of Nusselt number because of the low Reynolds and Eckert numbers in laminar flow.

In order to solve the above equations, the electric shear stress and the Joule heat must be expressed in terms of the electric potential. In an EHD pump, currents are very small so magnetic effects are negligible. The basic electrostatic relations for the complex amplitude of the electric potential can be reduced to (Seyed-Yagoobi, 1984)

$$\bar{\sigma}\frac{1}{r}\frac{d}{dr}\left(r\frac{dC}{dr}\right)+\frac{d\sigma}{dr}\frac{dC}{dr}-\bar{\sigma}K^2C=0 \tag{4}$$

where $C(r)$ is the complex amplitude of the electric potential expressed as (Krein, 1984)

$$\phi=\mathrm{Re}[Ce^{j(\Omega t-Kz)}]$$

and

$$\bar{\sigma}=\sigma+j\epsilon(\Omega-wK),\ K=\pm\frac{2\pi}{\lambda},\ \text{and}\ \Omega=2\pi f \tag{5}$$

where the plus and minus signs of the K term are for forward

Nomenclature

a = pipe radius, m
C = electrical potential, V
c_p = specific heat of fluid, J/kg°C
D = diameter, m
E = electric field intensity, V/m
f = frequency, Hz
f_e = electric force, N/m^2
g = gravitational acceleration = 9.81 m/s^2
j = complex operator = $\sqrt{-1}$
k = thermal conductivity, W/m°C
K = propagation constant, first harmonic = $2\pi/\lambda$, 1/m
$\dot{m}$ = mass flow rate, kg/s
P = pressure, N/m^2
Pr = Prandtl number
q = rate of heat transfer per unit area, W/m^2
q_e = electrical charge density, C/m^3
Re = Reynolds number or real value
r, θ, z = cylindrical coordinates
T = fluid temperature, °C
ΔT^* = characteristic temperature = qa/k, °C
u, v, w = dimensional velocities in r, θ, and z directions, m/s
U_c, W_c = characteristic velocities, m/s
z = distance from entrance, m
Z_c = characteristic length in axial direction, m
ϵ = electrical permittivity, F/m
λ = wavelength, m
μ = viscosity, kg/m − s
ρ = density, kg/m^3
σ = electrical conductivity, S/m
$\bar{\sigma}$ = complex electrical conductivity with velocity term, S/m
$\langle\tau_e\rangle$ = time-averaged electrical shear stress, N/m^2
ϕ = electrical field potential, V
Ω_n = angular frequency = $2n\pi f$, 1/s

Subscripts and Superscripts

b = bulk mean value
e = electrical value
0 = entrance condition
$0p$ = zero to peak value
P = peak value
$*$ = nondimensional value
$'$ = complex conjugate value

and backward pumping, respectively. In the derivation of equation (4), only the axial velocity term was retained. The electric shear stress $\tau_{e,rz}$ must be expressed in terms of electrical potential. In a linear dielectric, the force density is (Melcher, 1981)

$$\bar{f}_e = q_e\bar{E} - \frac{1}{2}E^2\nabla\epsilon \tag{6}$$

Since the permittivities of insulating oils are essentially constant in the operating regime under consideration, the last term in the above equation becomes negligible, indicating no momentum contribution to the medium by the dipoles. Expressing equation (6) as the Maxwell stress tensor, the time-averaged electric shear stress with a pure sinusoidal voltage excitation becomes

$$\langle\tau_{e,rz}\rangle = \frac{\epsilon}{2}\,\mathrm{Re}\left(-jKC\frac{dC'}{dr}\right) \tag{7}$$

where Re stands for the real value of a complex term and a prime denotes the complex conjugate.

The Joule heat, after taking the time average, becomes

$$\sigma E^2 = \frac{1}{2}\sigma\left(K^2|C|^2 + \left|\frac{dC}{dr}\right|^2\right) \tag{8}$$

where $||$ stands for the magnitude of a complex number.

Equations (1)–(8) must be solved simultaneously to determine the axial velocity, secondary velocity, and temperature distributions.

In order to nondimensionalize the electrical equations the following terms are introduced:

$$\sigma^* = \frac{\sigma}{\sigma_{b0}}, \quad \bar{\sigma}^* = \frac{\bar{\sigma}}{\sigma_{b0}}, \quad K^* = Ka, \quad r^* = \frac{r}{a}$$

$$E_{0P} = \frac{\phi_{e,P}}{a}, \quad \langle\tau_{e,rz}\rangle^* = \frac{\langle\tau_{e,rz}\rangle}{\frac{\epsilon E_{0p}^2}{2}} \tag{9}$$

$$C^* = \frac{C}{\phi_{e,P}}, \quad C'^* = \frac{C'}{\phi_{e,P}}$$

Then equations (4) and (7) become

$$\frac{d^2C^*}{dr^{*2}} + \frac{1}{r^*}\frac{dC^*}{dr^*} + \frac{1}{\sigma^*}\frac{d\sigma^*}{dr^*}\frac{dC^*}{dr^*} - K^{*2}C^* = 0 \tag{10}$$

$$\langle\tau_{e,rz}\rangle^* = \mathrm{Re}\left(-jK^*C^*\frac{dC'^*}{dr^*}\right) \tag{11}$$

To normalize the transport equations, the following terms are defined:

$$u^* = \frac{u}{U_c}, \quad w^* = \frac{w}{W_c}, \quad z^* = \frac{z}{Z_c} \tag{12}$$

$$\mu^* = \frac{\mu}{\mu_{b0}}, \quad \rho^* = \frac{\rho}{\rho_{b0}}, \quad c^* = \frac{c_p}{c_{p_{b0}}}$$

where

$$W_c = \frac{a}{\mu_{b0}}\frac{\epsilon E_{0p}^2}{2}, \quad U_c = \frac{\mu_{b0}}{\rho_{b0}a} \tag{13}$$

and

$$T^* = \frac{T - T_b}{\Delta T^*} \tag{14}$$

where $\Delta T^* = \dfrac{qa}{k}$.

From the continuity equation, it can be concluded that

$$Z_c = \rho_{b0}\left(\frac{a^3}{\mu_{b0}^2}\right)\left(\frac{\epsilon E_{0p}^2}{2}\right) \tag{15}$$

Then the nondimensional momentum and energy equations become

$$\rho^*\left(u^*\frac{\partial w^*}{\partial r^*} + w^*\frac{\partial w^*}{\partial z^*}\right)$$

$$= \frac{2a}{\epsilon E_{0p}^2}\rho_{b0}g\left(-\frac{dP}{dz}\frac{1}{\rho_{b0}g} - \frac{\rho_b}{\rho_{b0}} + \rho^*\right)$$

$$+ \left(\frac{\partial\mu^*}{\partial r^*}\frac{\partial w^*}{\partial r^*} + \frac{1}{r^*}\mu^*\frac{\partial w^*}{\partial r^*} + \mu^*\frac{\partial^2 w^*}{\partial r^{*2}}\right)$$

$$+ \left(\frac{\partial\langle\tau_{e,rz}\rangle^*}{\partial r^*} + \frac{\langle\tau_{e,rz}\rangle^*}{r^*}\right) \tag{16}$$

$$\rho^*\left(u^*\frac{\partial u^*}{\partial r^*} + w^*\frac{\partial u^*}{\partial z^*}\right) = 2\left(\frac{\mu^*}{r^*}\frac{\partial u^*}{\partial r^*}\right.$$

$$\left. + \frac{\partial\mu^*}{\partial r^*}\frac{\partial u^*}{\partial r^*} + \mu^*\frac{\partial^2 u^*}{\partial r^{*2}} - \mu^*\frac{u^*}{r^{*2}}\right)$$

$$+ \left(\frac{\partial\mu^*}{\partial z^*}\frac{\partial w^*}{\partial r^*} + \mu^*\frac{\partial^2 w^*}{\partial z^*\partial r^*}\right) + \frac{a^2}{Z_C^2}\frac{\partial\mu^*}{\partial z^*}\frac{\partial u^*}{\partial z^*} \tag{17}$$

$$u^*\frac{\partial T^*}{\partial r^*} + w^*\frac{\partial T^*}{\partial z^*} + w^*\frac{2Z_c}{a\mathrm{Re}_b\mathrm{Pr}_b}$$

$$= \frac{1}{\mathrm{Pr}_{b0}}\frac{1}{\rho^* c_p^*}\left(\frac{1}{r^*}\frac{\partial T^*}{\partial r^*} + \frac{\partial^2 T^*}{\partial r^{*2}}\right)$$

$$+ \frac{1}{2}\frac{\sigma_{b0}}{\mu_{b0}c_{p_{b0}}}\frac{1}{\Delta T^*}\frac{\sigma^*}{\rho^* c_p^*}\phi_{e,p}^2\left(K^{*2}|C^*|^2\right.$$

$$\left. + \left|\frac{dC^*}{dr^*}\right|^2\right) \tag{18}$$

where

$$\mathrm{Re}_b = \frac{\rho_b w_b a}{\mu_b} \text{ and } \mathrm{Pr}_b = \frac{\mu_b c_{p_b}}{k} \tag{19}$$

Pr_{b0} is the Prandtl number evaluated at the bulk temperature at the entrance of the pipe.

The bulk temperature at any cross section of the pipe is determined from the following equation, which was obtained from an energy balance in a section of pipe:

$$T_b = T_{b0} + \frac{2\pi a}{\dot{m}c_{p_b}}zq$$

where T_{b0} is the bulk temperature at the entrance, and z is the distance from the entrance of the pipe.

The nondimensional boundary conditions for an axisymmetric flow at the centerline of the pipe are

$$r^* = 0: \frac{\partial w^*}{\partial r^*} = \frac{dC^*}{dr^*} = \frac{\partial T^*}{\partial r^*} = 0, \quad u^* = 0 \tag{20}$$

and at the wall, the nonslip conditions give

$$r^* = 1: \; u^* = w^* = 0 \tag{21}$$

The pipe wall is being either cooled or heated uniformly, and the electric potential has a known value at the surface of the pipe; therefore:

$$C^* = 1, \quad \frac{\partial T^*}{\partial r^*} = 1 \tag{22}$$

We assume that the flow enters the pipe with a known temperature profile. The axial velocity at the entrance of the pipe is unknown but should correspond to the entrance temperature profile because for a given dp/dz, the velocity profile is related to the temperature profile by the axial momentum and energy equations. The secondary velocity is assumed to be zero at the entrance.

Equations (16)–(18) are elliptic in the radial direction and parabolic in the flow direction since the axial diffusion terms

Table 1 Reference operating characteristics

Heat flux	$q = \pm 100$ W/m^2
Temperature at the center of the pipe at the entrance	$T_c = 60$°C
Peak electric potential at the wall	$\phi_{e,0p} = 10^4$ V
Frequency	$f = 5$ Hz
Wavelength	$\lambda = 0.04$ m
External pressure drop or gain per unit length of the pump	$dP/dz = 0$ Pa/m
Pipe radius	$a = 0.01$ m

Table 2 Properties of pure Sun #4 transformer oil

Conductivity	$k = 0.126$ W/m°C
Density	$\rho = 906.70 - 0.63571T$ kg/m^3
Specific heat	$C_p = 1587.3 + 3.3186T$ J/kg°C
Kinematic viscosity	$\nu = (4.7681 - 0.1836T + 2.7038 \times 10^{-3} T^2 - 1.3750 \times 10^{-5} T^3) 10^{-5}$ m^2/s
Permittivity	$\epsilon = 2.2135 \times 10^{-11}$ F/m
Electric conductivity	$\sigma = 1.05 \times 10^{-3} \exp(-5553/T_k)$ S/m

Note: T is in °C and T_k is in K.

are sufficiently weak. Collins (1975), among others, also concluded that the elliptic character of the flow field was negligible in the analysis of combined natural and forced convection in internal laminar flows. Therefore, a marching method in the flow direction was employed.

The detail of the method of computation is given in Seyed-Yagoobi (1984). A finite difference technique was used to solve equations (16)–(18). The ordinary differential equation given by equation (10), with its boundary conditions, equations (20) and (22), is a two-point boundary value problem. The nondimensional electric potential C^*, which has real and imaginary components, was calculated from these equations by a second-order Runge–Kutta formula and a shooting technique.

The transport and electrical equations presented above are coupled. An iteration procedure overcame this problem. A convergence criterion on the order of 10^{-4} (m/s) was applied to the axial velocity. The differential form of the continuity equation was used in both the transport and electric equations. To ensure that the mass conservation is satisfied at every cross section, the continuity equation in the integral form was used.

The number of nodes in the radial direction was chosen to be eleven. In testing a greater number of nodes, the results differed by less than two percent. The nondimensional step in the axial direction was 2×10^{-6}, and no significant difference in the results was observed when the step size was further decreased.

Numerical Results

The controlling factors in the operation of an induction EHD pump fall into the following three categories:

I Thermal
- (a) Entrance temperature profile
- (b) Magnitude of the entrance bulk temperature
- (c) Heat flux at the wall of the pipe
- (d) Transport properties of the working fluid

II Electrical
- (a) Voltage
- (b) Wavelength
- (c) Frequency
- (d) Electric properties of the working fluid

III Physical
- (a) Load or pressure drop
- (b) Piping (radius, length, and fittings)

The effects of these terms on a vertical induction EHD pump are detailed in Seyed-Yagoobi (1984). Typical results are

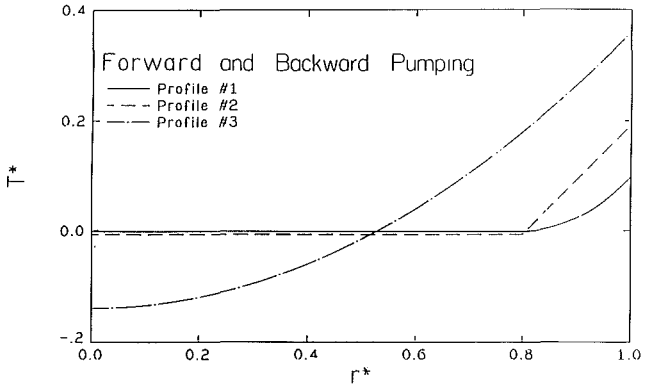

Fig. 3 Nondimensional temperature profiles at the entrance

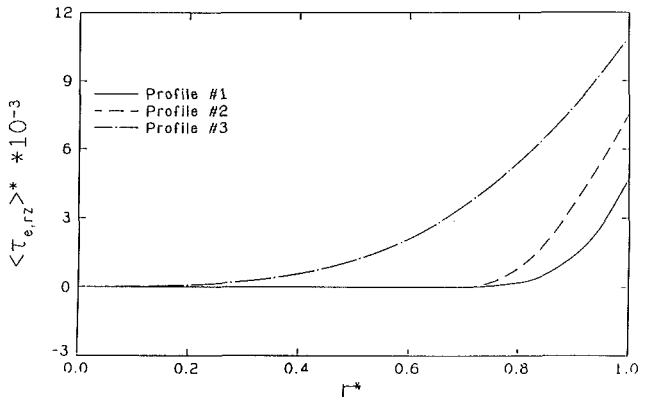

Fig. 4 Nondimensional electric shear stress distribution at the entrance, forward pumping

presented in this paper. Unless otherwise noted in the figures, the reference operating characteristics are as in Table 1.

The working fluid in Sun #4 transformer oil; its properties are given in Table 2 (Chato et al., 1977; Seyed-Yagoobi, 1984). Since the results obtained in the forward and backward modes are similar, only the forward mode is presented.

Three different entrance temperature profiles are considered. The first and second profiles have constant temperature in the central region, and are, respectively, parabolic and linear close to the wall. The third temperature profile is fully parabolic as shown in Fig. 3. These profiles satisfy the two boundary conditions given in equations (20) and (22).

The electric shear stress is a function of the electric conductivity gradient. A greater temperature difference gives a greater conductivity gradient. Therefore, the electric shear stress is the largest in profile No. 3 (Fig. 4), which in turn gives the highest velocity as illustrated in Fig. 5. The important conclusion is that the temperature profile of the fluid at the entrance of the pump has a considerable effect on the bulk velocity.

The viscosity of the fluid decreases as the temperature increases. Lower viscosity means lower viscous shear stress. Therefore, operating the EHD pump at a higher fluid temperature allows a greater velocity, as shown in Fig. 6. Since for our working fluid the change of electric conductivity at a higher temperature becomes negligible, the highest value of the bulk temperature is limited. In practice, the magnitude of the bulk temperature is determined by the heat balance in the system.

Higher heat flux at the wall of the pipe gives a higher bulk velocity because the temperature distribution becomes steeper with increased heat flux. The heat flux is limited by the size of the pipe and the transport properties of the fluids.

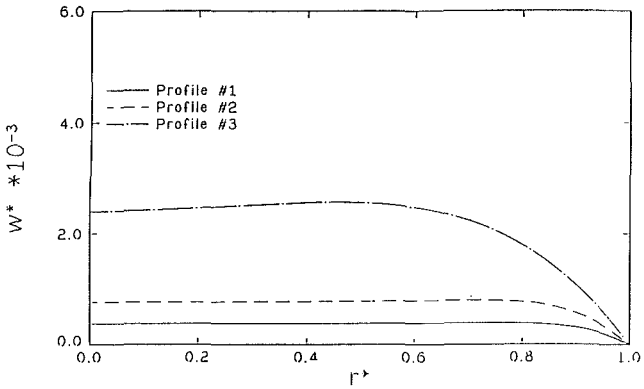

Fig. 5 Nondimensional axial velocity distribution at the entrance, forward pumping

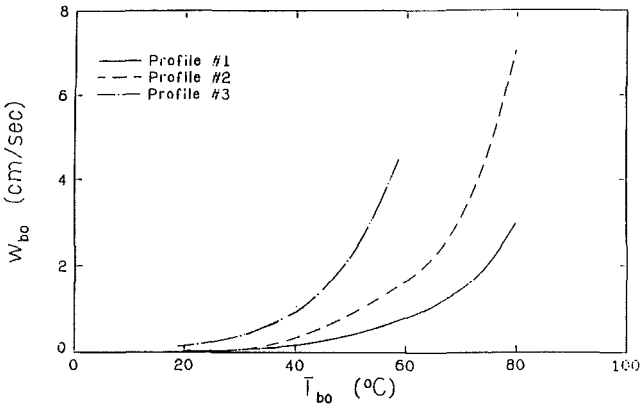

Fig. 6 Bulk velocity as a function of bulk temperature, forward pumping

For a given frequency and wavelength, equation (7) shows that the electric shear stress is proportional to the square of the peak voltage. Therefore, a higher voltage tends to give a higher veolcity. The upper limit of the voltage is constrained by the breakdown strength of the fluid at a given wavelength.

Figure 7 shows the bulk velocity as a function of wavelength while keeping the electric field strength, ϕ_e/λ, constant. The bulk velocity rises to its peak with increasing wavelength and then slowly decreases because at smaller wavelengths the electric forces are limited to a smaller space, giving lower fluid velocity. At longer wavelengths, the fluid velocity is lower since the electric field is not confined to the pipe because of large distances between the electrodes. The electric field, ϕ_e/λ, is limited by the fluid breakdown strength.

The electric conductivity is the only property of the fluid that can be readily altered by adding impurities such as antistatic agents. Figure 8 shows the velocity as a function of frequency at different conductivity levels. Increasing the conductivity extends the frequency range. At the lower electric conductivity levels, the peak velocity increases with increasing electric conductivity. Figure 8 shows that at a given electric conductivity level, as the frequency increases, the fluid velocity rises rapidly and then falls rather abruptly after reaching a maximum at an optimum frequency. The optimum frequency is lower with a higher wavelength. For example, the optimum frequency is 1.4 Hz in forward pumping with profile No. 1 and a wavelength of 4 cm. Increasing the wavelength from 4 cm to 5 cm lowers the optimum frequency to 0.9 Hz, as illustrated in Fig. 9.

At a given frequency there is an optimum level of electric conductivity that gives the peak velocity, as illustrated in Fig. 10. This phenomenon is due to the charge relaxation time ϵ/σ. If the electric conductivity is too small, then either the charges are moving too slowly to reach the thermal gradient layer or

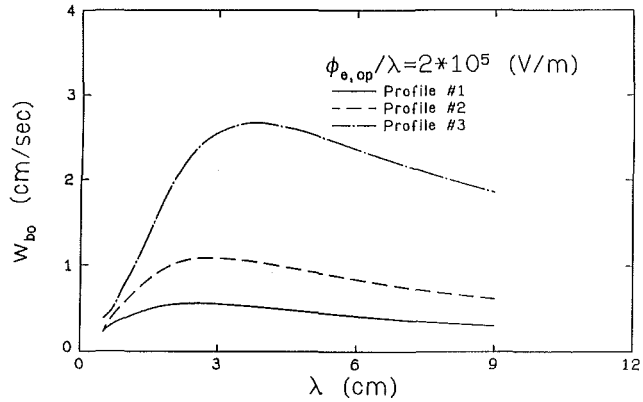

Fig. 7 Bulk velocity as a function of wavelength with a constant $\phi_{e,0p}/\lambda$, forward pumping

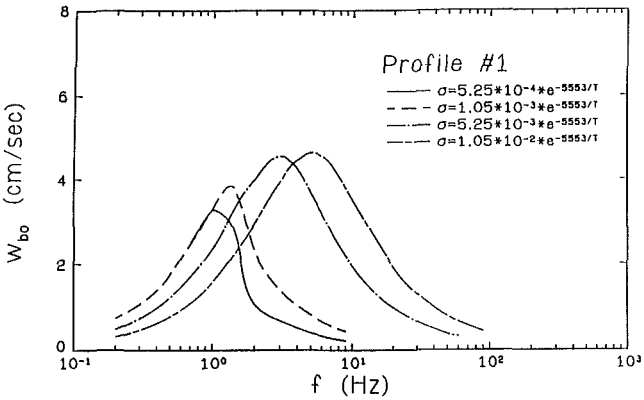

Fig. 8 Bulk velocity as a function of frequency at different electric conductivity levels, forward pumping

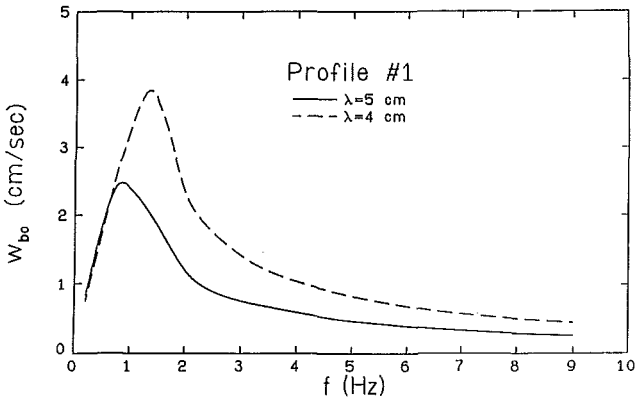

Fig. 9 Bulk velocity as a function of frequency at two wavelengths, forward pumping

there are too few to exert electrical shear stress. If the electric conductivity is very large, charges can "short circuit" too quickly to allow time for the particles to drag the fluid. In addition, the "short circuit" also increases the electric losses.

The results presented thus far were obtained for an unloaded EHD pump (see Table 1). The load, or pressure drop, plays an important role in operating the EHD pump. Figure 11 shows the bulk velocity versus the external pressure drop or gain per unit length of the pump. A negative dP/dz is a favorable load that speeds the pumping; the positive dP/dz is unfavorable and tends to lower the velocity.

Figure 12 shows the local velocity distributions at different values of dP/dz. As the load increases, the fluid starts to flow in two opposite directions, which is undesirable. Therefore, in designing an EHD pump, the external load (pressure drop)

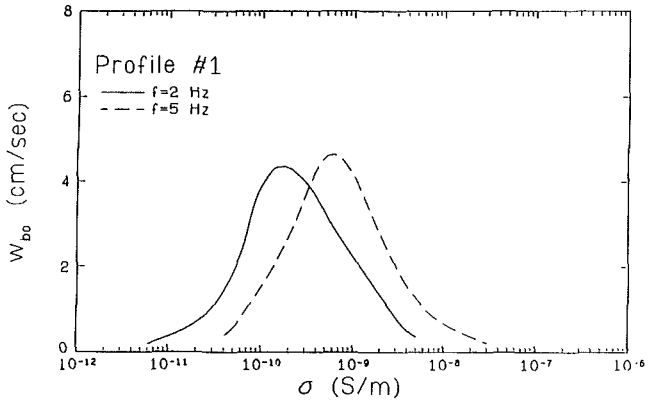

Fig. 10 Bulk velocity as a function of fluid electric conductivity, forward pumping

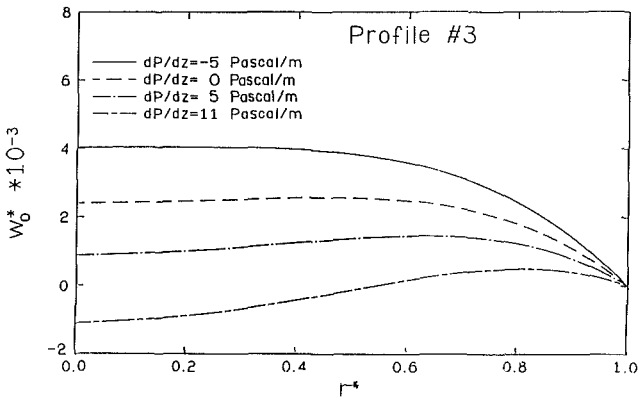

Fig. 12 Axial velocity distribution at different external pressure loads, forward pumping

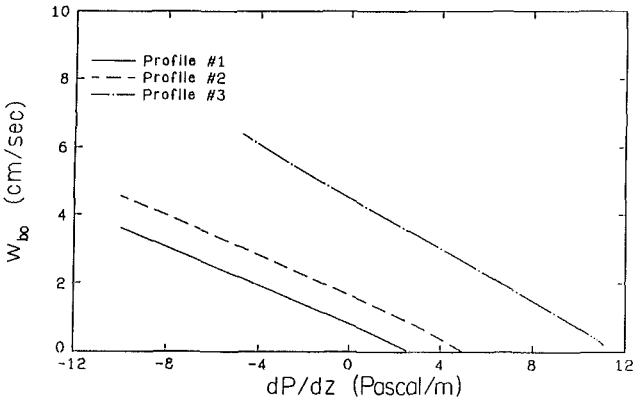

Fig. 11 Bulk velocity as a function of external pressure load, forward pumping

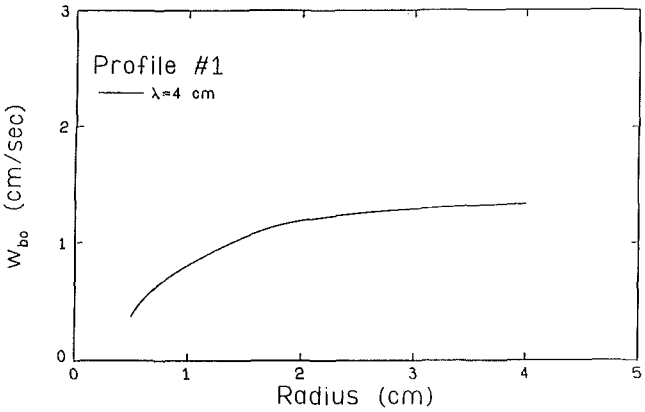

Fig. 13 Bulk velocity as a function of pipe radius, forward pumping

should not exceed its limit in order to prevent this occurrence. If the external load is too high, the pump length may have to be increased.

A higher bulk fluid velocity can be obtained for identical entrance temperature profiles by increasing the pump radius as shown in Fig. 13. By increasing the pipe size, the central, high-velocity area is increased roughly as the square of the radius whereas the boundary layer thickness remains about the same although the circumference increases.

For the electric conductivity and voltage levels of interest, including the Joule heat in the analysis proved to be insignificant. The effect of Joule heat may be significant at higher electric conductivity (above 10^{-6} S/m) and voltage (above 30 kV).

Conclusions

A theoretical model for EHD heat exchanger pumps has been developed. The numerical results show that higher velocities in an induction EHD pump can be achieved by increasing voltage, heat flux, and fluid temperature, and by decreasing external pressure load. These velocities may also be obtained at a higher electric field, ϕ_e/λ, i.e., by increasing the voltage or decreasing the wavelength. The electric field is limited, however, by the breakdown strength of the working fluid.

For a given ϕ_e/λ, the pump must be operated near the optimum wavelength. The pump must also be operated near the critical frequency and electrical conductivity level. The critical frequency drops as the wavelength increases. The entrance temperature profile plays an important role in the operation of the pump; steeper profiles produce higher velocities. For application, this result indicates the need for an "unpumped" heat exchanger section upstream from the EHD pump.

Acknowledgments

This work was supported in part by Grant No. CBT-84-11596 from the National Science Foundation.

References

Chato, J. C., et al., 1977, "Free and Forced Convective Cooling of Pipe-Type Electric Cables," EPRI EL-147, Project 7821, Final Report.

Chato, J. C., Crowley, J. M., et al., 1981, "Free and Forced Convection Cooling of Pipe-Type Electric Cables," EPRI EL-1872, Project 7853-1, Final Report, Vol. 1.

Collins, M. W., 1975, "An Analysis of Combined Natural and Forced Convection and Other Problems in Internal Laminar Flows," PhD Thesis, The City University of London, United Kingdom.

Crowley, J. M., Chato, J. C., et al., 1983, "Electrohydrodynamic Pumping in Cable Pipes," EPRI EL-2834, Project 781-1, Final Report.

Krein, P. T., 1984, "A Theoretical Study of the Thermal Electrohydrodynamic Induction Pump With Harmonics and Inhomogeneous Fluids," *Phys. Fluids*, Vol. 27, pp. 315-318.

Kuo, B. S., Chato, J. C., and Crowley, J. M., 1984, "Temperature Induced Electrohydrodynamic Pumping in Horizontal Pipes," ASME JOURNAL OF HEAT TRANSFER, Vol. 106, pp. 78-84.

Melcher, J. R., 1966, "Traveling-Wave Induced Electro-Convection," *Phys. Fluids*, Vol. 9, pp. 1548-1555.

Melcher, J. R., 1981, *Continuum Electromechanics*, MIT Press, Cambridge, MA, pp. 3.1-3.26 and Chap. 5.

Seyed-Yagoobi, J., 1984, "Theoretical, Numerical, and Experimental Study of Electrohydrodynamic Pumping in Vertical Configuration," PhD Thesis, Department of Mechanical Engineering, University of Illinois at Urbana-Champaign.

Sharbaugh, A. H., and Walker, G. H., 1983, "The Design and Evaluation of an Ion-Drag Dielectric Pump to Enhance Cooling in a Small Oil-Filled Transformer," *Proceedings, IEEE-IAS Annual Meeting*, Mexico City, pp. 1161-1165.

Test, F. L., 1968, "Laminar Flow Heat Transfer and Fluid Flow for Liquids With Temperature Dependent Viscosity," ASME JOURNAL OF HEAT TRANSFER, Vol. 90, pp. 385-392.

J. Seyed-Yagoobi
Texas A&M University,
College Station, TX 77843

J. C. Chato

J. M. Crowley

P. T. Krein

University of Illinois,
Urbana, IL 61801

Induction Electrohydrodynamic Pump in a Vertical Configuration: Part 2—Experimental Study

An induction electrohydrodynamic (EHD) pump in axisymmetric, vertical configuration was designed and built. The flow rates were measured for various temperature profiles and several values of frequency, voltage, wavelength, and electric conductivity. The experimental data are generally in good agreement with the theoretical model presented in Part 1. With the present apparatus at relatively low voltages, velocities four times higher than natural circulation velocity are easily obtained. The external pressure load and entrance temperature profile play important roles on the operation of the pump and must be considered carefully in the design.

Introduction

The theoretical model of the induction electrohydrodynamic (EHD) pump in vertical, axisymmetric configuration was developed in Part 1. A set of numerical solutions was also presented to show the effect of the controlling factors in operating an induction EHD pump. This presentation of the experimental results compares the data in the forward modes to the numerical solutions.

Experimental Apparatus

Figure 1 shows the experimental apparatus for induction EHD pumping in an axisymmetric, vertical configuration (Seyed-Yagoobi, 1984a). The total length of the loop is 5.2 m; the vertical sections are 2.1 m each. The pump was cooled or heated by a secondary loop. In forward mode, the oil in the main loop was cooled by the secondary loop and heated with electric heating tape. In the backward mode, the oil was heated by the secondary loop and cooled with the ice-filled tank No. 1.

Thermocouples No. 1 and No. 2 (TC1 and TC2) measure the temperature profiles at the top and bottom of the pump. The temperatures were taken when the pump was not operating because the common thermometry devices, which depend on electric signals, cannot be applied in the presence of a strong electrostatic field. The ice-filled tank No. 2 enables alteration of the entrance temperature profile of the pump in the forward mode. Thermocouples No. 3 to No. 6 (TC3 to TC6) enable determination of the heat flux at the wall of the pump.

The pumping section contains 99 electrodes separated by glass tubes 8 mm long, as shown in Fig. 2. The electrodes are made of copper gaskets with rectangular cross sections, with an inside diameter of 16 mm, an outside diameter of 21 mm, and a thickness of 2 mm. The glass tubes have the same inside and outside diameters as the electrodes. After rounding of the edges, the electrodes were electropolished to help prevent partial discharge. They were soldered to the six bus lines as shown in the figure. With the three-phase power supply used in the experiment, it is possible to generate either three-phase sine or square waves with amplitudes up to ±30 kV, from 0 to 100 Hz.

The fluid velocity was measured outside the pumping section by observing the particles in the oil and timing them over a distance of 4 to 5 cm. In most cases, the pumping was filmed for further analysis. Conventional flowmeters are impracticable because of the very low range of Reynolds numbers ($Re < 100$) and the electrical interference from the traveling wave. In addition, the flowmeters produce adverse pressure drop in the system.

The fluids in the main and secondary loops were the same to prevent contamination by leakage in the pumping section. In the main loop, the pipes exposed to ambient conditions were insulated.

Sun #4 oil at three electrical conductivity levels was used in the experiments. The d-c conductivity of Sun #4 oil was varied by the addition of Shell ASA-3 antistatic additive. The temperature dependencies of the electric conductivity in S/m measured at the three doping levels are as follows:

(1) Undoped, $\sigma = 7.956 \times 10^{-4} \exp(-5583.40/T_K)$;

(2) Moderately doped (83 parts per million), $\sigma = 7.790 \times 10^{-4} \exp(-4822.36/T_K)$;

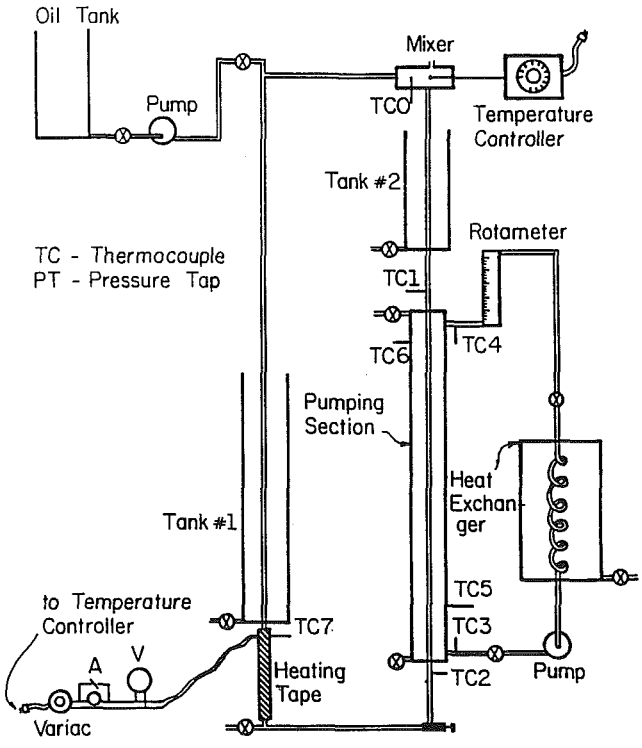

Fig. 1 Experimental apparatus

Contributed by the Heat Transfer Division for publication in the JOURNAL OF HEAT TRANSFER. Manuscript received by the Heat Transfer Division December 1, 1987. Keywords: Forced Convection, Heat Exchangers, Mixed Convection.

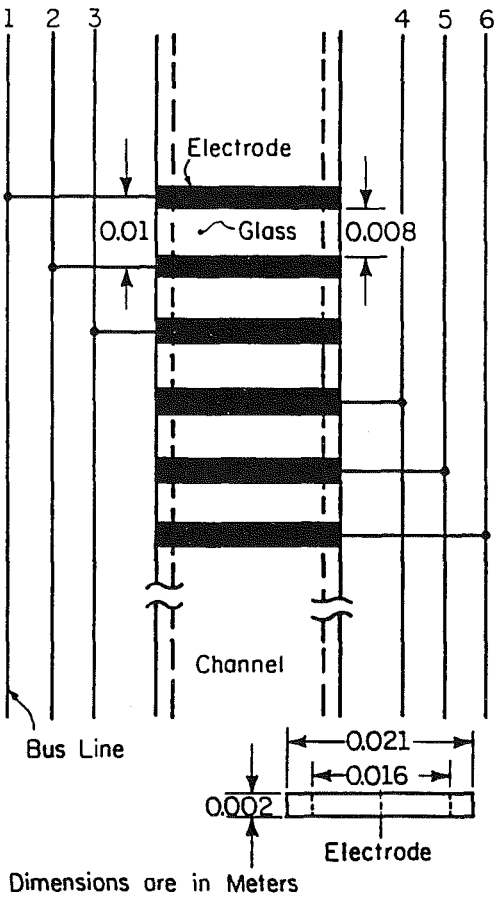

Fig. 2 Electric connections of electrodes to the bus lines

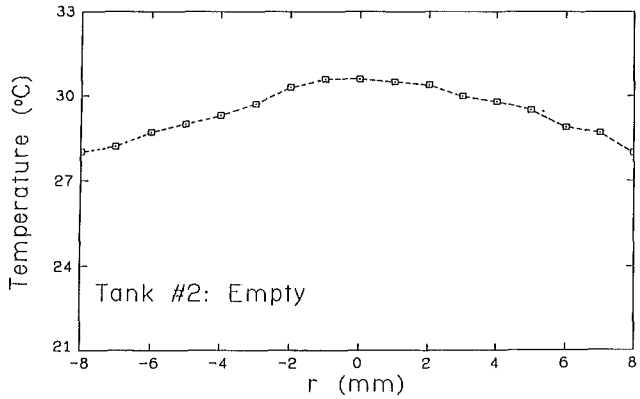

Fig. 3 Entrance temperature profile, forward pumping

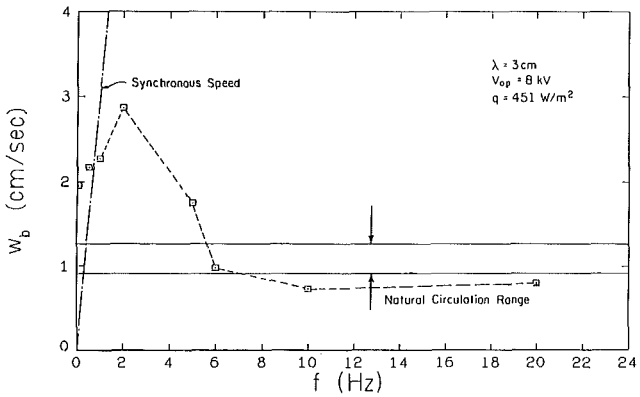

Fig. 4 Bulk velocity versus frequency, forward pumping, moderately doped oil

Table 1 Typical operating conditions

	Forward mode	Backward mode
Heat exchanger temperature °C	0	40
TCO, °C	29.5–30.5	26–28
TC3, °C	9–11	36–38
TC4, °C	12–14	33.5–35.5
TC5, °C	17–19	24–26
TC6, °C	17–19	24.8–26.8
TC7, °C	≤115	---
Ambient temperature, °C	20	20
Flow rate in secondary loop, kg/min	0.56–0.63	0.56–0.09
Power from heating tape, W	$84 \leq q \leq 158$	---

(3) Heavily doped (369 parts per million), $\sigma = 3.226 \times 10^{-2} \exp(-5543.087/T_K)$
where T_K is in degree Kelvin.

The permittivity of Sun #4 oil is not a function of temperature and has a value of 19.8 pF/m. The transport properties are given in Part 1.

Experimental Results

The detailed experimental results for induction EHD pumping in an axisymmetric, vertical configuration are given by Seyed-Yagoobi (1984a).

The experimental objective was to measure the fluid bulk velocity with respect to frequency and voltage at different values of heat flux, wavelength, and fluid temperature. Only a sinusoidal electric traveling wave was applied.

The experimental uncertainties were as follows. The maximum standard deviations of the velocities were 0.095 cm/s when pumped and 0.037 cm/s in natural convection. The temperatures were estimated to be accurate to within 0.1°C. The peak voltage and frequency were within ±5 percent of true value. Oil from a single barrel was used throughout the study to eliminate any variability in its properties. The electrical and thermal properties were accurate within ±4 percent. The repeatability of the results was verified by repeating the experiments several times. Within the experimental error, no change occurred in the pumping speed.

Theoretically, the induction pump requires a temperature gradient, but some flow could be detected with no heating or cooling of the channel. The highest fluid velocity observed was less than 3 mm/s obtained at a voltage of 10 kV and a frequency of 1 Hz. This is possibly due to corona discharge from the electrodes or induction pumping due to a residual temperature gradient in the channel. The flow was much faster, however, with heating. Typical operating conditions are shown in Table 1.

The direction of natural circulation was from top to bottom of the pumping section in the forward mode. A typical entrance temperature profile in the forward mode measured with thermocouple No. 1 is shown in Fig. 3. Velocities measured with the undoped oil in the forward and backward modes were slightly higher than the natural circulation velocity. The data follow the same trend as those discussed in Part 1. The bulk velocity tends to increase slowly as the voltage increases. Also, a higher heat flux produces higher velocities. The optimum frequency was near 1.0 Hz. Similar results were obtained with heavily doped oil in both modes. The velocities were higher than the natural circulation velocity by a factor of two or less. The optimum frequency was near 5 Hz.

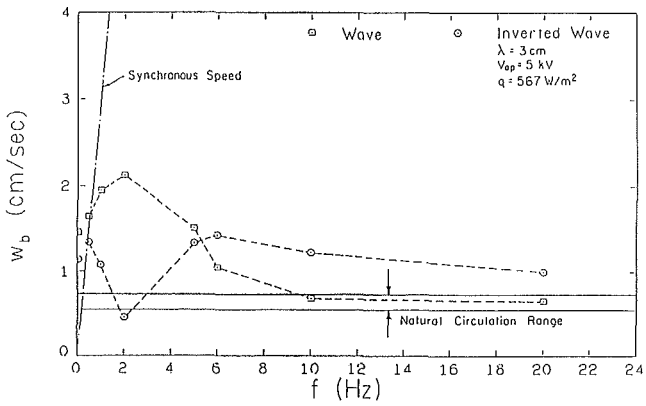

Fig. 5 Bulk velocity versus frequency, inverted wave, forward pumping, moderately doped oil

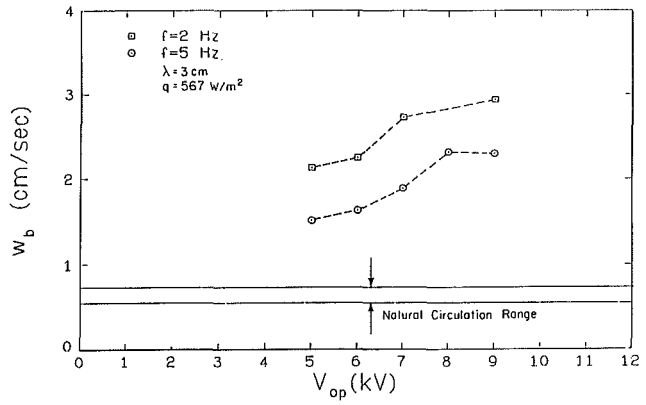

Fig. 6 Bulk velocity versus voltage, forward pumping, moderately doped oil

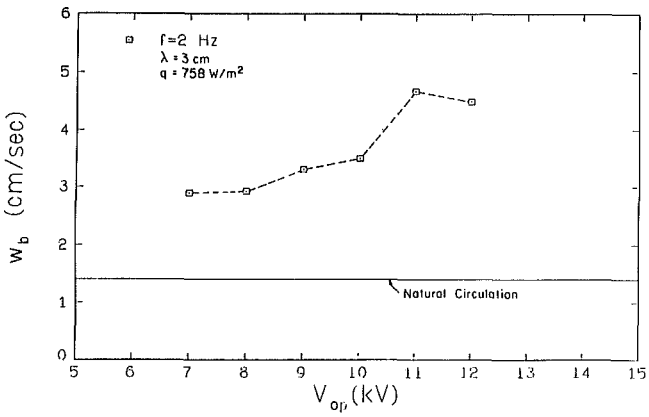

Fig. 7 Bulk velocity versus voltage, forward pumping, moderately doped oil

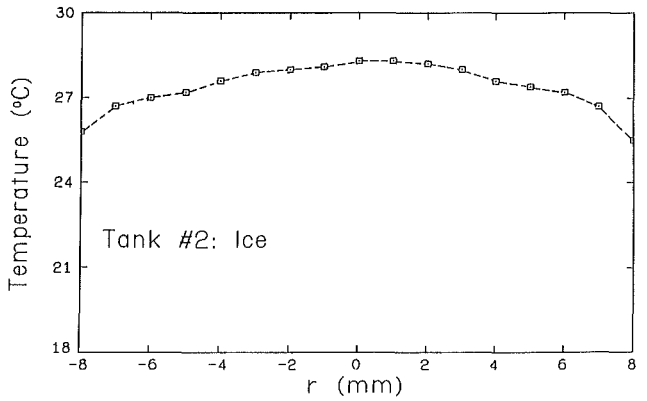

Fig. 8 Entrance temperature profile, forward pumping, ice-filled tank No. 2

The velocities measured with moderately doped Sun #4 oil are considerably higher than those with undoped or heavily doped oils. This was expected from the theoretical model. The results obtained in the backward mode are similar to those in the forward mode; therefore the following results with the moderately doped oil are presented in the forward mode only. Figure 4 shows the bulk velocity as a function of frequency. The optimum frequency, which was near 2 Hz, produced a considerably higher velocity than the natural circulation velocity. From the above experimental results, it can be concluded that the magnitude of the critical frequency depends on the electrical conductivity of the working fluid. This agrees with the results discussed in Part 1. The synchronous speed indicated in Fig. 4 is the speed of the moving electrical field defined as the product of the frequency and wavelength.

In a horizontal induction EHD pump, the flow can be reversed by simply inverting the direction of the traveling electric wave (Kervin, 1981). This is not necessarily the case with a vertical induction EHD pump, where a strong natural circulation exists. In order to reverse the flow by inverting the wave direction, the EHD pump should have enough power to overcome both the frictional losses and the pressure load caused by the natural circulation. When the natural circulation opposes the pumping, there is a possibility of the flow becoming unstable. This is a typical double diffusive problem: two forces acting in opposite directions. Although Turnbull (1968) investigated these electroconvection instabilities with a stabilizing temperature gradient, further work is needed in this area.

Figure 5 shows the results obtained when the wave direction was reversed so as to oppose thermal convection. The direction of the wave was reversed by simply switching phases B and C in the patch panel. This figure shows that the pump is incapable of reversing the flow since the dP/dz term is too high. The optimum frequency of 2 Hz, where the highest electric force occurs, gives the slowest resultant velocity. If the flow reversal were possible, the entrance temperature profile might be hotter near the wall and colder in the center (see Fig. 1). This profile is the opposite of that needed in the forward mode. This problem can be solved by adding another mixer to the lower end of the vertical leg in the apparatus, similar to the one at the top (see Fig. 1). The fluid then would exit the mixer with a uniform temperature.

Figure 6 shows the relation between fluid velocity and voltage measured at the two frequencies, 2 Hz (optimum) and 5 Hz. As expected, the velocity increases as the voltage increases.

Figure 7 is a similar plot, with the oil temperature in the mixer, TCO, set at 35°C. The entrance temperature profile for this particular case is like Fig. 3 with the exception that the magnitude is approximately 5°C higher. In Fig. 7, the velocities achieved are on the order of 5 cm/s, which is almost four times the natural circulation velocity.

The entrance temperature profile could be changed by filling tank No. 2 with ice, as shown in Fig. 8. This profile is similar to that shown in Fig. 3, with 2°C lower magnitude and steeper profile near the wall.

Figures 9 and 10 compare the frequency and voltage effects obtained with the two entrance temperature profiles shown in Figs. 3 and 8. The velocities are higher for precooling with ice in tank No. 2 despite the lower heat flux and bulk

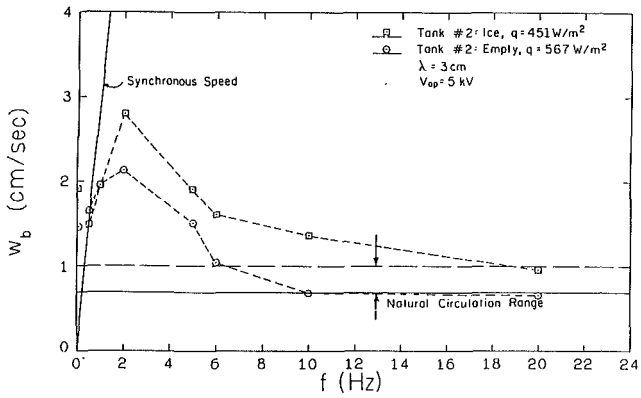

Fig. 9 Bulk velocity versus frequency, forward pumping, moderately doped oil

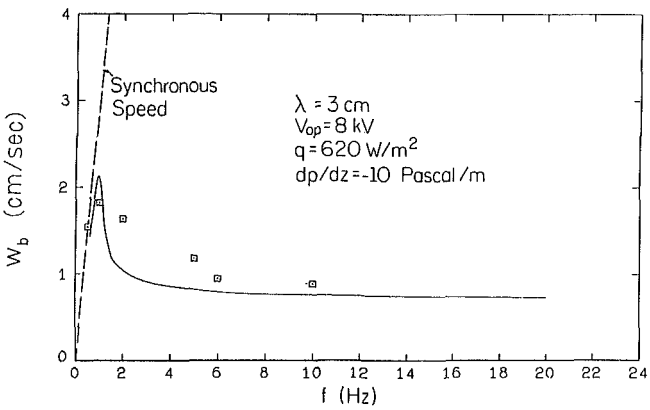

Fig. 12 Bulk velocity versus frequency, forward pumping, undoped oil

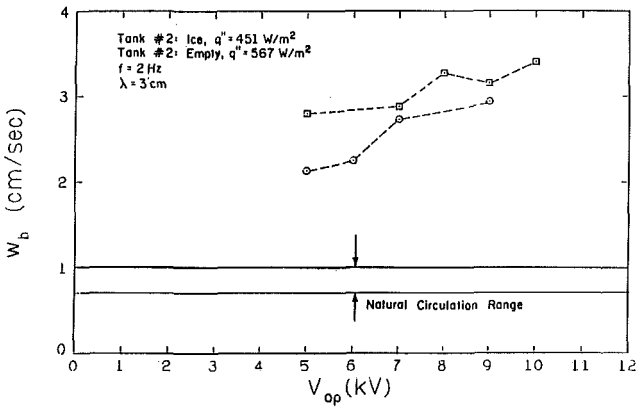

Fig. 10 Bulk velocity versus voltage, foward pumping, moderately doped oil

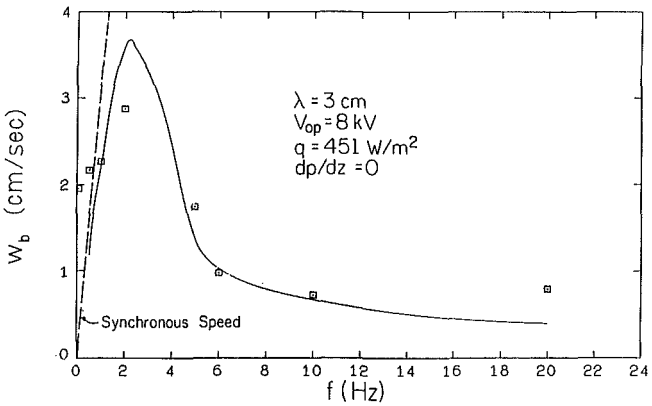

Fig. 13 Bulk velocity versus frequency, forward pumping, moderately doped oil

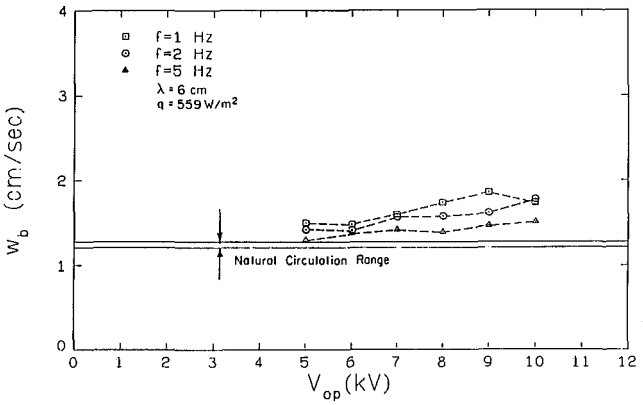

Fig. 11 Bulk velocity versus voltage, forward pumping, heavily doped oil

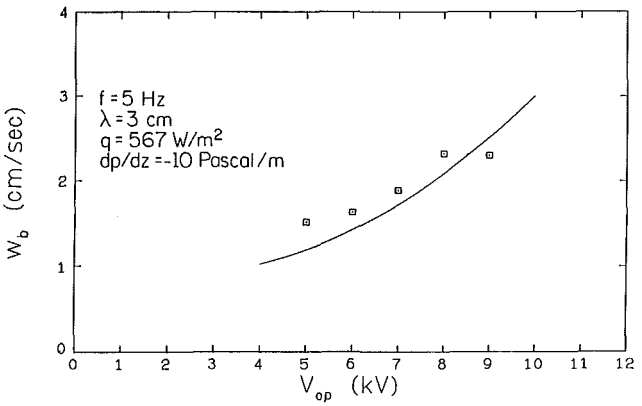

Fig. 14 Bulk velocity versus voltage, forward pumping, moderately doped oil

temperature, probably because of the steeper temperature profile at the entrance of the pump; the increase in the natural circulation velocity is also a contributing factor.

Figure 11 shows the bulk velocity as a function of voltage at three different frequencies and a wavelength of 6 cm with the heavily doped oil. The optimum frequency in this case is close to 1.0 Hz. The cause of this decrease (from 5.0 Hz to 1.0 Hz) is the increase in the wavelength (from 3 cm to 6 cm). This agrees with the numerical results presented in Part 1, Fig. 9.

Comparison of Numerical and Experimental Results

Figures 12 through 14 compare typical experimental results for the undoped and moderately doped oil to the numerical solution.

The data follow the numerical solutions qualitatively everywhere and quantitatively in most ranges. As shown in Fig. 12, for the undoped oil the correspondence between experimental and numerical results is good in the low (< 1 Hz) and high (> 6 Hz) frequency ranges. The experimental velocities, however, drop off more gradually in the intermediate range than the numerical values. Variations in oil purity are probably the main reason for this discrepancy.

The correspondence is good for the entire range of the moderately doped oil (Fig. 13) except that the very narrow

peak could not be completely explored because of the frequency limitations of the apparatus. Figure 13 shows finite experimental velocities at zero frequency, indicating a d-c pumping effect not included in the theory. This phenomenon may be due to some charge injection, even though we attempted to eliminate such effects. The voltage dependence of velocity, as shown in Fig. 14, was predictable.

Discrepancies in the low frequency range (< 0.5 Hz) can be attributed in part to time averaging of the electric shear stress being invalid in this range. Other small discrepancies are due to the fact that the entrance temperature profiles used in the numerical predictions were measured when the pump was not in operation. The temperature profile changes when the pump is operated (Seyed-Yagoobi et al., 1984b).

Conclusions

The experimental results are in reasonably good agreement with the numerical solutions presented in Part 1, confirming the conclusions of Part 1.

The experimental apparatus enabled running the EHD pump in the forward and backward modes. The results obtained in these two modes are similar. At relatively low voltages, less than 10 kV, velocities on the order of 5 cm/s (four times higher than the natural circulation velocity) were easily obtained. Velocities can be increased further by increasing the pipe diameter, particularly in the "unpumped" sections, to reduce friction losses.

Experimentally, the flow could not be reversed by inverting the direction of the traveling electric wave in either the forward or backward modes. This effect was primarily due to higher adverse pressure load caused by the natural circulation and frictional losses in the sections without electrodes. With the EHD pump aiding the natural convection, however, the flow rate could be quadrupled, indicating a large increase in heat transfer capabilities.

Acknowledgments

This work was supported in part by Grant No. CBT-84-11596 from the National Science Foundation. The oil in the experiments was furnished by the Sun Oil Company.

References

Kervin, D. J., 1981, "Three-Phase Variable Parameter Electrohydrodynamic Pumping," Master of Science Thesis, Department of Electrical Engineering, University of Illinois.

Seyed-Yagoobi, J., 1984a, "Theoretical, Numerical, and Experimental Study of Electrohydrodynamic Pumping in Vertical Configuration," PhD Thesis, Department of Mechanical Engineering, University of Illinois at Urbana-Champaign.

Seyed-Yagoobi, J., Chato, J. C., and Crowley, J. M. 1984b, "Viscometric Temperature Measurement in Electric or Magnetic Fields," *Review of Scientific Instruments*, Vol. 55, pp. 1471-1474.

Turnbull, R. J., 1968, "Electroconvective Instability With a Stabilizing Temperature Gradient. I. Theory," *Phys. Fluids*, Vol. 11, pp. 2588-2596.

Combined Forced and Free Upward-Flow Convection in the Entrance Region Between Inclined Parallel Plates

E. Naito
Associate Professor,
Department of Mechanical Engineering,
Shiga Prefecture Junior College,
Shiga 522, Japan

Y. Nagano
Professor,
Department of Mechanical Engineering,
Nagoya Institute of Technology,
Nagoya 466, Japan
Mem. ASME

The effects of buoyancy on upward-flow laminar convection in the entrance region between inclined parallel plates are studied by a numerical method. Solutions are given for three thermal conditions of parallel plates: lower wall heated and upper wall insulated; vice versa; and both walls heated equally. Results are presented to show how the developing upward-flow and thermal field in the entry region are affected by buoyancy in terms of the various inclination angles of parallel plates. Correlation equations applicable in practice are also developed for the skin-friction coefficient and the local Nusselt number.

1 Introduction

Recent discussion in heat transfer has expanded from the conventional problems related to the best use of thermal energy to those in high technology and power engineering, such as cooling of electronic devices. The heat transfer in the entrance region between parallel plates is an essential problem for a broad spectrum of thermal energy equipment and modern electronic devices. The studies on this problem have been summarized by Shah and London (1978). Since the reports so far have dealt mostly with laminar flow and laminar forced convection based on the boundary layer theory, the effects of leading edge, secondary flow, and buoyancy on heat transfer are not fully understood. Therefore, detailed information not available by the classical boundary layer theory is now much awaited. In a previous paper (Naito, 1983), attention was focused on the behavior of momentum and heat in the vicinity of the leading edge between parallel plates, and the influence of axial diffusion of momentum and heat on the velocity and thermal fields at the location upstream from the leading edge was studied for different Reynolds numbers.

In general, buoyancy effects cannot be disregarded for forced convection at low Reynolds numbers. Combined forced and free convection between parallel plates have been reported by many investigators. The developing laminar combined convection flow between semi-infinite and finite vertical parallel plates have been studied by Savkar (1971), Quintiere and Mueller (1973), Cebeci et al. (1982), Dalbert (1982), Yao (1983), Aung and Worku (1986), and Habchi and Acharya (1986). Similar problems for horizontal parallel plates have been investigated by Kiya et al. (1971), Nguyen et al. (1981), and Naito (1984, 1985).

The influence that buoyancy exerts in developing velocity and thermal fields between "inclined" parallel plates is changed by both the inclination angle and the flow direction in relation to the gravity field. However, few studies have been published for combined forced and free convection in the entrance region between inclined parallel plates. Therefore, the present report has dealt systematically with how the two-dimensional, developing flow and heat transfer in the entrance region between inclined parallel plates are affected by buoyancy due to the inclination angle. It is well known that the critical Rayleigh number for the onset of secondary flow between horizontal parallel plates is at 1708 (Mori and Uchida, 1965). Recently, Maughan and Incropera (1987) investigated experimentally the effect of thermal instability on Nusselt number of fully developed airflow in a parallel plate channel heated uniformly from below, and confirmed that the Nusselt number at $Gr^* = g' \cdot \beta' \cdot q'_w \cdot (2s')^4/(\lambda' \cdot \nu'^2) \leq 7000$ became finally equal to the forced convection limit. This value of Gr^* is equivalent to $Ra \leq 1600$ (see Appendix A). Thus, from judgment based on the critical Rayleigh number as usual or the result of Maughan and Incropera, the numerical results below $Ra = 1500$ are obtained for the present inclined channel except for the vertical position.

From the results obtained, we have developed correlation equations for skin-friction coefficient and local Nusselt number at the arbitrary channel inclination, streamwise location, and Reynolds and Rayleigh numbers.

2 Governing Equations

Consider the heat transfer phenomenon of combined forced and free convection in the entrance region between parallel plates with uniform wall temperature, which is set at an angle ϕ to the horizontal. This paper deals with upward laminar flow for $0 \text{ deg} \leq \phi \leq 90$ deg. As shown in Fig. 1, the incompressible fluid enters the channel at the inlet with a uniform velocity and temperature. The developing flow is assumed to be two dimensional. The three thermal conditions are as follows: (1) the lower wall maintained at constant temperature with the upper wall insulated; (2) vice versa; (3) both walls maintained at constant temperature (referred to as "lower wall heated, upper wall heated, and both walls heated,"

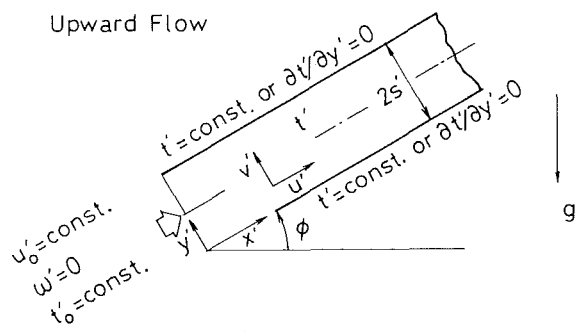

Fig. 1 Coordinate system

Contributed by the Heat Transfer Division for publication in the JOURNAL OF HEAT TRANSFER. Manuscript received by the Heat Transfer Division November 24, 1987. Keywords: Forced Convection, Mixed Convection, Natural Convection.

respectively). Using the usual Boussinesq approximation, the dimensionless governing equations of continuity, momentum, and energy can be written as

$$\partial u/\partial x + \partial v/\partial y = 0 \tag{1}$$

$$u\frac{\partial u}{\partial x} + v\frac{\partial u}{\partial y} = -\frac{1}{2}\frac{\partial p}{\partial x} + \frac{2}{\mathrm{Re}}\nabla^2 u + \frac{4\mathrm{Ra}}{\mathrm{Pe}\cdot\mathrm{Re}}(1-\theta)\sin\phi \tag{2}$$

$$u\frac{\partial v}{\partial x} + v\frac{\partial v}{\partial y} = -\frac{1}{2}\frac{\partial p}{\partial y} + \frac{2}{\mathrm{Re}}\nabla^2 v + \frac{4\mathrm{Ra}}{\mathrm{Pe}\cdot\mathrm{Re}}(1-\theta)\cos\phi \tag{3}$$

$$u(\partial\theta/\partial x) + v(\partial\theta/\partial y) = 2\nabla^2\theta/\mathrm{Pe} \tag{4}$$

The dimensionless variables and parameters are chosen as follows:

$$\left.\begin{aligned} &x = x'/(2s'),\quad y = y'/(2s'),\quad u = u'/u_0',\quad v = v'/u_0',\\ &p = 2(p' + \rho_0' g' y'\cos\phi + \rho_0' g' x'\sin\phi)/(\rho_0' u_0'^2),\\ &\theta = (t_w' - t')/(t_w' - t_0'),\quad \mathrm{Re} = 4s'u_0'/\nu',\quad \mathrm{Pe} = \mathrm{Pr}\cdot\mathrm{Re},\\ &\mathrm{Ra} = 8c_p'\rho_0' g'\beta'(t_w' - t_0')s'^3/(\lambda'\nu') \end{aligned}\right\} \tag{5}$$

The solution domain has to map the infinite region onto a finite one, and it is also advisable to expand the region near the inlet. Thus, a axial transformation of the type $\xi = (0.8x)^{0.8}/\{1+(0.8x)^{0.8}\}$ is used (Wang and Longwell, 1964). The dimensionless stream function ψ and vorticity ω are defined as follows:

$$u = \partial\psi/\partial y,\quad v = -(d\xi/dx)\partial\psi/\partial\xi \tag{6}$$

$$\omega = \partial v/\partial x - \partial u/\partial y = -\nabla^2\psi \tag{7}$$

where the Laplacian operator ∇^2 is written as

$$\nabla^2 \equiv (d\xi/dx)^2\partial^2/\partial\xi^2 + (d^2\xi/dx^2)\partial/\partial\xi + \partial^2/\partial y^2$$

Elimination of the pressure gradients from equations (2) and (3) gives the following dimensionless vorticity transport equation:

$$\frac{d\xi}{dx}\left\{\frac{\partial}{\partial\xi}\left(\omega\frac{\partial\psi}{\partial y}\right) - \frac{\partial}{\partial y}\left(\omega\frac{\partial\psi}{\partial\xi}\right)\right\} = \frac{2}{\mathrm{Re}}\nabla^2\omega + \frac{4\mathrm{Ra}}{\mathrm{Pe}\cdot\mathrm{Re}}\left(\frac{\partial\theta}{\partial y}\sin\phi - \frac{d\xi}{dx}\frac{\partial\theta}{\partial\xi}\cos\phi\right) \tag{8}$$

In a similar manner, equation (4) is rewritten as

$$\frac{d\xi}{dx}\left\{\frac{\partial}{\partial\xi}\left(\theta\frac{\partial\psi}{\partial y}\right) - \frac{\partial}{\partial y}\left(\theta\frac{\partial\psi}{\partial\xi}\right)\right\} = \frac{2}{\mathrm{Pe}}\nabla^2\theta \tag{9}$$

The boundary conditions of velocity and thermal fields for governing equations at inlet, at infinite downstream, and at lower and upper walls are, respectively, as follows:

At $\xi = 0$ ($x = 0$) and $0 < y < 1$,

$$u = 1,\quad \omega = 0,\quad \psi = y,\quad \theta = 1 \tag{10}$$

At $0 \le \xi < 1$ ($0 \le x < \infty$), and $y = 0$ and 1,

$$\left.\begin{aligned} &u = 0,\quad v = 0,\quad \psi_0 = 0,\quad \psi_1 = 1,\quad \partial\psi/\partial\xi = \partial\psi/\partial y = 0\\ &\theta = 0 \text{ (at heated wall)},\quad \partial\theta/\partial y = 0 \text{ (at insulated wall)} \end{aligned}\right\} \tag{11}$$

For $\xi = 1$ ($x \to \infty$) and $0 \le y \le 1$,

$$\left.\begin{aligned} &u = 6y(1-y),\quad v = 0,\quad \psi = 6y^2(1/2 - y/3),\\ &\omega = -6(1-2y),\quad \theta = 0 \end{aligned}\right\} \tag{12}$$

Note that the inlet conditions will affect the skin friction and heat transfer very near the inlet. However, practical difficulties arise from consideration of various conditions at the inlet in order to investigate the effects of buoyancy and in-

Nomenclature

a, b = grid sizes in the ξ and y directions
C_{f0}, C_{f1} = skin-friction coefficient at the lower and upper walls, equations (19) and (20)
C_f^* = skin-friction coefficient for isothermal flow
c_p = specific heat
Gr = Grashof number
g = gravitational acceleration
h = heat transfer coefficient
L = hydrodynamic entrance length
$\mathrm{Nu}_0, \mathrm{Nu}_1$ = Nusselt number at the lower and upper walls, equations (21) and (22)
Nu^* = Nusselt number for pure forced convection
Pe = Peclet number, equation (5)
Pr = Prandtl number $= c_p'\cdot\rho_0'\cdot\nu'/\lambda'$
p = pressure
q = heat flux
Ra = Rayleigh number, equation (5)
Re = Reynolds number, equation (5)
s = one half the spacing between parallel plates
t = temperature
u, v = velocity components in the x and y directions
x, y = axial and transverse coordinates
β = coefficient of thermal expansion
θ = dimensionless temperature, equation (5)
λ = thermal conductivity
ν = kinematic viscosity
ξ = dimensionless axial coordinate $= (0.8x)^{0.8}/\{1+(0.8x)^{0.8}\}$
ρ = density
ϕ = inclination angle
ψ = stream function, equation (6)
ω = vorticity, equation (7)

Subscripts

0 = value at inlet
b = bulk mean temperature
c, w = values a centerline and at wall
h, t = values of flow and thermal fields

Superscripts

$'$ = dimensional variable
$*$ = values of isothermal flow and pure forced convection

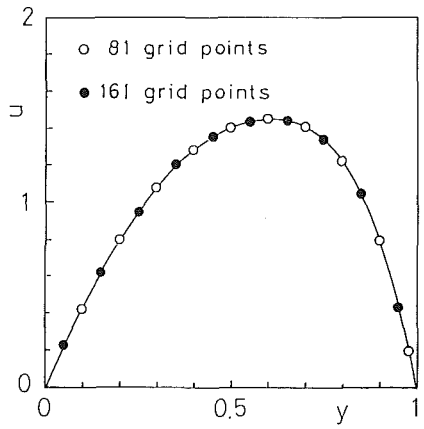

Fig. 2 Vertical velocity distribution for different grid intervals at $x = 1.871$ for $Re = 100$ and $Ra = 1500$ when one wall heated (at $y = 1$)

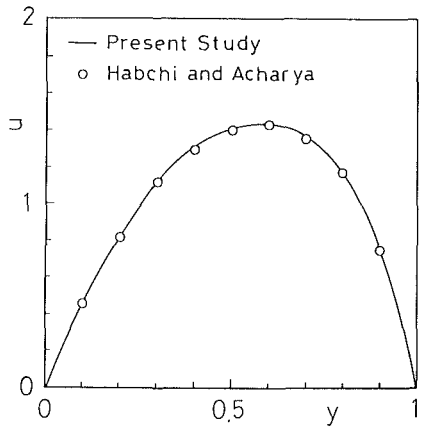

Fig. 3 Comparison of the vertical velocity at $x = 1.131$ for $Re = 75$ and $Ra = 1000$ when one wall heated (at $y = 1$)

clination angle on various physical quantities. Since the effects of axial diffusion of momentum and heat on the upstream and/or downstream region of the inlet were investigated previously (Naito, 1983), we used the most usual inlet condition considered appropriate for this kind of study as in the past. Furthermore, when finite plates are not very short, the condition at the exit exerts little influence on the upstream region. Therefore, the above boundary conditions and an axial transformation are adopted.

3 Numerical Method of Solution

Equations (7), (8), and (9) were approximated by finite difference equations using a central difference form. The finite difference forms for the derivations of ψ and θ at a grid point inside and nearest the boundary wall were derived in the same way by Naito (1984, 1987). Thus, the accuracy of these solutions was improved by consideration of several boundary conditions. The velocity at the wall was obtained from the Taylor series expansions for the stream function. The boundary vorticity, which has a truncation error of the third order, can be finally expressed by the following equations:

When only the lower wall is heated, at $y = 0$ ($j = 1$),

$$\omega_{i,1} = \frac{3}{b^2}(\psi_{i,1} - \psi_{i,2}) - \frac{\omega_{i,2}}{2} - \frac{b \cdot \mathrm{Ra}}{264 \cdot \mathrm{Pe}}(108\theta_{i,2} - 27\theta_{i,3} + 4\theta_{i,4})\sin\phi \tag{13}$$

at $y = 1$ ($j = n + 1$),

$$\omega_{i,n+1} = \frac{3}{b^2}(\psi_{i,n+1} - \psi_{i,n}) - \frac{\omega_{i,n}}{2} + \frac{b^2 \cdot \mathrm{Ra}}{8a \cdot \mathrm{Pe}} \frac{d\xi}{dx}(\theta_{i+1,n+1} - \theta_{i-1,n+1})\cos\phi \tag{14}$$

When only the upper wall is heated, at $y = 0$ ($j = 1$),

$$\omega_{i,1} = \frac{3}{b^2}(\psi_{i,1} - \psi_{i,2}) - \frac{\omega_{i,2}}{2} + \frac{b^2 \cdot \mathrm{Ra}}{8a \cdot \mathrm{Pe}} \frac{d\xi}{dx}(\theta_{i+1,1} - \theta_{i-1,1})\cos\phi \tag{15}$$

at $y = 1$ ($j = n + 1$),

$$\omega_{i,n+1} = \frac{3}{b^2}(\psi_{i,n+1} - \psi_{i,n}) - \frac{\omega_{i,n}}{2} + \frac{b \cdot \mathrm{Ra}}{264 \cdot \mathrm{Pe}}(108\theta_{i,n} - 27\theta_{i,n-1} + 4\theta_{i,n-2})\sin\phi \tag{16}$$

When both walls are heated, at $y = 0$ ($j = 1$),

$$\omega_{i,1} = \frac{3}{b^2}(\psi_{i,1} - \psi_{i,2}) - \frac{\omega_{i,2}}{2} - \frac{b \cdot \mathrm{Ra}}{264 \cdot \mathrm{Pe}}(108\theta_{i,2} - 27\theta_{i,3} + 4\theta_{i,4})\sin\phi \tag{17}$$

at $y = 1$ ($j = n + 1$),

$$\omega_{i,n+1} = \frac{3}{b^2}(\psi_{i,n+1} - \psi_{i,n}) - \frac{\omega_{i,n}}{2} + \frac{b \cdot \mathrm{Ra}}{264 \cdot \mathrm{Pe}}(108\theta_{i,n} - 27\theta_{i,n-1} + 4\theta_{i,n-2})\sin\phi \tag{18}$$

where the symbols i and j indicate the grid point of location in the ξ and y directions, respectively, and n is the number of partitions between the lower and upper walls. As obvious from equations (13)–(18), these equations for boundary vorticity contain the term due to buoyancy.

A mesh size of 51×51 (ξ, y) was normally used. In order to improve the accuracy of numerical calculation, the mesh size was again reduced by one-fourth for $0 \le y \le 0.1$ and $0.9 \le y \le 1$ near the walls, respectively. To confirm the grid independence of the results, the cross-stream grid interval was cut in half for the combined vertical convection case at $Re = 100$ and $Ra = 1500$ when one wall was heated. This comparison is shown in Fig. 2, where the axial-velocity distributions are plotted at $x = 1.871$. No significant differences were seen in the results. Also, to determine the numerical accuracy of the solution, Fig. 3 gives a comparison of the axial velocity in the vertical channel for $Re = 75$ and $Ra = 1000$ with the results of Habchi and Acharya (1986) with only one wall heated. A good agreement between the two results is obtained. The iteration was continued until the convergence criteria, $|\psi_{i,j}^{k+1} - \psi_{i,j}^{k}|_{\max} < 10^{-6}$ and $|\theta_{i,j}^{k+1} - \theta_{i,j}^{k}|_{\max} < 10^{-6}$, were satisfied simultaneously; where k is the kth iteration of computations, and the subscript max means the maximum value in all mesh point values of the network for each iteration.

4 Results and Discussion

This report dealt with air ($Pr = 0.71$) flow, and the numerical calculations were carried out for each condition given in Table 1. The symbols $A \sim I$ in the succeeding figures of velocity and temperature are those at typical axial locations given in Table 2.

4.1 Velocity Profiles and Hydrodynamic Entrance Length. The airflow that enters at a uniform velocity is deformed by buoyancy in addition to the usual displacement action of boundary layer. As a result, the developing velocity profiles become asymmetric. Far downstream, the buoyancy effect diminishes and the velocity profile attains the symmetric distribution of a parabola (Poiseuille flow). In order to visualize the buoyancy effects due to the inclination angle, the developing profiles of axial velocity u are illustrated in Fig. 4. Because the fluid near the lower wall in the horizontal parallel plates, irrespective of thermal conditions, is accelerated by buoyancy, the velocity profile is distorted and becomes vertically asymmetric. However, the asymmetry is very small. In

Table 1 Inclination angles and parameters for calculations

ϕ	Re	Ra				
		500	1000	1500	2000	3000
0°	50			o		
	100	o	o	o		
15°	100			o		
30°	100			o		
45°	50			o		
	100	o	o	o		
60°	100			o		
75°	100			o		
90°	50			o		
	100	o	o	o	o	o
	300			o		

Table 2 Locations where velocity and temperature profiles are given

	x'/(2s')
A	0.080 19
B	0.220 97
C	0.608 92
D	1.25
E	1.871 62
F	2.305
G	6.081 34
H	19.485 5
I	∞

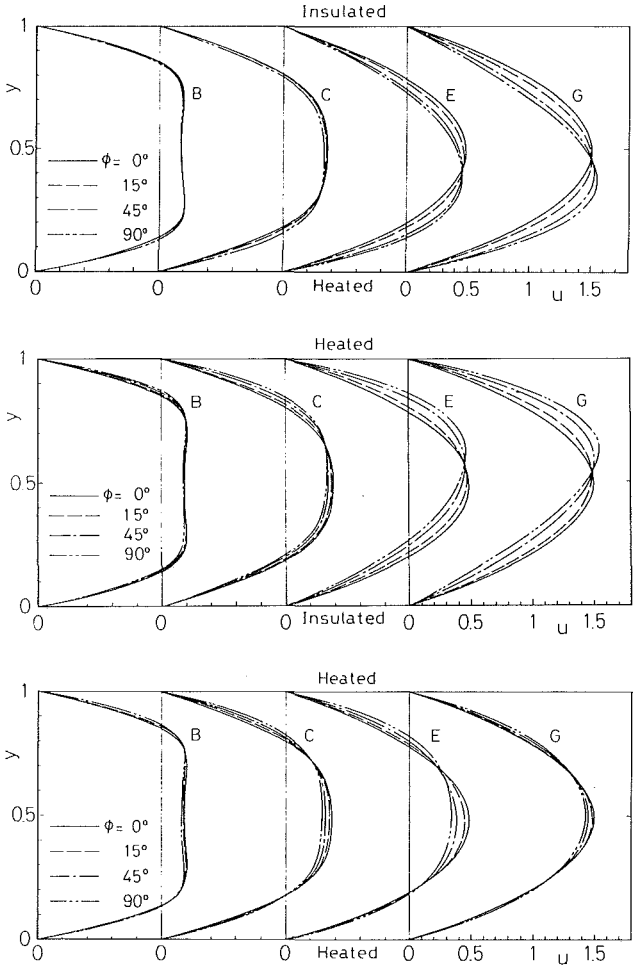

Fig. 4 Effects of inclination angle on developing velocity profiles for Re = 100 and Ra = 1500: (a) lower wall heated; (b) upper wall heated; (c) both walls heated

case the lower wall is heated, the location of maximum velocity u_{max} approaches the lower wall more and more with increasing inclination angles. Contrary to this, when the upper wall is heated, it is seen from the distributions of E and G that the locations of maximum velocity shift from within the lower half to the upper half of the channel. On the other hand, the location of u_{max} when both walls are heated moves toward the channel centerline, and the velocity profile approaches symmetry. Also, in the vertical position, the acceleration of the central part is smaller than at an inclined position, and the velocity profile becomes the flattest. Appendix B describes why such an asymmetric velocity profile occurs.

Figure 5 displays the effects of buoyancy on the developing velocity of upward flow between vertical parallel plates with one or both walls heated. The results for Ra = 0, 1500, and 3000 are plotted in this figure, while the Reynolds number is fixed at 100. The location of maximum velocity when only one wall is heated comes closer to the heated wall, and the velocity profile becomes remarkably asymmetric, as the Rayleigh number increases. When both walls are heated, on the other hand, the decrease of displacement action is seen in comparison with the pure forced convection, because the fluid near both heated walls is accelerated by free convection. In particular, the concave velocity profile for Ra = 3000 is maintained up to a far downstream position.

The developing velocity profile of vertical upward flow for three Reynolds numbers (50, 100, and 300) is shown in Fig. 6. The Rayleigh number is fixed at 1500. With one wall heated, the influence of free convection on the velocity becomes stronger with decreasing Reynolds number. With both walls heated, however, the variation of velocity profiles for

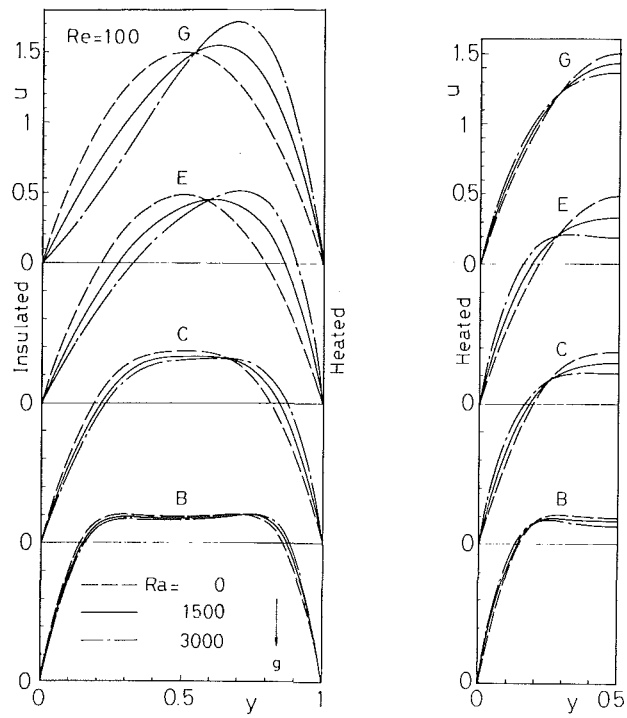

Fig. 5 Effects of Rayleigh number on developing vertical velocity profiles for Re = 100: (a) one wall heated; (b) both walls heated

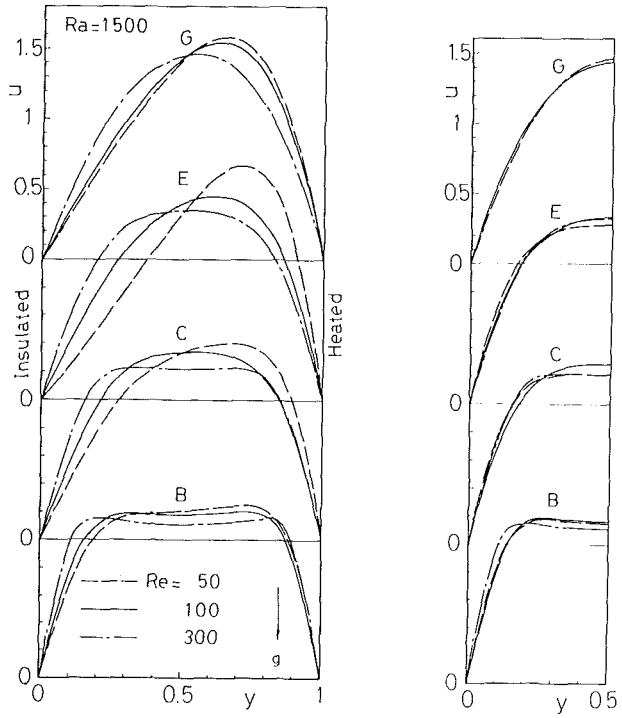

Fig. 6 Effects of Reynolds number on developing vertical velocity profiles for Ra = 1500: (*a*) one wall heated; (*b*) both walls heated

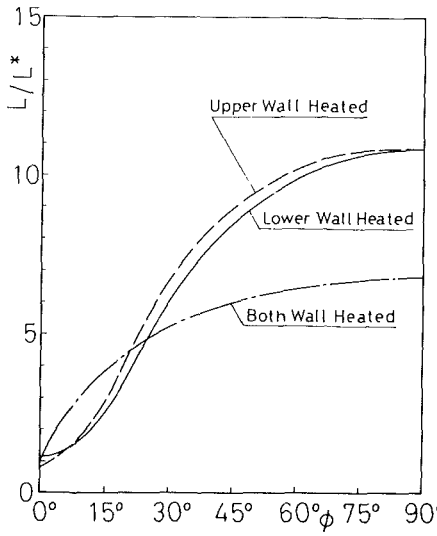

Fig. 7 Variation of hydrodynamic entrance length with inclination angle for Re = 100 and Ra = 1500

Reynolds numbers is not so appreciable as in the case of one wall heated. For Re = 50, the velocity profile overlaps at the position of *B* with that of Re = 100, but the velocity profile at *C* overlaps that for Re = 300.

Here, the influence of buoyancy on the hydrodynamic entrance length is investigated. The hydrodynamic entrance length is defined as the distance from the inlet to the axial location that it takes for the centerline velocity to reach $u_c = 1.485$ (that is, 99 percent of centerline velocity of Poiseuille flow), Figure 7 shows the hydrodynamic entrance length, L/L^*, for typical inclination angles that are normalized by isothermal flow ($L^* = 1.99$). The Reynolds and Rayleigh numbers are fixed at Re = 100 and Ra = 1500. For a horizontal channel, the hydrodynamic entrance length of a lower heated wall ($L = 2.22$) is longer than that of isothermal flow, while that of an upper heated wall ($L = 1.7$) is shorter

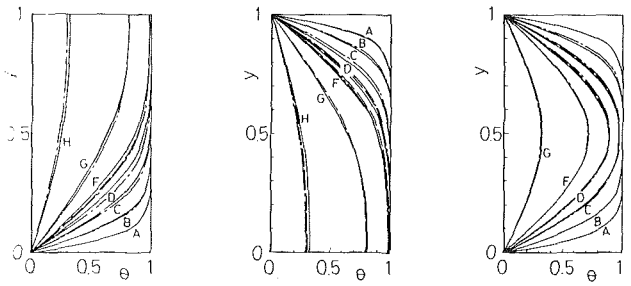

Fig. 8 Effects of inclination angle on developing temperature profiles for Re = 100 and Ra = 1500; ——, $\phi = 0$ deg; – – –, $\phi = 45$ deg; – · –, $\phi = 90$ deg: (*a*) lower wall heated; (*b*) upper wall heated; (*c*) both walls heated

than $L^* = 1.99$. The hydrodynamic entrance length when both walls are heated ($L = 1.96$) becomes nearly identical to that for isothermal flow. When only one wall is heated, a slight distortion of velocity profile remains, and the maximum velocity is at the position under the centerline. However, except in the horizontal position, the hydrodynamic entrance length is affected significantly by buoyancy and is longer than that of isothermal flow. When the parallel plates are made vertical, the value of L is the same for heating of either the lower or the upper wall. Then L/L^* is 10.8. The hydrodynamic entrance length ratio when both walls are heated, L/L^*, is much shorter than when only one wall is heated.

4.2 Temperature Profiles. Figure 8 gives a comparison of the developing temperature profile for the inclination angle under three thermal conditions. Reynolds and Rayleigh numbers are fixed at Re = 100 and Ra = 1500. As seen from the comparison of Figs. 8 and 4, the influence of inclination angles on temperature profile is not so appreciable as the velocity profile. Although the temperature profiles corresponding to Figs. 5 and 6 are omitted in this paper, the larger difference between temperature profiles for the three Reynolds numbers is recognized, whereas the variations of temperature profiles for Rayleigh numbers are smaller.

4.3 Skin-Friction Coefficient and Local Nusselt Number. The influence of buoyancy on the skin-friction coefficient and local Nusselt number is investigated, because the flow resistance and heat transfer are important in the practical technique of heat exchanger. To begin with, the skin-friction coefficient C_f and the local Nusselt number Nu are defined as follows:

$$C_{f0} = 4(\partial u/\partial y)_{y=\theta}/\mathrm{Re} \tag{19}$$

$$C_{f1} = -4(\partial u(\partial y)_{y=1}/\mathrm{Re} \tag{20}$$

$$\mathrm{Nu}_0 = 4s'h_0'/s' = 2(\partial\theta/\partial y)_{y=0}/\theta_b \tag{21}$$

$$\mathrm{Nu}_1 = 4s'h_0'/\lambda' = -2(\partial\theta/\partial y)_{y=1}/\theta_b \tag{22}$$

where the dimensionless bulk temperature θ_b in equations (21) and (22) is given by

$$\theta_b = (t_w' - t_b')/(t_w' - t_0') = \int_0^1 \theta u \cdot dy \tag{23}$$

The effects of buoyancy on the skin-friction coefficient and the local Nusselt number are evaluated by each ratio of C_f^* for the isothermal flow and Nu* for pure forced convection, respectively. Hence, C_f^* and Nu* are shown in Fig 9.

The skin-friction coefficients of three thermal conditions for Re = 100, Ra = 1500, and 0 deg $\leq \phi \leq$ 90 deg are shown in Fig. 10. The influence of buoyancy increases with flow downstream from the entrance and peaks in the region $x = 0.3 \sim 5$. The buoyancy effect diminishes gradually with downstream distance. At a far downstream position, C_f approaches asymptotically the value of Poiseuille flow. Then,

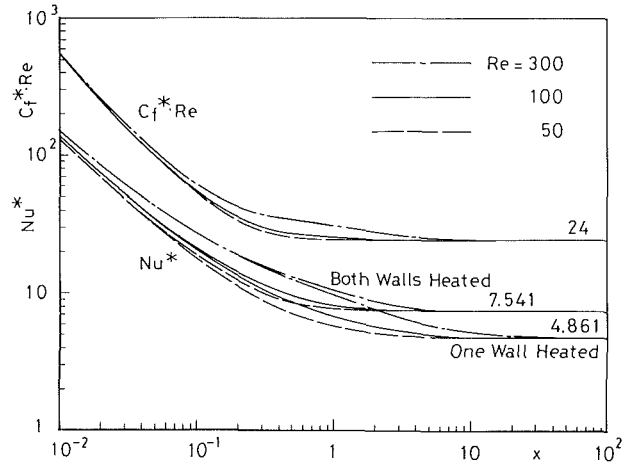

Fig. 9 Skin-friction coefficient for isothermal flow and local Nusselt number for pure forced convection

the skin-friction coefficient is larger at the horizontal lower wall and smaller at the horizontal upper wall than that of isothermal flow. This corresponds to the velocity gradients at the wall. With increasing inclination angles, $(C_f/C_f^*)_{max}$ at the heated wall is larger and $(C_f/C_f^*)_{min}$ at the insulated wall is smaller. This is because the fluid near the heated wall is accelerated by free convection. At $\phi = 15$ deg, there exists a region in the vicinity of the inlet where the ratios of the skin-friction coefficients become $C_{f0}/C_f^* < 1$ when the upper or both walls are heated.

Figure 11 depicts the distributions of local Nusselt number for typical inclination angles at Re = 100 and Ra = 1500. Although the influence of buoyancy on local Nusselt number is an order of magnitude smaller than that on skin-friction coefficient, these show a similar tendency. In other words, in the case of horizontal parallel plates with the upper or both walls heated, the axial variation of local Nusselt number at the upper wall exhibits the presence of a local valley at some axial position due to buoyancy. When the parallel plates are tilted, $(Nu/Nu^*)_{max}$ is larger than at $\phi = 0$ deg. With the upper wall heated, it is also known that the local Nusselt number for $\phi > 15$ deg is larger than that of pure forced convection.

In order to utilize the results of friction loss and heat transfer in the development or design of thermal energy devices, the correlation equations are obtained. At an inclination angle, a skin-friction coefficient $|1 - C_f/C_f^*|$ and the corresponding location x are normalized by use of $|1 - C_f/C_f^*|_{max}$ and its location $(x_h)_{max}$, respectively. Subsequently, $\chi = x/(x_h)_{max}$ is rewritten by $\zeta = \chi/(1+\chi)$. This distribution of normalized skin friction coefficient shows good agreement with that of local Nusselt number. Thus, the numerical results of skin-friction coefficient and local Nusselt number can be expressed by the following correlation equations.

1 When only one wall is heated,

$$C_f = C_f^*[1 + A\{F + (B + 0.101)f\}] \tag{24}$$

$$\mathrm{Nu} = \mathrm{Nu}^*[1 + 0.21A\{F + (B + 0.101)f\}] \tag{25}$$

$$F = 4\zeta(1-\zeta), \qquad 0 \le \zeta \le 1$$

$$f = 89\zeta(0.212 - \zeta), \qquad 0 \le \zeta \le 0.106$$

$$= (0.5 - \zeta)/\{0.796 - \zeta(6.581 - 26.32\zeta)\}, \qquad 0.106 \le \zeta \le 0.5$$

$$= 0, \qquad 0.5 \le \zeta \le 1$$

where A and B are given by the following equations: for the lower wall heated:

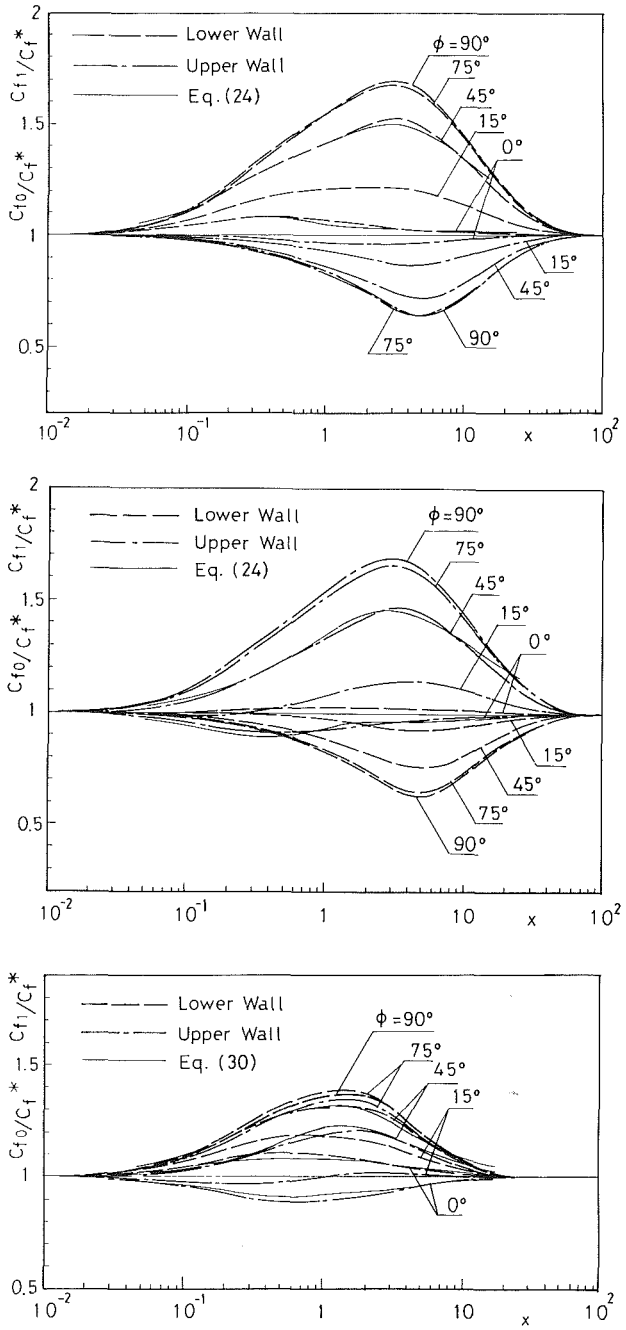

Fig. 10 Effects of buoyancy in terms of inclination angle on skin-friction coefficient for Re = 100 and Ra = 1500: (a) lower wall heated; (b) upper wall heated; (c) both walls heated

$$\left.\begin{aligned} A &= (0.0438\sin\phi + 0.0022)\mathrm{Ra/Re} \\ B &= \chi(0.772 - 5.156\chi + 19.69\chi^2 - 31.91\chi^3 + 18.66\chi^4) \end{aligned}\right\} \tag{26}$$

for the upper wall heated:

$$\left.\begin{aligned} A &= \{0.046\sin\phi - 0.0028\sqrt{(1-\sin^2\phi)}\}\mathrm{Ra/Re} \\ B &= -\chi(0.627 - 3.803\chi + 14.36\chi^2 \\ &\quad - 23.36\chi^3 + 14.34\chi^4) \end{aligned}\right\} \tag{27}$$

The location of $|1 - C_f/C_f^*|_{max}$ and $|1 - \mathrm{Nu}/\mathrm{Nu}^*|_{max}$ are given by

$$(x_h)_{max} = 0.0432\mathrm{Re}^{0.9} \tag{28}$$

$$(x_t)_{max} = 0.0479\mathrm{Re}^{0.9} \tag{29}$$

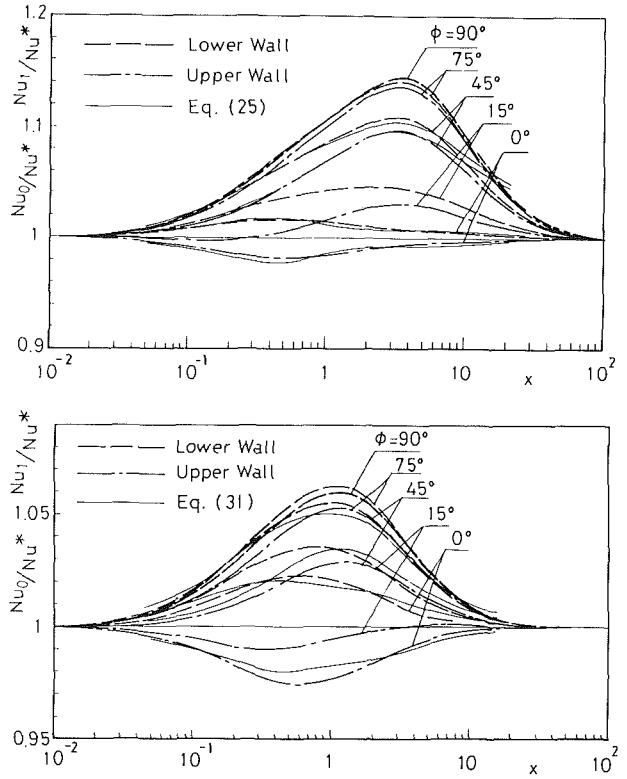

Fig. 11 Effects of buoyancy in terms of inclination angle on local Nusselt number for Re = 100 and Ra = 1500: (a) lower or upper wall heated; (b) both walls heated

2 When both walls are heated

$$C_f = C_f^*\{1 + A(F + Bf)\} \tag{30}$$

$$\mathrm{Nu} = \mathrm{Nu}^*\{1 + 0.15A(F + Bf)\} \tag{31}$$

$$\begin{aligned} F &= \zeta/\{0.286 - \zeta(0.145 - 1.145\zeta)\}, && 0 \le \zeta \le 0.5 \\ &= (1-\zeta)/\{1.566 - \zeta(3.266 - 2.266\zeta)\}, && 0.5 \le \zeta \le 1 \end{aligned}$$

At the lower wall for 0 deg $\le \phi < 90$ deg

$$\left.\begin{aligned} f &= 40.57\zeta(0.314 - \zeta), && 0 \le \zeta \le 0.157 \\ &= (0.5-\zeta)/\{0.621 - \zeta(2.546 - 4.924\zeta)\}, && 0.157 \le \zeta \le 0.5 \\ &= 0, && 0.5 \le \zeta \le 1 \\ A &= (0.0194 \sin\phi + 0.0072)\mathrm{Ra}/\mathrm{Re} \\ B &= \chi(0.784 - 3.513\chi + 9.134\chi^2 - 10.44\chi^3 + 4.543\chi^4) \end{aligned}\right\} \tag{32}$$

At the upper wall for 0 deg $\le \phi \le 90$ deg,

$$\left.\begin{aligned} f &= 25.77\zeta(0.394 - \zeta), && 0 \le \zeta \le 0.197 \\ &= (0.5-\zeta)/\{0.782 - \zeta(3.863 - 7.268\zeta)\}, && 0.197 \le \zeta \le 0.5 \\ &= 0, && 0.5 \le \zeta \le 1 \\ A &= (0.0322 \sin\phi - 0.0072)\mathrm{Ra}/\mathrm{Re}, \\ B &= -\chi(0.9083 - 3.168\chi + 7.911\chi^2 - 5.207\chi^3) \end{aligned}\right\} \tag{33}$$

Also $(x_h)_{\max}$ and $(x_t)_{\max}$ are expressed as follows:

$$(x_h)_{\max} = 0.027\mathrm{Re}^{0.854} \tag{34}$$

$$(x_t)_{\max} = 0.0222\mathrm{Re}^{0.854} \tag{35}$$

where $\chi = 1 - \sin\phi$. The application range of these equations is $0.05 \le x \le 10$. At the upper wall, except for the case of a heated lower wall, the sign of B is changed when A has the negative sign. Note that the values of $(x_h)_{\max}$ and $(x_t)_{\max}$ at the vertical position are used in the above formulation.

When only one wall was heated, C_f and Nu for $\phi = 45$ deg were approximated within 1.7 and 1 percent, respectively. When the values of C_f^* and Nu* are determined from Fig. 9, the C_f and Nu values at arbitrary inclination angle, streamwise location, and Reynolds and Rayleigh numbers within this analysis condition can be produced by using the proper equations (24) ~ (35). Note that the application of these equations is below the onset of thermal instability. Therefore, attention should be paid to use at low inclination angles.

5 Conclusions

A numerical investigation has been made of combined forced and free laminar convection of upward airflow in the entrance region between inclined parallel plates with uniform wall temperature. The results are summarized as follows:

1 The developing velocity profiles are distorted by the buoyancy. In the horizontal parallel plates, the fluid near the lower wall is always accelerated, irrespective of thermal condition. With increasing inclination angles, the position of $u_{\max}$ approaches the lower wall when only the lower wall is heated and toward the upper wall when only the upper wall is heated. When both walls are heated equally, the developing velocity profiles change from asymmetric to symmetric forms with an increase of the inclination angle.

2 The hydrodynamic entrance length becomes longer with an increase of buoyancy and inclination angle.

3 The variation of temperature profiles with inclination angle is not so remarkable as the velocity profile. Rayleigh number variations also give smaller differences in the temperature profile.

4 In the heated horizontal parallel plates, the skin-friction coefficients C_f at the lower and upper walls take consistently higher and lower values, respectively, than the isothermal flow. As the inclination angle increases, C_f values at the heated and insulated walls become larger and smaller, respectively, than for the horizontal parallel plates.

5 The effects of buoyancy on the local Nusselt number increase with increasing inclination angles. When the inclination angle is over 15 deg, the reduction of heat transfer at the upper wall observed in the horizontal parallel plates almost disappears due to free convection effects.

6 In order to estimate the value of skin-friction coefficient readily at the heated wall and of local Nusselt number, the correlation equations (24)–(35) are provided.

References

Aung, W., and Worku, G., 1986, "Developing Flow and Flow Reversal in a Vertical Channel With Asymmetric Wall Temperature," ASME JOURNAL OF HEAT TRANSFER, Vol. 108, pp. 299-304.

Cebeci, T., Khattab, A. A., and LaMont, R., 1982, "Combined Natural and Forced Convection in Vertical Ducts," *Heat Transfer 82, Proceedings of 7th International Heat Transfer Conference*, Munich, Federal Republic of Germany, Vol. 2, pp. 419-424.

Dalbert, A. M., 1982, "Natural, Mixed and Forced Convection in a Vertical Channel With Asymmetric Uniform Heating," *Heat Transfer 82, Proceedings of 7th International Heat Transfer Conference*, Munich, Federal Republic of Germany, Vol. 3, pp. 431-434.

Habchi, S., and Acharya, S., 1986, "Laminar Mixed Convection in a Symmetrically or Asymmetrically Heated Vertical Channel," *Numerical Heat Transfer*, Vol. 9, pp. 605-618.

Kiya, M., Fukusako, S., and Arie, M., 1971, "Effects of Buoyancy on Laminar Developing Flow in the Entrance Region of a Horizontal Parallel Plate Channel," *Trans. JSME*, Vol. 37, pp. 1947-1958.

Maughan, J. R., and Incropera, F. P., 1987, "Experiments on Mixed Convection Heat Transfer for Airflow in a Horizontal and Inclined Channel," *Int. J. Heat Mass Transfer*, Vol. 30, pp. 1307-1318.

Mori, Y., and Uchida, Y., 1966, "Forced Convective Heat Transfer Between Horizontal Flat Plates," *Int. J. Heat Mass Transfer*, Vol. 9, pp. 803-817.

Naito, E., 1983, "Fluid Flow and Heat Transfer Near the Leading Edge of Parallel Plates," *Proceedings of the ASME/JSME Thermal Engineering Joint Conference*, Honolulu, HI, Vol. 3, pp. 35-41.

Naito, E., 1984, "Buoyant Force Effects on Laminar Flow and Heat Transfer in the Entrance Region Between Horizontal Parallel Plates," *Heat Transfer Japanese Research*, Vol. 13, pp. 80-96.

Naito, E., 1985, "The Effect of Buoyancy on Laminar Flow and Heat Transfer in the Entrance Region Between Horizontal, Parallel Plates," *International Chemical Engineering*, Vol. 25, pp. 315-323.

Naito, E., 1987, "Laminar Forced Convection Heat Transfer in the Air Flow Through a Cascade of Parallel Plates: The Case of Uniform Heat Flux," *Heat Transfer Science and Technology*, Bu-Xuan Wang, ed., Hemisphere, Washington, DC, pp. 228–236.

Nguyen, T. V., Maclaine-cross, I. L., and de Vahl Davis, G., 1981, "The Effect of Free Convection on Entry Flow Between Horizontal Parallel Plates," *Numerical Methods in Heat Transfer*, R. W. Lewis, K. Morgan, and O. C. Zienkiwicz, eds., Wiley, New York, pp. 349–372.

Savkar, S. D., 1970, "Developing Forced and Free Convective Flow Between Two Semi-infinite Parallel Plates," *Proceedings of the Fourth International Heat Transfer Conference*, Paper No. NC 3.8.

Shah, R. K., and London, A. L., 1978, *Laminar Flow Forced Convection in Ducts*, Academic Press, New York.

Wang, Y. L., and Longwell, P. A., 1964, "Laminar Flow in the Inlet Section of Parallel Plates," *AIChE Journal*, Vol. 10, pp. 323–329.

Yao, L. S., 1983, "Free and Forced Convection in the Entry Region of a Heated Vertical Channel," *Int. J. Heat Mass Transfer*, Vol. 26, pp. 65–72.

APPENDIX A

When a horizontal parallel plate channel is heated from below with a uniform wall heat flux, the dimensionless temperature profile in the fully developed velocity and temperature fields may be written (Naito, 1984) as

$$\frac{t'_{w0}-t'}{\dfrac{q'_w\cdot s'}{\lambda'}}=2y-2y^3+y^4-\frac{2}{3}\,\frac{\mathrm{Gr}}{\mathrm{Pr}\cdot\mathrm{Re}^2}\left(\frac{y^3}{3}-\frac{y^4}{2}+\frac{y^5}{5}\right) \tag{A1}$$

where t'_{w0} is a lower wall temperature and $\mathrm{Gr}=8g'\cdot\beta'\cdot(q'_w\cdot s'/\lambda')\cdot s'^3/\nu'^2$. Thus, from equation (A1), the dimensionless temperature difference between the lower wall temperature t'_{w0} (at $y=0$) and upper wall temperature t'_{w1} (at $y=1$) is given by

$$\frac{t'_{w0}-t'_{w1}}{\dfrac{q'_w\cdot s'}{\lambda'}}=1-\frac{1}{45}\,\frac{\mathrm{Gr}}{\mathrm{Pr}\cdot\mathrm{Re}^2} \tag{A2}$$

In the meantime, the dimensionless temperature difference between lower wall temperature t'_{w0} and bulk temperature t'_b becomes:

$$\frac{t'_{w0}-t'_b}{\dfrac{q'_w\cdot s'}{\lambda'}}=\frac{26}{35}-\frac{1}{45}\,\frac{\mathrm{Gr}}{\mathrm{Pr}\cdot\mathrm{Re}^2}+\frac{1}{2835}\left(\frac{\mathrm{Gr}}{\mathrm{Pr}\cdot\mathrm{Re}^2}\right)^2 \tag{A3}$$

Maughan and Incropera (1987) obtained the transitory enhancement of Nusselt number at $\mathrm{Gr}^*=g'\cdot\beta'\cdot q'_w\cdot(2s')^4/(\lambda'\cdot\nu'^2)=7000$ and $\mathrm{Re}^*=2s'\cdot u'/\nu'=250$. The corresponding critical Rayleigh number based on $t'_{w0}-t'_b$ was $\mathrm{Ra}'=8c'_p\cdot\rho'\cdot g'\cdot\beta'\cdot(t'_{w0}-t'_b)\cdot s'^3/(\lambda'\cdot\nu')\simeq 1200$. Now, we estimate the value of $\mathrm{Ra}=8c'_p\cdot\rho'_0\cdot g'\cdot\beta'\cdot(t'_w-t'_0)\cdot s'^3/(\lambda'\cdot\nu')$ equivalent to the above value.

With $\mathrm{Gr}^*=7000$ and $\mathrm{Re}^*=250$, we have:

$$\mathrm{Gr}=\mathrm{Gr}^*/2=3500 \text{ and } \mathrm{Re}=2\mathrm{Re}^*=500$$

which yields

$$\mathrm{Gr}/(45\mathrm{Pr}\cdot\mathrm{Re}^2)=4.4\times10^{-4}<<26/35$$

and

$$\{\mathrm{Gr}/(\mathrm{Pr}\cdot\mathrm{Re}^2)\}^2/2835=1.4\times10^{-7}<<26/35$$

Thus, the second term of equation (A2) and the second and third terms of equation (A3) can be neglected.

Consequently, from equations (A2) and (A3), we obtain the following value:

$$(t'_{w0}-t'_{w1})/(t'_{w0}-t'_b)\simeq 35/26 \tag{A4}$$

With $\mathrm{Ra}'\simeq 1200$ and equation (A4), we then have

$$\mathrm{Ra}^*=8c'_p\cdot\rho'\cdot g'\cdot\beta'\cdot(t'_{w0}-t'_{w1})\cdot s'^3/(\lambda'\cdot\nu')\simeq 1600 \tag{A5}$$

Hence, the condition for the nonoccurrence of secondary flow is expressed as

$$\mathrm{Ra}^*\le 1600 \tag{A6}$$

In the present case, the following relations hold:

$$t'_{w0}=t'_w \text{ and } t'_{w1}\ge t'_0$$

which is equivalent to

$$\mathrm{Ra}^*\le \mathrm{Ra} \tag{A7}$$

Therefore, in the present definition, we comply with the following requirement in order to consistently satisfy equation (A6):

$$\mathrm{Ra}\le 1600 \tag{A8}$$

APPENDIX B

It is well known that the fluid near the lower wall for horizontal parallel plates with both walls heated is accelerated by buoyancy (Kiya et al., 1971; Nguyen et al., 1981), so the asymmetric velocity profile for heating of either the lower or the upper wall alone is discussed here.

As seen from Fig. 4, the fluid near the lower wall is accelerated by buoyancy as follows:

$$(\partial u/\partial y)_{y=0}>-(\partial u/\partial y)_{y=1} \tag{B1}$$

(*i*) When only the lower wall is heated, equations (13) and (14) are rewritten as follows:

$$(\partial u/\partial y)_{y=0}=3(\psi_{i,2}-\psi_{i,1})/b^2+\omega_{i,2}/2+\Delta_0 \tag{B2}$$

$$-(\partial u/\partial y)_{y=1}=3(\psi_{i,n+1}-\psi_{i,n})/b^2-\omega_{i,n}/2+\Delta_1 \tag{B3}$$

In the case of pure forced convection, the following equations are obtained:

$$\left.\begin{aligned}\psi_{i,2}-\psi_{i,1}&=\psi_{i,n+1}-\psi_{i,n}\\ \omega_{i,2}&=-\omega_{i,n}\end{aligned}\right\} \tag{B4}$$

The final terms on the right sides of equation (B2) and (B3) represent the effects of free convection and are expressed, respectively, as follows:

$$\left.\begin{aligned}\Delta_0&=b^2\cdot\mathrm{Ra}\{(\partial\theta/\partial y)_{y=0}\cdot\sin\phi\}/(4\mathrm{Pe})\\ \Delta_1&=b^2\cdot\mathrm{Ra}\{(\partial\theta/\partial x)_{y=1}\cdot\cos\phi\}/(4\mathrm{Pe})\end{aligned}\right\} \tag{B5}$$

$(\partial\theta/\partial x)_{y=1}\le 0$ at the upper wall (insulated wall) and $(\partial\theta/\partial y)_{y=0}>0$ at the lower wall. Therefore, from equations (B2) and (B3), we obtain: $(\partial u/\partial y)_{y=0}>-(\partial u/\partial y)_{y=1}$. This unequal relation increases with increasing inclination angles. In other words, the fluid near the lower wall is accelerated as the inclination angle and the value of parameter, Ra/(Pr•Re), increase.

(*ii*) When only the upper wall is heated, the final terms of equations (B2) and (B3) are expressed as follows:

$$\left.\begin{aligned}\Delta_0&=-b^2\cdot\mathrm{Ra}\{(\partial\theta/\partial x)_{y=0}\cdot\cos\phi\}/(4\mathrm{Pe})\\ \Delta_1&=-b^2\cdot\mathrm{Ra}\{(\partial\theta/\partial y)_{y=1}\cdot\sin\phi\}/(4\mathrm{Pe})\end{aligned}\right\} \tag{B6}$$

The temperature gradients in these equations maintain $(\partial\theta/\partial x)_{y=0}\le 0$ at the lower wall (insulated wall) and $(\partial\theta/\partial y)_{y=1}<0$ at the upper wall, respectively. In the same way as (*i*), $(\partial u/\partial y)_{y=0}>-(\partial u/\partial y)_{y=1}$ is derived for the horizontal parallel plates. However, the inequality between $(\partial u/\partial y)_{y=0}$ and $-(\partial u/\partial y)_{y=1}$ is reversed with increasing inclination angles. As discussed earlier in this report, it means that the vertical location for maximum velocity of developing flow is displaced toward the upper wall with increasing inclination angles.

L. S. Yao

B. B. Rogers

Department of Mechanical and Aerospace Engineering,
Arizona State University,
Tempe, AZ 85287

Mixed Convection in an Annulus of Large Aspect Ratio

Mixed convection in an annulus of large aspect ratio is studied. At an aspect ratio of 100, the effect of wall curvature is minimal, and both the base flow and the stability characteristics approach those of a two-dimensional channel flow. The linear-stability results demonstrate that the fully developed flow is unstable in regions of practical interest in an appropriate parameter space. Consequently, commonly assumed steady parallel countercurrent flows in many idealized numerical and analytical studies are unlikely to be observed experimentally.

1 Introduction

Mixed convection in vertical ducts is a fundamental problem in heat transfer. Unfortunately, the fluid motions and associated heat transfer mechanisms for these problems are frequently treated incorrectly. For example, many researchers have simplified the problem by assuming that the flow is parallel, similar to the isothermal case. With such an assumption, the velocity and temperature distributions at any axial location become relatively easily predicted functions of the transverse coordinates only. However, the limits of this assumption have not been discussed in depth for nonisothermal flows. Consequently, physically unrealistic steady parallel reverse flow, induced by buoyancy, is discovered in some overly idealized numerical models. In this paper we will demonstrate that mixed convection in a vertical annulus of large aspect ratio (equivalent to a two-dimensional channel) is unstable in many regions of an appropriate parameter space, and that the assumption of a steady parallel fully developed flow is not appropriate for most flow conditions of practical interest.

Many studies of mixed convection in vertical slots and annuli have adopted the parallel flow assumptions (Shumway and McEligot, 1971; El-Shaarawl and Sarhan, 1980; Kim, 1985; Hashimoto, Akino and Kawamura, 1986; Quintiere and Mueller, 1973; Habchi and Acharya, 1986; Aung and Worku, 1986), and ignored the possible hydrodynamic instabilities that can lead to increased mixing of the fluid. Thus, the results obtained without accounting for these effects will tend to underpredict the actual heat transfer rates.

There is experimental evidence that this is, indeed, the case. For example, Maitra and Raju (1975) developed an exact solution for the Nusselt number for fully developed flow in an annulus, based on the parallel flow assumption. The analytical result was then compared to experiment and it was found that the measured heat transfer rates were significantly higher than those predicted with the theoretical model. This effect was observed at Reynolds numbers as low as 200. The discrepancy in the results was attributed, correctly we believe, to secondary flows induced by hydrodynamic instability. Detailed observations of the flow patterns induced by the instabilities, however, were not reported.

A related problem that has been studied more extensively is that of nonisothermal flow in a vertical pipe. An extensive list of references can be found in Zeldin and Schmidt (1972). Most studies have adopted the parallel flow assumption in their analysis. An important exception, however, is the work of Scheele and Hanratty (1962). In this work the authors observed experimentally that the stable flow in the inlet region of a heated vertical pipe can become unstable near the fully developed region. When the buoyancy forces oppose the motion of the fluid, such as upward flow in a cooled pipe, the transition to turbulence is abrupt. However, when the buoyancy forces aid the fluid motion, such as upward flow in a heated pipe, the transition is gradual, and the initial transition process leads to a new equilibrium laminar nonparallel flow. Thus, in the opposing-flow case the instability is subcritical, and in the aided-flow case it is supercritical. Kemeny and Somers (1962) observed flow patterns for the supercritical case and called them nonlaminar to distinguish them from turbulent flow. The nonlaminar heat transfer rates were found to be as much as 30 percent larger than those observed in laminar flow. In addition, it was found that the flow can become nonlaminar at Reynolds numbers as low as 30. Confirmation of these results analytically was achieved by Yao (1987a), who demonstrated that upward flow in a heated vertical pipe is unstable for certain parameters and that a supercritical instability will likely consist of a double-spiral structure.

In addition to the results summarized above, there are a number of other studies relevant to the present investigation. In particular, the stability of natural convection in a two-dimensional slot or annulus and the stability of plane Poiseuille flow are limiting cases of the present study. In the limiting case of the Reynolds number equal to zero, the flow becomes that of pure natural convection. In a two-dimensional slot it has been observed that when a small temperature difference is imposed between the vertical walls, the fluid near the hotter wall rises and that near the cooler wall descends, and the accompanying temperature profile is linear. However, as the temperature difference between the plates is increased, the motion becomes unstable, the fluid bifurcates, and the new flow consists of stationary recirculating eddys (Elder, 1965). The stability of this motion has been determined by Vest and Arpaci (1969), who found that the marginal stability boundary occurs at a Grashof number of about 8000, and is a very weak function of Prandtl number. Korpela et al. (1973) confirmed these results for small Prandtl number, but they found that at Prandtl numbers above 12.7, thermally induced instability becomes dominant, the cells begin to drift, and a significant Prandtl number dependence appears. As discussed by Hart (1971) there are two distinct physical mechanisms that lead to instabilities. The instability that occurs at higher values of Pr is one in which the disturbance energy is gathered primarily from the potential energy associated with the buoyant forces, while with the instability that occurs at lower values of Pr, the disturbance energy is gained from the action of the shear forces in the mean flow. The drift of these cells for large Pr may be due to the fact that cells are produced in the thin thermal boundary layer and are carried away by the induced forced flow outside of it.

In the case of steady recirculating eddies in natural convection, as the Reynolds number is increased these cells will begin

Contributed by the Heat Transfer Division for publication in the JOURNAL OF HEAT TRANSFER. Manuscript received by the Heat Transfer Division January 5, 1988. Keywords: Flow Instability, Mixed Convection.

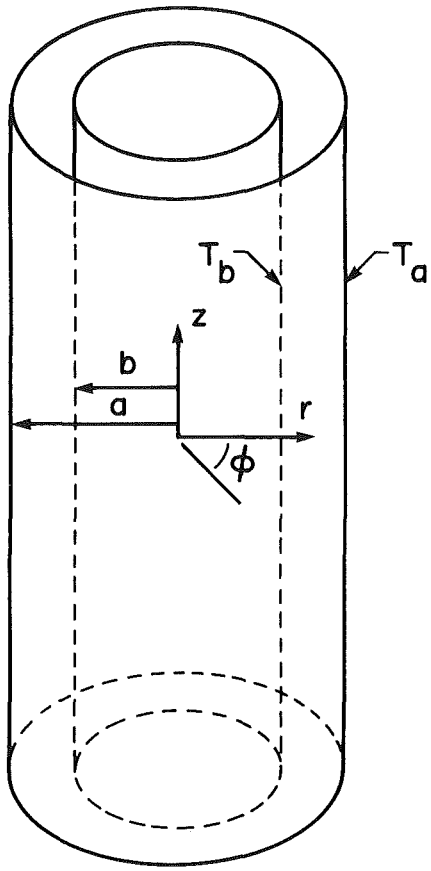

Fig. 1 Geometry and coordinates

to drift with the mean flow. As the Reynolds number is increased further these drifting cells will be "washed out" by the forced flow and the secondary motion will become vertical spirals. It is important to note that the flow above critical Gr/Re will not be steady and attempts to predict the detailed flow patterns that do not account for the unsteady nature of the flow will not be successful.

In many studies, the most unstable disturbances are assumed to be two-dimensional. This is a consequence of Squire's theorem, which is valid for two-dimensional isothermal flows and states that the growth rate of an unstable three-dimensional wave is equal to that of a two-dimensional wave at a smaller Re. Consequently, stability studies on plane Poiseuille flow are usually limited to two-dimensional disturbances. This result can also be derived for the problem of natural convection in a two-dimensional slot (Vest and Arpaci, 1969). Even though in the limiting cases of natural convection and plane Poiseuille flow in a two-dimensional channel the theorem is valid, an analogy of Squire's theorem for two-dimensional mixed convection can not be proved rigorously due to the presence of the buoyant term in the axial momentum equation. Therefore, both axial and azimuthal disturbances are investigated. While it is found that the first few azimuthal modes can be as unstable as the axisymmetric one, the linear stability boundary predicted by the analysis of two-dimensional disturbances is sufficient. The higher harmonic modes are needed, however, to study the nonlinear behavior beyond the onset of instability.

A linear stability analysis of fully developed mixed convection in a vertical annulus with an aspect ratio of 100 and a Prandtl number of 0.71 is carried out in the next section. The analysis accounts for both axisymmetric and nonaxisymmetric disturbances. The results show that the flow is unstable for certain parameter ranges (see Fig. 4). It is found that the aspect ratio investigated is sufficiently large so that a two-dimensional vertical slot is approximated. The effect of curvature is investigated in a related paper (Yao and Rogers, 1988).

2 Problem Formulation

Consider the annular geometry illustrated in Fig. 1. If we define a dimensionless radial coordinate as $\eta=(r-b)/(a-b)$ and an aspect ratio as $A=b/(a-b)$, where a and b are, respectively, the outer and inner radii of the cylinders, the dimensionless Navier–Stokes, continuity, and energy equations in terms of annular-cylindrical coordinates (η, ϕ, z) are

$$\frac{\partial u}{\partial \eta}+\frac{u}{\eta+A}+\frac{1}{\eta+A}\frac{\partial v}{\partial \phi}+\frac{\partial w}{\partial z}=0 \tag{1a}$$

$$\frac{\partial u}{\partial t}+D_1 u-\frac{v^2}{\eta+A}=-\frac{\partial P}{\partial \eta}+\frac{1}{\mathrm{Re}}\left[D_2^2 u-\frac{1}{(\eta+A)^2}\left(2\frac{\partial v}{\partial \phi}+u\right)\right] \tag{1b}$$

$$\frac{\partial v}{\partial t}+D_1 v+\frac{uv}{\eta+A}=-\frac{1}{\eta+A}\frac{\partial P}{\partial \phi}+\frac{1}{\mathrm{Re}}\left[D_2^2 v+\frac{1}{(\eta+A)^2}\left(2\frac{\partial u}{\partial \phi}-v\right)\right] \tag{1c}$$

$$\frac{\partial w}{\partial t}+D_1 w=-\frac{\partial P}{\partial z}+\frac{1}{\mathrm{Re}}[D_2^2 w]+\frac{\mathrm{Gr}}{\mathrm{Re}^2}\theta \tag{1d}$$

$$\frac{\partial \theta}{\partial t}+D_1\theta=\frac{1}{\mathrm{RePr}}D_2^2\theta \tag{1e}$$

where

$$D_1=u\frac{\partial}{\partial \eta}+\frac{v}{\eta+A}\frac{\partial}{\partial \phi}+w\frac{\partial}{\partial z} \tag{2a}$$

and

$$D_2^2=\frac{\partial^2}{\partial \eta^2}+\frac{1}{\eta+A}\frac{\partial}{\partial \eta}+\frac{1}{(\eta+A)^2}\frac{\partial^2}{\partial \phi^2}+\frac{\partial^2}{\partial z^2} \tag{2b}$$

The pressure in equation (1) is the thermodynamic pressure plus the quantity $\rho_a g z$. The z coordinate is nondimensionalized by the gap width $a-b$, the velocities by the mean axial velocity W_m, the pressure by ρW_m^2, and the time by $(a-b)/W_m$. The dimensionless temperature is given by $\theta=(T-T_a)/(T_b-T_a)$, where T_a and T_b are the outer and inner wall temperatures, respectively. The parameters appearing in the equations are the Reynolds number $\mathrm{Re}=(a-b)W_m/\nu$, Prandtl number $\mathrm{Pr}=\nu/\alpha$, and the Grashof number $\mathrm{Gr}=\beta g(a-b)^3(T_b-T_a)/\nu^2$, where g is the gravitational acceleration, β the thermal expansion coefficient, α the coefficient of thermal diffusivity, and ν the viscosity.

Investigation of the governing equations and their subsequent nondimensionalization reveals that if $T_b>T_a$, Gr is positive; if $T_a>T_b$, the outer cylinder temperature is higher than that of the inner cylinder, and the only change that occurs in the governing relations is that Gr changes sign. Further investigation of the problem reveals that there are two distinct base-flow situations that may occur. These are upward flow with the outer cylinder heated (which is analogous to downward flow with the outer cylinder cooled) and upward flow with the inner cylinder heated (which is analogous to downward flow with the inner cylinder cooled). Therefore, by investigating the stability behavior for both positive and negative values of Gr, the complete stability boundary for mixed convection in an annulus of a particular geometry is determined.

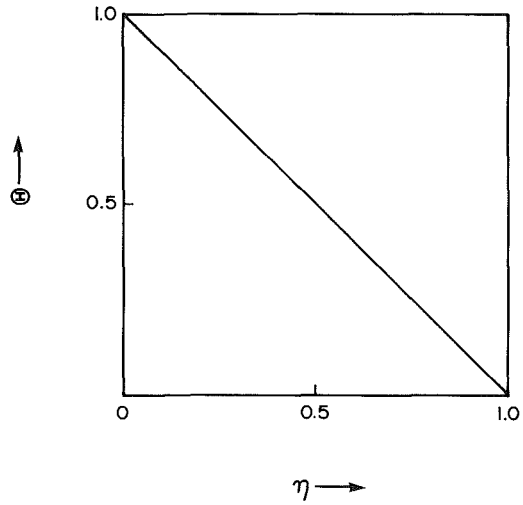

Fig. 2 Basic-state temperature profile

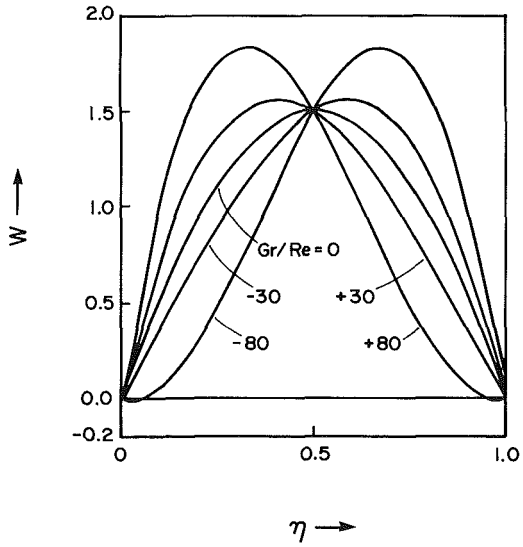

Fig. 3 Basic-state velocity profiles

In this paper, a geometry with an aspect ratio of $A = 100$ is investigated. The results show that there is little difference in the solutions for the inner and outer wall heated cases, indicating that the curvature does not have a significant effect on the results and the solution is a close approximation to the stability of mixed convection in a vertical, two-dimensional channel.

2.1 Basic State. Since we are interested in studying the stability of nonisothermal, fully developed flow in an annular region, we split the dependent variables in the governing equations into two parts: basic state and disturbance. If the classical assumption of fully developed flow is applied to equations (1*a*)-(1*e*), the basic state is independent of the axial and azimuthal coordinates. The governing equations are

$$\frac{\mathrm{Gr}}{\mathrm{Re}^2}\Theta - \frac{\partial P}{dz} + \frac{1}{\mathrm{Re}}\left[\frac{\partial^2 W}{\partial \eta^2} + \frac{1}{\eta + A}\frac{\partial W}{\partial \eta}\right] = 0 \tag{3a}$$

$$\frac{\partial^2 \Theta}{\partial \eta^2} + \frac{1}{\eta + A}\frac{\partial \Theta}{\partial \eta} = 0 \tag{3b}$$

The axial-pressure gradient can be determined with the use of the requirement of global mass conservation

$$\int_0^1 (\eta + A) W d\eta = \frac{1}{2}(1 + 2A) \tag{3c}$$

Where W and Θ are, respectively, the basic state velocity and temperature. The solution of equations (3*a*)-(3*c*) is accomplished by first solving equation (3*b*) for the temperature profile. This profile is then substituted into equation (3*a*) and, since the pressure gradient is independent of the radial coordinate, the equation is easily integrated to obtain an expression for the velocity profile, which includes a term proportional to the axial pressure gradient. Equation (3*c*) is then used to obtain an expression for the pressure gradient. While the solution is straightforward, the resulting expressions are algebraically complicated, and, since we are concerned with the stability of the laminar motion, the expressions themselves are not presented here. The results show that the basic state velocity and temperature profiles are functions of only the aspect ratio A and Gr/Re. A plot of the basic temperature profile for $A = 100$ is given in Fig. 2. It is seen from Fig. 2 that the temperature profile is almost linear, indicating that a two-dimensional basic state is being approached. Typical basic velocity profiles for $A = 100$ are given in Fig. 3. For $\mathrm{Gr/Re} = 80$ and -80, the velocity profiles contain points of inflection. Thus, increased heat transfer across the duct leads to profiles that contain an increased potential for instability.

2.2 Disturbance. The linear equations governing the infinitesimal disturbances are obtained by subtracting the basic state equations from the full equations and neglecting nonlinear terms. They are

$$\frac{\partial \hat{u}}{\partial \eta} + \frac{\hat{u}}{\eta + A} + \frac{1}{\eta + A}\frac{\partial \hat{v}}{\partial \phi} + \frac{\partial \hat{w}}{\partial z} = 0 \tag{4a}$$

$$\frac{\partial \hat{u}}{\partial t} + W\frac{\partial \hat{u}}{\partial z} = -\frac{\partial \hat{P}}{\partial \eta} + \frac{1}{\mathrm{Re}}\left[D_2^2 \hat{u} - \frac{\hat{u}}{(\eta + A)^2} - \frac{2}{(\eta + A)^2}\frac{\partial \hat{v}}{\partial \phi}\right] \tag{4b}$$

$$\frac{\partial \hat{v}}{\partial t} + W\frac{\partial \hat{v}}{\partial z} = -\frac{1}{\eta + A}\frac{\partial \hat{P}}{\partial \phi} + \frac{1}{\mathrm{Re}}\left[D_2^2 \hat{v} - \frac{\hat{v}}{(\eta + A)^2} + \frac{2}{(\eta + A)^2}\frac{\partial \hat{u}}{\partial \phi}\right] \tag{4c}$$

$$\frac{\partial \hat{w}}{\partial t} + \hat{u}\frac{\partial W}{\partial \eta} + W\frac{\partial \hat{w}}{\partial z} = -\frac{\partial \hat{P}}{\partial z} + \frac{1}{\mathrm{Re}}D_2^2 \hat{w} + \frac{\mathrm{Gr}}{\mathrm{Re}^2}\hat{\theta} \tag{4d}$$

$$\frac{\partial \hat{\theta}}{\partial t} + \hat{u}\frac{\partial \Theta}{\partial \eta} + w\frac{\partial \hat{\theta}}{\partial z} = \frac{1}{\mathrm{RePr}}D_2^2 \hat{\theta} \tag{4e}$$

Where the $\hat{}$ denotes a disturbance quantity. The continuity equation is satisfied by the choice of two streamfunctions, f and g, which are defined by

$$\hat{v} = \frac{\partial g}{\partial \eta} \tag{5a}$$

$$\hat{u} = -\left(\frac{\partial f}{\partial z} + \frac{1}{\eta + A}\frac{\partial g}{\partial \phi}\right) \tag{5b}$$

$$\hat{w} = \frac{\partial f}{\partial \eta} + \frac{f}{\eta + A} \tag{5c}$$

The remaining four equations can be reduced to three by the elimination of pressure through cross-differentiation. The number of independent variables is then reduced to one with the assumption that the disturbances are of the usual normal-mode form

$$\phi = \phi(\eta) e^{i[\alpha(z - ct) + n\phi]} \tag{6}$$

where $\phi = f$, g, or θ, and α and n are the axial and azimuthal wavenumbers, respectively. Equations (4*a*) – (4*e*) then become

$$f^{(4)} + \frac{2}{\eta + A} f''' + \left[-2\alpha^2 - \frac{(3+n^2)}{(\eta+A)^2} - i\alpha \mathrm{Re} W \right] f''$$
$$+ \left[-2\alpha^2 + \frac{(3+n^2)}{(\eta+A)^2} - i\alpha \mathrm{Re} W \right] \frac{f'}{\eta + A}$$
$$+ \left[\frac{2\alpha^2 + \alpha^2 n^2}{(\eta+A)^2} + \frac{3n^2 - 3}{(\eta+A)^4} + \alpha^4 \right.$$
$$\left. + i\alpha \mathrm{Re} \left(\frac{W}{(\eta+A)^2} + \alpha^2 W + W'' - \frac{W'}{\eta + A} \right) \right] f$$
$$+ \left(\frac{-\eta\alpha}{\eta + A} \right) g'' + \left[\frac{-n\alpha}{(\eta+A)^2} + in\mathrm{Re} \frac{W'}{\eta + A} \right] g' + \left[\frac{n^3 \alpha}{(\eta+A)^3} \right.$$
$$\left. + \frac{\alpha^3 n}{\eta + A} + i\mathrm{Re} \left(\frac{\alpha^2 n}{\eta + A} W + \frac{nW}{\eta + A}'' - \frac{nW'}{(\eta+A)^2} \right) \right] g + \frac{\mathrm{Gr}}{Re} \hat{\theta}'$$
$$= i\alpha \mathrm{Re} c \left[-f'' - \frac{1}{\eta + A} f' + \left(\frac{1}{\eta + A^2} + \alpha^2 \right) f + \frac{\alpha n}{\eta + A} g \right] \quad (7a)$$

$$nf''' + \frac{2n}{\eta + A} f'' + \left[-\frac{n^3 + n}{(\eta+A)^2} - \alpha^2 n - i\alpha n \mathrm{Re} W \right] f'$$
$$+ \left[-\frac{3\alpha^2 n}{\eta + A} - \frac{n^3 - n}{(\eta+A)^3} + i\alpha n \mathrm{Re} \left(-\frac{W}{\eta + A} + W' \right) \right] f$$
$$+ (-\alpha(\eta + A)) g''' - \alpha g'' + \left[\alpha^3 (\eta + A) + \frac{\alpha + \alpha n^2}{\eta + A} \right.$$
$$\left. + i\alpha^2 \mathrm{Re} W (\eta + A) \right] g' + \left[-\frac{2n^2 \alpha}{(\eta+A)^2} + in^2 \mathrm{Re} \frac{W'}{\eta + A} \right] g$$
$$+ n \frac{\mathrm{Gr}}{\mathrm{Re}} \theta = i\alpha \mathrm{Re} c \left[-nf' - \frac{n}{\eta + A} f + \alpha(\eta + A) g' \right] \quad (7b)$$

$$\hat{\theta}'' + \frac{1}{\eta + A} \hat{\theta}' + \left[-\frac{n^2}{(\eta+A)^2} - \alpha^2 - i\alpha \mathrm{RePr} W \right] \hat{\theta}$$
$$+ [i\alpha \mathrm{RePr} \Theta'] f + \left[in\mathrm{RePr} \frac{\Theta'}{\eta + A} \right] g = -i\alpha c \mathrm{RePr} \hat{\theta} \quad (7c)$$

where a prime denotes differentiation with respect to η.

These equations represent a ninth-order system. Eight boundary conditions, which reflect the no-slip, no-penetration, and constant-temperature conditions on the inner and outer cylinders, are given below:

$$g'(0) = \alpha f(0) + \frac{n}{A} g(0) = f'(0) + \frac{f(0)}{A} = \theta(0) = 0 \quad (8a)$$

$$g'(1) = \alpha f(1) + \frac{n}{1 + A} g(1) = f'(1) + \frac{f(1)}{1 + A} = \theta(1) = 0 \quad (8b)$$

The ninth boundary condition establishes a datum for the streamfunctions and is by

$$g(0) = 0 \quad (8c)$$

Equations (6*a*) through (6*c*) and the boundary conditions form a complex eigenvalue problem. The stability boundary in the (Re, Gr, n, α) space is determined by the point at which the imaginary component of the complex wave speed c_i is equal to zero, with the disturbance being unstable for c_i greater than zero. This also forms a minimax problem with $c_i = 0$ where Re and Gr/Re are local minima for various wave numbers α and η. A large number of calculations is required to establish the projection of the stability boundary on the (Gr/Re, Re) plane. The computational method is described in the next section.

3. Method of Solution

A pseudospectral Chebyshev method is used to discretize the equations and incorporate the boundary conditions (Orszag, 1971). The collocation points are selected to be the extrema of the Nth order Chebyshev polynomial so that the truncation error is minimized. The eigenvalues of the resulting matrix are determined with the aid of a complex QR algorithm as described by Moler and Stewart (1973).

The convergence of the numerical scheme has been checked by varying the number of collocation points. It has been found that 51 terms are usually sufficient. For large N, more terms are needed to avoid spurious roots. It was observed that true roots always appear when the number of discretization terms is changed. On the other hand, the spurious roots usually appear as a group and their values change drastically when N is altered. A great deal of care was exercised to ensure the most unstable eigenvalues were identified.

The accuracy and validity of the numerical scheme was checked by favorable comparisons with published results in the limiting cases mentioned earlier: (1) plane Posieuille flow, and (2) natural convection in a two-dimensional slot.

To compare our results with those of a two-dimensional channel, we set $A = 1000$. In this case, as $\mathrm{Gr} \to 0$, the basic flow approaches plane Poiseuille flow. In a careful numerical study of this problem, Orszag (1971) found the wave speed of the most unstable disturbance at $\mathrm{Re} = 13333$, $\alpha = 2.0$, and $n = 0$. Our calculation of this parameter agrees with his result to five significant figures.

With $A = 1000$, as $\mathrm{Re} \to 0$ the situation becomes that of natural convection between infinite parallel plates maintained at different temperatures. Korpela et al. and (1973) have determined that the critical point lies at $\mathrm{Gr} = 8038$ and $\alpha = 2.8$. Using a linear interpolation of the imaginary component of the complex wave speed between its values at $\mathrm{Gr} = 8000$ and $\mathrm{Gr} = 8100$ at wavenumbers of $\alpha = 2.7$, 2.8, and 2.9, then using a quadratic interpolation in α of these results, we find the critical condition to be $\mathrm{Gr} = 8015$ at $\alpha = 2.8$, a difference in the critical Grashof number of about 0.3 percent. The critical wave speed that we predict at this condition is $c_r \approx 10^{-5}$. This is consistent with the results of Korpela et al. (1973) for natural convection in a two-dimensional slot, in which it is found that the Prandtl number less than 12.7, the disturbances are stationary.

4 Results and Discussion

The following results are for $\mathrm{Pr} = 0.71$ and $A = 100$. The complete stability boundary on the (Re, Gr/Re) plane is shown in Fig. 4. Positive Gr indicates that the inner cylinder is heated while negative Gr implies that the outer cylinder is at a higher temperature. Axial wavenumber and the disturbance wave speed are plotted as functions of the Reynolds number in Figs. 5 and 6 for positive Gr.

In all cases, it was found that the first several azimuthal modes become unstable at the same time. For example, at $\mathrm{Re} = 7000$, the critical value of Gr/Re is found to be 47.43 for the first five azimuthal modes ($n = 0$–4). At $n = 5$, this value increases to 47.44; at $n = 10$, $\mathrm{Gr/Re} = 47.45$; at $n = 15$, $\mathrm{Gr/Re} = 47.48$; and at $n = 30$, $\mathrm{Gr/Re} = 47.60$. Thus, the trend is that the higher azimuthal modes are slightly more stable than those at smaller n. As the disturbance grows, however, it is not clear which mode will be dominant. Thus, even though the linear stability boundary is sufficiently determined from investigation of the axial disturbances only, a nonlinear stability analysis must account for all of the relevant azimuthal modes as well.

Investigation of Fig. 4 reveals that the instability boundary is similar for both positive and negative Gr. This indicates that the effect of wall curvature is minimal and the stability

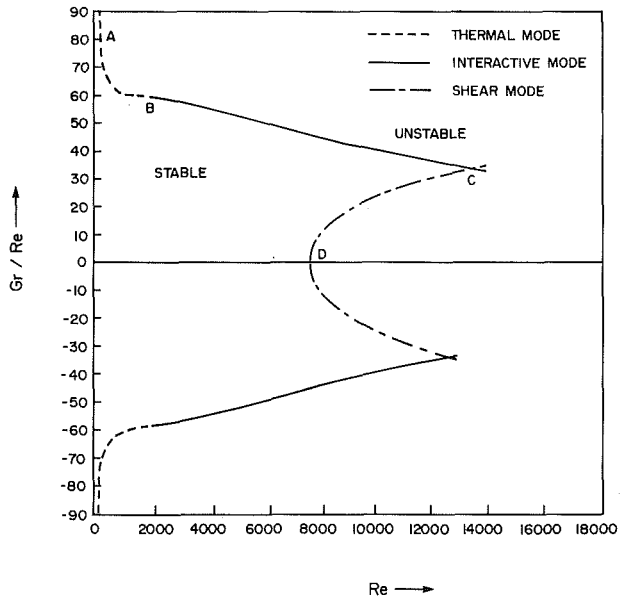

Fig. 4 Marginal stability boundary for $A = 100$

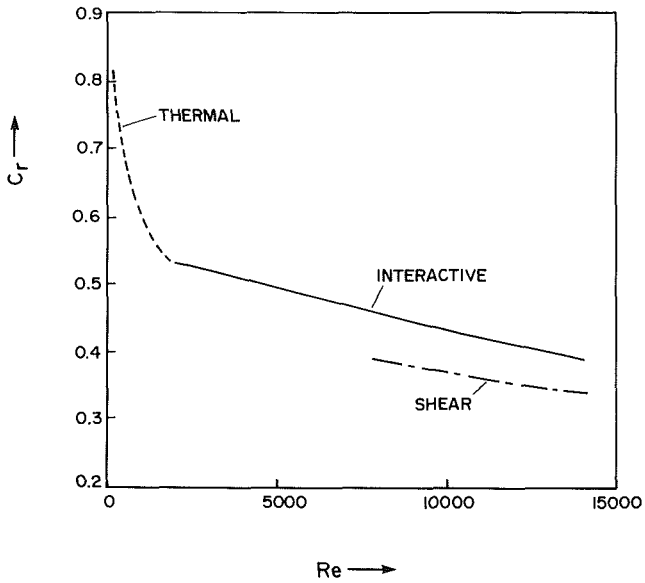

Fig. 6 Disturbance wave speed versus Re for thermal, interactive, and shear instabilities

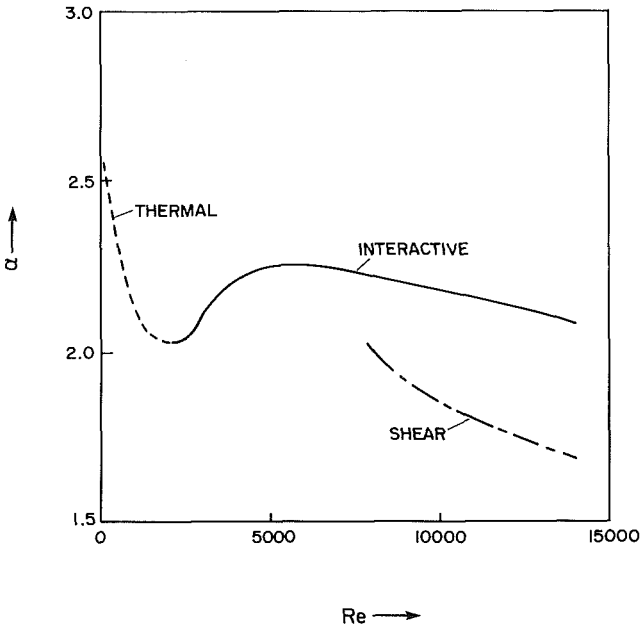

Fig. 5 Axial wavenumber versus Re for thermal, interactive, and shear instabilities

behavior is very close to that of a two-dimensional channel flow. In addition to the symmetry of the instability curves about the Gr = 0 axis, the other parameters of interest, such as axial and azimuthal wavenumbers and the disturbance wave speed, are also similar for each case. Thus, only the results for positive Gr will be discussed in detail in this paper.

The instability boundary shown in Fig. 4 can be separated into three distinct curves. The instability that occurs at small Gr is labeled as the shear instability since it occurs due to the shear flow in the duct. At small Reynolds numbers and larger Grashof numbers the instability is referred to as the thermal mode since the buoyant forces play a dominant role. In between these regions is the interactive instability. The shear and interactive instabilities are clearly identifiable in the region in which they intersect. The curves are distinct and they continue beyond the point of intersection. However, the boundary between the interactive and thermal instabilities is not so obvious. The curves blend smoothly together and no distinguishing characteristics, such as wavenumber or disturbance velocity, can be used to separate the instabilities. At small Re, the instability boundary curve is very steep, and small changes in Re lead to substantial changes in the critical Gr/Re. After about Re = 2000, however, the curve changes slope so that a nearly straight line of moderate slope is formed. In addition, investigation of the axial wavenumber and wave speed as functions of Re, plotted on Figs. 5 and 6, shows that, even though the curves are continuous, the evolution of these properties changes significantly at about Re = 2000. The critical disturbance wave speed decreases rapidly with increasing Re at small Re. After about Re = 2000, however, the curve changes slope and the decrease becomes more moderate. The axial wavenumber also initially decreases rapidly with increasing Re to about Re = 2000, after which point the shape of the curve changes. Thus, it is clear that the instability changes character at about Re = 2000, and the boundary between the thermal and interactive instabilities is assumed to be this point, with the thermal instability governing for small Re and the interactive for larger.

Near the point labeled *D* in Fig. 4, it is seen that the heating initially stabilizes the flow. With no heating, the shear flow becomes unstable at about Re = 7730, which is in close agreement with the results of Thomas (1953) for the linear stability of plane Poiseiulle flow. As Gr increases, however, the critical Re for the shear instability also increases up to a maximum value of about Re = 13,600 at Gr/Re = 34, at which point the shear and interactive instability curves intersect.

In Fig. 5 it is shown that the wave number decreases with increasing Re, from $\alpha = 2.03$ at Re = 7730 to $\alpha = 1.69$ at Re = 14,000. The wave speed, shown in Fig. 6, also decreases with increasing Re, from $c_r = 0.39$ at Re = 7730 to $c_r = 0.34$ at Re = 14,000.

With the interactive instability, investigation of Fig. 4 reveals that increasing Re has a slight destabilizing effect on the flow. As Re increases, the critical value of Gr/Re decreases. The curve forming the interactive instability boundary forms very nearly a straight line from Re = 2000, Gr/Re = 60 to Re = 14,000 and Gr/Re = 33, near the intersection with the shear instability curve.

The interactive axial wave number initially increases from $\alpha = 2.02$ at Re = 2000 to $\alpha = 2.25$ at Re = 5000, as shown on Fig. 5. After this point, the wavenumber decreases to $\alpha = 2.08$

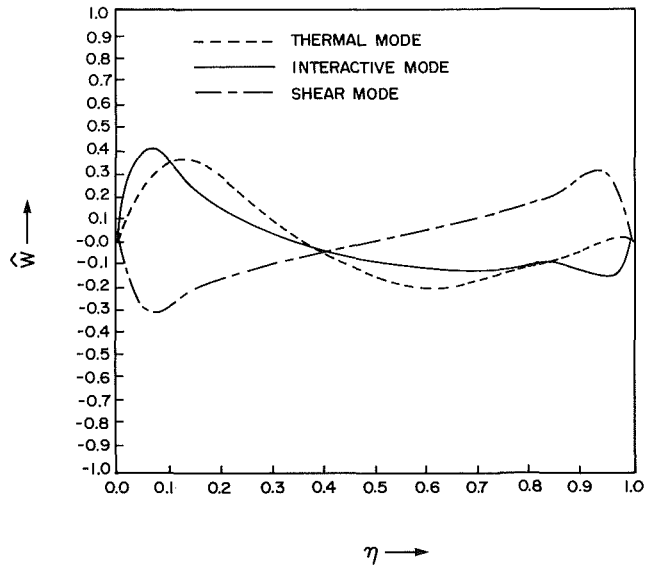

Fig. 7 Eigenfunctions of *w*: thermal mode—Re = 150, Gr/Re = 90.1, $\alpha = 2.55$; Interactive mode—Re = 7000, Gr/Re = 47.4, $\alpha = 2.24$; shear mode—Re = 7730, Gr/Re = 0, $\alpha = 2.03$

at Re = 14,000. The wave speed for the interactive instability decreases with increasing Re, as shown on Fig. 6, from a value of $c_r = 0.53$ at Re = 2000 to $c_r = 0.39$ at Re = 14,000. At Re = 14,000, the shear disturbance wave speed is $c_r = 0.34$ and the shear wave number is $\alpha = 1.69$. Thus, in the region of intersection with the shear instability, the interactive disturbance can be identified from the shear disturbance by a larger wave speed and a shorter wavelength.

Investigation of the curve for the thermal instability in Fig. 4 shows that the critical Gr/Re is quite sensitive to Re. The value of Gr/Re decreases from 90 at Re = 150 to 60 at Re = 2000. The disturbance wave speed c_r also decreases significantly with increasing Re, as shown in Fig. 6. At Re = 150, the wave speed is 0.82, and at Re = 2000 this value has decreased to 0.53. Extrapolation of the wave speed versus Re curve in Fig. 6 shows that as Re goes to zero, the wave speed approaches the mean velocity, which in the case of Re = 0 corresponds to a stationary disturbance. This agrees with the result from the instability of natural convection in a slot (Vest and Arpaci, 1969). As the Reynolds number increases, the cells begin to drift with the mean flow, but the dimensionless velocity, the ratio of the absolute speed to that of the mean flow, decreases. As the mass flow rate increases, the structure of the secondary flow will be modified by nonlinear effects and it is expected that the eventual state will be that of vertical spirals (Yao, 1987a). The axial wave number α decreases from 2.55 at Re = 150 to 2.02 at Re = 2000. Thus, the thermal instability will occur at small Re and will be characterized in part by higher dimensionless wave speeds than those occurring with the interactive and shear instabilities.

Insight into the shape of the disturbances in the radial direction can be gained from investigation of the shape of the most unstable eigenvectors. These results are plotted for each mode in Fig. 7. The eigenfunction of the axial disturbance velocity for the thermal instability is plotted at Re = 150, Gr/Re = 90, and $\alpha = 2.55$. Investigation of Fig. 7 reveals that the disturbance consists of a large rotating vortex with its streamlines concentrated near the inner, or heated, wall. Near the outer wall the flow is quite stagnant, but there may be a smaller vortex near this wall rotating in the opposite direction from the large vortex near the inner wall. The shear instability eigenvector is plotted at Re = 7728 and Gr/Re = 0. In this case, the disturbance is a single rotating vortex the shape of which is symmetric with respect to the center of the duct. The interactive instability is plotted at Re = 7000 and Gr/Re = 47.4. This disturbance also consists of a single vortex, but in this case, thermal effects have caused the streamlines to be concentrated near the warmer wall.

5 Conclusion

It has been demonstrated that the linear stability of mixed convection in an annulus with an aspect ratio of 100 approaches that of a two-dimensional vertical slot, and the flow is unstable in regions of practical interest in an appropriate parameter space. Therefore, steady parallel mixed convection flows with reverse flow regions, predicted by some idealized numerical and analytical models, are unlikely to be observed experimentally, except possibly at extremely small Re. Heat transfer correlations developed from numerical techniques that fail to account for mixing caused by unsteady secondary flows induced by hydrodynamic instabilities are likely to underpredict the actual heat transfer rates.

The marginal stability boundary is found to be formed by three types of instability. At low speeds, the thermal instability is dominant. At higher speeds and low heating, the flow becomes unstable to a shear instability. Between these cases is the interactive instability. The shear and interactive instabilities can be identified from each other in the regions in which they intersect by different disturbance wave speeds and axial wave numbers, with the shear instability disturbance being characterized by a slower wave speed and a smaller axial wave number than that of the interactive instability. The intersection of the shear and interactive instabilities can be clearly identified since the curves continue past their point of intersection. The intersection of the thermal and interactive instabilities is not as easy to identify, however. The boundary between the thermal and interactive instabilities is determined by a change in the evolution, with increasing Re, of the disturbance wave speed and the axial wave number. The thermal instability disturbance will have a higher wave speed than that of the interactive instability, but the value of the axial wave number can not be used to distinguish between the instabilities.

The most unstable azimuthal disturbance was not determined accurately by this analysis. In the limit of either a two-dimensional isothermal channel flow or a two-dimensional natural convection flow between vertical walls maintained at different temperatures, Squire's theorem predicts that the most unstable mode is two-dimensional. It might be expected that the most unstable mode for a mixed convection flow, which lies between these two limiting cases, will also be two-dimensional. However, because of the presence of the Gr/Re term in the axial momentum equation, the derivation of a corresponding result for mixed convection in a vertical duct cannot be achieved.

References

Aung, W., and Worku, G., 1986, "Developing Flow and Flow Reversal in a Vertical Channel With Asymmetric Wall Temperatures," ASME JOURNAL OF HEAT TRANSFER, Vol. 108, pp. 299-304.

Aung, W., and Worku, G., 1986, "Theory of Fully Developed Combined Convection Including Flow Reversal," ASME JOURNAL OF HEAT TRANSFER, Vol. 108, pp. 485-488.

Elder, J. W., 1965, "Laminar Free Convection in a Vertical Slot," *J. Fluid Mechanics*, Vol. 23, pp. 77-98.

El-Shaarawl, M. A. I., and Sarhan, A., 1980, "Free Convection Effects on the Developing Laminar Flow in Vertical Concentric Annuli," ASME JOURNAL OF HEAT TRANSFER, Vol. 102, pp. 617-622.

Habchi, S., and Acharya, S., 1986, "Laminar Mixed Convection in a Symmetrically or Asymmetrically Heated Vertical Channel," *Numerical Heat Transfer*, Vol. 9, pp. 605-618.

Hart, J. E., 1971, "Stability of the Flow in a Differentially Heated Inclined Box," *J. Fluid Mechanics*, Vol. 47, pp. 547-576.

Hashimoto, K., Akino, N., and Kawamura, H., 1986, "Combined Forced Free Laminar Heat Transfer to a Highly Heated Gas in a Vertical Annulus," *Int. J. Heat Mass Transfer*, Vol. 29, No. 1, pp. 145–151.

Kemeny, G. A., and Somers, E. V., 1912, "Combined Free and Forced Convective Flow in Vertical Circular Tubes—Experiments With Water and Oil," ASME JOURNAL OF HEAT TRANSFER, Vol. 84, pp. 339–346.

Kim, J. H., 1985, "Analysis of Laminar Natural Convection Superimposed on Downward Flow in a Vertical Tube Annulus," ASME Paper No. 85-WA/HT-13.

Korpela, S. A., Gozum, D., and Chandrakant, B. B., 1973, "On the Stability of the Conduction Regime of Natural Convection in a Vertical Slot," *Int. J. Heat Mass Transfer*, Vol. 16, pp. 1683–1689.

Maitra, D., and Raju, K. S., 1975, "Combined Free and Forced Convection Laminar Heat Transfer in a Vertical Annulus," ASME JOURNAL OF HEAT TRANSFER, Vol. 97, pp. 135–137.

Moler, C. B., and Stewart, G. W., 1973, "An Algorithm for Generalized Matrix Eigenvalue Problems," *SIAM J. Numer. Anal.*, Vol. 10, pp. 241–256.

Orszag, S. A., 1971, "Accurate Solution of the Orr-Sommerfeld Stability Equation," *J. Fluid Mech*, Vol. 50, pp. 689–703.

Quintiere, J., and Mueller, W. K., 1973, "An Analysis of Laminar Free and Forced Convection Between Finite Vertical Parallel Plates," ASME JOURNAL OF HEAT TRANSFER, Vol. 95, pp. 53–59.

Scheele, G. F., and Hanratty, T. J., 1962, "Effect of Natural Convection on Stability of Flow in a Vertical Pipe," *J. Fluid Mech.*, Vol. 14, pp. 244–256.

Shumway, R. W., and McEligot, D. M., 1971, "Heat Laminar Gas Flow in Annuli With Temperature Dependent Transport Properties," *Nuc. Sci. Eng.*, Vol. 46, 1953, pp. 394–407.

Thomas, L. H., 1953, "The Stability of Plane Poiseuille Flow," *Physical Review*, Vol. 91, pp. 780–783.

Vest, C. M., and Arpaci, V. S., 1969, "Stability of Natural Convection in a Vertical Slot," *J. Fluid Mech.*, Vol. 36, pp. 1–15.

Yao, L. S., 1987, "Is Fully-Developed and Non-isothermal Flow Possible in a Vertical Pipe?" *Int. J. Heat Mass Transfer*, Vol. 30, pp. 707–716.

Yao, L. S., 1987, "Linear Stability Analysis for Opposing Mixed Convection in a Vertical Pipe," *Int. J. Heat Mass Transfer*, Vol. 30, pp. 810–811.

Yao, L. S., and Rogers, B. B., 1988, "The Linear Stability of Mixed Convection in a Vertical Annulus," *Journal of Fluid Mechanics*, in press.

Zeldin, B., and Schmidt, F. W., 1972, "Developing Flow With Combined Forced Free Convection in an Isothermal Vertical Tube," ASME JOURNAL OF HEAT TRANSFER, Vol. 94, pp. 211–223.

Prediction of Conjugate Heat Transfer in a Solid-Liquid System: Inclusion of Buoyancy and Surface Tension Forces in the Liquid Phase

J. R. Keller

T. L. Bergman
Assistant Professor.
Assoc. Mem. ASME

Department of Mechanical Engineering,
The University of Texas at Austin,
Austin, TX 78712

Numerical predictions have been obtained for steady-state conjugate heat transfer in an open rectangular cavity. For the geometry considered, fluid motion is driven by augmenting buoyancy and surface tension forces. Predictions of the steady-state solid volume fraction and various solid thicknesses were obtained for a high Prandtl number fluid characterized by various Rayleigh and Marangoni (Ma) numbers. Due to numerical difficulties associated with large surface tension effects, a limited range of Ma was investigated ($Ma \leq 250$). The predictions show that surface tension induced flow can affect the solid geometry and, ultimately, freezing or melting rates. Specifically, the solid-liquid interface shape is altered, the steady-state solid volume fraction is decreased, and the solid thickness at the top surface is smaller, compared to the pure buoyancy-driven case. The dimensionless solid volume fraction and solid thicknesses are related to the governing dimensionless parameters of the problem. Finally, predictions are made for high Marangoni number flows ($Ma >> 250$) to demonstrate the potential governing influence of surface tension effects in phase-change systems.

Introduction

Natural convection is known to play an important role in the solid-liquid phase-change process (Viskanta, 1985). For example, casting and crystal growth applications are affected by the fluid motion induced by buoyancy forces in the melt. The fluid motion and heat transfer associated with natural convection affect freezing or melting rates, the solid-liquid interface shape (Sparrow et al., 1977), and, ultimately, the final solid properties such as its strength or elasticity (Zierep and Oertel, 1982).

Many solid-liquid phase-change processes are characterized by systems with free liquid surfaces. If a temperature gradient exists along the free surface, thermal variations in the surface tension can induce a shear stress at the free surface and, in turn, drive fluid motion in the melt (Zebib et al., 1985); Schwabe et al., 1978). This thermocapillary or Marangoni convection can, in general, augment or oppose the buoyancy driven flow and significantly enhance or reduce local and overall heat transfer rates (Villers and Platten, 1985; Bergman and Ramadhyani, 1986). Since surface tension forces can affect heat transfer rates and since these rates, in turn, govern the solidification or melting process, it follows that combined surface tension-buoyancy flows will induce solidification or melting phenomena that are different from the pure buoyancy-driven case. An extreme example is that of welding, where surface tension forces dominate over buoyancy forces (Oreper and Szekely, 1984). The extreme cases of negligible surface tension or buoyancy effects will not be emphasized here; rather, the case of combined effects is of primary interest.

Phenomena due to combined buoyancy and surface tension forces in the liquid phase were first considered by Stanek and Szekely (1970) who were interested in a process similar to the phase-change problem; erosion of a vertical slab subjected to convection in an adjacent fluid layer driven by solutal surface tension and buoyancy forces. Their numerical predictions showed that surface tension induced convection was responsible for significant solid erosion near the free surface. Other applications have been identified that are characterized by combined surface tension-buoyancy driven flows within the melt (Hurle and Jakeman, 1984; McNiel et al., 1986; Kou, 1987); however, the convection effect on the phase-change process was not investigated. To the authors' knowledge, the only work to specifically address the effect of combined buoyancy-surface tension flow and its influence on the solidification process has dealt with *n*-octadecane but did not systematically examine surface tension effects on the phase change process in a quantitative manner (Munakata and Tanasawa, 1986).

It is interesting to note that the influence of surface tension on solid-liquid phase change has been largely ignored in the literature. For example, Webb and Viskanta (1985) have discussed the difficulties that occur when attempting to correlate liquid volume fractions with dimensionless convection parameters, which exclude surface tension effects. Perhaps the inclusion of appropriate surface tension related parameters would lead to more successful collapse of the data.

Since little systematic work has been done to investigate combined buoyancy-surface tension flow and its impact on solid-liquid phase change, the present study was conducted. As a first step, consideration is given to a steady-state solid-liquid system in order to focus attention on the influence of surface tension forces on the heat transfer at a solid-liquid interface. Although the transient problem is, of course, more relevant, the influence of surface tension is clouded by the introduction of additional dimensionless parameters, such as the Stefan number and subcooling parameter, which also govern the system response.

The system considered here is a partial solid-liquid material contained in a rectangular enclosure. The case of augmenting buoyancy and surface tension forces will be examined since

Contributed by the Heat Transfer Division for publication in the JOURNAL OF HEAT TRANSFER. Manuscript received by the Heat Transfer Division June 14, 1988. Keywords: Materials Processing and Manufacturing Processes, Natural Convection, Thermocapillary Flows.

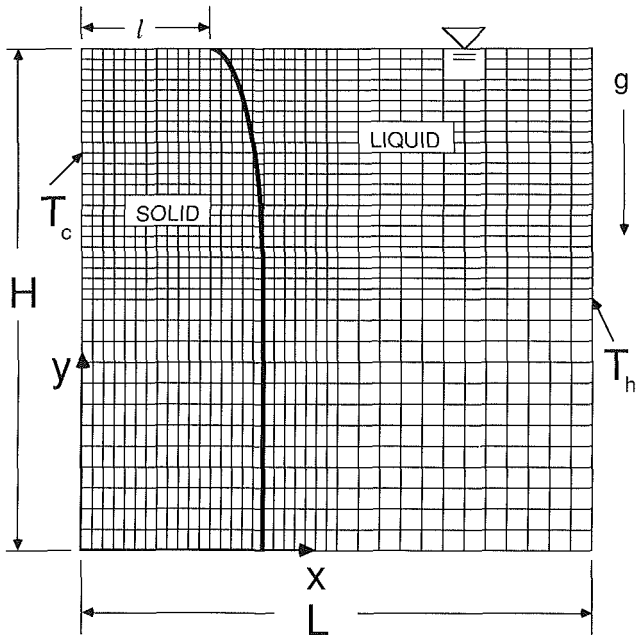

Fig. 1 Schematic of the physical and coordinate systems

opposing surface tension and buoyancy forces occur almost exclusively in binary fluids (Jasper, 1972), which would require a transient analysis (since solidification is history dependent in binary systems) and the possible inclusion of a two-phase mushy zone.

Analysis

As a first step in understanding the effect of liquid surface tension and buoyancy forces on phase change processes, a simple system, shown in Fig. 1, is considered. A solid and liquid of the same material are contained in a two-dimensional rectangular enclosure of height H and length L. The left and right walls are maintained at temperatures T_c and T_h, respectively. Here, T_c is below the fusion temperature T_f, and T_h is above the fusion temperature. The free surface ($y = H$) and the bottom boundary ($y = 0$) are adiabatic. With the prescribed boundary conditions, the thermally induced variation of surface tension along the free surface and buoyancy forces within the liquid will induce fluid motion. Variations in the local heat transfer rates at the solid-liquid interface will lead to variations in the thickness of the solid material.

In order to simplify the analysis, certain assumptions, consistent with recent numerical analyses of combined surface tension-buoyancy driven flow (Villers and Platten, 1985; Bergman and Ramadhyani, 1986), and phase-change processes (Benard et al., 1986) have been made. For the melt, the free surface is assumed to be flat and nondeformable. The Boussinesq approximations are employed in treating the thermal density variations, surface tension is assumed to vary lineraly with temperature, and the densities of the solid and liquid phases are identical. The flow is assumed to be steady and laminar and viscous dissipation is neglected.

With these assumptions, the governing equations for the fluid are:

Continuity:

$$\frac{\partial u}{\partial x}+\frac{\partial v}{\partial y}=0 \tag{1}$$

x Momentum:

$$\frac{\partial}{\partial x}(\rho uu)+\frac{\partial}{\partial y}(\rho uv)=\frac{\partial}{\partial x}\left(\mu\frac{\partial u}{\partial x}\right)+\frac{\partial}{\partial y}\left(\mu\frac{\partial u}{\partial y}\right)-\frac{\partial P}{\partial x} \tag{2}$$

y Momentum:

$$\frac{\partial}{\partial x}(\rho uv)+\frac{\partial}{\partial y}(\rho vv)=\frac{\partial}{\partial x}\left(\mu\frac{\partial v}{\partial x}\right)+\frac{\partial}{\partial y}\left(\mu\frac{\partial v}{\partial y}\right)-\frac{\partial P}{\partial y}+g\beta\rho(T-T_{\text{ref}}) \tag{3}$$

Energy:

$$\frac{\partial}{\partial x}(\rho uT)+\frac{\partial}{\partial y}(\rho vT)=\frac{\partial}{\partial x}\left(\frac{k_1}{c_{p,1}}\frac{\partial T}{\partial x}\right)+\frac{\partial}{\partial y}\left(\frac{k_1}{c_{p,1}}\frac{\partial T}{\partial x}\right) \tag{4}$$

Nomenclature

A = aspect ratio $= H/L$
Bo = Bond number $= g\beta\rho L^2/(\partial\sigma/\partial T)$
c_p = specific heat
g = gravitational acceleration
H = height
h = liquid heat transfer coefficient $= q''/(T_h - T_f)$
k = thermal conductivity
k^* = conductivity ratio $= k_s/k_1$
l = solid thickness
L = cavity length
L^* = normalized solid thickness $= (l/L)/(l/L)_{cs}$
Ma = Marangoni number $= (\partial\sigma/\partial T)\Delta TL/\mu\alpha$
$\overline{\text{Nu}}$ = average Nusselt number $= hL/k$
P = pressure
Pr = Prandtl number $= \nu/\alpha$
q'' = wall heat flux
Ra = Rayleigh number $= g\beta\Delta TL^3/\nu\alpha$
T = temperature
u = horizontal velocity
v = vertical velocity
V = volume fraction
V^* = normalized volume fraction $= V/V_{cs}$
x = horizontal direction
y = vertical direction
α = thermal diffusivity
β = thermal expansion coefficient
θ = dimensionless liquid temperature $= (T - T_f)/(T_h - T_f)$
θ^* = dimensionless cavity temperature $= (T_f - T_c)/(T_h - T_c)$
μ = dynamic viscosity
ν = kinematic viscosity
ρ = density
σ = surface tension
Ψ = stream function

Subscripts

b = bottom
c = cold wall
cs = conduction solution
dif = diffusion methodology solution
f = fusion temperature
h = hot wall
l = liquid
max = maximum
ref = reference
s = solid
T = top

For the solid:

$$\frac{\partial}{\partial x}\left(\frac{k_s}{c_{p,s}}\frac{\partial T}{\partial x}\right)+\frac{\partial}{\partial y}\left(\frac{k_s}{c_{p,s}}\frac{\partial T}{\partial y}\right)=0 \tag{5}$$

The hydrodynamic boundary conditions include the no-slip requirement at the hot wall, cold wall, and the cavity bottom. The free surface hydrodynamic boundary conditions are

$$\mu\frac{\partial u}{\partial y}\bigg|_{y=H}=\frac{\partial\sigma}{\partial T}\frac{\partial T}{\partial x}\bigg|_{y=H} \tag{6}$$

$$v|_{y=H}=0 \tag{7}$$

The shear stress on the left-hand side of equation (6) is responsible for the surface tension convection and occurs whenever the surface tension of the liquid phase varies with the liquid temperature.

The thermal boundary conditions are

$$T=T_c|_{x=0} \qquad T=T_h|_{x=L} \tag{8}$$

and

$$\frac{\partial T}{\partial y}=0\bigg|_{y=0,\,y=H}$$

As will become evident, the solution techniques used in the analysis do not require implementation of coupling conditions at the solid–liquid interface.

If the governing equations and boundary conditions are normalized with appropriate scaling factors, the following dimensionless parameters are found to govern system behavior:

Rayleigh number $\quad \mathrm{Ra}=g\beta\Delta TL^3/(\nu\alpha)$ (9)

Prandtl number $\quad \mathrm{Pr}=\nu/\alpha$ (10)

Marangoni number $\quad \mathrm{Ma}=\left(\frac{\partial\sigma}{\partial T}\right)\frac{\Delta TL}{\mu\alpha}$ (11)

Cavity aspect ratio $\quad A=H/L$ (12)

Conductivity ratio $\quad k^*=k_s/k_1$ (13)

where $\Delta T=T_h-T_f$. The dynamic Bond number, which is the ratio of buoyancy forces to surface tension forces in the melt, is useful to consider when examining the predictions and is defined as

$$\mathrm{Bo}=\mathrm{Ra}/\mathrm{Ma}=\rho g\beta L^2/(\partial\sigma/\partial T) \tag{14}$$

Relatively large Bond numbers indicate buoyancy-dominated flow, while smaller Bond numbers suggest surface tension dominated conditions.

It is noted that the dimensionless parameters of the problem are based on the cavity length L, whereas a more relevant length scale might be the average liquid layer thickness. Selection of L as the characteristic length is necessary since the liquid layer thickness is not known *a priori*. In addition, most relevant studies of phase change are concerned with the transient system response. By considering the steady-state problem, three dimensionless parameters, the Fourier number, the Stefan number, and the subcooling parameter, are no longer relevant to the problem. With the elimination of these parameters, attention can be focused on the interaction of surface tension and buoyancy forces on the conjugate heat transfer in the system. This approach is taken here.

Solution Technique

Solution of the governing equations was obtained numerically by employing the control volume based discretization technique and the SIMPLER algorithm (Patankar, 1980). A composite grid, shown in Fig. 1, with fixed, equally spaced control volumes in each quadrant, was used to resolve the important details of the flow and predict the interface shape and location.

In order to predict the solid–liquid interface location as well as the heat conduction in the solid, the governing equations of mass, momentum, and energy are applied to the entire calculation domain. Since the velocities in the solid are zero, the conservation of energy equation (4) reduces to the heat equation (5). To achieve this simplification numerically, the dynamic viscosity μ is set to a very large value in the solid region.

The initial guess for the temperature distribution in the domain is the conduction solution. Control volume properties are evaluated and assigned by assuming the individual control volumes are either solid or liquid, depending on the control volume temperature. Upon solution of the equations, a new temperature distribution is predicted, the control volume properties are reassigned, and the governing equations are resolved. The procedure of control volume property reassignment and subsequent solution of the governing equations is repeated until the interface location is fixed and the heat transfer rates at the cold and hot walls agree to within 2 percent. The solid thickness at any y location is ultimately determined by locating T_f with a linear interpolation scheme.

The modified orthogonal grid provides fine node spacing near the solid–liquid interface to resolve the shape and location of the interface. Although employment of a gradually varying grid size adjacent to the solid–liquid interface may provide increased resolution of the details of the flow, this scheme was not employed since the interface location is not know *a priori*. Cartesian grids are commonly used in conjugate heat transfer problems with nonorthogonal boundaries (Patankar, 1980) and it is noted that Cartesian grids are employed in enthalpy-based phase change simulations (Bennon and Incropera, 1987). While the orthogonal grid does not align with the position of the interface, the model gives reasonable results if the grid is made acceptably fine and, as will become evident, the results are nearly grid independent. In far-field regions away from the solid–liquid interface, a more coarse grid (characteristic dimensions of the course grids are twice those of the fine grids) is used.

The numerical limitations associated with the use of the Cartesian grid are perhaps overshadowed by a serious numerical difficulty, which occurs when surface tension effects are considered in any convective heat transfer problem. A numerical singularity occurs at the cold wall boundary (i.e., the free surface–solid–liquid intersection, Zehr et al., 1987), which requires an even finer grid spacing at this location than is normally demanded due to considerations associated with grid alignment at the solid–liquid interface. Specifically, care must be taken to ensure that maximum horizontal surface velocities do not occur in the computational grid adjacent to the solid–liquid interface. Even with the grid packing scheme described here, a maximum Ma of 250 was determined to be allowable by way of a grid dependence study. A detailed description of the surface tension related difficulty is in the Appendix.

Due to the numerical approximations and difficulties associated with the problem, the model was validated to insure proper interpretation of the predicted results. The buoyancy-induced convective portion of the model was verified by comparing the predicted heat transfer across a square, air-filled cavity with heated endwalls to a benchmark numerical solution (de Vahl Davis, 1983). Average Nusselt numbers predicted by the model were within 2 percent of the benchmark values for $\mathrm{Ra}<10^5$. The surface tension convective portion of the model was verified by comparing predictions with those reported by Zebib et al. (1985). Predicted average Nusselt numbers were in agreement within 2 percent for $\mathrm{Ma}<10^4$. The solid–liquid model predictions were compared with the steady-state conduction solution. Various conductivi-

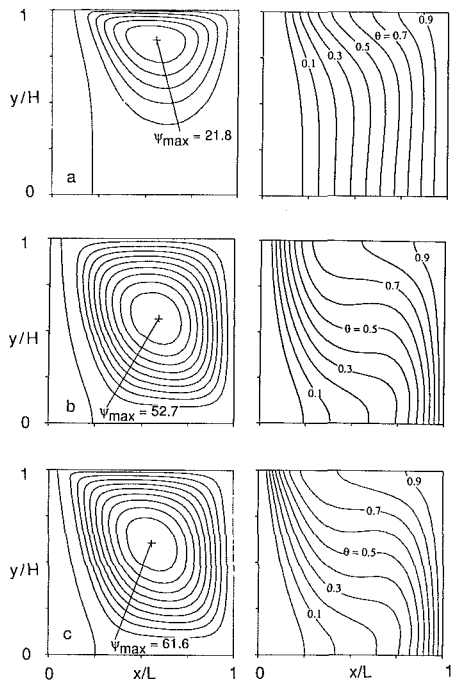

Fig. 2 Predicted streamlines (left) and isotherms (right) for $A = 1.0$, $Pr = 100$, $\theta^* = 0.2$ for (*a*) $Ra = 0$, $Ma = 250$, (*b*) $Ra = 10^4$, $Ma = 0$, and (*c*) $Ra = 10^4$, $Ma = 250$

ty ratios and temperature differences were considered and the predicted volume fractions were within 1 percent of the analytical solutions. An adequately small grid size was determined by simulating conditions for an extreme case, $Ma = 250$ and $Ra = 0$. Local and overall quantities, consisting of the solid thickness at $y = H$, solid thickness at $y = 0$, solid volume fraction, fluid velocities, and overall Nusselt number were examined to determine the grid dependence of the solution. Simulations were made using 32×32, 42×42 and 52×52 grid networks. A 32×32 grid was found to be sufficient to predict the overall quantities; however, a 42×42 grid is required to predict local quantities within an acceptable accuracy. For example, a 15 percent difference in the solid thickness at $y = H$ was noted when the 32×32 results were compared with the 52×52 results, while a 2 percent difference in this quantity was noted between the 42×42 and the 52×52 results. Although a 20 percent decrease in the control volume size (from the 42×42 to the 52×52 grid) may not be sufficient to guarantee a grid-independent solution, a further decrease in the control volume size was deemed prohibitively expensive in light of the number of simulations that were to be performed.

Results

To provide an initial understanding of how surface tension and buoyancy forces may affect fluid motion in the melt and, ultimately, the phase change process, simulations were performed using a high Pr fluid ($Pr = 100$). Low Prandtl number melts were not considered extensively since excessive, yet realistic, Ma values are required to overshadow the relative dominance of conduction in the liquid. Although phenomena associated with liquid metals cannot be quantitatively predicted here, several results are reported, but care must be taken in their interpretation.

For the numerical predictions associated with the $Pr = 100$ results, the conductivity ratio k^* is unity. Simulations were made for $0 \le Ma \le 250$ and $0 \le Ra \le 10^4$ with cavity aspect ratios of 1.0 and 0.5. A dimensionless temperature, describing the relationship between the fusion temperature and the cavity wall temperatures, is defined as

$$\theta^* = (T_f - T_c)/(T_h - T_c) \tag{15}$$

and is held at 0.2 to insure a relatively large liquid fraction and, in turn, placement of the solid-liquid interface inside the fine grid region of the calculation domain.

The figures illustrate the predicted steady-state streamline and isotherm distributions in the liquid phase. The dimensionless streamfunction is determined from the equations

$$\Psi_{x,\,y=0} = \Psi_{x=0,\,y=0} - \frac{1}{\nu}\int_{x=0}^{x} v\,dx \tag{16}$$

$$\Psi_{x,\,y} = \Psi_{x,\,y=0} + \frac{1}{\nu}\int_{y=0}^{y} u\,dy \tag{17}$$

with $\Psi_{x=0,\,y=0}$ taken to be zero. The dimensionless liquid temperature distribution is shown and is defined as

$$\theta = (T - T_f)/(T_h - T_f) \tag{18}$$

with $\theta = 0$ corresponding to the solid-liquid interface.

Predicted System Behavior. Figure 2 includes predicted streamlines, liquid isotherms, and the solid-liquid interface position for the extreme Ra and Ma and $A = 1.0$. Figure 2(*a*), which corresponds to the case of $Ra = 0$ and $Ma = 250$, shows the counterclockwise melt convection resulting from surface tension forces at the liquid free surface. The surface tension induced stress at $y/H = 1$ pulls liquid from the hot enclosure wall to the cool solid-liquid interface. Due to the fluid motion, warm temperatures are advected to the solid-liquid interface near $y/H = 1$. As a result, local heat transfer rates along the solid-liquid interface are maximized near the free surface and the thickness of the solid is minimized at $y/H = 1$. This phenomenon can lead to a significant decrease in the solid thickness at $y/H = 1$ (notching) and will be discussed in more detail later.

Since buoyancy forces are not included in the results of Fig. 2(*a*), fluid motion is relatively slow in the lower half of the enclosure and the center of rotation is at $y/H \cong 0.80$. Since convective effects are most prevalent near the free surface, the solid thickness near $y/H = 0$ is the same as the conduction solution and is located at $x/L = 0.2$.

As buoyancy forces are included in the analysis and surface tension effects are ignored ($Ra = 10^4$, $Ma = 0$; Fig. 2*b*), convective motion occurs throughout the melt. Due to the absence of shear at the free surface, the center of rotation is slightly above $y/H = 0.5$. Local heat transfer at the solid-liquid interface is again maximized at $y/H = 1$, but the solid thickness is decreased everywhere except near the bottom of the enclosure, where a slight increase in its thickness is evident, corresponding to local heat transfer rates slightly less than that which would occur for the conduction solution.

Predicted system behavior when both surface tension and buoyancy forces are considered ($Ra = 10^4$, $Ma = 250$, $Bo = 40$) is shown in Fig. 2(*c*). As expected, the predicted results indicate increased system velocities relative to those in Fig. 2(*b*) ($\Psi_{max} = 61.6$ in Fig. 2*c* while $\Psi_{max} = 52.7$ in Fig. 2*b*) and the center of rotation is between those of Figs. 2(*a*) and 2(*b*). Although the overall heat transfer across the cavity increases ($\overline{Nu} = 8.05$ and 8.29 for Figs. 2*b* and 2*c*, respectively) it is interesting to note that the solid thickness at $y/H = 0$ is greater when surface tension is included in the analysis. This observation is consistent with results predicted for combined buoyancy-surface tension flow in enclosures with differentially heated side walls in the absence of phase change, which show reduced local Nusselt numbers at the lower portions of the cold vertical surface (Bergman and Ramadhyani, 1986).

From the results shown in Fig. 2, it is evident that surface tension and buoyancy forces can interact to vary the steady-state solid fraction and the local solid thickness within the

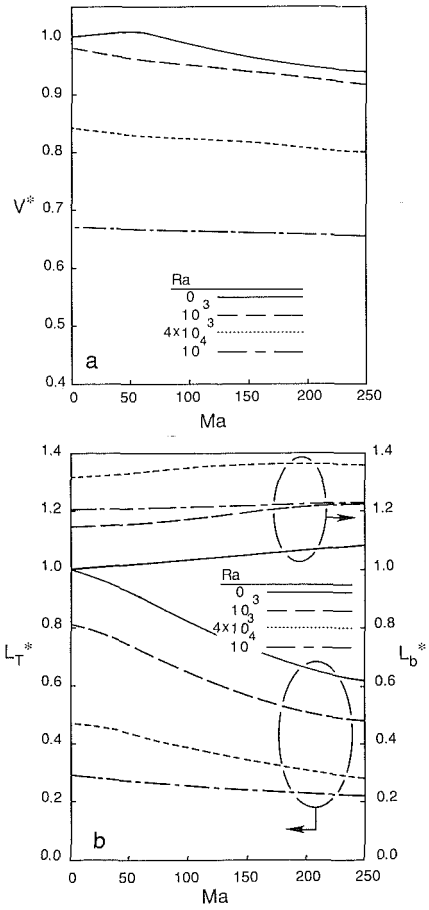

Fig. 3 Predicted normalized (*a*) volume fractions and (*b*) solid thicknesses for the simulations of Fig. 2

system. Figure 3 presents predicted solid volume fractions (Fig. 3*a*) and local solid thicknesses at $y/H=0$ and $y/H=1$ for various Ma and Ra for $A=1.0$ and $\mathrm{Pr}=100$. Again, the results are restricted to $\theta^*=0.2$ and the quantities are normalized by the conduction solution volume fraction and solid thicknesses.

Figure 3(*a*) reveals that, for the ranges of parameters considered here, the normalized solid fraction is nearly independent of surface tension effects. Indeed, as Ra (Bo) is increased, surface tension forces can, for most cases, be ignored. A slight dependence on Ma is evident for the smallest Ra and can be explained in terms of increased Nu as the free surface shear stress, induced by Marangoni phenomena, is included in the analysis.

Although the solid fraction is nearly independent of surface tension effects, local solid thicknesses vary considerably with Ma. Figure 3(*b*) includes the normalized solid thickness at $y/H=1$, L_T^*, and at $y/H=0$, L_b^*. It is evident that L_T^* and L_b^* vary as surface tension is included in the analysis. Specifically, a 35 percent decrease in L^*_T occurs at $\mathrm{Ra}=10^4$ and $\mathrm{Ma}=250(\mathrm{Bo}=40)$ while, at higher Bond numbers, surface tension forces become less influential on system behavior, as expected.

Since the overall solid fraction is nearly independent of surface tension considerations and L_T^* decreases with Ma, it is seen that the increase in solid thickness at $y/H=0$, noted in Fig. 2(*c*), is not an anomaly but is typical of systems of this nature. Inspection of Fig. 3(*b*) shows this effect, with L_b^* increasing with increased surface tension forces for all of the results associated with $A=1.0$.

The results for $A=1.0$ show that surface tension forces may or may not be deemed important, but their influence is more pronounced if local, rather than global, phenomena are of interest. Since surface tension effects are most prevalent at large y/H it is probable that these effects will be amplified for enclosures characterized by a smaller aspect ratio (Kirdyashkin, 1984).

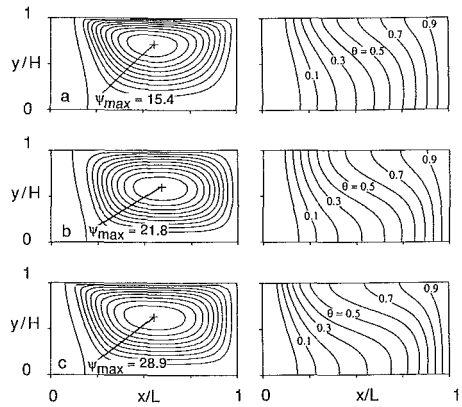

Fig. 4 Predicted streamlines (left) and isotherms (right) for $A=0.5$, $\mathrm{Pr}=100$, $\theta^*=0.2$ for (*a*) $\mathrm{Ra}=0$, $\mathrm{Ma}=250$, (*b*) $\mathrm{Ra}=10^4$, $\mathrm{Ma}=0$, and (*c*) $\mathrm{Ra}=10^4$, $\mathrm{Ma}=250$

Figure 4 presents streamlines, liquid isotherms, and solid-liquid interfaces for conditions identical to those of Fig. 2, except the cavity aspect ratio is reduced to $A=0.5$.

The results of Fig. 4 exhibit phenomena that are similar to that noted in Fig. 2. That is, surface tension forces augment the convection induced by buoyancy effects, resulting in increased fluid velocities near the free surface and a slightly elevated center of fluid rotation. Differences in the results of Figs. 2 and 4 exist, however, and are attributed to the relative strength of the surface tension flow throughout the enclosure. Most notably, inspection of Fig. 4 indicates that L_T^* and L_b^* are all decreased as surface tension forces are included in the analysis.

Figure 5(*a*) shows the normalized solid fraction for conditions bounded by the results of Fig. 4. In contrast to the results of Fig. 3(*a*), the normalized solid fraction decreases as Ma is increased for all Ra considered here. This result is expected, since surface tension effects propagate more readily to small y/H for reduced A. Although enhanced heat transfer and, in turn, thinner solids occur near the free surface (Fig. 4*b*), decreased heat transfer rates and thicker solids do not occur at $y/H=0$ as were noted in the results for $A=1.0$. As such, inclusion of surface tension forces in the analysis of solidification or melting will, in general, have different effects on the local phase change rates, depending on the geometry being considered.

Comparison of the Model to an Existing Methodology. The results reported so far show that surface tension forces in the liquid phase can affect heat transfer rates at the solid-liquid interface and, in turn, the local solid thickness. These effects are most pronounced at the free surface, $y/H=1$. In general, therefore, surface tension effects should be included in conjugate systems characterized by small dynamic Bond numbers. Combined surface tension–buoyancy induced convection and its effect on the solid–liquid interface morphology has been considered previously and differences between the present analysis and that of the original work by Stanek and Szekely (1970) will now be discussed.

In their analysis, Stanek and Szekely predict the solid–liquid interface location by analyzing the surface tension–buoyancy induced flow in a rectangular cavity characterized by dimensions that are approximately the same as the liquid volume in the conjugate system. Local heat transfer rates are evaluated along the cold wall of the rectangular enclosure and are presumed to be similar to those that occur along the solid–liq-

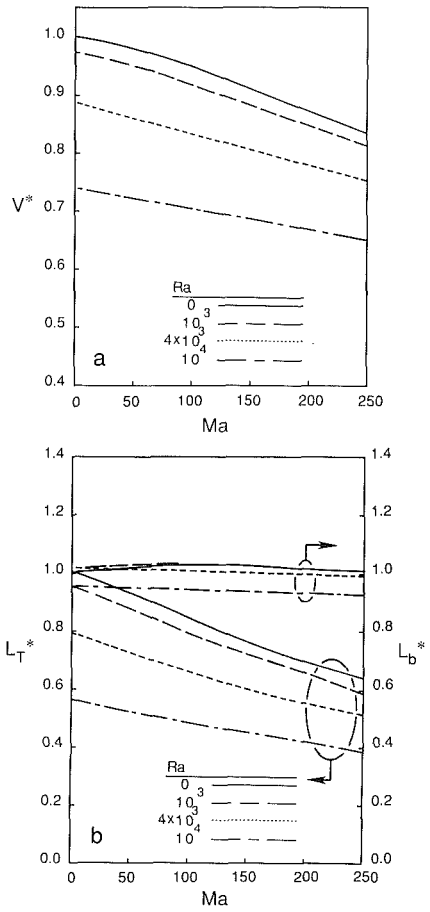

Fig. 5 Predicted normalized (*a*) volume fractions and (*b*) solid thicknesses for the simulations of Fig. 4

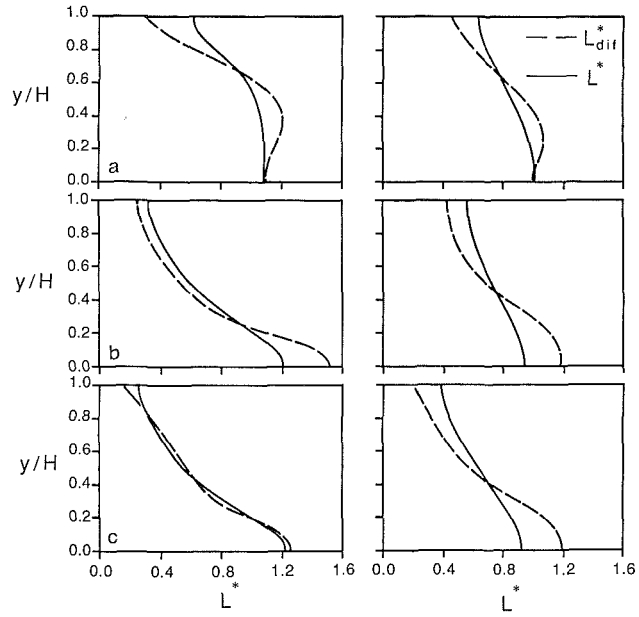

Fig. 6 Comparison of the predicted interface morphologies due to the diffusion method and the present model. The results are for $A = 1$ (left panel) and $A = 0.5$ (right panel). (*a*) Ra = 0, Ma = 250, (*b*) Ra = 10^4, Ma = 0, (*c*) Ra = 10^4, Ma = 250.

uid interface in the multiphase system. The interface location is determined by equating the horizontal diffusive heat transfer through the solid to the local cold wall heat transfer obtained for the rectangular cavity (Szekely and Chhabra, 1970). Due to the very large local Nu at $y/H = 1$ in the cavity (Bergman and Ramadhyani, 1986) the predicted notching is severe.

Use of the "diffusion" methodology does not account for the effect of the notch on the hydrodynamics of the liquid layer or the two-dimensional heat transfer in the solid. In reality, the long, thin notches that are predicted by the diffusion method serve to increase viscous forces in the melt, slow the flow at the interface, and decrease the horizontal heat transfer at $y/H = 1$. Two-dimensional heat transfer in the solid also decreases the horizontal heat transfer due to the presence of T_f below the liquid in the notch. Hence, although potentially important, events attributed to surface tension phenomena will be overestimated if the effect of the solid-liquid interface curvature is neglected.

To demonstrate this notion, the solid-liquid interface location was predicted using the diffusion method for the range of parameters associated with the results of Figs. 3 and 5. To provide a meaningful comparison between the results of the two methodologies, an iterative procedure was used so that, for a given cavity height and applied thermal boundary conditions, the predicted liquid volume *after* locating the interface by the diffusion method is identical to the predicted liquid volume of the present analysis.

Figure 6 shows the dimensionless solid-liquid interface locations predicted for the extreme Ra and Ma considered so far, for $A = 1$ and 0.5.

Figure 6(*a*), associated with Ma = 250 and Ra = 0, shows that the diffusion method overpredicts notching and can predict physically unrealistic interface morphologies. The solid bulge at $Y/H \approx 0.5$ is an artifact of bottom corner recirculations in the rectangular cavity, resulting in minimum local Nu halfway up the cold wall (Bergman and Ramadhyani, 1986) as well as enforcement of solid volume fraction conservation. It is also noted that the interface slope at $y = H$, predicted by the diffusion method, is not consistent with the adiabatic top boundary condition.

Results for buoyancy-dominated conditions are shown in Fig. 6(*b*). Although significant errors occur in the predicted local solid thickness when using the diffusion method, the resulting interface shapes are physically plausible.

Predictions for Ra = 10^4, Ma = 250, Bo = 40 are presented in Fig. 6(*c*). For both aspect ratios, the solid thickness at $y/H = 1$ is significantly less than shown in Fig. 6(*b*). By chance, the predicted interface locations resulting from the two methods agree quite well for $A = 1$, with notching slightly overpredicted by the diffusion method. In contrast, the degree of agreement in the predicted interface location for $A = 0.5$ is similar to that in Fig. 6(*b*). Again, the solid thickness at the free surface is substantially reduced due to the inclusion of surface tension in the analysis.

Comparisons of the predicted solid-liquid interface positions due to the two solution methods are summarized in Figs. 7 and 8 for $A = 1$ and 0.5, respectively. These figures relate the ratio of the normalized solid thickness predicted by the diffusion method, L^*_{dif}, to the normalized solid thickness associated with Figs. 3(*b*) and 5(*b*), L^*. Results are included for the top and bottom of the solid.

For $A = 1$ (Fig. 7), significant overprediction of notching results when the diffusion method is incorporated. However, as buoyancy forces become larger, the notching error becomes independent of Ma, as expected. As discussed in relation to Fig. 6, errors in the predicted bottom solid thickness decrease as Ma increases. For $A = 0.5$ (Fig. 8), surface tension induced notching errors remain important for all Ra considered here since surface tension forces are more robust in the smaller aspect ratio cavity. The response of surface tension convection effects to variations in the cavity aspect ratio leads to signifi-

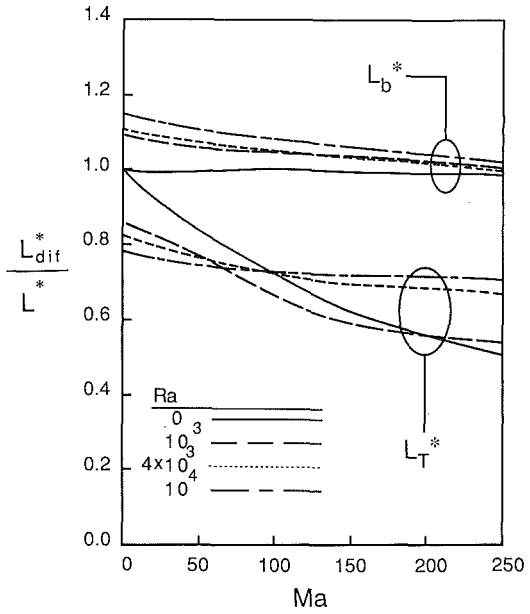

Fig. 7 Relative error in the solid thickness at $y/H = 0$ and $y/H = 1$ for $A = 1$

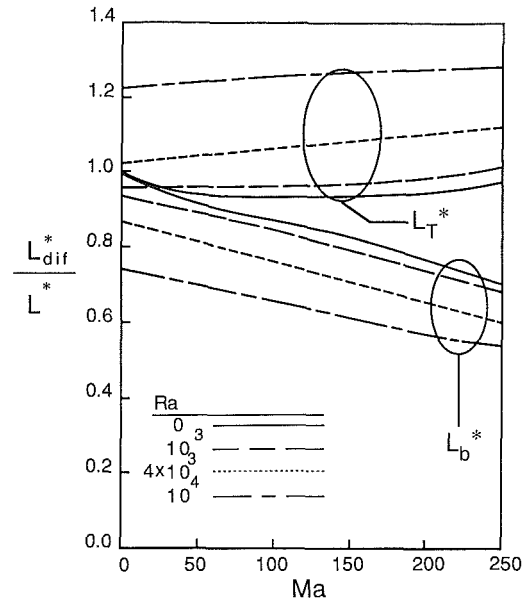

Fig. 8 Relative error in the solid thickness at $y/H = 0$ and $y/H = 1$ for $A = 0.5$

cant errors attributable to the diffusion method along the entire solid-liquid interface.

Predictions of High Ma Flows. As emphasized in previous discussions, the model is quantitatively restricted to low-Ma simulations due to the numerical singularity at the free surface–solid–liquid interface intersection. Despite this restriction, the model was used qualitatively to illustrate the potentially severe impact of surface tension effects in solid-liquid phase-change systems. The results of Figs. 9 and 10 show the predicted results for two common phase change materials, *n*-octadecane and aluminum. These materials were selected to consider a common, relatively high Pr phase change material (*n*-octadecane; Pr = 55.9) and to investigate a relevant low Pr fluid (aluminum; Pr = 0.015). An aspect ratio of 0.5 was used in the simulations and the thermophysical properties of the materials are shown in Table 1.

Figure 9 shows streamlines, liquid isotherms, and the solid-liquid interface for *n*-octadecane. The dimensional

Table 1 Thermophysical properties of *n*-octadecane and aluminum

	n-Octadecane	Aluminum
T_f	300.65 K	933.52 K
ρ	776.5 kg/m^3	2542.5 kg/m^3
$c_{p,s}$	2150 J/kg•K	1076 J/kg•K
$c_{p,l}$	2180 J/kg•K	1080 J/kg•K
k_s	0.358 W/m•K	238.0 W/m•K
k_l	0.152 W/m•K	94.03 W/m•K
μ	3.9×10^{-3}kg/m•s	1.3×10^{-3}kg/m•s
β	8.5×10^{-4}K^{-1}	1.2×10^{-4}K^{-1}
$\partial\sigma/\partial T$	0.835×10^{-4}N/m•K	-0.35×10^{-3}N/m•K

Note: All property data are from Bennon and Incropera (1987) except $\partial\sigma/\partial T$ for *n*-octadecane (Vargaftik, 1975) and aluminum (Smithells, 1983).

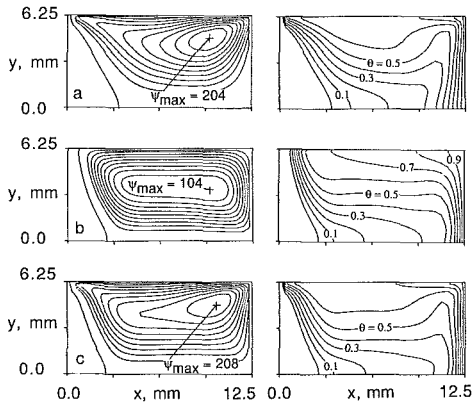

Fig. 9 Predicted streamlines (left) and isotherms (right) for *n*-octadecane at relatively large Ma: (*a*) with surface tension forces only; (*b*) with buoyancy forces only; (*c*) with simultaneous surface tension and buoyancy forces

parameters associated with the simulation are $L = 12.5$ mm, $H = 6.25$ mm, $T_h = 304.65$ K, and $T_c = 299.65$ K. The dimensionless parameters describing the system are Pr = 55.9, $A = 0.5$, $\mathrm{Ra} = 1.45\times10^5$, $\mathrm{Ma} = 1.19\times10^4$, Bo = 12.1, and $\theta^* = 0.2$. The predicted flow characteristics are remarkably similar to those reported for a similar range of dimensionless parameters by Zebib et al. (1985). Note that Ma is large compared to the acceptable values described in the Appendix.

The results of Fig. 9 show that surface tension forces can profoundly influence phase change in typical test fluids when a free surface is present. The solid-liquid interface shape that is predicted to occur when both buoyancy and surface tension forces are included in the analysis (Fig. 9*c*) bears little resemblance to the interface shapes in either Fig. 9(*a*) or 9(*b*). The solid is very thin at $y/H = 1$ as isotherm compaction in the melt, resulting from surface tension phenomena, notches the solid layer. The solid-liquid interface exhibits an inflection near $y/H = 0.5$, which is presumably due to the superposition of the convex and concave interfaces associated with the pure surface tension (Fig. 9*a*) and pure buoyancy (Fig. 9*b*) results. Both of these interface characteristics, notching and inflection, are evident in experimental phase-change studies involving *n*-octadecane with free liquid surfaces as seen in Ho and Viskanta (1984). Normalized solid fractions and top and bottom solid thicknesses are $V^* = 0.409$, 0.329, 0.315, $L_T^* = 0.040$, 0.153, 0.038, and $L_b^* = 0.709$, 0.570, 0.568 for the results of Figs. 9(*a*, *b*, and *c*), respectively.

Figure 10 shows the predictions for aluminum in an enclosure with $L = 12.5$ mm, $H = 6.25$ mm, $T_h = 1033.52$ K, and $T_c = 908.52$ K. The dimensionless parameters describing the system are Pr = 0.015, $A = 0.5$, $\mathrm{Ma} = 9.8\times10^3$, $\mathrm{Ra} = 1.3\times10^4$, Bo = 1.34, and $\theta^* = 0.2$.

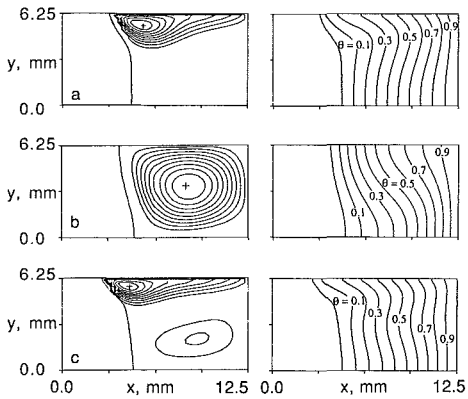

Fig. 10 Predicted streamlines (left) and isotherms (right) for aluminum at relatively large Ma: (*a*) with surface tension forces only, $\Psi_{max} = 3.16 \times 10^5$; (*b*) with buoyancy forces only, $\Psi_{max} = 2.26 \times 10^5$; (*c*) with simultaneous surface tension and buoyancy forces, $\Psi_{max} = 3.54 \times 10^5$

Figure 10(*a*) shows the notching phenomenon due to surface tension effects. In Fig. 10(*b*), where only buoyancy forces are included, the solid–liquid interface is relatively vertical and conduction dominates the heat transfer process. For combined surface tension and buoyancy forces, notching is again prevalent and multicellular convection, typical of low-Pr liquids, occurs. As in simulations reported for metal welding (Oreper and Szekely, 1984), the combined flow is dominated by surface tension effects and buoyancy forces are relatively unimportant in the analysis. Hence, the solid–liquid interface position is not much different from that of Fig. 10(*a*). The normalized solid fractions and top and bottom solid thicknesses are $V^* = 0.865$, 0.906, 0.821, $L_T^* = 0.646$, 0.800, 0.557, and $L_b^* = 0.948$, 1.012, 1.007 for the results of Figs. 10(*a*) through 10(*c*), respectively.

It should be noted that, although notching at $y/H = 1$ is evident for the simulations involving *n*-octadecane and aluminum, the severity of the effect is less than would be predicted by the diffusion methodology.

Conclusions and Summary

A numerical model has been developed that predicts the steady-state convection in a two-phase solid–liquid system including the effects of Marangoni and buoyancy-induced convection in the liquid phase. The model is limited in its application due to a singularity at the solid–liquid interface-free surface intersection. However, several conclusions may be drawn from the study.

Surface tension flow may cause local and overall variations in the heat transfer processes relevant to solid–liquid phase-change systems. The influence of surface tension effects is most important at the free surface where increased local heat transfer occurs and, in turn, decreased solid thickness exist. Depending on the aspect ratio of the system, the inclusion of surface tension effects in the analysis can lead to increased or decreased solid thickness at small y/H. If decreased local heat transfer occurs at small y/H, increases in the solid thickness at this location can offset decreases in the solid thickness at the free surface, resulting in little change in the total solid fraction. Surface tension induced phenomena cannot be accurately predicted if the influences of the solid–liquid interface curvature on the melt hydrodynamics and solid heat transfer are ignored.

Most relevant systems of interest are characterized by Ma and Bo outside of the range of quantitative applicability of the model. However, when the model is deliberately applied to these systems, surface tension effects begin to dominate the response of the system. Anomalies in solid–liquid interface shapes observed during experimental solidification and melting studies are predicted when surface tension and buoyancy forces are both included in the model. When applied to liquid metals, it is clear that surface tension forces can dominate buoyancy forces, and systems that are analyzed with conduction-based methodologies will underestimate convection effects attributable to surface tension phenomena.

It is important to discuss the relationship between the steady-state results of this study with solidification or melting processes that are transient in nature. Typically, transient solidification or melting analyses utilize quasi-steady models for the fluid flow and convection transport in the system (Sparrow et al., 1977). Hence the predictions included here would be relevant to an actual solid–liquid phase-change problem at a given time during solidification or melting. However, it must be noted that, as with the buoyancy flow parameters, the relevant length scale associated with Marangoni flow (the melt free surface length) steadily decreases (increases) with time during solidification (melting). Since the relevant Bond number is proportional to the square of the length of the free surface, inclusion of surface tension in the analysis of solidification, for example, may be unnecessary at early times but crucial at later times when free surface lengths are small. Finally, the simulations associated with *n*-octadecane and aluminum multiphase systems demonstrate the need for the development of computational methodologies capable of resolving the numerical difficulties associated with surface tension-induced flow in enclosures.

Acknowledgments

The authors acknowledge the support of the National Science Foundation under Grant No. CBT-8552806 and thank the Department of Mechanical Engineering at the University of Texas at Austin for use of computational facilities.

References

Bernard, C., Gobin, D., and Zanoli, A., 1986, "Moving Boundary Problem: Heat Conduction in the Solid Phase of a Phase-Change Material During Melting Driven by Natural Convection in the Liquid," *International Journal of Heat and Mass Transfer*, Vol. 29, pp. 1669–1681.

Bennon, W. D., and Incropera, F. P., 1987, "Developing Laminar Mixed Convection With Solidification in a Vertical Channel," presented at the National Heat Transfer Conference, Pittsburgh, Pa, Paper No. 87-HT-3.

Bergman, T. L., and Ramadhyani, S., 1986, "Combined Buoyancy- and Thermocapillary-Driven Convection in Open Square Cavities," *Numerical Heat Transfer*, Vol. 9, pp. 441–451.

de Vahl Davis, G. E., 1983, "Natural Convection of Air in a Square Cavity: A Bench Mark Numerical Solution," *International Journal for Numerical Methods in Fluids*, Vol. 3, pp. 249–264.

Ho, C. J., and Viskanta, R., 1984, "Heat Transfer During Melting From an Isothermal Slab," ASME JOURNAL OF HEAT TRANSFER, Vol. 106, pp. 12–19.

Hurle, D. T. J., and Jakeman, E., 1981, "Introduction to the Techniques of Crystal Growth," *Physico Chemical Hydrodynamics*, Vol. 2, pp. 237–244.

Jasper, J. J., 1972, "The Surface Tension of Pure Liquid Compounds," *Journal of Physical Chemical Reference Data*, Vol. 1, pp. 841–1009.

Kirdyashkin, A. G., 1984, "Thermogravitational and Thermocapillary Flows in a Horizontal Liquid Layer Under the Conditions of a Horizontal Temperature Gradient," *International Journal of Heat and Mass Transfer*, Vol. 27, pp. 1205–1218.

Kou, S., 1987, *Welding Metallurgy*, Wiley, New York.

McNeil, T. J., Cole R., and Subramanian, R. S., 1985, "Surface-Tension-Driven Flow in a Glass Melt," *Journal of the American Ceramic Society*, Vol. 68, pp. 254–259.

Munakata, T., and Tanasawa, I., 1986, "Buoyancy and Surface Tension Driven Natural Convection With Solidification," *Proceedings, 8th International Heat Transfer Conference*, C. L. Tien et al., eds., Hemisphere Publishing Corp., Washington, DC, Vol. 4, pp. 1733–1738.

Oreper, G. M., and Szekely, J., 1984, "Heat- and Fluid-Flow Phenomena in Weld Pools," *Journal of Fluid Mechanics*, Vol. 147, pp. 53–79.

Patankar, S. V., 1980, *Numerical Heat Transfer and Fluid Flow*, Hemisphere Publishing Corp., Washington, DC.

Schwabe, D., Scharmann, A., Preisser, F., and Oeder, R., 1978, "Experiments on Surface Tension Driven Flow in Floating Zone Melting," *Journal of Crystal Growth*, Vol. 43, pp. 305–312.

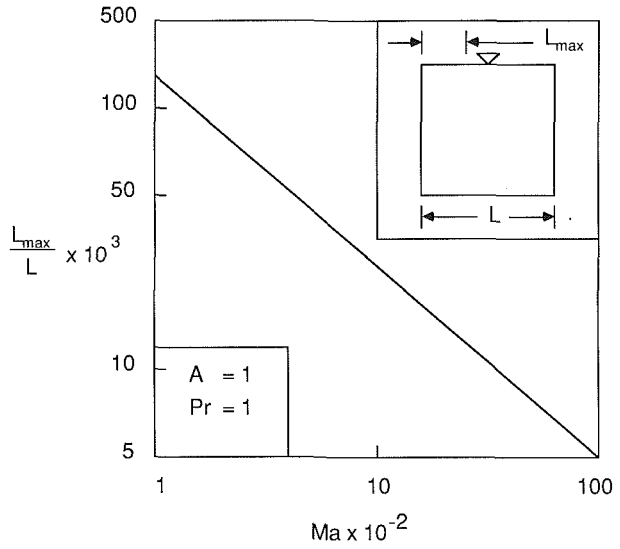

Fig. 11 Predicted locations of the maximum free surface velocity for Ra = 0 (from Zehr et al., 1987)

Smithell's Metal Reference Book, 1985, 6th ed., E. A. Brandes, ed., Butterworths, London.

Sparrow, E. M., Patankar, S. V., and Ramadhyani, S., 1977, "Analysis of Melting in the Presence of Natural Convection in the Melt Region," ASME JOURNAL OF HEAT TRANSFER, Vol. 99, pp. 520–526.

Stanek, V., and Szekely, J., 1970, "The Effect of Surface Driven Flows on the Dissolution of a Partially Immersed Solid in a Liquid-Analysis," *Chemical Engineering Science*, Vol. 25, pp. 699–715.

Szekely, J., and Chhabra, P. S., 1970, "The Effect of Natural Convection on the Shape and Movement of the Melt-Solid Interface in the Controlled Solidification of Lead," *Metallurgical Transactions*, Vol. 1, pp. 1195–1203.

Vargaftik, N. B., 1975, *Tables on the Thermophysical Properties of Liquids and Gases*, 2nd. ed., Hemisphere Publishing Corp., Washington, DC.

Villers, D., and Platten, J. K., 1985, "Marangoni Convection in Systems Presenting a Minimum in Surface Tension," *Physico Chemical Hydrodynamics*, Vol. 6, pp. 435–451.

Viskanta, R., 1985, "Natural Convection in Melting and Solidification," in: *Natural Convection: Fundamentals and Applications*, S. Kakac et al., eds., Hemisphere Publishing Corp., Washington, DC, pp. 845–877.

Webb, B. W., and Viskanta, R., 1985, "On the Characteristic Length Scale for Correlating Melting Heat Transfer Data," *International Communications in Heat and Mass Transfer*, Vol. 12, pp. 637–646.

Zebib, A., Homsy, G. M., and Meiburg, E., 1985, "High Marangoni Number Convection in a Square Cavity," *Physics of Fluids*, Vol. 12, pp. 3467–3476.

Zehr, R. L., Chen, M. M., and Mazumder, J., 1987, "Thermocapillary Convection of a Differentially Heated Cavity at High Marangoni Numbers," presented at the National Heat Transfer Conference, Pittsburgh, PA, Paper No. 87-HT-29.

Zierep, J., and Oertel, H., 1982, *Convective Transport and Instability Phenomena*, G. Braun Publishers, Karlsruhe, Federal Republic of Germany.

APPENDIX

Zehr et al. (1987) report that a numerical singularity occurs when Marangoni flows occur at a horizontal free surface that is adjacent to a vertical surface. Due to the Marangoni boundary condition, equation (6), and isotherm compaction at the cold wall, the location of the maximum horizontal free surface velocity tends to be near the cold wall. If a coarse grid is used, the maximum velocity will be at the control surface of the control volume adjacent to the fixed cold wall, which is, of course, characterized by $u = 0$. This sharp jump in velocities over one control volume width adversely affects the predicted hydrodynamics and heat transfer at the cold wall in the region near the free surface (Zehr et al., 1987). It is especially important in phase-change processes to predict local heat transfer rates accurately here, since local heat transfer rates determine the system behavior.

In order to minimize the numerical error associated with the singularity, an adequate number of control volumes must be placed between the location of the maximum surface velocity and the cold wall. In general, this procedure demands that a very fine grid be used to predict realistic surface tension flows (for example, a 51×51 uniform grid is inadequate for $\mathrm{Ma} = 3000$ according to Zehr et al., 1987).

To estimate the grid size required to overcome effects associated with the singularity, the location of the maximum velocity must first be approximated. Figure 11, reduced from data presented by Zehr et al. (1987), shows the normalized location of the maximum free-surface velocity for $10^2 \leq \mathrm{Ma} \leq 10^4$, $A = 1$, and $\mathrm{Pr} = 1$. A least-squares curve fit of the relationship yields $L_{max}/L = 14.8\ \mathrm{Ma}^{-0.852}$.

In this study, approximately four control volumes were placed between the L_{max}/L location and the solid-liquid interface. The grid size determined by this procedure yields grid-independent results for $\mathrm{Ma} < 250$.

M. Prud'homme

T. Hung Nguyen

Département de Génie Mécanique,
Ecole Polytechnique,
Université de Montréal,
Montréal, Québec, Canada, H3C-3A7

D. Long Nguyen

Institut de Recherche d'Hydro-Québec,
Varennes, Québec, Canada, J0L-2P0

A Heat Transfer Analysis for Solidification of Slabs, Cylinders, and Spheres

The method of strained coordinates is applied to the inward solidification problem. Constant thermal properties are assumed throughout the analysis for the liquid, which is initially at the fusion temperature. A unified approach is adopted that allows the simultaneous treatment of the problem in plane, cylindrical, and spherical geometries for three different types of boundary condition. A general recurrence formula is derived for the determination of the series solutions up to any desired order of the Stefan number. A comparison is made with numerical and regular perturbation solutions in the plane case to illustrate the usefulness and the validity of the method.

Introduction

Recently, there has been a growing interest in the heat transfer analysis of phase change problems (Sparrow and Chuck, 1984; Bénard et al., 1986; Toda et al., 1986). Solidification is of practical interest in such diverse areas as refrigeration, electrochemistry, metal casting and welding, etc. Studies in this field are based on various mathematical as well as physical approximations, which need to be continuously improved. Difficulties are due to the fact that real problems usually involve both conduction and convection, taking place separately in their respective domains whose interface is moving and of unknown form. As these problems are governed by nonlinear differential equations, they are usually solved numerically. The solidification process is then treated in a quasi-static manner, i.e., during a short time step, the temperature field in each phase is solved with a fixed interface. The amount of heat transferred across the interface during this time interval is then used to determine the progression of the solidification front. Variations on this theme were continuously proposed to improve the accuracy of the results according to the type of boundary conditions and geometry considered.

Although numerical solutions seem quite convenient, their accuracy is often difficult to assess, and the results are less enlightening and systematic than those obtained from an analytical approach. Exact closed-form solutions are, however, not available, except in the simplest case of a semi-infinite medium with a fixed temperature imposed at the boundary (Carslaw and Jaeger, 1959). Approximate analytical solutions are still possible for other problems using perturbation methods. These solutions fall into two main categories. There are first the so-called small time solutions for arbitrary Stefan number ϵ, which are only valid at the beginning of solidification. Then, there are solutions for the complete process, which are only valid for a limited range of ϵ values. Leaving aside the small time solutions, which are not the main concern of this work, cylindrical and spherical solidification has been investigated so far only for the fixed wall temperature boundary condition. The purpose of this paper is therefore to provide a brief survey of the methods and to lay the groundwork to close the gaps in the literature.

Assuming the above boundary condition, Pedroso and Demoto (1973a) obtained regular perturbation solutions for outward and partial inward spherical solidification, to second order in ϵ. The inward solution had a singularity at $r = 0$, which they tried to remove with an Euler transformation involving an unknown parameter. This parameter was evaluated numerically for a given epsilon from a transcendental equation based on an energy balance. The transformed solution was bounded, but discontinuous at $r = 0$, and hence violated the boundary condition at the interface at the instant of freezing to the center. Despite this undesirable feature, they still obtained freezing times in good agreement with the numerical values of Tao (1967), up to $\epsilon = 1$.

The same authors (1973b) used subsequently the method of strained coordinates to derive a new second-order solution, which satisfied all the boundary conditions. They found closed-form expressions for the temperature profiles and the freezing time. At the instant of freezing to the center, and up to $\epsilon = 1$, the temperature profile turned out to be in good agreement with the computations of Tao everywhere, except near the center where the numericals appear dubious. The results for the freezing time agreed with the numerical data for $\epsilon = 0.1$ and 0.5 but diverged for $\epsilon = 1$. A Shanks (1955) transformation was applied to the solution in order to extend its range of validity. It may be estimated that this action doubled the range, at least.

Riley et al. (1974) carried out the investigation of inward solidification a step further for spheres and cylinders. Using matched asymptotic expansions, they showed that the solution requires the matching of two inner expansions with the outer regular solution. The leading term of each inner expansion was obtained from which several closed-form results were deduced for the freezing time at the final temperature profile. Higher order terms could not always be obtained in closed form, even though some order of magnitude estimates could still be made. Nevertheless, the basic matched solution compared well with the numerical data of Beckett (1971) for a sphere at $\epsilon = 0.1$ and a cylinder at $\epsilon = 0.1$ and 0.05. Although this technique brings a lot of insight into the physical and mathematical behavior of the solution near the center, it is strictly asymptotic in nature and thus limited to $\epsilon << 1$.

For large ϵ this time, a noteworthy contribution is that of Beckett (1981) who extended the small time solutions of Poots (1962) for cylinders and spheres. Unlike the previous methods that use ϵ as a perturbation parameter, this approach relies on an expansion using time as a parameter. The expansion coefficients for the interface position and the temperature profile are determined from a differential equation that is better solved numerically beyond the first few terms. The series are slowly converging and a lot of terms are required in order to estimate the freezing time, typically 25 for a cylinder at $\epsilon = 10$. Also, the smaller ϵ is, the more terms will be needed.

The strained coordinates method emerges as the most in-

Contributed by the Heat Transfer Division and presented at the 24th AIChE/ASME National Heat Transfer Conference, Pittsburgh, Pennsylvania, August 9–12, 1987. Manuscript received by the Heat Transfer Division October 9, 1987. Keywords: Moving Boundaries, Phase-Change Phenomena.

teresting one for several reasons. It is not strictly asymptotic, that is, limited to very small ϵ. It does not require the matching of two or more solutions over the domain. It does not require the evaluation of a large number of terms in the solution to get meaningful results. Furthermore, each term in the series can be expressed in closed form instead of being itself another series. In the present study, we shall adopt the strained coordinates method to study inward solidification under boundary conditions that have not been considered so far with this or any of the methods described above. A general formulation is employed to treat the problem of solidification for a fluid initially at its fusion temperature contained in either a slab, a cylinder, or a sphere under three typical boundary conditions: constant wall temperature, constant heat flux at the wall, and constant convective heat transfer between the wall and the surrounding medium.

The strained coordinates method is then used to derive a unified recurrence formula for the three geometries and boundary conditions, which allows the calculation of the series solutions up to any desired order in ϵ. We will present explicitly the second-order solutions for a slab only, since our main goal here is to illustrate the general formulation and compare it with other results. The perturbation solutions will be compared with some numerical results obtained by solving directly the governing equations according to the recommendations of Sparrow and Chuck. The first Shanks transformation will be applied to the singular perturbation solution. A comparison with regular perturbation solutions will also be made.

Formulation of the Problem

The solidification process will now be studied formally for a liquid initially at the freezing temperature. It is assumed that the solidified shell grows in a symmetric manner as sketched in Fig. 1. The heat flow within the solid phase is then governed by the unsteady, one-dimensional heat conduction equation. For constant thermal properties

$$\frac{\partial T}{\partial t}=\frac{\kappa}{R^n}\frac{\partial}{\partial R}\left(R^n\frac{\partial T}{\partial R}\right) \tag{1}$$

with $n = 0, 1, 2$, for plane, cylindrical, and spherical configuration, respectively. An energy balance at the solid-liquid interface yields

$$\frac{dR_f}{dt}=\frac{k}{\rho L}\frac{\partial T}{\partial R}\bigg|_{R=R_f} \tag{2}$$

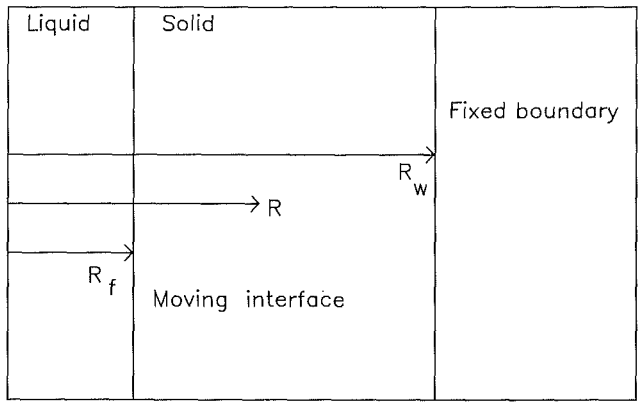

Fig. 1 Geometry and coordinate system

Furthermore,

$$T=T_f; \qquad R=R_f \tag{3}$$

The initial condition for the problem is simply $T=T_f$ at $t = 0$. Three different types of boundary condition can be considered at the fixed wall. Namely, one might assume either: (*a*) a constant temperature T_w, or (*b*) a constant heat flux q, or (*c*) a constant heat transfer coefficient h. Thus, for inward solidification:

$$(a)\quad T=T_w\ ;\ R=R_w \tag{4a}$$

$$(b)\quad -k\frac{\partial T}{\partial R}=q\ ;\ R=R_w \tag{4b}$$

$$(c)\quad -k\frac{\partial T}{\partial R}=h(T-T_\infty)\ ;\ R=R_w \tag{4c}$$

It is possible to recast the problem in nondimensional form using

$$U=(T-T_0)/\Delta T,\ \tau=tk\Delta T/(\rho LR_w^2)$$
$$r=R/R_w,\ r_f=R_f/R_w \tag{5}$$

where

$$(a)\quad \Delta T=T_f-T_w,\ T_0=T_w \tag{6a}$$

$$(b)\quad \Delta T=\dot{Q}''R_w/k,\ T_0=T_f-\Delta T \tag{6b}$$

$$(c)\quad \Delta T=T_f-T_\infty,\ T_0=T_\infty \tag{6c}$$

Changing to dimensionless variables and eliminating τ from equation (1) using equation (2) yields

Nomenclature

c = specific heat
h = convective heat transfer coefficient
k = thermal conductivity
L = latent heat of fusion
N = number of grid points
q = wall heat flux
R = position in the solidified material
R_f = position of the freezing front
R_w = position of the fixed boundary
T = temperature distribution
T_f = freezing temperature
T_w = temperature at the fixed boundary
T_0 = reference temperature
T_∞ = temperature at infinity
t = time
κ = thermal diffusivity $= k/(\rho c)$
ρ = density

Dimensionless Quantities

C = integration constant
Bi = Biot number $= hR_w/k$
n = exponent
r = normalized position $= R/R_w$
r_f = normalized freezing front position $= R_f/R_w$
S = thickness of solid phase $=1-r_f$
U = normalized temperature distribution $= (T-T_0)/\Delta T$
X = transformed coordinate $= (1-r)/S$
δ = initial thickness
Δ = increment
ϵ = Stefan number $= c\Delta T/L$
σ_i = coefficient of ϵ^i in power series expansion of r
τ = normalized time $= tk\Delta T/\rho LR_w^2$
ϕ, ψ = strained coordinates

$$\epsilon \frac{\partial U}{\partial r_f}\frac{\partial U}{\partial r}\Big|_{r=r_f} = \frac{1}{r^n}\frac{\partial}{\partial r}\left(r^n \frac{\partial U}{\partial r}\right);\ n=0,\ 1,\ 2 \tag{7}$$

$$\frac{dr_f}{d\tau} = \frac{\partial U}{\partial r}\Big|_{r=r_f} \tag{8}$$

where $\epsilon = c\Delta T/L$ is the Stefan number.

The set of boundary conditions in nondimensional form reads

$$U=1;\ r=r_f \tag{9}$$

and

$$(a)\quad U=0;\ r=1 \tag{10a}$$

$$(b)\quad \frac{\partial U}{\partial r} = -1;\ r=1 \tag{10b}$$

$$(c)\quad \frac{\partial U}{\partial r} = -\mathrm{Bi}U;\ r=1 \tag{10c}$$

Equations (7) and (8) with the associated boundary conditions (9) and (10*a-c*) constitute the mathematical statement of the problem.

Analytical Solutions

There is an exact similarity solution to the set of equations (7) and (8) in the plane case ($n=0$) that satisfies equations (9) and (10*a*). Without loss of generality, let $\tau = 0$ for $r_f = 1$. Then for any Stefan number, U and r_f are given by

$$U(r, r_f) = \sqrt{\frac{\pi C}{2\epsilon}}\exp\left(\frac{\epsilon C}{2}\right)\mathrm{erf}\left(\sqrt{\frac{\epsilon C}{2}}\ \frac{1-r}{1-r_f}\right) \tag{11a}$$

and

$$r_f(\tau) = 1-\sqrt{2C\tau} \tag{11b}$$

respectively, where C can be evaluated using equation (9). For small values of ϵ, equation (11*a*) can be written as

$$U(X, \epsilon) = X + (X+X^3)\frac{\epsilon}{6} + \left(-\frac{19}{90}X + \frac{1}{9}X^3 + \frac{1}{10}X^5\right)\frac{\epsilon^2}{4} + \ldots \tag{11c}$$

where $X=(1-r)/(1-r_f)$ and the freezing time becomes

$$\tau_m(\epsilon) = \frac{1}{2} + \frac{\epsilon}{6} - \frac{\epsilon^2}{45} + \ldots \tag{11d}$$

In the other cases there are no exact solutions, as we already know. Perturbation solutions are then quite instructive in showing the initial influence of ϵ on the solidification process and its evolution as ϵ increases.

Regular perturbation methods where an expansion of the form

$$U(r, r_f; \epsilon) = \sum_{i=0}^{\infty} \epsilon^i U_i(r, r_f) \tag{12}$$

is assumed for the temperature distribution are straightforward and will yield uniformly valid solutions in the case of outward solidification. But the solutions will diverge for inward cylindrical and spherical solidification as the r_f approach zero. This does not occur in the plane case, however, and useful comparisons with the present method can be made. For the fixed temperature condition, the regular perturbation solution is identical to the expansion equation (11*c*). It is a simple matter to derive second-order solutions for the remaining two cases, which may be found in Prud'homme and Nguyen (1987).

In order to derive uniformly valid solutions for inward solidification in the three geometries one must turn toward the singular methods. The method of stretched coordinates is one of the most powerful singular perturbation methods (see, for instance, Van Dyke, 1975). The approach is as follows.

The stretched variables ϕ and ψ, which must reduce to r and r_f in the limit as ϵ tends toward zero, are defined formally as

$$\begin{aligned}\phi &= f(r, r_f)\\ \psi &= f(r_f, r_f)\end{aligned} \tag{13}$$

so that $\phi = \psi$ when $r=r_f$. Instead of expanding the function U itself in powers of ϵ, an expansion of r and r_f is made

$$\begin{aligned} r &= \sum_{i=0}^{\infty} \epsilon^i \sigma_i(\psi, \phi)\\ r_f &= \sum_{i=0}^{\infty} \epsilon^i \sigma_i(\psi, \psi)\end{aligned} \tag{14}$$

A solution of the form $U(\psi, \phi)$ is sought that satisfies the problem and the boundary conditions in terms of ϕ and ψ at the zeroth order. The σ_i's can be calculated afterward.

The stretching has been arbitrary so far. It can conveniently be assumed to vanish at the fixed wall. In other words, for all values of r_f, $\phi = \partial\phi/\partial r = 1$ at $r=1$. With this condition the set of equations (7) and (8) and the boundary conditions equations (9) and (10) transform to

$$\epsilon\left[\frac{\partial U}{\partial \phi}\frac{\partial \phi}{\partial r}\right]_{\phi=\psi}\left(\frac{\partial U}{\partial \phi}\frac{\partial \phi}{\partial r_f} + \frac{\partial U}{\partial \psi}\frac{d\psi}{dr_f}\right) = \frac{\partial^2 U}{\partial \phi^2}\left(\frac{\partial \phi}{\partial r}\right)^2 + \frac{\partial U}{\partial \phi}\frac{\partial^2 \phi}{\partial r^2} + \frac{n}{r}\frac{\partial U}{\partial \phi}\frac{\partial \phi}{\partial r} \tag{15}$$

$$\frac{dr_f}{d\psi}\frac{d\psi}{d\tau} = \left[\frac{\partial U}{\partial \phi}\frac{\partial \phi}{\partial r}\right]_{\phi=\psi} \tag{16}$$

and

$$U=1;\ \phi=\psi \tag{17}$$

$$(a)\quad U=0;\ \phi=1 \tag{18a}$$

$$(b)\quad \frac{\partial U}{\partial \phi} = -1;\ \phi=1 \tag{18b}$$

$$(c)\quad \frac{\partial U}{\partial \phi} = -\mathrm{Bi}U;\ \phi=1 \tag{18c}$$

The condition of zero stretching at the wall further requires that for all ψ's

$$\sigma_i(\psi, 1) = \frac{\partial \sigma_i}{\partial \phi}(\psi, 1) = 0; \qquad i \geq 1 \tag{19}$$

It is possible to eliminate r and r_f from equation (15) using equation (14). This yields a power series equation in ϵ involving U, σ_i, ϕ, ψ. Equating the coefficients of like powers of ϵ gives a recurrence relation for the σ_i's and an equation for U. At the zeroth order therefore

$$\phi\frac{\partial^2 U}{\partial \phi^2} + n\frac{\partial U}{\partial \phi} = 0 \tag{20}$$

which can be integrated easily after multiplication of equation (20) by ϕ^{n-1}. The solution for $U(\psi, \phi)$ will involve two arbitrary functions of ψ, which can be determined using the boundary conditions equations (17) and (18).

Once $U(\psi, \phi)$ is known, $\sigma_i(\phi, \psi)$ can be calculated for $i \geq 1$ from the recurrence relation

$$\frac{\partial}{\partial\phi}\left\{-\phi^{2-n}\frac{\partial}{\partial\phi}\left(\phi^{n-1}\frac{\partial U}{\partial\phi}\sigma_i\right)\right\}$$

$$=\sum_{j=0}^{i-1}\sum_{k=0}^{i-j-1}\sum_{l=0}^{i-j-k-1}\left(\frac{\partial U}{\partial\psi}\frac{\partial\sigma_j}{\partial\phi}-\frac{\partial U}{\partial\phi}\frac{\partial\sigma_j}{\partial\psi}\right)$$

$$\left[\frac{\partial U}{\partial\phi}\right]_{\phi=\psi}\frac{\partial\sigma_k}{\partial\phi}\frac{\partial\sigma_l}{\partial\phi}\sigma_{i-j-k-l-1}-\sum_{j=0}^{i-1}\sum_{\substack{k=0\\k\neq i}}^{i-j}\sum_{\substack{l=0\\k\neq i}}^{i-j-k}$$

$$\left(\left[\sigma_j\frac{\partial\sigma_k}{\partial\phi}-\phi\frac{\partial\sigma_j}{\partial\phi}\frac{\partial\sigma_k}{\partial\phi}\right]\frac{\partial^2U}{\partial\phi^2}-\sigma_j\frac{\partial^2\sigma_k}{\partial\phi^2}\frac{\partial U}{\partial\phi}\right)$$

$$\left[\frac{\partial\phi_l}{\partial\phi}\right]_{\phi=\psi}\sigma'_{i-j-k-l} \tag{21}$$

where the prime represents the total derivative of the function (evaluated at $\phi=\psi$) with respect to ψ. The zeroth-order stretching requirements, equation (19), at $\phi = 1$ provide two boundary conditions for the integration of equation (21). Consequently σ_i (ψ, ϕ) is determined explicitly in terms of $\sigma_{i-1}, \sigma_{i-2}, \ldots, \sigma_0$ and U as

$$\sigma_i(\psi,\phi)=\left(\frac{\partial U}{\partial\phi}\phi^{n-1}\right)^{-1}\int_1^\phi\int_1^\zeta-\xi^{n-2}f_i(\psi,\xi)d\xi\ d\zeta \tag{22}$$

where $f_i(\psi, \phi)$ stands for the right-hand side of equation (21), for all the geometries and boundary conditions considered so far in this study. The influence of the latter on the stretching is felt only indirectly through the zeroth order solution U.

A power series for $d\tau/d\psi$ is obtained by eliminating r and r_f from equation (16) with the help of equation (14) as before.

$$\frac{d\tau}{d\psi}=\left[\frac{\partial U}{\partial\phi}\right]_{\phi=\psi}^{-1}\sum_{i=0}^{\infty}\epsilon^i\sum_{j=0}^{i}\left[\frac{\partial\sigma_j}{\partial\phi}\right]_{\phi=\psi}\sigma'_{i-j} \tag{23}$$

The explicit relationship for $\tau(\psi)$ follows from the integration of equation (23) using the initial condition $\tau=0$ at $\psi=1$. It is possible to proceed up to any desired order in ϵ with the equations (14) and (23) using the general recurrence relations equations (21) and (22) for σ_i. These recurrence relations, together with U, represent a uniformly valid perturbation solution to the inward solidification problem in the plane, cylindrical, and spherical geometries, for three types of boundary conditions at the fixed wall.

Calculations were carried out up to second order in ϵ for the purpose of the present investigation. The results for U, σ_1, and σ_2 are presented below for $n = 0$ and each type of boundary condition. For boundary condition equation (18*a*)

$$U(\psi,\phi)=(\phi-1)/(\psi-1)$$
$$\sigma_1(\psi,\phi)=\frac{1}{6}\frac{(\phi-1)^3}{(\psi-1)^2} \tag{24}$$
$$\sigma_2(\psi,\phi)=\frac{(\phi-1)^3}{(\psi-1)^2}\left[\frac{7}{120}\frac{(\phi-1)^2}{(\psi-1)^2}-\frac{1}{9}\right]$$

For equation (18*b*)

$$U(\psi,\phi)=1-\phi+\psi$$
$$\sigma_1(\psi,\phi)=-(\phi-1)^2/2 \tag{25}$$
$$\sigma_2(\psi,\phi)=(\phi-1)^3/2-(\phi-1)^2(\psi-1)$$

For equation (18*c*)

$$U(\psi,\phi) = (\phi-\alpha)/(\psi-\alpha), \qquad \alpha=1+1/\mathrm{Bi}$$
$$\sigma_1(\psi,\phi) = \frac{1}{6}\frac{(\phi-1)^2}{(\psi-\alpha)^2}[(\phi-1)+3(1-\alpha)] \tag{26}$$
$$\sigma_2(\psi,\phi) = \frac{1}{120}\frac{(\phi-1)^3}{(\psi-\alpha)^4}[7(\phi-1)^2$$
$$+ 35(1-\alpha)(\phi-1)+60(1-\alpha)^2]$$
$$-\frac{(\phi-1)^2(\psi-1)}{9(\psi-\alpha)^5}[(\phi-1)$$
$$+ 3(1-\alpha)][(\psi-1)^2+3(1-\alpha)(\psi-\alpha)]$$

A more comprehensive application of the method to the cylindrical and spherical cases may be found in a companion paper by Prud'homme and Nguyen (1988). For the time being, a comparison will be made with numerical solutions in order to establish the range of validity of the low-order perturbation solutions for the slab.

Numerical Method

The governing equations (1) and (2) are first rewritten in terms of the dimensionless variables defined in equation (5). The dimensionless set of equations and boundary conditions is better solved numerically in a system of coordinates X, τ where the position of the freezing front remains fixed. The coordinate X is defined by the transformation

$$X=(1-r)/S \tag{27}$$

where $S=1-r_f$ is the thickness of the solid phase. The moving interface is thus immobilized at $X = 1$ and the governing equations are solved within the fixed domain $0 \le X \le 1$. The transformed set of equations is then

$$\epsilon\left(\frac{\partial U}{\partial\tau}-\frac{X}{S}\frac{dS}{d\tau}\frac{\partial U}{\partial X}\right)=\frac{1}{S^2(1-SX)^n}\frac{\partial}{\partial X}$$
$$\left[(1-SX)^n\frac{\partial U}{\partial X}\right] \tag{28}$$

$$\frac{dS}{d\tau}=\frac{1}{S}\frac{\partial U}{\partial X}\Big|_{X=1} \tag{29}$$

The boundary conditions are given by

$$U=1 \quad \text{at} \quad X=1 \tag{30}$$

and

$$(a)\quad U=0;\ X=0 \tag{31a}$$
$$(b)\quad \frac{\partial U}{\partial X}=S;\ X=0 \tag{31b}$$
$$(c)\quad \frac{\partial U}{\partial X}=S\mathrm{Bi}U;\ X=0 \tag{31c}$$

The above equations can be discretized using finite difference techniques with an implicit scheme for the heat conduction equation and an explicit scheme for the interface energy balance. The coupling between these equations will be treated following a procedure recently proposed by Sparrow and Chuck (1984). The numerical approach can be summarized as follows. Let U_i be the value of U at time τ and at grid point $X_i = (i - 1)\,\Delta X$ $(i = 1, 2, \ldots, N)$. During the time interval $\tau_0 \le \tau \le \tau_0 + \Delta\tau$, we suppose that

$$\frac{\partial U_i}{\partial\tau}=\frac{U_i-U_i^0}{\Delta\tau} \tag{32}$$

where U_i^0 stands for the value at time τ_0, while all spatial derivatives of U are evaluated at time $\tau = \tau_0 + \Delta\tau$ in agreement with the implicit scheme.

At this point, it is interesting to notice that equation (32) can be considered as a central difference representation in time at $\tau = \tau_0 + \Delta\tau/2$. Sparrow and Chuck proposed that the term $dS/d\tau$ in equation (28) should be evaluated accordingly at $\tau = \tau_0 + \Delta\tau/2$.

If second-order central differences are used to approximate the spatial derivatives, equation (28) can be readily transformed to

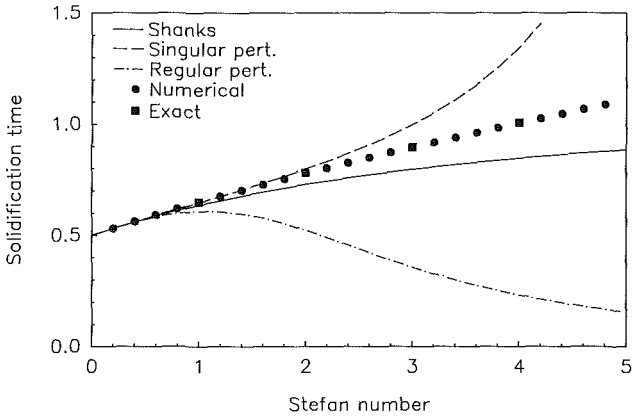

Fig. 2 Solidification time τ_m versus ϵ for boundary condition given by equation (10*a*)

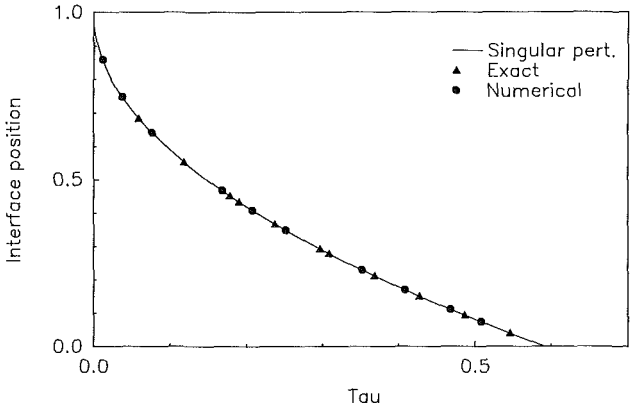

Fig. 3 Interface position r_f versus time τ for $\epsilon = 0.6$ and boundary condition given by equation (10*a*)

$$\epsilon\left(\frac{U_i-U_i^0}{\Delta\tau}-\frac{X_i}{S}\left(\frac{dS}{d\tau}\right)^{1/2}\frac{U_{i+1}-U_{i-1}}{2\Delta X}\right)$$

$$=\frac{-n}{(1-SX_i)S}\frac{U_{i+1}-U_{i-1}}{2\Delta X}+\frac{U_{i+1}-2U_i+U_{i-1}}{S^2\Delta X^2} \tag{33}$$

where $(dS/d\tau)^{1/2}$ stands for the value at $\tau_0 + \Delta\tau/2$, which can be determined with the help of equation (29). Starting from

$$\left(\frac{dS}{d\tau}\right)^0=\frac{1}{S^0}\frac{1-U_{N-1}^0}{\Delta X} \tag{34}$$

which yields

$$S^{1/2}=S^0+\left(\frac{dS}{d\tau}\right)^0\frac{\Delta\tau}{2} \tag{35}$$

one finds

$$\left(\frac{dS}{d\tau}\right)^{1/2}=\frac{1}{S^{1/2}}\frac{1-U_{N-1}^0}{\Delta X} \tag{36}$$

Finally, the thickness of the solid phase at time $\tau = \tau_0 + \Delta\tau$ is approximated by

$$S=S^0+\left(\frac{dS}{d\tau}\right)^{1/2}\Delta\tau \tag{37}$$

At this point, we are ready to determine the temperature field and the thickness of the solidified region by performing calculations in the following sequence: Starting with known values U_i^0 and S^0 at time $\tau=\tau_0$, the derivative $(dS/d\tau)^{1/2}$ is calculated from equations (35) and (36). S is given next by equation (37). Substituting these values into equation (33), the new values of U_i are readily obtained using the well-known Thomas algorithm for tridiagonal matrices.

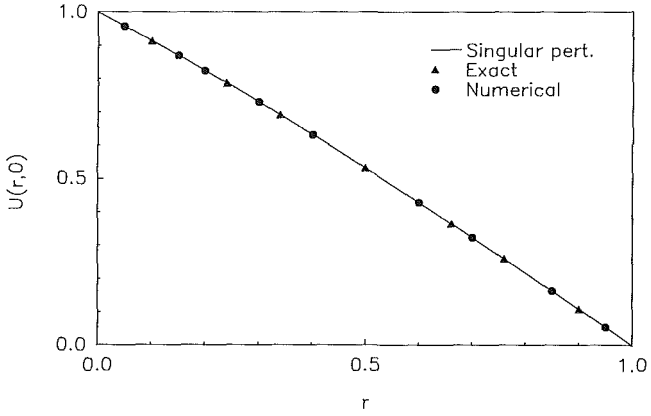

Fig. 4 Temperature profile U versus r at the end of solidification for $\epsilon = 0.6$ and boundary condition given by equation (10*a*)

To initiate the calculations, instead of starting from $\tau = 0$ at which $S = 0$, we have to begin computations at a certain (small) time $\tau=\tau^*$ with $S=\delta$. For a given choice of δ, τ^* and U are evaluated using leading order regular perturbation solutions. These solutions are given in the Appendix for all the boundary conditions and geometries.

Calculations were performed starting with $\delta=10^{-5}$. Successive time steps were chosen such that the interface only moved about 2 percent after each time interval. The solution domain was covered with a 101 point uniform mesh. Computations were done in double precision arithmetic. Execution time on an IBM/PC-AT was around 2 min per run. Validation and accuracy of the numerical program will be discussed in the next section.

Results and Discussion

In this section we present the analytical and numerical results obtained for a slab of thickness $2R_w$. Symmetric boundary conditions are assumed on both faces, i.e., either equations (10*a*), (10*b*), or (10*c*). Hence the freezing process will be symmetric with respect to the center plane and we need to consider only one half of the slab ($0\le r\le 1$).

Results are first presented for the constant temperature boundary condition equation (10*a*) for which the similarity solution, equation (11), holds. In this case, the numerical method may be directly validated against an exact solution. Figure 2 displays the normalized freezing time τ_m, i.e., the time required for complete solidification, versus the Stefan number $\epsilon = c\Delta T/L$. Figure 3 shows the progression of the moving solid-liquid interface r_f with time τ for $\epsilon = 0.6$. Figure 4 gives the dimensionless temperature profile $U = (T-T_w)/(T_f-T_w)$ within the solid phase for $\epsilon = 0.6$ at the instant of freezing to the center plane, when $\tau = \tau_m$ and $r_f = 0$.

Figure 2 shows the excellent agreement between the numerical calculations based on equations (28) and (29) and the exact solution equation (11). The second-order perturbation solution equation (24) is accurate within the range $0 \le \epsilon \le 2$. When $\epsilon = 3.15$, the stretching fails. That is, ψ vanishes at $r_f = 0$, which is precisely what the stretching is intended to prevent. The solution starts to diverge very rapidly afterward. Applying a Shanks transformation to the solution slows the divergence considerably, as can be seen on the graph. Also represented is the result of a calculation based on the regular perturbation equation (11*c*) to order ϵ^2. The latter diverges beyond $\epsilon = 0.8$. It appears from this figure that τ_m increases almost linearly with ϵ. This behavior is confirmed for low values of ϵ by the expansion of the similarity solution, which shows that τ_m behaves initially as $\tau_m \approx 1/2+\epsilon/6$ (cf. equation (11*d*)). It may then be deduced noting that $\tau=\kappa\epsilon t/R_w^2$ that the dimensional freezing time will behave as $t_m = R_w^2(1/6+1/2\epsilon)/\kappa$.

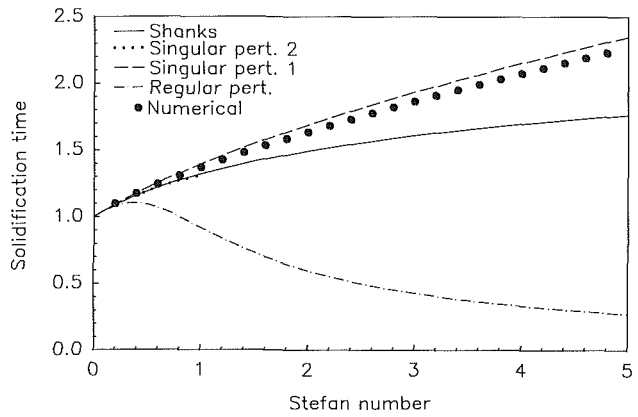

Fig. 5 Solidification time τ_m versus ϵ for boundary condition given by equation (10*b*)

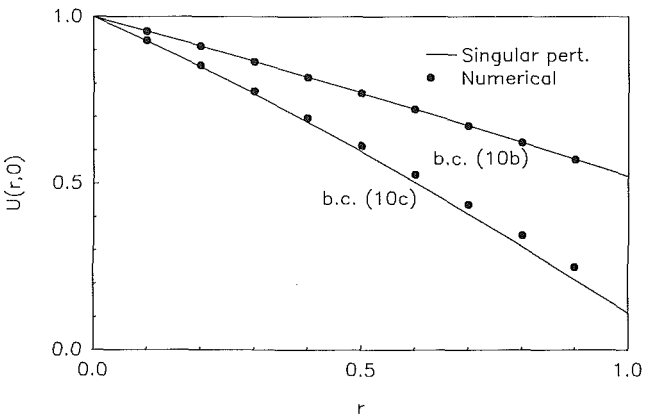

Fig. 7 Temperature profiles U versus r at the end of solidification for $\epsilon = 0.6$ and boundary conditions given by equations (10*b*) and (10*c*)

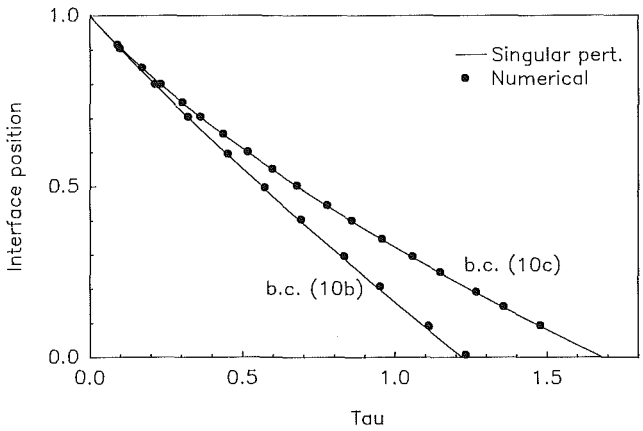

Fig. 6 Interface positions r_f versus time τ for $\epsilon = 0.6$ and boundary conditions given by equations (10*b*) and (10*c*)

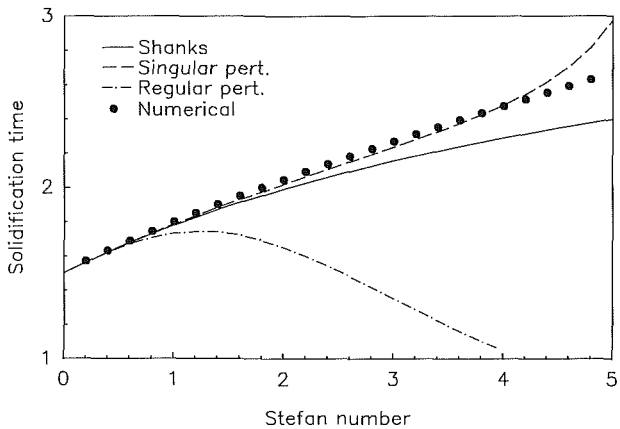

Fig. 8 Solidification time τ_m versus ϵ for boundary condition given by equation (10*c*)

Figure 3 shows that both the numerical and the perturbation solution are virtually undistinguishable from the exact solution for $\epsilon = 0.6$. The latter shows that $r_f \sim \sqrt{\tau}$ (cf. equation (11*b*)) so that the freezing process is faster at the beginning. For instance, it takes four times longer to complete the solidification than it takes to solidify half of the slab. Figure 4 shows the temperature profile when the solidificaton is completed. The agreement is excellent between the three solutions. The temperature profiles are quasi-linear for the low value of the Stefan number (0.6) for which we present our results.

For the constant flux boundary condition, equation (10*b*), there is no exact solution available. Given the perfect agreement between the numerical prediction and the exact solution in the previous case however, it may be reasonably assumed that the numerical solutions will be reliable for the other boundary conditions as well. Figure 5 reveals that for the second type of boundary condition, equation (10*b*), the perturbation solution, equation (25), only agrees with the numerical calculations up to $\epsilon \approx 1.0$. The curve terminates abruptly at $\epsilon = 1.05$ where the stretching fails. It would fall almost vertically beyond this value if it were shown on the graph. If the Shanks transformation is used there is no failure of the stretching for this range of Stefan numbers and the solution remains smooth. Oddly enough, the first-order solution neglecting σ_2 is more accurate. Therefore the perturbation series might be slowly divergent in this case. The regular second-order perturbation solution for this case diverges almost immediately.

Figure 6 demonstrates that the effects of imposing a constant heat flux are in contrast with those of imposing a constant temperature. It will be noticed from this figure that r_f changes almost linearly with τ. Figure 7 presents the temperature profile at $\epsilon = 0.6$, which is again almost linear. It will be seen from the graph that U is not zero at $r = 1$. In fact, a simple iteration on equation (13) using equation (25) will show that for $\epsilon = 0.6$ and $r_f = 0$, $\approx \epsilon(1-\epsilon)/2 = 0.12$ at $r = 1$, which is indeed verified on the figure. The average temperature gradient $(T_w - T_f)/R_w$ is thus smaller than for a fixed T_w.

Numerical calculations are further compared with the perturbation solution equation (26) for the last type of boundary condition, equation (10*c*). The results are presented for a Biot number $\mathrm{Bi} = hR_w/k = 1$. This last case shares the characteristics of the two previous cases. As a matter of fact, the solutions for constant T_w are a special case of the solutions for constant h when the Biot number becomes infinite. This may be readily verified by setting $\alpha = 1$ in equation (26). Figure 8 illustrates that the perturbation solution remains valid up to $\epsilon = 4.0$ without the Shanks transformation. With the transformation, divergence is slowed when $\epsilon \approx 5$ and beyond. A second-order regular perturbation solution was again plotted. Let us also mention briefly that for $\epsilon = 0.5$, 1, equation (26) is as accurate as the fourth-order regular solution that Pedroso and Demoto (1973c) evaluated numerically for the freezing time at various r_f when $\mathrm{Bi} = 1$.

Figure 6 shows that r_f increases faster once again at the beginning of the solidification, but not as much as for the constant T_w condition. The freezing time is about twice as long and the average temperature gradient is only half as large. This may be inferred from Fig. 7, which displays much higher values of U at $r = 1$ for $\epsilon = 0.6$ than in the other cases. The profile is once again almost linear.

Concluding Remarks

- The numerical method based on Sparrow and Chuck's proposals is accurate and will be useful for further investigations of the general perturbation solutions at higher order.
- Second-order solutions may be used with accuracy over a significantly wider range of ϵ than regular perturbation solutions of the same order.
- The boundary conditions have a significant effect on τ_m, $r_f(\tau)$, and $U(r_f, r)$ as well as on the average temperature gradient within the solidified shell.
- The Shanks transformation appears to be a simple and efficient method of slowing divergence. For the plane case, it did not extend the domain of validity of the solutions given by the stretched coordinate method.

Acknowledgments

This work was supported by the National Sciences and Engineering Research Council of Canada through grant No. NRC A-0626.

References

Beckett, P. M., 1971, "Problems Involving Heat Transfer with Change of Phase," Ph.D. Thesis, Hull University, United Kingdom.

Beckett, P. M., 1981, "On the Use of Series Solutions Applied to Solidification Problems," *Mech. Res. Commun.*, Vol. 8(3), pp. 169–174.

Bénard, C., Gobin, D., and Zanoli, A., 1986, "Moving Boundary Problem: Heat Conduction in the Solid Phase of a Phase-Change Material During Melting Driven by Natural Convection in the Liquid," *Int. J. Heat Mass Transfer*, Vol. 29, pp. 1169–1681.

Carslaw, H. S., and Jaeger, J. C., 1959, *Conduction of Heat in Solids*, Oxford University Press, Oxford, United Kingdom.

Pedroso, R. I., and Demoto, G. A., 1973a, "Perturbation Solutions for Spherical Solidification of Saturated Liquids," ASME JOURNAL OF HEAT TRANSFER, Vol. 95, pp. 42–46.

Pedroso, R. I., and Demoto, G. A., 1973b, "Inward Spherical Solidification – Solution by the Method of Strained Coordinates," *Int. J. Heat Mass Transfer*, Vol. 16, pp. 1037–1043.

Pedroso, R. I., and Demoto, G. A., 1973c, "Exact Solution by Perturbation Method for Planar Solidification of a Saturated Liquid with Convection at the Wall," *Int. J. Heat Mass Transfer*, Vol. 16, pp. 1816–1819.

Poots, G., 1962, "On the Application of Integral-Methods to the Solution of Problems Involving the Solidification of Liquids Initially at Fusion Temperature," *Int. J. Heat Mass Transfer*, Vol. 5, p. 525.

Prud'homme, M., and Nguyen, T. H., 1987, "Solutions de Perturbation Généralisées pour le Problème de Solidification en Milieu Semi-infini," EPM/RT-87-13, Ecole Polytechnique de Montréal, Montréal, Québec, Canada.

Prud'homme, M., and Nguyen, T. H., 1988, "Solutions par Perturbations Singulières pour un Problème de Stefan Généralisé," to be published in the *Int. J. Heat Mass Transfer*.

Riley, D. S., Smith, S. T., and Poots, G., 1974, "The Inward Solidification of Spheres and Circular Cylinders," *Int. J. Heat Mass Transfer*, Vol. 17, pp. 1507–1516.

Shanks, D., 1955, "Non-Linear Transformations of Divergent and Slowly Convergent Sequences," *J. Math. Physics*, Vol. 34, pp. 1–42.

Sparrow, E. M., and Chuck, W., 1984, "An Implicit–Explicit Numerical Solution Scheme for Phase-Change Problems," *Num. Heat Transfer*, Vol. 7, pp. 1–15.

Tao, L. C., 1967, "Generalized Numerical Solutions of Freezing a Saturated Liquid in Cylinders and Spheres," *AIChE J.*, Vol. 13(1), p. 165.

Toda, S., Sugiyama, H., Owada, H., Kurokawa, M., and Hori, Y., 1986, "Laminar Flow Heat Transfer in a Tube With Internal Solidification," *Proc. 8th Int. Heat Transfer Conf.*, Vol. 4, pp. 1745–1750.

Van Dyke, M., 1975, *Perturbation Methods in Fluid Mechanics*, Parabolic Press, Stanford, CA.

APPENDIX A

Initial Temperature Profile and Interface Position to Start Numerical Computations

Temperature profile at $\tau = \tau^*$

	$n=0$	$n=1$	$n=2$
Case *a*	$\dfrac{r-1}{r_f-1}$	$\dfrac{\ln r}{\ln r_f}$	$\dfrac{1/r-1}{1/r_f-1}$
Case *b*	$1-r+r_f$	$1-\ln r+\ln r_f$	$1+1/r-1/r_f$
Case *c*	$\dfrac{r-\alpha}{r_f-\alpha}$	$\dfrac{\ln r-\alpha}{\ln r_f-\alpha}$	$\dfrac{1/r-\alpha}{1/r_f-\alpha}$

Initial time τ^* when $S=\delta$

	$n=0$	$n=1$	$n=2$
Case *a*	$\delta^2/2$	$\dfrac{(1-\delta)^2}{2}\ln(1-\delta)+\dfrac{2\delta-\delta^2}{4}$	$\dfrac{\delta^2}{2}-\dfrac{\delta^3}{3}$
Case *b*	δ	$\delta-\delta^2/2$	$\delta-\delta^2+\delta^3/3$
Case *c*	$\dfrac{\delta^2}{2}+(\alpha-1)\delta$	$\dfrac{(1-\delta)^2}{2}\ln(1-\delta)+\dfrac{(1+2\alpha)(2\delta-\delta^2)}{4}$	$(1-\alpha)\delta+(2\alpha-1)\dfrac{\delta^2}{2}-\delta\dfrac{\alpha^3}{3}$

where

$$\alpha = \begin{cases} 1+1/\mathrm{Bi}, & \text{if } n=0 \\ 1/\mathrm{Bi}, & \text{if } n=1 \\ 1-1/\mathrm{Bi}, & \text{if } n=2 \end{cases}$$

W. D. Bennon
Aluminum Company of America,
Alcoa Center, PA 15069
Mem. ASME

F. P. Incropera
Heat Transfer Laboratory,
School of Mechanical Engineering,
Purdue University,
West Lafayette, IN 47907

An Experimental Investigation of Binary Solidification in a Vertical Channel With Thermal and Solutal Mixed Convection

Experimental measurements and photographic observations are presented for the solidification of a binary, aqueous ammonium chloride solution in a vertical channel. Transient liquidus front progressions and temperature measurements are used to characterize the influences of flow rate, superheat, composition, and chill wall temperature on binary phase-change behavior. Experimental results are compared with previously reported model predictions and discrepancies are used to critically assess model assumptions and limitations.

Introduction

Qualitative experimental observations (Jackson et al., 1966; McDonald and Hunt, 1969; Asai and Muchi, 1978; Szekely and Jassal, 1978) and recently reported numerical predictions (Bennon and Incropera, 1987a) clearly illustrate the complex transport behavior associated with multiconstituent phase change. Even for static systems, complex interactions between thermal and solutal natural convection in the bulk fluid and multiphase regions can lead to significant variations in resultant as-cast structure (Bennon and Incropera, 1987b). Conditions are further complicated by the fact that, in many applications, such as the production of continuously cast ingot, buoyancy-driven flows combine with an externally imposed velocity field.

Reviews of recent literature reveal that, while limited, efforts to predict multiconstituent phase change far surpass efforts to obtain quantitative data. However, the availability of a reliable experimental data base is crucial to the development of accurate methods for predicting multiconstituent phase change. Hence, the goals of this study are twofold. The first objective is to establish a quantitative data base for mixed convection multiconstituent phase change that, in itself, contributes to an improved understanding of related processes. The second objective is to compare the experimental results with existing predictions (Bennon and Incropera, 1988a) and, in the process, to assess the validity of a recently established continuum model for multiconstituent phase change.

Experimental Methods

Experiments on solidification in the presence of an externally imposed forced flow were conducted using the test cell of Fig. 1(*a*). Components of the assembly included a main chill section and entrance and exit headers, each with an internal cross section of 5 cm × 5 cm. The entrance and exit headers were fabricated from 1.27-cm-thick lexan and provided unchilled flow lengths of 8.9 cm. A permeable sponge, 4 cm long, was inserted in each header to provide a more uniform entrance velocity field to the chill section and to minimize the channeling of fluids at the chill section exit.

Each header assembly was equipped with an array of stainless steel compression fittings, staggered on 5-mm centers, for accommodating the vertical insertion of 1.6-mm-dia stainless steel thermocouple probes. Additional fittings, mounted in each of the header side walls, permitted the insertion of thermocouple probes for fluid temperature measurements at the chill section entrance and exit. Specific temperature measurement locations, including those associated with the chill wall, are shown in Fig. 1(*b*). The copper-constantan thermocouples were accurate to ±0.5°C.

The 10-cm length of the chill section, which consisted of two chill plates and two observation windows, was limited by heat extraction requirements. The chill plates were machined from copper with internal serpentine passages used to provide for recirculation of the coolant. Each chill plate was machined to a thickness of 11.1 mm and was coated with a thin layer of corrosion-resistant paint. The three thermocouples permanently mounted in each plate were installed 0.38 mm from the internal surface and were used for measurement and control of the plate temperature. A low-temperature recirculating bath (Neslab Model ULT-80DD) was used to extract energy from the chill plates. The bath provided a recirculating flow of coolant (ethanol) and could maintain the plates at temperatures between +10°C and −80°C, with a stability of ±0.03°C.

The observation windows were constructed of double-paned 6.4-mm-thick lexan with a 6.4-mm air space. The double-pane arrangement minimized heat transfer from the environment to the chill section. Nitrogen gas was used to purge air from the window assembly, thereby eliminating internal condensation.

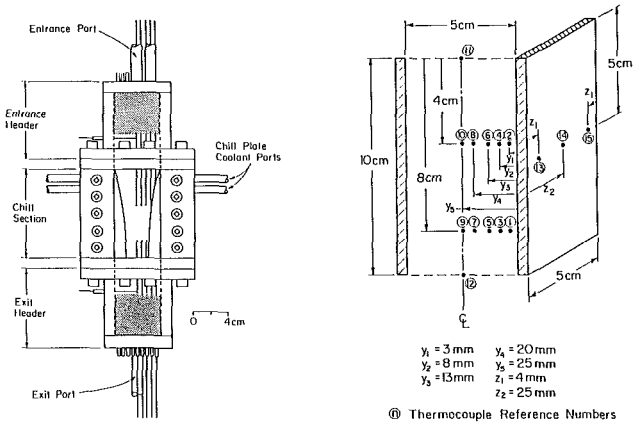

Fig. 1 Experimental test cell: (*a*) schematic, (*b*) thermocouple locations

Contributed by the Heat Transfer Division for publication in the JOURNAL OF HEAT TRANSFER. Manuscript received by the Heat Transfer Division April 26, 1988. Keywords: Mass Transfer, Mixed Convection, Phase-Change Phenomena.

Table 1 Experimental conditions for mixed convection solidification of binary NH_4Cl-H_2O solutions

Experiment	Chill Wall Temperature (T_c), °C	Reynolds Number (Re)	Entry Temperature (T_o), °C	Entry Composition ($f_{l,o}^{H_2O}$)	Liquidus Temperature (T_{liq}), °C
1	-20	200	25	0.73	18.8
2	-40	200	25	0.73	18.8
3	-40	800	25	0.73	18.8
4	-40	200	35	0.73	18.8
5	-40	200	25	0.76	4.7

A transparent grid was mounted on the front observation window to facilitate quantifying the transient solidification process from photographic records.

Liquid phase change material (NH_4Cl-H_2O) was stored in a temperature-controlled holding tank, and a magnetically driven centrifugal pump and calibrated (±1 percent) rotometer were used to maintain steady flow through a closed loop, which included the test cell. The temperature of the isothermal holding tank was set according to the desired superheat at the chill section entrance.

For each experiment, approximately 35 liters of NH_4Cl-H_2O solution were prepared by mixing pure NH_4 Cl reagent with deionized and demineralized water. The solution was degassed prior to filling the isothermal holding tank. Solidification was induced by initiating a flow of precooled ethanol through the internal serpentine passages of the chill plates. To minimize the time required to achieve a prescribed chill plate temperature, the ethanol bath was initially operated at a temperature below the set point.

During each experiment, the thermocouple readings were continuously monitored using a Hewlett-Packard 3054A data acquisition system. Two-milliliter samples of phase-change material were periodically extracted from the isothermal holding tank and tested gravimetrically to verify the mixture composition. Deviations in the mass fraction of water from the desired nominal were less than 0.56 percent. Back lighting of the test cell was provided by a high-intensity incandescent lamp with a diffuse cover, and photographs of the liquidus interface were obtained at selected times during each experiment. The photographs provided a quantitative measure of the liquidus progression, as well as a qualitative description of liquidus morphology.

Experimental conditions of the study, summarized in Table 1, were selected to evaluate the influences of entry liquid superheat (T_o), entry composition ($f_{l,o}^{H_2O}$), flow rate (Re), and chill wall temperature (T_c) on phase-change behavior. The NH_4Cl-H_2O system has a eutectic composition of $f_{l,o}^{H_2O} = 0.803$ and a eutectic temperature of $T_e = -15.4$°C. Each experiment was terminated at 3600 s, beyond which significant changes were not observed.

Experimental Results

Figures 2–5 illustrate the influence of chill wall temperature (T_c) for Re = 200, T_o = 25°C, and $f_{l,o}^{H_2O} = 0.73$. Photographs of solidification behavior are shown in Figs. 2 and 3 for $T_c = -20$°C and -40°C, respectively, while the corresponding temperature histories are illustrated in Figs. 4 and 5. Liquidus (T_{liq}) and eutectic (T_e) temperatures are included on each temperature history to aid in determining the extent of the mushy region and in contrasting the temperature measurements with the photographic observations. However, it should be noted that the liquidus temperature (T_{liq} = 18.8°C) corresponds to the entry composition, $f_{l,o}^{H_2O} = 0.73$, while local phase change behavior is governed by local compositions which, due to the transient redistribution of species, can deviate from the entry composition. Experimental limitations precluded establishment of an instantaneous step change in the chill plate temperature T_c. As illustrated by the chill plate temperatures (thermocouples 13–15) in Figs. 4 and 5, a cooling rate of approximately 0.6°C/s was achieved.

Figures 2 and 3 reveal the expected trend of increasing solidification rate with decreasing chill wall temperature. Due to interference of the entrance and exit header flanges (Fig. 1*a*), photographic observations were restricted to the 10-cm chill section. However, due to axial diffusion, solidification occurred both upstream and downstream of the chill section, with the most significant growth occurring in the downstream region. Liquidus front irregularities observed by previous investigators (Szekely and Jassal, 1978; Jackson et al., 1966; McDonald and Hunt, 1969) for static phase-change systems appear in each figure, particularly for times just following the onset of solidification. While these irregularities persist throughout each experiment, they become less pronounced during the later stages, when growth rates are small.

Except for local interfacial irregularities and distortions near the chill region entrance and exit, solidification at early times ($T < 240$ s) is characterized by a nearly planar propagation of the liquidus front, suggesting that early transport is unidirectional and diffusion-dominated. For later times, significant deviations from planar, diffusion-dominated behavior can be observed, particularly for small chill wall temperatures (Fig. 3). Similar trends may be inferred from the temperature histories. For example, in Fig. 5, thermocouples 1 and 2, which are at different axial positions, record almost identical temperatures, suggesting that isotherms are nearly planar and parallel to the vertical chill surface. In contrast, differences for thermocouples 5 and 6 suggest a significant deviation from planar, diffusion-dominated conditions in the outer extent of the mushy region.

Irrespective of chill wall temperature, temperature measurements nearest the chill plates (thermocouples 1 and 2) indicate that the influence of the cold boundary quickly propagates into the phase-change medium. Significant deviations from the entry temperature occur as early as 50 s from the start of solidification. In contrast thermocouples further from the chill plate experience delays before recording values below the entry temperature. The extent of the delay varies inversely with the rate of solidification and hence increases with increasing chill plate temperature. Times for which temperatures drop below T_{liq} can be contrasted with photographically observed liquidus front positions and the results are consistent. For example, thermocouples 3 and 4 of

Nomenclature

D_h = hydraulic diameter = $2W$
f = mass fraction
L = chill region length
Re = Reynolds number = $u_o D_h/\nu_l$
t = time
t^* = dimensionless time
T = temperature
u_o = entry velocity
W = plate spacing
x, y, z = Cartesian coordinates
δ = thickness
ν = kinematic viscosity

Subscripts

c = chilled wall
e = eutectic
l = liquid
liq = liquidus
o = entry

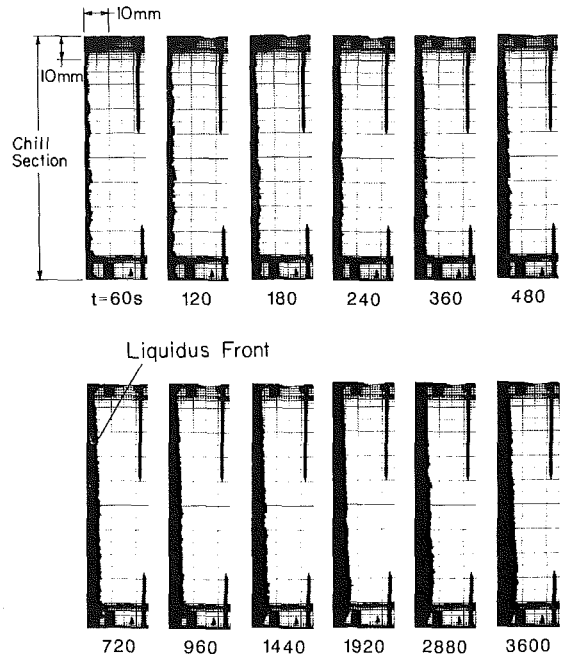

Fig. 2 Photographically observed solidification behavior for experiment 1

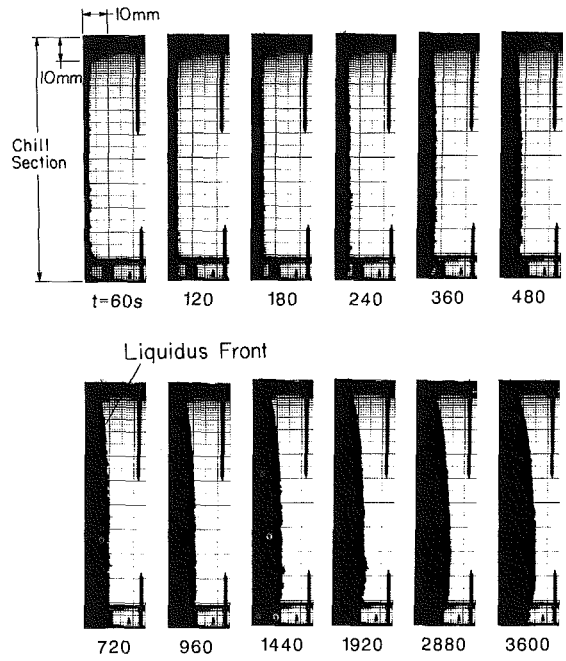

Fig. 3 Photographically observed solidification for experiment 2

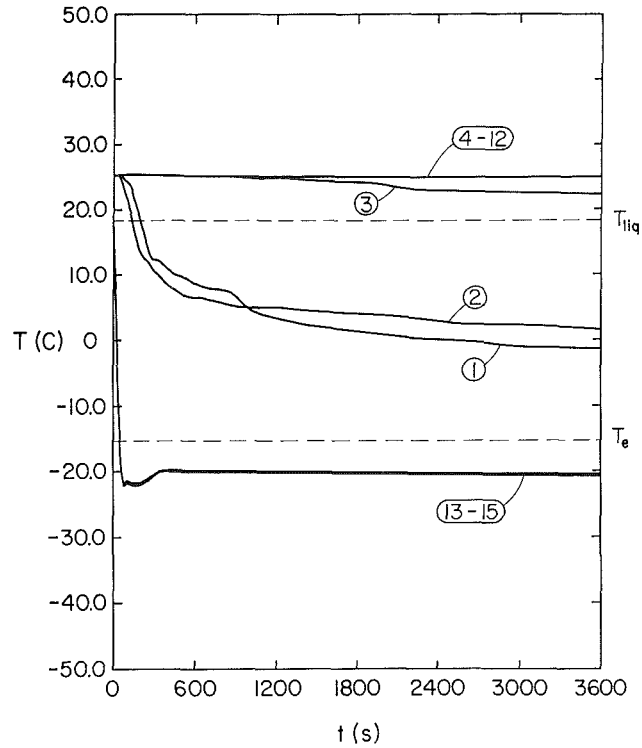

Fig. 4 Experimental temperature histories for experiment 1

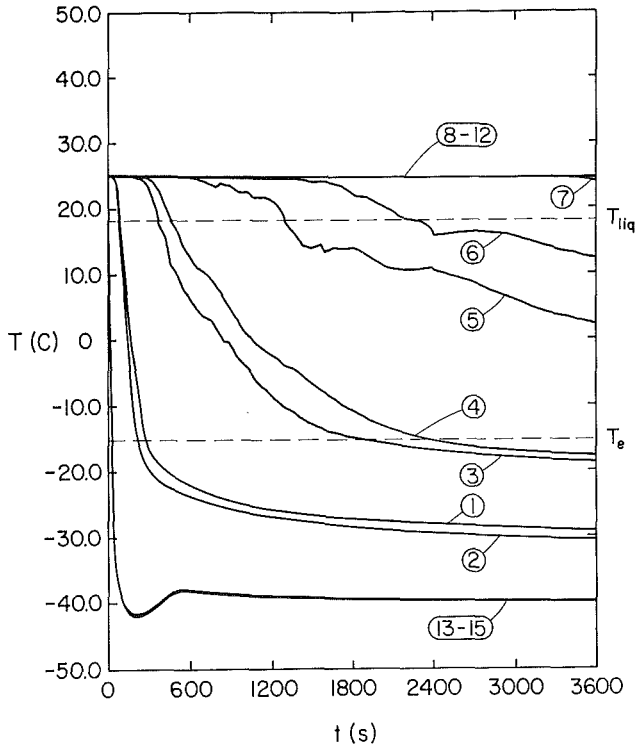

Fig. 5 Experimental temperature histories for experiment 2

Fig. 5, which are 8 mm from the chilled wall, drop below T_{liq} at times ranging from approximately 350 to 450 s. While irregularities in the liquidus interface of Fig. 3 make it difficult to assess the precise time at which the front crosses 8 mm, crossing does occur between 360 and 480 s.

Fluctuations in thermocouple readings within the mushy region are attributed to variations in the interdendritic flows. With large temperature gradients in the mushy region, transient changes in interdendritic flows can induce temperature fluctuations. Supporting evidence of fluctuating behavior in statically cast NH_4Cl–H_2O systems has been provided by previous investigators (Jackson et al., 1966) and is attributed to local growth rate variations and remelting. Localized remelting is due to the advection of water-rich interdendritic fluids from cold regions near the chilled wall. Due to the accompanying liquidus temperature depression, solid in warmer regions near the liquidus interface may be melted.

Figures 3 and 6 and the corresponding temperature histories, Figs. 5 and 7, illustrate the influence of Reynolds number on binary phase-change behavior. The photographs suggest that Reynolds number has little influence on development of the liquidus front for early times, and for $t < 480$ s, the

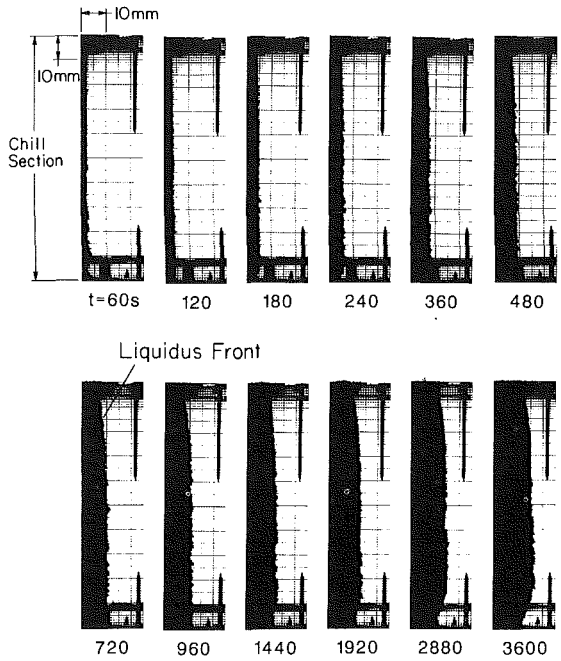

Fig. 6 Photographically observed solidification behavior for experiment 3

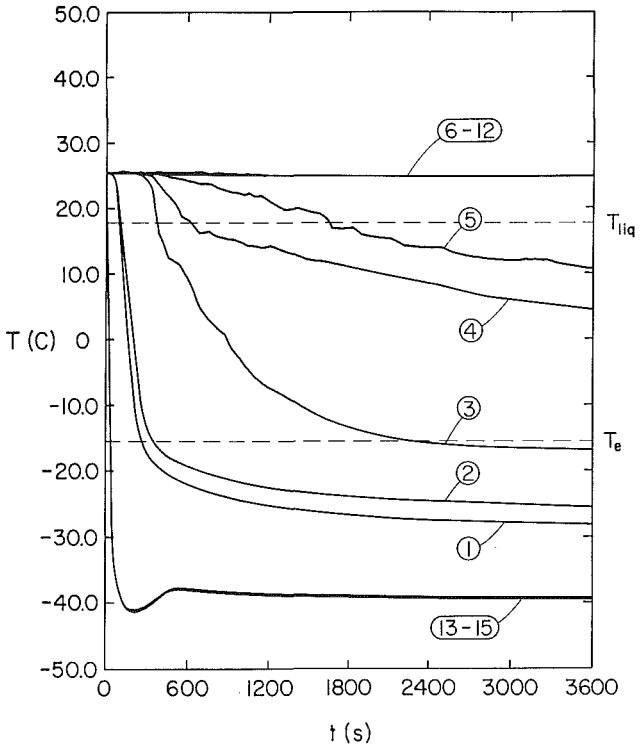

Fig. 7 Experimental temperature histories for experiment 3

maximum difference in front locations is approximately 1 mm. The temperature histories confirm this observation, and for $t < 480$ s, differences are less than 3°C. However, for $t > 480$ s deviations from a planar liquidus front and thinning of the mushy region near the entrance become more pronounced with increasing Re. Thermocouple measurements at the two axial locations (40 and 80 mm from the chill section entrance) confirm this observation. For example, while temperatures recorded by thermocouples 3 and 4 for Re = 200 (Fig. 5) exhibit only modest differences (<5°C) throughout

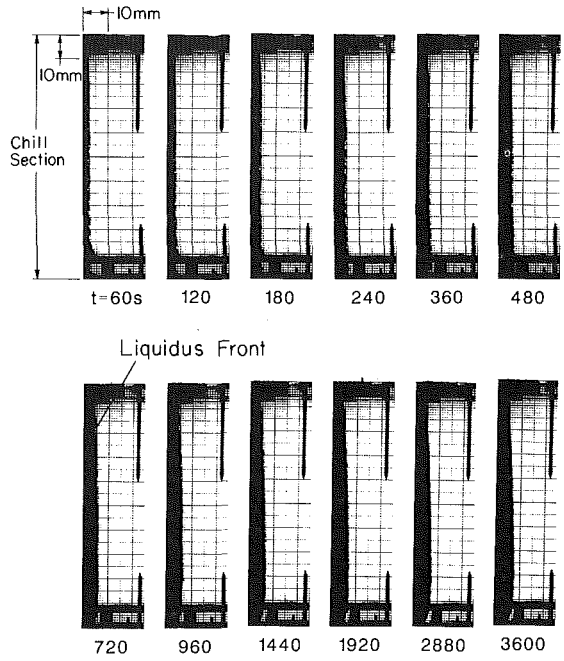

Fig. 8 Photographically observed solidification for experiment 4

the experiment, differences are as large as 25°C for Re = 800 (Fig. 7). An indication of nonplanar liquidus front progression is also provided by thermocouple 6, which is located 13 mm from the chilled wall. While this thermocouple enters the mushy region at $t \approx 2200$ s (Fig. 5) for Re = 200, its recorded temperature for Re = 800 (Fig. 7) never deviates from the entrance temperature.

Figures 3 and 6 also reveal that irregularities in the liquidus front become less pronounced with increasing Reynolds number. This trend is attributed to an increase in shear forces at the liquidus interface with increasing Re. These forces will inhibit the formation of and/or shear off fragile dendrites that protrude from the interface. Furthermore, since the extent of propagation of dendrites into a melt depends strongly on the existence of local temperature and concentration gradients, the thinning of temperature and concentration boundary layers that accompanies an increase in core liquid velocities can contribute to the finer structures and smoother appearance of the liquidus front at the larger Reynolds number.

Figures 3 and 8 and the corresponding temperature histories, Figs. 5 and 9, reveal the influence of entry temperature T_o on phase-change behavior. In addition to impeding solidification, elevated entry temperatures reduce the time required to achieve quasi-steady conditions. For T_o = 35°C (Fig. 8), liquidus front positions exhibit only a modest change between 1440 and 3600 s, while significant growth occurs beyond 1440s for T_o = 25°C (Fig. 3). Figures 3 and 8 further suggest that elevated entry temperatures act to smooth the liquidus front during the latter stages of solidification. Smooth liquidus front morphologies, which accompany elevated entry temperatures, are again attributed to the existence of large shear forces. In this case, however, the increased interfacial shear is attributed to an increase in the localized, thermally induced fluid acceleration near the liquidus front. Acceleration near the interface is induced by an assisting (downward) thermal buoyancy force, which results from the temperature difference $(T_o - T_{liq})$.

The influence of entry composition $f_{l,o}^{H_2O}$ is shown in Figs. 3 and 10 and the corresponding temperature histories of Figs. 5 and 11. As the photographs suggest, an increase in entry composition alters solidification in much the same manner as an increase in entry temperature. This similarity is attributed

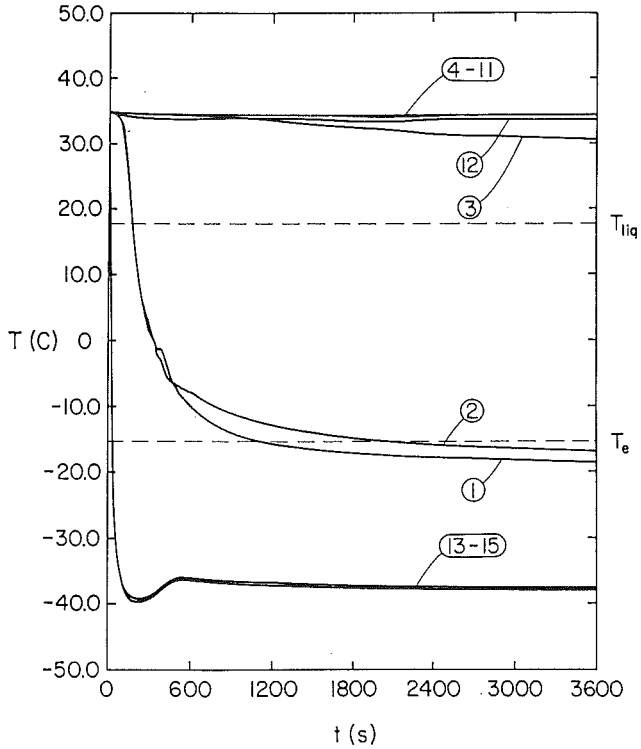

Fig. 9 Experimental temperature histories for experiment 4

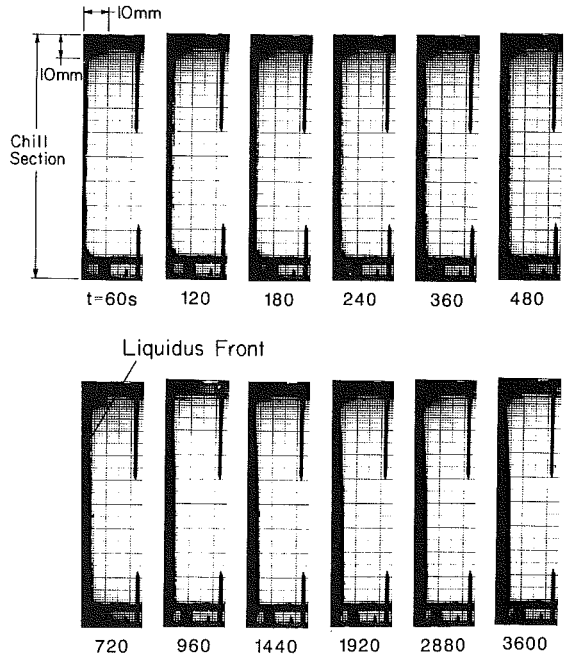

Fig. 10 Photographically observed solidification for experiment 5

the depression in liquidus temperature that accompanies increased composition. Due to the extremely large liquidus slope associated with the NH_4Cl–H_2O system, a change in $f_{l,o}^{H_2O}$ from 0.73 (Fig. 3) to 0.76 (Fig. 10) results in a 14.1°C depression in liquidus temperature. Since the temperature difference ($T_o - T_{liq}$), which strongly influences transport between the fluid core and liquidus interface, increases with either increasing T_o or decreasing T_{liq}, a 10°C increase in entry temperature is approximately equivalent to a 3 percent increase in entry water composition. In fact, except for the slightly greater solidification rate observed in Fig. 8 ($T_o - T_{liq} = 16.2$°C),

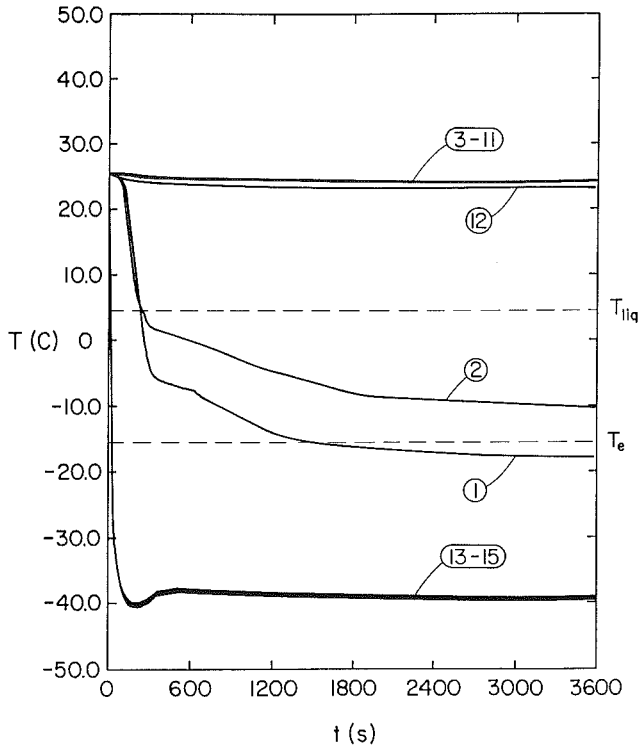

Fig. 11 Experimental temperature histories for experiment 5

visually observed phase change behavior differs little from that of Fig. 10 ($T_o - T_{liq} = 20.3$°C). Hence, observed changes in solidification that accompany an increase in $f_{l,o}^{H_2O}$, such as smoothing of the liquidus front, are attributed to the same mechanisms previously identified for an increase in the entry temperature T_o.

Comparisons With Predictions

Experimental results may be compared with previously reported numerical predictions (Bennon and Incropera, 1988a) based on a continuum model of mixed convection, binary phase change. The model views the multiphase region as an isotropic, stress free, porous mass. In addition, simplifying assumptions, which include local thermal and constitutional equilibrium and constant phase thermophysical properties, are invoked. An assessment of model assumptions and limitations, as they relate to quantitative comparisons of numerical and experimental results, will be subsequently discussed. Details of the numerical solution methodology are provided elsewhere (Bennon and Incropera, 1988b).

Several difficulties are associated with comparing predicted and measured results. A major difficulty relates to the extreme sensitivity of solidification to entry composition ($f_{l,o}^{H_2O}$). Figure 12(*a*) compares predicted and experimental results for the liquidus front propagation (δ_{liq}) at the axial midpoint of the chilled section ($x/L = 0.5$) for Re = 800, $T_c = -40$°C, and $T_o = 25$°C. The experimental results correspond to an inlet composition of $f_{l,o}^{H_2O} = 0.7300 \pm 0.0056$, while the predicted results correspond to values of 0.72 and 0.73. The predicted liquidus front progression is initially more rapid than that observed experimentally and, for $f_{l,o}^{H_2O} = 0.73$, the predicted front rapidly approaches a value that is well below that observed experimentally. Discrepancies between the initial rate of liquidus front progression and the time required to approach a steady condition are, in part, due to the inability to achieve an instantaneous step change experimentally in the chill wall temperature T_c. As shown in Fig. 7 (thermocouples

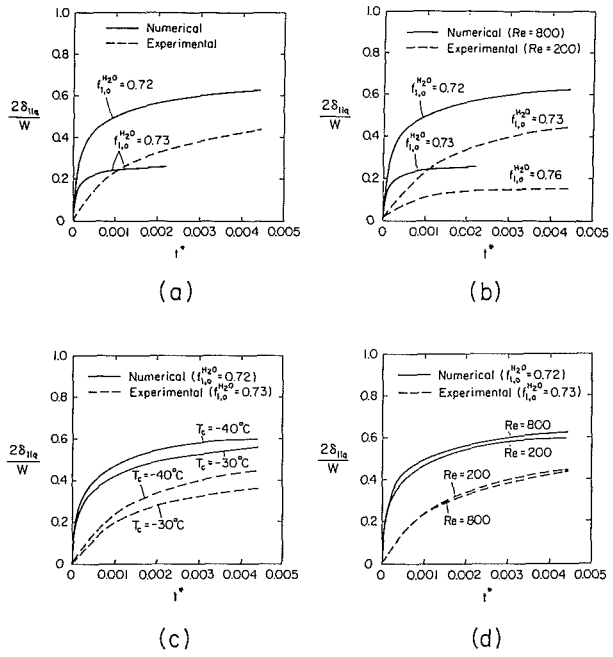

Fig. 12 Comparison of experimental and predicted liquidus front locations at x/L = 0.5; (a) Re = 800, $T_c = -40°C$, and $T_o = 25°C$; (b) $T_c = -40°C$ and $T_o = 25°C$; (c) Re = 200 and $T_o = 25°C$; (d) $T_c = -40°C$ and $T_o = 25°C$

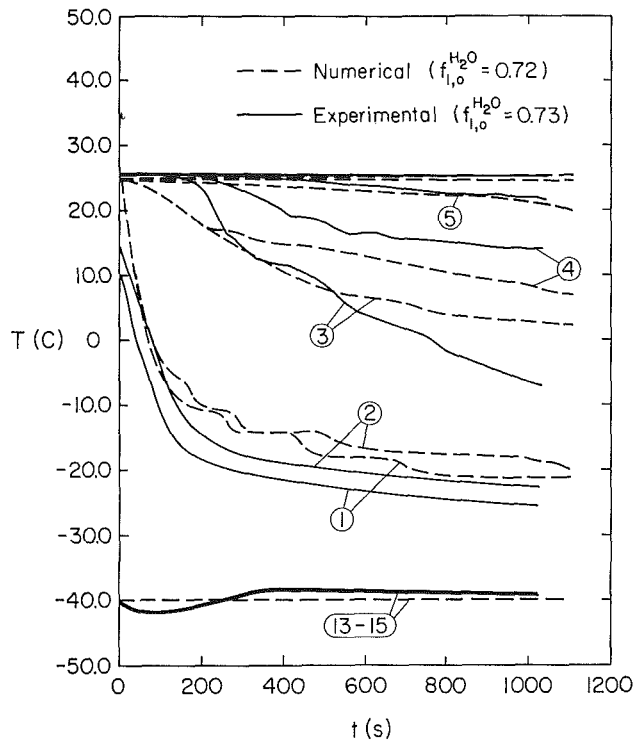

Fig. 13 Comparison of predicted and measured temperature histories with a 110 s experimental time shift for Re = 800, $T_c = -40°C$, and $T_o = 25°C$

13–15), approximately 110 s pass before the chill plates can be reduced to the desired setpoint of $T_c = -40°C$. This limitation cannot, however, explain underprediction of the extent of liquidus front propagation. Additional calculations performed for $f_{l,o}^{H_2O} = 0.72$ suggest that the discrepancy may be due more to the strong dependence of solidification on $f_{l,o}^{H_2O}$. As shown in Fig. 12, a 1 percent decrease in entry composition more than doubles the predicted liquidus front position after only 480 s ($t^* = 2.20 \times 10^{-3}$) and causes a substantial overprediction of the measured results. Hence, at least in part, the discrepancies may be attributed to the 0.56 percent uncertainty in the experimental entry composition. Although the numerical model could be *tuned* by selecting values of $f_{l,o}^{H_2O}$ slightly smaller than the nominal value of 0.73, such tuning would be somewhat arbitrary and was hence deemed inappropriate.

Figure 12(*b*) illustrates the influence of entry composition on both predicted and experimental liquidus front progressions. While the numerical and experimental results correspond to different Reynolds numbers, several important observations can be made. The strong sensitivity of the predicted liquidus front progression to changes in $f_{l,o}^{H_2O}$ for Re = 800 is confirmed by the data for Re = 200. In both cases a small increase in entry composition significantly reduces both the time required to achieve steady conditions and the corresponding liquidus front progression. The strong dependence of solidification on entry composition is due to the liquidus temperature depression that accompanies an increase in $f_{l,o}^{H_2O}$. The large decrease in T_{liq} resulting from a small increase in $f_{l,o}^{H_2O}$ for the NH_4Cl-H_2O system significantly increases the temperature difference ($T_o - T_{liq}$) and hence energy transport from the bulk fluid to the mushy region. This enhancement of interfacial energy transport is responsible for the decline in solidification rates.

Figure 12(*c*) illustrates the influence of chill wall temperature on liquidus front progression. The discrepancy in absolute liquidus front positions is attributed to the previously described influence of uncertainties in the entry composition. However, both numerical and experimental results exhibit a similar reduction in liquidus front growth rate and a corresponding reduction in the extent of liquidus front progression as T_c is increased from $-40°C$ to $-30°C$.

The influence of Reynolds number is shown in Fig. 12(*d*). Although the influence of entry composition again compromises absolute quantitative comparisons, both the experimental results for $f_{l,o}^{H_2O} = 0.73$ and the numerical results for $f_{l,o}^{H_2O} = 0.72$ indicate that Re has little influence (less than 1 mm) on liquidus front progression. While experimental results suggest a slight decline in liquidus front growth with increasing Re, the numerical results suggest a slight increase. Due to the irregular nature of the liquidus front, experimental difficulties associated with extracting precise positions preclude the establishment of definitive conclusions based on such small differences.

Figure 13 compares temperature histories for which numerical results correspond to $f_{l,o}^{H_2O} = 0.72$ and experimental results correspond to a nominal entry composition of $f_{l,o}^{H_2O} = 0.73$. Recalling the strong sensitivity of results to the entry composition, predictions for $f_{l,o}^{H_2O} = 0.72$ were chosen on the basis of their better agreement with data. Moreover, since the inability to impose a step change experimentally in the chill wall temperature from T_o to T_c causes significant differences between the measured and predicted initial cooling rates, the experimental results were modified by shifting the experimental time axis by 110 s. That is, the modified experimental results of Fig. 13 begin ($t = 0$) when the chill plates attain the desired setpoint of $T_c = -40°C$.

Predicted and measured trends of Fig. 13 are consistent. For example, both predicted and measured temperature differences between thermocouples 1 and 2, each of which is located 3 mm from the vertical chill plate, are less than 4°C. Since the two locations correspond to different axial positions, this observation suggests that both measured and predicted isotherms remain nearly planar (and parallel) close to the chilled wall. The gradual divergence with time of both predicted and measured temperatures for thermocouples 3 and

4 indicates a departure from planar isotherms at distances farther from the chill wall (8 mm) during latter stages of solidification. Both predicted and measured results indicate a significant delay for further propagation of the chilled wall thermal condition into the bulk fluid (thermocouple 5). Similar consistency between predicted and measured trends was obtained for Re = 200.

Although the foregoing comparison suggest that the continuum model is able to predict major trends, they do not confirm its ability to predict quantitative results accurately. While the strong influence of composition on solidification of the NH_4Cl–H_2O system has been cited as a likely source of differences between predictions and measurements, model assumptions undoubtedly contribute to the discrepancies. A major assumption relates to the existence of thermal and compositional equilibrium between coexisting phases (Bennon and Incropera, 1987a, 1987b). Its validity depends on phase thermophysical properties and solidification rates, with large property differences and rapid solidification rates acting to violate the assumption. For example, if the thermal diffusivity of the solid phase exceeds that of the liquid phase, solid within the multiphase region would respond more rapidly to an imposed temperature change than the coexisting interdendritic liquid. In the NH_4Cl–H_2O system, the thermal diffusivity of solid phase exceeds that of liquid by approximately 40 percent and, in view of the rapid solidification rates of this study, deviations from local thermal equilibrium may be partially responsible for observed numerical/experimental discrepancies. Violations of the assumption of local compositional equilibrium are more difficult to assess, since they are influenced not only by differences in phase mass diffusivities, but also by the rate at which solute atoms are incorporated or rejected from the atomic lattice structures of the coexisting phases. It is likely, however, that the rapid solidification rates of this study are conducive to nonequilibrium conditions and hence may also contribute to numerical/experimental discrepancies.

Due to the absence of pertinent data, the predictions also neglect variations of phase thermophysical properties with temperature and composition. For systems with moderate temperature and concentration gradients, the assumption of constant phase properties may be satisfactory. However, for the conditions of this study, which correspond to large temperature and composition variations, the constant property assumption is suspect. For example, liquid temperature variations in the experimental studies were as large as 85°C. Furthermore, due to the water enrichment of interdendritic fluids within the mushy region, variations in liquid composition generally exceeded 10 percent. Hence, a dependence of properties such as phase-specific heats and thermal conductivities on temperature and composition would undoubtedly influence predicted transport behavior and hence numerical/experimental comparisons.

Another factor that could influence model predictions is the uncertainty associated with the multiphase region permeability. The prescription of phase interaction forces through Darcy's law is a major model assumption, which permits the description of momentum transport within the mushy region. By adopting this approximation, however, description of the complex, microscopic structure of the mushy region is linked to a single parameter (the permeability). The significant influence of interdendritic fluid motion on species redistribution, and hence on overall solidification behavior, renders the permeability an important model parameter. Moreover, due to limitations in available data, predictions of this study have been based on the assumption of an isotropic permeability. However, the dependence of growth mechanisms on gradients of temperature and composition, as well as on the scalar quantities themselves, suggests that the permeability of the dendritic system is anisotropic. Uncertainties in the permeability model itself and in related coefficients therefore compromise the ability to obtain accurate numerical predictions.

Conclusions

Experimental results characterizing the influence of flow rate, liquid superheat, liquid composition, and chill wall temperature on the mixed convection solidification of a binary aqueous ammonium chloride solution have been presented. Although trends are consistent with those predicted by a continuum model, quantitative agreement between experimental and predicted results has been compromised by several factors. One factor relates to strong dependence of solidification behavior on composition for the NH_4Cl–H_2O system. Other factors include inadequately characterized thermophysical properties, as well as model assumptions related to thermal/compositional equilibrium and momentum transport in a porous medium. The results of this study represent a first step in identifying potential model limitations and in establishing a rational basis for improving means of predicting the complex phenomena associated with solidification in binary substances.

Acknowledgments

Support of this work by the U.S. Department of Energy under Award No. DE-FG02-87ER13759 is gratefully acknowledged. The research was conducted at Purdue University while one author (WDB) was on a supported technical leave of absence from the Aluminum Company of America.

References

Asai, S., and Muchi, I., 1978, "Theoretical Analysis and Model Experiments on the Formation Mechanism of Channel-Type Segregation," *Transactions ISIJ*, Vol. 18, pp. 90–98.

Bennon, W. D., and Incropera, F. P., 1987a, "A Continuum Model for Momentum Heat and Species Transport in Binary Solid–Liquid Phase Change Systems—II. Application to Solidification in a Rectangular Cavity," *International Journal of Heat and Mass Transfer*, Vol. 30, pp. 2171–2187.

Bennon, W. D., and Incropera, F. P., 1987b, "The Evolution of Macrosegregation in Statically Cast Binary Ingots," *Metallurgical Transactions*, Vol. 18B, pp. 611–619.

Bennon, W. D., and Incropera, F. P., 1987c, "A Continuum Model for Momentum, Heat and Species Transport in Binary Solid–Liquid Phase Change Systems—I. Model Formulation," *International Journal of Heat and Mass Transfer*, Vol. 30, pp. 2161–2169.

Bennon, W. D., and Incropera, F. P., 1988a, "Numerical Simulation of Binary Solidification in a Vertical Channel With Thermal and Solutal Mixed Convection," *International Journal of Heat and Mass Transfer*, in press.

Bennon, W. D., and Incropera, F. P., 1988b, "Numerical Analysis of Binary Solid–Liquid Phase Change Using a Continuum Model," *Numerical Heat Transfer*, in press.

Jackson, K. A., Hunt, J. D., Uhlmann, D. R., and Seward, T. P., III, 1966, "On the Origin of the Equiaxed Zone in Castings," *Transactions Metallurgical Society AIME*, Vol. 236, pp. 149–158.

McDonald, R. J., and Hunt, J. D., 1969, "Fluid Motion Through the Partially Solid Regions of a Casting and Its Importance in Understanding A Type Segregation," *Transactions Metallurgical Society AIME*, Vol. 245, pp. 1993–1997.

Szekely, J., and Jassel, A. S., 1978, "An Experimental and Analytical Study of the Solidification of a Binary Dendritic System," *Metallurgical Transactions B*, Vol. 9B, pp. 389–398.

Transient Radiative Heat Transfer From a Sphere Surrounded by a Participating Medium

Y. Bayazitoglu
Professor.
Mem. ASME

P. V. R. Suryanarayana
Student Mem. ASME

Mechanical Engineering and
Materials Science Department,
Rice University,
Houston, TX 77251

Transient radiative cooling of a solid or liquid sphere in space, surrounded by a radiatively participating vapor cloud, is considered. A quasi-steady assumption is applied to the radiation transfer in the medium, with the unsteadiness being retained at the inner spherical boundary. The problem is solved by applying the third-order (P_3) spherical harmonics approximation to the radiative transfer equation for the participating cloud, and a finite difference scheme for transient conduction in the sphere. In general, the presence of a participating medium decreases the cooling rate of the sphere, and cooling curves are presented to show this effect. Effective emissivity of the surface in the presence of a surrounding medium is evaluated, and an approximate explicit equation is given.

Introduction

In problems involving radiative cooling of conductive bodies in space, the presence of a nonlinear boundary condition at the surface makes an analytical, closed-form solution difficult to obtain, except under highly restrictive assumptions. Crosbie and Viskanta (1966) and Ayers (1970) have presented numerical solutions to the problem of cooling with a radiation boundary, and this is a well-understood problem. However, the presence of a surrounding radiatively participating medium, and its effect on the transient cooling of the body, have not been reported in the literature. An understanding of such a problem has many practical applications, such as manufacturing processes in space, combustion systems (for example coal particles enclosed within a soot cloud), noncontact temperature measurement techniques, and nuclear engineering. In space manufacturing, particularly electromagnetic levitation and induction melting of metals and some nonmetals, we often have a liquid droplet surrounded by its own vapor, inert gases, boiling impurities, and some particles that may be thrown off by the droplet, which rotates in response to the electromagnetic torque. Thus, it is possible to have millimeter to meter sized droplets surrounded by a participating medium. This situation may also be present in some volatilization studies.

Many noncontact temperature measurements often rely on a measurement of the brightness and intensity of radiation emitted by the surface whose temperature is of interest. When such a surface is surrounded by a participating medium, either at a higher or lower temperature than the surface, the radiant energy reaching the diagnostic instrument is a function of the optical properties of the medium, in addition to the surface properties. This situation may also arise in some liquid droplet radiators (Mattick and Hertzberg, 1981), where the droplet stream is contained in micron thick bounding plates as suggested by recent work (White, 1987). In all these cases, the effect of the medium on the transient cooling of the enclosed object becomes important.

In this study, the transient cooling of a single sphere at high temperatures, surrounded by a radiatively participating medium, is addressed. The spherical harmonics method is employed to obtain a system of differential equations for the medium radiative transfer, and its solution is coupled with the conduction in the sphere. Transient temperature at the surface of the sphere is compared with the no-cloud case, and the effect of the cloud is discussed. An expression for the effective emissivity of the surface, which accounts for the presence of a participating vapor, is also derived.

Contributed by the Heat Transfer Division for publication in the JOURNAL OF HEAT TRANSFER. Manuscript received by the Heat Transfer Division July 26, 1988. Keywords: Microgravity Heat Transfer, Radiation.

Analysis

A schematic representation of the geometry of the problem considered is given in Fig. 1. A sphere of radius R_1 is surrounded by a finite cloud of a gray, absorbing-emitting-scattering medium, of outer radius R_2. The sphere is at an initial temperature T_i, and at time $t>0$, is exposed to the radiatively cooling environment of space, at temperature $T_e=0$. Heat transfer is by conduction in the sphere, and it is assumed to have no heat sources or sinks.

In general, the problem is coupled with transient conduction in the sphere, transient radiation in the vapor medium, and matching conditions at the interface. The governing equations then become

$$\frac{1}{r^2}\frac{\partial}{\partial r}\left(r^2\frac{\partial T}{\partial r}\right)=\frac{1}{\alpha_s}\frac{\partial T}{\partial t},\ \text{for } 0<r\le R_1 \tag{1}$$

$$\mu\frac{\partial i}{\partial r}(\mu, r)+\frac{(1-\mu^2)}{r}\frac{\partial i(r,\mu)}{\partial \mu}+\beta i(r,\mu)$$

$$=\sigma_a i_b(T)+\tfrac{1}{2}\sigma_s\int_{-1}^{1}P(\mu,\mu')i(r,\mu')d\mu',\ \text{for } R_1\le r\le R_2 \tag{2}$$

and

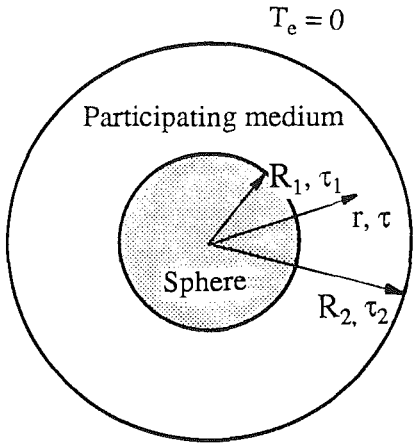

Fig. 1 Geometry of the problem

$$\rho_g C_{p,g} \frac{DT}{Dt} = \nabla \cdot (k \nabla T - q^r) + \gamma T \frac{DP}{DT} + q''' + \phi', \text{ for } R_1 < r \leq R_2 \quad (3)$$

where α_s is the thermal diffusivity of the sphere, and the subscript g refers to parameters in the surrounding vapor. Here, equation (1) is the equation governing transient conduction in the sphere, equation (2) is the equation for the radiative intensity for systems with spherical symmetry (Ozisik, 1973), and equation (3) is the transient energy balance equation. The optical thickness τ and the single scattering albedo ω are defined as

$$\tau = (\sigma_a + \sigma_s) r, \quad \omega = \frac{\sigma_s}{\sigma_a + \sigma_s}$$

In addition, for a nonstagnant medium, the mass and momentum conservation equations have to be satisfied. However, in this work, the medium is assumed to be stagnant. Most vapors have a very low thermal conductivity, and at high temperatures radiation dominates the heat transfer, especially in the near-wall regions. Hence, conduction may be neglected. Thus, the energy balance of equation (3) reduces to

$$\rho_g C_{p,g} \frac{\partial T}{\partial t} = -\nabla \cdot q^r + q''', \text{ for } R_1 < r \leq R_2 \quad (4)$$

Even a numerical solution of the above system of equations (1), (2), and (4) appears quite formidable. In order to make this system more tractable, it is assumed that the energy transfer in the medium is quasi-steady. Accordingly, internal heat generation is assumed to be absent, and the medium is assumed to be at radiative equilibrium at any given time. The unsteadiness in the medium is thus removed to the inner spherical boundary, and the transient effect is felt only through the time-dependent boundary condition. This assumption is frequently invoked in studies of radiation in combustion systems. It is a matter of detail to include internal heat generation in the medium, and the analysis that follows can be extended fairly easily for the case of a volumetric heat source in the medium, $q''' \neq 0$.

Using the spherical harmonics method for the solution of the radiative transfer equation in the medium, the phase function $P(\mu, \mu')$ is expressed as

$$P(\mu, \mu') = \sum_{n=0}^{\infty} a_n P_n(\mu) P_n(\mu') \quad (5)$$

and the radiation intensity $i(\tau, \mu)$ is expanded in Legendre polynomials, as

$$i(\tau, \mu) = \sum_{m=0}^{\infty} \frac{2m+1}{4\pi} P_m(\mu) \Psi_m(\tau) \quad (6)$$

Substituting equations (4), (5), and (6) into equation (2), and using the orthogonality and recurrence relationships for Legendre polynomials (Abramowitz and Stegun, 1965), one obtains

$$(m+1)\frac{d\Psi_{m+1}(\tau)}{d\tau} + (m+1)(m+2)\frac{\Psi_{m+1}(\tau)}{\tau} + (2m+1)(1-\omega a_m)\Psi_m(\tau) + m\frac{d\Psi_{m-1}(\tau)}{d\tau} - \frac{(m-1)m}{\tau}\Psi_{m-1}(\tau) - (1-\omega)4\pi i_b(T)\delta_{om} = 0, \quad m = 0, 1, 2, \ldots \quad (7)$$

The Marshak boundary conditions are used with the ODE's from the P_N approximation as follows:

$$\int_0^1 i(\tau_1, \mu)\mu^{2l-1} d\mu = \int_0^1 f_1(\mu)\mu^{2l-1} d\mu, \quad \mu > 0 \quad (8a)$$

and

$$\int_{-1}^0 i(\tau_2, \mu)\mu^{2l-1} d\mu = \int_{-1}^0 f_2(\mu)\mu^{2l-1} d\mu, \quad \mu < 0 \quad (8b)$$

where $l = 1, 2, 3 \ldots 1/2(N+1)$, consistent with the order of the approximation.

Nomenclature

a_n = angular distribution coefficients in the scattering phase function
C_1, C_2, C_3, C_4 = constants of integration in P_3 solution
C_p = specific heat at constant pressure
d_1, d_2 = constants of integration in P_1 solution
F_1 = coefficient in the expression for C_1
G = incident radiation intensity
i = radiation intensity
i_b = blackbody intensity
I = modified spherical Bessel functions of the first kind
k = thermal conductivity of sphere
K = modified spherical Bessel functions of the second kind
n = optical thickness ratio $= \tau_2/\tau_1$
n_{ri} = refractive index of the medium
Nr = conduction-to-radiation ratio parameter $= \beta k/4\bar{\sigma} T_i^3 n_{ri}^2 \epsilon_1$
P = pressure
$P(\mu, \mu')$ = phase function in the radiative transfer equation
P_n = Legendre polynomial of order n
q^r = radiation heat flow
q''' = volumetric heat generation rate
t = time
t^* = nondimensional time $= \alpha_s \beta^2 t$
T = temperature
r = radius
R_1 = radius of the sphere
R_2 = outer radius of the surrounding medium
T_e = temperature of the environment
T_i = initial temperature
T_s = surface temperature of e the sphere
α_s = thermal diffusivity of the sphere
β = extinction coefficient
γ = coefficient of volumetric expansion
δ_{0m} = Kronecker delta
ϵ_1 = boundary emissivity at the surface of the sphere
ϵ_{eff} = effective emissivity of the surface of the sphere
μ = direction cosine corresponding to the angle between beam direction and radius vector
ρ = density
$\bar{\sigma}$ = Stefan–Boltzmann constant
σ_a = absorption coefficient
σ_s = scattering coefficient
τ = optical thickness
τ_1, τ_2 = optical inner and outer radius of the medium, respectively
ϕ' = viscous dissipation
$\Psi_m(\tau)$ = function in the spherical harmonics expansion of i
ω = single scattering albedo

For the P_N approximation, the series of equation (7) is truncated at N, resulting in $N+1$ ordinary differential equations. Higher-order approximations have been discussed by Bayazitoglu and Higenyi (1979), and the third-order approximation is shown to be quite accurate for spherical media. The P_3 approximation is addressed in the following section.

In the P_3 approximation, four ordinary differential equations result from equation (7), which are

$$\frac{d\Psi_1}{d\tau} + \frac{2\Psi_1}{\tau} = 0 \tag{9a}$$

$$\frac{2d\Psi_2}{d\tau} + \frac{6\Psi_2}{\tau} + 3(1-\omega a_1)\Psi_1 + \frac{d\Psi_0}{\tau} = 0 \tag{9b}$$

$$\frac{3d\Psi_3}{d\tau} + \frac{12\Psi_3}{\tau} + 5(1-\omega a_2)\Psi_2 + \frac{2d\Psi_1}{d\tau} - \frac{2\tau_1}{\tau} = 0 \tag{9c}$$

$$7(1-\omega a_3)\Psi_3 + \frac{3d\Psi_2}{d\tau} - \frac{6\Psi_2}{\tau} = 0 \tag{9d}$$

where, by definition, $\Psi_0(\tau)$ and $\Psi_1(\tau)$ are seen to be the incident radiation and the radiant heat flux, respectively. For this work, the radiant heat flux is of greater interest than the intensity, and a complete solution for $\Psi_1(\tau)$ will suffice.

The boundary conditions for a reflective inner boundary and zero incident energy at the outer (vacuum) boundary are

$$i(\tau_1, \mu) = \frac{\epsilon_1 \bar{\sigma} n_{ri}^2 T_1^4}{\pi} + \rho_1 i(\tau_1, -\mu), \quad \mu > 0, \tag{10a}$$

and

$$i(\tau_2, \mu) = 0, \quad \mu < 0 \tag{10b}$$

where ρ_1, the reflectivity of the surface, includes specular and diffuse components. Substitution of equations (10) into equations (8) gives four boundary conditions. The solution for the ODEs of equation (9), for radiative equilibrium and no heat source (Tong and Swathy, 1988) is

$$\Psi_0(\tau) = \frac{3}{\tau} C_1 + \frac{6}{5} (\xi\tau^{-1/2})[C_2 I_{1/2}(\xi\tau) - C_3 K_{1/2}(\xi\tau)] + C_4 \tag{11a}$$

$$\Psi_1(\tau) = \frac{C_1}{\tau^2} \tag{11b}$$

$$\Psi_2(\tau) = \frac{1}{5}\left\{\frac{6C_1}{\tau^3} - 3\,\xi\,\tau^{-1/2}[C_2 I_{5/2}(\xi\,\tau) - C_3 K_{5/2}(\xi\,\tau)]\right\} \tag{11c}$$

and

$$\Psi_3(\tau) = \tau^{-1/2}[C_2 I_{7/2}(\xi\,\tau) + C_3 K_{7/2}(\xi\,\tau)] + \frac{10\,C_1}{\tau^4 \xi^2} \tag{11d}$$

where $\xi = \sqrt{35/9}$, and the I's and K's are the Bessel function of the first and third kind, respectively. In writing equations (11), isotropic scattering ($a_0 = 1$, a_n, $(n>0) = 0$) has been assumed. If anisotropic scattering is to be investigated, nonzero values for a_n $(n>0)$ are chosen depending upon the type of scattering considered, and the degree of the P_N approximation employed. For the P_1 case, the effect of anisotropic scattering is studied by Bayazitoglu and Suryanarayana (1988).

The constants C_1, C_2, C_3, and C_4 can be obtained by applying the boundary conditions of equations (10). C_1, which is the only constant that appears in the solution for $\Psi_1(\tau)$, is of interest here. It must be noted that an explicit dependence on T_1 in the solution for $\Psi_1(\tau)$ makes the coupling with the conduction problem much easier. This is possible only through an analytical solution. Here, the system of equations is analytically solved (Appendix A), and C_1 is obtained in the form

$$C_1 = F_1\ 4\ n_{ri}^2 \bar{\sigma} \epsilon_1 T_1^4 \tag{12}$$

It now remains to solve the conduction problem of equation (2) in the sphere, subject to the following boundary conditions:

$$\text{at } r=0, \quad t>0: \quad \frac{\partial T}{\partial r} = 0 \tag{13a}$$

$$\text{at } r=R_1, \quad t>0: \quad -k\frac{\partial T}{\partial r} = q^r \tag{13b}$$

and the initial condition

$$T(t=0,\ r) = T_i \tag{13c}$$

The boundary conditions of equation (13) can be nondimensionalized and rearranged as

$$\text{at } \tau=0, \quad t>0: \quad \frac{\partial \bar{T}}{\partial \tau} = 0 \tag{14a}$$

$$\text{at } \tau=\tau_1, \quad t>0: \quad \frac{\partial \bar{T}}{\partial \tau} = \frac{-F_1 \bar{T}_1^4}{Nr\,\tau_1^2} \tag{14b}$$

In equation (14b), since the explicit dependence on T_1 is retained, the conduction problem becomes easier to solve. The conduction problem is solved using an explicit finite difference scheme. Milton and Gross (1973) have studied explicit finite difference schemes for problems with nonlinear boundary conditions, and derived stability criteria. In general, explicit schemes are less complicated, less expensive, and are better suited to such problems, although they restrict the size of the time step. In this work, a nondimensional time step of 0.0001 is employed, and the scheme is stable for conservative choices of the space step.

In summary, the assumptions made in this analysis are as follows:

(*i*) The sphere is surrounded by a finite, gray, absorbing-emitting-isotropically scattering medium, with a spatially independent albedo.

(*ii*) Heat transfer is by conduction within the sphere, and radiation in the medium. Convection and conduction are neglected in the medium.

(*iii*) Neither the sphere, nor the medium have volumetric heat sources.

(*iv*) Quasi-steady energy transfer prevails in the medium.

Results and Discussion

Numerical solutions that were obtained by the analysis of the previous section are presented. Results include the effect of cloud optical thickness and the conduction to radiation parameter (Nr) on the transient temperature, and the effective emissivity of the sphere in the presence of a surrounding participating vapor.

No Cloud (Nonparticipating Medium). The solution for the transient surface temperature for the case of a sphere radiating directly to space is important because it can be used for comparison with existing solutions. For the case of $\tau_1 = \tau_2 = 1$, the problem is identical to the one solved by Ayers (1970), with the only difference being that due to a slightly different definition, the conduction to radiation parameter Nr differs from the one used in this work by a factor of 4. In Fig. 2, the transient nondimensional surface temperature for various values of Nr is shown, for the case where no cloud surrounds the sphere. The results obtained by using the finite difference scheme of this work were compared wherever possible with those of Ayers, and agreed within 2 percent.

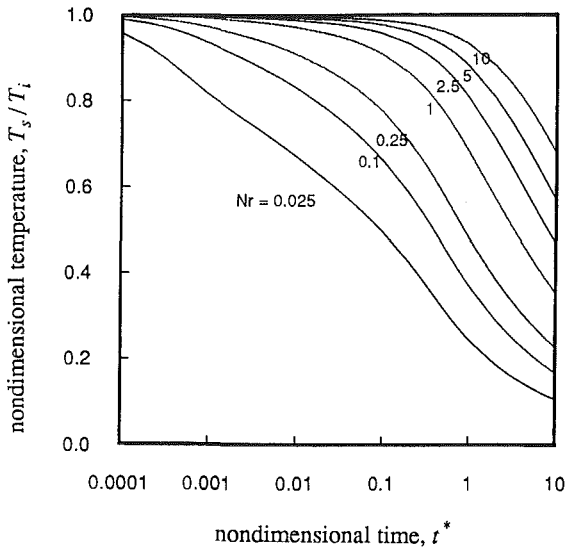

Fig. 2 Transient temperature at the surface for the case of no cloud ($\tau_1 = \tau_2$)

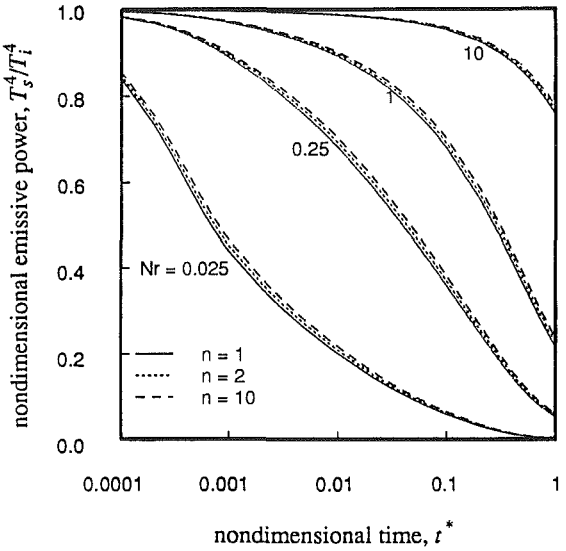

Fig. 3(a) Transient temperature at the surface for the case $\tau_1 = 1$

Participating Medium. The effect of a participating medium surrounding the material was investigated quantitatively for various optical thickness ratios. In all calculations, an ω of 0.8 was used, with $\rho_1 = 0.7$ and $\epsilon_1 = 0.3$. The values of ρ_1 and ϵ_1 chosen are typical of liquid metal surfaces, which are usually specularly reflective, and $\omega = 0.8$ allows for scattering. It should be noted that the radius of the sphere corresponding to a given τ_1 depends on the extinction coefficient β of the medium. In the context of liquid metals processing and space manufacturing, $\tau_1 = 10$ represents a very large sphere, and $\tau_1 = 0.1$ represents a very small sphere. It is the intermediate sizes ($\tau_1 \sim 1$–5) that are of practical interest. In this work, results were obtained for four different sizes of the sphere, $\tau_1 = 0.1$, 1, 5, and 10. It was found that for $\tau_1 = 0.1$ the change in the emissive power at the surface was very small when compared to the case where the medium is transparent. The effect for $\tau_1 = 1$, 5, and 10 for various optical thickness ratios is depicted by the cooling curves of Figs. 3(*a*), 3(*b*), and 3(*c*). As τ_1 increases, the vapor cloud begins to have a more pronounced effect. The cloud acts as a radiative insulator, and the sphere takes much longer to cool to a given temperature, in comparison to the no-cloud case. As the conduction to radiation parameter *Nr* increases, the sphere takes longer to feel the effect of the cloud.

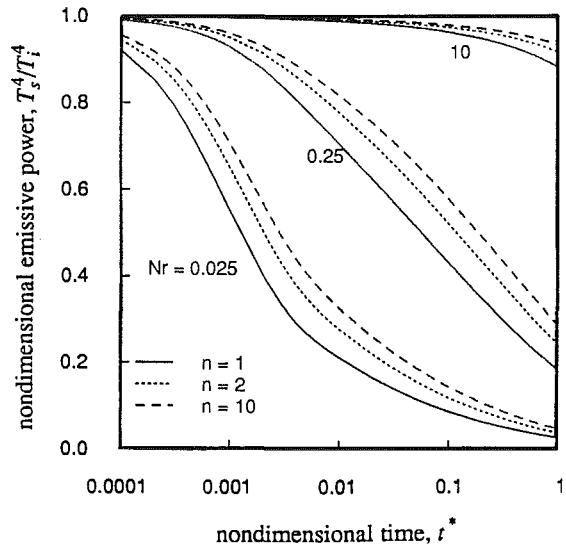

Fig. 3(b) Transient temperature at the surface for the case $\tau_1 = 5$

The effect of varying the optical thickness of the cloud is shown in Fig. 4, at $Nr = 0.025$ and $t^* = 0.001$. For spheres with larger τ_1, an increase in the optical thickness ratio causes at first a rapid, and then a gradual increase in the temperature at the surface. From Fig. 4, it is observed that increasing the optical thickness beyond a point has no significant effect on the surface temperature.

In comparison with the no-cloud case, the effect of the cloud can be included in an effective emissivity of the surface, which is a function of the optical thickness parameters and surface properties of the sphere. This enables one to state the boundary condition of equation (13*b*) in the form

$$\text{at } r = R_1, \quad t > 0: \quad -k \frac{\partial T}{\partial r} = \epsilon_{\text{eff}} \bar{\sigma} T^4 \tag{15}$$

where, for the no-cloud case, $\epsilon_{\text{eff}} = \epsilon_1$. From the P_3 solution of equation (10*a*), this effective emissivity ϵ_{eff} can be expressed as

$$\epsilon_{\text{eff}} = \frac{4 F_1 \epsilon_1 n_{ri}^2}{\tau_1^2} \tag{16}$$

The effective emissivity at the surface is indicative of the

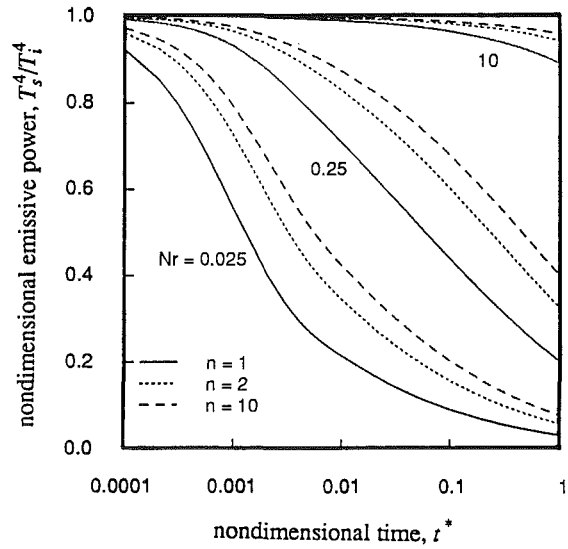

Fig. 3(c) Transient temperature at the surface for the case $\tau_1 = 10$

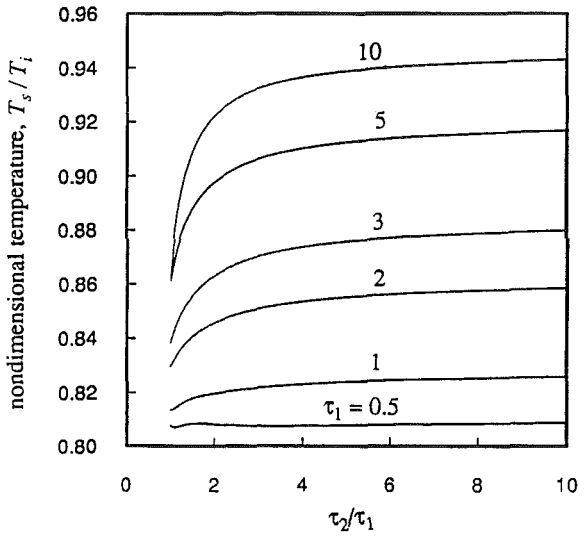

Fig. 4 Surface temperature variation with optical thickness ratio, for $Nr = 0.025$ and $t^* = 0.001$

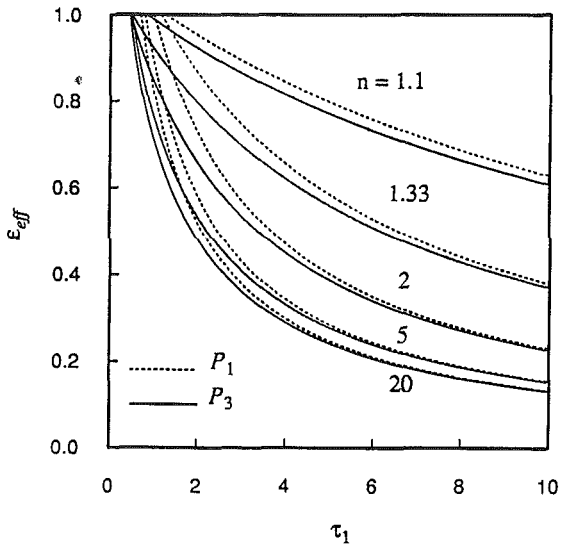

Fig. 5 Effective emissivity of the surface of the sphere

reduction in the heat transfer from the surface of the sphere, as a result of the insulating effect of the cloud. By using ϵ_{eff} instead of ϵ_1 in the earlier solutions for radiative cooling problems in space, solutions can be obtained for the cases where a participating vapor surrounds the body.

The expression for effective emissivity from the P_3 approximation is rather involved, as F_1 is a long, cumbersome coefficient involving Bessel functions of fractional order. The P_1 approximation, on the other hand, gives a simple, algebraic expression. A brief description of the derivation of the effective emissivity expression using the P_1 approximation follows.

P_1 Approximation. In the P_1 approximation, the two ODEs for radiative equilibrium are

$$\frac{dq^r}{d\tau} + \frac{2q^r}{\tau} = 0 \tag{17a}$$

and

$$\frac{dG}{d\tau} = -3(1-\omega a_1)q^r \tag{17b}$$

Equations (17) can easily be solved for G and q^r to give

$$q^r = \frac{d_1}{3(1-\omega a_1)\tau^2} \tag{18a}$$

and

$$G = \frac{d_1}{\tau} + d_2 \tag{18b}$$

where d_1 and d_2 are constants, which are obtained by applying the boundary conditions of equations (8). Once the constants are obtained, the expression for effective emissivity from the P_1 solution can be easily shown to be

$$\epsilon_{eff} = \frac{4\epsilon_1}{\left\{(1-\rho_1)\left[\frac{1}{\tau_1} - \frac{1}{\tau_2}\right] + \frac{2}{3(1-\omega a_1)}\left[\frac{1-\rho_1}{\tau_2^2} + \frac{1+\rho_1}{\tau_1^2}\right]\right\}3(1-\omega a_1)\tau_1^2} \tag{19}$$

The simplicity of equation (19) makes it attractive to use in preference to the P_3 solution whenever a quick, practical solution is desired. A comparison of the effective emissivity results from P_1 and P_3 (Fig. 5) shows that the modest P_1 agrees quite well with the P_3 solution, especially when τ_1 and τ_2/τ_1 are large. As expected, the P_1 solution overestimates the heat transfer, and hence the effective emissivity of the surface. At $\tau_1 = 2$, for example, the error when compared to P_3 is of the order of 15 percent. Such an error may be sufficient for many engineering applications, and either Fig. 5 or equation (19) can be used in design calculations.

It must be borne in mind that both P_1 and P_3 are approximate solutions, and are not very accurate at the boundaries, especially for radiative equilibrium. The P_3 approximation yields a solution with an accuracy of the order of 8 to 15 percent, for spherical symmetry (Bayazitoglu and Higenyi, 1979). The employment of either higher-order P_N approximations or some other more accurate approximations will lead to better solutions for the wall heat flux, if a highly accurate solution is desired. However, for P_N approximations beyond P_3 the solutions are numerical, and explicit solutions for the temperature profile, heat flux, or the effective emissivity cannot be obtained.

Conclusion

The transient radiative cooling of a conductive sphere, surrounded by a gray, radiatively participating medium has been studied. The spherical harmonics method was used to solve the equation of radiative transfer, and a finite difference scheme was used to solve the conduction problem. Solutions have been obtained for various optical thicknesses, using the third-order differential approximation. It has been found that the medium has a very small effect on the transient temperature at the surface of the sphere for small τ_1. For spheres with larger τ_1, the cloud has a significant effect, even when the cloud is a thin blanket.

An expression was obtained for the effective emissivity of the surface in the presence of a participating cloud, using both P_3 and P_1 approximations. This can be readily used to include the effect of a cloud when solving problems of radiative cooling in space. The expression derived from the P_1 approximation is simple, and sufficiently accurate for engineering applications.

Acknowledgments

The authors wish to acknowledge the partial support by the Houston Area Research Center (HARC).

References

Abramowitz, M., and Stegun, I. A., eds., 1965, *Handbook of Mathematical Functions*, Dover, New York.

Ayers, D. L., 1970, "Transient Cooling of a Sphere in Space," ASME JOURNAL OF HEAT TRANSFER, Vol. 92, pp. 180–182.

Barmatz, M., 1982, "Overview of Containerless Processing Technologies," *Materials Processing in the Reduced Gravity Environment of Space*, Guy E. Rindone, ed., North Holland, New York, p. 25.

Bayazitoglu, Y., and Higenyi, J., 1979, "Higher Order Differential Equations of Radiative Transfer: P_3 Approximation," *AIAA Journal*, Vol. 17, pp. 424–431.

Bayazitoglu, Y., and Suryanarayana, P. V. R., 1988, "Transient Cooling of a Sphere Surrounded by a Participating Medium," presented at the ASME Winter Annual Meeting, Nov. 28–Dec. 3, 1988, Chicago, IL.

Choi, S., and Kruger, C. H., 1985, "Modeling of Coal Particle Behavior Under Simultaneous Devolatilization and Combustion," *Combustion and Flame*, Vol. 61, pp. 131–144.

Crosbie, A. L., and Viskanta, R., 1966, "Transient Heating or Cooling of One-Dimensional Solids by Thermal Radiation," *Proceedings of the Third International Conference*, AIChE, Vol. 5, pp. 146–153.

Mattick, A. T., and Hertzberg, A., 1981, "Liquid Droplet Radiators for Heat Rejection in Space," *Journal of Energy*, Vol. 5, pp. 387–393.

Milton, J. L., and Gross, W. P., 1973, "Stability Criteria for Explicit Finite Difference Solutions of the Parabolic Diffusion Equation With Nonlinear Boundary Conditions," *International Journal for Numerical Methods in Engineering*, Vol. 7, pp. 57–67.

Ozisik, M. N., 1973, *Radiative Transfer*, Wiley, New York, p. 263.

Tong, T. W., and Swathi, P. S., 1987, "Radiative Heat Transfer in Emitting-Absorbing-Scattering Spherical Media," *AIAA J. Thermophysics and Heat Transfer*, Vol. 1, pp. 162–170.

White, A. K., III, 1987, "Liquid Droplet Radiator Development Status," NASA Technical Memorandum 89852.

APPENDIX

On applying the boundary conditions of equations (10), the equations (11) reduce to a linear system of four simultaneous algebraic equations

$$\sum_{j=1}^{4} a_{ij}c_j = b_j, \quad i=1, \ldots, 4 \tag{A1}$$

where the a_{ij} are given by

$$a_{11} = (1-\rho_1)\left(\frac{3}{\tau_1} + \frac{3}{2\tau_1^3}\right) + (1+\rho_1)\frac{2}{\tau_1^2}$$

$$a_{12} = (1-\rho_1)\xi\,\tau_1^{-1/2}\left[\frac{6}{5} I_{1/2}(\xi\,\tau_1) - \frac{3}{4} I_{5/2}(\xi\,\tau_1)\right]$$

$$a_{13} = (1-\rho_1)\xi\,\tau_1^{-1/2}\left[-\frac{6}{5} K_{1/2}(\xi\,\tau_1) + \frac{3}{4} K_{5/2}(\xi\,\tau_1)\right]$$

$$a_{14} = (1-\rho_1)$$

$$a_{21} = (1-\rho_1)\left(\frac{3}{\tau_1} + \frac{3}{\tau_1^3}\right) + (1-\rho_1)\left(\frac{12}{5\tau_1^2} + \frac{16}{\xi^2\tau_1^4}\right)$$

$$a_{22} = (1-\rho_1)\xi\,\tau_1^{-1/2}\left[\frac{6}{5} I_{1/2}(\xi\,\tau_1) - \frac{3}{2} I_{5/2}(\xi\,\tau_1)\right] + \frac{8}{5}(1+\rho_1)\tau_1^{-1/2} I_{7/2}(\xi\,\tau_1)$$

$$a_{23} = (1-\rho_1)\xi\,\tau_1^{-1/2}\left[-\frac{6}{5} K_{1/2}(\xi\,\tau_1) + \frac{3}{2} K_{5/2}(\xi\,\tau_1)\right] + (1+\rho_1)\frac{8}{5}\tau_1^{-1/2} K_{7/2}(\xi\,\tau_1)$$

$$a_{24} = (1-\rho_1)$$

$$a_{31} = \frac{3}{\tau_2} - \frac{2}{\tau_2^2} + \frac{3}{2\tau_2^3}$$

$$a_{32} = (\xi\,\tau_2^{-1/2}\left[\frac{6}{5} I_{1/2}(\xi\,\tau_2) - \frac{3}{4} I_{5/2}(\xi\,\tau_2)\right]$$

$$a_{33} = (\xi\,\tau_2^{-1/2})\left[-\frac{6}{5} K_{1/2}(\xi\,\tau_2) + \frac{3}{4} K_{5/2}(\xi\,\tau_2)\right]$$

$$a_{34} = 1$$

$$a_{41} = \frac{3}{\tau_2} - \frac{12}{5\tau_2^2} + \frac{3}{\tau_2^3} - \frac{16}{\xi^2\tau_2^4}$$

$$a_{42} = \xi\,\tau_2^{-1/2}\left[\frac{6}{5} I_{1/2}(\xi\,\tau_2) - \frac{3}{2} I_{5/2}(\xi\,\tau_2)\right] - \frac{8}{5}\tau_2^{-1/2} I_{7/2}(\xi\,\tau_2)$$

$$a_{43} = \xi\,\tau_2^{-1/2}\left[-\frac{6}{5} K_{1/2}(\xi\,\tau_2) + \frac{3}{2} K_{5/2}(\xi\,\tau_2)\right] - \frac{8}{5}\tau_2^{-1/2} K_{7/2}(\xi\,\tau_2)$$

$$a_{44} = 1$$

The right-hand terms b_j are

$$b_1 = b_2 = 4\,n_{ri}^2\bar{\sigma}T_1^4$$

and

$$b_3 = b_4 = 0$$

A convenient way of expressing equation (A1) is

$$[A]\{C\} = \{B\} \tag{A2}$$

Cramer's rule can now be applied to equation (A2), and the constants c_i can be found.

Heat and Mass Transfer During Piloted Ignition of Cellulosic Solids

A. Atreya

I. S. Wichman

Department of Mechanical Engineering,
Michigan State University,
East Lansing, MI 48824

This study presents the results of an experimental and theoretical investigation into the heat and mass transfer processes that occur during piloted ignition of cellulosic materials. The experiments were conducted on both horizontal and vertical samples of thick pieces of wood initially at ambient temperature. The time required to ignite the sample in the presence of a pilot flame and the surface temperature–time history of the sample were recorded. The data so obtained were used to identify the critical surface temperature at ignition. These results compare well with those previously reported in the literature. Based on the experimental observations an approximate analytical model for the piloted ignition process was developed. The model predictions are in good agreement with the experimental measurements. This model is based on the following observations: (i) Critical conditions at ignition are achieved solely by external radiation and surface radiant emission plays a dominant role in determining the surface temperature at ignition, and (ii) although the heat lost by the flame to the solid at the instant of ignition is significant and may cause thermal quenching its contribution to the enthalpy rise of the solid is negligible. Also, to simplify the description of the gas-phase combustion process the concepts of nearly constant limit diffusion flame temperature at extinction and nearly constant heat of combustion of oxygen for most hydrocarbons are profitably employed. The approximate model presented here provides simple formulas that show good agreement with the experiments. It also provides some justification for the use of critical surface temperature and critical fuel mass flux as ignition criteria.

Introduction

The ease with which cellulosic materials such as wood, paper, and cotton may be ignited is important in determining the fire hazard and fire growth rate in buildings. Hence it is necessary to understand how combustible solids ignite, and to develop a model capable of predicting the ignition characteristics of materials in a fire environment. Typically, in building fires, thermal radiation from the flames, the ceiling layer of hot gases, and the hot walls is the primary cause of ignition of the as-yet-unburned materials. This ignition may be spontaneous or piloted. In this work, the heat and mass transfer processes that occur during piloted ignition of solids that are exposed to external radiation are examined both experimentally and theoretically.

A considerable amount of work on piloted ignition of solids has been done in the past, and several reviews have also been published. The review by Kanury (1972) and the recent work of Kashiwagi (1981, 1982) provide excellent sources of general information. Thus, only the relevant aspects are considered here.

Numerous experimental methods have been developed to investigate the piloted ignition phenomenon. Essentially, the sample (vertical or horizontal) is exposed to external radiation in the presence of a pilot (a small flame or an electrical heat source) and the time required for sustained flaming and the surface temperature of the sample are measured. The data are then correlated to deduce an empirical ignition criterion. Several criteria, such as critical surface temperature at ignition (Atreya et al., 1985), critical fuel mass flux (Bamford et al., 1945), critical char depth (Sauer, 1965), critical mean solid temperature (Martin, 1965), etc., have been proposed. Of these, the critical fuel mass flux at ignition seems to be physically the most correct, but surface temperature has proved to be the most useful, since it can be conveniently related to the fire spread rate (Quintiere, 1981).

It is important to note that all of the above criteria are indirect quantities assumed to be closely related to ignition. The actual process is quite complex. The solid must first chemically decompose to inject fuel gases into the boundary layer. These fuel gases must then mix with the surrounding air to produce a flammable mixture that is ignited by the pilot flame. To achieve sustained ignition the fuel production rate must enable the heat released by the flame to overcome the heat losses to the surface and the ambient surroundings. A theoretical description of the piloted ignition process will therefore require a time-dependent model for the simultaneous processes of solid-phase thermal decomposition and gas-phase mixing and combustion in the two-dimensional boundary layer. The absence of such comprehensive models has necessitated the various attempts to develop the empirical ignition criteria discussed above. In this paper a simplified analytical approach is sought in order to (i) establish a relationship between the critical surface temperature and the critical fuel mass flux at ignition, and (ii) determine the critical surface temperature at ignition by examining processes occurring in the gas phase.

Experiments

Experiments were conducted in both horizontal and vertical configurations on thick samples of various woods (0.75 in. thick) initially at ambient temperature. Figure 1 schematically shows the experimental arrangement. Further details of the experimental setup are given by Atreya (1984) for the horizontal mode and Robertson (1979) for the vertical mode. These samples were suddenly exposed to a known constant external radiation flux F. Infrared heaters at a radiation temperature of $850 \pm 50°C$ were used to provide external radiation and the heat flux F was continuously measured by a water-cooled wide-angle total heat flux transducer. The time required to ignite the sample in the presence of a pilot flame and the surface temperature–time history of the sample were recorded by thermocouples (TC; Fig. 1). These data were used to identify the critical surface temperature at ignition and the lower limit of the incident heat flux.

Contributed by the Heat Transfer Division and presented at the 2nd ASME-JSME Thermal Engineering Joint Conference, Honolulu, Hawaii, March 1987. Manuscript received by the Heat Transfer Division March 10, 1988. Keywords: Combustion, Mass Transfer.

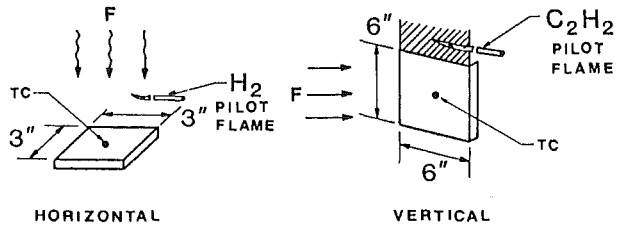

Fig. 1 Schematic of ignition experiments; black dot marked *TC* represents the surface thermocouple

Experimental Observations

It is instructive to examine in detail the surface temperature history during the last few instants preceding ignition. Figure 2 shows an enlarged view of the measured surface temperature profile at the time of sustained ignition for the horizontal case. A similar result was obtained for the vertical case, although the flashes (unsustained flaming) were far less pronounced. This is because for the horizontal case the flashes occurred in the middle of the sample, directly above the thermocouple, whereas for the vertical case they often did not cover the entire sample and remained close to the pilot flame far from the thermocouple. For the low heat flux experiment shown in Fig. 2 one observes that there was sufficient time between flashes for the surface to achieve thermal equilibrium with the external radiation, since between flashes the surface temperature resumes its steady increase. Figure 2 also shows that the extrapolated surface temperature[1] at the time of sustained flaming is *less* than the momentary rise in temperature caused by the flashes and yet sustained flaming was not achieved. In other words, for sustained flaming to occur it is necessary for the surface temperature, *caused by external radiation*, to rise to some critical value (372°C in Fig. 2). The contributions of gas phase exothermicity must not be included in the determination of this critical value. Furthermore, the total heat contribution to the solid because of the flashes (which is proportional to the area under the peaks) is small compared to that due to external radiation. Thus, it may be concluded that although the heat lost by the flame to the solid at the instant of ignition is significant (and may cause thermal quenching, resulting in a flash) its contribution to enthalpy rise of the solid is negligible and, consequently, the critical conditions for ignition are achieved primarily by the externally applied radiation.

[1]This is the surface temperature that would have been achieved solely by external radiation in the absence of ignition. In Fig. 2, it has a value of 372°C and is defined as the temperature of ignition.

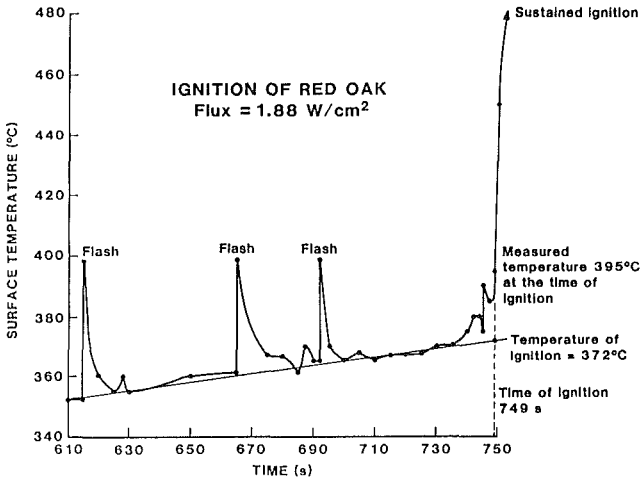

Fig. 2 Enlarged view of the surface temperature-time history at the time of sustained ignition for the horizontal case. Intersection of the time for sustained ignition and the extrapolated surface temperature is defined as the temperature of ignition

Analysis

The preceding experimental observations suggest that, to a first approximation, the piloted ignition problem may be decoupled into the following two physical processes: (*i*) solid-phase thermal decomposition, caused by external radiation, to produce fuel gases, and (*ii*) establishment of a diffusion flame in the gas-phase boundary layer under the influence of heat losses.

Solid-Phase Model. In the solid-phase model presented here the sample is assumed to be moisture-free, opaque, and sufficiently thick to enable the semi-infinite approximation to be made. Surface oxidation and internal heat transfer between the pyrolysis gases and the solid matrix are ignored. The thermal properties are assumed to be temperature-independent and the net heat required to decompose a unit mass of wood thermally is taken to be zero (Atreya, 1983). The decomposition is assumed to occur according to a first-order global chemical reaction with a known and fixed final char density ρ_f^* (the superscript "*" identifies dimensional quantities).

With these approximations the equations describing the one-dimensional decomposition process are:

Mass balance

$$\frac{\partial M^*}{\partial x^*} = \frac{\partial \rho^*}{\partial t^*} \tag{1}$$

Nomenclature

A = pre-exponential factor
c = specific heat of solid
c_{pg} = specific heat of gas
E = activation energy
F = externally applied radiative heat flux
h = average heat transfer coefficient
H = nondimensional value of h
ΔH = heat of combustion
L = length scale
M = fuel mass flux
R = ideal gas constant
t = time
T = temperature
x = position coordinate
y = nondimensional mass flux, see equation (21), et seq.
Y_O = oxidizer mass fraction
δ = char yield
ϵ = surface emissivity
θ = nondimensional temperature difference $= T - 1$
λ = thermal conductivity
ν = mass-based stoichiometric coefficient
ρ = density
σ = Stefan–Boltzmann constant
Σ = nondimensional σ
Φ_s = total heat flux into solid at surface

Subscripts

d = diffusion
f = flame, final value
g = gas
p = penetration depth
s = surface value
∞ = ambient value

Superscripts

$*$ = dimensional quantity

Energy balance

$$\rho^* c^* \frac{\partial T^*}{\partial t^*} = \frac{\partial}{\partial x^*}\left(\lambda^* \frac{\partial T^*}{\partial x^*}\right) \tag{2}$$

Decomposition kinetics

$$\frac{\partial \rho^*}{\partial t^*} = -A^*(\rho^* - \rho_f^*)\exp(-E^*/RT^*) \tag{3}$$

The boundary and initial conditions are

$$T^*(x^*, 0) = T^*(\infty, t^*) = T_\infty^*, \rho^*(x^*, 0) = \rho_\infty^*, M^*(\infty, t^*) = 0 \tag{4}$$

and the net heat flux into the solid is given by

$$-\lambda^* \frac{\partial T^*}{\partial x^*}(0, t^*) = \epsilon\left[F^* - \frac{h^*}{\epsilon}(T_s^* - T_\infty^*) - \sigma^*(T_s^{*4} - T_\infty^{*4})\right] \tag{5}$$

Here h^* is the average convective heat transfer coefficient.

The evaluation of h^* is complicated because (*i*) the surface temperature of the sample is continuously changing, and (*ii*) the heat losses from the surface do not occur primarily by free convection. In fact, a major portion of the incident heat flux is lost by radiative emission. Thus, the use of correlations for h^* obtained from either constant surface temperature or constant heat flux (all of which is lost by free convection) is questionable. Furthermore, there are blowing effects from the evolution of pyrolysis gases, although these are expected to be negligible for piloted ignition.

In view of the above complications only an approximate value of h^* can be obtained from the Nusselt number correlations available in the literature. Also it seems more appropriate to use the constant surface temperature condition because: (*i*) The surface temperature at piloted ignition is nearly constant, and (*ii*) for the range of heat fluxes of concern here (2 to 6 W/cm^2) the rate of change of surface temperature is small when it is in the neighborhood of the piloted ignition temperature (see Fig. 2). Thus, for laminar free convection over vertical and horizontal surfaces the suggested correlations (Kanury, 1982) are $\overline{\mathrm{Nu}} = 0.59\ \mathrm{Ra}^{1/4}$, and $\overline{\mathrm{Nu}} = 0.54\ \mathrm{Ra}^{1/4}$, respectively. For the horizontal case the characteristic length in the Rayleigh number (Ra) is obtained by dividing the surface area by the perimeter.

To nondimensionalize the above equations a length scale is defined as $L^* = \lambda_\infty^* T_\infty^*/\epsilon F^*$, which is obtained as the ratio of thermal conduction and incident heat flux. Also, a diffusion time is defined as $t_d^* = L^{*2}/(\lambda_\infty^*/\rho_\infty^* c^*)$. The remaining nondimensional variables are defined as follows:

$$\left.\begin{aligned} &T = T^*/T_\infty^*, \quad \rho = \rho^*/\rho_\infty^*, \quad x = x^*/L^*, \quad t = t^*/t_d^*, \\ &E = E^*/RT_\infty^*, \quad A = A^* t_d^*, \quad \delta_f = \rho_f^*/\rho_\infty^*, \quad H = \frac{h^* T_\infty^*}{\epsilon F^*} \\ &M = M^* t_d^*/\rho_\infty^* L^*, \quad \Sigma = \sigma^* T_\infty^{*4}/F^*, \quad \lambda = \frac{\lambda^*}{\lambda_\infty^*} \end{aligned}\right\} \tag{6}$$

Hence, the nondimensional equations become

Mass balance

$$\frac{\partial M}{\partial x} = \frac{\partial \rho}{\partial t} \tag{7}$$

Energy balance

$$\rho \frac{\partial T}{\partial t} = \frac{\partial}{\partial x}\left(\lambda \frac{\partial T}{\partial x}\right) \tag{8}$$

Decomposition kinetics

$$\frac{\partial \rho}{\partial t} = -A(\rho - \delta)e^{-E/T} \tag{9}$$

The initial and boundary conditions become

$$\left.\begin{aligned} &T(x, 0) = T(\infty, t) = \rho(x, 0) = 1, \quad M(\infty, t) = 0 \\ &-\lambda \frac{\partial T}{\partial x}(0, t) = 1 - H(T_s - 1) - \Sigma(T_s^4 - 1) \end{aligned}\right\} \tag{10}$$

Solution of this nonlinear set of equations will yield the transient temperature and density distributions inside the solid. The problem contains five nondimensional parameters. Of these, the activation energy E, the pre-exponential factor A, and the char yield δ control the decomposition kinetics, and H and Σ control the heat loss from the sample surface.

Integral Solution. Because of the highly nonlinear nature of the problem an exact analytical solution cannot likely be found. Thus, approximate integral methods are employed. Considerable simplification of the problem is obtained by noting that during the initial stages of thermal decomposition, it is necessary to consider only the inert heating of the solid, whereby $\rho = 1$ (which makes equation (9) unnecessary) and $\lambda = 1$. The result is a linear heat conduction equation with a nonlinear boundary condition. It is convenient to define $\theta = T - 1$ so that equations (8) and (10) become

$$\frac{\partial \theta}{\partial t} = \frac{\partial^2 \theta}{\partial x^2} \tag{11}$$

and

$$\left.\begin{aligned} &\theta(x, 0) = \theta(\infty, t) = 0 \\ &-\frac{\partial \theta}{\partial x}(0, t) = 1 - H\theta_s - \Sigma[(\theta_s + 1)^4 - 1] \equiv \Phi_s \end{aligned}\right\} \tag{12}$$

Defining $x_p(t)$ as the penetration distance such that for $x > x_p(t)$, for all practical purposes, $T = 1$ (i.e., $\theta = 0$). The temperature profile

$$\theta = \frac{\theta_s}{x_p^2}(x_p - x)^2 \tag{13}$$

satisfies the conditions $\theta(0, t) = \theta_s$, $\theta(x_p, t) = 0$, and $[\partial\theta/\partial x]_{x_p} = 0$. From the heat-flux boundary condition at $x = 0$ one finds $x_p(t) = 2\theta_s/\Phi_s$, where Φ_s is given by equation (12). Substituting this into equation (13) gives

$$\theta = T - 1 = \theta_s(t)\left(1 - x\frac{\Phi_s}{\theta_s} + x^2 \frac{\Phi_s^2}{4\theta_s^2}\right) \tag{14}$$

Thus, the problem is now reduced to finding θ_s as a function of time. This is done by satisfying the energy balance expressed by equation (11) in an integral sense. By integrating equation (11) with respect to x from 0 to $x_p(t)$ and substituting $x_p = 2\theta_s/\Phi_s$ one finds $(\theta_s/\Phi_s^2)d\theta_s/dt + d(\theta_s^2/2\Phi_s^2)/dt = 3/2$. Integration of this result over time from 0 to t and using $\theta_s(t = 0) = 0$ gives

$$I \equiv \int_0^{\theta_s} \frac{\theta_s d\theta_s}{\Phi_s^2} = \frac{3t}{2} - \frac{\theta_s^2}{2\Phi_s^2} \tag{15}$$

This integral can be solved by using partial fraction expansions; the results, however, are cumbersome and impractical. In order to obtain a simple and reasonably accurate formula for $\theta_s(t)$ in the temperature range of interest (300 K $\lesssim T^* \lesssim$ 600 K, i.e., $0 \lesssim \theta_s \lesssim 1$) equation (12) is rewritten as

$$\Phi_s = 1 - (H + 4\Sigma)\theta_s - \Sigma\theta_s^2[\theta_s^2 + 4\theta_s + 6] \tag{16}$$

Here the factor in square brackets varies slowly from a value of 6, for $\theta_s = 0$, to 11, for $\theta_s = 1$. Thus, by replacing this factor with its integrated average, 25/3, Φ_s given by equation (16) can be approximated to within ±3 percent in the range $0 \le \theta \le 1$. Hence, equation (15) becomes, approximately,

$$\int_0^{\theta_s} \frac{\theta_s d\theta_s}{[1 + A\theta_s + B\theta_s^2]^2} \simeq \frac{3t}{2} - \frac{\theta_s^2}{2\Phi_s^2} \tag{17}$$

where $A = -(H + 4\Sigma)$ and $B = -(25/3)\Sigma$. This integral is evaluated in various mathematical handbooks (Gradshteyn and Rhyzik, 1965); thus equation (17), after simplifications, reduces to

$$t = \frac{1}{3}\left\{\frac{\theta_s^2}{\Phi_s^2} - \frac{10AB\theta_s}{\beta^2} - \frac{2\theta_s(A + 2B\theta_s)}{\beta\Phi_s}\right\} \tag{18}$$

where $\beta = (A^2 - 4B) > 0$ and $\Phi_s = 1 + A\theta_s + B\theta_s^2$. Equation (18) enables the determination of $\theta_s(t)$. The in-depth temperature profile is then obtained from equation (14).

It will be shown in the section on comparison with experiments that the predicted temperature distribution given by equations (14) and (18) can be used in equations (7) and (9) to calculate the fuel mass production rate in the initial stages of decomposition. From equations (7) and (9), one finds, upon integration,

$$M_s = A(1 - \delta)\int_0^{\infty} e^{-E/(\theta+1)} dx \tag{19}$$

where $\rho = 1$ was used and θ is given by equations (14) and (18). For small x, $\theta \approx \theta_s - x\Phi_s$; therefore, the upper limit of integration is replaced by $x_{\max} = \theta_s/\Phi_s = x_p/2$, the distance from the surface where $\theta = 0$. By substituting this into equation (19), integrating, and keeping only the lowest-order terms of the asymptotic expansion for large E, one obtains

$$M_s = \frac{A(1 - \delta)}{\Phi_s E} T_s^2 e^{-E/T_s}\left\{1 - \frac{\exp[-E(1 - 1/T_s)]}{T_s^2}\right\} \tag{20}$$

[Note that nearly all the contribution to the asymptotic expansion comes from the interval near $x = 0$; the choice of the upper limit for x does not affect the result.]

Equation (20) shows that $M_s(T_s = 1) = 0$, and that M_s increases exponentially with increasing $T_s(t)$. However, the attainment of a maximum value of M_s and the subsequent decay usually observed in the experiments is not obtained because equation (20) is *valid only for the initial stage of the decomposition process*, [since $\rho = 1$ is used in equation (10)]. Equation (20) relates the measurable quantities M_s and T_s to the chemical parameters (A, E, δ) and the heat-loss parameters (H, Σ) contained in Φ_s. The parametric dependence of M_s on A, E, δ, T_s, and Φ_s is similar to the inert-stage formula of Wichman and Atreya (1987). Note that equation (20) also relates the surface temperature at ignition (if known) to the critical fuel mass flux.

Gas-Phase Energy Balance. The fuel injected into the gas-phase boundary layer by thermal decomposition of the solid will sustain a diffusion flame only if the heat produced by the flame is equal to or greater than the heat losses. Otherwise the flame is thermally quenched, resulting in a flash. By assuming that the equality holds at the instant of sustained ignition, the highest possible temperature of the diffusion flame can be obtained simply by an energy balance (Kanury, 1982). Also, extensive studies on extinction of opposed-flow diffusion flames (Ishizuka and Tsuji, 1981) have shown that near extinction the limit flame temperature is remarkably constant for most hydrocarbons and is about 1550 K. This empirical result, when combined with the gas-phase energy balance, yields an equation for determining the critical fuel mass flux. The energy balance is written as

$$M_s^* c_{pg}^*(T_f^* - T_s^*) + \frac{M_s^*}{\nu Y_{O\infty}} c_{pg}^*(T_f^* - T_\infty^*) + h^*(T_f^* - T_s^*)E(y) = \Delta H^* M_s^* \tag{21}$$

where T_f^* is the limit flame temperature, ν is the fuel-to-oxygen ratio by mass, $Y_{O\infty}$ is the oxygen mass fraction and $E(y)$ [$= y/(e^y - 1)$, where $y = M_s^* c_{pg}^*/h^* = (M_s/H)(c_{pg}^*/c^*)$ from equation (6)] is the correction factor required for the heat transfer coefficient in the presence of mass transfer (Bird et al., 1960). For low mass transfer rates (i.e., small M_s), which is the case for ignition, $E(y) \approx 1$. By simplifying and rewriting equation (21) in a nondimensional form one obtains

$$M_s = \frac{\nu Y_{O\infty} H(T_f - T_s)}{[\Delta H - (T_f - 1) - \nu Y_{O\infty}(T_f - T_s)]} \tag{22}$$

where $T_f = T_f^*/T_\infty^*$ is the normalized limit flame temperature and $\Delta H = \Delta H^* \nu Y_{O\infty}/c_{pg}^* T_\infty^*$ is the normalized heat of combustion of air.[2] It has been found that ΔH is very nearly constant for most hydrocarbons (Huggett, 1980; Rasbash, 1976) and its value is approximately equal to 9.25 (where the average specific heat of the gas c_{pg}^* and ambient temperature T_∞^* are taken as 1.12 J/gK and 20°C, respectively). For a given fuel, $\nu Y_{O\infty}$ is also a constant and for wood its value is approximately 0.29 (Atreya, 1984). Thus, equation (22) relates M_s to T_s with H as a parameter. Physically, the right-hand side of equation (22) is the ratio of heat lost by the flame to the sample surface divided by the excess combustion heat available after accounting for the heat required to bring both fuel and air to the flame temperature T_f. At ignition both equations (20) and (22) must be satisfied. Together they provide a unique solution for the piloted ignition problem. These equations may also be used for determining the critical fuel mass flux and the critical surface temperature at ignition. Furthermore, once the critical surface temperature has been determined the ignition time can be obtained from equation (18).

Comparison with Experiments

Figure 3 shows a comparison of the measured and predicted surface temperatures. The curves marked E_1 and E_2 are for experiments conducted on "dry" wood (dried at 105°C for 12 h) and on wood at equilibrium with laboratory air (70 percent R.H. and 22°C), respectively. The weight lost during these low-heat-flux experiments is primarily because of the loss of moisture and is almost linear for the time duration of these tests. Note that the two distinct evaporation rates of moisture produce a difference of about 15°C in the surface temperature and that the evaporation rate is nonzero even for "dry" wood.

Theoretical predictions for dry wood from Carslaw and Jaeger (1959) for the cases of pure conduction and conduction with convective losses are also shown in Fig. 3 as the curves marked T_1 and T_2, respectively. The curve T_3 shows the calculations based on equation (18) for experiment E_2.

The linear theories (T_1 and T_2) considerably overpredict the surface temperature. For the calculation of T_3 a correction for the energy required to evaporate moisture was made. This quantity was estimated by using the constant weight-loss rate and latent heat of evaporation for water. The result (0.05

[2] The energy released upon complete combustion of a unit mass of fuel is called the heat of combustion of the given fuel. This energy when calculated per unit mass of the stoichiometric amount of air required for combustion is termed the heat of combustion of air.

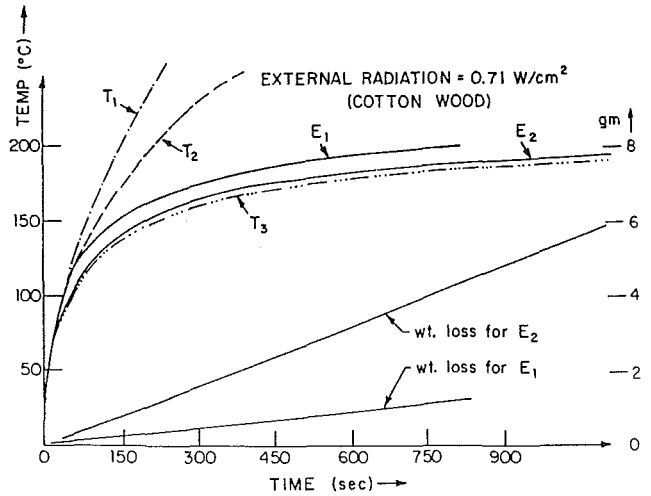

Fig. 3 A comparison of measured and predicted surface temperature showing the effect of radiant emission. Weight loss shown is due to desorption of moisture. E_1: experiments on wood dried at 105°C for 12 hours; E_2: experiments on wood at 70 percent R. H. and 22°C; T_1, T_2 and T_3 are theoretical calculations for a semi-infinite solid based on pure conduction, conduction with convective losses, and conduction with convective and reradiative losses, respectively. Properties used were: $\rho^* = 470$ kg/m^3, $\epsilon = 0.85$, $c^* = 1.38$ J/gK, $\lambda^* = 0.126$ W/mK, and $h^* = 8.4$ W/m^{2}K. All temperatures shown are above ambient (22°C).

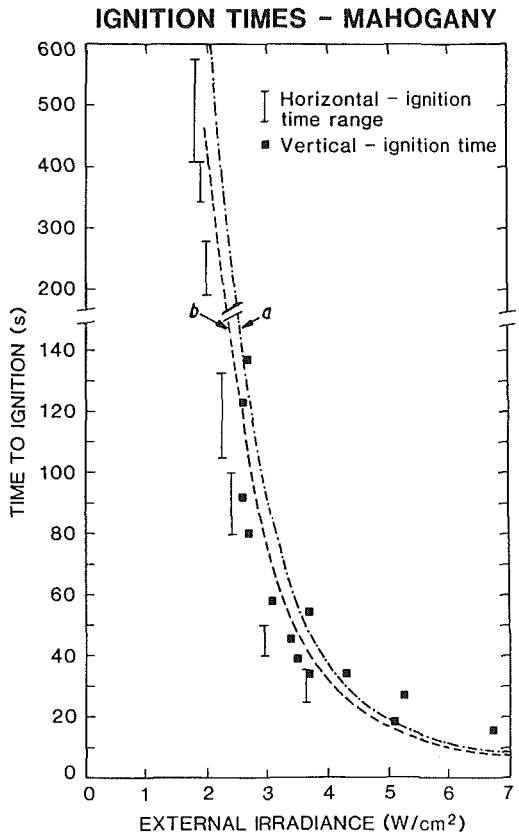

Fig. 4 Measured and predicted time for piloted ignition as a function of external rediation: curve *a* is for $h^* = 15$ W/m^{2}K and curve *b* is for $h^* = 10$ W/m^{2}K

W/cm^2) was then subtracted from the incident heat flux to obtain the corrected heat flux used to generate the curve T_3. This procedure is mathematically correct because equation (18) was obtained by satisfying the energy balance in an integral sense, and because the evaporation rate is very nearly constant for these tests.[3] The comparison between E_2 and T_3 is, however, better than expected.

A further test of equation (18) is made by comparing the predicted and measured times for piloted ignition, which occur at an approximately constant surface temperature. Figure 4 shows such a comparison for tests conducted on horizontal and vertical samples of mahogany. Curve *a* is calculated for the vertical case using a heat transfer coefficient of 15 W/m^2 K (Quintiere et al., 1983) while curve *b* is calculated for the horizontal case with an estimated heat transfer coefficient of 10 W/m^2 K. For both calculations an average measured piloted ignition temperature of 375°C was used and thermal properties were obtained from Atreya (1984). (The choice of this piloted ignition temperature is not arbitrary. The value of 375°C is completely justified by the graphic solution of the governing equations, shown in Fig. 6.) Once again, the comparisons are encouraging, even though enough decomposition took place during these experiments to allow piloted ignition to occur (recall that equation (18) was derived for the inert-heating stage). This provides justification for using $\rho = 1$ in equation (19).

Equations (18), (20), and (22) together provide an approximate solution for the piloted ignition problem. They relate the time, surface temperature, and mass flux at ignition to the conditions of the experiment and the thermophysical and thermochemical properties of the solid and the gas phases. It is revealing to compare these predictions with the experiments.

Figure 5 shows the measured surface temperatures at ignition for mahogany at different levels of external radiation for both the horizontal and the vertical sample orientations (further details of effect of sample orientation on piloted ignition are given by Atreya et al., 1985). These temperatures are well within the range reported in the literature (300°C–540°C) and, for reasons already stated, they do not include any contributions from gas-phase exothermic reactions. In terms of the nondimensional surface temperature T_s the measured range is between 2.05 and 2.3. This measured range is also shown on Fig. 6, which represents a graphic solution of equations (18), (20), and (22).

In Fig. 6, the calculations were carried out for three different levels of external radiation (2, 3, and 4 W/cm^2) and two different values of the nondimensional pre-exponential factor A in equation (9) (this was done to cover the range quoted in the literature). The values of other properties taken from various handbooks were $\epsilon = 0.85$, $T^*_\infty = 293$ K, $H^* = 10$ W/m^{2}K, $E = 123$kJ/g mole, $\delta = 0.25$, $c^* = 1.38$ J/gK, $\rho^*_\infty = 500$ kg/m^3, and $h^* = 15$ W/m^{2}K. The curves labeled gas-phase (M) are obtained from equation (22) whereas the curves labeled solid-phase (M) are obtained from equation (20). The intersection of these curves is the ignition point, which yields a unique solution for the fuel mass flux and surface temperature at ignition. Once the latter is known the time for piloted ignition is obtained from the bottom graph.

It is interesting to note that the predicted ignition temperatures lie within the measured range and that for a given set of parameters they are indeed very nearly constant. Note that from Fig. 6 the average predicted critical surface temperature for $A = 10^{10}$ is 325°C and for $A = 10^9$ is 375°C. The latter value of surface temperature at piloted ignition was used in the calculations of curves *a* and *b* shown in Fig. 4.

The results shown in Fig. 6 also indicate that though the

[3] The total energy flux required to evaporate moisture may be obtained by rewriting equation (8) as $\partial T/\partial t = \partial^2 T/\partial x^2 + Q_{EVAP}\partial\rho_m/\partial t$, where ρ_m is the moisture density, and $\rho = \lambda = 1$ has been used for dry wood. Now, by integrating over x from $x = 0$ to $x = \infty$ and using $\partial\rho_m/\partial t = \partial M_{EVAP}/\partial x$, one finds

$$\int_0^\infty \frac{\partial T}{\partial t} dx = \Phi_s - Q_{EVAP} M_{EVAP,s}.$$

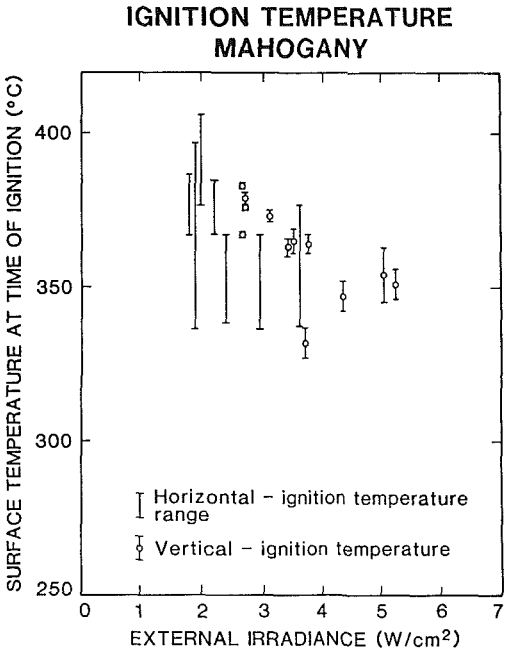

Fig. 5 Measured surface temperatures at the time of ignition for different external radiation conditions

nondimensional fuel mass flux M_s shows a considerable variation with external radiation, its dimensional counterpart M_s^* is almost constant, with a value of about 1.8 g/m^2 s. Furthermore, variations in the decomposition kinetics (which may cause a change in the value of A from 10^9 to 10^{10}) seem to produce a larger variation in the surface temperature at ignition but only a minor change in the critical fuel mass flux at ignition.

Conclusions

In this work the results of an experimental and theoretical investigation into the heat and mass transfer processes that occur during piloted ignition are presented. The predictions of the integral model developed herein show good agreement with the experimental measurements. This model is based on the following observations: (*i*) Critical conditions at ignition are achieved solely by external radiation and surface radiant emission plays a dominant role in determining the surface temperature at ignition. (*ii*) Although the heat lost by the flame to the solid at the instant of ignition is significant and may cause thermal quenching, its contribution to the enthalpy rise of the solid is negligible. This permits a decoupling of the gas and the solid phase equations. (*iii*) The concepts of nearly constant limit diffusion flame temperature at extinction and the nearly constant heat of combustion of air for most hydrocarbons can be profitably employed to approximate the extremely complicated gas phase combustion process by a simple energy balance. Finally, although more comprehensive models for the piloted ignition process are sorely needed the approximate model presented here provides simple formulas that show good agreement with the experiments. It also provides the conditions under which the often-used critical surface temperature and critical fuel mass flux ignition criteria are valid.

Acknowledgments

The first author would like thankfully to acknowledge the help and support provided by Professor H. W. Emmons and Dr. J. G. Quintiere. This material is based upon the work supported by the Center for Fire Research, National Bureau of Standards under grant No. 60NANB5D0578.

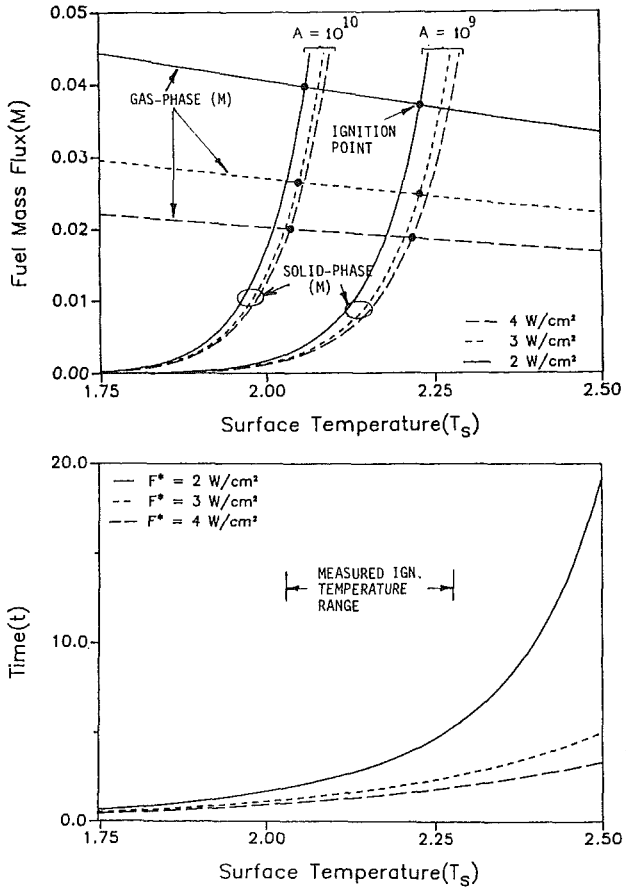

Fig. 6 Graphic solution of equations (18), (20), and (22)

References

Atreya, A., 1983, "Heat of Decomposition in Wood Pyrolysis," *Proceedings of the Eastern States Section of the Combustion Institute*, paper No. 37.

Atreya, A., 1984, "Pyrolysis, Ignition and Fire Spread on Horizontal Surfaces of Wood," NBS-GCR-83-449, National Bureau of Standards, Washington, DC.

Atreya, A., Carpentier, G., and Harkleroad, M., 1985, "Effect of Sample Orientation on Piloted Ignition and Flame Spread," *First International Symposium on Fire Safety Science*, pp. 97–109.

Bamford, C. H., Crank, J., and Malan, D. H. 1945, "The Combustion of Wood," *Proceedings of the Cambridge Philosophical Society*, Vol. 42, pp. 166–182.

Bird, R. B., Stewart, W. E., and Lightfoot, E. N., 1960, *Transport Phenomena*, Wiley, New York.

Carslaw, H. S., and Jaeger, J. C., 1959, *Conduction of Heat in Solids*, 2nd ed., Oxford University Press, London, United Kingdom.

Gradshteyn, I. S., and Ryzhik, I. M., 1965, *Table of Integrals, Series and Products*, Academic Press, New York.

Huggett, C., 1980, "Estimation of Rate of Heat Release by Means of Oxygen Consumption Measurement," *Fire and Materials*, Vol. 4, pp. 61–65.

Ishizuka, S., and Tsuji, H., 1981, "An Experimental Study of Effect of Inert Gases on Extinction of Laminar Diffusion Flames," *Eighteenth Symposium (International) on Combustion*, The Combustion Institute, Pittsburgh, PA, pp. 695–703.

Kanury, A. M., 1972, "Ignition of Cellulosic Solids—A Review," *Fire Research Abstracts and Reviews*, Vol. 14, No. 1, pp. 24–52.

Kanury, A. M., 1982, *Introduction to Combustion Phenomena*, Gordon and Breach Science Publishers, New York.

Kashiwagi, T., 1981, "Radiative Ignition Mechanism of Solid Fuels," *Fire Safety Journal*, Vol. 3, pp. 185–200.

Kashiwagi, T., 1982, "Effects of Sample Orientation on Radiative Ignition," *Combustion and Flame*, Vol. 44, pp. 223–245.

Martin, S., 1965, "Diffusion-Controlled Ignition of Cellulosic Materials by Intense Radiant Energy," *Tenth Symposium (International) on Combustion*, The Combustion Institute, Pittsburgh, PA, pp. 877–896.

Quintiere, J. G., 1981, "A Simplified Theory for Generalizing Results From a Radiant Panel Rate of Flame Spread Apparatus," *Fire and Materials*, Vol. 5, pp. 52–60.

Quintiere, J. G., Harkleroad, M., and Walton, D., 1983, "Measurement of Material Flame Spread Properties," *Combustion Science and Technology*, Vol. 32, pp. 67–89.

Rasbash, D. M., 1976, "Theory in the Evaluation of Fire Properties of Combustible Materials," *Proceedings of the 5th International Fire and Protection Seminar*, Karlsruhe, Federal Republic of Germany, Sept., pp. 113–130.

Robertson, A. F., 1979, "A Flammability Test Based on Proposed ISO Spread of Flame Test," Third Progress Report, Intergovernmental Maritime Consultative Organization, IMCO FP/215.

Sauer, F. M., 1956, "The Charring of Wood During Exposure to Thermal Radiation: Correlation Analysis for Semi-infinite Solids," Interim T. R. AFSWP-868, USDA Forest Service.

Tsuji, H., 1982, "Counterflow Diffusion Flames," *Progress in Energy and Combustion Science*, Vol. 8, pp. 93–119.

Wichman, I. S., and Atreya, A., 1987, "A Simplified Model for the Pyrolysis of Charring Materials," *Combustion and Flame*, Vol. 68, pp. 231–247.

Energy Storage in a Fluidized Bed

N. Merry

B. Rubinsky

Department of Mechanical Engineering,
University of California at Berkeley,
Berkeley, CA 94720

An experimental study was performed to investigate the possible use of a compound that undergoes solid-to-solid phase transformation for energy storage in a fluidized bed configuration, and to determine the heat transfer characteristics of this system. It was shown that the heat transfer coefficients from a surface immersed in the fluidized bed are a function of the bed temperature and of the temperature of the immersed surface. The heat transfer process is enhanced by the phase transformation by as much as a factor of four relative to the heat transfer in the same material without phase transformation. The experimental results suggest the possible existence of a thermal resistance between the surface immersed in the fluidized bed and the particles, which is responsible for the particular experimentally observed thermal behavior.

Introduction

Thermal energy storage systems provide more efficient use of energy through conservation of otherwise wasted energy for later use. The systems are employed in industrial processes that use or reject low-grade energy, with time varying energy sources such as solar and wind, and with time varying energy users such as heating and cooling of building systems. It is common to use in energy storage devices materials that have large energy storage capability per unit volume, such as materials that undergo solid-to-liquid phase transformation with large changes in enthalpy. There are however several practical problems with the use of the these materials. For example, the molten material must be confined to retain the structural integrity of the system, which increases the cost of the energy storage process. Also, since in these systems energy is transferred from the outer surface by diffusion heat transfer, only a limited region in the material, corresponding to the temporal position of the change of phase interface, is engaged in the energy storage process. This leads to a low energy storage capacity per unit time.

Murrill and Breed (1969) have studied compounds that undergo solid-to-solid phase transition (STSPT) associated with large changes in enthalpy, for use as thermal capacitors to buffer the temperature change of earth orbiting satellites passively. The materials identified were plastic crystals that exhibit mesocrystalline phases and high transitional enthalpy during solid-to-solid phase transition, between the crystalline and plastic crystalline states. These materials reversibly absorb large amounts of energy during solid state phase transformation at specific temperatures below their melting temperature, and therefore can be used for energy storage without being confined.

Since most of the STSPT materials are produced as small crystals, Rubinsky (1983) suggested using these materials for energy storage in a fluidized bed configuration. A gas–solid fluidized bed contains particulate matter through which a gas is passed. Sufficiently high flows of gas produce vigorous mixing of the solid particulates, which yields good heat transfer between the fluidized bed and surfaces immersed in the fluidized bed. The use of the STSPT materials for energy storage in a fluidized bed configuration should therefore yield high heat transfer between any heat exchanger surfacer immersed in the fluidized bed and the solid particulates. Furthermore, there should be an active participation in the energy storage process of the whole fluidized bed and a higher and uniform energy storage rate per unit volume.

Contributed by the Heat Transfer Division for publication in the JOURNAL OF HEAT TRANSFER. Manuscript received by the Heat Transfer Division November 17, 1987. Keywords: Packed and Fluidized Beds, Phase-Change Phenomena, Thermal Energy Storage.

Numerous studies have been reported on the heat transfer in a fluidized bed and comprehensive descriptions can be found in several publications such as Zabrodsky (1966), Abuaf and Gutfinger (1974), Botterfill (1975), Saxena et al. (1978), and Saxena and Ganzha (1984). Abuaf and Gutfinger (1974) have shown that the heat transfer coefficients in fluidized beds increase with an increase in the heat capacity of the fluidized particles. Botterill et al. (1981) have demonstrated experimentally that in a thermal regime not dominated by radiation or gas convection, the maximal heat transfer coefficients on a surface immersed in the fluidized bed increase only slightly with an increase in surface temperature. (The small increase is attributed to the increase in the thermal conductivity of the gas with temperature.) In a fluidized bed of STSPT compounds the change in enthalpy during phase transformation is large and it should have a similar effect on heat transfer coefficients as a large heat capacity, i.e., the heat transfer coefficients should increase when the STSPT particles undergo phase transformation. The STSPT particles will undergo phase transformation if the temperature of the immersed surface is above the phase transition temperature while the particles are at a temperature below the phase transition. Therefore, heat transfer coefficients in a fluidized bed of STSPT particles should be dependent on the temperature of the immersed surface relative to the phase transition temperature. This will obviously be different from the behavior in fluidized beds of particles that do not undergo phase transformation.

In this study a new experimental system was designed and experiments were performed to demonstrate that the STSPT materials undergo phase transformation in a fluidized bed configuration and to determine the effect of the immersed surface temperature on the heat transfer. The experimental apparatus was tested first in a fluidized bed of glass particles.

Experiments with glass particles have verified that in materials that do not undergo phase transformation the maximal heat transfer coefficients are not dependent on the temperature of the immersed surface. Experiments with STSPT particles have shown that the heat transfer coefficients were strongly dependent on both the surface temperature and the fluidized bed temperature. A possible qualitative explanation of the results is presented.

Experimental System. Several of the materials that can be of potential use for energy storage and their thermal properties are listed in Table 1 (Murrill and Breed, 1969). The material chosen for this study was neopentyl glycol (2, 2-dimethyl-1,3-propanediol) a material that could become useful for residential energy storage because of its thermal properties and low cost and because it is relatively innocuous. The material was purchased from the Aladine Company and is readily available from many other suppliers.

Table 1 Thermal properties of different materials that undergo solid-to-solid phase transformation

Compound	T, K	ΔH, kJ/kg	T, K	ΔH, kJ/kg
Pentaerythritol 12,2-Bis (hydroxymethyl 1,3 propanediol)	457–458	303.4	531–533	36.8
Pentaglycerin (2-hydroxymethyl-2 methyl-1,3-propanediol)	354	263	470–471	42
2-amino-2 methyl 1,3-propanediol	349–351	222.9	383–385	28.2
Neopentyl glycol (2,2-dimethyl-1,3-propanediol)	313–316	131	398–399	42

Microscopic observations of the neopentyl glycol crystals have shown that the crystals have a boxlike shape with a ratio of approximately five to one between the long and short sides of the box. The mean diameter of the particles was determined to be 0.4 mm by sieving using the averaging formula by Botterill (1979). The size distribution was between 0.05 and 0.65 mm. The plastic crystals are soft, waxy, and hygrophobic.

The experiments reported in this study were performed in a two-dimensional fluidized bed with a cross section of 3.5 cm by 22.9 cm and a height of 83.2 cm, described earlier by Rubinsky and Sterns (1983). The experimental system is shown schematically in Fig. 1. The air to the fluidized bed was supplied from a central compressor at 6.81 Pa through a pressure regulator, a Drierite air drier, oil filters, and a custom designed air heater. The air flow rate was measured with a Fisher–Porter rotometer. The pressure drop across the fluidized bed was measured by a Merriam Instruments manometer filled with measurement oil using a glass tube capped with a 40 μm porous plug at the bottom of the fluidized bed. In typical fluidized bed experiments it is observed that the temperature of surfaces immersed in the fluidized bed fluctuates in time (e.g., Richardson and Shakiri, 1979; Baskakov et al., 1979; Botterill, 1975). This temperature fluctuation, which is acceptable in experiments with materials with weak dependence of thermal properties on temperature, is not acceptable in experiments with STSPT compounds, in particular when the temperature of the surface is near the compound's phase transition temperature. To eliminate the surface temperature fluctuation we have designed a special computer-controlled experimental system that can maintain a probe at a constant surface temperature during the experiments while recording the instantaneous heat dissipation required to maintain the constant temperature.

A schematic diagram of the heat transfer probe used in this work is shown in Fig. 2. The probe was constructed by encasing an N-type (120 Ohm) thermofoil Minco heater by a rectangular 0.05 mm copper shell (3.5 cm by 3 cm). The thin copper foil was chosen to produce a probe with a low thermal mass to facilitate the determination of the instantaneous heat transfer to the fluidized bed. Thermal compound was used to assure uniform thermal distribution in the probe and good thermal contact between the heater and the copper walls. The probe temperature was measured by two 0.0254 mm type K thermocouples soldered on the inner side of the copper wall, one at the center of the probe, and the other on the long axis of symmetry of the heat transfer surface, at a distance of 1 cm from the first thermocouple. The probe was positioned in the fluidized bed, with the heat transfer surface normal to the larger (22.9 cm by 83.2 cm) surfaces of the fluidized bed, and in the direction of the air flow. The probe was pressed between the two larger surfaces of the fluidized bed with its center at a height of 15 cm from the bottom of the fluidized bed, at an equal distance from the narrow sides of the chamber.

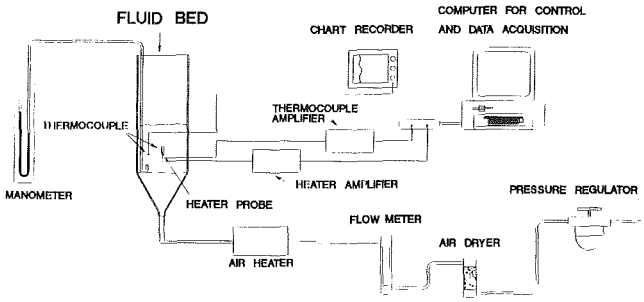

Fig. 1 Schematic of the experimental system

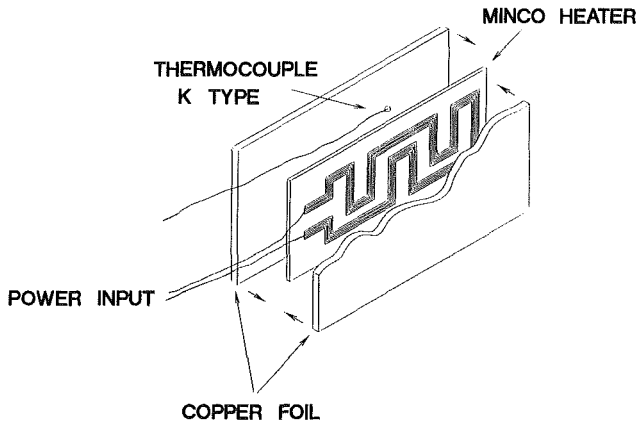

Fig. 2 Schematic of the heat transfer probe

The unsteady heat transfer in fluidized beds required maintaining the heat transfer probe at a constant temperature while varying rapidly the power dissipation and at the same time recording both the surface temperature and the power consumption. This was accomplished by a parallel data acquisition and control system. The heart of the system was a Z-Tech Systems personal microcomputer equipped with an IBM data acquisition and control board. The signals from the probe thermocouples were amplified by a Cole Palmer Model 20B thermocouple amplifier. The thermocouple amplifier, which incorporates also a multiplexer, was controlled by the computer. The multiplexer allowed the program to sample all the thermocouples involved in the experiment together with an electronic cold junction. Among the temperature data sampled was also the bulk temperature of the fluidized bed, which was measured with an additional thermocouple located 10 cm away from the center of the probe, at the same height.

The control system operated at a temperature sampling rate of 28 samples per second. This sampling rate was proven sufficiently high to stabilize the temperature of the immersed surface and counteract the fluctuations in heat transfer. The translation of the control output signal into a high-power signal was accomplished by a custom-designed amplifier that operated the heater probe. The computer output was a digital signal in the range of 0V to 10 V, which was translated to an analog current signal by the amplifier. The heater probe used direct current with a maximum power consumption of 42.72 W.

The software required to run the experiment is primarily a proportional-integral control algorithm written in the C programming language and can be found in Merry (1988). In a typical experimental protocol the computer program collects the temperature of the probe and the bulk temperature of the fluidized bed and, without recording the data, echoes these values to the computer monitor. In the program, the temperature of the probe is compared to the desired value and

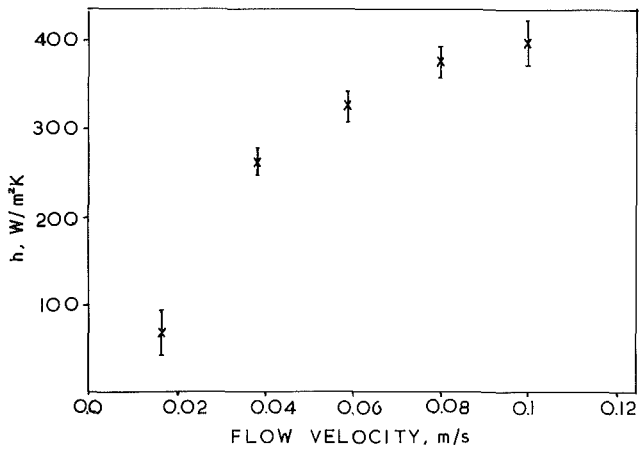

Fig. 3 Heat transfer coefficients in a fluidized bed of glass particles as a function of air flow rate

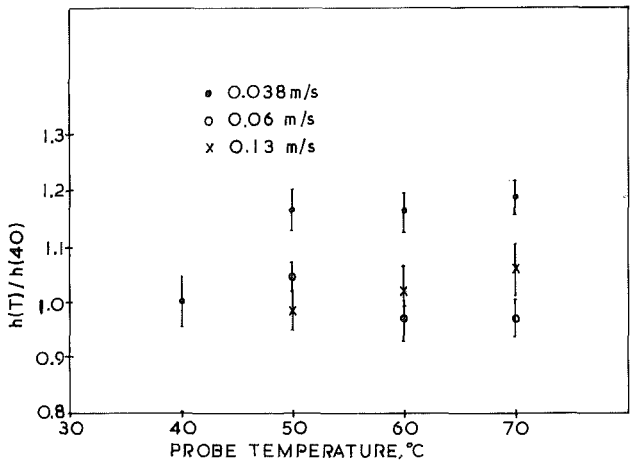

Fig. 4 Dimensionless heat transfer coefficients in a fluidized bed of glass particles as a function of surface temperature

the power consumption needed to maintain a constant probe temperature is determined by the proportional-integral control algorithm. A discrete voltage value is sent by the computer to the amplifier, which delivers the direct current flowing through the probe. The known current can be used together with the known constant value of the probe resistance to evaluate the instantaneous power dissipation by the probe, which is also displayed on the terminal. Once the temperature of the probe has stabilized at the desired value, the command to start recording the data is given from the terminal. During the data acquisition part, the probe temperature fluctuations were found to be less than 0.5°C peak to peak. The uniformity of the temperature distribution in the probe was confirmed by the measurements of the two thermocouples in the probe and was found to be within the range of the temperature fluctuations. The sampling period was 40 seconds, during which the instantaneous temperature of the surface and the heat dissipated were recorded for 1120 sampling points. In addition to the data acquisition and the control program, the computer calculated the standard deviation of the heat flux and the probe temperature from the 1120 data points and displayed the standard deviation and average heat transfer from the surface, calculated using the formula

$$h = \left(\sum_{i=1}^{1120} q_i / (T_i - T_b) \right) / (nA) \qquad (1)$$

where h is the average heat transfer coefficient, q and T_i are the heat flux and the temperature of the ith sample, T_b is the bulk temperature of the fluidized bed, A is the probe surface area, and the summation is over n sample points.

Between three and six experiments were performed for each of the experimental results shown in the figures of this publication. The error bars in the different figures represent the value of 2σ (i.e., two standard deviations). The standard deviation was calculated from the distribution of values of the instantaneous heat transfer coefficients evaluated for each sampling point and represents the variation of 3360 to 6720 data measurements. The major cause for the experimental uncertainty is the nonuniform heat transfer, typical to fluidized beds, which is caused by the intermittent interaction of the immersed surface with air bubbles and the particles.

Experimental Results and Discussion

Preliminary experiments have shown that despite the relative large mean diameter of the particles, the neopentyl glycol crystals fluidize in a way that resembles fluidization in fine powders (Richardson and Shakiri, 1979). First, with an increase in air flow rate, channels form through the fluidized bed. The channeling continues with an increase in air flow rate until suddenly bubbles start forming and a fully fluidized bubbling bed results.

Experiments were performed to evaluate and calibrate the experimental system. Since the neopentyl glycol particles fluidize in a channeling, powderlike form, a spherical glass powder was used for the preliminary experiments. The mean diameter of the glass particles was 78 μm and the size range was between 52 μm and 100 μm. For each experiment the height of the fluidized bed was measured together with the pressure drop across the fluidized bed. A set of experiments was performed in which the heat transfer coefficients were determined as a function of the fluidizing air flow velocity and the probe surface temperature.

Figure 3 shows the heat transfer coefficients as a function of air flow rate. The experiments were performed with a fluidized bed at a temperature of 22°C and for a probe with a surface temperature of 40°C. The initial height of the fluidized bed was 260 mm and the bed expanded to 289 mm. The minimal fluidization velocity, evaluated from the expansion of the bed and the pressure drop across the bed, was 0.018 m/s. The maximal heat transfer coefficient in this figure is 390 W/m²K, which compared well with the experimental results obtained by Richardson and Shakiri (1979, Table 3), who determined experimentally, for similar glass particles, a maximal heat transfer coefficient of 353 W/m²K.

Additional experiments were performed to determine the effect of probe temperature and bed temperature on heat transfer coefficients in a fluidized bed of glass particles. Figure 4 shows dimensionless heat transfer coefficients, in a fluidized bed at 22°C, as a function of probe surface temperature for different air flow velocities. The heat transfer coefficients in Fig. 4 were normalized with respect to the heat transfer coefficients for the same air flow rates in Fig. 3. It is evident that, as anticipated (Botterill et al., 1981), the heat transfer coefficients increase very little with an increase in the temperature of the probe. Increasing the temperature of the fluidized bed to 25°C and 35°C did not produce results significantly different from those shown in Fig. 4.

The special mode of fluidization of pure neopentyl glycol has been described earlier. First channeling occurs, and then, with an increase in air flow rates, fluidization starts suddenly. Initially, a high air flow rate was required to start the fluidization. However, once the fluidization was started, lower air flow rates could sustain the fluidization process. Because of this fluid flow behavior, we were able to perform experiments only with the fully fluidized, bubbling bed, which is a state in

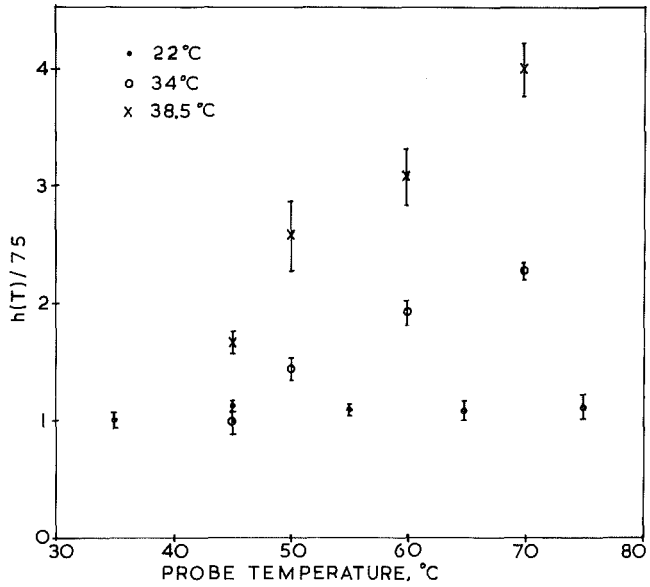

Fig. 5 Dimensionless heat transfer coefficients in a fluidized bed of neopentyl glycol as a function of surface temperature

which maximal heat transfer is expected, and in which the air flow rate does not have a significant effect on heat transfer coefficients.

Seven different air flow rates between 0.1 m/s and 0.55 m/s were used in this work. The initial height of the fluidized bed was 214 mm and the bed expanded during fluidization to 240 mm. The results of the experiments are given in Fig. 5.

Figure 5 shows heat transfer coefficients as a function of probe surface temperature for fluidized beds with initial temperatures of 22°C, 34°C, and 38.5°C. The heat transfer coefficients have been normalized with respect to 75 W/m^2K, which is the heat transfer coefficient for fluidization without phase transformation determined in a fluidized bed of neopentyl glycol in which the initial fluidized bed temperature was 22°C and the probe surface temperature was 35°C. The data for all the flow rates was concentrated in a single curve since the air flow rates, in the range studied in this work, did not affect the heat transfer coefficients in a systematic way.

The special behavior of the heat transfer coefficients in fluidized beds of neopentyl glycol becomes evident when Fig. 5 is compared with Fig. 4. The dramatic effects of the probe temperature and of the initial fluidized bed temperature on the heat transfer coefficients can be attributed only to the solid to solid phase transformation in neopentyl glycol.

A comparison between the different curves in Fig. 5 shows that a small increase in the initial temperature of the fluidized bed has a large effect on the behavior of the heat transfer coefficients as a function of probe surface temperature. The heat transfer coefficients for a fluidized bed at an initial temperature of 22°C are practically independent of the probe surface temperature. This behavior is typical to fluidized beds of particles that do not undergo phase transformation as demonstrated in Fig. 4. However, when the initial temperature of the fluidized bed is 38.5°C the heat transfer coefficients are a strong function of the probe surface temperature and increase by a factor of four with an increase in probe surface temperature from 45°C to 70°C. The only possible explanation for this behavior is that phase transformation occurred in the fluidized bed and this, as predicted, resulted in a significant increase in the heat transfer coefficients. Obviously the STSPT particles can be used for energy storage and the heat transfer coefficients increase significantly when energy is stored in the fluidized bed.

A possible explanation for the experimental results described earlier will be given next. Heat transfer with phase transformation is characterized by the propagation of an interface on which the phase transition occurs from the outer surface of the domain, on which the heat is applied, to the interior. In a fluidized bed of STSPT particles, the phase transition interface will propagate from the point of contact between the particles and the immersed surface into the particle. The propagation of the solid-to-solid phase transition interface is obviously slow because of the large change in enthalpy during phase transformation and because the associated energy must be introduced by diffusion from the outer surface. Numerous studies are available on the propagation of the phase transition interface. A simplified equation for the position of the interface as a function of time can be found in Lunardini (1981)

$$S=\sqrt{\frac{2kt(T_s-T_{ph})}{\rho L}} \tag{2}$$

where k, the thermal conductivity of the STSPT particle, is 0.324 J/mK; ρ, the density, is 720 kg/m^3; L, the change in enthalpy upon phase transformation, is 131 kJ/kg; and T_s-T_{ph}, the difference in temperature, between the probe surface temperature and the phase transition, in this experiment was 40°C. The time of contact between the particles and the probe surface has the same order of magnitude as the experimentally determined fluctuation in the heat flux. These fluctuations were on the order of 0.1 seconds. It can be found from equation (2) that during the time a particle resides near the immersed surface, the phase transition interface will penetrate no more than 0.15 mm from the outer surface. Obviously this penetration is less than the average size of a particle and therefore the heat transfer in fluidized beds of STSPT particles will be dominated by the energy transfer process on the interface between the first layer of particles and the probe surface.

In order to explain the heat transfer process in fluidized beds, many researchers have postulated the existence of a thermal resistance between a surface immersed in the fluidized bed and the fluidized bed (Baskakov et al., 1971; Gabor, 1970; Yoshida et al., 1968). This thermal resistance was attributed by researchers to different mechanisms, all of which are related to the existence of a layer of air between the particles and the immersed surface. Kubie (1985) suggested that this resistance is a consequence of the increased voidage near the surface, while Glicksman and his co-workers (Decker and Glicksman, 1981; Gloski et al., 1984) have shown that this resistance is due to the contact resistance between the particles and the surface.

The experiments with the STSPT particles show that the heat transfer coefficients do not increase when the temperature of the fluidized bed or the probe temperature are low relative to the phase transition temperature. In a fluidized bed at 22°C the heat transfer coefficients do not increase even when the probe surface is at 75°C. This implies that under certain circumstances the STSPT particles do not undergo phase transition even when the probe surface is above the phase transition temperature. These results can be explained by the existence of the thermal resistance between the particles and the surface, across which there is a temperature drop and through which the heat must be transferred to the particles. When the temperature drop across the thermal resistance is too large the particles do not reach the phase transition temperature.

Figure 5 shows that when the initial temperature of the bed was 34°C and 38.5°C, the heat transfer coefficients started increasing for probe surface temperatures higher than 50°C and 45°C, respectively. These results can be explained qualitatively in terms of the transient process of heat transfer between the particles and the fluidized bed. In fluidized beds particles spend a relatively short time near the probe surface. During

the time a particle is near the probe surface it will be heated and its temperature will increase as a function of time. If the time of residence of the particle near the surface is long enough relative to the time required to heat the particle to the phase transition temperature, phase transition will occur and the heat transfer coefficients will start to increase. Obviously, in our experiments with fluidized beds at 35°C and 38.5°C, the particles reached the phase transition temperature, while in the fluidized beds at 22°C the phase transition temperature was not reached even for the highest probe surface temperature used in our experiments. A higher probe surface temperature will result in more material undergoing phase transformation during the time a particle is near the probe. This might explain the observed increase in heat transfer coefficients with probe surface temperature.

Conclusions

An experimental study was performed on the heat transfer in a fluidized bed of neopentyl glycol, a compound that undergoes solid-to-solid phase transformation with a large change in enthalpy. A new experimental system was designed to determine the heat transfer coefficients from a probe immersed in the fluidized bed and maintained at a constant temperature. The results show that the heat transfer is enhanced by the phase transformation process and that the heat transfer coefficients are a strong function of both the fluidized bed temperature and the probe surface temperature. These results can be explained qualitatively by the existence of a thermal resistance between the surface immersed in the fluidized bed and the fluidized bed. The results of this study indicate that the neopentyl glycol could be used effectively for energy storage.

Acknowledgments

This study was supported by NSF Grant No. CBT-8609946.

References

Abuaf, N., and Gutfinger, C., 1974, "Heat Transfer in Fluidized Beds," *Advances in Heat Transfer*, Vol. 10, pp. 167–218.

Baskakov, A. P., Berg, B. V., Vitt, O. K., Filippovsky, N. F., Kirakosyan, V. A., Goldobin, J. M., and Maskaev, V. K., 1973, "Heat Transfer to Objects Immersed in Fluidized Beds," *Powder Technology*, Vol. 8, pp. 273–282.

Botterill, J. S. M., 1975, *Fluidized Bed Heat Transfer*, Academic Press, New York.

Decker, N. A., and Glicksman, L. R., 1981, "Conduction Heat Transfer at the Surface of Bodies Immersed in Gas Fluidized Beds of Spherical Particles," *AIChE Symposium Series*, No. 208, Vol. 77, pp. 341–349.

Gabor, J. D., 1970, "Wall to Bed Heat Transfer in Fluidized and Packed Beds," *Chem. Eng. Progress Symposium Series*, Vol. 66, No. 105, pp. 76–86.

Gloski, D., Glicksman, L., and Decker, N., 1984, "Thermal Resistance at a Surface in Contact With Fluidized Bed Particles," *Int. J. Heat Mass Transfer*, Vol. 27, No. 4, pp. 599–610.

Kubike, J., 1985, "Heat Transfer Between Gas Fluidized Beds and Immersed Surfaces," *Int. J. Heat Mass Transfer*, Vol. 28, No. 7, pp. 1345–1353.

Lunardini, V., 1981, *Heat Transfer in Cold Climates*, Van Nostrand Reinhold, New York.

Mathur, A., and Saxena, S. C., 1987, "Total and Radiative Heat Transfer to an Immersed Surface in a Gas-Fluidized Bed," *AIChE J.*, Vol. 33, No. 7, pp. 1124–1135.

Merry, N., 1988, "Heat Transfer in Fluidized Beds of Solid to Solid Phase Transformation Materials," M.Sc. Thesis, Department of Mechanical Engineering, U. C. Berkeley, CA.

Murrill, E., and Breed, L. W., 1969, "Space Thermal Control by Use of Solid/Solid-Phase Change Materials," Annual Summary Report No. 1, NASA Contract No. NASA-21452DCN-1-8-28-0053.

Richardson, J. F., and Shakiri, K. J., 1979, "Heat Transfer Between a Gas–Solid Fluidized Bed and a Small Immersed Surface," *Chem. Eng. Sci.*, Vol. 34, pp. 1019–1029.

Rubinsky, B., 1983, "Energy Storage Systems Using Solid to Solid Phase Transformation Materials in an Air Fluidized Bed Configuration," Internal report, University Energy Research Group, University of California, UCB Grant Eng-5788.

Rubinsky, B., and Sterns, G. L., 1983, "Experimental Comparison of Heat Transfer Data With Flow Visualization on the Heat Transfer From a Flat Surface in a Fluidized Bed," ASME JOURNAL OF HEAT TRANSFER, Vol. 105, pp. 809–816.

Saxena, S. C., and Ganzha, V. L., 1984, "Heat Transfer to Immersed Surfaces in Gas-Fluidized Beds of Large Particles and Powder Characterization," *Powder Technology*, Vol. 39, pp. 199–208.

Yoshida, K., Kunii, D., and Levenspiel, O., 1975, "Heat Transfer Mechanisms Between Wall Surface and Fluidized Bed," *Int. J. Heat Mass Transfer*, Vol. 12, p. 529.

Zabrodsky, S., 1966, *Hydrodynamics and Heat Transfer in Fluidized Beds*, M.I.T. Press, MA.

Void Fraction Measurements During Saturated Pool Boiling of Water on Partially Wetted Vertical Surfaces

S. P. Liaw
Student Mem. ASME

V. K. Dhir
Mem. ASME

Mechanical, Aerospace and Nuclear Engineering Department,
School of Engineering and Applied Science,
University of California,
Los Angeles, CA 90024-1597

Void fraction profiles adjacent to a vertical wall 6.3 cm wide and 10.3 cm high were measured during nucleate boiling. The experiments were conducted in saturated water at 1 atm pressure. In the experiments, the wettability of the surface was varied by controlling the degree of oxidation of the surface. Static contact angle was used as an indicator of the surface wettability. The void fraction was measured with a gamma densitometer. The experimental results show that the maximum void fraction occurs about 1–1.5 mm away from the heater surface. The wall void fraction, the maximum void fraction, and the thickness of the void layer increase with wall heat flux. It is found that for a given heat flux, the wall void fraction increases as the surface becomes less wettable, whereas the maximum heat flux decreases with increase in contact angle.

Introduction

Of all the modes of boiling, nucleate boiling is associated with the highest heat transfer coefficients. As a result, this process is of great interest with regard to applications as well as basic understanding. Numerous studies of nucleate boiling heat transfer have been reported in the literature. The results of these studies have generally been given in the form of correlations. So far, relatively few attempts have been made to describe the nucleate boiling process in a mechanistic way, and those efforts have met with little success. The primary cause for the very limited success of those attempts is a lack of understanding of the interaction of several surface and fluid parameters. To facilitate further development of mechanistic models of nucleate boiling and maximum heat fluxes, the purpose of the present work is to determine experimentally the interplay between the wall void fraction, surface wettability, and vapor flow dynamics away from the wall.

The earliest correlation for nucleate boiling is that of Rohsenow (1952). This correlation, though not based on sound reasoning of the physical mechanisms, has been very successful in predicting the observed nucleate boiling data. According to this correlation, the dependence of wall heat flux on wall superheat is written as

$$q = \mu_l h_{fg} \sqrt{\frac{g(\rho_l - \rho_v)}{\sigma}} \left(\frac{c_{pl} \Delta T}{C_s h_{fg}} \right)^m (\mathrm{Pr}_l)^{-n} \qquad (1)$$

In equation (1), the parameters C_s, m, and n are obtained empirically. The parameter C_s accounts for the effect of surface finish and wettability and as such varies with fluid-surface combination. The constants n and m have generally been found to vary between 3 and 4 for water. One reason for the success of this correlation is that it combines a correct length scale with appropriate thermophysical properties. Subsequent work has led to some modifications (Dwyer, 1974) of the above correlation but not in any significant way.

A prerequisite to the development of a mechanistic model for nucleate boiling is the delineation of various mechanisms by which energy can be transferred from the heater surface. It has generally been accepted that transient conduction and evaporation at nucleation sites and convection over the inactive regions of the heater are the relevant mechanisms. However, at higher heat fluxes, evaporation dominates over the two mechanisms. A comparison of the magnitudes of heat transfer rates associated with these mechanisms and related discussion is given by Hsu and Graham (1976).

Although most of the energy at high heat fluxes is transferred by evaporation, the location at which evaporation occurs at the bubble surface was a controversial topic in the 1960s. Two points of view have been that evaporation occurs over the upper surface of a bubble as opposed to underneath a bubble. Subsequent work lends credence to the earlier contention of Moore and Mesler (1961) that most of the evaporation occurs underneath the bubbles.

Apart from a detailed description of the modes of heat transfer, a mechanistic model also requires a knowledge of the site density as a function of wall superheat, vapor bubble size and its area of influence, bubble release frequency or superficial vapor velocity, and the vapor flow dynamics in the vicinity of the heater. The site density and bubble size and shape are strongly influenced by surface characteristics such as finish, wettability, cleanliness, etc. Because of the involvement of numerous variables and their interactions, the development of a totally mechanistic model for nucleate boiling has been an insurmountable task. Fath and Judd (1978) attempted to predict nucleate boiling heat flux on a mechanistic basis. However, they employed several of the parameters inferred from the experiments and as a result simply established the self-consistency of their model.

Further progress in the development of mechanistic models for nucleate boiling strongly depends not only on the correct modeling of the various transport processes but also on the parameters that characterize the heater surface and the fluid flow conditions away from the wall. In this context, the purpose of the present work is twofold:

(*i*) to determine the effect of surface wettability on nucleate boiling heat fluxes; and

(*ii*) to delineate the interaction between the boiling process at the wall and the vapor flow dynamics away from the wall. The second objective is met through the measurement of void profiles adjacent to the heated vertical wall. This study was designed to lay the ground work for our future efforts toward

Contributed by the Heat Transfer Division and presented at the ASME Winter Annual Meeting, Boston, Massachusetts, December 13–18, 1987. Manuscript received by the Heat Transfer Division September 24, 1987. Keywords: Boiling, Multiphase Flows.

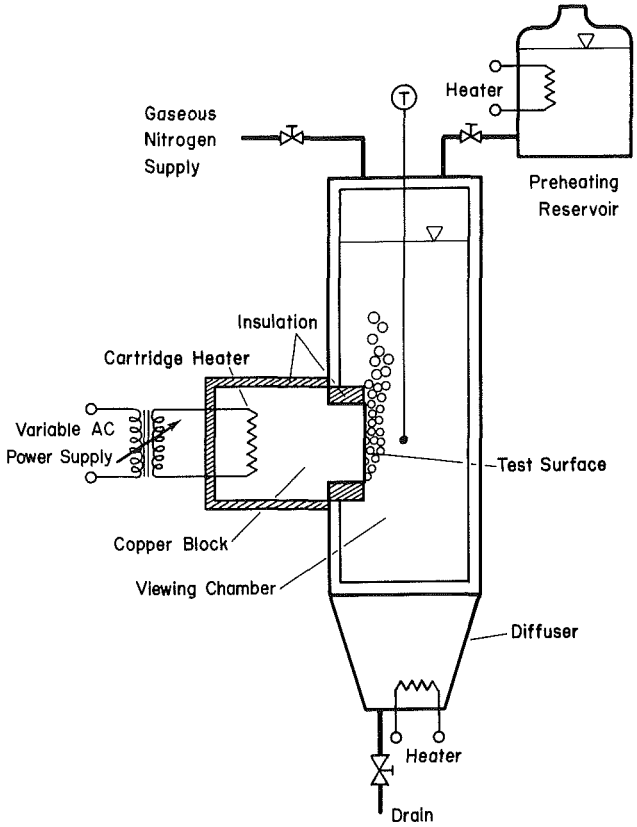

Fig. 1 Schematic diagram of the test setup for pool boiling study

development of a theoretical model for the complete boiling curve.

Experiments

The experimental apparatus used in this study was essentially the same as that described earlier by Bui and Dhir (1985) and by Liaw and Dhir (1986). Figure 1 shows a schematic diagram of the apparatus. The test surface is rectangular in shape and has a width of 6.3 cm and a height of 10.3 cm. The surface was machined from one end of a cooper rod having a purity of 99.9 percent. Eight cartridge heaters, four rated at 2 kW and the other four rated at 1 kW, are embedded in the copper rod. Thirty-gage chromel-alumel thermocouples are positioned along the vertical axis of the rectangular boiling surface at four locations, 8, 26, 52, and 77 mm from the lower edge. At each vertical location, four thermocouples were embedded at various depths normal to the boiling surface. The test section is mounted on one side of a viewing and liquid holding chamber. Glass plates are placed on the remaining three sides of the chamber for simultaneous observation of the front and side views of the boiling phenomena on the test surface. The liquid holding and viewing chamber is a square duct with a 14 cm by 14 cm cross section.

Startup of a typical experimental run began with deaeration of the test liquid by vigorous boiling in a reservoir and with preheating of the test section. The chamber was then filled with the test liquid from the reservoir and the boiling process was commenced. The power to the heaters was controlled with an autotransformer and was determined by voltmeter and ammeter readings. A steady-state condition was assumed to exist when the temperature of the test section changed less than 1 K in 5 min. All of the tests reported in this work were carried out in a steady-state mode. For these tests, the thermocouple output was recorded directly on a Fluke data logger. The wall heat flux was determined by knowing the temperature gradient, which was linear through the copper block except near the edges. The surface temperature was obtained by extrapolating the known temperature profile at a given vertical location. A balance between the energy input in the cartridge heaters and the energy lost at the boiling surface and the copper block surface was also made. At a boiling surface heat flux of 74 W/cm^2, the calculated energy loss rate agreed to within 5 percent of the energy input rate.

Surface Preparation and Measurement of Contact Angles. A well-defined procedure already described in detail (Liaw and Dhir, 1986) was used to obtain surfaces of different degrees of wettability. In this procedure, the polished surface of a copper disk (secondary surface) was heated in air while increasing the surface temperature at about 6 K/min until the surface temperature reached a desired value. The surface was then maintained at that temperature for a predetermined period and was subsequently cooled at a rate of about 2 K/min to the temperature at which the contact angle was to be measured. The inset in Fig. 2 shows the surface oxidation procedure. Thereafter a liquid droplet 0.2 cm^3 in volume was placed on the test surface. The initial temperature of the droplet was the same as the test surface. The contact angle was determined from a photograph of the droplet placed on the test surface. Figure 2 shows the contact angles measured at room temperature as a function of the maximum temperature to which the secondary surface was heated. To obtain a desired degree of wettability of the primary test surface, the same procedure as described above was repeated. To assure that the surface conditions were indeed duplicated, in one instance the contact angles on the secondary and the primary surface were measured and found to be within the measurement uncertainty, which was about ±3 deg.

Nomenclature

C_1, C_2 = constants
C_s = empirical constant characterizing a surface
c_{pl} = specific heat of liquid
g = gravitational acceleration
h_{fg} = latent heat of vaporization
I = beam intensity
I_g = beam intensity after it passes through gas or vapor
I_l = beam intensity after it passes through liquid
L = spacing of vapor stems
l = thermal layer thickness
Pr_l = Prandtl number of liquid
q = heat flux
T_{sat} = saturation temperature of liquid
T_w = wall temperature
U_c = vapor velocity in a continuous passage
$\bar{U}_c$ = average vapor velocity in the continuous passages
U_H = Helmholtz critical velocity
U_t = terminal velocity of a bubble
$\bar{U}_v$ = superficial velocity of vapor
x = distance normal to the wall
z = distance along the wall
z' = dimensionless distance along the wall
α = void fraction
α_{max} = maximum void fraction at wall
α_w = void fraction at wall
γ = ratio of width of test surface to width of test chamber
ΔT = wall superheat
$\bar{\delta}$ = effective vapor layer thickness
μ_l = viscosity of liquid
ρ_l = density of liquid
ρ_v = density of vapor
σ = surface tension
ϕ = contact angle

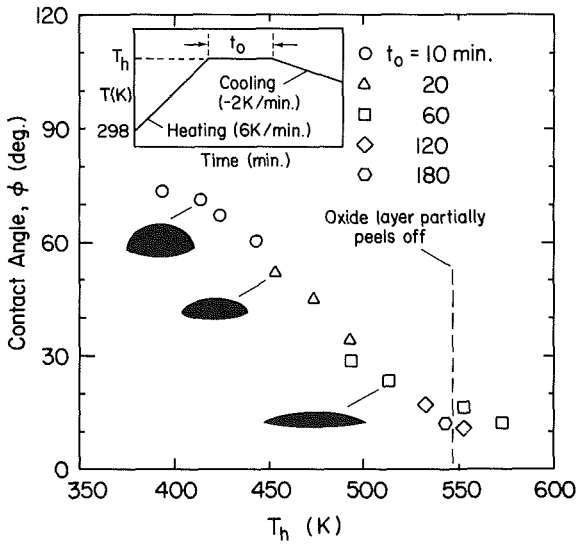

Fig. 2 Dependence of the contact angle measured at room temperature on the highest temperature attained during oxidation (the dark symbols are photographs of droplets)

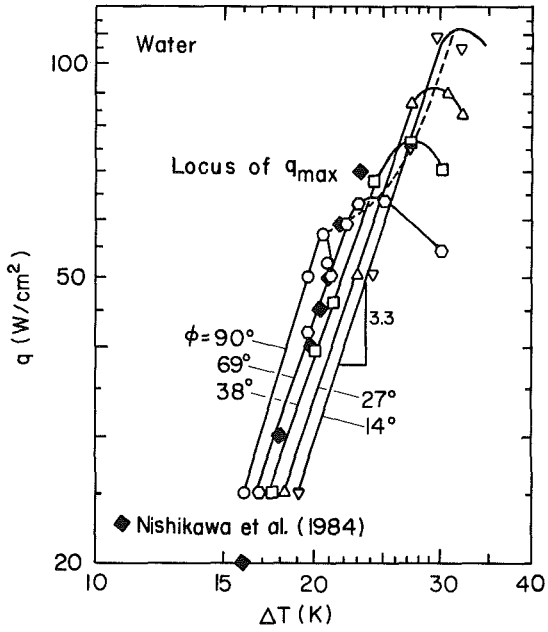

Fig. 4 Variation of heat flux with wall superheat for various contact angles

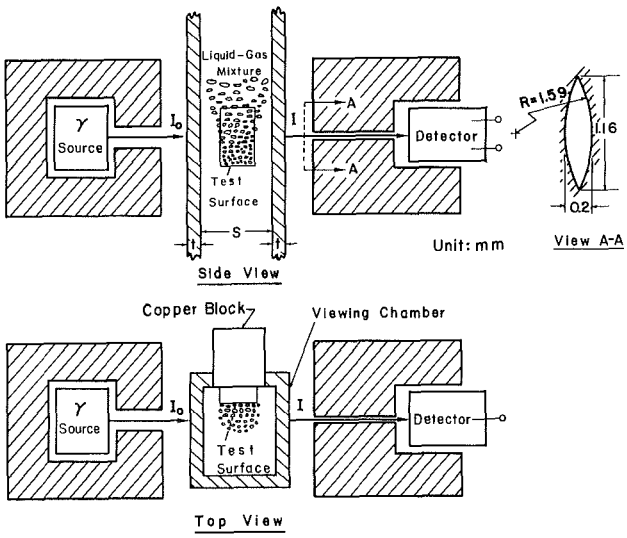

Fig. 3 Schematic diagram of orientation of gamma beam with respect to test surface

Void Fraction Measurement. The void fraction profiles adjacent to the boiling surface were obtained with a gamma densitometer. Figure 3 shows the orientation of the gamma beam with respect to the surface. The gamma densitometer consists of a 150-milli-Curie cesium-137 source and a NaI detector, both encased in lead. The diameter of the source collimeter is 6.25 mm (1/4 in) and that of the detector is 3.18 mm (1/8 in). The source and the detector are placed 0.62 m (2 ft) apart on a base plate, which in turn is mounted on a lift truck. The base plate is moved vertically upward or horizontally across the test surface by rotating threaded spindles. In this way the beam can be made to traverse the test section at several horizontal and vertical locations along the plate. After passing through the test chamber the gamma beam is absorbed in the detector and produces a pulsed signal. The circular area over which the signal is received and the area of the detector are experimentally found to have an eccentricity of about 2.9 mm. As such, the pulsed signal is representative of nearly point value of the void fraction rather than an average over the cross-sectional areas corresponding to the source or the detector. The signal magnitude was analyzed and sorted in an HP model 401D pulse analyzer. The signal output was printed on a TMC model 500A printer.

Prior to the measurement of void fractions on the boiling surface, calibration for the attenuation of the beam intensity was made when the test section had only air or water in it. The density of air is not much different from that of water vapor. As a result little error (0.03 percent) is made in assuming that attenuation of beam intensity in water vapor will be the same as in air. If γ is the ratio of the width of the test surface to that of the test chamber (see Fig. 3), the average void fraction across the cross section of the surface can be written as

$$\alpha = \gamma \frac{\ln(I/I_l)}{\ln(I_g/I_l)} \tag{2}$$

The variability in the void fraction due to uncertainty in the value of I is calculated to be ± 1.4 percent. All of the distances normal to the wall were measured from the test surface. The position of the test surface ($x=0$) was established by aligning the centerline of the gamma beam with the test surface. The beam center was assumed to be tangent to the surface when the rate at which attenuation of the beam intensity was maximum. The uncertainty in location of the surface is estimated to be 0.05 mm. This introduces a calibration error as well as an error in the measured void fraction. The total error in the void fraction as a result of statistical error (± 1.4 percent) as stated earlier, and taking into account the uncertainty in the location at which the void fraction is measured, is calculated to be less than ± 0.05 at 0.4 mm from the surface. Since the uncertainty in the measured void fractions at distances shorter than 0.4 mm was large, all of the reported data were limited to distances greater than 0.4 mm from the surface. The error in void fraction, however, decreases with distance from the wall and is calculated to be ± 0.03 at 20 mm from the wall.

The wall void fractions were determined by extrapolation of the data obtained at locations farther than 0.4 mm from the wall. The maximum uncertainty in the wall void fraction is found to be ± 0.06 and was obtained by extrapolating the mean and upper and lower bounds of the data representing the void profiles at distances greater than 0.4 mm from the wall. It

Table 1 Values of C_s for different contact angles

ϕ,deg	C_s
14	0.0209
27	0.0202
38	0.0194
69	0.0186
90	0.0172

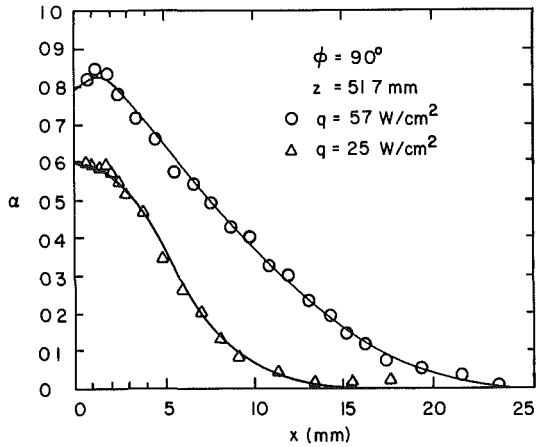

Fig. 5 Void profiles at midplane of the test surface for a contact angle of 90 deg

should be stressed here that for well-wetted surfaces the interface shape could change rapidly very near the wall. For these surfaces the uncertainty in the wall void fraction could conceivably be higher than that evaluated in this work.

Results and Discussion

The nucleate boiling data were obtained under steady-state conditions at a system pressure of 1 atm with saturated water as the test liquid. The reported void fractions represent an average over the width of the plate and over time. The reported heat transfer data were obtained under steady-state conditions.

Figure 4 shows dependence of nucleate boiling heat flux on wall superheat for contact angles of 90, 69, 38, 27, and 14 deg. The reported data are for the higher end of nucleate boiling and no attempt was made to obtain data near inception of nucleate boiling. In all cases, the dependence of wall heat flux on wall superheat is similar, i.e., $q \sim \Delta T^{3.3}$. However, as the surface wettability improves, the approach to maximum heat flux becomes gradual and a higher superheat is required to attain the same heat flux. The maximum heat flux nevertheless increases as the surface wettability improves. Although it is not the purpose of this work to develop a correlation, it is found that the constant C_s in Rohsenow's equation (1) varies almost linearly with contact angle. The values of C_s are given in Table 1. In Fig. 4, the data of Nishikawa et al. (1984) for saturated water at one atmosphere pressure boiling on a copper plate are also plotted. The contact angle of water with polished copper is 90 deg. It is seen that their data lie between the 69 and 90 deg data obtained in the present work. Their data also show the same dependence of heat flux on wall superheat as do the present data. It should also be mentioned that at high nucleate boiling heat fluxes, Nishikawa et al. observed little effect of the orientation of the heater surface.

Figure 5 shows the wall void fraction profiles at the midplane of the test surface for a contact angle of 90 deg and for heat fluxes of 25 and 57 W/cm^2. At both heat fluxes, the

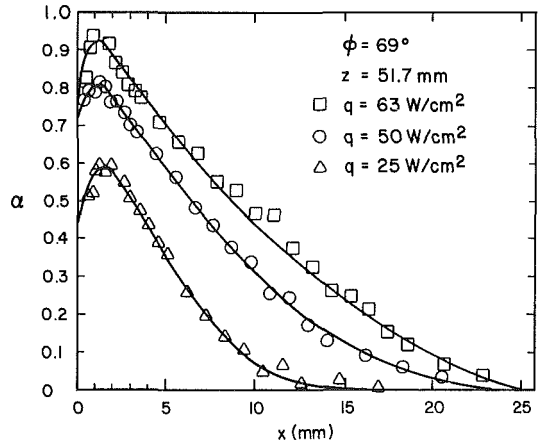

Fig. 6 Void profiles at midplane of the test surface for a contact angle of 69 deg

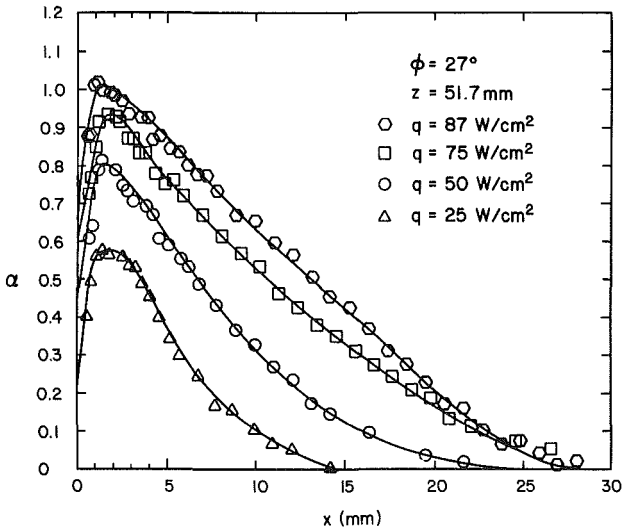

Fig. 7 Void profiles at midplane of the test surface for a contact angle of 27 deg

void fraction is nearly constant in the region immediately next to the wall. Thereafter it decreases nearly exponentially. The wall void fraction and thickness of the voided region increase with heat flux. Figures 6 and 7 show the midplane void profiles for contact angles of 69 and 27 deg. General features shown by these profiles are similar to those observed earlier for a contact angle of 90 deg. However, for contact angles less than 90 deg, the maximum void fraction occurs at about 1 to 1.5 mm away from the wall. For a given contact angle, the steepness of the profile appears to be independent of heat flux. However, the steepness increases with decrease in contact angle. This is a clear manifestation of the shape of the interface near the heater surface.

It is also noted that for contact angles less than 90 deg, the location of maximum void fraction shows little change as heat flux is increased. Another interesting observation that can be made from Figs. 5, 6, and 7 is that though in each case the highest heat flux is very close to the maximum heat flux for that contact angle, the maximum void fraction is never equal to unity except when the heat flux is 87 W/cm^2 for a contact angle of 27 deg. Since in the absence of a void fraction equal to unity, liquid is always available, the maximum heat flux must then be caused by some limitation occurring at the surface itself. In fact, a detailed theoretical investigation of the

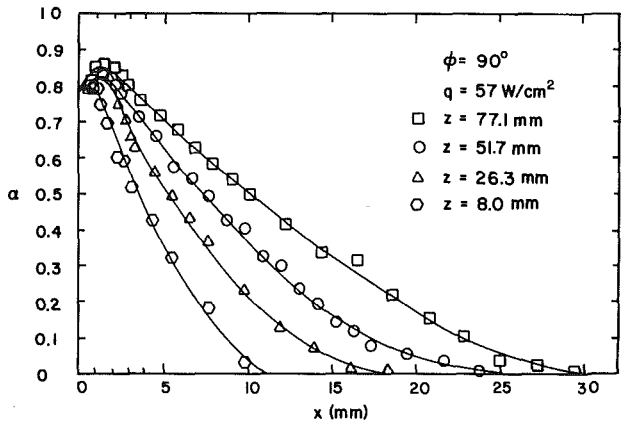

Fig. 8 Void profiles at several vertical locations for a contact angle of 90 deg

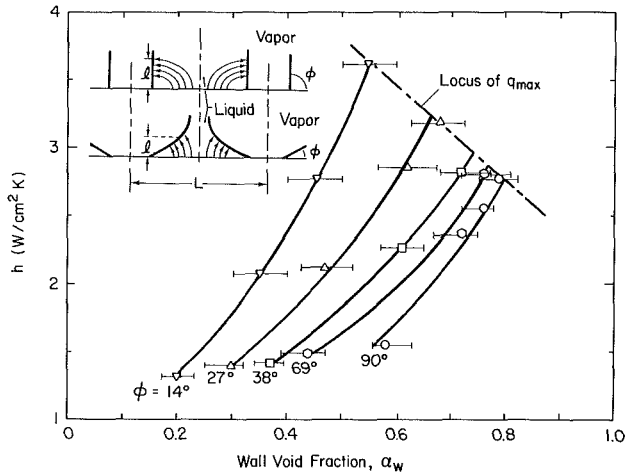

Fig. 10 Heat transfer coefficient as a function of wall void fraction for several contact angles

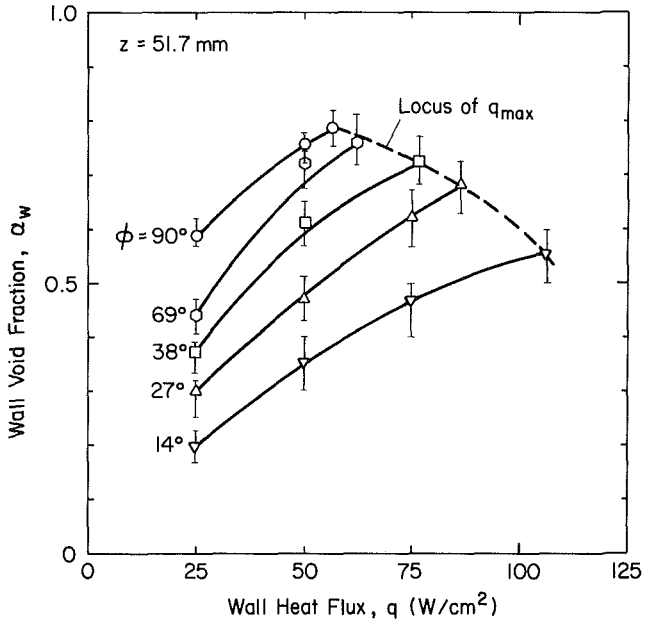

Fig. 9 Dependence of wall void fraction on wall heat flux

surface limited maximum heat flux is the topic of the companion paper. Occurrence of a void fraction of unity implies formation of a continuous vapor layer away from the surface. The continuous vapor layer inhibits the flow of liquid to the surface, hence leading to a critical heat flux condition. Thus it appears that a heat flux of 87 W/cm² for a contact angle of 27 deg represents a demarcation between surface-controlled maximum heat flux and that controlled by vapor flow dynamics away from the surface.

The void fractions as a function of distance from the bottom edge of the vertical plate are plotted in Fig. 8. The plotted data are for a contact angle of 90 deg and for a heat flux very near the maximum heat flux. The wall void fraction is observed to be independent of the vertical distance. This is consistent with the observed uniformity of the wall heat flux and the temperature along the plate. The maximum void fraction increases slightly with distance but there is a large increase in the extent of the voided region with distance. This is mainly because of addition of vapor along the direction of flow. It should be noted that in order to avoid clutter, the variability in the measured void fractions has not been shown in Figs. 5–8.

The wall void fractions obtained by extrapolating the profiles such as those shown in Figs. 5, 6, and 7 are plotted in Fig. 9 as a function of wall heat flux. For all of the contact angles, the wall void fractions increase with heat flux. Near the maximum heat flux condition, the wall void fraction for all the contact angles lies between 0.55 and 0.8. Since the plotted void fractions are averaged over time and width of the plate, they represent the dry fraction of the heater at a given instant.

Before proceeding further, it is pertinent to compare the void fractions measured in the present work with the data reported in the literature. Earlier attempts to measure void fractions during nucleate and/or transition boiling are those of Iida and Kobayasi (1969), Hasegawa et al. (1973), Ragheb and Cheng (1979), Nishikawa et al. (1984) and Dhuga and Winterton (1985). Both Iida and Kobayasi and Hasegawa et al. used a 0.04-mm-dia movable probe to measure the void fractions in the vicinity of a 2.9-cm-dia horizontal disk. Distilled water was used as the test liquid. Surprisingly, in both cases the maximum heat flux was only 25 W/cm². Because of lack of information on the contact angles in these studies, it is difficult to make a meaningful comparison of the measured void fractions. Nevertheless if a contact angle of 69 deg is assumed, in the present work the mean values of α_w and α_{max} at a heat flux of 25 W/cm² are found to be 0.44 and 0.6, respectively. In comparison, Iida and Kobayasi and Hasegawa et al. measured void fractions of 0.53 and 0.71, respectively, at 0.1 mm away from the wall. The maximum void fractions in the two studies were 0.94 and 0.85, respectively, and occurred at 0.5 to 1.0 mm away from the wall.

Ragheb and Cheng (1979) used a 1.02-mm zirconium wire embedded in a copper block to measure the fractional surface area occupied by liquid during subcooled forced flow transition boiling. In their work the void fraction measured at the maximum heat flux was only 0.15 to 0.2. Similar values of void fraction near the maximum heat flux on a horizontal plate have been reported by Dhuga and Winterton (1985). Nishikawa et al. (1984) used an electric probe to measure void fraction at 0.5 mm away from the heated plates oriented at different angles to the vertical. For their nucleate boiling data, which were plotted earlier in Fig. 4, a mean void fraction at a heat flux of 25 W/cm² is found to be 0.58. This value is very close to the value obtained in the present work at 0.5 mm from a surface with a contact angle of 69 deg.

In Fig. 10, the heat transfer coefficients are plotted as a function of wall void fraction for contact angles of 14, 27, 38, 69, and 90 deg. From the plotted data, it is seen that for a fixed void fraction, the heat transfer coefficient increases as the contact angle decreases or the surface becomes more wet-

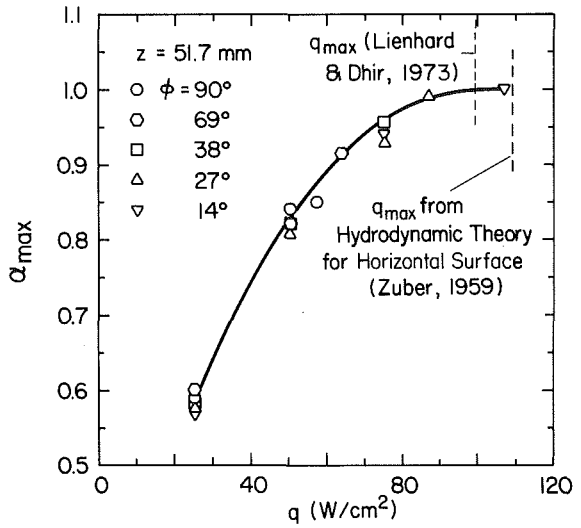

Fig. 11 Maximum void fraction as a function of heat flux for several contact angles

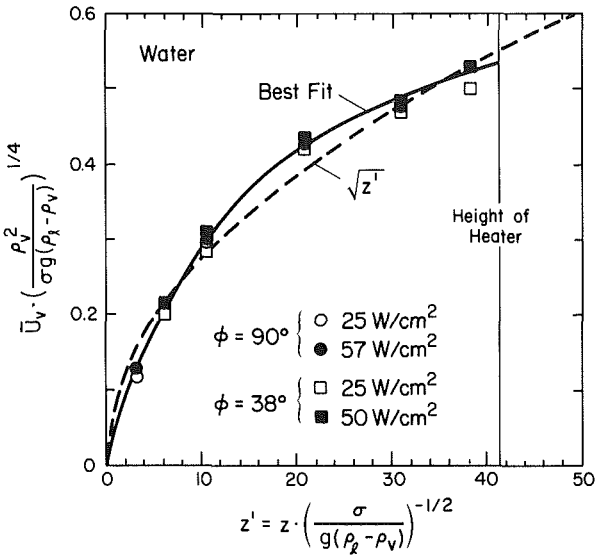

Fig. 12 Dependence of superficial vapor velocity on dimensionless distance from the leading edge

table. Since transport of energy occurs at the heater surface, one can infer that for a fixed wall void fraction an increase in heat transfer coefficient as the contact angle becomes small implies thinning of the liquid layer intervening between the vapor–liquid interface and the wall. This is shown qualitatively in the inset in Fig. 10. The inference drawn here also implies that it is the evaporation of the liquid layer (macro/micro) adjacent to the wall that controls the vapor volume flux leaving the heater.

The maximum void fraction for all of the contact angles is plotted in Fig. 11 as a function of wall heat flux. The maximum void fraction is seen to become unity as the observed heat fluxes approach those given by the hydrodynamic theory. Contrary to the wall void fraction, the maximum void fraction is found to be independent of the contact angle. The maximum void fraction depends only on the magnitude of the vapor volume flux leaving the heater or conceivably on the vapor flow behavior in the pool. The location of maximum void fraction thus represents the boundary beyond which flow dynamic effects dominate. This is elaborated further in the following paragraphs.

Vapor Flow Dynamics

An assessment of vapor flow behavior away from the heater surface is made from the observed superficial velocity of the vapor. The observed superficial velocity of vapor is compared with the terminal velocity of a single bubble, the vapor velocity in a continuous passage, and the critical velocity for Kelvin-Helmholtz instability of a vapor jet. If an effective vapor layer thickness is defined as

$$\bar{\delta} = \int_0^\infty \alpha \, dx \tag{3}$$

the vapor superficial velocity at a vertical location z can be written as

$$\bar{U}_v = \frac{qz}{\rho_v h_{fg} \bar{\delta}} \tag{4}$$

The terminal velocity of a bubble or slug of vapor can be written by balancing liquid inertia with the buoyancy force on a bubble as

$$U_t = C_1 \sqrt[4]{\frac{\sigma g(\rho_l - \rho_v)}{\rho_l^2}} \tag{5}$$

where the constant C_1 is generally assigned a value of 2.9 (see Lahey and Moody, 1977) for churn turbulent bubbly flow. On the other hand, for an inviscid vapor the velocity in a continuous passage surrounded by an inviscid liquid is obtained by balancing the hydrostatic head with the inertia of the vapor as

$$U_c = \sqrt[4]{\frac{\sigma g(\rho_l - \rho_v)}{\rho_v^2}} \sqrt{2z'} \tag{6}$$

where z' is defined as

$$z' = z \Big/ \sqrt{\frac{\sigma}{g(\rho_l - \rho_v)}} \tag{7}$$

and is measured from the location at which vapor starts to move in the vertical direction. The characteristic length used in equation (7) was also used to define the diameter of the bubble while obtaining equation (5). Since vapor is added to the pool uniformly along the plate, the average vapor velocity in the jets along the plate can be obtained by integrating equation (6) as

$$U_c = 0.94 \sqrt[4]{\frac{\sigma g(\rho_l - \rho_v)}{\rho_v^2}} \sqrt{z'} \tag{8}$$

z' is measured from the leading edge of the plate.

The critical velocity at which a vapor jet with axis parallel to the gravitational acceleration becomes Helmholtz unstable can be written (see Lamb, 1945) as

$$U_H = C_2 \sqrt[4]{\frac{\sigma g(\rho_l - \rho_v)}{\rho_v^2}} \tag{9}$$

where the constant C_2 is of the order of unity. In writing equation (9) the diameter of the jet is assumed to be proportional to the characteristic length used in equation (7).

The average superficial velocity calculated from equation (4) is plotted as a function of vertical distance in Fig. 12. The velocity has been nondimensionalized with the characteristic velocity in equations (8) or (9). The superficial velocity is found to increase as the square root of the distance from the leading edge and is independent of the magnitude of the heat flux and the contact angle. The independence of the super-

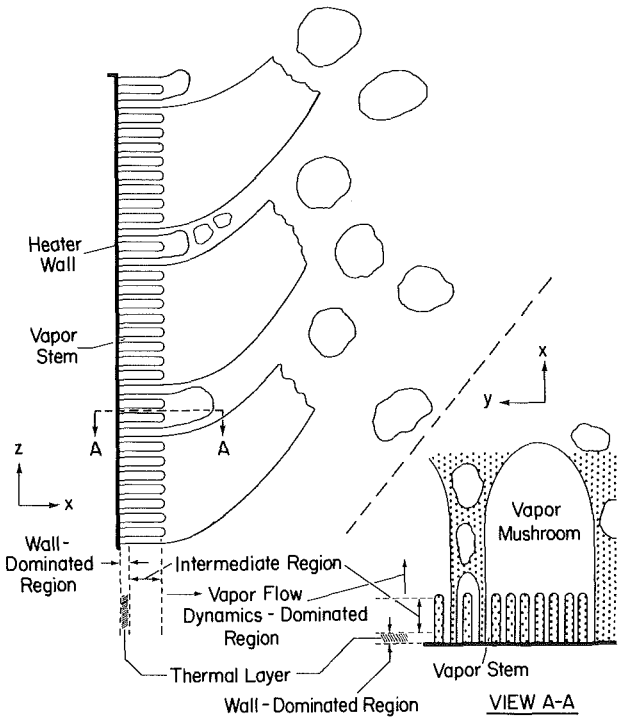

Fig. 13 Conceptualization of three regimes during pool boiling on a vertical surface for a contact angle of 90 deg

ficial vapor velocity from the contact angle is indicative of the fact that conditions on the wall do not influence the flow behavior away from the wall. The nondependence of vapor velocity on heat flux implies that once the vapor velocity reaches a certain allowable value, more vapor flow passages develop to accommodate a higher vapor volume flux. As a result, the flow area or $\bar{\delta}$ increases with heat flux. Although the observed superficial velocity shows the same dependence on distance from the leading edge as is given by equation (8), the observed velocity is about an order of magnitude smaller than that predicted from equation (8). This is not unexpected since all of the flow area is not occupied by vapor jets. The observed maximum velocity at the top of the vertical plate is about eight times higher than that given by equation (5) for the terminal velocity of a bubble. This suggests that a large fraction of vapor definitely moves through continuous vapor passages. The most probable location of these passages is the region close to the wall. Although, according to equation (8), vapor velocity in the jets could continue to increase indefinitely with distance, the upper limit on the average superficial velocity will be set by equation (9).

It should be stressed here that the above evaluation does not represent a model of the vapor flow dynamics but an assessment of the prevailing vapor flow configurations.

From the results presented above, the boiling phenomenon on a heater surface can be subdivided into three regions. The region strongly influenced by the wall characteristics extends up to the outer edge of the thermal layer, which as shown in the companion paper has a thickness of the order of 10^{-5} m. The vapor flow dynamics dominates the region beyond the location at which maximum void fraction occurs. The maximum void fraction occurs at about 10^{-3} m away from the wall. The intermediate region between the outer edge of the thermal layer and the location at which α_{max} occurs is influenced by both the wall and the vapor flow dynamics away from the wall. Figure 13 shows the conceptualization of the process.

For partially wetted surfaces, $\phi > 27$ deg, the maximum heat flux condition occurs as a result of the limitation on the energy that can be removed from the liquid-occupied region of the heater. For these surfaces, the void fraction in the vicinity of the surface is always less than unity. Hence liquid has an easy access to the surface. The maximum as well as the nucleate boiling heat fluxes are only weakly affected by the flow conditions away from the wall as long as vapor can find its way out of the wall region unhindered.

For relatively well-wetted surfaces, $\phi < 20$ deg, the vapor flow dynamics away from the surface may control the maximum heat flux. In the present study, the data point for $\phi = 27$ deg appears to approach that limiting condition, whereas the surface with $\phi = 14$ deg appears to meet that condition. From these data points, it is found that at maximum heat flux on well-wetted surfaces the void fraction away from the wall reaches a value of unity. At a void fraction equal to unity, an obstruction to the flow of liquid to the interior regions of the vertical wall can develop. This condition appears to be analogous to what has been assumed in the past with respect to hydrodynamically controlled boiling crisis in pool boiling. In the hydrodynamic theory originally proposed by Zuber (1959), it was assumed that the maximum heat flux occurs when vapor escape velocity and vapor flow area fraction reach their critical values. A critical value can be assigned to the average vapor layer thickness $\bar{\delta}$ when maximum void fraction reaches unity. The present observations, however, show that local vapor velocity attains its maximum value at relatively low heat fluxes and remains constant thereafter.

A void fraction of unity slightly away from the heater may be a preferable criterion for maximum heat fluxes on well-wetted surfaces. This criterion will eliminate separate specification of average vapor velocity and fractional vapor flow area. Such a criterion will also provide a natural link between pool and forced flow boiling since void fraction can be related to the drift velocity in both cases. To develop a totally analytical model for nucleate and transition boiling, attention needs to be paid to all of the three regions identified in this work and as shown in Fig. 13. The maximum heat flux and the corresponding wall superheat will be a natural outcome of such an analysis.

Summary and Conclusions

1 The effect of surface wettability on nucleate boiling and maximum heat fluxes has been quantified.

2 Void fractions adjacent to a heated vertical wall have been measured for several heat fluxes and contact angles.

3 At a given heat flux, the wall void fraction is found to be sensitive to contact angle. For the contact angles studied in this work, the data suggest wall void fractions of 55–80 percent at the onset of maximum heat flux condition.

4 For contact angles less than 90 deg, the maximum void fraction occurs at about 1–1.5 mm away from the wall and is found to be independent of contact angle.

5 The void fraction everywhere in the vicinity of the surface is found to be less than unity at maximum heat flux for all of the surfaces except the surfaces with $\phi = 27$ and 14 deg. This confirms that for partially wetted surfaces the maximum heat flux condition is controlled by surface effects.

6 Based on the observations, the boiling phenomenon on a heater is subdivided into three regions: the wall-dominated region, the vapor flow dynamics dominated region, and the intermediate region.

Acknowledgments

This work received support from the NSF under Grant No. CBT-84-17684.

References

Bui, T. D., and Dhir, V. K., 1985, "Transition Boiling Heat Transfer on a Vertical Surface," ASME JOURNAL OF HEAT TRANSFER, Vol. 107, pp. 756–763.

Dhuga, D. S., and Winterton, R. H. S., 1985, "Measurement of Surface Contact Transition Boiling," *Int. J. Heat Mass Transfer*, Vol. 28, pp. 1869–1880.

Dwyer, O. E., 1974, *Boiling Liquid Metal Heat Transfer*, American Nuclear Society, Hinsdale, IL.

Fath, H. S., and Judd, R. L., 1978, "Influence of System Pressure on Microlayer Evaporation Heat Transfer," ASME JOURNAL OF HEAT TRANSFER, Vol. 100, pp. 49–55.

Hasegawa, S., Echigo, R., and Takegawa, T., 1973, "Maximum Heat Fluxes for Pool Boiling on Partly Ill-Wettable Heating Surfaces," *Bulletin of JSME*, Vol. 16, No. 97, pp. 1076–1084.

Hsu, Y. Y., and Graham, R. W., 1976, *Transport Processes in Boiling and Two-Phase Systems*, McGraw-Hill, New York.

Iida, Y., and Kobayasi, K., 1969, "Distribution of Void Fraction Above a Horizontal Heating Surface in Pool Boiling," *Bulletin of JSME*, Vol. 12, No. 50, pp. 283–290.

Lahey, R. T., and Moody, F. J., 1977, *The Thermal Hydraulics of a Boiling Water Nuclear Reactor*, American Nuclear Society, Hinsdale, Illinois.

Lamb, H., 1945, *Hydrodynamics*, 6th ed., Dover Publications Inc., New York.

Liaw, S. P., and Dhir, V. K., 1986, "Effect of Surface Wettability on Transition Boiling Heat Transfer From a Vertical Surface," *Proc. Eighth Int. Heat Transfer Conference*, Vol. 4, pp. 2031–2036.

Moore, F. D., and Mesler, R. B., 1961, "The Measurement of Rapid Surface Temperature Fluctuations During Nucleate Boiling of Water," *AIChE J.*, Vol. 7, No. 4, pp. 620–624.

Nishikawa, K., Fujita, Y., Uchida, S., and Ohta, H., 1984, "Effect of Surface Configuration on Nucleate Boiling Heat Transfer," *Int. J. Heat Mass Transfer*, Vol. 27, pp. 1559–1571.

Ragheb, H. S., and Cheng, S.C., 1979, "Surface Wetted Area During Transition Boiling in Forced Convective Flow," ASME JOURNAL OF HEAT TRANSFER, Vol. 101, pp. 381–383.

Rohsenow, W. M., 1952, "A Method of Correlating Heat Transfer Data for Surface Boiling of Liquids," *Trans. ASME*, Vol. 74, pp. 969–976.

Tong, L. S., 1978, "Heat Transfer in Reactor Safety," *Proc. Sixth Int'l. Heat Transfer Conf.*, Vol. 6, pp. 285–309.

Zuber, N., 1959, "Hydrodynamic Aspects of Boiling Heat Transfer," Ph.D. dissertation, University of California, Los Angeles; also published as U.S. Atomic Energy Commission Report No. AECU-4439.

Framework for a Unified Model for Nucleate and Transition Pool Boiling

V. K. Dhir
Mem. ASME

S. P. Liaw
Student Mem. ASME

Mechanical, Aerospace and Nuclear Engineering Department, University of California, Los Angeles, Los Angeles, CA. 90024-1597

An area and time-averaged model for saturated pool boiling heat fluxes has been developed. In the model, which is valid in the upper end of nucleate boiling and in transition boiling, the existence of stationary vapor stems at the wall is assumed. The energy from the wall is conducted into the liquid macro/micro thermal layer surrounding the stems and is utilized in evaporation at the stationary liquid-vapor interface. The heat transfer rate into the thermal layer and the temperature distribution in it are determined by solving a two-dimensional steady-state conduction equation. The evaporation rate is given by the kinetic theory. The heater surface area over which the vapor stems exist is taken to be dry. Employing experimentally observed void fractions, not only the nucleate and transition boiling heat fluxes but also the maximum and minimum heat fluxes are predicted from the model. The maximum heat fluxes obtained from the model are valid only for surfaces that are not well wetted and includes the contact angle as one of the parameters.

Introduction

Numerous studies of pool and forced flow boiling have appeared in the literature in the past. Those studies no doubt provide us information about many intricate features of this complex process, but they also point to the limited understanding we have of the process. For example, at present nucleate, transition, and maximum heat fluxes are treated as disjoint processes and we know little about their interdependence. Similarly, no logical treatment unifying pool and forced flow boiling exists. The purpose of the present work is to provide a framework with which interlinking features of nucleate and transition boiling can be assessed.

In the nucleate boiling, several mechanisms such as transient conduction into liquid, evaporation, and natural convection have been identified to contribute to the overall heat transfer rate. At a given wall superheat, the relative contribution of these mechanisms is influenced by surface characteristics (i.e., surface finish, surface wettability, surface cleanliness, etc.) and the vapor flow dynamics away from the wall. Because of the involvement of many variables and their interactions, as yet no successful mechanistic model for nucleate boiling heat transfer has been reported in the literature. However, the correlation developed by Rohsenow (1952) is used very often to predict the nucleate pool boiling data. This correlation is of the form

$$q=\mu_l h_{fg}\sqrt{\frac{g(\rho_l-\rho_v)}{\sigma}}\left[\frac{c_{pl}\Delta T}{C_s h_{fg}}\right]^m (\mathrm{Pr}_l)^{-n} \qquad (1)$$

In the correlation, the constants C_s, m, and n are determined empirically. The constant C_s accounts for the variations in the surface properties.

The most successful models for the upper limit of the nucleate boiling heat fluxes on horizontal (infinite) plates are those by Kutateladze (1948) and Zuber (1959). Both models are based on the dynamics of vapor outflow. Zuber employed stability of vapor jets to determine the maximum possible vapor velocity. Kutateladze on the other hand developed dimensionless groups from the equations governing the flow of vapor and liquid. The analyses of Zuber and Kutateladze yielded an identical expression for the maximum heat flux on flat plates as

$$q_{\max F}=C_1\rho_v h_{fg}[\sigma g(\rho_l-\rho_v)/\rho_v^2]^{1/4} \qquad (2)$$

Zuber obtained a value of $\pi/24$ for the constant C_1 whereas Kutateladze correlated the data and found the constant C_1 to have a value of 0.16. Equation (2) with a modification in the constant C_1 has been used to predict maximum heat fluxes on heaters of different geometry, size, and orientation. A summary of the methodology developed to evaluate constant C_1 has been given by Lienhard and Dhir (1973).

Equation (2) has a purely hydrodynamic basis as processes away from the heater surface are believed to control the maximum heat flux. However, according to equation (1), nucleate boiling heat fluxes strongly depend on the surface properties. As a result, at the maximum heat flux the wall superheat obtained by equating equations (1) and (2) can vary over a wide range. Ambiguity with respect to $\Delta T_{\max}$ makes the prediction of transition boiling heat flux extremely uncertain. For this reason, transition boiling correlations such as those developed by Kalinin et al. (1976) and Bjornard and Griffith (1977) become very specific to the data on which they are based.

Recently, it has been shown by Bui and Dhir (1985a) and the present authors (1986) that equation (2) fails to predict maximum heat fluxes for water boiling on surfaces that are not well wetted. Thus development of a consistent model for transition boiling strongly hinges on our ability simultaneously to model the processes taking place at and near the wall and away from the wall. Such an approach having a total analytical basis can be very potent, but extremely involved.

The present work represents a first step in that direction. In this paper, the thermal processes occurring at and near the surface are modeled. The modeling effort relies on the experimental observations of void fractions as reported in the companion paper (Liaw and Dhir, 1989). Although the dynamic behavior of vapor flow is not included in the analysis, its implications are discussed. Also, in this study no effort is made to predict nucleate boiling heat fluxes at low wall superheats when convective effects can be important.

Analysis

The present model, which is applicable only to ordinary

Contributed by the Heat Transfer Division and presented at the ASME Winter Annual Meeting, Boston, Massachusetts, December 13-18, 1987. Manuscript received by the Heat Transfer Division September 24, 1987. Keywords: Boiling, Multiphase Flows.

liquids at high heat fluxes for which nucleate boiling is fully established on the heater surface, is based on the visual observations made in the present work and those made by Gaertner (1965) about two decades ago. From photographic records of the process, Gaertner noted the existence of large bubbles attached to the surface via numerous vapor stems and described these bubbles as vapor mushrooms. The vapor stems were planted in the thermal layer and were nourished by evaporation at the vapor–liquid interface of the stems. The diameter and length of vapor stems were also measured by Gaertner (1965). The vapor stems occupy the nucleation sites. The number of active sites as a function of wall heat flux was measured by Gaertner and Westwater (1960). The number density of active sites was found to increase with wall heat flux. In a subsequent paper, Gaertner (1963) related the average nearest neighbor distance between active sites with the average population density of the cavities.

Figure 13 of the companion paper shows conceptualization of the boiling process on a vertical surface submerged in a pool of saturated liquid. The interface shape near the wall is shown for a contact angle of 90 deg. The boiling phenomenon near the wall is divided into three regions. The thermal layer occupies the region immediately next to the wall. Energy from the heater wall is transferred to this layer by conduction and is in turn utilized for evaporation at the vapor–liquid interface of the vapor stems. The intermediate region spans from the outer edge of the thermal layer to the location at which vapor stems merge into large vapor mass. For contact angles less than 90 deg, it is the location at which void fraction is maximum. The surface and vapor flow dynamics influence the intermediate region and this region is the most difficult to analyze. The third region extends away from the stem merger location and into the liquid pool. In this region, vapor moves in nearly continuous passages and vapor dynamics controls the void profile.

As stated earlier, in this work attention is focused only on the region adjacent to the wall. Main resistance to the transport of heat from the wall comes from the thermal layer. At high heat fluxes, the thermal layer is very thin ($\sim 10^{-5}$ m) in comparison to the stem diameter and length, and as a result the effect of gravity and flow field away from the wall on the thermal layer can be ignored. The gravity can influence the stem diameter; however, its effect on the heat transfer process should be small as long as vapor can escape away from the wall. This suggests that except for an infinite downward-facing horizontal plate, the model should be applicable to various orientations of the surface with respect to gravitational acceleration. The upper limit on the heat flux in nucleate boiling, however, will be set either by the vapor escape rate or by the vapor generation rate. If the limit is set by the vapor escape rate, the maximum heat flux may depend on the orientation of the surface with respect to gravitational acceleration. Similarly, gravity can influence the heat removal at low nucleate boiling heat fluxes by affecting the agitation created by bubbles leaving sparsely populated nucleation sites.

In the model, the vapor stems are assumed to be located on a square grid. The vapor stems adhere to the wall and provide a stationary interface at all times. The pressure inside the stems is assumed to be very close to the system pressure. The temperature on the heater surface is assumed to be uniform such that the variation of temperature underneath the stem and on the liquid-occupied region is neglected. As will be discussed later, this is a realistic assumption when a high-thermal-conductivity solid such as copper is used and no heat is generated in the solid itself. The upper portion of Fig. 1 shows the plan view of a typical cell supporting one stem. The spacing L between stems is the average spacing between nucleation sites. Prior to merger, the stem diameter D_w and spacing L are related to the wall void fraction as

$$\alpha_w = \frac{\pi}{4}\frac{D_w^2}{L^2} \tag{3}$$

The dependence on D_w/L of the dimensionless circumference P_s/L of the stems in contact with the liquid and of the wall void fraction α_w is shown in Fig. 1. It is seen that a wall void fraction of $\pi/4$ corresponds to merger of the stems at the wall. After merger, the stem circumference in contact with liquid decreases very rapidly with increase in stem diameter.

Assuming that a two-dimensional analysis is sufficient for the level of accuracy desired here, the average heat transfer coefficient over the liquid-occupied region is expressed as

$$\bar{\bar{h}}_l = \frac{8}{L^2(1-\alpha_w)}\int_0^{\pi/4}\int_{D_w/2}^{(L\sec\psi)/2} h_l(r,\psi)\cdot r\, dr\, d\psi \tag{4}$$

Nomenclature

a_1 = evaporation coefficient
b = width of thermal layer
$C(r)$ = local Nusselt number
$\bar{C}$ = dimensionless heat transfer coefficient defined in equation (17)
C_1 = constant
C_k = evaporation heat transfer coefficient
C_s = constant characterizing a surface
c_{pl} = specific heat of liquid
D = vapor stem diameter
D_w = vapor stem diameter at wall
g = gravitational acceleration
h = average heat transfer coefficient over the heater surface
h_{fg} = latent heat of vaporization
$\bar{\bar{h}}_l$, $\bar{\bar{h}}_v$ = average heat transfer coefficients over liquid-occupied and vapor-occupied regions
k_l = thermal conductivity of liquid
k_v = thermal conductivity of vapor
L = vapor stem spacing
M = molecular weight
m = constant
m_1 = constant
N = active site density
n = constant
n_1 = coordinate normal to the interface
$\bar{n}_1$ = dimensionless coordinate normal to the interface
Pr_l = Prandtl number of liquid
P_s = stem circumference
q = average heat flux over the heater
$q_{\max F}$ = maximum heat flux on a flat plate
R = universal gas constant
T = temperature
T_{sat} = saturation temperature
T_w = wall temperature
x, r = coordinates along and normal to the surface
$\bar{x}, \bar{r}$ = dimensionless coordinates along and normal to the surface
α = void fraction
α_w = wall void fraction
β = parameter defined in equation (12)
ΔT = wall superheat
$\Delta T_{\max}$ = wall superheat at maximum heat flux
θ = dimensionless temperature
λ = eigenvalue
μ_l, μ_v = viscosity of liquid and vapor, respectively
ρ_l, ρ_v = density of liquid and vapor, respectively
σ = surface tension
ϕ = contact angle
ψ = angular coordinate

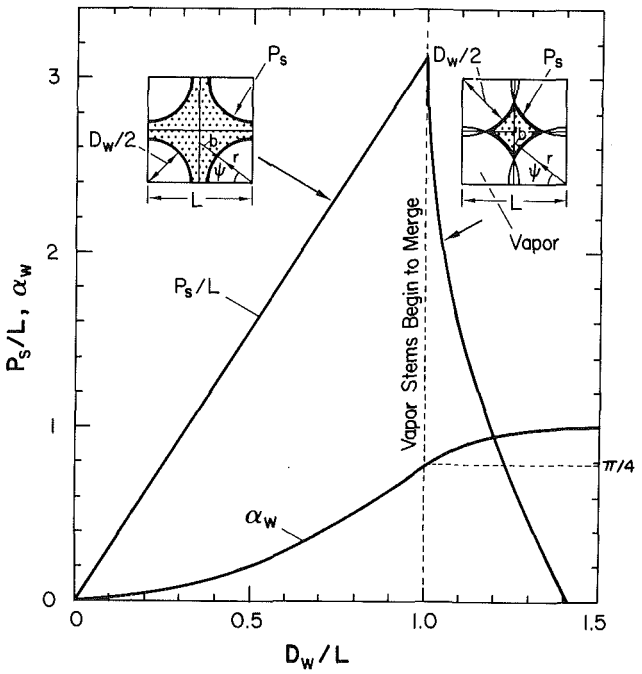

Fig. 1 Dependence of stem periphery and void fraction on stem diameter

The heat transfer coefficient $h_l(r, \psi)$ for a given value of ψ is obtained by solving the two-dimensional conduction equation for the liquid-occupied region.

Thermal Model for a Contact Angle of 90 deg

Figure 2(*a*) shows a sketch of the two-dimensional slab representing the thermal layer adjacent to the heater wall. The two-dimensional steady-state conduction equation for the slab is written in dimensionless form as

$$\theta_{\bar{x}\bar{x}} + \theta_{\bar{r}\bar{r}} = 0 \tag{5}$$

The four boundary conditions are

$$\theta(0, \bar{r}) = 1 \tag{6}$$

$$\theta(\infty, \bar{r}) = 0 \tag{7}$$

$$\theta_{\bar{r}}\left(\bar{x}, \frac{L}{2b}\sec\psi\right) = 0 \tag{8}$$

$$\theta_{\bar{r}}\left(\bar{x}, \frac{D_w}{2b}\right) = \frac{C_k b}{k_l}\,\theta\left(\bar{x}, \frac{D_w}{2b}\right) \tag{9}$$

In the above equations, the dimensionless parameters have been defined as

$$\theta = \frac{T - T_{\text{sat}}}{T_w - T_{\text{sat}}}$$

$$\bar{x} = x/b$$

$$\bar{r} = r/b$$

and the width b is defined as

$$b = \frac{1}{2}\,(L\sec\psi - D_w)$$

The last boundary condition, equation (9), represents an equality of the conductive heat flux at the interface to the evaporative heat flux. The evaporative heat flux is calculated by using the expression obtained from kinetic theory such that parameter C_k is written as

$$C_k = a_1 \rho_v h_{fg}^2 \left[\frac{M}{2\pi R\, T_{\text{sat}}^3}\right]^{1/2} \tag{10}$$

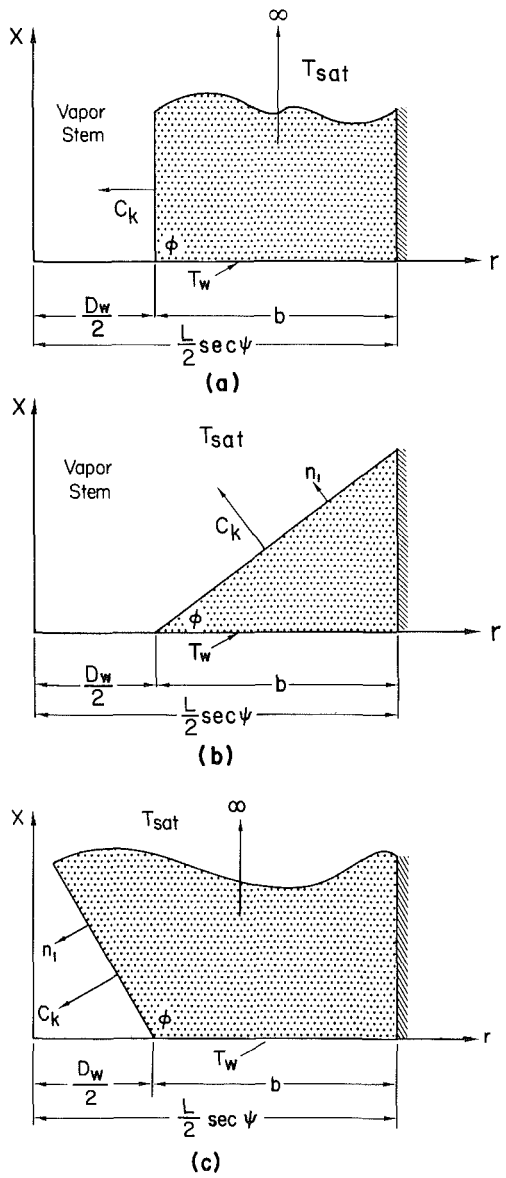

Fig. 2 Liquid layer configuration for different contact angles: (*a*) contact angle equal to 90 deg; (*b*) contact angle less than 90 deg; (*c*) contact angle greater than 90 deg

In the above equation, a_1 is the evaporation coefficient. Its values varying from 0.04 to 1 have been reported in the literature (Hsu and Graham, 1976). In this work, a value of unity has been assumed for a_1.

The resulting temperature distribution in the thermal layer is obtained by using the method of separation of variables as

$$\theta = 2\sum_{n=1}^{\infty}\left[\frac{\sin\lambda_n b}{\lambda_n b + \sin\lambda_n b\,\cos\lambda_n b}\right] e^{-\lambda_n x}\cos\lambda_n\left(\frac{L}{2}\sec\psi - r\right) \tag{11}$$

where the eigenvalues are the roots of the equation

$$\lambda_n b\,\tan\lambda_n b = \frac{C_k b}{k_l} \equiv \beta \tag{12}$$

The local heat transfer coefficient is obtained from the temperature profile given by equation (11) as

$$h_l(r, \psi) = \frac{q}{(T_w - T_{\text{sat}})} = \frac{-k_l \left.\dfrac{\partial T}{\partial x}\right|_{x=0}}{(T_w - T_{\text{sat}})} = \frac{C(r)k_l}{b} \tag{13}$$

where

$$C(r)=\sum_{n=1}^{\infty}\frac{2\lambda_n b\,\sin\lambda_n b\cdot\cos\lambda_n\left(\frac{L}{2}\sec\psi-r\right)}{\lambda_n b+\sin\lambda_n b\,\cos\lambda_n b} \tag{14}$$

Substitution of h_l from equation (13) into equation (4) yields $\bar{\bar{h}}_l$.

The average heat transfer coefficient over the width b of the liquid layer can be written as

$$\bar{h}_l(\psi)=\frac{-\int_{D_w/2}^{(L\sec\psi)/2}k_l\left.\frac{\partial T}{\partial x}\right|_{x=0}dr}{b(T_w-T_{\text{sat}})} \tag{15}$$

Using the temperature profile given by equation (11), the above equation yields

$$\bar{h}_l(\psi)=\frac{\bar{C}k_l}{b} \tag{16}$$

where

$$\bar{C}=\sum_{n=1}^{\infty}\frac{2\sin^2\lambda_n b}{\lambda_n b+\sin\lambda_n b\,\cos\lambda_n b} \tag{17}$$

Thermal Model for Contact Angles Different From 90 deg

A sketch of the wedge-shaped liquid layer that would exit adjacent to the heater wall for a contact angle less than 90 deg is shown in Fig. 2(*b*), whereas Fig. 2(*c*) shows the liquid layer shape for a contact angle greater than 90 deg. For these cases, the governing two-dimensional steady-state conduction equation is the same as that for a contact angle equal to 90 deg. However, the boundary conditions are replaced by

For $\phi<90$ deg

$$\theta(0,\bar{r})=1 \tag{18}$$

$$\theta_{\bar{r}}\left(\bar{x},\frac{L}{2b}\sec\psi\right)=0 \tag{19}$$

$$\theta_{\bar{n}_1}(\bar{x},\bar{r})=-\beta\theta(\bar{x},\bar{r})\ \text{ at }\ \bar{r}-\bar{x}\cot\phi=\frac{D_w}{2b} \tag{20}$$

For $\phi>90$ deg

$$\theta(0,\bar{r})=1 \tag{21}$$

$$\theta(\infty,\bar{r})=0 \tag{22}$$

$$\theta_{\bar{r}}\left(\bar{x},\frac{L}{2b}\sec\psi\right)=0 \tag{23}$$

$$\theta_{\bar{n}_1}(\bar{x},\bar{r})=-\beta\theta(\bar{x},\bar{r})\ \text{ at }\ \bar{r}-\bar{x}\cot\phi=\frac{D_w}{2b} \tag{24}$$

The temperature distribution in the thermal layers for contact angles different from 90 deg is obtained numerically by using the S.O.R. method. Figure 3 shows for several contact angles the variation of $C(\bar{r})$ with $\bar{r}$ for $\beta=100$ and 1000. It is seen that for a given r, the value of $C(\bar{r})$ increases as the contact angle becomes small or the interface becomes closer to the wall. This is indicative of the fact that the heat transfer process improves as the surface becomes more wettable. Local wall Nusselt number or $C(\bar{r})$ decreases with distance from the location where the vapor stem attaches to the wall. Figure 4 shows the calculated values of $\bar{C}$ as a function of β for several contact angles. It is seen that the value of $\bar{C}$ that is proportional to the heat transfer coefficient averaged over width b increases as β or the width of the thermal layer is increased.

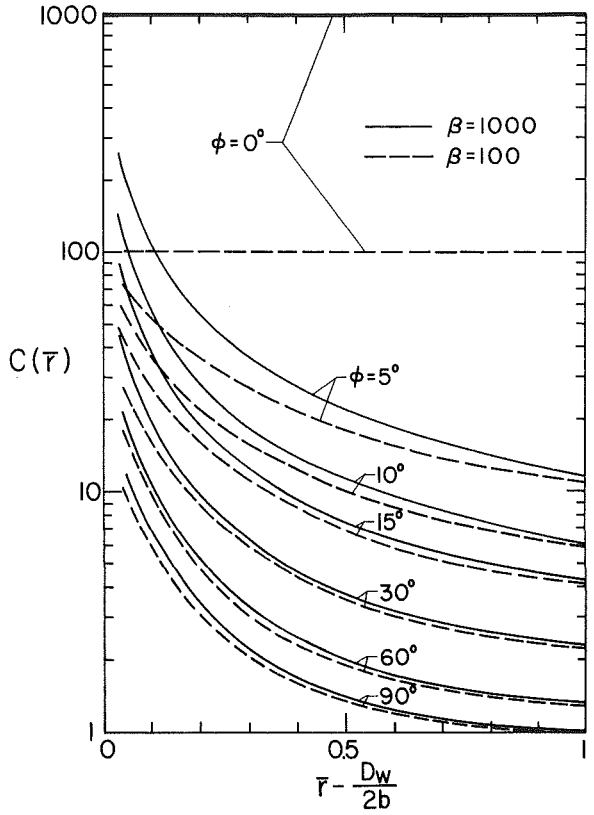

Fig. 3 Dependence of the parameter C on dimensionless distance from the location where stems attach to the surface

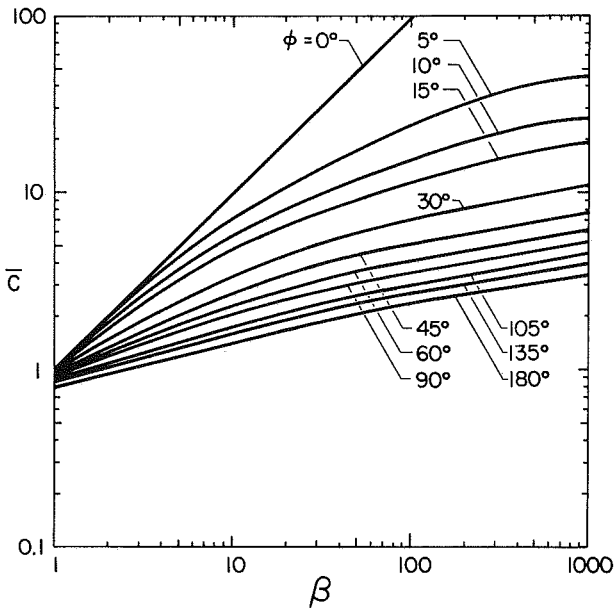

Fig. 4 Dependence of the parameter $\bar{C}$ on β for contact angles between 0 and 180 deg

Results and Discussion

Heat removal at both the wet and dry areas contributes to the overall heat transfer from the surface. Although the temperatures over the dry and wet areas may differ slightly, it is not unrealistic to assume that the temperature is uniform over the heater surface. Using this assumption combined with the fact that the heat flux is time and area-averaged, the wall heat flux can be written as

$$q=h\Delta T=\bar{\bar{h}}_l(1-\alpha_w)\Delta T+\bar{\bar{h}}_v\,\alpha_w\,\Delta T \tag{25}$$

In the above equation, $\bar{\bar{h}}_l$ can be obtained from the model and results presented in the analysis section. However, for a particular fluid, $\bar{\bar{h}}_l$ can only be determined if the width of the liquid layer is known. The evaluation of the width b requires a knowledge of the wall void fraction and the spacing or the diameter of the vapor stems. The heat transfer coefficient $\bar{\bar{h}}_v$ over the dry region is much smaller than $\bar{\bar{h}}_l$ and can be neglected as long as the wall void fraction is not close to unity. As the wall void fraction approaches unity, the wall heat flux or vapor volume flux drops very rapidly. This in turn eliminates the long continuous vapor escape paths shown in Fig. 1 of the companion paper. For this situation, the vapor stem height can be assumed to be of the same order as the vapor film thickness in film boiling. In the present work, the heat transfer coefficient on the dry region is evaluated from the study of Bui and Dhir (1985b) for film boiling on a vertical surface. The approximate form of $\bar{\bar{h}}_v$ from their work is

$$\bar{\bar{h}}_v \simeq 0.37\left[\frac{k_v^3\rho_v(\rho_l-\rho_v)g\ h_{fg}}{\mu_v\Delta T\sqrt{\sigma/g(\rho_l-\rho_v)}}\right]^{1/4} \tag{26}$$

As stated above, the determination from equation (25) of the wall heat flux as a function of wall superheat requires an explicit knowledge of the stem spacing and the stem diameter. Alternatively we may use the wall void fraction and have the option of using either the stem spacing or the stem diameter. The stem spacing depends on the wall superheat, the surface finish, and the contact angle. In the present work no attempt was made to measure the cavity size distribution and as such it is difficult to determine the stem spacing explicitly. The stem diameter is influenced by the contact angle and probably by the vapor flow dynamics near the wall as well. As such it can only be determined if the intermediate region is analyzed. Such an evaluation, however, is beyond the scope of the present work.

To demonstrate the application of the present model, the time and area-averaged void fraction data reported in the companion paper (Liaw and Dhir, 1989) are used. Figure 5 shows the extrapolated values of the wall void fractions for contact angles of 90, 38, and 14 deg. The void fractions were measured only in the nucleate boiling region and represent a significant extrapolation in the transition boiling region.

For a square grid, the stem spacing, L is related to the nucleation site density and the wall heat flux as

$$L \sim N^{-0.5} \sim q^{-0.5m_1} \tag{27}$$

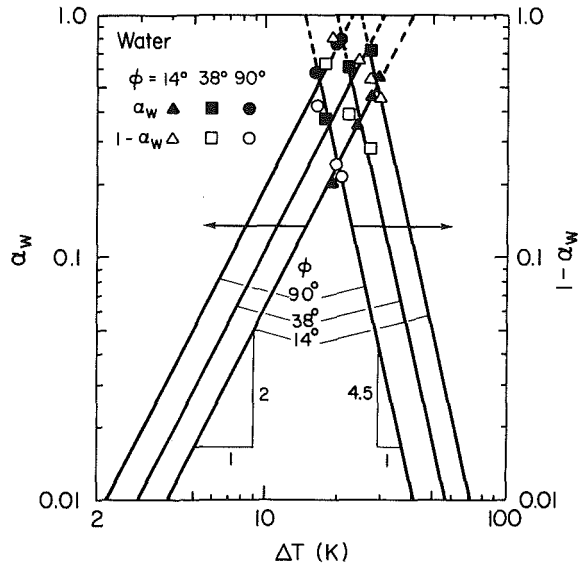

Fig. 5 Void fraction data for contact angles of 14, 38, and 90 deg

Hsu and Graham (1976) have presented a summary of results regarding the dependence of site density on wall heat flux. The observations of various investigators show that m_1 varies from 1.5 to 2 for water boiling on a copper surface. In the present work, a value of 1.5 was used for m_1.

The proportionality constant in equation (27) is determined by matching the model predictions of heat flux with data at one wall superheat in nucleate boiling. As seen earlier in Fig. 1, the vapor stems begin to merge at the wall when $\alpha_w = \pi/4$. For contact angles between 27 and 90 deg, the wall void fraction at maximum heat flux was found to vary between 0.68 and 0.8 (Liaw and Dhir, 1989). This implies that the maximum heat flux condition approximately coincided with the merger of vapor stems. It does not seem physically realistic that vapor stem spacing will change after merger of the stems. Hence, stem spacing L is assumed to remain constant after the stems merge. Here it should also be pointed out that for contact angles different from 90 deg, the shape of the vapor stems changes with distance from the wall. Thus for contact angles other than 90 deg, a correction to values of $\bar{C}$ obtained from Fig. 4 needs to be made to account for the deviation of the shape (see Fig. 10 of the companion paper) from that used in the analysis. Maximum deviation occurs in the central portion of a unit cell. The overall deviation is a function of the contact angle. The correction becomes large as the contact angle becomes small or the wall void fraction exceeds $\pi/4$. For example, for a contact angle of 14 deg, the average value of $\bar{\bar{h}}_l$ near the maximum heat flux had to be reduced by 16 percent. The corresponding value for a contact angle of 38 deg was 10 percent. This suggests that for surfaces with small contact angles (well wetted surfaces), not only the wall void fractions but also the variation of the void fraction in the vicinity of the wall is needed for precise evaluation of the heat transfer coefficient as a function of wall superheat.

A comparison of the model predictions with the data for contact angles of 90 and 38 deg is made in Figs. 6 and 7, respectively. The transition boiling data used in these figures are given by Liaw (1988). In Fig. 6, the heat fluxes over the wet region and the dry region are also plotted. In both cases, the model predictions appear to be in good agreement with the

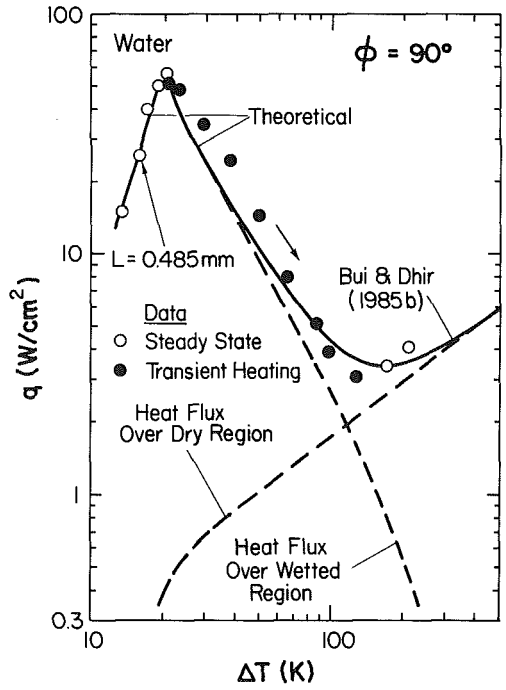

Fig. 6 Comparison of predicted and observed boiling curves for a contact angle of 90 deg

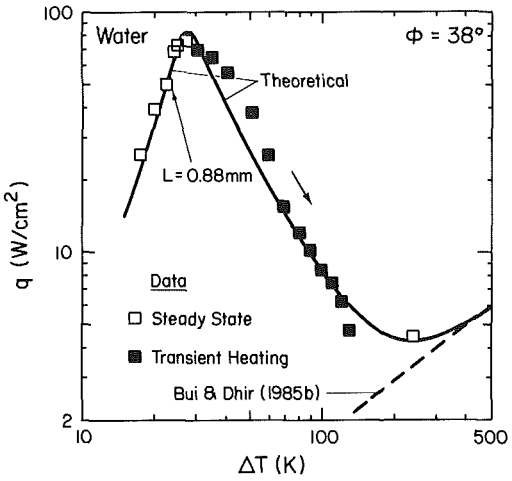

Fig. 7 Comparison of predicted and observed boiling curves for a contact angle of 38 deg

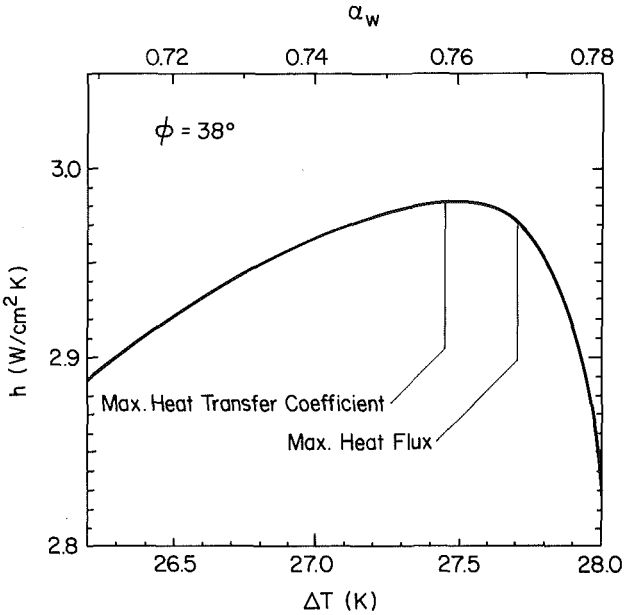

Fig. 8 Predicted dependence of heat transfer coefficient in nucleate boiling for a contact angle of 38 deg

heat flux data in nucleate, transition, and the lower end of film boiling. The maximum heat flux, which is a natural outcome of the model, also agree well with the data. In contrast to the hydrodynamic theory, the maximum heat flux predicted from the present model depends on the wall superheat. For a particular contact angle, the maximum heat flux occurs at a wall superheat in nucleate boiling at which the ratio of the evaporating interface area per unit area of the heater is nearly maximum. The minimum heat flux condition, on the other hand, is dictated by the rate at which the relative magnitudes of the heat fluxes in the wet and dry regions change with wall superheat.

In the upper end of the transition boiling, the model generally tends to underpredict the data. Three sources leading to underprediction of the data are possible:

(*i*) The wall temperature under the vapor stems is higher than that under the liquid-occupied region. As a result the average temperature used in the model is different from the wall temperature that existed in the experiments.

(*ii*) The transition boiling data were obtained in the transient mode whereas the present model is a steady-state one.

(*iii*) Deviations on the heater surface exist with respect to the extrapolated values of the wall void fraction, the square grid model, and the liquid–vapor interface shape assumed in the model. These differences become important when the wetted area is very small, as is the case in transition boiling.

To assess the contribution of the first source, the steady-state two-dimensional conduction equation was solved for the solid and the liquid-occupied region. It was found that for copper, which was the material of the test block in the experiments, the wall superheat under a vapor stem was never higher by more than 2 percent than that under the liquid occupied region (Liaw, 1988). This provides a justification for the use of the same temperature for vapor stems and the liquid-occupied region and eliminates the first source of discrepancy.

In the transient heating experiments, the rate of change of the boiling surface temperature was always less than 10 K/s. For a thermal layer of thickness of the order of 10^{-5} m, the diffusion time constant is of the order of 10^{-3} s. During this period, the change in surface temperature is very small and as such, little error should have resulted from the use of the steady-state model. The degree to which the transient in the hydrodynamic process away from the wall affects the vapor stem diameter has not been evaluated.

The more probable source that could lead to the difference between the prediction and the data is the deviations that may exist on the surface with respect to the extrapolated values of the wall void fraction and to the square grid. It is found that in transition boiling a slight uncertainty in the liquid fraction can influence the predicted heat fluxes significantly. A small correction to the relationship between the void fraction and D_w/L as a result of statistical variations in the spacing between stems in the square grid model, or due to the existence of a triangular or a hexagonal grid on a portion of the surface, could be very meaningful in the upper end of the transition boiling. As pointed out earlier, uncertainty with respect to the assumed shape of the interface could have also contributed to the difference between the predicted and the observed transient boiling heat fluxes. However, in the present work, which mainly provides a framework for modeling of nucleate and transition boiling heat fluxes, no systematic corrections with respect to these sources of uncertainty have been made.

In Fig. 8, the predicted heat transfer coefficient is plotted as a function of wall superheat for a contact angle of 38 deg. The heat transfer coefficient is found to attain its maximum value prior to occurrence of maximum heat flux condition. This is in agreement with what has been reported in the literature and has been found from the data obtained in this study for contact angles less than 90 deg.

Figure 9 shows a comparison of the model predictions with the nucleate and transition boiling data for a contact angle of 14 deg. The predictions are again seen to compare well with the data. For this surface, which can be called a well-wetted surface, the predicted maximum heat flux is about 30–40 percent higher than that obtained from the hydrodynamic theory. As it was observed from the experimental results described in the companion paper, the void fraction at about 1 to 1.5 mm away from the wall becomes unity when the wall heat flux approaches that given by the hydrodynamic models. Thus for this surface, the limit on the wall heat flux is set by the rate at which vapor can escape without totally blocking the liquid flow paths, rather than by the surface itself. Hence, while exercising the present model, the nucleate and transition boiling heat fluxes in excess of the maximum heat flux obtained from the hydrodynamic analysis were not allowed.

The vapor stem spacing and stem base diameter obtained from the model are plotted in Fig. 10 as a function of wall superheat for several contact angles. The data points correspond to the experimental values of the wall void fractions, whereas the solid lines correspond to the best fit to the void

data as shown in Fig. 5. While making the prediction of the boiling curves, the proportionality constant for the stem spacing was obtained by utilizing one of the heat flux data points in nucleate boiling. The stem diameter is found to show a weaker dependence on wall superheat in comparison to that shown by the stem spacing. The stem diameter and spacing decrease with superheat as more sites with smaller cavity size nucleate. The average stem base diameter and spacing increase as the surface becomes more wettable. The magnitudes of stem diameter D_w and stem spacing L, deduced from the present model for a contact angle of 14 deg, are compared in Table 1 with the data of Gaertner and Westwater (1960). In Gaertner and Westwater's experiments, nickel salts were dissolved in water and boiling was observed on a 5-cm-dia horizontal copper surface. A value of contact angle was not given, but it is expected that the contact angle in their experiments was relatively small and probably much less than 14 deg. It is seen from Table 1 that in general the predicted magnitudes of stem spacing and diameter compare favorably with the data for wall superheats of 25 and 30°C. However, the stem diameter reported by Gaertner and Westwater at a wall superheat of 30°C is about four times smaller than that predicted from the present model. It appears that something is amiss with this data point since the data show a reduction in wall void fraction with increase in wall superheat and heat flux. This is contrary to the observations made in the present work and to the trend reported in the literature by several other investigators. It should also be mentioned that the heat flux data of Gaertner and Westwater show a much stronger dependence on wall superheat than that found in the present data. Furthermore, the maximum void fraction measured in their work was only about 20 percent. This value is considerably smaller than that

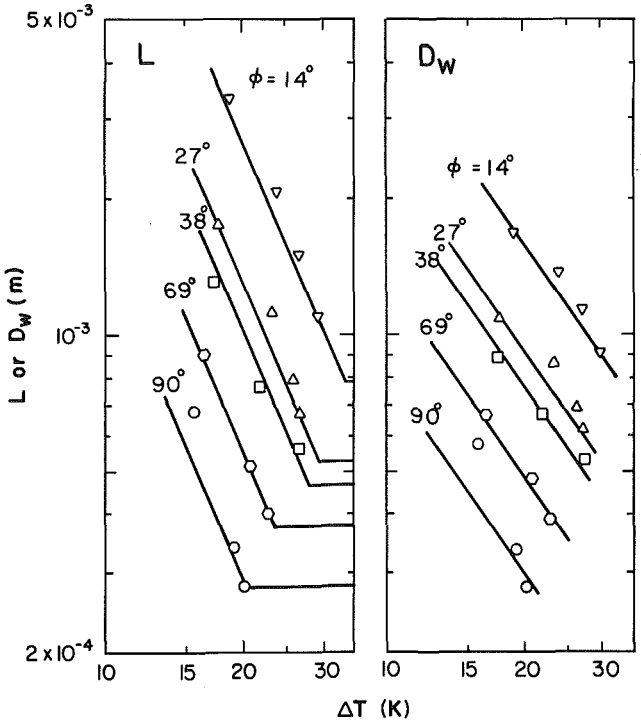

Fig. 10 Variation of stem diameter and spacing with wall superheat and contact angle

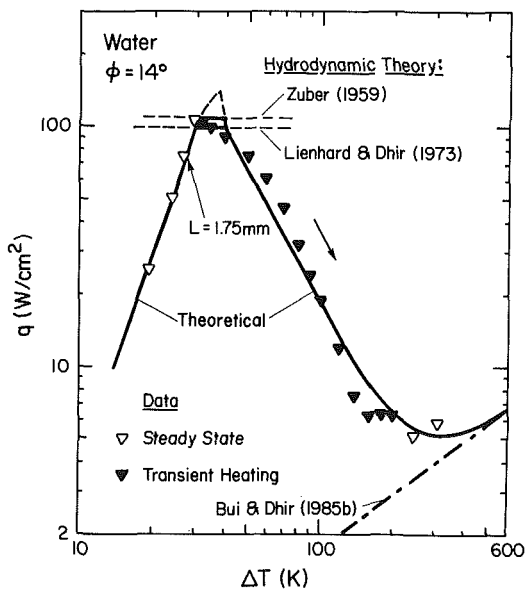

Fig. 9 Comparison of predicted and observed boiling curves for a contact angle of 14 deg

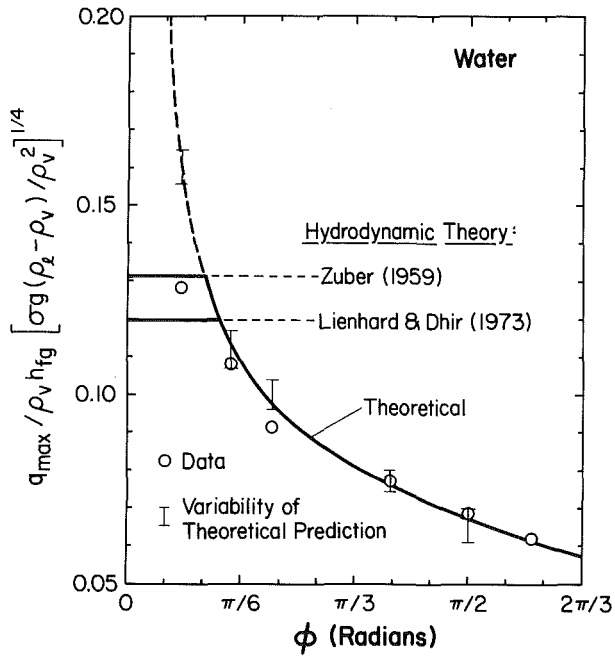

Fig. 11 Comparison of predicted and observed maximum heat fluxes on vertical surfaces of different degrees of wettability

Table 1 Comparison of magnitudes of stem diameter and spacing with the data reported in the literature

	Present work $\phi = 14$ deg			Data of Gaertner and Westwater (1960)		
ΔT, °C	q, W/cm²	D_w, m	L, m	q, W/cm²	D_w, m	L, m
25	61	1.18×10^{-3}	1.57×10^{-3}	44	9.50×10^{-4}	2.27×10^{-3}
30	103	9.11×10^{-4}	1.09×10^{-3}	96	2.48×10^{-4}	1.10×10^{-3}

and is reflective of the existence of a very small contact angle in their experiments.

The thermal layer thickness over the liquid-occupied region of the heater is found to vary as ΔT^{-6}. This dependence is in agreement with the observations made several years ago by Bobst and Colver (1968). At nucleate boiling heat fluxes well below the maximum, the calculated thermal layer thickness is of the order of 10^{-5} m.

In Fig. 11, the maximum heat fluxes predicted from the present model are compared with the data obtained on surfaces of different degrees of wettability. The predicted values are found to be in good agreement with the data. Here it should be stated again that the inherent assumption made in the present model is that vapor escape paths away from the wall are available and the vapor escape rate from the wall imposes no limitation on the heat transfer rate from the wall as long as the predicted heat flux does not exceed that obtained from the hydrodynamic analysis (Zuber, 1959; Lienhard and Dhir, 1973).

Summary and Conclusions

1 A thermal model for pool boiling has been developed. The model provides a framework for theoretical prediction of the boiling curve.

2 In the model, which does not apply in the isolated bubble regime of nucleate boiling, static vapor stems are assumed to be implanted in the thermal layer.

3 The heat transferred from the wall to the thermal layer is utilized in evaporation at the stationary vapor–liquid interface of the stems.

4 The model predictions of the boiling curve compare quite well with the data when observed values of void fraction and spacing of stems at one superheat are used as input to the model.

5 The model predicted values of the vapor stem spacing and diameter and temperature dependence of the thermal layer thickness are found to be in general agreement with those reported in the literature.

6 The maximum heat fluxes predicted from the model compare well with those observed in the experiments.

Acknowledgments

This work received support from NSF under Grant No. CBT-84-17684.

References

Bjornard, T. A., and Griffith, P., 1977, "PWR Blowdown Heat Transfer," *Symposium on the Thermal and Hydraulic Aspects of Nuclear Reactor Safety*, Vol. 1, pp. 17–39.

Bobst, R. W., and Colver, C. P., 1968, "Temperature Profiles up to Burnout Adjacent to a Horizontal Heating Surface in Nucleate Pool Boiling of Water," *Chem. Engr. Progr. Symposium Ser.*, Vol. 64, pp. 26–32.

Bui, T. D., and Dhir, V. K., 1985a, "Transition Boiling Heat Transfer on a Vertical Surface," ASME JOURNAL OF HEAT TRANSFER, Vol. 107, pp. 756–763.

Bui, T. D., and Dhir, V. K., 1985b, "Film Boiling Heat Transfer on an Isothermal Vertical Surface," ASME JOURNAL OF HEAT TRANSFER, Vol. 107, pp. 764–771.

Gaertner, R. F., 1965, "Photographic Study of Nucleate Pool Boiling on a Horizontal Surface," ASME JOURNAL OF HEAT TRANSFER, Vol. 87, pp. 17–29.

Gaertner, R. F., 1963, "Distribution of Active Sites in the Nucleate Boiling of Liquids," *Chem. Engr. Progr. Symposium Ser.*, Vol. 59, pp. 52–161.

Gaertner, R. F., and Westwater, J. W., 1960, "Population of Active Sites in Nucleate Boiling Heat Transfer," *Chem. Eng. Progr. Symposium Ser.*, Vol. 56, pp. 39–48.

Hsu, Y. Y., and Graham, R. W., 1976, *Transport Processes in Boiling and Two-Phase Systems*, McGraw-Hill, NY.

Kalinin, E. K., Berlin, I. I., Kostyuk, V. V., and Nosova, E. M., 1976, "Heat Transfer During Transition Boiling of Cryogenic Liquids," *High Temperature*, Vol. 14, No. 2, pp. 372–374.

Kutateladze, S. S., 1948, "On the Transition to Film Boiling Under Natural Convection," *Kotloturbostroenie*, No. 3, p. 10.

Liaw, S. P., and Dhir, V. K., 1986, "Effect of Surface Wettability on Transition Boiling Heat Transfer From a Vertical Surface," *Proc. Eighth Int'l. Heat Transfer Conference*, San Francisco, CA, Vol. 4, pp. 2031–2036.

Liaw, S. P., and Dhir, V. K., 1989, "Void Fraction Measurements During Saturated Pool Boiling of Water on Partially Wetted Vertical Surfaces," ASME JOURNAL OF HEAT TRANSFER, this issue.

Liaw, S. P., 1988, "Experimental and Analytical Study of Nucleate and Transition Boiling on Vertical Surfaces," Ph.D. dissertation, University of California, Los Angeles, CA.

Lienhard, J. H., and Dhir, V. K., 1973, "Extended Hydrodynamic Theory of the Peak and Minimum Pool Boiling Heat Fluxes," NASA Rept., CR-2270.

Rohsenow, W. M., 1952, "A Method of Correlating Heat Transfer Data for Surface Boiling of Liquids," *Trans. ASME*, Vol. 74, pp. 969–976.

Zuber, N., 1959, "Hydrodynamic Aspects of Boiling Heat Transfer," Ph.D. Thesis, University of California, Los Angeles [also published as U.S. Atomic Energy Commission Report AECU-4439].

The Influence of Subcooling on the Frequency of Bubble Emission in Nucleate Boiling

R. L. Judd
Professor of Mechanical Engineering,
McMaster University,
Hamilton, Ontario, Canada

The experimental results reported in Ibrahim and Judd (1985) in which bubble period first increased and then decreased as subcooling varied over the range $0 \leq \theta_{sat} \leq 15°C$ is interpreted by means of a comprehensive boiling heat transfer model incorporating the contributions of nucleate boiling, natural convection, and microlayer evaporation components. It is shown that bubble emission frequency varies to accommodate the impressed heat load in the manner described above because changes in subcooling cause the heat flux within the area influenced by the formation and departure of bubbles to change in the opposite sense to the fraction of the surface area within which bubble formation and departure occurs. The mechanism responsible for the nucleation of bubbles at exactly the frequency required at each level of subcooling is the object of continuing research.

Introduction

The ability to predict nucleate boiling heat transfer rates depends upon a knowledge of the mechanisms involved in the transport of heat away from the boiling surface and the way in which these mechanisms interact as superheat and subcooling change. Undoubtedly, the growth and departure of the bubbles is responsible for the transfer of the heat, and while bubble dynamics is understood reasonably well, the interrelationship between the rate of bubble formation and the rate of heat transfer is not well understood at all. In a situation where the generation of heat is impressed as in a research experiment, the rate at which bubbles are nucleated must change continually in order to accommodate changes in subcooling so that the rate of heat transfer will always be equal to the impressed flux. However, the way in which this is accomplished has not yet been ascertained.

Ibrahim and Judd (1985) boiled water on a horizontal copper surface at atmospheric pressure and reported the results of an investigation of bubble growth and waiting time. At the beginning of the research, a boiling apparatus constructed by Wiebe (1971) and later modified by Sultan (1977) was adapted for the present investigation. No particular attention was given to the finish of the boiling surface except that just prior to the collection of the data reported in Ibrahim and Judd (1985), the surface was once more cleaned with a soft cloth moistened with liquid silver polish after which the residue was rinsed away with a stream of methanol from a squeeze bottle.

The most peculiar aspect of the results that were reported was the way in which waiting time first increased and then decreased with increasing subcooling as seen in Fig. 1. This behavior was evident at all seven of the active nucleation sites that were studied in detail. Ibrahim (1983) estimated the accuracy to be approximately ± 10 percent in the determination of the time intervals and ± 5 percent in the determination of the subcooling. Considering the relatively small uncertainty associated with these quantities that is represented by error bars in Fig. 1, it must be concluded that the variation of bubble waiting time with liquid subcooling is authentic. While the low subcooling results are consistent with the transient conduction of heat from the surface to the liquid that periodically replaces

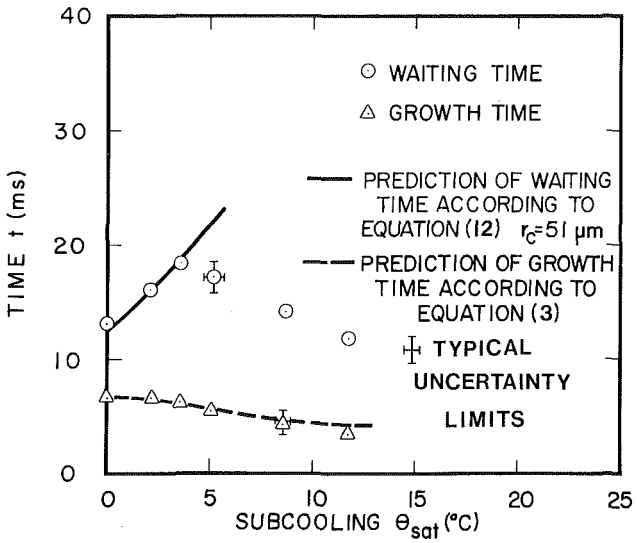

Fig. 1 Waiting and growth time correlations for site C at 166 kW/m² presented by Ibrahim and Judd (1985)

a bubble after its departure, it is not apparent how this mechanism could explain the high subcooling results, which suggests that a different mechanism was acting. Nevertheless, although the mechanisms that were operative are not understood at the present time, it is possible to interpret the behavior observed without understanding them, as will be demonstrated in this paper.

According to Mikic and Rohsenow (1969), heat transfer by nucleate boiling is accomplished by the periodic removal of energy accumulated in the liquid that replaces each departing bubble and can be predicted by the relationship

$$\frac{q_{NB}}{A_T} = \left(\frac{q_{NB}}{A_{NB}}\right)\left(\frac{A_{NB}}{A_T}\right) = \left(\frac{2}{\sqrt{\pi}}\sqrt{\rho_l C_l k_l}\,\theta_w \sqrt{f}\right)\left(4\pi R_d^2 \frac{N}{A_T}\right) \quad (1)$$

which is much the same as the Han and Griffith (1965) relationship

Contributed by the Heat Transfer Division for publication in the JOURNAL OF HEAT TRANSFER. Manuscript received by the Heat Transfer Division November 1, 1987. Keywords: Boiling.

$$\frac{q_{NB}}{A_T} = 2\,\rho_l\,C_l\,\theta_w \sum_{i=1}^{N/A_T} \left\{ f\left[R_i^2\,\delta_d - \frac{1}{3} R_d^2\,(\delta_d - \delta_c)\right]\right\}_i$$

$$\simeq 2\,\rho_l\,C_l\,\theta_w\,f\sqrt{\pi\,\alpha_l\,(t_w+t_g)}\;R_i^2\,\frac{N}{A_T}\left[1 - \frac{1}{3}\left(\frac{R_d^2}{R_i^2}\right)\left(1 - \sqrt{\frac{t_w}{t_w+t_g}}\right)\right]$$

$$= \left(\frac{2}{\sqrt{\pi}}\sqrt{\rho_l\,C_l\,k_l}\,\theta_w\sqrt{f}\right)\left(4\pi\,R_d^2\,\frac{N}{A_T}\right)\left[1 - \frac{1}{3}\left(\frac{1}{4}\right)\left(1 - \sqrt{\frac{t_w}{t_w+t_g}}\right)\right] \qquad (2)$$

because $\delta_d = \sqrt{\pi\,\alpha_l\,(t_w + t_g)}$ and $\delta_c = \sqrt{\pi\,\alpha_l\,t_w}$. The factor in square brackets accounts for the fact that some of the liquid that replaced the last departing bubble was displaced as the succeeding bubble grew, but it is not a significant factor and can be considered equivalent to unity. This approach to modeling nucleate boiling heat transfer has been used successfully by Judd and Hwang (1976), Kenning and del Valle (1981), and Gorenflo et al. (1986) among others.

In both of these theories, the rate of heat transfer per unit area by nucleate boiling $q_{NB}/A_{NB} = (2/\sqrt{\pi})\sqrt{\rho_l\,C_l\,k_l}\,\theta_w\sqrt{f}$ and the fraction of the boiling surface $A_{NB}/A_T = 4\,\pi\,R_d^2\,N/A_T$ in which nucleate boiling is effective have been identified. Table 1 presents data for site C at $q/A_T = 166$ kW/m^2, which is one of the experimental data sets reported by Ibrahim and Judd (1985) that comprises all the parameters required to compute these expressions, with the exception of the departure radius R_d and the nucleation site density N/A_T. Although the departure radius was not determined explicitly in Ibrahim and Judd (1985) because it was not relevant to the theory being developed, it is readily obtainable from the growth time solution presented in that paper, which has been reproduced as equation (3) below

$$149.9\left\{1 - \frac{\theta_w}{\theta_w-\theta_{sat}}\left[\sqrt{\left(1+\frac{t_w}{t_g}\right)} - \sqrt{\left(\frac{t_w}{t_g}\right)}\right]\right\} t_g - \frac{46.8}{\theta_w-\theta_{sat}}\sqrt{t_g} + \frac{\theta_w}{\theta_w-\theta_{sat}}\sqrt{\left(1+\frac{t_w}{t_g}\right)} = 1 \qquad (3)$$

from which the departure radius R_d can be evaluated by the relationship

$$R_d = X\left\{1 + \frac{8.86\,Y}{\sqrt{t_g}}\left[1 - \frac{\theta_w}{\theta_w-\theta_{sat}}\sqrt{\left(1+\frac{t_w}{t_g}\right)}\right]\right\} \qquad (4)$$

where $X = 0.203\,\beta\sqrt{2\,\sigma\,g_c/g(\rho_l-\rho_v)}$ and $Y = 2\sqrt{3/\pi}$ Ja $\sqrt{\alpha_l}$ once the growth time t_g has been computed from equation (3). In equation (4), the contact angle β was taken to be 0.82 radians (47 deg) in keeping with values measured in previous investigations. The agreement of the growth time solution predictions with the measured results is excellent as seen in Fig. 1 so the departure radius predictions are expected to be reliable. These values have been presented in Table 1 as well. The trend in the variation of waiting time t_w with subcooling θ_{sat} that is evident in Table 1 is typical of that observed at all of the sites that Ibrahim and Judd (1985) investigated.

Table 1 Ibrahim and Judd (1985) results for site C

q/A_T (kW/m^2)	t_g (ms)	t_w (ms)	t_w+t_g (ms)	θ_{sup} (°C)	θ_{sat} (°C)	θ_w (°C)	R_d (mm)
166.00	6.74	13.01	19.75	13.70	.00	13.70	1.83
166.00	6.58	16.05	22.63	14.30	2.20	16.50	1.83
166.00	6.07	18.40	24.47	14.50	3.60	18.10	1.82
166.00	5.42	17.11	22.53	14.90	5.20	20.10	1.73
166.00	4.52	14.09	18.61	15.40	8.70	24.10	1.48
166.00	3.47	11.71	15.18	15.80	11.80	27.60	1.26

Nomenclature

A_{NB} = area influenced by nucleate boiling
A_{NC} = area influenced by natural convection
A_T = total heat transfer surface area
C = specific heat
f = bubble emission frequency
g = gravitational acceleration
g_c = gravitational constant
h_{fg} = latent heat
Ja = Jakob number = $\rho_l\,C_l\,(T_w - T_{sat})\,/\,\rho_v\,h_{fg}$
k = thermal conductivity
N/A_T = active site density
N'/A_T = potentially active site density
q_{NB} = nucleate boiling heat transfer rate
q_{NC} = natural convection heat transfer rate
q_{ME} = microlayer evaporation heat transfer rate
r = radius
r_c = nucleation cavity radius
r_e = radius of complete microlayer evaporation
$R(t)$ = bubble radius
R_i = radius of area of influence
R_d = radius of bubble at departure
t = time
t_g = bubble growth time
t_w = bubble waiting time
T = temperature
U_o = bubble growth velocity = $dR(t)/dt$
V_{ME} = volume of microlayer evaporated
X = parameter used in equation (4) = $0.203\,\beta\sqrt{2\sigma g_c/g(\rho_l - \rho_v)}$
Y = parameter used in equation (4) = $2\sqrt{3/\pi}$ Ja $\sqrt{\alpha_l}$
α = thermal diffusivity
β = contact angle or volumetric coefficient of expansion
$\delta_o(r)$ = initial microlayer thickness
$\delta(r, t)$ = instantaneous microlayer thickness
δ_c = parameter used in equation (2) = $\sqrt{\pi\,\alpha_l\,t_w}$
δ_d = parameter used in equation (2) = $\sqrt{\pi\,\alpha_l\,(t_w + t_g)}$
θ = temperature difference = $T - T_\infty$
μ = dynamic viscosity
ν = kinematic viscosity
ρ = density
σ = surface tension

Subscripts

l = liquid
sat = saturation
v = vapor
w = wall
∞ = bulk

Heat Transfer Modeling

When subcooling θ_{sat} increases, $q_{NB}/A_{NB} = (2/\sqrt{\pi})\sqrt{\rho_l C_l k_l}\,\theta_w\sqrt{f}$ increases because θ_w increases even though $\sqrt{f} = 1/\sqrt{t_w + t_g}$ decreases initially. At the same time, $A_{NB}/A_T = 4\pi R_d^2 N/A_T$ decreases. These trends are depicted in Fig. 2. For the computation of A_{NB}/A_T, the relevant values of N/A_T were not known because this parameter was not determined in connection with the experimental results reported by Ibrahim and Judd (1985). However, Judd and Hwang (1976) observed no more than ± 15 percent difference in active site density N/A_T over the subcooling range $0 \le \theta_{sat} \le 12°C$ at any of the levels of heat flux that they investigated in the range 20 kW/m² $\le q/A_T \le$ 60 kW/m² in connection with their study of dichloromethane boiling on an oxide coated glass surface and Sultan and Judd (1978) reported that the potentially active site density N'/A_T (continually active nucleation sites and all of the intermittently active sites surrounding them) changed about 10 percent as subcooling varied in the range $0 \le \theta_{sat} \le 40°C$ with respect to their study of water boiling on a copper surface using the same boiling apparatus. Consequently, it was felt to be reasonable to assume that N/A_T is independent of θ_{sat} over the range of subcooling under investigation and arbitrarily chosen values of active site density from N/A_T = 11,500 sites/m² to N/A_T = 21,500 sites/m² were used to demonstrate the variation.

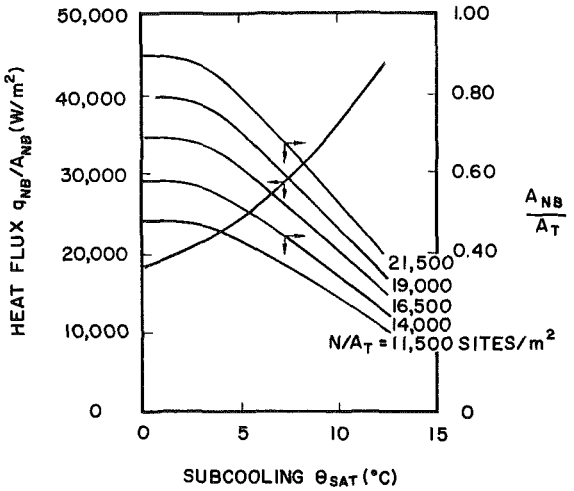

Fig. 2 Variation of nucleate boiling heat flux and area fraction with subcooling

It is logical to expect that the periodic removal of the energy accumulated in the liquid that replaces each departing bubble would predominate the nucleate boiling heat transfer process so that it is not unreasonable to assume that

$$\frac{q}{A_T} \approx \left(\frac{q_{NB}}{A_{NB}}\right)\left(\frac{A_{NB}}{A_T}\right) \tag{5}$$

where $q_{NB}/A_{NB} = (2/\sqrt{\pi})\sqrt{\rho_l C_l k_l}\,\theta_w\sqrt{f}$ and $A_{NB}/A_T = 4\pi R_d^2 N/A_T$. In order to evaluate this model, the heat flux predicted was set equal to the impressed heat flux q/A_T = 166 kW/m² and then for each of the active site density values under consideration N/A_T = 11,500, 14,000, 16,500, 19,000, and 21,500 sites/m², respectively, equation (5) was solved to determine the frequency f and the bubble period $t_w + t_g$ using the information presented in Table 1 as appropriate. The values so obtained were plotted in Fig. 3 for comparison with the experimentally determined values listed in Table 1. However, the quality of the agreement between the predictions of this model and the experimental results presented in Fig. 3 does not support this conclusion, although the rough agreement between the experimentally determined values and the predictions at N/A_T = 19,000 sites/m² confirms that the nucleate boiling heat transfer mechanism is the predominant factor in the prediction of heat transfer. Regrettably, the model is too simplistic inasmuch as it ignores the contribution of natural convection, which has to be significant, especially at the higher levels of subcooling.

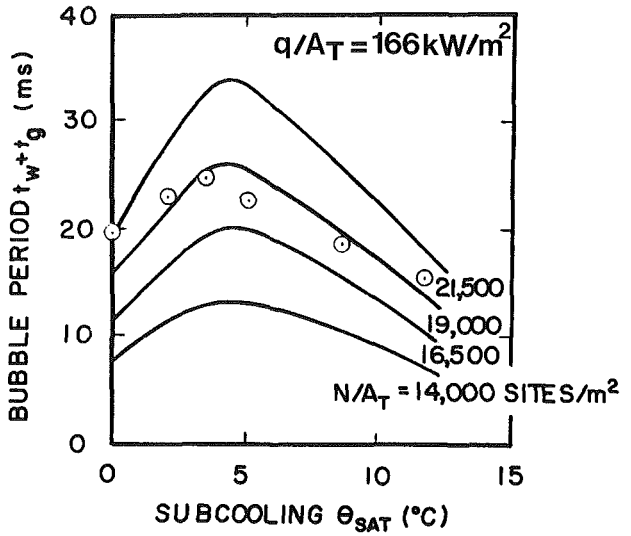

Fig. 3 Comparison of experimental results and predictions of a model involving nucleate boiling only

Han and Griffith (1965) and Judd and Hwang (1976) among others have presented boiling heat transfer models that incorporated a natural convection heat transfer component such that

$$\frac{q}{A_T} = \left(\frac{q_{NB}}{A_{NB}}\right)\left(\frac{A_{NB}}{A_T}\right) + \left(\frac{q_{NC}}{A_{NC}}\right)\left[1 - \left(\frac{A_{NB}}{A_T}\right)\right] \tag{6}$$

wherein $q_{NC}/A_{NC} = 0.14\,k_l\,[(g\beta/\nu_l^2)\,(\mu_l C_l/k_l)]^{1/3}\,\theta_w^{4/3}$ was introduced to predict the contribution of natural convection heat transfer. Again the heat flux predicted by this model was set equal to the impressed heat flux q/AT = 166 kW/m² and then for each of the active site density values under consideration N/A_T = 11,500, 14,000, 16,500, 19,000, and 21,500 sites/m², respectively, equation (6) was solved to determine frequency f and bubble period $t_w + t_g$ using the information in Table 1 as appropriate. The values so obtained were plotted in Fig. 4 for comparison with the experimentally determined values listed in Table 1. As seen in Fig. 4, while the agreement between the predictions of this model and the experimental results is better at the higher levels of subcooling, the overall agreement is not good enough to support this model either.

The investigations of Judd and Hwang (1976) and Fath and Judd (1978) have demonstrated that microlayer evaporation heat transfer ought to be included in a comprehensive heat transfer model as well. In the aforementioned references, it was possible to evaluate the microlayer evaporation heat transfer from interferometric measurements of the volume of microlayer evaporated because the bubbles formed on a transparent surface. However, this information is not available from Ibrahim and Judd (1985). While Cooper and Lloyd (1969) studied the formation and evaporation of microlayers underlying growing bubbles and developed a theory for predicting the volume of the microlayer evaporated that would seem to be relevant, the theory is not appropriate in the present case because the theory is predicated upon the assumption that the bubbles grow according to $R(t) = \text{const}\,t^n$, where the exponent n is a constant. This is not the case in the Ibrahim and Judd (1985) experiment in which the results are correlated by the Mikic and Rohsenow (1969) theory as evidenced by the ex-

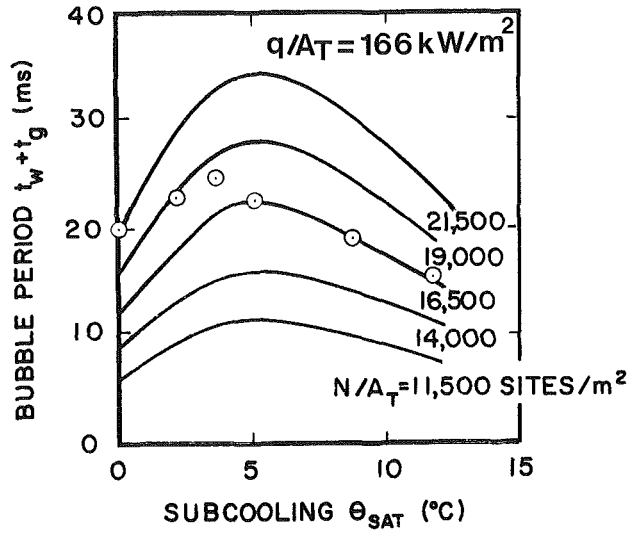

Fig. 4 Comparison of experimental results and predictions of a model involving nucleate boiling and natural convection

cellent agreement between the experimental results and the prediction of bubble growth time seen in Fig. 1. If bubble radius were fitted by a relationship of the form $R(t) = \text{const}\ t^n$, the exponent n would have to vary considerably depending on the level of subcooling and heat flux. The empirical correlation of Katto et al., (1973) is more applicable in the present case. The correlation is derived from experimental measurements pertaining to the growth and evaporation of microlayers that developed beneath bubbles forming on a copper heating surface on which water was boiling. The predictions of the relationship

$$\left.\frac{d\delta_o(r)}{dr}\right|_{r=R(t)} = 0.65\left\{\frac{\mu U_o}{\sigma}\right\}^{1/6}\left|\left\{\frac{U_o r}{\nu}\right|_{r=R(t)}\right\}^{1/2} \tag{7}$$

where $U_o = dR(t)/dt$ were shown to be in agreement with the initial microlayer thickness results reported by Cooper and Lloyd (1969) when the relationship that Katto et al. (1973) obtained by empirically fitting their bubble growth results according to $R(t) = \text{const}\ t^n$ was used to evaluate U_o and the obvious mathematical manipulation was performed to obtain $\delta_o(r)$. In the present case, $R(t)$ and U_o were obtained from the Mikic and Rohsenow (1969) relationship and equation (7) was solved numerically.

At the end of each time step, the instantaneous microlayer thickness $\delta(r, t)$ was computed by determining the portion of the initial microlayer thickness $\delta_o(r)$ that had been evaporated in the region $0 \le r \le R(t)$ since the microlayer was formed. The rate at which heat was transferred through the microlayer in order to cause evaporation at the liquid/vapor interface was considered to be governed by conduction through the microlayer at the location under consideration, resulting in the differential equation

$$\rho_l h_{fg}\left(\frac{d\delta(r, t)}{dt}\right) = -k_l\left(\frac{\theta_w - \theta_{sat}}{\delta(r, t)}\right) \tag{8}$$

where $t = 0$ at the moment that the initial microlayer was formed at $r = R(t)$ so that $\delta(r, 0) = \delta_o(r)$ served as the initial condition. At the end of the growth period, this equation yields the solution

$$\frac{\delta(r, t_g)}{\delta_o(r)} = \text{Real}\left\{\sqrt{1 - \frac{2\,k_l\,(\theta_w - \theta_{sat})}{\rho_l\,h_{fg}\,\delta_o(r)^2}\,(t_g - t)}\right\} \tag{9}$$

where t is the time that has elapsed since the microlayer was formed at $r = R(t)$ as explained above. The requirement that the solution be real has been invoked to allow for the complete evaporation of the microlayer in the region $0 \le r \le r_e$, wherein the equation would otherwise predict imaginary values. The derivation of these equations is presented by Cooper (1969) and others.

After the instantaneous microlayer profile $\delta(r, t_g)$ had been determined, the volume of the microlayer that had evaporated at $t = t_g$

$$V_{ME} = 2\pi\left[\int_0^{r_e}\delta_o(r)\,r\,dr - \int_{r_e}^{R_d}[\delta_o(r) - \delta(r, t_g)]\,r\,dr\right\} = \sum_{i=1}^{N}\Delta V_{ME_i} \tag{10}$$

was computed wherein $\Delta V_{ME_i} = 2\pi\,r_i\,[\delta_o(r)]_i\,\Delta r_i$ for $0 \le r \le r_e$ and $\Delta V_{ME_i} = 2\,\pi\,r_i\,[\delta_o(r) - \delta(r, t_g)]_i\,\Delta r_i$ for $r_e < r \le R_d$. In the above equation, r_e is the value of radius at which $\delta(r, t_g)/\delta_o(r)$ becomes real. This is the radius up to which complete evaporation has occurred at the departure time t_g and R_d is the bubble departure radius.

Accordingly, a boiling heat transfer model incorporating nucleate boiling, natural convection, and microlayer evaporation was formulated

$$\frac{q}{A_T} = \left(\frac{q_{NB}}{A_{NB}}\right)\left(\frac{A_{NB}}{A_T}\right) + \left(\frac{q_{NC}}{A_{NC}}\right)\left[1 - \left(\frac{A_{NB}}{A_T}\right)\right] + \left(\frac{q_{ME}}{A_T}\right) \tag{11}$$

wherein the relationship $q_{ME}/A_T = \rho_l\,h_{fg}\,V_{ME}\,N/A_T\,f$ was introduced to predict the contribution of microlayer evaporation heat transfer. In this model q_{NB}/A_T represents the periodic removal of the energy that accumulated in the liquid that replaced the previous bubble during the waiting period by entrainment in the wake of the subsequent bubble and q_{ME}/A_T represents the periodic removal of energy that was extracted from the surface during the growth period in order to evaporate the microlayer. The two effects are complementary and while they both occur in the vicinity of the nucleation site, the two mechanisms occur at different times and do not conflict. Once again, the heat flux predicted by this model was set equal to the impressed heat flux $q/A_T = 166\ \text{kW/m}^2$ and then for each of the active site density values under consideration, $N/A_T =$ 11,500, 14,000, 16,500, 19,000, and 21,500 sites/m^2, respectively, equation (11) was solved to obtain frequency f and

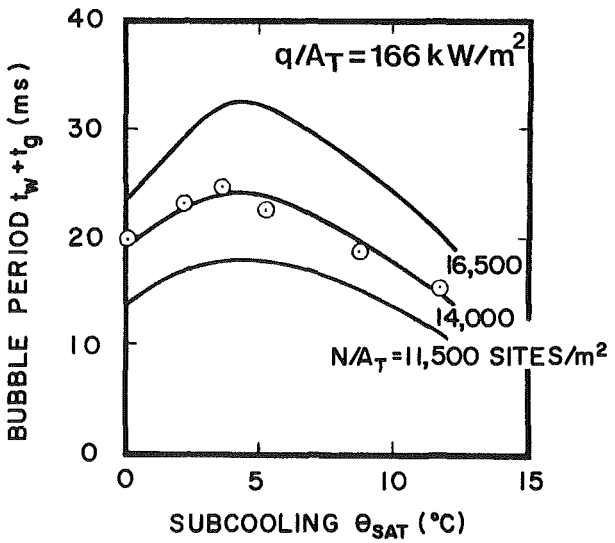

Fig. 5 Comparison of experimental results and predictions of a model involving nucleate boiling, natural convection, and microlayer evaporation

bubble period $t_w + t_g$ using the information in Table 1 as appropriate. The values so obtained were plotted in Fig. 5 for comparison with the experimental values listed in Table 1. Good agreement is seen in Fig. 5 between the experimental results and the theoretical predictions at $N/A_T = 14{,}000$ sites/m^2 over the entire range of subcooling values. The differences between measured and predicted values are less significant than they might appear inasmuch as the greatest deviation between measured and predicted values of the bubble period $t_g + t_w$ is less than 7 percent.

Active site density is very much dependent upon the finish of the boiling surface, which is impossible to quantify, so it is not surprising that two ostensibly identical surfaces might have different values of active site density under the same boiling conditions. Sultan and Judd (1978) obtained $N'/A_T \simeq 250{,}000$ sites/m^2 at $q/A_T = 166$ kW/m^2 but the results are not comparable. However, Westwater and Gaertner (1960) studied aqueous plating solutions boiling on a copper surface and reported $N/A_T \simeq 45{,}000$ sites/m^2 at $q/A_T = 166$ kW/m^2, whereas Kurihara and Myers (1960) reported $N/A_T \simeq 11{,}000$ sites/m^2 in connection with their study of water boiling on a copper surface at the same level of heat flux. Considering the variability of the active site density data presented, one may conclude that the value obtained in the present investigation $N/A_T = 14{,}000$ sites/m^2 is not unreasonable.

While there is no comparable value of active site density with which to compare the value obtained in the present investigation, similar analysis applied to all of the other data sets obtained at the same level of heat flux yielded the values listed in Table 2.

The self-consistency of these values does not prove the validity of the active site density value determined by the present analysis, but it does indicate that the value obtained is not peculiar to the particular data set that was chosen for detailed investigation.

Closing Remarks

The variation of bubble emission frequency is consistent with the predictions of a comprehensive boiling heat transfer model that incorporates nucleate boiling, natural convection, and microlayer evaporation components. The bubble emission period varies in the manner observed experimentally because the heat flux within the area influenced by the formation and departure of bubbles and the fraction of the surface area within which bubble formation and departure occurs change in the opposite sense as subcooling varies. Initially, as subcooling increases from the saturated condition, the ability to dissipate heat increases while the area fraction remains constant and as a consequence, the frequency of bubble emission decreases and the bubble emission period increases with increasing subcooling. Ultimately a level of subcooling is reached where the area fraction decreases and when the rate of decrease in area fraction becomes greater than the rate of increase in heat dissipation ability, bubble emission frequency increases once again and the bubble emission period decreases with increasing subcooling. The nucleation phenomenon whereby bubbles are generated at the rate required to dissipate the impressed heat flux at the low levels of subcooling is consistent with classical nucleation theory. In particular, the Han and Griffith (1965) nucleation theory correlates the results very well, as demonstrated in Fig. 1, in accordance with the relationship

$$t_w = \frac{9}{4\,\pi\,\alpha_l}\left\{\left[\frac{(T_w - T_\infty)}{(T_w - T_{sat}) - (2\sigma T_{sat}/\rho_v h_{fg} r_c)}\right] r_c\right\}^2 \qquad (12)$$

Table 2 Active site density values for data sets obtained at 166 kW/m²

Site A	Site B	Site C	Site D	Site E	Site F	Site G
13,100 sites/m^2	14,500 sites/m^2	14,000 sites/m^2	13,300 sites/m^2	13,300 sites/m^2	14,100 sites/m^2	13,300 sites/m^2

so long as the effective cavity radius r_c is assumed to be either 2.40 μm or 51 μm. In all of the classical nucleation theories, there are two values of nucleation cavity radius that will satisfy the theoretical relationships for a single value of waiting time. While Ibrahim (1983) arbitrarily chose $r_c = 51$ μm as the value of nucleation that would fit the experimental data best, $r_c = 2.40$ μm is more representative of the value of nucleation cavity radius that would be associated with an active cavity in a copper surface in the presence of boiling water. However, the nucleation phenomenon that causes bubbles to be generated at exactly the rate required to dissipate the impressed heat flux at each level of subcooling is not understood at the present time and remains the focus of continuing research.

References

Cooper, M. G., 1969, "The Microlayer and Bubble Growth in Nucleate Pool Boiling," *International Journal of Heat and Mass Transfer*, Vol. 12, pp. 915–933.

Cooper, M. G., and Lloyd, A. J. P., 1969, "The Microlayer in Nucleate Pool Boiling," *International Journal of Heat and Mass Transfer*, Vol. 12, pp. 895–914.

Fath, H. S., and Judd, R. L., 1978, "Influence of System Pressure on Microlayer Evaporation Heat Transfer," ASME JOURNAL OF HEAT TRANSFER, Vol. 100, No. 1, pp. 49–55.

Gorenflo, D., Knabe, V., and Bieling, V., 1986, "Bubble Density on Surfaces With Nucleate Boiling—Its Influence on Heat Transfer and Burnout Heat Flux at Elevated Saturation Pressures," *Proceedings of the Eighth International Heat Transfer Conference*, Hemisphere Publishing Company, Vol. 4, pp. 1995–2000.

Han, C. Y., and Griffith, P., 1965, "The Mechanism of Heat Transfer in Nucleate Pool Boiling," *International Journal of Heat and Mass Transfer*, Vol. 8, pp. 887–912.

Ibrahim, E. A., 1983, "An Experimental Investigation of the Effect of Subcooling on Bubble Growth and Waiting Time in Nucleate Boiling," M.Eng. Thesis, Department of Mechanical Engineering, McMaster University, Hamilton, Ontario, Canada.

Ibrahim, E. A., and Judd, R. L., 1985, "An Experimental Investigation of the Effect of Subcooling on Bubble Growth and Waiting Time in Nucleate Boiling," ASME JOURNAL OF HEAT TRANSFER, Vol. 107, No. 1, pp. 168–174.

Judd, R. L., and Hwang, K. S., 1976, "A Comprehensive Model for Nucleate Pool Boiling Heat Transfer Including Microlayer Evaporation," ASME JOURNAL OF HEAT TRANSFER, Vol. 98, No. 4, pp. 623–629.

Katto, Y., Takahashi, S., and Yokoya, S., 1973, "Law of Micro-Liquid-Layer Formation Between a Growing Bubble and a Solid Surface With Special Reference to Nucleate Boiling," *Bulletin of the Japanese Society of Mechanical Engineers*, Vol. 16, No. 97, pp. 1066–1075.

Kenning, D., and del Valle M., 1981, "Fully-Developed Nucleate Boiling: Overlap of Areas of Interference Between Bubble Sites," *International Journal of Heat and Mass Transfer*, Vol. 24, pp. 1025–1032.

Kurihara, H. M., and Myers, J. E., 1960, "The Effects of Superheat and Surface Roughness on Boiling Conditions," *AIChE Journal*, Vol. 6, No. 1, pp. 83–91.

Mikic, B. B., and Rohsenow, W. M., 1969, "A New Correlation of Pool Boiling Data Including the Effect of Heating Surface Characteristics," ASME JOURNAL OF HEAT TRANSFER, Vol. 91, No. 2, pp. 245–250.

Sultan, M., 1977, "Spatial Distribution of Active Sites and Bubble Flux Density," M. Eng. Thesis, Department of Mechanical Engineering, McMaster University, Hamilton, Ontario, Canada.

Sultan, M., and Judd, R. L., 1978, "Spatial Distribution of Active Sites and Bubble Flux Density," ASME JOURNAL OF HEAT TRANSFER, Vol. 100, No. 1, pp. 56–62.

Westwater, J. W., and Gaertner, R. F., 1960, "Population of Active Sites in Nucleate Boiling Heat Transfer," *Chemical Engineering Progress Symposium*, Vol. 30, No. 56, pp. 39–48.

Wiebe, J. R., 1971, "Superheat Layer Thickness Measurements in Saturated and Subcooled Nucleate Boiling," ASME JOURNAL OF HEAT TRANSFER, Vol. 93, No. 4, pp. 455–461.

Microelectronic Cooling by Enhanced Pool Boiling of a Dielectric Fluorocarbon Liquid

T. M. Anderson
Graduate Research Assistant.

I. Mudawar
Associate Professor and Director.
Assoc. Mem. ASME

Boiling and Two-Phase Flow Laboratory,
School of Mechanical Engineering,
Purdue University,
West Lafayette, IN 47907

An experimental study of boiling heat transfer from a simulated microelectronic component immersed in a stagnant pool of the dielectric Fluorinert (FC-72) is presented. Various enhancement surfaces were attached to an electrically heated copper calorimeter bar having a vertically oriented heat transfer surface area of 12.7 × 12.7 mm². A number of enhancement schemes aimed at a reduction of the incipience temperature overshoot were tested, employing various arrangements of fins, studs, grooves, and vapor-trapping cavities. Atmospheric pressure testing revealed a variation in the magnitude of boiling curve incipience temperature excursion as a function of both macro- and microcharacterization of the surface geometry and initial conditions (pressure and temperature history) prior to boiling. Increased incipience temperatures accompanied prolonged periods of nonboiling. It is assumed that this is due to vapor embryos within surface cavities collapsing to smaller radii. Large artificially created cavities (0.3 mm diameter) were found incapable of maintaining a stable vapor embryo for time periods greater than 10 min. In comparison to flat surfaces, low-profile surface geometries having a structure scale of the order of one bubble departure diameter resulted in significant enhancement of nucleate boiling while drilled surfaces had minimal effectiveness. Surface finish and artificial cavities had no effect on CHF, but levels of critical heat flux computed on base area were strongly dependent on macrogeometry, due in part to increased surface area.

Introduction

Recent advances in the electronics industry have led to rapid miniaturization of integrated circuits. The past two decades have seen chip power densities increase by five orders of magnitude as integration technologies advanced to the VLSI level. Consequently, thermal design of more powerful cooling systems must be developed to allow chip dissipation to exceed the current 5 to 40 W/cm² limits.

The current cutting-edge high-power mainframe cooling technologies have already reached their upper performance limits imposed by the thermal resistance between the chip and the coolant. The Thermal Conduction Module (TCM) implemented in the IBM 3090 computer series, for example, utilizes indirect cooling of a large array of chips in a single module. Spring-loaded convex-tipped pistons conduct heat away from individual chips to a water-cooled cold plate. However, expected increases in mainframe computer chip power density may force indirect cooling methods to succumb to direct immersion cooling by dielectrics fluids such as the 3M Fluorinerts. Substitution of an intermediate boiling fluid between the chip and an enlarged cold plate (or condenser) would drastically reduce the internal thermal resistance compared to diffusion through a long and complex conduction path.

While recent studies by Tuckerman and Pease (1981) and Ramadhyani and Incropera (1987) are strong evidence of the cooling potential of single-phase forced convection, the accompanying linear relationship between heat duty and chip temperature makes it less attractive compared to nucleate boiling in the medium VLSI heat flux range (50–100 W/cm²). Pool boiling heat transfer tends to maintain the chip temperature within a narrow range while dissipating a wide range of heat fluxes. This pool boiling feature is very desirable in electronic cooling since chip temperatures are limited to 85°C. Additionally, forced convection systems are often plagued by the need for large pumps and complex plumbing.

Enhanced pool boiling of fluorocarbon liquids appears to be a promising first generation mainframe cooling technique for removal of large amounts of heat from individual chips. Independent gravity-driven thermosyphon modules (Fig. 1) may be able to cool arrays of high-power chips without the need for expensive pumps or complex plumbing. However, advances in the control of the often anomalous behavior of the boiling curve will be required before pool boiling heat

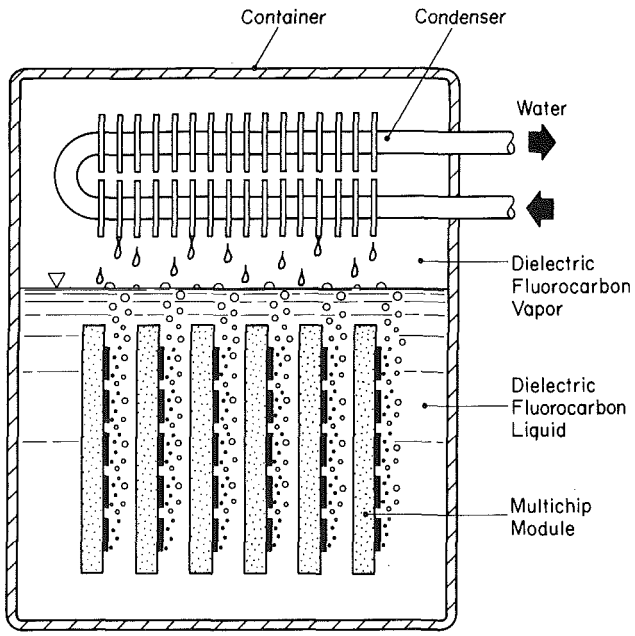

Fig. 1 Liquid-encapsulated gravity-driven thermosyphon cooling concept

Contributed by the Heat Transfer Division for publication in the JOURNAL OF HEAT TRANSFER. Manuscript received by the Heat Transfer Division March 11, 1988. Keywords: Boiling, Finned Surfaces, Phase-Change Phenomena.

transfer gains widespread popularity in the mainframe computer industry.

Presently much uncertainty exists in the prediction of the incipient boiling point. Flux levels corresponding to the cessation of boiling upon decreasing heat flux are usually much less than those encountered at the onset of boiling upon increasing heat flux. In other words, boiling incipience often occurs at temperatures much higher than expected and the excess superheat may quickly be dissipated by vigorous boiling resulting in potential damage to the heat source (chip) by thermal shock.

If a force balance is performed on a spherical bubble and it is assumed pressure is related to temperature by the Clausius–Clapeyron equation and that superheat is sufficiently small that $P_{sat} - T_{sat}$ linearity holds, then

$$\Delta T_i = \frac{T_{sat}\, v_{fg}}{h_{fg}} \frac{2\,\sigma}{r} \tag{1}$$

Equation (1) indicates that the superheat required to promote bubble growth and release is inversely proportional to the radius of the embryo within the cavity. Prevalent incipience theories (Hsu, 1962; Han and Griffith, 1965; Davis and Anderson, 1966) assume the smallest value of bubble radius (and therefore the greatest superheat) is equal or proportional to the radius of the cavity r_{cav}. Following this assumption the wall superheat necessary to cause boiling is determined by cavity size distribution on the boiling surface. But for the special case of dielectric fluorocarbons, the extremely low contact angle causes almost complete liquid flooding of surface cavities, leaving very small vapor embryos. These embryos require much higher superheat than predicted by equation (1) based on cavity radius (Bar-Cohen and Simon, 1986). Hence the key to estimation of the boiling incipience temperature for very wetting fluids lies in prediction of the distribution of embryo sizes rather than solely on the specification of surface characteristics.

The rapid temperature drop that often accompanies boiling incipience is a product of the large and rapid change in the heat transfer coefficient as the heat transfer mode shifts from natural convection to nucleate boiling. For a small fairly isothermal heat transfer surface undergoing both natural convection and boiling on separate areas, A_{nc} and A_b, the total heat load is comprised of a combination of natural convection and boiling components. That is,

$$\frac{qA}{\Delta T_{sat}} = h\,A = h_{nc}\,A_{nc} + h_b\,A_b \tag{2}$$

where h_{nc} and h_b are the heat transfer coefficients for natural convection and boiling, respectively. Defining the boiling area fraction as $A^* = A_b/A$

$$h = h_{nc}(1 - A^*) + h_b A^* \tag{3}$$

As A^* grows gradually toward unity in equation (3), the heat transfer coefficient h will likewise increase smoothly to the value of h_b.

The behavior of A^* with respect to time can be influenced by the size of the heat transfer surface and the pattern of boiling activation. Small heaters are often subject to large jumps in A^* since the area that is influenced by the boiling of a single site is a significant fraction of heater area. Rapid patterns of activation force large swings in A^* and therefore result in considerable incipience excursion. Blander and Katz (1975), Marto and Lepere (1982), and Hui and Thome (1985) reported explosive activation of boiling sites and considerable incipience temperature drop.

Conduction effects within the test heater can greatly influence the magnitude of the detected incipience excursion. Foil heaters such as those used by Park and Bergles (1986) allow little conduction along the heat transfer surface. Consequently, temperature measurements on these heaters are strongly affected by only a small localized area of the surface (smaller than the total heat surface area). The large change in the local heat transfer coefficient is sensed as a relatively large temperature fallback. Thick heaters, such as those of the present study, allow conduction within the heat transfer surface, which dampens the localized effect of the activation of a few boiling sites. Rapid activation of the entire surface may still result in incipience excursion but thermal shock is damped by the increased thermal capacitance.

The purpose of this study is to determine the effect of some types of surface roughness scheme and surface structure on pool boiling incipience, nucleate boiling, and critical heat flux (CHF) using FC-72 dielectric fluorocarbon liquid. Low-profile enhancements built upon a 12.7×12.7 mm^2 vertical surface were studied with flow visualization employed to facilitate interpretation of results.

Experimental Methods

A highly instrumented pool boiling facility was developed to simulate the microelectronic boiling module environment. A schematic of the power supply, data acquisition, test and charging vessels, and supporting plumbing in shown in Fig. 2. To maintain fluid purity, only stainless steel and fluorocarbon compatible materials were in direct contact with the working fluid. Leaks in the test chamber were detected by repeated application of vacuum and pressure and completely sealed.

A stainless steel pressure vessel rated for 22 bars at 200°C with three access nozzles was utilized as the test chamber. For optical access, quartz sight glass window flanges capped two of the access ports while the heater module was mounted through the third. The bulk of the natural convection heat loss from the vessel to the ambient was compensated by large flexible band heaters wrapped around the vessel. To maintain

Nomenclature

$A^* = A_b/A$
A = total heat transfer area
A_b = boiling fraction of total area
A_{nc} = natural convection fraction of total area
g = acceleration due to gravity
H = heater height
h = average heat transfer coefficient $= q/\Delta T_{sat}$
h_b = boiling heat transfer coefficient
h_{fg} = latent heat of vaporization
h_{nc} = natural convection heat transfer coefficient
k = thermal conductivity of liquid
Nu_c = Nusselt number at center of foil heaters $= h_{nc}H/2k$
P = pressure
q = heat flux
r = bubble radius
r_{cav} = cavity radius
Ra_c^* = modified Rayleigh number at center of foil heaters $= g\beta qH^4/(16k\nu\alpha)$
Δt^* = nonboiling time interval between boiling states
ΔT_h = incipient boiling temperature excursion
ΔT_i = incipient boiling superheat temperature
ΔT_{sat} = wall superheat $= (T_w - T_{sat})$
T_{sat} = saturation temperature
T_w = temperature of heater surface or fin base
v_{fg} = latent specific volume change
W = heater width
α = thermal diffusivity of liquid
β = coefficient of expansion of liquid
ν = kinematic viscosity of liquid
σ = surface tension

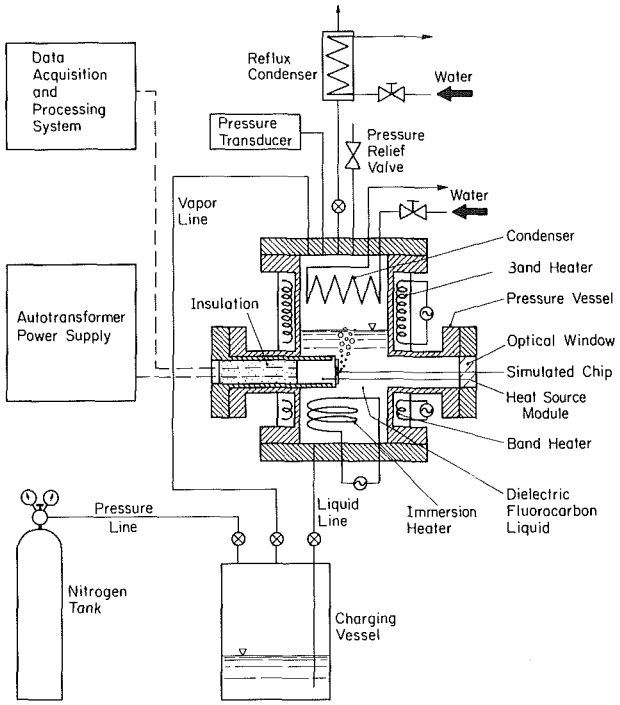

Fig. 2 Schematic of pool boiling facility

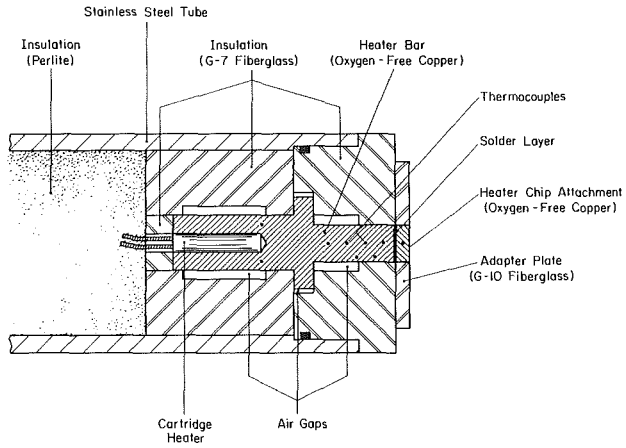

Fig. 3 Sectional diagram of the heat source module

precise control of the temperature and pressure a temperature controller powered an immersion heater located in the liquid pool near the base of the vessel. The bulk fluid temperature was measured by a set of type K thermocouples located below the test surface. Heat was removed from the vessel via a water-cooled condenser coiled within the upper section of the vessel. Combined use of the immersion heater and condenser allowed maintaining the fluid at atmospheric saturated conditions.

Between test runs the test fluid was stored in a charging vessel below the test section. Dry high-pressure nitrogen was employed to drive the stored liquid into the test chamber prior to each test. Deaeration of the fluid to remove entrained gases was performed within the test vessel by vigorous boiling for 30 min. The reflux condenser above the vessel recovered escaping FC-72 vapor and returned it directly to the test vessel. Danielson et al. (1987) employed a gas chromatographic technique to evaluate the effectiveness of this deaeration procedure on a similar system and found the residual air concentration to be less than 1 percent by volume after 3 min of degassing.

The heat source module, similar to those used by Nakayama et al. (1984) and Park and Bergles (1985), was fabricated from a copper bar, cartridge heater, two G-7 insulating plates, and a mounting tube as shown in Fig. 3. An oxygen-free copper assembly was employed to conduct heat from a Watlow cartridge heater through a calorimeter bar section and into the simulated chip attachment. Insulation and positioning of the copper bar were accomplished by a G-7 fiberglass plastic cap and collar arrangement. The interface between the bar and insulation was sealed with high-temperature silicone RTV. The G-7 cap was fitted within the stainless mounting tube using a Viton O-ring and held against the test vessel pressure by set screws.

Heat flux through the test surface was determined by a combination of electrical and thermal measurements. Power supplied to the cartridge heater by a 0–140 V autotransformer was measured by a Scientific Colombus Exceltronic Watt transducer to determine an electrical flux value within ±0.1 percent uncorrected for heat loss. Four electrically insulated 0.075 mm chromel-alumel wire thermocouples spaced 3.18 mm apart were used to determine the thermal heat flux through the calorimeter section of the copper bar by assuming one-dimensional heat conduction. The thermal conductivity of the copper was 391 W/m•K (±1.2 percent) as determined by the supplier. It was found that a least-squares parabolic fit of the four temperatures showed little nonlinearity. This result confirmed both the low level of heat loss and the validity of the one-dimensional heat flow assumption.

Plotting the percent heat loss (defined as the percent difference between the electrical and thermal flux) versus the electrical power input revealed a smooth function of heat loss with electric power. The low power region of the plot was somewhat scattered due to the limited resoluton of the thermocouples (±0.05°C). These random round-off errors were eliminated by fitting a curve through the data. The empirically derived relationship was then used to correct the electrical flux for heat loss. Thus, the heat flux data presented in this paper correspond to the *thermal flux* corrected only for thermocouple round-off errors. This procedure was utilized for each boiling curve since heat loss is a sensitive function of the detailed boundary conditions of the heater.

Several test conditions were repeated to verify the reproducibility of the data and validate the experimental technique. The variation in data sets was within ±0.05°C at heat fluxes smaller than 1 W/cm^2 and within ±0.1°C at higher heat fluxes.

Enhanced surface boiling chips were directly soldered to the heat source module. An adapter plate was fitted around the chip to provide a surface flush with the face of the chip and to insulate the chip sides. A relatively low temperature (180°C) lead/tin solder gave the best combination of strength, thermal conductivity, and operating temperature range for chip attachment. The thermal capacitance of the heater created a short time delay between the development of the vapor blanket at CHF and the temperature rise at the bond area. This delay allowed the operator to shut off power to the heater prior to melting of the solder.

All augmentation schemes were built upon a standard 4.78-mm-thick base chip with an area of 12.7×12.7 mm^2. A 0.075 mm wire type K thermocouple implanted in the center of the attachment was used to extrapolate an average surface temperature and evaluate the bond effectiveness. Experiments with multiple thermocouples within the chip confirmed numerical predictions that the central location of a single thermocouple bead well represented the average reference base surface temperature.

Three categories of enhanced surfaces were tested: smooth, drilled, and low-profile structures. Geometries were chosen on the basis of simplicity and repeatability, requiring only existing manufacturing technology. Three smooth surfaces were

examined to contrast the effects of surface roughness. A mirror finish was prepared by buffing a milled surface with 12,000 grit lapping compound. A similarly prepared mirror smooth surface was roughened by longitudinal sanding with a 600 grit silicon wet/dry sandpaper to investigate the impact of microscopic grooving of the surface. Examination of the sanded surface under a scanning electron microscope revealed the dense pattern of parallel 0.6–1.0 μm gouges (or scratches) shown in Fig. 4(a). The micrograph also shows a void within the copper that was exposed by machining. Surfaces marred by such void anomalies were not used for testing.

The seemingly random dendritic structure of Fig. 4(b) was the result of vapor blasting a water-base slurry of 12,000 grit silica particles onto a mirror polished surface by means of compressed air. Vapor blasting appears to replace any prior surface roughness such as marks left by polishing or sanding with a homogeneous structure having an effective pore size near 15 μm as determined by the ASTM F-316-80 testing procedure using a Coulter porometer. Cavity size distribution was determined by submerging the surface in a given mass of pressurized liquid and measuring the displacement of liquid toward the surface as more cavities were intruded with liquid with increasing pressure. All drilled and low-profile surfaces were vapor blasted to eliminate variations in surface finish.

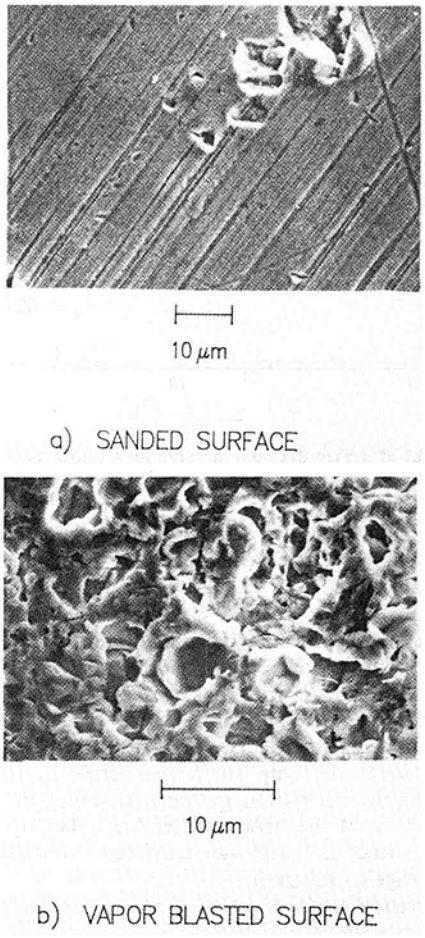

Fig. 4 Scanning electron microscope photographs of surface roughness

The effect of artificial cavities was examined using the three surfaces shown in Fig. 5. A uniform cavity pattern of seventeen 0.36-mm-dia holes on 0.72-mm centers was drilled into a vapor-blasted chip to simulate shallow 0.41-mm-deep artificial cavities. In an attempt to use gravity to aid retention of a stable vapor embryo, the holes of the inclined drill augmentation form a 30-deg angle with the surface.

Three low-profile enhancement structures were used in this study (Fig. 6). The microfin surface was characterized by twenty 0.305-mm-wide vertical fins of 0.508-mm length separated on 0.610-mm centers. This design was based on the enhanced surface geometries of Nakayama et al. (1984). The microstud geometry was formed by modifying a microfin surface with horizontal cross-cuts. Similar in concept to the inclined drill surface, the inclined microgroove was fabricated in an attempt to trap vapor pockets within nine grooves oriented at 30-deg angle to gravity.

The time, temperature, and pressure history prior to boiling was found to be the primary factor affecting the magnitude of incipient boiling hysteresis. To allow comparison of the hysteresis behavior of the various enhanced surfaces, a standardized test procedure was required. Unless otherwise noted, the presented data resulted from the following procedure:

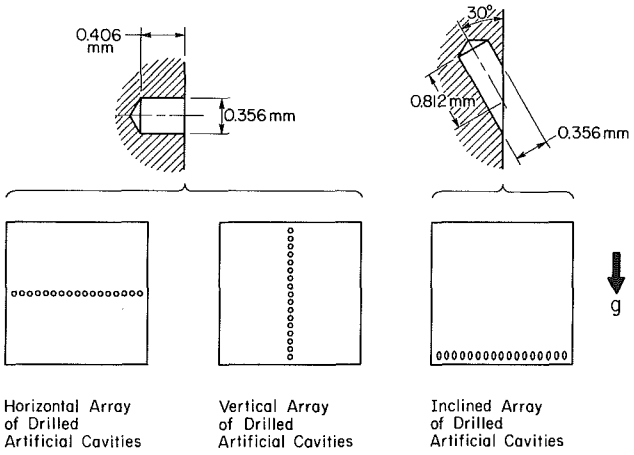

Fig. 5 Artificial cavity configurations

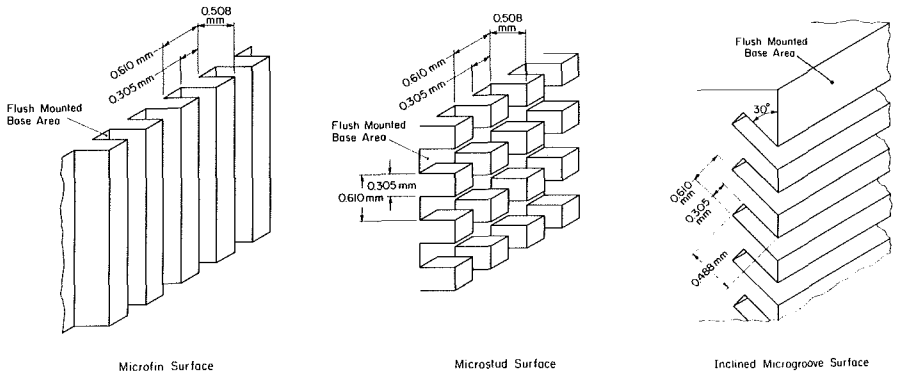

Fig. 6 Low-profile enhancement structures

1 The test chamber was charged then deaerted by 30 min of vigorous boiling at the immersion heater and test surface.

2 The system was closed and the immersion heater brought back to a nonboiling mode to maintain saturated conditions.

3 The test heater was shut off and the system allowed to stabilize for $\Delta t^* = 8$ h.

4 Power was supplied to the test heater in small increments.

5 The test continued to the critical heat flux condition or once within the fully developed region, the power to the heater was gradually decreased, and after waiting at the zero power level for $\Delta t^* = 10$ min, power was again increased toward CHF. The CHF condition was defined by the event where a small increment in power resulted in a rapid and large temperature rise as a film boiling mode was approached. The highest stable heat flux condition attainable prior to this event was designated to be the CHF point.

Results and Discussion

The influences of Δt^*, surface roughness, artificial cavities, and low-profile structures were examined for pool boiling of FC-72 on a vertical surface at atmospheric pressure. The data are presented in the form of heat flux versus wall superheat to allow comparison of such performance parameters as the natural convection heat transfer coefficient, incipience temperature, magnitude of incipience excursion, growth pattern of the boiling region, enhancement of nucleate boiling, and critical heat flux.

Effects of Nonboiling Waiting Period. The results of variations in Δt^*, the nonboiling time interval, were studied with the mirror polished surface to minimize the dependence on surface characteristics. Figure 7 shows natural convection heat transfer was unaffected by the nonboiling time interval, but as Δt^* was increased from 8 to 19 and 72 h, the boiling incipience temperature ΔT_i rose from 15.0 to 23.1 and 30.6°C, respectively. The authors suggest this variation indicates a dependence of boiling incipience on embryo size rather than cavity size for highly wetting fluids such as FC-72. Considering a decreasing flux situation, after an active cavity ceases boiling the vapor embryo shifts from a growth process into a collapsing mode as the vapor condenses into the surrounding liquid. As time progresses, the embryo radius decreases, thereby requiring a greater superheat to resume growing and re-initiate boiling. The data of Marto and Lepere (1982) also indicate the dependence of ΔT_i on the preboiling history. Sabersky and Gates (1955) examined the effect of an embryo-collapsing pressurization treatment and found high incipience temperatures resulted from shrunken vapor embryos.

The magnitude of incipience excursion detected for $\Delta t^* = 8$ and 19 h was less than 1°C but increased to greater than 10°C when the vapor embryos were allowed to shrink for 72 h. Visual observation of the growth patterns of the boiling patch revealed the correlation between the preboiling history with the time rate of change of the boiling area fraction A^*, the incipience superheat ΔT_i, and the incipience excursion ΔT_h. It is proposed that for shorter Δt^* insufficient condensation of the vapor into liquid caused little collapse of vapor embryos, thus allowing initial boiling to begin at modest surface superheat. The total heat transfer was adequately enhanced at the onset of boiling to stabilize the growth of A^*, resulting in gradual departure from the natural convection regime as the initial bubble nucleation front near the top edge of the heater spread slowly downward in response to increasing heat load. On the other hand, the average surface temperature for the longest condensation time examined, $\Delta t^* = 72$, was elevated beyond the $T_w = 85$°C electronic chip junction temperature limit to a point where a chain reaction of activation took place as boiling sites triggered nucleation at neighboring sites in rapid succession. The boiling region spread over approximately 45 percent of the surface within a few milliseconds, consistent with Marto and Lepere's observations of rapid activation on cylindrical commercial surfaces. The number of active sites dropped fourfold as the 10.4°C of excess superheat was reduced by a few seconds of vigorous boiling. The effect of the location of the active sites is evidenced by comparing the $\Delta t^* = 8$ and 19 h curves with the $\Delta t^* = 72$ h curve. Over the 3.5 to 6 W/cm² range of heat flux the $\Delta t^* = 72$ h curve shows marked enhancement because the active boiling sites are well distributed over the chip surface. Therefore, fluid mixing caused by bubble formation and departure may be influencing a large portion of the heat transfer area. The active boiling sites for the other Δt^* tests were confined to a small area near the upper edge of the chip.

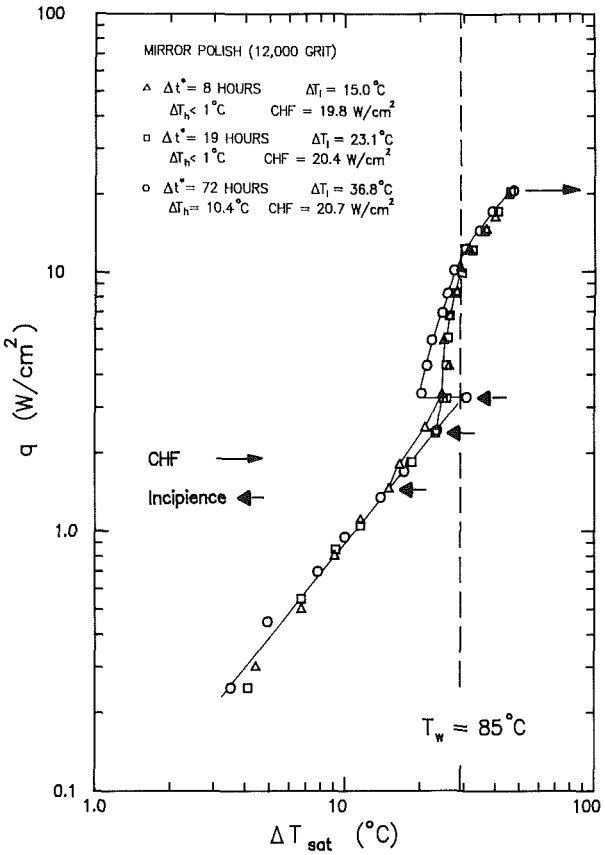

Fig. 7 Effect of Δt^* on the boiling curve for a mirror polished surface

As the mirror surface tests neared fully developed boiling ($q \approx 8$ W/cm²) the boiling curves converged indicating Δt^* affects the boiling performance only in the partially developed nucleate boiling regime. Similarly, identical CHF values were obtained for the three tests.

To facilitate comparison to subsequent tests, it should be noted that the nucleate boiling portion of these curves lay relatively close to the $T_w = 85$°C line and the heat fluxes at that temperature were only half of the peak values.

A strong argument against extending incipience theories based on cavity radius r_{cav} to fluids having very low contact angles can be built upon these incipience results since calculation of ΔT_i based on r_{cav} would predict equal incipience temperature values for each of the three cases shown in Fig. 8.

Effects of Surface Roughness. Surfaces can be characterized on a microscopic scale by determining the effect of roughness on boiling parameters. Comparing the mirror polished, sanded, and vapor blasted enhancements reveals a dependence of incipience temperature, incipience excursion, and nucleate boiling on microcharacteristics of the surface tex-

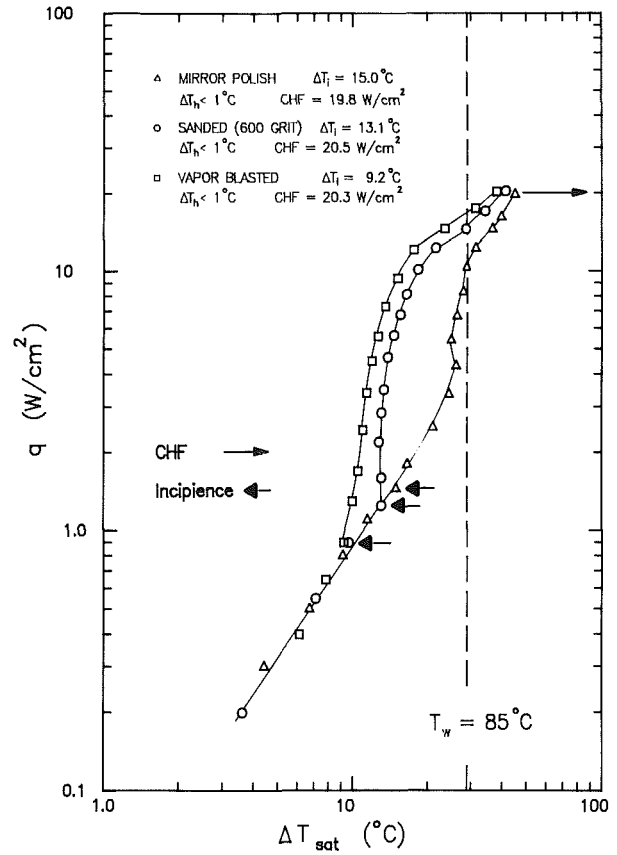

Fig. 8 Effect of surface roughness on the boiling curve for a flat vertical surface

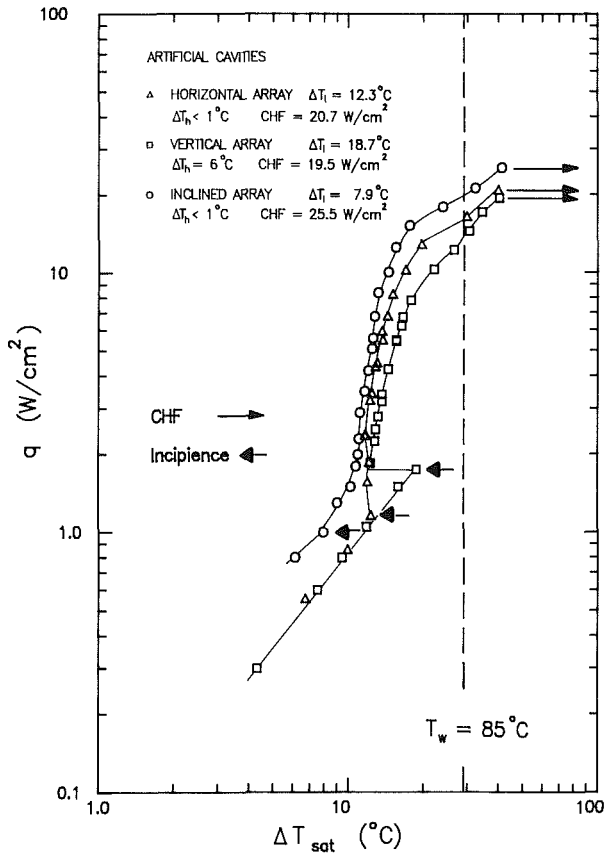

Fig. 9 Effect of artificial cavities on the boiling curve for a flat vertical surface

ture (Fig. 8). Contrasting the single-phase results suggests little effect of microroughness on natural convection; however, subject to equivalent initial conditions, increasing roughness promoted earlier incipience and therefore reduced incipience excursion. The depression of the vapor blasted surface incipience temperature is assumed to be evidence of a connection to embryo stability since within the distribution of the complex cavities on the surface may exist a number of configurations capable of maintaining stable vapor embryos by comparison to the mirror polished surface. In the regime of nucleate boiling, roughness significantly enhanced heat transfer (shifting the curve to the left) indicating a significant increase in the number of active sites at a given heat flux. Messina and Park (1981) reported similar boiling augmentation of R-113 on a copper surface etched with jagged pits or sanded with fine sandpaper. Increased roughness lowered the superheat at CHF, but did not alter the magnitude of CHF noticeably, in contrast to the investigations of Messina and Park (1981), who detected a significant increase in CHF with increased roughness. The surface treatment for the remainder of the surfaces discussed in this paper was vapor blasting. It was chosen for its advantages in controlling hysteresis and augmenting nucleate boiling heat transfer.

Effects of Artificial Cavities. A smooth vapor blasted surface modified by three unique drilled cavity patterns revealed the inability of large cavities to retain vapor embryos of FC-72. However, some amount of control over the propagation of the boiling area can be exercised by proper placement of the cavities. Figure 9 shows that the incipience temperature was most reduced for the inclined array of cavities. Tests were run after $\Delta t^* = 8$ h. Nucleation began near the upper edge of all three enhanced surfaces, not at the cavities, indicating that no moderately sized vapor embryo existed within the drilled holes. As with the smooth vapor blasted surface, the gradual growth of A^* was from top to bottom with increasing flux except for the vertically arrayed surface. Following incipience on the vertical cavity surface, the top cavity began to boil, releasing relatively large bubbles. These bubbles were sufficient in size to activate the hole immediately below it. Within 20 s at the same flux the entire vertical row and surrounding area were completely active, resulting in a 6.0°C surface temperature drop. The cavities of the horizontal and inclined array become active only as the front of the boiling patch passed over them. Despite their relative reluctance to become active before microscopic cavities when heat flux was increased, large cavities were the last to cease boiling as the flux was decreased. Similar to the trend seen for natural convection, nucleate boiling and CHF were most enhanced by the inclined array of artificial cavities. The magnitude of CHF and the associated superheat for the horizontal and vertical cavity arrays were almost identical to that of the plain (nondrilled) vapor blasted surface indicating that these particular cavity patterns had little or no effect on the formation of the vapor blanket. However, the inclined array was successful at increasing the maximum flux by 25 percent through enhancement of the boiling prior to the onset of transition to film boiling. In contrast, experiments with very shallow pits on a mirror surface by Messina and Park (1981) suggest an optimum cavity size and distribution can enhance CHF markedly. Further experimentation with placement and geometry of artificial cavities may result in more precise control of the growth of the active boiling area and enhancement of CHF.

Figure 10 shows a comparison of natural convection data for all the flat surfaces including those with artificial cavities. Except for the inclined cavity array, data for all the flat surfaces seem to follow a unique convection coefficient correlation indicating the weak effect surface roughness, vertical

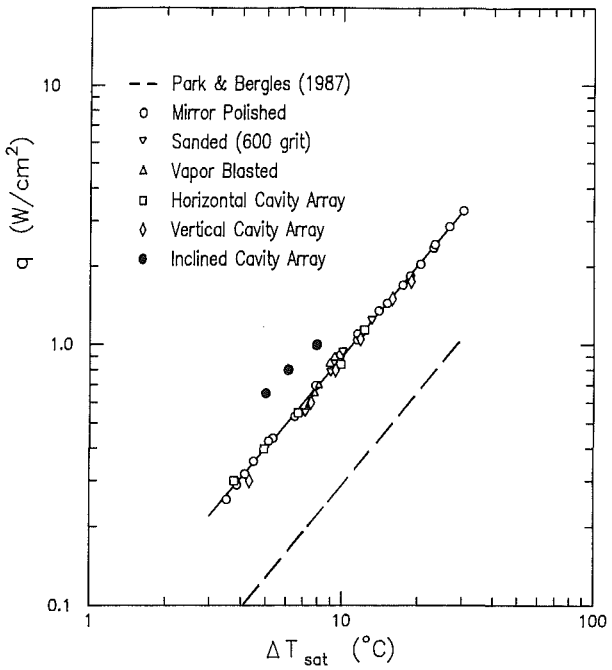

Fig. 10 Comparison of present natural convection data with the correlation of Park and Bergles (1987)

cavities, and horizontal cavities have on natural convection. Inclined cavities showed some enhancement over the other surfaces due, perhaps, to enhanced turbulent activity the orientation of these cavities imposes on vertical fluid motion near the upstream edge of the thermal boundary layer. Also shown in Fig. 10 is the empirical correlation

$$\mathrm{Nu}_c = 0.906\left[1+\frac{0.011}{(W/W_\infty)^{3.965}}\right]^{0.2745}\mathrm{Ra}_c^{*\delta} \tag{4}$$

where

$$\delta = 0.184\left[1+\frac{2.64\times10^{-5}}{(W/W_\infty)^{9.248}}\right]^{-0.0362}$$

$$W_\infty = 70\ \mathrm{mm}$$

developed by Park and Bergles (1987) for natural convection from a small foil heater of height H and width W (typical of electronic chip size) in R-113. The large deviation between the present data and the Park and Bergles correlation can be explained, in part, by the differences in thermal properties between the fluids used in the two studies, and by the fundamental differences in measuring the heat transfer coefficient. Unlike the isothermal surface condition of the present study, Park and Bergles utilized a thin foil heater, which imposed a constant heat flux boundary, and the wall temperature was measured only at the vertical center of the foil. Differences between the two correlations may also be traced back to the different three-dimensional pool geometries surrounding the two types of heater. These geometric effects are believed to influence the natural circulation pattern in the vicinity of the heater.

Effects of Low-Profile Surface Structures. Figures 11 and 12 show that low-profile microfin, microstud, and inclined microgroove structures significantly augment nucleate boiling heat transfer at the expense of increased incipience excursion. Although natural convection for the microfin is more efficient than for the smooth surface (due to the more than doubled surface area), still greater enhancement is caused by the development of *multiple boundary layers* on the lower edges of the microstud structure. Another advantage of the microstud geometry is related to the stagnation of the induced flow caused by the downward-facing sides of the studs. Ap-

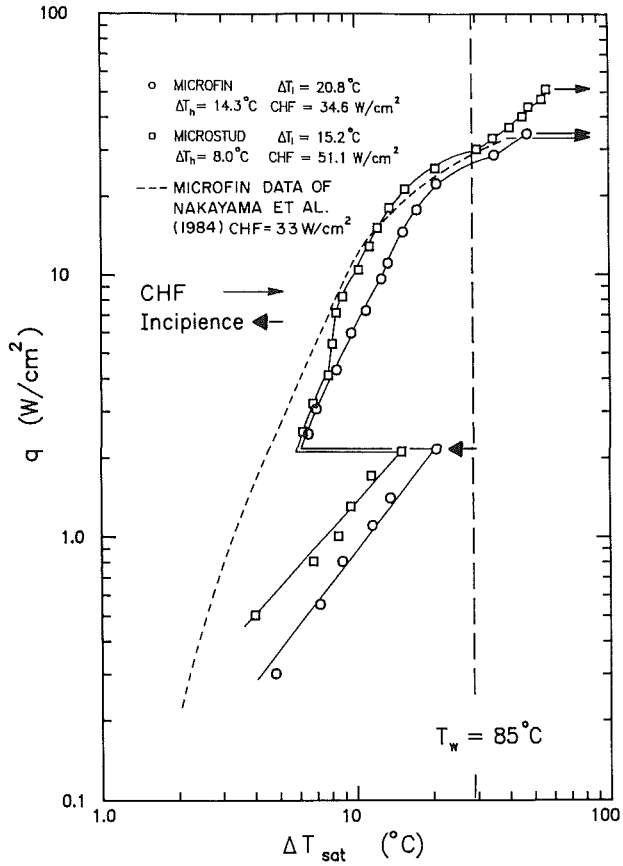

Fig. 11 Effect of microfin and microstud structures on the boiling curve

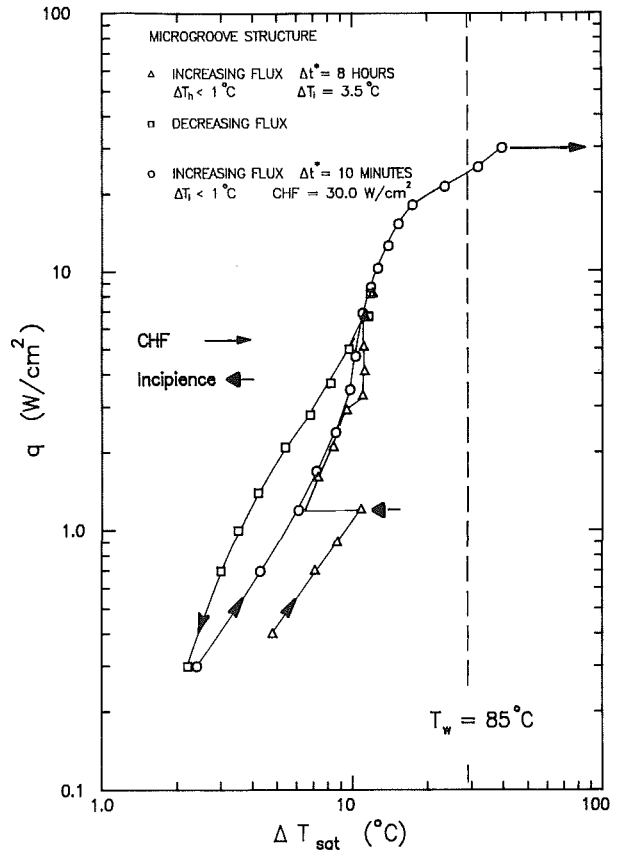

Fig. 12 Effect of inclined microgrooves on the boiling curve

parently the flow is slowed down allowing the liquid to be warmed to a temperature more favorable for activation of a vapor embryo. This effect is most clearly shown in the 5.6°C decrease in incipience temperature for the microstud compared to the microfin surface.

Incipience on the microfin and microstud were accompanied by 14.3 and 8.0°C of incipience excursion, respectively, as large portions of the chips rapidly activated. The quick growth of the boiling patch was caused by the growing bubbles' tendency to move downward along the surface through a combination of attachment to the neighboring studs and dryout of the area between the fins. The extreme levels of boiling enhancement associated with these structures will require significantly higher natural convection heat transfer coefficients to close the gap between the pre-incipience and post-incipience temperatures at typical values of incipient heat flux. Also shown in Fig. 11 are the data obtained by Nakayama for a similar microfin geometry oriented horizontally facing upward. The CHF values are close (33 versus 34.6 W/cm^2) but the horizontal orientation appears to enhance the nucleate boiling heat transfer slightly. However, the microstud surface resulted in a much higher CHF value of 51.1 W/cm^2. Comparison of the incipience performance of the two orientations is difficult since the Δt^* values of Nakayama's experiments were not reported; however, data taken with the vertical microfin after a short Δt^* period (10 min) display low incipience flux and temperature.

Multiple traverses of the inclined microgroove surface boiling curve (Fig. 12) show the dependence of curve hysteresis on Δt^*. The incipience temperature was further depressed compared to the microstud surface since stagnant pockets of warmed fluid were trapped within the grooves. The irregular shape of the inclined microgroove nucleate boiling curve is believed to be a product of the bubble activation pattern. As the initial bubble grew, they coalesced together very rapidly and activated the entire surface of the groove. The initial boiling from the uppermost groove was passed down to the next two grooves similar to the migration of activation seen with the vertical array of artificial cavities. The sudden jump in A^* resulted in a 3.5°C surface temperature drop. Further activation was more gradual as flux was increased to the fully developed region. Decreasing the heat flux revealed an additional augmentation in the heat transfer at lower power levels compared to the case of increasing heat flux as the majority of the grooves remained boiling. Very low values of the boiling cessation flux and superheat were echoed by low values at incipience as the heat flux was increased after 10 min of nonboiling. The third traverse of the boiling curve fell between the first two until a convergence at the point of fully developed boiling ($q \approx 8$W/cm^2) occurred. The lack of protruding structures to influence the onset of burnout explains the moderate peak flux, CHF = 39.8 W/cm^2.

The microfin and microstud surfaces experienced similar trends to the boiling curve when subjected to multiple traverses of the boiling curve with Δt^* first fixed at 8 h and then at 10 min.

Summary

This study was conducted to gain a good understanding of the trends associated with pool boiling of FC-72 on a vertical surface. Specific conclusions for the design of direct immersion electronic cooling packages are as follows:

1 Common incipience theories based on cavity radius do not apply to highly wetting fluids such as FC-72. Incipience is sensitive to the value of the effective radius of vapor embryos existing within the surface; however, that radius may be a very complex function of surface microstructure and the temperature/pressure history prior to boiling.

2 Increasing the nonboiling waiting period appears to increase the incipience temperature and incipient excursion.

3 Artificial cavities on the order of 0.3 mm diameter are ineffective in lowering the incipience temperature, enhancing nucleate boiling, or increasing CHF.

4 Microstructures significantly shift the boiling curve toward lower superheats while increasing the incipience excursion.

5 The maximum heat flux is a function of surface geometry and orientation but independent of initial conditions, surface roughness, or the presence of large artificial cavities. The microstud surfaces provided CHF values in excess of 50 W/cm^2.

Acknowledgments

Support of this work by a grant from the IBM Corporation is gratefully acknowledged. The assistance of Mr. Richard C. Chu, Mr. Robert E. Simons, and Dr. Dereje Agonafer of IBM is appreciated. The authors also thank Mr. R. D. Danielson of the Industrial Chemical Products Division of 3M for providing fluid samples and technical information on the test fluid.

References

Bar-Cohen, A., and Simon, T. W., 1986, "Wall Superheat Excursions in the Boiling Incipience of Dielectric Fluids," *Heat Transfer in Electronic Equipment*, A. Bar-Cohen, ed., ASME HTD-Vol. 57, pp. 83–94.

Blander, M., and Katz, J. L., 1975, "Bubble Nucleation in Liquids," *AIChE Journal*, Vol. 21, pp. 833–848.

Danielson, R. D., Tousignant, T., and Bar-Cohen, A., 1987, "Saturated Pool Boiling Characteristics of Commercially Available Perfluorinated Inert Liquids," *Proceedings of the 1987 ASME-JSME Thermal Engineering Joint Conference*, Honolulu, HI, Vol. 3, pp. 419–430.

Davis, E. J., and Anderson, G. H., 1966, "The Incipience of Nucleate Boiling in Forced Convection Flow," *AIChE Journal*, Vol. 12, pp. 774–780.

Han, C. Y., and Griffith, P., 1965, "The Mechanism of Heat Transfer in Nucleate Pool Boiling," *International Journal of Heat and Mass Transfer*, Vol. 8, pp. 887–903.

Hsu, Y. Y., 1962, "On the Size Range of Active Nucleation Cavities on a Heating Surface," ASME Journal of Heat Transfer, Vol. 84, pp. 207–216.

Hui, T. O., amd Thome, J. R., 1985, "A Study of Binary Mixture Boiling: Boiling Site Density and Subcooled Heat Transfer," *International Journal of Heat and Mass Transfer*, Vol. 28, pp. 919–928.

Marto, P. J., and Lepere, V. J., 1982, "Pool Boiling Heat Transfer From Enhanced Surfaces to Dielectric Fluids," ASME Journal of Heat Transfer, Vol. 104, pp. 292–299.

Messina, A. D., and Park, E. L., 1981, "Effects of Precise Arrays of Pits on Nucleate Boiling," *International Journal of Heat and Mass Transfer*, Vol. 24, pp. 141–145.

Nakayama, W., Nakajima, T., and Hirasawa, S., 1984, "Heat Sink Studs Having Enhanced Boiling for Cooling of Microelectronic Components," ASME Paper No. 84-WA/HT-89.

Park, K. A., and Bergles, A. E., 1985, "Heat Transfer Characteristics of Simulated Microelectronic Chips Under Normal and Enhanced Conditions," Iowa State College of Engineering Interim Technical Report HTL-35, submitted to IBM Data Systems Division.

Park, K. A., and Bergles, A. E., 1986, "Boiling Heat Transfer Characteristics of Simulated Microelectronic Chips With Detachable Heat Sinks," *Proceedings of the Eighth International Heat Transfer Conference*, San Francisco, CA, Vol. 4, pp. 2099–2104.

Park, K. A., and Bergles, A. E., 1987, "Natural Convection Heat Transfer Characteristics of Simulated Microelectronic Chips," ASME Journal of Heat Transfer, Vol. 109, pp. 90–96.

Ramadhyani, S., and Incropera, F. P., 1987, "Forced Convection Cooling of Discrete Heat Sources With and Without Surface Enhancement," *Proceedings of the International Symposium on Cooling Technology for Electronic Equipment*, Honolulu, HI, pp. 249–264.

Sabersky, R. H., and Gates, C. W., 1955, "On the Start of Nucleation in Boiling Heat Transfer," *Jet Propulsion, Journal of the American Rocket Society*, Vol. 25, pp. 67–70.

Tuckerman, D. B., and Pease, R. F. W., 1981, "High-Performance Heat Sinking for VLSI," *Electronic Device Letters*, EDL-2, pp. 126–129.

The Effect of Surface Motion on Forced Convection Film Boiling Heat Transfer

D. A. Zumbrunnen[1]

R. Viskanta

F. P. Incropera

Heat Transfer Laboratory,
School of Mechanical Engineering,
Purdue University,
West Lafayette, IN 47907

The growth in demand for high-quality metallic alloys has placed greater emphasis on the predictability of cooling methods used in manufacturing processes. Several methods involve forced convection film boiling, which can occur on metallic strips or plates cooled by water jet impingement or on strips inside cooling jackets of continuous annealing processes. Since surface temperatures are typically well above the boiling point of water, a substantial portion of the surface area can involve film boiling. The strip or plate speed often exceeds the water velocities and strongly influences boundary layer development in the vapor and liquid. The purpose of this paper is to estimate the effect of plate motion on heat transfer in the film boiling regime. Conservation equations for mass, momentum, and energy have been solved by the integral method for film boiling in forced convection boundary layer flow on a flat isothermal plate in motion parallel to the flow direction. Unlike previous studies, which have shown that heat transfer is chiefly governed by the plate and subcooled liquid temperatures, heat transfer is shown to also depend on the plate velocity. For large velocities, the importance of radiation heat transfer across the vapor layer is reduced. However, when the velocities of the plate and liquid are oppositely directed and of nearly equal magnitude, radiation across the vapor layer can become significant, even at low plate temperatures.

Introduction

In order to improve process control and product quality, increasing attention is being given to the development of accurate methods for predicting the thermal response of materials to cooling methods used in their manufacture. A good example is the hot rolling process in which a series of counterrotating cylindrical rollers (Fig. 1(*a*)) reduces a steel strip to its final thickness (McGannon, 1971). For low-carbon steels, rolling usually begins at about 1200°C and is completed well above 723°C, below which ferrite and iron carbide are formed. After rolling, the strip is typically cooled along a runout table by jets of water to about 650°C and is subsquently directed to a coiler. Coiling at this temperature preserves a fine ferritic grain size by limiting self-annealing in the roll. In addition to greater strength, smaller grain size improves weldability by allowing lower carbon alloys to be used, which in turn reduces the formation of iron carbide.

The mechanical properties of cold rolled steel are also affected by cooling methods used along the runout table, since the surface finish and thickness tolerance of a strip from the hot rolling mill are improved by cold rolling. Properties of cold rolled strip can be altered by using the continuous annealing process shown in Fig. 1(*b*). A strip moving at high speed is heated to permit recrystallization and is rapidly cooled by direct contact with a flowing liquid inside a compact heat exchanger. The strip is directed back and forth to accommodate a long length of strip inside the jacket.

Temperatures in the foregoing processes are high enough for film boiling to occur (Collier, 1981). Hence, it is useful to consider how film boiling can arise adjacent to an impinging planar jet on a stationary plate, since the mechanisms are similar to those on moving plates. This configuration is of primary concern to hot strips on runout tables, where planar jets of low turbulence water span the entire width of the strips. The jets provide uniform, controllable, and effective cooling, since splashing is minimized and contact of water with the strip is improved. Kohring (1985) cited measurements of cooling efficiencies in terms of heat removed per volume of water expended. He showed that planar jets are about 48 percent more efficient than circular jets in removing heat from a strip at 900°C and traveling at 10 m/s.

The relative locations of the anticipated heat transfer regimes are depicted in Fig. 2. Beneath the jet and extending several jet widths, heat transfer is by single-phase forced con-

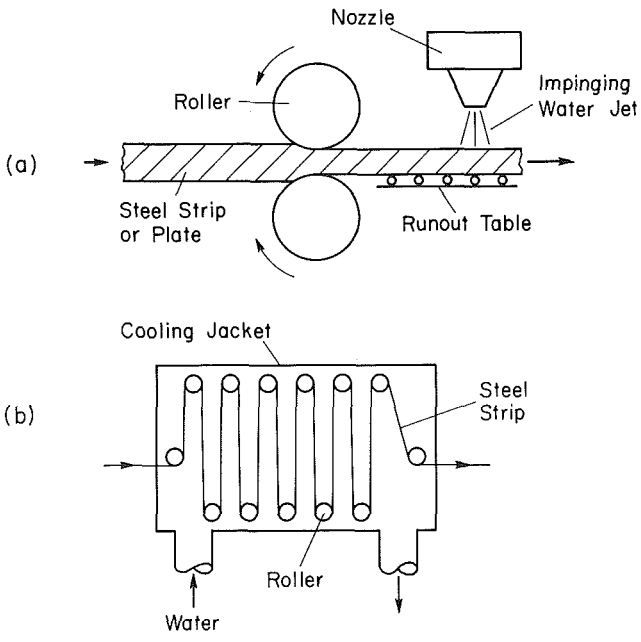

Fig. 1 Examples of forced convection film boiling on moving surfaces: (*a*) cylindrical rollers acting on hot plastic steel of rectangular cross section prior to cooling by jets of water, and (*b*) continuous annealing of cold rolled strip

[1]Currently with Department of Mechanical Engineering, Clemson University, Clemson, SC 29634.

Contributed by the Heat Transfer Division and presented at the ASME Winter Annual Meeting, Boston, Massachusetts, December 13–18, 1987. Manuscript received by the Heat Transfer Division May 10, 1988. Paper No. 87-WA/HT-5. Keywords: Boiling, Forced Convection, Materials Processing and Manufacturing Processes.

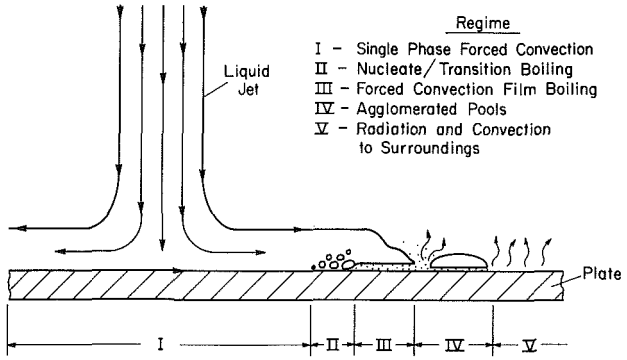

Fig. 2 Anticipated heat transfer regimes adjacent to an impinging jet on a stationary plate (note: lengths for each regime are not necessarily to scale)

vection. In this zone (region I), the cooling effectiveness of the jet is very high and the surface temperature is too low for boiling. Away from the stagnation streamline, the water near the plate is heated and the cooling effectiveness of the jet diminishes. The plate's surface temperature increases and the onset of boiling is eventually reached. A comparatively narrow region (II) of nucleate and transition boiling may separate region I from region III, where forced convection film boiling occurs. Eventually, water overriding the vapor layer agglomerates into pools (region IV) due to surface tension effects and a significant fraction of the surface is left void of liquid and vapor. Heat transfer occurs by convection and radiation beneath the pools and principally by radiation to the surroundings from the unwetted surface. The pools migrate in a random-walk fashion until they either evaporate or are lost at the edge of the plate. In region V, heat transfer occurs by radiation and convection from the dry plate to the surroundings. This description is consistent with observations made by Kokado et al. (1984) for a stationary plate cooled from 900°C by a circular water jet.

If the plate in Fig. 2 is made to move to the right, the thickness of the vapor layers beneath the pools and in the film boiling regime would decrease since vapor flow would be promoted by the plate motion. However, if the plate moves to the left with sufficient velocity, the vapor layer thickness may increase since vapor can be drawn *toward* the jet by the plate motion. Of course, both cases can occur simultaneously on moving strips or plates since an impinging jet divides on their surfaces.

Numerous studies of forced convection film boiling have been performed. Motte and Bromley (1957) experimentally studied the effects of subcooling on heat transfer from horizontal tubes in a turbulent flow. Nusselt numbers increased markedly with subcooling and approached those for nucleate boiling. Cess and Sparrow (1961a, 1961b) performed similarity analyses for forced film boiling in saturated and subcooled liquids on stationary isothermal plates. Their results also showed large increases in Nusselt number with increasing subcooling. They demonstrated that, if radiation across the vapor is neglected and the liquid is saturated, the Nusselt number decreases as the wall temperature is raised.

Radiation across the vapor film can be significant when the surface temperature is high. Sparrow (1964) considered separately cases where the vapor was both radiatively participating and nonparticipating in laminar film boiling by natural convection on a vertical isothermal plate immersed in a saturated liquid. Advection terms for energy transport were ignored, since they were deemed negligible relative to conduction across the vapor. In the nonparticipating case, the plate and vapor/liquid interface were treated as diffuse/gray parallel surfaces. In the participating case, the radiation term in the energy equation for the vapor was assumed to correspond to that for an optically thin vapor. Sparrow concluded that the effect of a radiatively participating steam vapor is "fully negligible" for pressures up to at least 10 atm.

The objective of this study is to assess the importance of surface motion on heat transfer by forced convection film boiling. Although heat is more effectively removed by single-phase forced convection near impinging jets, the film boiling region can span more than 50 jet widths on a strip in a hot rolling mill. Hence, reliable models are needed in order to determine the cooling of strips and plates in this regime.

Nomenclature

c_p = specific heat at constant pressure
h = heat transfer coefficient
h_c = convective heat transfer coefficient in the presence of radiation across vapor layer
h_{co} = convective heat transfer coefficient without radiation
h_{fg} = latent heat of vaporization
h_R = radiation heat transfer coefficient
h_T = total heat transfer coefficient $= h_c + h_R$
Ja = Jakob number $= c_{pv}(T_p - T_s)/h_{fg}$
k = thermal conductivity
L = plate length or length for film boiling
Nu_x = Nusselt number $= h_{co}x/k_v$
Nu_* = ratio of Nusselt number for moving plate to Nusselt number for stationary plate $= (\mathrm{Nu}_x\mathrm{Re}_x^{-1/2}\,\mu_v/\mu_l) / (\mathrm{Nu}_x\mathrm{Re}_x^{-1/2}\,\mu_v/\mu_l)|_{v=0}$
Pr = Prandtl number $= \mu c_p/k$
q = heat flux
Re_x = Reynolds number for liquid $= \rho_l u_\infty x/\mu_l$
T = temperature
u = x component of velocity
u_s = x component of velocity for vapor/liquid interface
$\bar{u}_s$ = velocity ratio $= u_s/u_\infty$
v_p = velocity of plate
$\bar{v}$ = velocity ratio $= v_p/u_\infty$
w = mass flow per unit width of plate
x = streamwise coordinate (Fig. 3)
y = vertical position above plate (Fig. 3)
y_1 = vertical position above vapor layer $= y - \delta_v$
Z = density-viscosity product ratio $= \rho_l\mu_l/\rho_v\mu_v$
β = subcooling parameter $= \mathrm{Pr}_v c_{pl}(T_s - T_\infty) / \mathrm{Pr}_l c_{pv}(T_p - T_s)$
Γ = boundary layer thickness ratio $= \Delta/\delta$
δ = velocity boundary layer thickness in liquid
δ_v = vapor layer thickness
Δ = thermal boundary layer thickness in liquid
ϵ = emissivity
η = dimensionless vertical coordinate $= y_1/\delta$
μ = dynamic viscosity
ρ = mass density
σ = Stefan–Boltzmann constant
Σ = dimensionless vertical coordinate $= y_1/\Delta$
τ_{yx} = shear stress $= \mu\,\partial u/\partial y$
Φ = parameter defined by equation (23)

Subscripts

av = average value
l = liquid
p = plate
s = vapor/liquid interface
v = vapor
y = y direction
∞ = liquid free stream

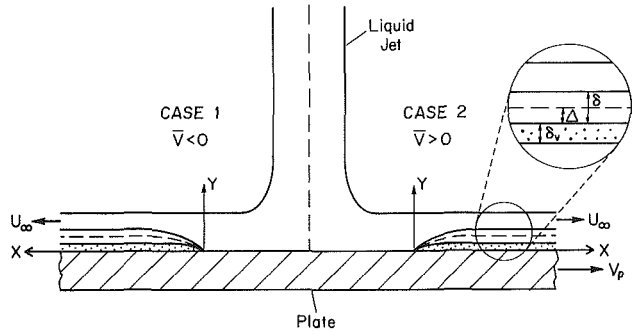

Fig. 3 Boundary layer development for forced convection film boiling adjacent to an impinging jet on a moving plate

Analysis

Rao and Prasad (1983) compared their integral solution for heat transfer due to forced convection film boiling over a flat stationary plate to a solution numerically generated by Ito and Nishikawa (1966). Differences between the solutions were indiscernible, leading Rao and Prasad to conclude that the integral solution provided an accurate analytical method for film boiling. An integral method was therefore utilized, with the realization that the accuracy of a film boiling model is necessarily limited by simplifying assumptions.

The integral method applied in this study was a generalization of one described by Arpaci and Larson (1984). The analysis is applied to boundary layers in the vapor and liquid adjacent to a jet impinging on a moving plate (Fig. 3). The point of vapor formation, which was fixed, served as the origin to the coordinate system and was sufficiently removed from the stagnation region where the free-stream velocity in the liquid is constant. In case 1, the plate's velocity is opposite to that of the liquid, while in case 2, the plate and liquid travel in the same direction. The bulk vapor and liquid flows can be oppositely directed in case 1 if the plate speed approaches or exceeds the jet impingement velocity. The vapor layer may form at the beginning of the agglomerated pool zone of Fig. 2, develop toward the jet, and terminate when the plate temperature near the jet decreases below the Leidenfrost point.

Nonuniform plate temperature and vapor collapse near the jet due to flow reversal are complications of case 1 that were not considered in this study. The model that follows pertains to case 1 only when the plate speed is sufficiently small to preclude reversal of the bulk vapor flow. Under these conditions the boundary layer equations are applicable. Moreover, a constant plate temperature is used over the film boiling regime due to the relatively small values of the associated heat transfer coefficients.

Instabilities in the vapor/liquid interface can arise due to the greater density of the liquid overriding the vapor in the presence of a gravitational field. The importance of these Taylor–Helmholtz instabilities (Berenson, 1961) is unknown when the flow velocity and plate temperature are high, as in the present case. For example, the waviness in the interface arising from the instabilities may be reduced by vaporization occurring preferentially whenever the liquid approaches the plate surface. This effect is enhanced at higher flow velocities and plate temperatures since heat transfer across the vapor layer is increased. Consequently, owing to the uncertain importance of interface instability and in order to simplify the analysis, the vapor/liquid interface is modeled as a smooth boundary with no waviness, as depicted in Fig. 3.

Further simplification is realized by considering only the case where the vapor and liquid flows are laminar. Thus, the analysis applies to locations prior to the point where turbulence begins in either the vapor or liquid. Unfortunately, appropriate transition criteria are not yet available for the complicated flow considered here. However, it is reasonable to expect that a fraction of the affected area adjacent to an impinging laminar jet will pertain to laminar flow, so long as the distance between the jet's stagnation point and the point where film boiling begins is not large.

The specific assumptions of the analysis are: (*i*) steady flow with u_∞ = const, (*ii*) constant thermophysical properties, (*iii*) negligible viscous heating, (*iv*) $\mathrm{Pr}_l \geq 1$, (*v*) negligible body forces in comparison to viscous forces, (*vi*) laminar, incompressible flow, (*vii*) negligible vapor loss from the vapor layer, (*viii*) a radiatively nonparticipating vapor layer, and (*ix*) opaque, diffuse/gray liquid and plate surfaces. Thermophysical properties are evaluated at the film temperature $T_f = (T_1 + T_2)/2$, where T_1 and T_2 are the temperatures across the boundary layer in the liquid or vapor.

An analysis was performed to validate assumption (*viii*) by determining whether the vapor can be regarded as radiatively nonparticipating in forced convection film boiling. The vapor was modeled as an optically thin planar layer (Cess, 1964). Volumetric absorption and emission by the vapor were found to be small for the temperatures and surface emissivities associated with the manufacture of steel strips and plates. The error in the heat flux predicted at the vapor/liquid interface caused by neglecting absorption and emission was less than 5 percent for a plate temperature of 1000°C. Smaller errors were associated with the heat flux predicted at the plate's surface. Hence, assumption (*viii*) was considered to be appropriate.

The mass vaporization rate of liquid per unit plate width w_s is related to the mass flow in the vapor layer by the expression

$$w_s = \frac{d}{dx}\int_0^{\delta_v} \rho_v u_v dy \tag{1}$$

Conservation of momentum and energy in the vapor and liquid layers of Fig. 3 may then be expressed as

$$\frac{d}{dx}\int_0^{\delta_v} \rho_v u_v^2 dy - w_s u_s = \tau_{yx}|_{y=\delta v} - \tau_{yx}|_{y=0} \tag{2}$$

$$\frac{d}{dx}\int_0^{\delta_v} \rho_v c_{pv} u_v (T_v - T_s) dy = q_y|_{y=0} - q_y|_{y=\delta v} \tag{3}$$

$$\frac{d}{dx}\int_0^{\delta} \rho_l u_l (u_\infty - u_l) dy_1 + (u_\infty - u_s) w_s = \tau_{yx}|_{y_1=0} \tag{4}$$

$$\frac{d}{dx}\int_0^{\Delta} \rho_l c_{pl} u_l (T_l - T_\infty) dy_1 + c_{pl}(T_s - T_\infty) w_s = q_y|_{y_1=0} \tag{5}$$

It is of interest to note that, even when thermophysical properties are independent of temperature, the conservation equations for energy and momentum in the vapor and liquid are coupled, since the velocity of the vapor/liquid interface depends on the vaporization rate.

The conservation equations are subject to conditions at the plate surface, the vapor/liquid interface, and the extremities of the liquid thermal and velocity boundary layers.

Plate surface ($y = 0$):

$$u_v = v_p \tag{6a}$$

$$T_v = T_p \tag{6b}$$

Vapor/liquid interface ($y = \delta_v$ *or* $y_l = 0$):

$$u_v = u_s \tag{7a}$$

$$T_v = T_s \tag{7b}$$

$$u_l = u_s \tag{8a}$$

$$T_l = T_s \tag{8b}$$

Edge of thermal boundary layer in liquid ($y_l = \Delta$):

$$T_l = T_\infty \tag{9a}$$

$$\frac{\partial T_l}{\partial y_1} = 0 \tag{9b}$$

Edge of velocity boundary layer in liquid ($y_l = \delta$):

$$u_l = u_\infty \tag{10a}$$

$$\frac{\partial u_l}{\partial y_1} = 0 \tag{10b}$$

Additional relationships are obtained by imposing force and energy balances at the vapor/liquid interface.

$$\mu_v \frac{\partial u_v}{\partial y}\Big|_{y=\delta v} = \mu_l \frac{\partial u_l}{\partial y_1}\Big|_{y_1=0} \tag{11}$$

$$w_s h_{fg} = -k_v \frac{\partial T_v}{\partial y}\Big|_{y=\delta v} + k_l \frac{\partial T_l}{\partial y_1}\Big|_{y_1=0} + q_R \tag{12}$$

In accordance with assumption (*ix*), the radiation heat flux q_R across the vapor layer is (Sparrow, 1964)

$$q_R = h_R (T_p - T_s) \tag{13a}$$

where

$$h_R = \left[\frac{\epsilon_p \epsilon_s}{\epsilon_p + \epsilon_s - \epsilon_p \epsilon_s}\right]\left[\frac{\sigma(T_p^4 - T_s^4)}{T_p - T_s}\right] \tag{13b}$$

Ordinary nonlinear differential equations for δ_v, δ, and Δ can be obtained by solving the foregoing equations subject to prescribed expressions for the velocity and temperature profiles. Cess and Sparrow (1961a) showed that the temperature and velocity profiles in the vapor are nearly linear for stationary plates when $\mathrm{Ja}/\mathrm{Pr}_v \ll 30$ and $\mathrm{Ja} \ll 12$, respectively. Since most vapors (and notably water vapor) have $\mathrm{Pr}_v \approx 1$ and $\mathrm{Ja} \lesssim 1$ for most applications, both conditions are frequently satisfied. The validity of this assumption is enhanced by conditions for which the velocity difference across the vapor layer is large. Assuming linear profiles in the vapor layer, the boundary conditions given by equations (6) and (7) give

$$\frac{u_v - v_p}{u_s - v_p} = \frac{y}{\delta_v} \tag{14}$$

and

$$\frac{T_v - T_s}{T_p - T_s} = 1 - \frac{y}{\delta_v} \tag{15}$$

Second-degree polynomials are prescribed for the velocity and temperature profiles in the liquid subject to conditions given by equations (8), (9), and (10).

$$\frac{u}{u_\infty} = (1 - \bar{u}_s)(2\eta - \eta^2) + \bar{u}_s \tag{16}$$

$$\frac{T - T_\infty}{T_s - T_\infty} = (\Sigma - 1)^2 \tag{17}$$

The resulting system of differential equations obtained from equations (1), (4), and (5) is

$$w_s = \frac{1}{2} \rho_v u_\infty \frac{d}{dx}[(\bar{u}_s + \bar{v})\delta_v] \tag{18}$$

$$\frac{2}{15}\frac{\delta}{(1-\bar{u}_s)}\frac{d}{dx}[\delta(1-\bar{u}_s)(1+3\bar{u}_s/2)] + \frac{\delta}{2}\frac{\rho_v}{\rho_l}\frac{d}{dx}[(\bar{u}_s + \bar{v})\delta_v] = \frac{2\mu_l}{\rho_l u_\infty} \tag{19}$$

$$\Delta \frac{d}{dx}\left[(1-\bar{u}_s)\left(\frac{\Delta^2}{6\delta} - \frac{\Delta^3}{30\delta^2}\right) + \frac{\bar{u}_s \Delta}{3}\right] + \frac{1}{2}\frac{\rho_v}{\rho_l}\Delta \frac{d}{dx}[(\bar{u}_s + \bar{v})\delta_v] = \frac{2k_l}{\rho_l c_{pl} u_\infty} \tag{20}$$

The vapor layer thickness δ_v is related to δ by equation (11), which with equations (14) and (16) gives

$$\frac{\delta_v}{\delta} = \frac{\mu_v}{2\mu_l}\frac{(\bar{u}_s - \bar{v})}{(1 - \bar{u}_s)} \tag{21}$$

In order to solve equations (18), (19), and (20), it is necessary to assume that the dimensionless interface velocity $\bar{u}_s$ ($= u_s/u_\infty$) and the boundary layer thickness ratio Γ ($= \Delta/\delta$) are constants. These assumptions are mathematically valid when $q_R = 0$, although the resulting solutions will be subsequently modified to include radiation. Physically, the assumptions are plausible, since for $\mathrm{Pr}_l = 1$, $\Delta = \delta$ and it can be shown that equations (19) and (20) are identical, in accordance with the Reynolds analogy, only when $\bar{u}_s$ is constant. Equations (19) and (21) yield an ordinary differential equation for $\delta(x)$ which, for $\delta(x=0) = 0$, has the solution

$$\delta(x) = \left[\frac{30\mu_l x}{\rho_l u_\infty \Phi}\right]^{1/2} \tag{22}$$

where

$$\Phi = 1 + \frac{3}{2}\bar{u}_s + \frac{15}{8Z}\left[\frac{\bar{u}_s^2 - \bar{v}^2}{1 - \bar{u}_s}\right] \tag{23}$$

In equation (23), $\bar{u}_s$, $\bar{v}$, and Z are constants related to the momentum transfer between the vapor and liquid.

Expressions relating Γ and $\bar{u}_s$ are found from equation (12) with $q_R = 0$ and equations (20) and (22),

$$\frac{\Gamma \mathrm{Pr}_l}{8\Phi} = \left[2(1-\bar{u}_s)\Gamma^2(5-\Gamma) + 20\Gamma\bar{u}_s + \frac{15}{Z}\frac{(\bar{u}_s^2 - \bar{v}^2)}{(1-\bar{u}_s)}\right]^{-1} \tag{24}$$

$$\frac{15}{8\Phi}\frac{\mathrm{Pr}_v}{\mathrm{Ja}Z}(\bar{u}_s + \bar{v})\left[\frac{\bar{u}_s - \bar{v}}{1 - \bar{u}_s}\right]^2 = 1 - \frac{\beta(\bar{u}_s - \bar{v})}{\Gamma(1 - \bar{u}_s)} \tag{25}$$

The local Nusselt number referenced to the temperature difference across the vapor is then

$$\mathrm{Nu}_x = \frac{h_{co} x}{k_v} = \left(\frac{2\Phi}{15}\right)^{1/2}\frac{\mu_l}{\mu_v}\frac{(1-\bar{u}_s)}{(\bar{u}_s - \bar{v})}\mathrm{Re}_x^{1/2} \tag{26}$$

where h_{co} is the convective heat transfer coefficient when radiation across the vapor is negligible. Specific values of $\bar{u}_s$ and Γ can be found from equations (23), (24), and (25) with a root-solving method once Pr_v, Pr_l, Ja, Z, and β are specified. (This approach is consistent with the earlier assumption that $\bar{u}_s$ and Γ are constants.) Calculated values of $\mathrm{Nu}_x \mu_v / \mu_l \mathrm{Re}_x^{1/2}$ were compared to those given by an existing similarity solution (Cess and Sparrow, 1961) for forced convection film boiling on a stationary isothermal plate in a saturated liquid ($\beta = 0$) with negligible radiation across the vapor layer. The values agreed to within 0.5 percent for $6.25 \le \mathrm{Ja}Z/\mathrm{Pr}_v \le 7610$.

Bromley (1950) included the effect of radiation in natural convection film boiling from horizontal tubes by using an approximate method that has since been widely used and shown to provide good results (Sparrow, 1964; Collier, 1981; Shigechi et al., 1984). In order to include radiation effects in this study, an analogous method is introduced for forced convection film boiling on a plate. In particular, an average *total* heat transfer coefficient across the vapor is defined as $(h_T)_{av} = (h_c + h_R)_{av}$, where an average heat transfer coefficient is related to the local value by $h_{av} = (\int_0^L h\, dx)/L$. For a linear temperature profile in the vapor, $(h_c)_{av} \propto 1/\delta_v$. If the heat transfer to the liquid is small, the vapor mass flow rate w_v is proportional to the vaporization rate. Hence, $w_v \propto (h_T)_{av}$ and since $w_v \propto \delta_v$ for a linear velocity profile in the vapor, $(h_c)_{av} \propto (1/h_T)_{av}$. If $(h_{co})_{av}$ is approximately constant (e.g., far from $x = 0$), the following relationship can be formed by noting that $(h_c)_{av} = (h_{co})_{av}$ when $h_R = 0$:

$$\left(\frac{h_{co}}{h_c}\right)_{av} = \left(\frac{h_c + h_R}{h_{co}}\right)_{av} \tag{27}$$

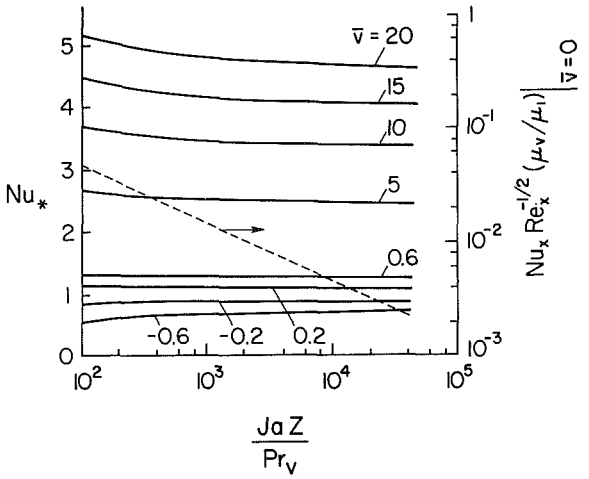

Fig. 4 Ratio of Nusselt number for moving plate to Nusselt number for stationary plate with Pr_l = 1.0, q_R = 0, and β = 0

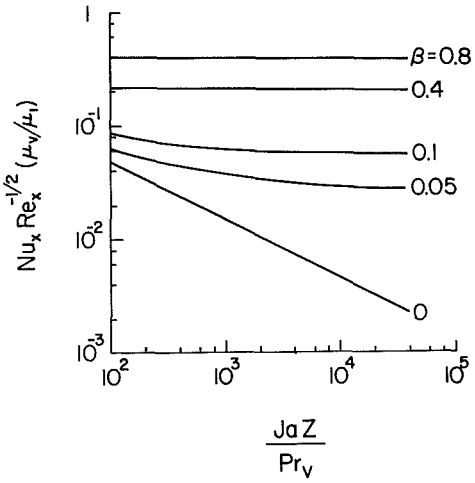

Fig. 5 Effect of subcooling on heat transfer for Pr_l = 1.0, $\bar{v}$ = 0, and q_R = 0

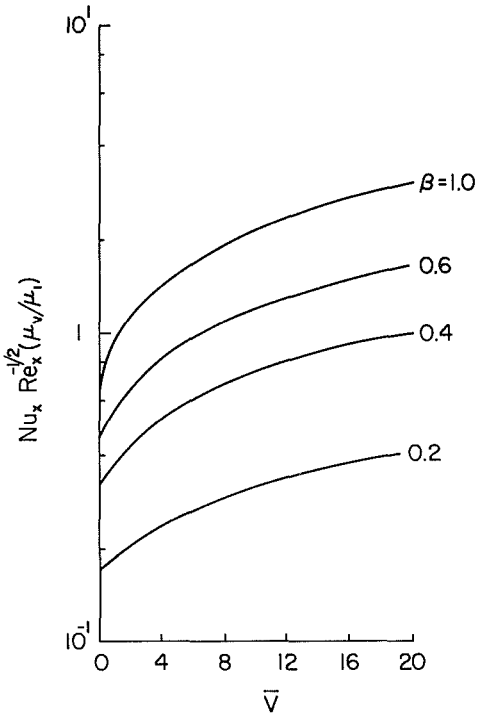

Fig. 6 Influence of subcooling on heat transfer from a moving plate for Pr_l = 2.7, JaZ/Pr_v = 30,000, and q_R = 0

It follows that, in the presence of radiation, the average convective heat transfer coefficient is approximated by

$$(h_c)_{av} = \left[\frac{-h_R + \sqrt{h_R^2 + 4h_{co}^2}}{2}\right]_{av} \tag{28a}$$

and the total heat transfer coefficient is

$$(h_T)_{av} = \left[\frac{h_R + \sqrt{h_R^2 + 4h_{co}^2}}{2}\right]_{av} \tag{28b}$$

Equation (28*b*) differs from Bromley's expression (Bromley, 1950), which applies to natural convection film boiling. The radiation heat transfer coefficient, in accordance with assumption (*ix*), is given by equation (13*b*).

Results and Discussion

Equation (26) can be rearranged to relate the local Nusselt and Reynolds numbers to the parameter Φ given by equation (23) and to the velocity ratios $\bar{u}_s$ and $\bar{v}$.

$$\frac{\mathrm{Nu}_x \mu_v/\mu_l}{\mathrm{Re}_x^{1/2}} = \left(\frac{2\Phi}{15}\right)^{1/2} \frac{(1-\bar{u}_s)}{(\bar{u}_s - \bar{v})} \tag{29}$$

Thus, for particular values of the subcooling parameter β, the density-viscosity product ratio Z, the parameter JaZ/Pr_v, and the Prandtl number for the liquid Pr_l, the interface velocity ratio $\bar{u}_s$ can be calculated for specific values of $\bar{v}$ from equations (23), (24), and (25). On runout tables, $|\bar{v}| \lesssim 10$, $20{,}000 \lesssim JaZ/Pr_v \lesssim 40{,}000$, and $0.05 \lesssim \beta \lesssim 0.2$. Values for $\mathrm{Nu}_x \mu_v/\mu_l \mathrm{Re}_x^{1/2}$ are presented for $10^2 \leq JaZ/Pr_v \leq 10^5$ to include results for lower plate temperatures, or equivalently, lower Jakob numbers, where film boiling can also occur.

The effect of plate velocity on heat transfer to a saturated liquid (β = 0) is presented in Fig. 4 in terms of a dimensionless Nusselt number ratio Nu_* defined by $[\mathrm{Nu}_x \mathrm{Re}_x^{-1/2} \mu_v/\mu_l] / [\mathrm{Nu}_x \mathrm{Re}_x^{-1/2} \mu_v/\mu_l]|_{\bar{v}=0}$. When the plate moves opposite to the liquid ($\bar{v} < 0$), vapor traveling with the plate increases the vapor layer thickness and Nu_* decreases as $|\bar{v}|$ increases. Information is not provided for $\bar{v} < -0.6$ since the bulk mass flow of vapor becomes directed toward $x = 0$ and solutions for $\bar{u}_s$ could no longer be found to equations (23), (24), and (25). Solutions were not possible since the boundary layer equations no longer apply when the bulk vapor flow is reversed.

Heat transfer is enhanced when the plate and liquid move in the same direction ($\bar{v} > 0$) since vapor flow is aided and the vapor layer is thinned. On runout tables, $|\bar{v}| \lesssim 10$ and the Nusselt number may be as much as 250 percent larger than that for a stationary plate. This enhancement can be more pronounced when flow velocities are small ($\bar{v} > 10$), as in heat exchangers used in continuous annealing processes or when the jet flow rates are reduced.

Figure 5 illustrates how subcooling can substantially increase heat transfer from a stationary plate. Typically, the subcooling parameter β is less than about 0.2 for a runout table. Higher values are possible at lower plate temperatures at which film boiling can still occur. Values for $\mathrm{Nu}_x \mathrm{Re}_x^{-1/2} \mu_v/\mu_l$ are nearly constant for $\beta \gtrsim 0.05$, indicating the importance of subcooling in determining the heat transfer rate.

As shown in Fig. 6, the plate velocity remains important even with high subcooling for typical values of JaZ/Pr_v and Pr_l on runout tables. The increase in $\mathrm{Nu}_x \mathrm{Re}_x^{-1/2}\ \mu_v/\mu_l$ is greater for $\bar{v}$ near zero in that plate motion promotes the vaporization of liquid.

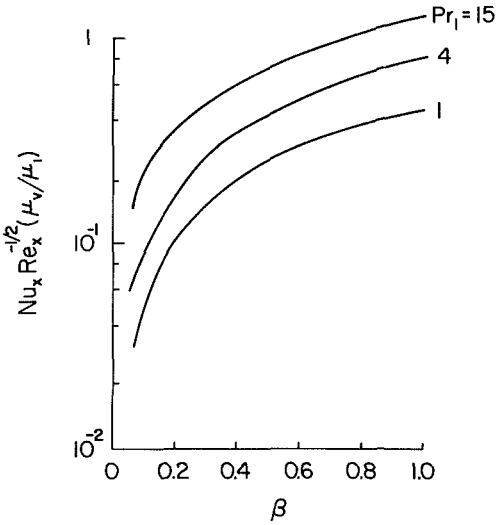

Fig. 7 Influence of the liquid Prandtl number on heat transfer at different subcoolings for $q_R = 0$, $\bar{v} = 0$, and $JaZ/Pr_v = 30{,}000$

Heat transferred from the vapor/liquid interface to the liquid decreases as the thermal boundary layer thickness Δ increases. The value of Δ depends largely on Pr_l, which affects heat transfer as shown in Fig. 7 for different values of the subcooling parameter β.

The derivation of equation (28) assumed that the heat transfer to the liquid is small. The effect of subcooling is to reduce the vapor layer thickness, since heat is lost to the liquid in lieu of vaporizing liquid at the vapor/liquid interface. Therefore, the importance of conduction relative to radiation across the vapor layer is increased when the liquid is subcooled. Analyses employing $(h_c)_{av}$ for saturated liquids ($\beta = 0$) can be used to conservatively estimate conditions where radiation is important in a subcooled liquid. Such analyses also reveal the effect of plate motion on the contribution of radiation to total heat transfer.

The effect of radiation across the vapor layer on the average total and convective heat transfer coefficients for water is shown in Fig. 8 as a function of plate temperature for $-0.6 \leq \bar{v} \leq 20$. Values representative of runout tables were used for the film boiling length L, the liquid velocity u_∞, and the emissivities ϵ_p and ϵ_s of the plate and vapor/liquid interface, respectively. The emissivity of the vapor liquid interface is nearly unity since water is strongly absorbing at the characteristic wavelengths for the plate temperatures considered. The emissivity ($\epsilon_p = 0.85$) of the plate is typical of highly oxidized steels (Touloukian and DeWitt, 1970). In the figure, the ratio of the average total heat transfer coefficient to the average convective heat transfer coefficient in the absence of radiation, $(h_T/h_{co})_{av}$, increases significantly with plate temperature due to higher radiative emission by the plate. The increase is most pronounced for $\bar{v} = -0.6$ since the vapor layer thickness is increased by vapor traveling with the plate against the liquid flow. However, the ratio $(h_T/h_{co})_{av}$ is smaller when the plate and liquid move in the same direction, since the combined motion of the plate and liquid decreases the vapor layer thickness and conduction across the vapor layer becomes more important. Radiation reduces the average convective heat transfer coefficient, as indicated by the results for $(h_c/h_{co})_{av}$. This reduction is due to larger vapor layer thicknesses, which arise when heat is transferred by both radiation and conduction to vaporize water more readily at the vapor/liquid interface. The effect is most pronounced for $\bar{v} = -0.6$, since the contribution due to radiation is greatest. For very high values of $\bar{v}$, radiation may be negligible, especially at lower plate temperatures.

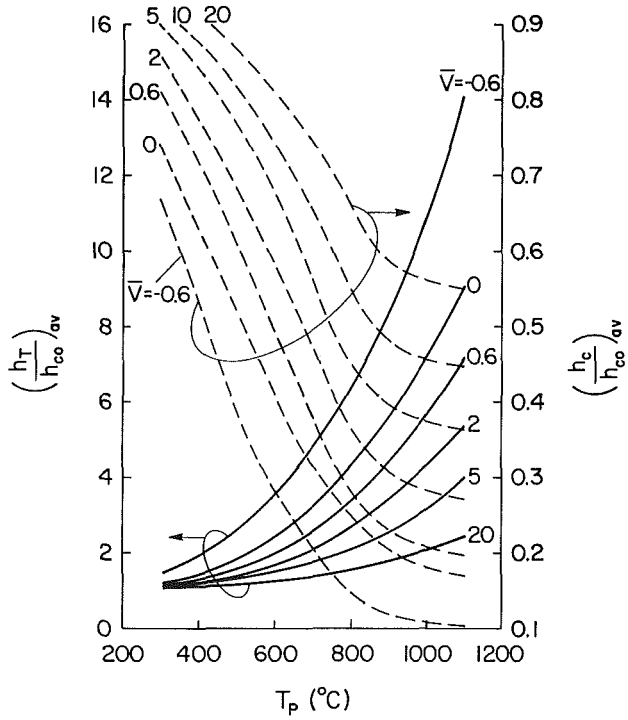

Fig. 8 Effect of radiation across the vapor layer on the average total and convective heat transfer coefficients for water with $L = 0.5$ m, $T_\infty = 100°C$, $u_\infty = 5$ m/s, $\beta = 0$, $\epsilon_p = 0.85$, and $\epsilon_s = 1.0$

It is important to note that Fig. 8 corresponds to a saturated liquid ($\beta = 0$). When the liquid is subcooled, the importance of radiation decreases, as explained earlier, and the values of $(h_T/h_{co})_{av}$ and $(h_c/h_{co})_{av}$ would be closer to unity than those in Fig. 8. However, the effect of plate velocity is correctly represented, and plate velocity must be incorporated into physical models in order to describe accurately the importance of radiation across the vapor layer.

Conclusions

Plate motion can significantly influence heat transfer in film boiling, even when the liquid is subcooled. The effect of subcooling is significant and depends on Pr_l, as well as plate speed. Radiation becomes less important at higher plate velocities and can in some cases be neglected unless the plate temperature is very high. For small plate velocities opposite to the flow of liquid, radiation becomes more important since the vapor layer thickness is increased. Larger plate velocities can reverse the vapor flow and possibly entrain vapor from partially wetted regions, greatly complicating theoretical models.

Accurate analytical estimates of heat transfer by film boiling should include the effects of plate motion when applicable. Plate motion is especially important when the plate speed greatly exceeds the liquid velocity. Hence, correlations for forced convection film boiling on stationary surfaces may provide inaccurate heat transfer estimates when applied to manufacturing processes where the cooled material is in motion.

Acknowledgments

We are grateful for support of this work by the National Science Foundation under Grant No. CPE-8414613. We also appreciate the consultation of Mr. Timothy A. Veslocki of the Inland Steel Company in matters related to the cooling methods used in hot rolling mills.

References

Arpaci, V. S., and Larsen, P. S., 1984, *Convection Heat Transfer*, Prentice-Hall, Inc., Englewood Cliffs, NJ, pp. 182–187.

Berenson, P. J., 1961, "Film-Boiling Heat Transfer From a Horizontal Surface," ASME JOURNAL OF HEAT TRANSFER, Vol. 83, pp. 351–358.

Bromley, L. A., 1950, "Heat Transfer in Stable Film Boiling," *Chemical Engineering Progress*, Vol. 46, No. 5, pp. 221–227.

Cess, R. D., 1964, "The Interaction of Thermal Radiation With Conduction and Convection Heat Transfer," in: *Advances in Heat Transfer*, Vol. 1, Academic Press, New York, pp. 1–50.

Cess, R. D., and Sparrow, E. M., 1961a, "Film Boiling in a Forced Convection Boundary Layer Flow," ASME JOURNAL OF HEAT TRANSFER, Vol. 83, pp. 370–376.

Cess, R. D., and Sparrow, E. M., 1961b, "Subcooled Forced Convection Film Boiling on a Flat Plate," ASME JOURNAL OF HEAT TRANSFER, Vol. 83, pp. 377–379.

Collier, J. G., 1981, *Convective Boiling and Condensation*, 2nd ed., McGraw-Hill, New York, pp. 121–139.

Ito, T. and Nishikawa, K., 1966, "Two Phase Boundary Layer Treatment of Forced Convection Film Boiling," *International Journal of Heat and Mass Transfer*, Vol. 9, pp. 117–130.

Kohring, F. C., 1985, "Waterwall Water-Cooling Systems," *Iron and Steel Engineer*, June, pp. 30–36.

Kokado, J., Hatta, N., Hirohiko, T., Harada, J., and Yasuhira, N., 1984, "An Analysis of Film Boiling Phenomena of Subcooled Water Spreading Radially on a Hot Steel Plate," *Arch. Eisenhuttewesen*, Vol. 55, No. 3, pp. 113–118.

McGannon, H. E., ed., 1971, *The Making, Shaping, and Treating of Steel*, 9th ed., United States Steel Corp., Herbick and Held, Pittsburgh.

Motte, E. I., and Bromley, L. A., 1957, "Film Boiling of Flowing Subcooled Liquids," *Industrial and Engineering Chemistry*, Vol. 49, No. 11, pp. 1921–1928.

Rao, J. R., and Prasad, K. K., 1983, "Integral Method Solutions for Forced Convection Film Boiling," in: *Proceedings of Seventh National Heat and Mass Transfer Conference*, Oxford and IBH Publishing Co., New Delhi, India, Vol. F3, pp. 335–339.

Shigechi, T., Ito, T., and Nishikawa, K., 1984, "The Effect of Radiation in Film Boiling Heat Transfer," *Bulletin of JSME*, Vol. 27, No. 227, pp. 939–944.

Sparrow, E. M., 1964, "The Effect of Radiation on Film Boiling Heat Transfer," *International Journal of Heat and Mass Transfer*, Vol. 7, pp. 229–238.

Touloukian, Y. S., and DeWitt, D. P., 1970, *Thermophysical Properties of Matter*, Vol. 7, IFI/Plenum, New York.

M. Golafshani
Morton Thiokol Corporation,
Gas Dynamics Section,
Brigham City, UT 84302

H. R. Jacobs
The Pennsylvania State University,
Department of Mechanical Engineering,
University Park, PA 16802

Stability of a Direct-Contact Spray Column Heat Exchanger

The governing equations for the transient multiphase flow in a liquid–liquid spray column are developed. Using the model, numerical calculations are presented that represent typical fluctuations observed in the operation of the direct contact tower of the U.S. Department of Energy's 500-kW_e geothermal power plant at East Mesa, CA. The response time is determined for the column and conditions leading to local flooding are determined.

Introduction

In the 1960s, the use of spray columns in desalination systems initiated a renewal of interest in them as heat exchangers (Kern, 1967; M. W. Kellogg Co., 1971; Sukhatine and Hurwitz, 1971). The energy crisis of the 1970s and 1980s led to further investigations. Of particular interest was their application to extracting heat from geothermal brines (Jacobs and Boehm, 1977, 1980), and for use with solar ponds (Wright, 1982). These interests were based on the need to avoid the fouling and scaling problems associated with these hot fluids, and to develop means of maximizing the efficiency of heat extraction. Early studies based their design on mass transfer analogies (Treybal, 1953). Later studies attempted to develop correlations for volumetric heat transfer coefficients (Plass et al., 1979), and to use simplistic models to estimate the column's hydrodynamic behavior (Letan and Kehat, 1968; Jacobs and Boehm, 1980).

Using these simplified methods, this paper's second author carried out the design for the East Mesa DCHX Binary Cycle Geothermal Facility's large spray column. The column was designed to operate with a minimum approach temperature between the low-salinity geothermal brine (< 2000 ppm) and the isobutane working fluid of 5°F or 2.8°C. This minimum approach temperature occurred within the preheating section of the column, which was used as a combined preheater–boiler. Data acquired during the nearly three years of operation of the system indicated that its performance was equal to or greater than expected. However the temperature profiles along the length of the column did not follow closely those predicted from the correlations used in its design (Ohlander et al., 1983). It was obvious that further studies were necessary to interpret the results. The U.S. D.O.E. requested the present authors to commence such a study.

In an attempt to understand the operation of the East Mesa spray column better, it was decided to formulate the problem in terms of the governing equations for multiphase flow. For the preheater section of the column, models were developed for steady-state operation using different methods to describe the heat transfer to the drops. In the preceding paper (Jacobs and Golafshani, 1989), it was shown that the heat transfer was controlled by the conduction within the drops of the dispersed phase. Attempts to determine a physical model to describe the heat transfer in the boiler section of the column have not met with much success (Jacobs and Boehm, 1980). In fact, Walter (1981) concludes, "There appears to be no way to calculate a heat transfer coefficient." Thus, the simple correlation of Jacobs and Boehm (1980) was used for the boiling of isobutance in brine. The correlation is a simple expression for volumetric heat transfer coefficient as a function of holdup

$$U_v = 8.38 \times 10^5 \phi \quad \text{W/m}^3\,^\circ\text{C} \tag{1}$$

Since dchx's are designed to operate near flooding conditions, it is important to determine how changes in operating conditions might influence the column's performance. This is particularly true in geothermal systems where changes in the well head conditions are beyond the control of the operator. Fluctuations in brine flow rate, pressure, and temperature can all occur. Adjustments must be made before the column goes unstable. In addition, for a combined preheater–boiler spray column such as at East Mesa, it is necessary to ascertain how such changes affect the needed length of the preheater so that carryover of liquid brine with the working fluid vapor does not occur as this could damage the working fluid turbine. Based on this need to understand the transient operation, the present study was undertaken utilizing a transient multiphase model.

In modeling the direct contact preheater-boiler combination used at East Mesa, we note that the boiler volume is very small compared to that of the preheater. This is, of course, due to the intensity of the heat transfer in the boiler as compared to the preheater and the large temperature increase that is required across the preheater. Typically the vaporization process is completed in less than a meter of column height while the preheating takes nearly 7 m. Thus, as a first approximation, it is reasonable to assume a rapid adjustment in the boiler while the preheater provides the major time delay. (It should be noted that for solar pond applications, the low temperature increase across the preheater would make the boiler and preheater sections nearly identical in length.) In the present study, we restrict ourselves to a situation where the boiler section adjusts nearly instantaneously to the conditions of the fluids entering it. Thus, we can concentrate on the response of the preheater section.

Mathematical Modeling

Consider the column shown in Fig. 1. It is of constant diameter and ideally the dispersed phase, which we assume is lighter than the continuous phase, rises in continuous streams from the injector nozzles. Unless strong recirculation regions occur due to improper design of the continuous phase inlet, it is clear that the flow is essentially one dimensional. However, for our problem, there is the possibility of time dependence. Thus, the continuity equations for the continuous phase and dispersed phase are, respectively,

$$\frac{\partial[(1-\phi)\rho_c]}{\partial t} + \frac{\partial[(1-\phi)\rho_c V_c]}{\partial x} = 0 \tag{2}$$

and

$$\frac{\partial \rho_d \phi}{\partial t} + \frac{\partial \rho_d \phi V_d}{\partial x} = 0 \tag{3}$$

For each phase the conservation of momentum can be writ-

Contributed by the Heat Transfer Division and presented at the ASME/AIChE National Heat Transfer Conference, Denver, Colorado, August 1985. Manuscript received by the Heat Transfer Division July 10, 1987. Keywords: Evaporation, Multiphase Flows.

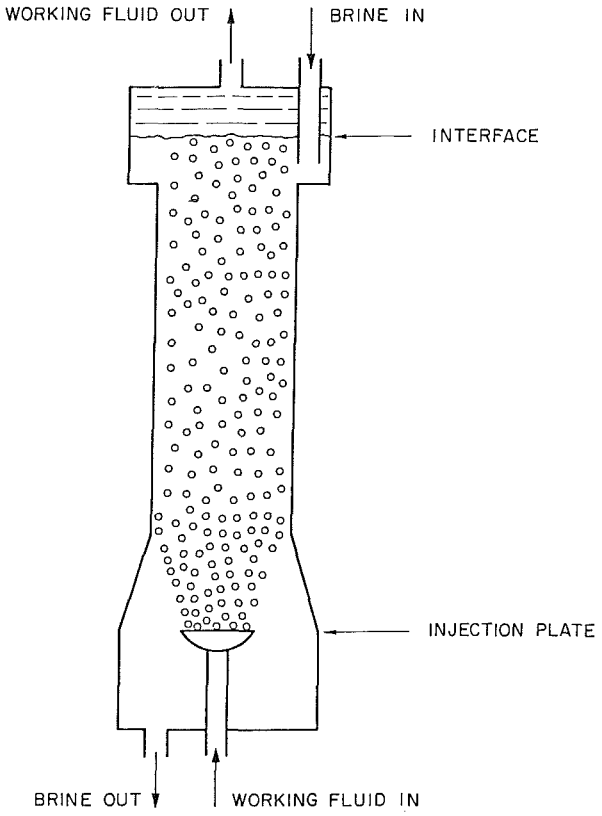

Fig. 1 Schematic of a countercurrent spray column heat exchanger

ten; however, in a two-component system, it is only necessary to write the momentum equation for one phase and for the mixture. Thus, for the dispersed phase

$$\frac{\partial \rho_d \phi V_d}{\partial t} + \frac{\partial \rho_d \phi V_d^2}{\partial x} = -\phi \frac{\partial P}{\partial x} - K(V_d - V_c) - \phi \rho_d g \quad (4)$$

where K is the interphase friction factor.

For the mixture as a whole, we have

$$\frac{\partial[(1-\phi)\rho_c V_c]}{\partial t} + \frac{\partial[(1-\phi)\rho_c V_c^2]}{\partial x} + \frac{\partial \rho_d \phi V_d}{\partial t} + \frac{\partial \rho_d \phi V_d^2}{\partial x} = -\frac{\partial P}{\partial x} - [(1-\phi)\rho_c + \phi \rho_d]g \quad (5)$$

Note in equation (5), that the interphase friction term disappears as the interphase forces on each phase are equal and opposite. Note also that we write the pressure gradient as a partial derivative. This is due to the fact that during a transient the amount of mass of each fluid can vary in the column and thus the hydrostatic pressure can vary with time as well as axial location. As the continuous phase flows downward, V_c is a negative value.

The energy equations also need only be written for the dispersed phase and the mixture as a whole, thus for the dispersed phase

$$\frac{\partial \rho_d \phi h_d}{\partial t} + \frac{\partial \rho_d \phi h_d V_d}{\partial x} = \frac{\partial (\phi P)}{\partial t} - \frac{Q_i}{\text{Vol}} \quad (6)$$

and for the mixture

$$\frac{\partial[(1-\phi)\rho_c h_c]}{\partial t} + \frac{\partial[(1-\phi)\rho_c V_c h_c]}{\partial x} + \frac{\partial \phi \rho_d h_d}{\partial t} \frac{\partial \phi \rho_d V_d h_d}{\partial x} = \frac{\partial P}{\partial t} \quad (7)$$

The set of partial differential equations given in equations (2)–(7) has to be solved in conjunction with equations of state for the two fluids and using appropriate relations for the interphase friction factor K and the interfacial heat transfer Q_i/Vol. Jacobs and Golafshani (1989) give for K

$$K = \frac{3}{8} \frac{\phi}{R_d} C_D \rho_C \mid V_d - V_c \mid \quad (8)$$

where $\mid V_d - V_c \mid$ is the absolute value. The value for C_d is found from Grace (1983) for single drops. It is consistent with Steiner and Hartland's equation (29*a*) (1983) for drop swarms.

For an organic fluid as a dispersed phase in water or brine, Jacobs and Golafshani (1989) have shown for droplets of ~3.0–4.0 mm in diameter that the heat transfer is governed by conduction within the drops and that, at least for isobutane, drop growth, due to decreased density when the drops are being heated, must be taken into account. Thus, for the droplets, it is also required to solve the transient conduction problem

$$\frac{\partial (\rho c_p T)_d}{\partial t_1} = \frac{1}{r^2} \frac{\partial r^2 k_d \frac{\partial T_d}{\partial r}}{\partial r} \quad (9)$$

where here t_1 is defined as the elapsed time from the point of origin of the drop to x, or

$$t_1 = \int_o^x \frac{dx}{V_d} \quad (10)$$

The associated initial and boundary conditions are

$$T_d = T_{do} \text{ at } t_1 = 0$$
$$T_d \text{ is finite at } r = 0 \quad (11)$$

and

$$T_d = T_c \text{ at } r = R_d$$

Nomenclature

C_D = drag coefficient
C_p = specific heat
G = volumetric flow rate
g = gravitational acceleration
h = enthalpy
k = thermal conductivity
K = interphase friction factor
LMTD = log mean temperature difference
m = mass flow rate
N_d = number of droplets of dispersed phase
P = pressure
Pr = Prandtl number
Q = heat transfer rate
r = radial coordinate
R_d = radius of droplets
Re_{D_C} = Reynolds number $= \rho_c \mid (V_c - V_d) \mid D/\mu_c$
t = time
t_1 = time for a droplet to rise through the column $= x/V_d$
T = temperature
V = velocity in x direction
Vol = volume
x = vertical coordinate measured from the bottom of the column
α = thermal diffusivity
μ = dynamic viscosity
ρ = density
ϕ = holdup, fraction of volume occupied by the disperse phase

Subscripts

b = brine
c = continuous phase
d = dispersed phase
f = conditions at flooding
i = at the interface between the droplets and continuous phase
o = at entrance conditions
w = working fluid

It should be noted that since the density of the drops changes that

$$R_d = R_{do}\left(\frac{\rho_{do}}{\rho_d}\right)^{1/3} \quad (12)$$

It is clear that even for steady-state operation, the above-described equations must be solved numerically, since T_c varies with x as does V_d. For transient behavior of the column, we have a doubly complex problem. However, for a given system of droplets released at a specified time, the problem is in fact no worse in regards to solving equations (9)–(12).

At each location along the column, the droplets' mean temperature is found after solving equations (9)–(12). From this, the value of the dispersed phase enthalpy can be obtained, and from the mixture energy equation (7), the enthalpy of the continuous phase. Equation (6), therefore, is only used to check convergence. Thus, the actual governing equations for solution of the problem are equations (2)–(5) and equations (7)–(12) subject to the constraints of the equations of state for the two fluids and the imposed boundary conditions.

Numerical Solution

In carrying out the numerical solutions, the governing equations are first converted into a set of algebraic equations using a spacewise upwind differencing technique with the exception of the droplet conduction equations where central differencing is used. The transients are expressed in an implicit formulation. As the finite difference equations are strongly coupled and nonlinear they have to be solved by an iterative guess and correct technique at each time step. The method used closely follows that of Spalding (1980) and is described in detail by Golafshani (1984). Details of the programming can be found there as well.

Typically in carrying out an analysis, due to the added complexity of having to solve the droplet conduction problem simultaneously, we initiated our analyses by first solving for a steady-state solution around which we wished to study a transient response. In carrying out an analysis for the design of a spray column, the two fluids, their mass flow rates, and their temperatures as they enter the column are specified as well as the pressure at the top of the column. The column diameter is also specified in such a way as to insure that flooding would not take place in an isothermal column. This is normally done utilizing the equation (13) experimentally derived correlation due to an empirical formula (Minard and Johnson, 1952)

$$(m+1)\,(1-G_D/G_c)\,\phi_f^2 + (m+2)\,\frac{G_D}{G_c}\,\phi_f\,\frac{G_D}{G_c} = 0 \quad (13)$$

where $m = 1.39$ for $\mathrm{Re}_{Dc} > 500$.

Next one can specify the exit temperature desired for one of the fluids or the column length. It is, of course, much easier to do the latter since defining one exit temperature in fact defines the other. However, the length would be unknown. Thus, initially a length would be guessed. Such a guess could be obtained by using an empirical expression for a volumetric heat transfer coefficient such as given by Plass et al.

$$U_v = 22.4 \times 10^4\,\phi \quad \mathrm{W/m^3\,°C} \quad (\text{for } \phi < 0.05) \quad (14)$$

$$U_v = [83.9 \times 10^4\,(\phi - 0.05)_e^{-0.57}\,\frac{G_D}{G_c} + 1.12 \times 10^4) \quad \mathrm{W/m^3°C} \quad (15)$$

In this case, equation (6) could be used in place of equations (9)–(12) in solving the problem. Even greater simplification could result by assuming the fluid properties ρ and C_p constant at inlet conditions; however, for many systems such as isobutane–water, the results could be quite erroneous and lead to a long iteration time to converge to the actual length required for the variable property conduction model.

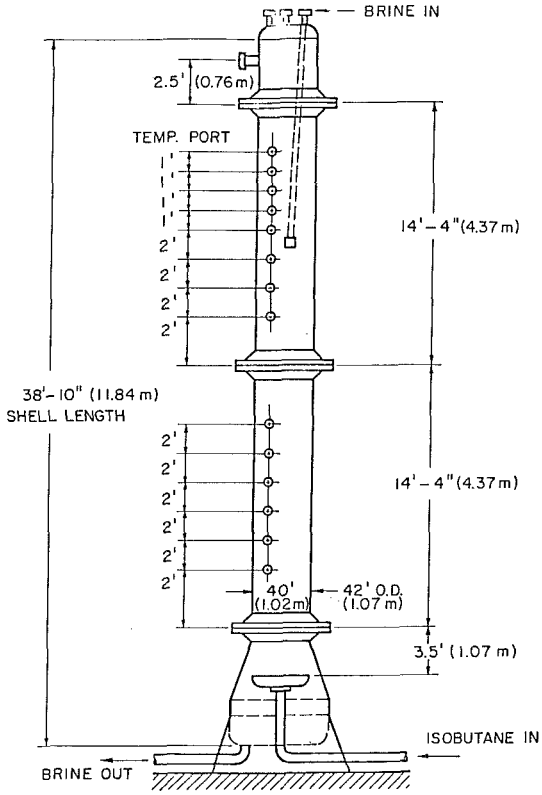

Fig. 2 Schematic of 500-kWe direct-contact heat exchanger

After obtaining a steady-state solution for the column operation, the transient behavior can be obtained by imposing a change in one of the input variables or in the column pressure. In the work presented by Golafshani (1984), changes in mass flow rates, pressure, and temperature were considered.

Results and Discussion

The transient response analyses reported herein correspond to operating conditions reported by Olander et al. (1983) for the 500-kW_e Direct Contact Geothermal Power Plant at East Mesa, CA. The spray column, as shown in Fig. 2, is a combined preheater–boiler arrangement. The design is such that liquid level is controlled primarily by adjusting flow rates. The boiling section is relatively short, in the range of 1.0–1.5 m (3–5 ft.) with the greater portion of the length being the preheater. Fluctuations in flows, temperatures, and column pressure can occur as the continuous phase is brine and the dispersed phase is isobutane. Although the system ideally should operate in a steady-state mode, the geothermal wells at East Mesa produce time-varying amounts of CO_2 as well as hot brine. The CO_2 needs to be purged by flashing, which can induce changes in brine temperature and flow rate and even pressure although the wells are pumped. Carryover of CO_2 to the condenser can also cause fluctuations in isobutane inlet temperature. Thus, at least small fluctuations can occur at regular intervals and the column must adjust to them. Since the column operation attempts to control fluid height, and the preheater required length can vary, it is possible to cause buildup of isobutane in the boiler section of the column since, as the preheater lengthens, there may not be sufficient boiler length or contact time between the saturated isobutane drops and the brine. This can cause a drop in column pressure as less vapor is generated. Adjustments would thus have to be made to the turbine controls, etc., until the column re-equilibrated. It is thus necessary to determine the response time for the column as well as changes

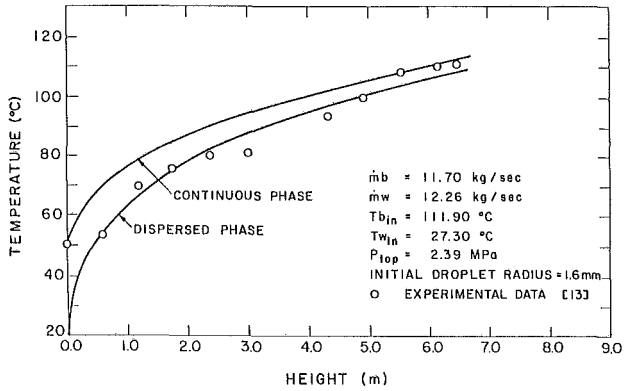

Fig. 3 Temperature profile of the brine and the working fluid along the length of the column using variable radius model, $\dot{m}b$ = 11.70 kg/s, $\dot{m}w$ = 12.26 kg/s

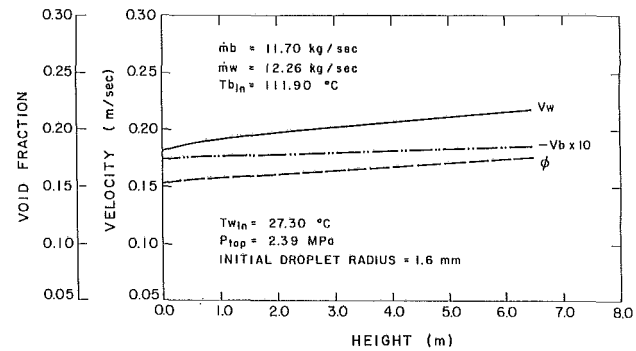

Fig. 4 Variation of velocity of the brine and the working fluid as well as holdup along the length of the column, $\dot{m}b$ = 11.70 kg/s, $\dot{m}w$ = 12.26 kg/s

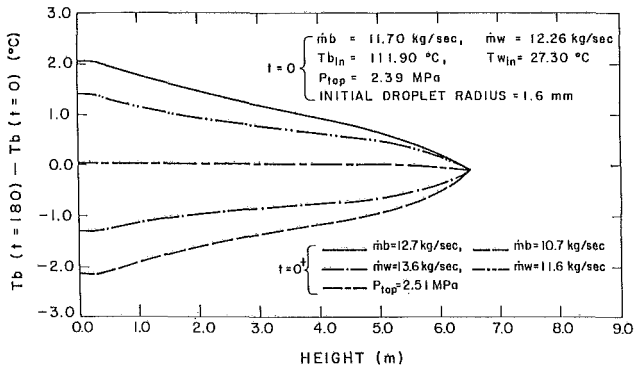

Fig. 5 Effect of change in mass flow rate and column pressure on the brine temperature, $\dot{m}b$ = 11.70 kg/s, $\dot{m}w$ = 12.26 kg/s

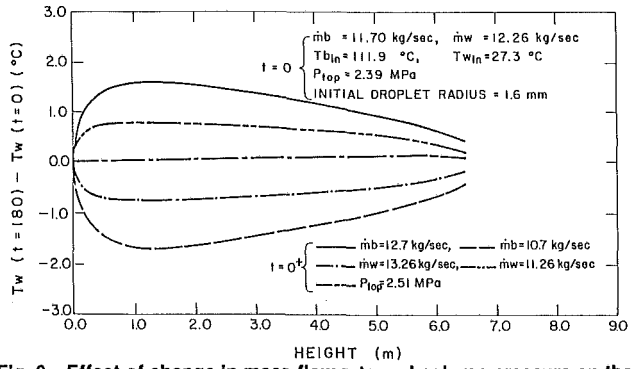

Fig. 6 Effect of change in mass flow rate and column pressure on the working fluid temperature, $\dot{m}b$ = 11.70 kg/s, $\dot{m}w$ = 12.26 kg/s

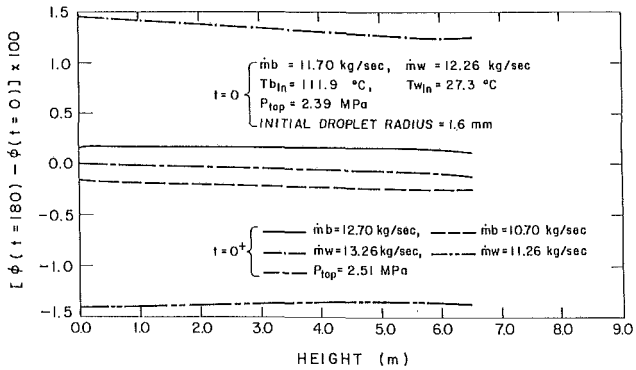

Fig. 7 Effect of change in mass flow rate and column pressure on holdup, $\dot{m}b$ = 11.70 kg/s, $\dot{m}w$ = 12.26 kg/s

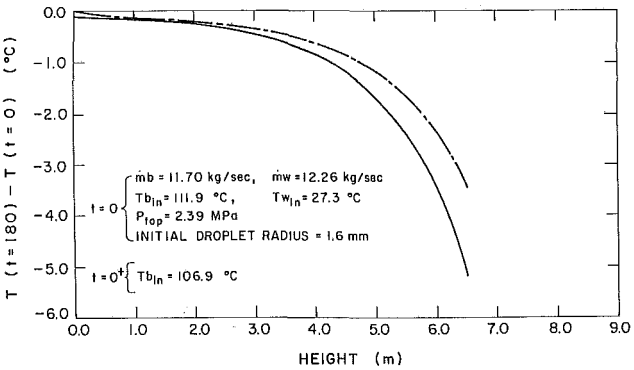

Fig. 8 Effect of change in the brine inlet temperature on temperature profile of the brine and the working fluid, $\dot{m}b$ = 11.698 kg/s, $\dot{m}w$ = 12.259 kg/s

in holdup and required preheater length to reach the saturation conditions for the isobutane.

Figures 3 and 4 present the steady-state preheater temperature, void fraction, or holdup and the velocities predicted throughout the 500-kW_e spray column. In Fig. 3, there are also presented temperature measurements made with resistance thermometers located in the column (Olander et al., 1983). The higher temperature curve is for the brine and the lower temperature curve is for the isobutane. The experimental data appear to represent the isobutane drops in this case, except at $x = 0$, which is the extraction temperature of the brine. This was not always the case, however. Usually the experimental data lie between the two curves, indicating that normally some sort of weighted average is measured.

Figures 5–7 indicate changes observed after 180 seconds for the brine temperature, isobutane temperature, and holdup for step changes in mass flow rates or column pressure. It is clear that the preheater is relatively insensitive to pressure, whereas changes in the mass flow rates as low as ±1 kg/s can yield temperature variations within the column of ±2°C. Figure 8 shows the effect of a 5°C decrease in brine inlet temperature. Near the bottom of the column, the temperatures remain unchanged, but near the top, changes of each fluid are seen. For the East Mesa column, all such changes in flow rates and brine inlet temperature can occur, and they can occur rapidly as the controllers were not sufficiently sensitive to respond. Thus, it is impossible to state that steady-state operation is ever really achieved. Due to this, it was remarkable that Jacobs and Golafshani (1989) were able to achieve the comparison shown in Fig. 3 and better in many cases (Golafshani, 1984) between their model and measured temperatures. Table 1 indicates how each variation discussed influences the preheater length requirement.

Table 1 Changes in column height after a sudden change in input characteristic of the column. Steady-state conditions are: mb = 11.70 kg/s, mw = 12.26 kg/s, Tb_{in} = 111.9°C, Tw_{in} = 27.3°C, P_{top} = 2.39 MPa, and initial droplet radius = 1.6 mm.

Change in input characteristic	$H(t=180)-H(t=0)$ (m)
mb increased by 1 kg/s	−0.87
mb decreased by 1 kg/s	0.1
mw increased by 1 kg/s	0.04
mw decreased by 1 kg/s	−0.04
P_{top} increased by 5 percent	0.9
Tb_{in} decreased by 5°C	1.04

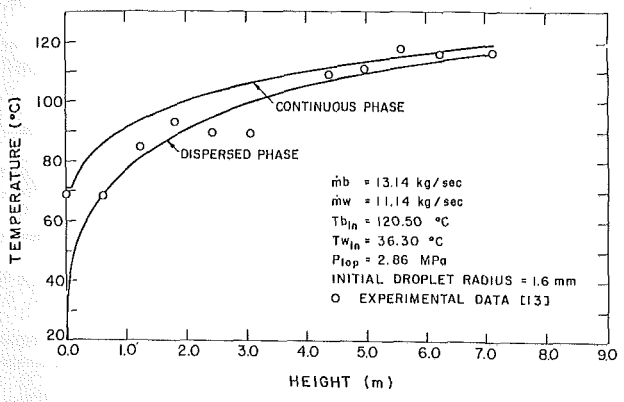

Fig. 9 Temperature profile of the brine and the working fluid along the length of the column using variable radius model, $\dot{m}b$ = 13.14 kg/s, $\dot{m}w$ = 11.14 kg/s

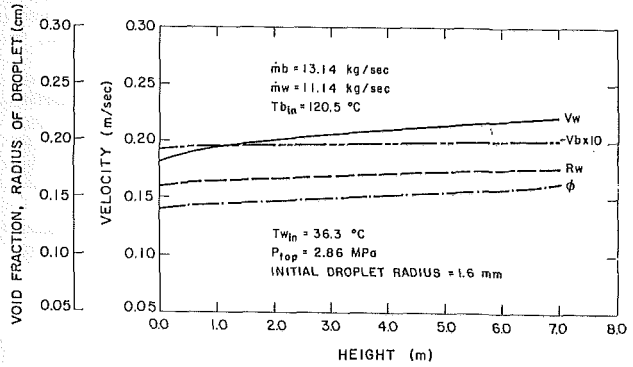

Fig. 10 Variation of velocity of the brine and the working fluid as well as holdup and drop radius along the length of the column

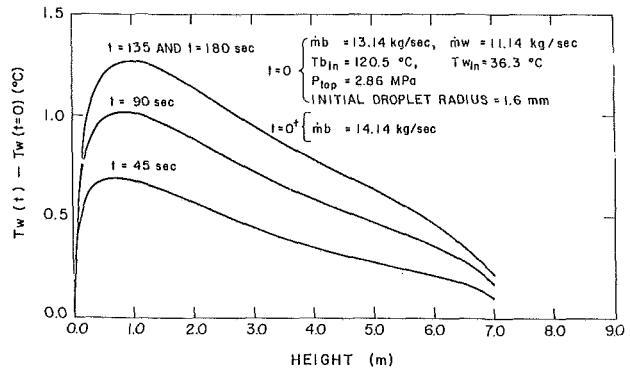

Fig. 11 Transient response of the working fluid temperature after an increase in mass flow rate of the brine

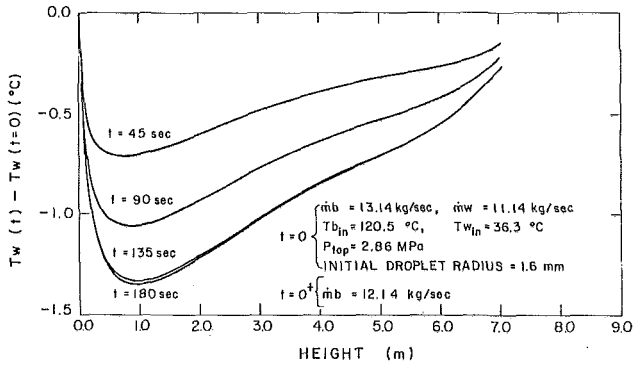

Fig. 12 Transient response of the working fluid temperature after a decrease in mass flow rate of the brine

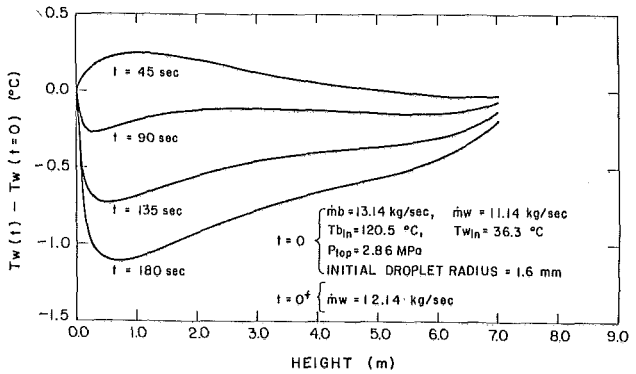

Fig. 13 Transient response of the working fluid temperature after an increase in mass flow rate of the working fluid

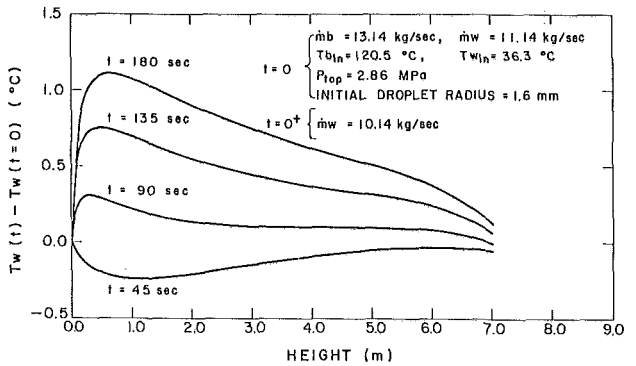

Fig. 14 Transient response of the working fluid temperature after a decrease in mass flow rate of the working fluid

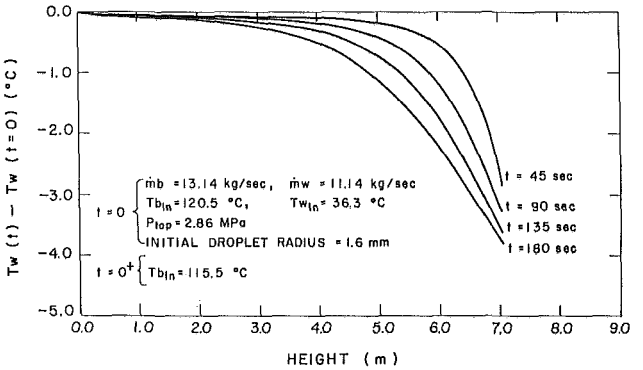

Fig. 15 Transient response of the working fluid temperature after a decrease in the brine inlet temperature

Figures 9 and 10 illustrate another steady-state calculation for an additional operating condition. Figures 11–15 show the response of T_w to changes in mass flows and inlet brine temperature as a function of time. The trends are all as expected for the increase in working fluid flow rate. The early time response indicates an increase in temperature at the bottom of the column. This is due to the time that it takes the mass flux wave to traverse the column height. At 45 seconds, the increased number of droplets per unit volume will be occupying a greater fraction, i.e., ϕ will be higher and the drag on the drops greater. There will be a longer exposure to a hotter brine. However, as the higher mass flux works its way up the column, there will be a cooling of the continuous fluid approaching the bottom and the temperatures will be depressed. It is clear that a longer preheater length will be required to bring the isobutane up to its saturation temperature as was indicated by the previous case studied.

For all cases studied, a new equilibrium steady state was achieved after approximately 180 seconds. Thus, the analysis indicates that this is the effective response time for the preheater section of the column. As the boiler section is always very short for the East Mesa facility, this is a good approximate value for the column itself.

Conclusions

A one-dimensional transient multiphase model appears to be adequate to describe the performance of a spray column such as that at the East Mesa 500-kW_e Direct Contact Binary Cycle Power Plant. Changes in preheater length of up to one meter can easily occur due to modest changes in the input conditions. The response time for the direct contactor is of the order of 180 seconds. For changes occurring in shorter times than this, there should be a lag time such that a true equilibrium steady state is not achieved. Thus, observed temperature measurements in the column are not necessarily at steady state. For small changes in various input parameters that are likely to occur, the long response time of 180 seconds should allow for reasonable control if adequate space is provided for the boiler and a vapor accumulator. As this was the case for the 500 kW_e facility spray column, there occurred no adverse operational effects to the power plant due to the direct contactor.

Acknowledgments

This work was carried out under contract with the U.S. Department of Energy, Contract No. DE-AS07-76ID01523. The data supplied by Mr. Robert Olander of Barber-Nichols Engineering were appreciated as was the technical encouragement of Mr. Judson Whitbeck of EG&G-Idaho, Inc.

References

Bruckner, A. P., and Hertzberg, A., 1982, "Direct Contact Droplet Heat Exchangers for Thermal Management in Space," *Proceedings of the 17th IECEC*, pp. 107–111.

Golafshani, M., 1984, "Stability of a Direct Contact Heat Exchanger," Ph.D. Dissertation, University of Utah, Salt Lake City, UT.

Grace, J. R., "Hydrodynamics of Liquid Drops in Immiscible Liquids," *Handbook of Fluids in Motion*, N. P. Cheremisinoff and R. Gupta, eds., Ann Arbor Science, The Butterfield Group, Ann Arbor, MI, Chap. 38, pp. 1003–1025.

Jacobs, H. R., Boehm, R. F., and Hansen, A. C., 1977, "Application of Direct Contact Heat Exchangers to Geothermal Power Production Cycles—Project Review 1974–1977," U.S. ERDA Report IDO/1549-8.

Jacobs, H. R., and Boehm, R. F., 1980, "Direct Contact Binary Cycles," *Sourcebook on the Production of Electricity From Geothermal Energy*, J. Kestin, ed., DOE/RA/4051-1, Washington, DC, Section 4.26.

Jacobs, H. R., and Golafshani, M., 1989, "A Heuristic Evaluation of the Governing Mode of Heat Transfer in a Liquid–Liquid Spray Column," ASME JOURNAL OF HEAT TRANSFER, Vol. 111, this issue.

M. W. Kellogg Company, Nov. 1971, *Saline Water Conversion Engineering Data Handbook*, 2nd ed., Office of Saline Water, Washington, DC, U.S. Government Printing Office.

Kern, D. Q., 1967, "Evaluation of Liquid–Liquid Heat Transfer for Large Scale Desalination," Office of Saline Water, Research and Development Progress Report No. 261.

Letan, R., and Kehat, E., 1968, "The Mechanism of Heat Transfer in a Spray Column Heat Exchanger," *AIChE Journal*, Vol. 14, No. 3, pp. 398–405.

Minard, G. W., and Johnson, A. I., 1952, "Limiting Flow and Holdup in a Spray Extraction Column," *Chemical Engineering Progress*, Vol. 48, No. 2, pp. 62–74.

Olander, R., Oshmyansku, S., Nichols, K., and Werner, D., 1983, "Final Phase Testing and Evaluation of the 500KW_e Direct Contact Heat Exchange Pilot Plant at East Mesa," ERDA Report/DOE/SF/11700-T1, Arcada, CO.

Plass, S. B., Jacobs, H. R., and Boehm, R. F., 1979, "Operational Characteristics of a Spray Column Type Direct Contact Preheater," *AIChE Symposium Series*, No. 189, pp. 227–234.

Spalding, D. B., 1980, "Numerical Computation of Multiphase Fluid Flow and Heat Transfer," *Recent Advances in Numerical Methods in Fluids*, C. Taylor and K. Morgan, eds., Pineridge Press, Swansea, United Kingdom, pp. 139–167.

Steiner, L., and Hartland, S., 1983, "Hydrodynamics of Liquid–Liquid Spray Columns," *Handbook of Fluids in Motion*, N.P. Cheremisinoff and R. Gupta, eds., Ann Arbor Science, The Butterfield Group, Ann Arbor, MI, Chap. 40, pp. 1049–1091.

Sukhatine, S. P., and Hurwitz, M., 1971, "Heat Transfer in the Liquid-Liquid Spray Tower," Office of Saline Water, Washington, DC, U.S. Government Printing Office.

Treybal, R. E., 1953, *Liquid Extraction*, 1st ed., McGraw-Hill, New York.

Walter, D. B., 1981, "An Experimental Investigation of Direct Contact Three Phase Boiling Heat Transfer," Ph.D. Dissertation, The University of Tennessee, Knoxville, TN.

Wright, J. D., 1982, "Selection of a Working Fluid for an Organic Rankine Cycle Coupled to a Salt Gradient Solar Pond by Direct-Contact Heat Exchange," ASME *Journal of Solar Energy Engineering*, Vol. 104, pp. 286–291.

A Heuristic Evaluation of the Governing Mode of Heat Transfer in a Liquid-Liquid Spray Column

H. R. Jacobs
The Pennsylvania State University,
Department of Mechanical Engineering,
University Park, PA 16802

M. Golafshani
Morton Thiokol Corporation,
Gas Dynamics Section,
Brigham City, UT 84302

A steady-state one-dimensional multiphase flow model is developed to describe the characteristics of a spray column type direct-contact liquid-liquid heat exchanger. Several models are assumed to describe the interphase heat exchange between water as the continuous phase and organic liquids as the dispersed phase. For small-diameter droplets, it is shown that existing experimental data are best described by a model that assumes the heat transfer is controlled by conduction within the drops.

Introduction

Direct-contact heat exchangers of the spray column type have many potential uses in industry. Among them is the extraction of heat from low-temperature sources such as geothermal brines. Since the 1960s, a number of investigators have proposed correlations to predict the volumetric heat transfer rate in such devices.

Spray column liquid-liquid heat exchanger experiments have been conducted in laboratory scale equipment for the following fluids as the dispersed phase with water as the continuous phase: benzene (Garwin and Smith, 1953), toluene (Treybal, 1953), CCl_4 (Johnson et al. 1957), Shell Oil A and spray base and kerosene (Woodward, 1961), kerosene (Letan and Kehat, 1968), mercury (Pierce et al., 1959), isobutane (Suratt and Hart, 1977), hexane (Holt, 1977), R-113 and insulating oil (Plass et al., 1979), and also pentane in recent design studies carried out at the University of Utah. Defining a volumetric heat transfer coefficient as

$$U_v = \frac{Q/\text{Vol}}{\text{LMTD}} \tag{1}$$

several different correlations have been proposed based on moderate temperature changes and overall column heat transfer. These correlations for U_v have generally been written as a function of holdup ϕ, and the ratio of the volumetric flow rates of the dispersed and continuous phases G_D/G_C (Garwin and Smith, 1985; Woodward, 1961; Plass et al., 1979). In many of the experiments the actual holdup was not measured, but was instead calculated based on drop size and relative buoyancy as well as flow rates and ratios for a given column (Jacobs and Boehm, 1980). This was due to the difficulty in making actual holdup measurements.

Garwin and Smith (1953) presented two correlations for their experiments for benzene dispersed in water. For the benzene being heated their data showed

$$U_v = 20.3 \times 10^4 \phi \quad \text{W/m}^3\text{°C} \tag{2}$$

and for benzene being cooled

$$U_v = 31.1 \times 10^4 \phi \quad \text{W/m}^3\text{°C} \tag{3}$$

However, their experiments were conducted with two different size drops. For the benzene being heated the drops were 7.34 mm in diameter and for the benzene being cooled the diameter of the drops was 6.71 mm. Rosenthal's (Treybal, 1953) data for toluene show a similar trend. Rosenthal used two different orifice diameters for his injection plates, 7.2 mm and 3 mm. Higher heat transfer was achieved with the smaller drops.

Woodward's (1961) data for Shell Oil A, spray base, and kerosene were accumulated for a single volumetric flow ratio, $G_D/G_C = 2.5$, and a single drop diameter, 3.5 mm. For this condition, the data correlate as

$$U_v = 22.4 \times 10^4 \phi \quad \text{W/m}^3\text{°C} \tag{4}$$

In 1979, a research team at the University of Utah carried out a study of liquid-liquid heat transfer characteristics of a 6′ × 6″ diameter spray column using water as the continuous phase and insulating oil as the dispersed phase (Plass et al., 1979). An orifice plate was chosen that yielded 1.75-2.00 mm radius drops. Data were acquired for very small holdups up to near the flooding limit. Using their data and all of the existing data for organic liquids, they arrived at the following correlations:

$$U_v = 22.4 \times 10^4 \phi \quad \text{W/m}^3\text{°C (for } \phi < 0.05) \tag{5}$$

and

$$U_v = [83.9 \times 10^4 (\phi - 0.05) e^{-0.57 G_D/G_C} + 1.12 \times 10^4] \quad \text{W/m}^3\text{°C (for } \phi > 0.05) \tag{6}$$

The above correlations yielded conservative results and appeared to be accurate to within ±20 percent not only for those organic fluids lighter than water, but also for the data for R-113, which is 1.4 times as heavy as water. No attempt was made to use the correlations for the existing liquid metal-water system (Pierce et al., 1959).

Letan and Kehat (1968) were involved in designing a spray column using kerosene dispersed in a continuous water phase. Due to difficulties in rationalizing their data, they sought a hydrodynamic explanation based on single drops and a wake shedding model. This model assumed that a drop rising through a continuous phase would have a wake forming phase followed by a wake shedding phase and then would, in a spray column, have an agglomeration stage. This model was to explain apparent high heat transfer at the top and bottom of their column. Their model assumed perfect mixing within the drops, and the heat transfer governed by the wake buildup and shedding. Empirical relations for wake size and shedding rate were incorporated in the model. For very long columns, the model led to a constant heat transfer rate. The problems with this model include the fact that for small drops, ~ 1.75 mm radius, little internal circulation occurs (Grace, 1983), and for moderate holdup $\phi \sim 0.15$-0.30, the distance between drops would not allow for wake sizes typical of those assumed in the model. In fact, studies reported by Steiner and Hartland (1983) indicate that the flow field external to the drops resembles flow over a closely spaced staggered tube bundle with no wakes being formed.

In 1980, Barber-Nichols Engineering, under U.S. Depart-

Contributed by the Heat Transfer Division and presented at the ASME/AIChE National Heat Transfer Conference, Denver, Colorado, August 1985. Manuscript received by the Heat Transfer Division July 10, 1987. Keywords: Evaporation, Multiphase Flows.

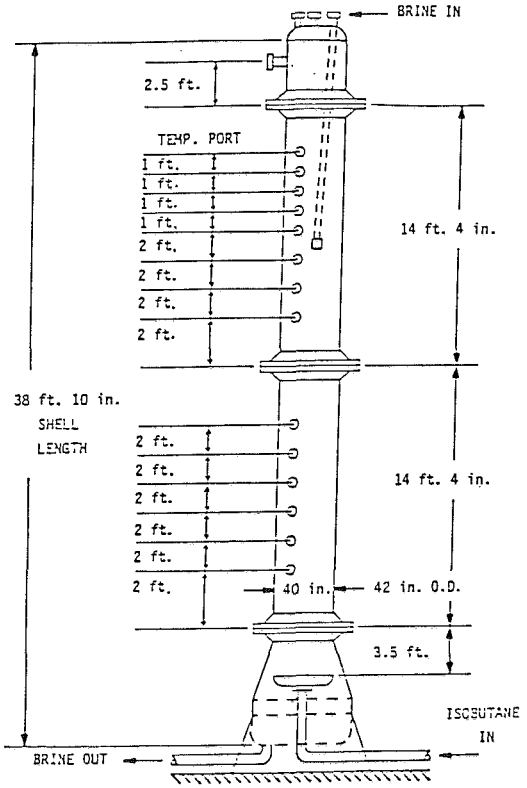

Fig. 1 Schematic of 500-kWe direct contact heat exchanger

ment of Energy funding, began construction of a direct contact geothermal demonstration power plant at East Mesa, CA (Ohlander et al., 1980). The direct-contact heat exchanger for this system was designed by this paper's first author. The column (see Fig. 1) combined a boiler section at the top of the column with a liquid–liquid preheater section. Isobutane was injected at the bottom of the column as the dispersed phase and the geothermal brine at the top. For operation at 90 percent of flooding with a pinch point temperature of 5°F (2.8°C), equation (6) indicated a preheater (liquid–liquid) length of about 22 feet (6.7 m) above the isobutane distributor plate assuming 1.75 mm radius drops. The nature of the potential drop behavior was studied using a small distributor plate in a glass column with normal pentane as the working fluid instead of isobutane. This was done so that the experiments could be conducted near atmospheric pressure. Drops of 1.6 mm radius ± 0.1 mm were formed. They maintained a nearly spherical shape with no fluctuation or oscillation, which is contrary to the empirical curve of Grace (1983). The column was successfully operated over a 2.5 year period. However, temperature profiles measured in the preheater section appeared to be anomalous from that expected for a constant value of U_v.

In order to gain some insight into the operational characteristics of the East Mesa Column, the largest spray column yet constructed, the U.S. Department of Energy funded the present authors to carry out the study described herein. In this paper, we concentrate on the preheater section of the column. Rather than using the simple correlation equations that have normally been used for design for both the hydrodynamics and heat transfer, we have formulated the problem in terms of the basic conservation equations for multiphase flows. We then investigated several models for the interphase heat transfer.

Mathematical Modeling

In a spray column, where the column diameter is very much larger than the droplet size, and if the continuous phase does not have significant recirculation zones, the flow can be assumed to be effectively one dimensional.

Assuming steady state, the one-dimensional continuity equations for the continuous phase and dispersed phase are, respectively,

$$\frac{d}{dx}((1-\phi)\rho_c V_c)=0 \tag{7}$$

and

$$\frac{d}{dx}(\phi\rho_d V_d)=0 \tag{8}$$

The conservation of momentum equations for a two-component system of immiscible fluids can be written in terms of the conservation of momentum of one fluid and for the mixture as a whole. Thus, we have for the dispersed phase

$$\frac{d}{dx}(\phi\rho_d V_d^2)=-\phi\frac{dP}{dx}-K(V_c-V_d)-\phi\rho_d g \tag{9}$$

and for the mixture as a whole

$$\frac{d}{dx}((1-\phi)\rho_c V_c^2)+\frac{d}{dx}(\phi\rho_d V_d^2)$$

$$=-\frac{dp}{dx}-((1-\phi)\rho_c+\phi\rho_d)g \tag{10}$$

Nomenclature

C_D = drag coefficient
C_p = specific heat
G = volumetric flow rate
g = gravitational acceleration
h = enthalpy
h_m = mean surface heat transfer coefficient
k = thermal conductivity
K = interphase friction factor
LMTD = log mean temperature difference
m = mass flow rate
Nu_D = average surface Nusselt number
N_d = number of droplets of dispersed phase
P = pressure
Pr = Prandtl number
Q = heat transfer rate
r = radial coordinate
R_d = radius of droplets
Re_{D_C} = Reynolds number = $\rho_c\lvert(V_c - V_d)\rvert D/\mu_c$
t = time
t_1 = time for a droplet to rise through the column $= x/V_d$
T = temperature
U_v = volumetric heat transfer coefficient
V = velocity in x direction
Vol = volume
x = vertical coordinate measured from the bottom of the column
α = thermal diffusivity
μ = dynamic viscosity
ρ = density
ϕ = holdup, fraction of volume occupied by the dispersed phase

Subscripts

c = continuous phase
d = disperse phase
i = at the interface between the droplets and continuous phase
o = at entrance conditions

where K is the interphase friction factor. Note that the interphase friction factor does not occur in the mixture equation as it acts with equal magnitude but opposite direction on each of the two phases.

The energy equation for the droplets is

$$\frac{d}{dx}(\phi\rho_d V_d h_d) = -Q_i/\text{Vol} \tag{11}$$

and for the mixture

$$\frac{d}{dx}((1-\phi)\rho_c V_c h_c) + \frac{d}{dx}(\phi'_d V_d h_d) = 0 \tag{12}$$

where Q_i/vol is the rate of interfacial heat transfer per unit volume. As was the case for the interfacial friction, no interfacial heat transfer term occurs in the mixture equation.

The set of differential equations given in equations (7)–(12) has to be solved in conjunction with observance of variables represented by algebraic relations. The density and temperature for each fluid must be represented by an equation of state written in terms of that fluid's enthalpy and pressure. (Riemer et al., 1976a, 1976b).

The interfacial friction factor K may be written as

$$K = N_d \pi R_d^2 C_d \, 1/2\rho_c \left| V_d - V_c \right| \tag{13}$$

where the number of droplets per unit volume N_d is

$$N_d = \frac{\phi}{\frac{4\pi}{3} R_d^3} \tag{14}$$

Substituting equation (14) into equation (13) yields

$$K = \frac{3\phi}{8R_d} C_D \rho_c \left| V_d - V_c \right| \tag{15}$$

The drag coefficient C_D is in general a function of the Reynolds number of the droplet, which in turn is a function of the droplet radius, kinematic viscosity of the continuous phase, and the relative velocity between phases. However, in the present analysis, the drag coefficient can be assumed to be of a constant value of 0.4, which is approximately valid for a droplet Reynolds number in the range of $10^3 - 10^5$. This range is typical of that calculated for the rise of hydrocarbon liquid droplets in water or geothermal brine.

There are several ways of establishing the interfacial heat transfer per unit volume, Q_i/Vol. *Utilizing the concept of a volumetric heat transfer coefficient* U_v, we could write

$$Q_i/\text{Vol} = U_v(T_d - T_c) \tag{16}$$

in equation (11). In so doing, we would be able to utilize any of the correlations found in the literature. The correlations most representative of all existing data are those given in equations (5) and (6). As these correlations were not based on actually measured values of holdup, but rather on empirical correlation, we could use that correlation instead of the calculated values of ϕ from the governing equations.

A second possible way to evaluate U_v *is to assume that the heat transfer to the working fluid droplets is controlled by the convective heat transfer outside of the drop.* This is essentially the same as assuming no resistance to heat transfer within the drop. (While this may be accurate for liquid metal drops, organic liquids such as refrigerants, oils, or hydrocarbons normally have very low thermal conductivity, and thus, such an assumption is suspect.) If we were to use such a model, Sideman (1966) recommends the following correlation for the mean surface heat transfer coefficient h_m:

$$\text{Nu}_{Dp} = 2.0 + 0.6 \, \text{Re}_{DC}^{1/2} \, \text{Pr}_{DC}^{1/3} \tag{17}$$

The relationship between U_v and h_m can be shown to be

$$U_v = 4N_d \pi R_d^2 h_m \tag{18}$$

Another method for establishing Q_i*/Vol that we will consider for establishing the mechanism of heat transfer between the phases is to assume that the outside heat transfer coefficient is large and that the heat transfer inside the drop is the controlling mechanism.* Since the droplets remain spherical as noted earlier, the internal circulation should be small. For such fluids as refrigerants and hydrocarbons, which are notoriously poor conductors, a small radius could well cause conduction to dominate at Re_{D_C} above 500. (Note: This would require only a small shift in the boundary of the empirical curves of Grace (1983), which are used to define drop behavior.) In order to facilitate the use of this idea, one could use the one-dimensional transient spherical conduction equation with a time-dependent boundary condition. This equation is

$$\frac{\partial(\rho C_p T)_d}{\partial t_1} = \frac{1}{r^2}\frac{\partial r^2 k_d \frac{\partial T_d}{\partial r}}{\partial r} \tag{19}$$

Here t_1 is defined as the elapsed time from the point of origin to x, which is equal to x/V_d. The associated initial and boundary conditions are

$$T_d = T_{do} \text{ at } t_1 = 0$$
$$T_d \text{ is finite at } r = 0 \tag{20}$$

and

$$T_d = T_c \text{ at } r = R_d$$

T_{do} is the temperature of the droplets at the injection point.

In order to solve equation (19) subject to the conditions given in equation (20), one may assume two different approaches. If ρ_d, Cp_d, and k_d do not change significantly, there would result an analytical solution for the mean temperature of the droplet utilizing the Duhammel superposition integral

$$T_{dm}(t_1) = T_{do} + \frac{6\alpha_d}{R_d^2}\left(\sum_{n=1}^{\infty} e^{\frac{-\alpha_d n^2}{R_d^2}}\right)\left(\int_0^{t_1} e^{\frac{\alpha_d n^2 \pi^2 S}{R_d^2}}(T_c - T_{do})ds\right) \tag{21}$$

Obtaining the solution of equation (19) in this manner precludes the solution of equation (11). However, equation (19) must be solved subject to simultaneously satisfying equations (7), (8), (10), and (12).

If the integration is done along sufficiently small steps in time, t_1, then T_c could be considered constant during each of these intervals and the resulting expression for T_{dm} would be

$$T_{dm}(t_1) = T_{do} + \frac{6}{\pi^2}\sum_{n=1}^{\infty}\frac{1}{n^2} e^{\frac{-\alpha_d n^2 \pi^2 t_1}{R_d^2}}\left(\sum_{i=1}^{M}(T_c - T_{do})\right.$$
$$\left.(e^{\frac{\alpha_d n^2 \pi^2}{R_d^2}}(\Delta t_i - \Delta t^{i-1}))\right), \tag{22}$$

where Δt = time step equal to $\Delta x/V_w$ and M = number of time steps to reach time t_1.

The second method for solving equation (19) subject to the conditions of equation (20) is to account for the change of the dispersed phase properties ρ_d, Cp_d, *and* k_d *as the droplet traverses the height of the column.* When this is required due to a density change, then the droplet radius also changes

$$R_d = R_{d_o}\left(\frac{\rho_{do}}{\rho_d}\right)^{1/3} \tag{23}$$

The change in radius leads to changes in drag, holdup, and phase velocity along the length of the column resulting in a computationally much more difficult problem.

A fourth way of determining Q_i/Vol is to account for both the internal and external heat transfer. This would be to solve equation (19) subject to the boundary conditions

$$T_d = T_{di} \text{ at } t_1 = 0$$
$$T_d \text{ is finite at } r = 0 \tag{24}$$

and

$$-K \frac{\partial T_d}{\partial r} \Big|_{R_d} = h_D (T_d - T_c) \Big|_{R_d}$$

Equation (19) subject to equation (24) and including the drop growth defined by equation (23) requires numerical solution in a separate subroutine. h_D can be obtained from equation (17).

Typically in carrying out an analysis for the design of a direct contact liquid–liquid heat exchanger, the two fluids, their mass flow rates, and their temperatures as they enter the column are specified, as well as the pressure at the top of the column. The column diameter is also specified in such a way as to insure that flooding would not take place in an isothermal column. Next one can specify the exit temperature of one of the fluids or the length of the column. This is, of course, analogous to the procedures used in designing shell and tube heat exchangers. For the latter case, one must worry about excessive pressure drop; however, for direct-contact heat exchangers one must concern himself with flooding. If such a condition exists, one must change either the flow rates or the column diameter. Although in an isothermal column it is only necessary to check the flooding condition at one axial location, in a column with heat exchange the holdup may change anywhere along its length. Thus, one does not design at the flooding point, although the correlations for U_v would indicate the higher the value of holdup, the higher the heat transfer. Typically, one designs for 90 percent of holdup as a maximum with the column.

For steady-state operation of a spray column with inlet and outlet temperatures specified the unknowns are the length of the column and the holdup, temperature distributions, and pressure along the length of the column.

Numerical Solution

In carrying out the numerical solutions the governing equations are first converted into a set of algebraic equations using an upwind differencing technique. As the finite difference equations are strongly coupled and nonlinear they have to be solved by an iterative guess and correct technique. The method used closely follows that of Spalding and co-workers (Spalding, 1976, 1980; Kurosaki and Spalding, 1979). An outline of the procedure follows. Details of the programming may be found in Golafshani's (1984) dissertation.

1 Determine the boundary conditions at the upper and lower limits of the solution domain. Estimate a length for the exchanger.
2 Select appropriate guesses for all dependent variables.
3 Determine the pressure distribution appropriate to the finite difference equation of the mixture momentum equation.
4 Solve the energy equations for the dispersed phase and the mixture and update the densities of the fluids.
5 Using the pressure distribution, solve for the velocity of the working fluid droplets.
6 Check for continuity of the two fluids. Assume any error is due to pressure. The net error when the two fluid continuity equations are added together is a "source term." This term is used to modify the pressure so that continuity is assured.
7 Corrections are made to the velocities and densities using the pressure corrections and the two momentum equations.
8 Using the corrected densities and velocities the holdup is calculated along the column using the continuity equation for the dispersed phase.
9 A second phase of correction is introduced by using the continuous phase continuity equation to find $V_c(x)$.
10 Steps (3)–(9) are repeated until the continuity errors computed at step (6) are sufficiently small.

The finite difference equations for a given variable, over the integration domain, at a given stage of the whole solving procedure are solved using a tridiagonal algorithm.

Results and Discussion

In order to evaluate the six methods of predicting the heat transfer in a direct-contact preheater discussed in this paper, it is necessary to compare the predictions with experimental data. The final report on the operation of the 500-kW_e facility at East Mesa (Olander et al., 1983) provides such information.

The 500-kW_e direct-contact heat exchanger, shown schematically in Fig. 1, is a 40-in. (1.02-m) inside diameter spray column. The East Mesa brine contains typically less than 2000 ppm dissolved solids and a small amount of CO_2 gas. The brine was preflashed to drive off most of the CO_2 prior to entering the heat exchanger. The perforated plate distributor was designed to deliver the isobutane as 1.6-mm-radius drops. Laboratory experiments using pentane indicated that for a range of ± 10 percent of design flow rates that this radius was obtained for virtually all of the droplets.

The column was operated as a combined preheater–boiler. Inlet and outlet temperatures for the two fluids as well as flow rates and pressure were reported. In addition, temperatures were recorded using resistance thermometers along the length of the column. As the resistance thermometers were relatively large, ~ 3.2 mm in diameter, they recorded neither the continuous nor the dispersed phase temperature, but rather some sort of time and flow-based average. Thus, the resistance thermometer data should lie between the values calculated for the continuous and dispersed phases. An adequate heat transfer model for the preheater should be able to predict these temperatures as well as heights of the preheater. No attempt was made to analyze the boiler section. It was assumed to start when the dispersed phase reached its saturation temperature and continue up the column. Assuming complete evaporation of the isobutane and partial evaporation of the brine according to equilibrium thermodynamics, the brine temperature at the top of the preheater can be calculated.

Figures 2–4 show data from three different operating conditions of the 500-KW_e direct-contact heat exchanger assuming 2.0-mm-radius drops. Figure 2 compares the three possible methods described earlier for calculating U_v. Method I utilizes equations (5) and (6) with the holdup calculated by

$$0.81(m+1)((1-\phi)V_c - \phi V_d)\delta + 0.09(m+2)V_d\phi - V_d = 0 \tag{25}$$

where $m = 1.39$ for droplet $Re_{D_C} > 500$. Method II utilizes equations (5) and (6) with the holdup as calculated from equations (7)–(10). Method III results from the use of equations (17) and (18) and is applicable to a perfectly mixed drop. It is clear from Fig. 2 that the latter model is unacceptable as it overpredicts the heat transfer. This is illustrated by the fact that the ebullition temperature is reached far below the length required experimentally. Thus, Model III was eliminated from further consideration.

If one looked only at Figs. 2 and 3 he would think that the entirely empirical Model I would best describe the heat transfer; however, Fig. 4 indicates that Model II best fits the data. The primary difference between the operating conditions for Figs. 2 and 3 as opposed to Fig. 4 is in the flow rate.

As the heat transfer was clearly not governed by the external

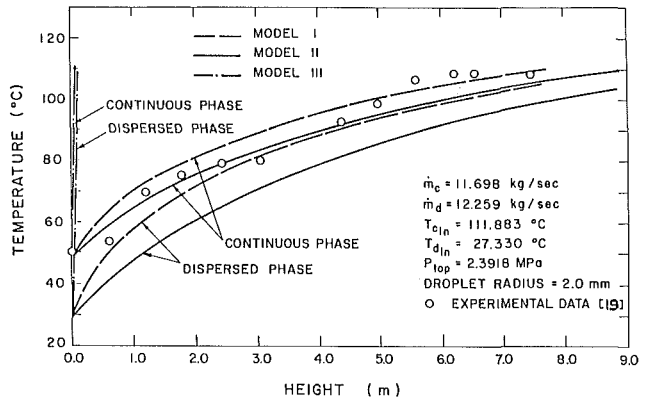

Fig. 2 Temperature profile of the brine and the working fluid along the length of the column for comparison of models I, II, and III

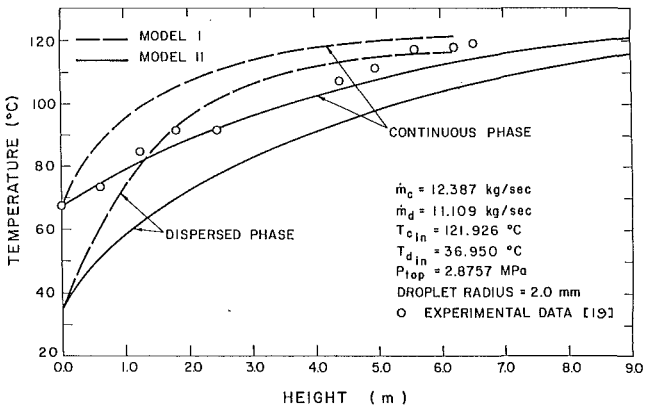

Fig. 3 Temperature profile of the brine and the working fluid along the length of the column for comparing models I and II; $\dot{m}c$ = 12.387 kg/s, $\dot{m}d$ = 11.109 kg/s

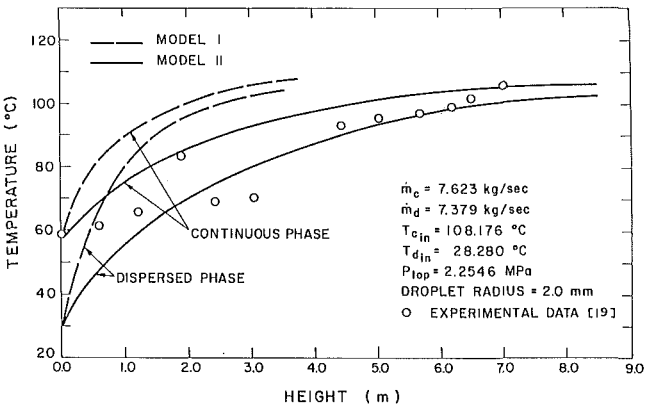

Fig. 4 Temperature profile of the brine and the working fluid along the length of the column for comparing models I and II; $\dot{m}c$ = 7.623 kg/s, $\dot{m}d$ = 7.379 kg/s

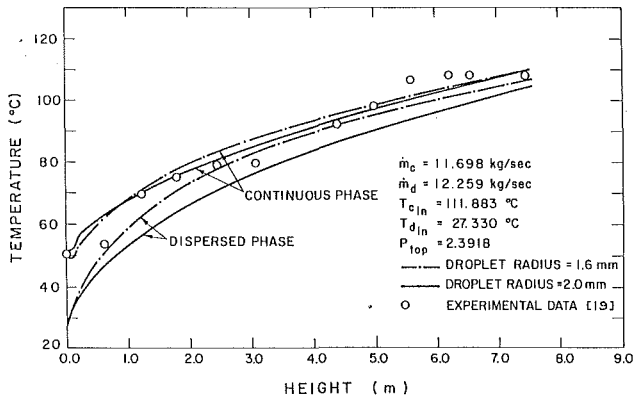

Fig. 5 Temperature profile of the brine and the working fluid along the length of the column using constant-diameter model; $\dot{m}c$ = 11.698 kg/s, $\dot{m}d$ = 12.259 kg/s

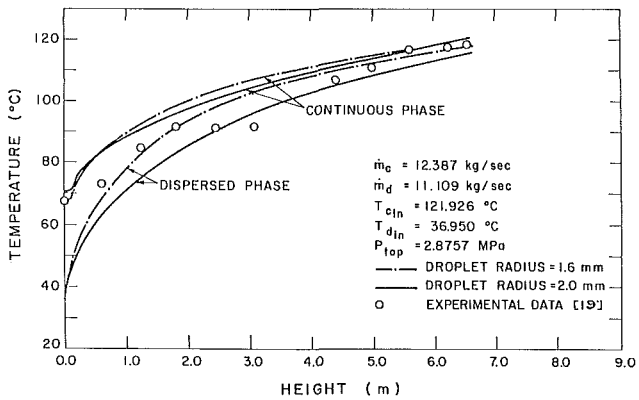

Fig. 6 Temperature profile of the brine and the working fluid along the length of the column using constant-diameter model; $\dot{m}c$ = 12.387 kg/s, $\dot{m}d$ = 11.109 kg/s

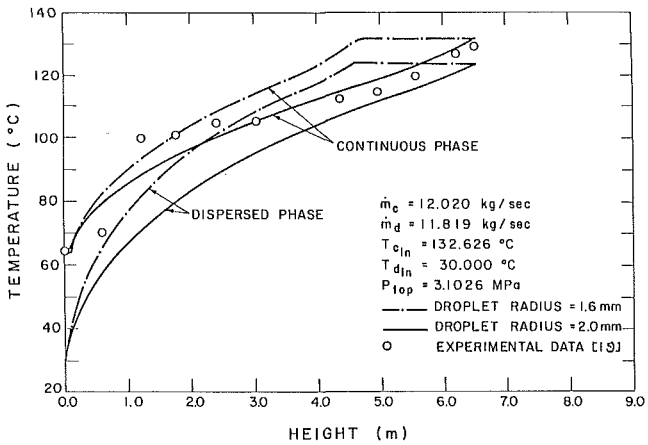

Fig. 7 Temperature profile of the brine and the working fluid along the length of the column using constant-diameter model; $\dot{m}c$ = 12.02 kg/s, $\dot{m}d$ = 11.819 kg/s

heat transfer coefficient, at least as described by equations (17) and (18), a fourth model was introduced. If one postulates that the dispersed phase was made up of droplets that had no internal circulation, then the heat transfer could be dominated by internal conduction. This is Method IV. The heat transfer would then be described by a transient conduction model such as the one described by equations (19) and (20). Initially such a model was developed by assuming the droplets would be of constant diameter even though it was known that a considerable change in density would be experienced by the isobutane for the operating conditions of the 500-kW_e direct-contact heat exchanger. The reason for this assumption was to cut down on the computer time of the solution, since an analytical solution was available as indicated by equations (21) and (22). Golafshani (1984) analyzed more than nine different experi-

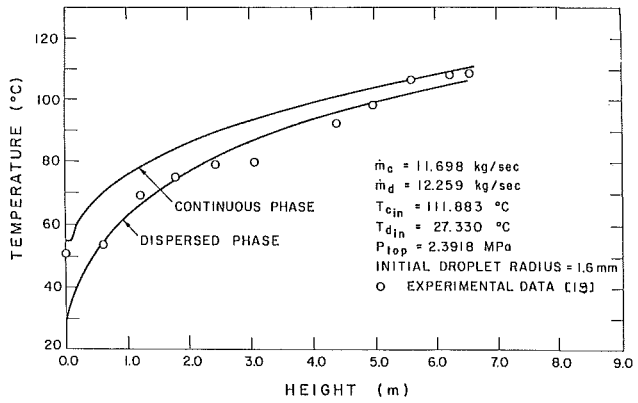

Fig. 8 Temperature profile of the brine and the working fluid along the length of the column using variable radius model; $\dot{m}c$ = 11.698 kg/s, $\dot{m}d$ = 12.259 kg/s

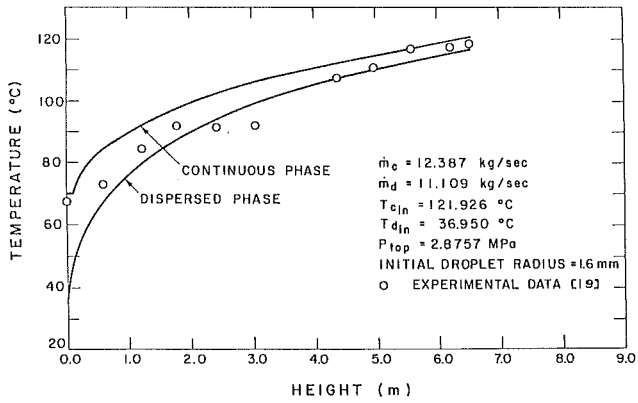

Fig. 9 Temperature profile of the brine and the working fluid along the length of the column using variable radius model; $\dot{m}c$ = 12.387 kg/s, $\dot{m}d$ = 11.109 kg/s

ments assuming constant drop radii of 1.6 mm and 2.0 mm. Figures 5 and 6 illustrate typical results. It is clear that to approach duplicating all of the date neither choice of constant radius is always acceptable. Figure 7 illustrates a clear example where the heat transfer near the bottom of the column was well represented by the smaller radius, yet the total preheater length and temperature distribution at the top was better represented by the larger radius. Since both the higher temperature and lower pressure that occur as the isobutane droplets approach the top might explain this behavior, the fifth model tried was the variable property, variable radius conduction model, Method V. Figures 8–10 are the same cases as presented in Figs. 5–7. It is clear that this latter model accurately predicts the preheater length as well as the temperature except for the depression of temperature near the 3-m location. This depression appears in all of the East Mesa 500-kW_e direct contactor data. It could be due to recirculation within the column or temperature depression due to the massive central flange located just above it. In order to ascertain which, it would be necessary to carry out two-dimensional multiphase analyses.

The last model tried was the solution of equation (19) subject to the boundary conditions given in equation (24) and accounting for drop growth, Method VI. No significant difference was found from that when the boundary conditions given in equation (20) were used. This clearly indicates that the internal resistance to heat transfer dominates the results.

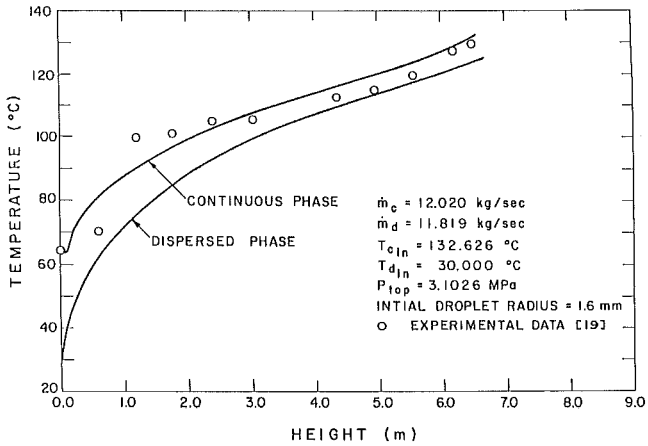

Fig. 10 Temperature profile of the brine and the working fluid along the length of the column using variable radius model; $\dot{m}c$ = 12.02 kg/s, $\dot{m}d$ = 11.819 kg/s

Conclusions

Previous investigators, including the first author, have attempted to argue that the rate of heat transfer from water to dispersed organic liquids or vise versa in a spray column was governed primarily by flow phenomena. The current study, however, clearly indicates that the controlling mechanism for small diameter drops is the internal transfer of heat. For drops that remain spherical little circulation takes place. Thus, the mechanism is probably controlled by conduction. Variable properties as a function of temperature and pressure must be accounted for in order to predict preheater length accurately in isobutane systems.

Since in large drops internal circulation can take place, it may be possible to reduce the preheater length in spray columns by going to larger drop sizes than the 1.5–2.0 mm radius currently being used in the design of direct contactors for geothermal or solar applications. Care would have to be taken to insure that drop integrity is maintained. Continued studies of internal drop heat transfer are warranted.

Further studies using two-dimensional multiphase modeling are recommended so as to investigate the prevalent temperature depression in the middle of the East Mesa 500-kW_e direct contact heat exchanger. Such a model should investigate the role of the mass of the direct contactor and the external environment, as well as potential internal recirculation and droplet agglomeration and redivision, as possible sources of the anomaly.

Acknowledgments

This work was carried out under contract with the U.S. Department of Energy, Contract number DE-AS07-761D01523. The data supplied by Mr. Robert Olander of Barber-Nichols Engineering were appreciated as was the technical encouragement of Mr. Judson Whitbeck of EG&G-Idaho, Inc.

References

Garwin, L., and Smith, B. D., 1953, "Liquid–Liquid Spray Tower Operation in Heat Transfer," *Chemical Engineering Progress*, Vol. 49, No. 11, pp. 591–601.

Golafshani, M., 1984, "Stability of a Direct Contact Heat Exchanger," Ph.D. Dissertation, University of Utah, Salt Lake City, UT.

Grace, J. R., 1983, "Hydrodynamics of Liquid Drops in Immiscible Liquids," *Handbook of Fluids in Motion*, N. P. Cheremisinoff and R. Gupta, eds., Ann Arbor Science, The Butterfield Group, Ann Arbor, MI, Chap. 38, pp. 1003–1025.

Holt, B., 1977, "A Preliminary Study of Direct Contact Heat Exchangers for Geothermal Power Production," a report submitted to ERDA by the Ben Holt Company, Pasadena, CA.

Jacobs, H. R., and Boehm, R. F., 1980, "Direct Contact Binary Cycles," *Sourcebook on the Production of Electricity From Geothermal Energy*, J. Kestin, ed., DOE/RA/4051-1, Washington, DC, Section 426.

Johnson, A. I., Mirand, G. W., Huang, C. J., Hansuld, J. H., and Mc-

Namara, V. M., 1957, "Spray Extraction Tower Studies," *AIChE J.*, Vol. 3, pp. 101–110.

Kurosaki, Y., and Spalding, D. B., 1979, "One Dimensional Two-Phase Flows," 2nd Multiphase Flow and Heat Transfer Symposium Workshop, "Multiphase Transport: Fundamentals, Reactor Safety, Application," Hemisphere Publishing, Washington, DC, Vols. 1–5.

Letan, R., and Kehat, 1968, "The Mechanism of Heat Transfer in a Spray Column Heat Exchanger," *AIChE J.*, Vol. 14, No. 3, pp. 398–405.

Olander, R., Oshmyansku, S., Nichols, K., and Werner, D., 1983, "Final Phase Testing and Evaluation of the 500kW$_e$ Direct Contact Pilot Plant at East Mesa," U.S.D.O.E. Report DOE/SF/11700-T1, Arvada, CO.

Pierce, R. D., Dywer, O. E., and Martin, J. J., 1959, "Heat Transfer and Fluid Dynamics in Mercury-Water Spray Columns," *AIChE J.*, Vol. 5, p. 257.

Plass, S. B., Jacobs, H. R., and Boehm, R. F., 1979, "Operational Characteristics of a Spray Column Type Direct Contact Preheater," *AIChE Symposium Series*, No. 189, pp. 227–234.

Riemer, D. H., Jacobs, H. R., and Boehm, R. F., 1976a, "A Computer Program for Determining the Thermodynamic Properties of Water," University of Utah, U.S. D.O.E. Report IDO/1549-2.

Riemer, D. H., Jacobs, H. R., Boehm, R. F., and Cook, D. S., 1976b, "A Computer Program for Determining the Thermodynamic Properties of Light Hydrocarbons," University of Utah, U.S. D.O.E. Report IDO/1549-3.

Sideman, S., 1966, "Direct Contact Heat Transfer Between Immiscible Liquids," *Advances in Chemical Engineering*, Vol. 6, Academic Press, New York, pp. 207–286.

Spalding, D. B., 1980, "Numerical Computation of Multiphase Fluid Flow and Heat Transfer," *Recent Advances in Numerical Methods in Fluids*, C. Taylor and K. Morgan, eds., Pineridge Press, Swansea, United Kingdom, pp. 139–167.

Spalding, D. B., 1976, "The Calculation of Free Convection Phenomena in Gas-Liquid Mixtures," Lecture at ICHMT Seminar, Dubrovnik, Yugoslavia.

Steiner, L., and Hartland, S., 1983, "Hydrocarbons of Liquid-Liquid Spray Columns," *Handbook of Fluids in Motion*, N. P. Cheremisinoff and R. Gupta, eds., Ann Arbor Science, The Butterfield Group, Ann Arbor, MI, Chap. 40, pp. 1049–1091.

Suratt, W. B., and Hart, G. K., 1977, "Study and Testing of Direct Contact Heat Exchangers for Geothermal Brines," *DSS Engineers*, Fort Lauderdale, FL, ERDA Report No. ORO-4893-1.

Treybal, R. E., 1953, *Liquid Extraction*, 1st ed., McGraw-Hill, New York.

Woodward, T., 1961, "Heat Transfer in a Spray Column," *Chemical Engineering Progress*, Vol. 57, pp. 52–57.

Direct Contact Evaporation Between Two Immiscible Liquids in a Spray Column

K. N. Seetharamu

P. Battya

Department of Mechanical Engineering,
Indian Institute of Technology,
Madras, India

The present investigation deals with the direct contact evaporation of refrigerant 113 and n-pentane in a stagnant column of distilled water. The operational parameters investigated in the experimental study are the operating column height, the temperature difference, the dispersed phase flow rate, and the diameter and number of orifices in the distributor. The effects of these parameters on volumetric heat transfer coefficient, holdup, and agglomeration are investigated. A modified relation, based on the theoretical analysis of Smith et al. (1982), is also developed for predicting the theoretical volumetric heat transfer coefficient. Comparison with related works available in the literature shows reasonable agreement.

Introduction

Direct contact heat transfer between two immiscible liquids has the advantage of eliminating metallic heat transfer surfaces that are prone to corrosion and fouling. The main features of direct contact heat exchangers are: relative simplicity of design, fewer scaling problems, higher heat transfer rates, and capacity to operate at relatively small temperature driving forces. The practical applications are found in water desalination, geothermal heat recovery, ocean thermal energy conversion, and thermal energy storage systems. A critical review of the investigations carried out in direct contact heat transfer is given by Sideman (1966).

Considerable work has been done to study the phenomenon of single drop evaporation in a stagnant column of immiscible liquid. Only a limited number of experimental and theoretical investigations dealing with multiple drops undergoing vaporisation in an immiscible liquid are available in the literature. Sideman et al. (1965) studied the effect of initial size of *n*-pentane drops evaporating in water in a counterflow direct contact heat exchanger. Sideman and Gat (1966) studied the performance of a counterflow spray column with a pentane-water system. The effect of the water flow rate was found to be relatively small. Heat transfer characteristics of a direct contact volume boiler were studied by Blair et al. (1966). They used water as the continuous phase and R-113, which is denser than water, as the dispersed phase. The volumetric heat transfer coefficients obtained in their study were lower than those obtained by Sideman and Gat (1966) for water–pentane systems.

Smith et al. (1982) developed an analytical model for the evaluation of the volumetric heat transfer coefficient in direct contact evaporation between two immiscible liquids in a spray column. They also conducted experiments with cyclopentane as the dispersed phase and stagnant water as the continuous phase. Experiments were carried out using two distributor plates. The second distributor, with closer spacing of holes, resulted in considerable agglomeration requiring higher column heights for complete evaporation of the dispersed phase at a given temperature difference.

The present investigation is aimed at the study of the effects of the various operating parameters on volumetric heat transfer coefficient. Two different liquids, refrigerant-113 and n-pentane, are used as the dispersed phase to study the effects of the physical properties of the dispersed phase on the heat transfer process. A modified relation, based on the theoretical analysis of Smith et al. (1982), is also developed for predicting the volumetric heat transfer coefficient.

Experimental Apparatus

The experimental setup is shown schematically in Fig. 1. It consists of a test vessel, hot water supply system, dispersed phase supply system, and condensation system. The details of the test vessel are shown in Fig. 2. It is made of Corning glass with an inside diameter of 10.5 cm and a length of 40 cm. Perspex end plates with O-ring seals are secured to the glass tubing with four threaded steel rods.

The dispersed phase is injected into the test vessel from a brass injection manifold located at the bottom of the vessel. The manifold consists of a main and an interchangeable perforated plate or distributor. The dispersed phase liquid is supplied to the injection manifold through a tube penetration in the lower perspex plate from a graduated supply tank. The supply tank is pressurized using nitrogen or air and the pressure is maintained constant using a pressure regulator. The dispersed phase flow rate is measured using a rotameter. The dispersed phase vapor is collected from the top of the vessel and condensed in a water-cooled, tube-in-shell heat exchanger. The condensate is collected in a storage tank.

Hot water is supplied to the test vessel by a Haake constant-temperature circulating bath equipped with a thermostatically controlled heater. The distributor disks are 90 mm in diameter and 4 mm thick. Four different types of configuration are used for the arrangement of orifices in the distributor. The number of orifices in the four configurations are 4, 7, 19, and 36 respectively. In each configuration, four different orifice diameters of 0.35, 0.5, 1.0, and 1.5 mm are employed. The arrangement of holes in the distributor is shown in Fig. 3.

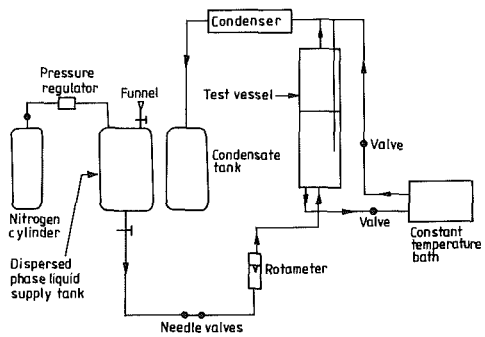

Fig. 1 Schematic diagram of experimental setup

Contributed by the Heat Transfer Division for publication in the JOURNAL OF HEAT TRANSFER. Manuscript received by the Heat Transfer Division May 27, 1986. Keywords: Direct-Contact Heat Transfer, Evaporation.

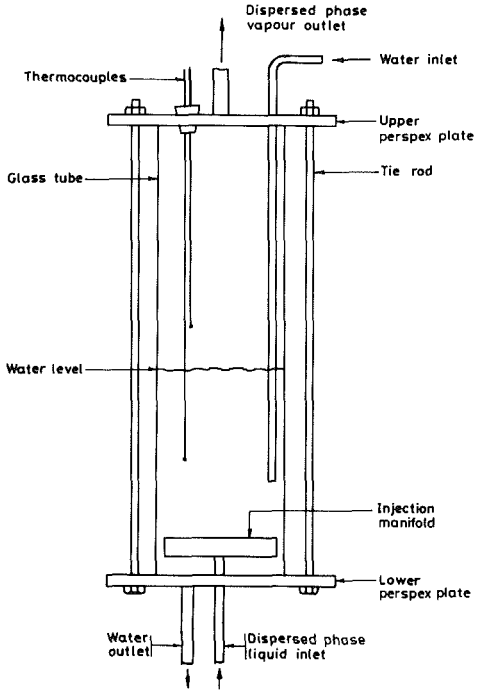

Fig. 2 Assembly drawing of test vessel

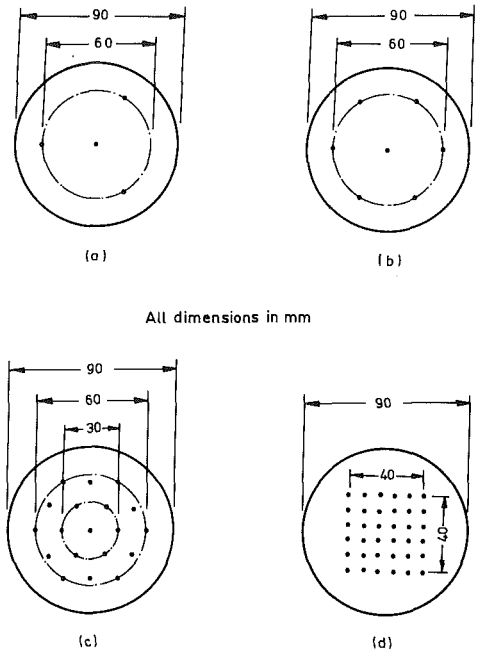

Fig. 3 Orifice configurations

Operation of the Experiment

The experiment is conducted as follows. Water is heated in the constant-temperature bath to the desired temperature. The dispersed phase liquid supply tank is pressurized to 0.5 $kg_f/cm^2 \cdot g$ using a nitrogen cylinder and a pressure regulator. The distributor is filled with the dispersed phase liquid using the needle valves. Hot water from the constant temperature bath is circulated through the test vessel. When the water in the test vessel attains a temperature of about 30 K above the dispersed phase saturation temperature, the vessel is filled with water to the desired level and the circulation is stopped. The needle valve is then adjusted to give the required flow rate of the dispersed phase liquid through the distribution. The dispersed phase liquid drops evaporate in the stagnant column of water and the superheated vapor leaves the test vessel. The heat transfer process progressively reduces both the water temperature and the dispersed phase vapor temperature. The evaporation is allowed to proceed until the dispersed phase escapes as a saturated vapor. The water temperature is measured at the instant when the dispersed phase vapor escapes at its saturation temperature. This gives the temperature of the water column required for complete evaporation of the dispersed phase. The dispersed phase flow rate and the length of the water column are also noted and the experimental run is completed. The experiment is repeated by varying the following parameters to study their effect on temperature difference, holdup, and volumetric heat transfer coefficient:

Nomenclature

A = surface area of evaporating drops, m^2
B = parameter in equation (4) $= 2h_{bo}T(\rho_{dl} - \rho_{dv})/u_o D_o L_d(\rho_{dl} \cdot \rho_{dv})$
C = constant in equation (10)
C_p = specific heat of continuous phase liquid, J/kg-K
d_h = orifice diameter, m
$D_{o,D}$ = initial and instantaneous diameters of evaporating drop, m
h_{bo} = individual droplet heat transfer coefficient, W/m^2-K
h_v = volumetric heat transfer coefficient, W/m^3-K
Ja = Jakob number $= \rho Cp\Delta T/\rho_{dv} L_d$
k = thermal conductivity of continuous phase liquid, W/m-k
L_d = latent heat of evaporation of dispersed phase, J/kg
m_a = parameter in equation (4) $= \frac{1}{2}(5 - 3x)$
Nu = Nusselt number $= h_{bo}D/k$
Pe = Peclet number = Re Pr
Pr = Prandtl number $= \mu Cp/k$
Q = mass flow rate of dispersed phase, kg/s
r = diameter ratio $= D/D_o$
Re = Reynolds number $= \rho uD/\mu$
s = spacing of orifices, m
u_o, u, u_r = initial, instantaneous, and relative drop velocities, m/s
U = overall surface heat transfer coefficient, W/m^2-K
v = orifice velocity, m/s
x = exponent of Re in equation (5)
Z = column height, m
α = average holdup
γ = constant in equation (5)
ΔT = temperature difference between continuous phase liquid and saturation temperature of dispersed phase liquid, K
μ = viscosity of continuous phase liquid, Ns/m^2
ρ = density of continuous phase liquid, kg/m^3
ρ_{dl} = density of dispersed phase liquid, kg/m^3
ρ_{dv} = density of dispersed phase vapor, kg/m^3

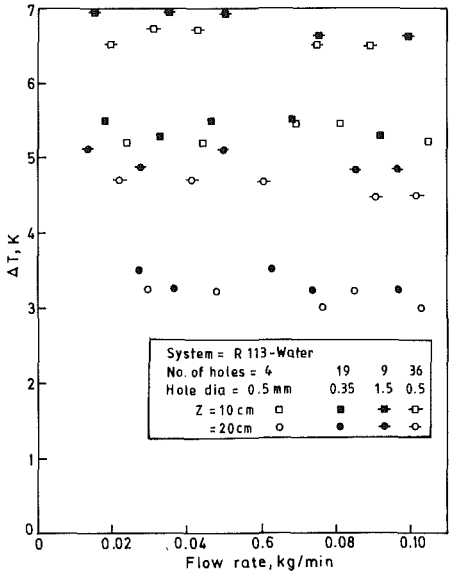

Fig. 4 Variation of ΔT with column height and flow rate

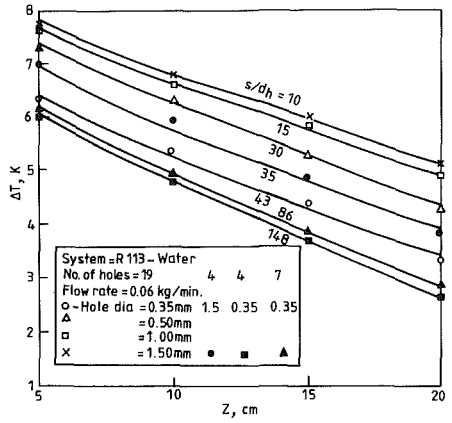

Fig. 5 Variation of ΔT with Z at different s/d_h ratios

1. Size, number, and spacing of orifices
2. Operating column height
3. Dispersed phase flow rate
4. Dispersed phase liquid

It is observed that there is no significant axial temperature gradient along the column. This was also observed by Smith et al. (1982) and may be attributed to the presence of turbulence during the evaporation process. Hence, a thermocouple located at the center of the water column is used to measure the water temperature. The thermocouple to measure the vapor temperature is located sufficiently above the water surface so that the bubbling action at the water surface does not affect the temperature measurement.

The uncertainties in the experimental measurements and the transport property values combine to give errors in the calculation of volumetric heat transfer coefficient of ±5 percent. The maximum error in the measurements of holdup value is about ±4 percent due to the changes in active level. The data were collected over a period of 6 months by a single individual. The reproducibility of the data was checked and found to be better than the uncertainty in the measurements.

Results and Discussion

The experimental results of direct contact evaporation of R-113 and pentane in a stagnant column of distilled water are discussed.

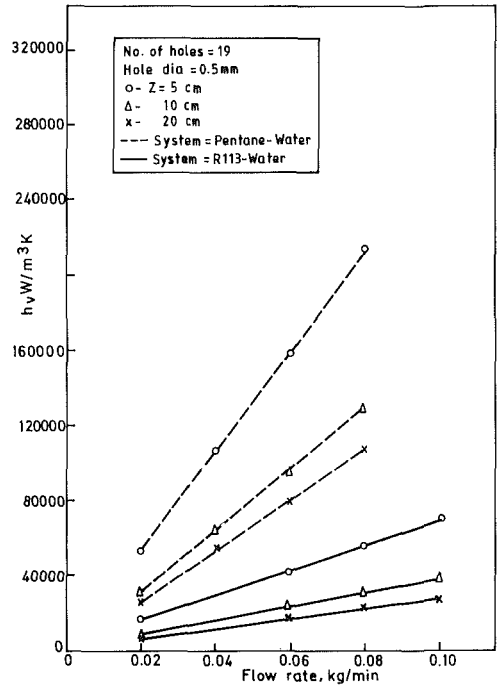

Fig. 6 Variation of h_v with column height and flow rate

Figure 4 shows, for an R-113–water system, the effect of column height and dispersed phase flow rate on the temperature difference, ΔT, required for complete evaporation for various orifice diameters and number of holes. It can be observed that as the column height decreases, ΔT increases. For a given column height, the change in dispersed phase flow rate is found to have small effect on ΔT. However, the hole diameter and spacing of holes have an effect on ΔT. Similar trends are also observed with a pentane–water system. Figure 5 illustrates, for an R-113–water system, the effect of column height and s/d_h ratios on ΔT at a constant dispersed phase flow rate of 0.06 kg/min. ΔT increases with a reduction in column height and with a decrease in s/d_h ratio. A lower s/d_h ratio results in increased agglomeration. The closeness of the curves for s/d_h ratios of 10 and 15 in Fig. 5 indicates the presence of agglomeration at small s/d_h ratios. The injection velocities also have an influence on ΔT. The velocities corresponding to the above s/d_h ratios are 0.0192 and 0.0432 m/s, respectively, whereas for the two s/d_h ratios of 148 and 86 the velocities are 1.676 and 0.058 m/s, respectively.

The performance of direct contact heat exchangers is usually represented by the volumetric heat transfer coefficient. Figure 6 shows the variation of volumetric heat transfer coefficient with column height and dispersed phase flow rate. The results obtained with a distributor having 19 holes 0.5 mm in diameter are shown in the figure. The volumetric heat transfer coefficient increases with a decrease in column height. A lower column height is associated with larger temperature differences, greater acceleration of the drops, and increased turbulence. The increase in turbulence causes better heat transfer and higher volumetric heat transfer coefficients. The volumetric heat transfer coefficient increases with an increase in the flow rate of the dispersed phase. This is in agreement with the experimental results of Sideman and Gat (1966), Blair et al. (1976), and Smith et al. (1982). The volumetric heat transfer coefficients are lower for an R-113–water system than for a pentane–water system. The trends are the same for both systems. Figure 7 shows the variation of volumetric heat transfer coefficient with column height and number of holes for 0.5 mm hole diameter and dispersed phase flow rate of 0.06 kg/min. The volumetric heat transfer coefficient

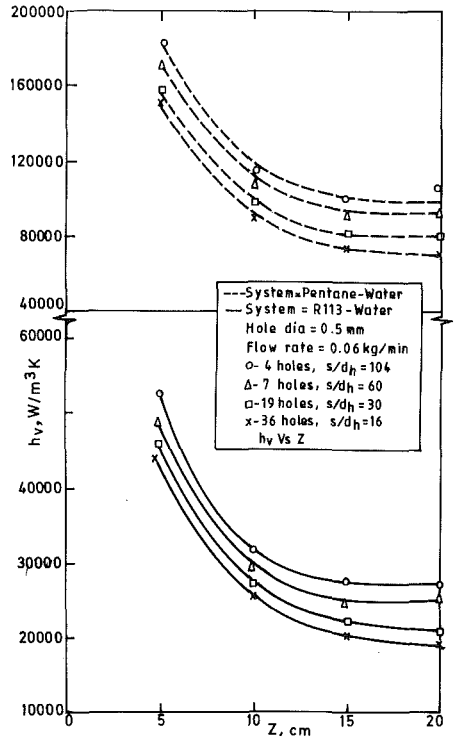

Fig. 7 Variation of h_v with column height and s/d_h ratios

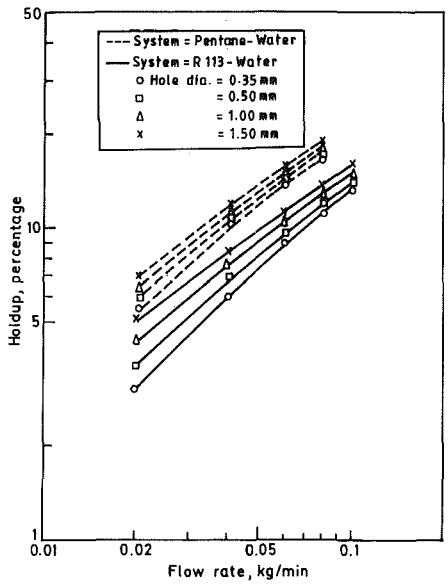

Fig. 8 Variation of holdup

decreases with an increase in column height, but the decrease is not considerable beyond a column height of 10 cm. For a given flow rate of 0.06 kg/min, the volumetric heat transfer coefficient decreases with an increase in the number of holes since the velocity of the dispersed fluid decreases. The volumetric heat transfer coefficient is lower for an R-113-water system than for a pentane-water system. The trends are the same for both systems.

Variation of Holdup. The average holdup is defined as the ratio of the volume of the dispersed phase to that of the total fluid volume. If Z_o is the column height before the injection of the dispersed phase and Z is the column height when the dispersed phase escapes as a saturated vapor, the average holdup is given by

$$\alpha = \frac{Z - Z_o}{Z} \tag{1}$$

The average holdup is found to depend considerably on the dispersed phase flow rate. At a given dispersed phase flow rate, the variation of average holdup with column height and spacing of the holes is found to be negligible. However, an increase in holdup is observed with an increase in the hole diameter. It is also found that for the same mass flow rate, the pentane-water system gives higher values for the average holdup. This may be due to the lower density of *n*-pentane compared to R-113. Figure 8 shows the variation of average holdup on a log-log scale for both systems. As the holdup-flow rate relation is observed to follow a power law, a multiple linear regression analysis is carried out and the following relations for the holdup are obtained for the R-113-water and pentane-water systems, respectively:

$$\text{R-113-water: } \alpha = 1.115 Q^{0.838} d_h^{0.185} \tag{2}$$

$$\text{Pentane-water: } \alpha = 1.313 Q^{0.764} d_h^{0.106} \tag{3}$$

where Q is the flow rate in kg/min and d_h is the hole diameter in mm. The correlation coefficient is both cases is about 0.995.

Comparison of the Experimental Results With the Theoretical Model. Smith et al. (1982) have developed an analytical model for calculating the volumetric heat transfer coefficient in direct contact evaporation in a spray column. The theoretical model uses single droplet correlations for the Nusselt number and a drift flux model for the fluid dynamics. On the basis of their analysis, the following relation for the volumetric heat transfer coefficient is obtained for direct contact evaporation in a spray column in the presence of agglomeration:

$$h_v = \frac{2h_{bo}\alpha}{D_o BZ(1-\alpha)}\left[\{1 + 6(1-\alpha)^{1-x} m_a BZ\}^{1/2m_a} - 1\right] \tag{4}$$

In the present experimental investigation, agglomeration was observed even at the beginning of the evaporation process. The use of equation (4) requires the value of α, D_o, and h_{bo}. The experimentally determined value of average holdup is taken as α. The initial diameter D_o of the drops formed at the orifices was difficult to determine. Sideman et al. (1965) have reported that attempts to determine the initial drop diameter in their system accurately were unsuccessful due to the presence of partially evaporated drops and entrained vapor bubbles in the bottom part of the column. Blair et al. (1976) and Smith et al. (1982), who have conducted similar experiments, also did not attempt to determine the initial drop diameters. Because of the uncertainty in the initial drop diameters, the theoretical volumetric heat transfer coefficients are calculated assuming different initial drop diameters and a comparison is made with the experimentally determined volumetric heat transfer coefficients.

Smith et al. (1982) have used the following relation for calculating h_{bo}, the single droplet heat transfer coefficient at the beginning of evaporation:

$$\text{Nu} = \frac{h_{bo} D}{K} = \gamma \text{Re}^x \text{Pr}^{1/3} \tag{5}$$

where γ depends on the drop diameter and the value of the exponent x.

Sideman and Taitel (1964) have obtained the following relation for the instantaneous Nusselt number for single drop evaporation in an immiscible liquid:

$$\text{Nu} = 0.272 \text{Pe}^{0.5} \tag{6}$$

The use of this relation for Nu does not give satisfactory agreement with the available experimental results under all

Table 1 Comparison of experimental and predicted values of h_v

System and authors	Flow rate, kg/min	Holdup, percent	Z, cm	ΔT, K	Orifice diameter mm	No. of orifices	h_v, W/m^{3}K experimental	Predicted
Cyclopentane–water	0.386	12	10	12–13.5	0.5	19	5.65 to 5.0×10^4	5.1 to 4.6×10^4
Smith et al. (1982)	0.386	12	15	8–9.5	0.5	19	5.65 to 4.75×10^4	5.3 to 4.66×10^4

Table 2 Comparison of experimental values of h_v

	Sideman and Gat (1966)	Blair et al. (1976)	Smith et al. (1982)	Present work	Present work
Dispersed phase	n-pentane	R-113	Cyclo-pentane	R-113	n-pentane
Continuous phase flow rate, kg/min	1.295	1.370	0	0	0
Dispersed phase flow rate, kg/min	0.042	0.101	0.257–0.386	0.02–0.10	0.02–0.08
h_v, W/m^{3}K	18×10^4	12.2×10^4	4.52–6×10^4	0.5–9×10^4	2–22×10^4

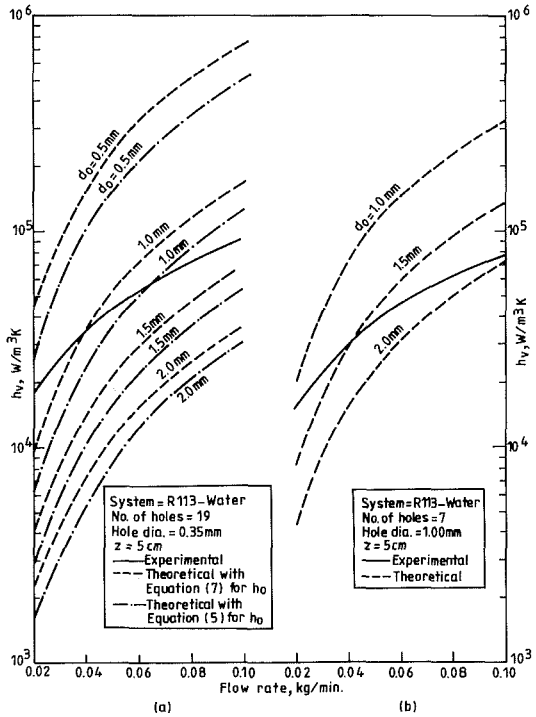

Fig. 9 Comparison of theoretical and experimental values of h_v

operating conditions. The available experimental results on single drop evaporation indicate the dependence of Nu on temperature difference. Sideman and Taitel (1964) have calculated, based on their experimental studies, the instantaneous heat transfer coefficients for three different systems at several temperature differences and at various percentages of evaporation. A regression analysis of their results was carried out and the following correlation was obtained by Battya et al. (1984):

$$\mathrm{Nu} = 0.64\mathrm{Pe}^{0.5}\mathrm{Ja}^{-0.35} \tag{7}$$

Equations (5) and (7) were used in the present analysis to calculate h_{bo}.

Figure 9 shows the experimentally determined volumetric heat transfer coefficients along with the theoretical values calculated assuming four different initial drop diameters for R-113–water systems. Figure 9(a) shows the variation of h_v with dispersed phase flow rate at a column height of 5 cm for a distributor with 19 holes 0.35 in diameter. The theoretical h_v predicted using equation (5) for h_{bo} is comparatively lower than that predicted using equation (7). Both the experimental and theoretical results show an increase of volumetric heat transfer coefficient with flow rate. It can be observed that initial drop diameter increases with increasing dispersed phase flow rate and hence with increasing injection velocities. This is in agreement with the results of Hayworth and Treybal (1950) in their studies on drop formation in immiscible liquids. Figure 9(a) indicates a variation of initial drop diameter from about 0.8 to 1.3 mm in the flow rate range considered in the present investigation for an orifice diameter of 0.35 mm. Figure 9(b) shows similar curves at a column height of 5 cm and with a distributor containing 7 holes 1.0 mm in diameter. The trends of the curves are similar to those in Fig. 9(b) and the variation of initial drop diameter is from about 1.2 to 1.9 mm in this case.

The initial drop diameters determined in this manner for several cases are found to depend mainly on the orifice velocity and orifice diameter. A multiple linear regression analysis of these results gives the following relation for the initial drop diameter:

$$D_o = 0.376 v^{0.35} d_h^{0.72} \tag{8}$$

where D_o is the initial drop diameter in cm, v the orifice velocity in cm/s, and d_h the orifice diameter in cm. The correlation coefficient is 0.998.

A similar analysis for the pentane–water system resulted in the following relation with a correlation coefficient of 0.994:

$$D_o = 0.307 v^{0.35} d_h^{0.72} \tag{9}$$

Equations (8) and (9) indicate that the initial drop diameter can be predicted by the following relation in the range of flow rates considered in this work:

$$D_o = C v^{0.35} d_h^{0.72} \tag{10}$$

where C is an empirical constant, the value of which depends on the physical properties of the system.

Using the above relations for D_o, α, and h_{bo}, the volumetric heat transfer coefficients are predicted corresponding to the experimental conditions of Smith et al. (1982) and the comparison is shown in Table 1. The predicted values are lower than the experimental values by about 10 percent. This is mainly due to the high injection velocities in their experiments and partly to the use of equation (9) for the cyclopentane-water system.

Table 2 shows a comparison of the present work with similar works by other investigators. The volumetric heat transfer coefficients in the present work are of the same order as those obtained by others. However, the table reveals that the countercurrent operation increases the volumetric heat transfer coefficient (due to increased turbulence). The present work covers much wider ranges of holdup and flow rates compared to the work of Smith et al. (1982).

Conclusions

Direct contact evaporation of refrigerant-113 and *n*-pentane in a stagnant column of distilled water is experimentally investigated and a modified relation is proposed for the calculation of the theoretical volumetric heat transfer coefficient. The following conclusions are reached.

1 The temperature difference required for the complete evaporation of the dispersed phase is found to depend considerably on the column height, turbulence, and agglomeration. The s/d_h ratio is found to influence the degree of agglomeration or coalescence.

2 The average holdup is found to depend mainly on the dispersed phase flow rate and the orifice diameter.

3 The volumetric heat transfer coefficient is seen to increase almost linearly with dispersed phase flow rate in the flow rate ranges considered in the investigation. The volumetric heat transfer coefficient is found to be higher at lower column heights.

4 At high rates of coalescence, the initial drop diameter has only a small effect on column performance.

5 The initial drop diameter is found to depend mainly on the orifice velocity, orifice diameter, and the physical properties of the system.

6 A lighter dispersed phase is found to yield higher volumetric heat transfer coefficients. A lighter dispersed phase also gives higher holdup ratios for the same mass flow rate.

7 The method proposed for the prediction of the volumetric heat transfer coefficient is fairly successful.

References

Battya, P., Raghavan, V. R., and Seetharamu, K. N., 1984, "Parametric Studies on Direct Contact Evaporation of a Drop in an Immiscible Liquid," *Int. J. Heat Mass Transfer*, Vol. 27, pp. 263–272.

Blair, C. K., Boehm, R. F., and Jacobs, H. R., 1976, "Heat Transfer Characteristics of a Direct Contact Volume Type Boiler," ASME Paper No. 76-HT-23.

Hayworth, C. B., and Treybal, R. E., 1950, "Drop Formation in Two Liquid-Phase Systems," *Ind. Engg. Chem.*, Vol. 42, pp. 1174–1181.

Sideman, S., and Taitel, Y., 1964, "Direct Contact Heat Transfer With Change of Phase: Evaporation of Drops in an Immiscible Liquid Medium," *Int. J. Heat Mass Transfer*, Vol. 7, pp. 1273–1289.

Sideman, S., Hirsch, G., and Gat, Y., 1965, "Direct Contact Heat Transfer With Change of Phase: Effect of the Initial Drop Size in Three-Phase Heat Exchangers," *AIChE Journal*, Vol. 11, pp. 1081–1087.

Sideman, S., 1966, "Direct Contact Heat Transfer Between Immiscible Liquids," *Adv. Chem. Engg.*, Vol. 6, pp. 207–286.

Sideman, S., and Gat, Y., 1966, "Direct Contact Heat Transfer With Change of Phase: Spray Column Studies of a Three-Phase Heat Exchanger," *AIChE Journal*, Vol. 12, pp. 296–303.

Smith, R. C., Rohsenow, W. M., and Kazimi, M. S., 1982, "Volumetric Heat Transfer Coefficients for Direct Contact Evaporation," ASME JOURNAL OF HEAT TRANSFER, Vol. 104, pp. 264–270.

Modeling the Thermally Governed Transient Flow Surges in Multitube Condensing Flow Systems With Thermal and Flow Distribution Asymmetry

G. L. Wedekind
Mem. ASME

B. L. Bhatt
Mem. ASME

School of Engineering and Computer Science, Oakland University, Rochester, MI 48309

In a tube-type condenser involving complete condensation, small changes in the inlet vapor flow rate momentarily cause very large transient surges in the outlet liquid flow rate. An equivalent single-tube model is proposed that predicts these transient flow surges for a multitube system. The model, based upon a system mean void fraction model developed earlier, includes the effects of thermal and flow distribution asymmetry associated with each individual condenser tube in the multitube system. Theoretical and experimental verification for a two-tube system is presented.

Introduction

This paper is concerned with multiple, in-tube condensing flow systems involving complete condensation. The transient characteristics and stability of such multitube condensers are important in many energy conversion processes including reheat, reboiler, and submerged evaporator systems associated with nuclear or conventional power plants. Sufficiently large excursions, or oscillations, could affect the performance of the processes taking place within these devices, cause damage to mechanical equipment, and endanger the safety of such systems. For example, large flow oscillations in the subcooled liquid at the end of the condensation process, including the possibilities of flow reversals, are likely to be associated with large impulse loads that may cause substantial damage to various components involved in the overall system.

Motivation for the present research was generated in part by the successful results of earlier experimental and theoretical studies on thermally governed transient flow surges (Wedekind and Bhatt, 1977), influence of compressibility on transient and frequency response characteristics (Bhatt and Wedekind, 1980a), and self-sustained limit-cycle-type flow instabilities associated with two-phase condensing flows in a single-tube condenser system (Bhatt and Wedekind, 1980b). To the best knowledge of the authors, there do not appear to be any theoretical models in the literature addressing the transient flow surge characteristics of multitube condensers. Therefore, since most practical applications of in-tube condensation involve multiple-tube geometries, consisting of parallel tubes connected to common headers, there was a natural motivation to find a means for extending the predictive capability of these previously developed single-tube models to multitube systems possessing the possibility for thermal and flow distribution asymmetry.

The purpose of this paper is to describe the development and capability of such a model. The approach will be first to summarize the formulation of the governing equations for a two-tube condensing flow system. Then, results will be presented for a parametric study on the two-tube system in an effort to gain physical insight into the influence on the transient flow surges of various geometric, thermal, and fluid parameters, including the relative flow distribution within the two tubes. Utilizing the insight gained from the parametric study, an equivalent single-tube model will be proposed and verified both theoretically and experimentally for the two-tube condenser. Finally, by mathematical induction, the equivalent single-tube model is generalized for an n-tube condensing flow system, which still includes the effects of flow distribution and other relevant geometric, thermal, and fluid parameters associated with each individual tube in the multitube system.

Contributed by the Heat Transfer Division and presented at Symposium of Heat and Mass Transfer, University of Illinois, Champaign-Urbana, October 1-2, 1987. Manuscript received by the Heat Transfer Division November 30, 1987; revised version received July 1988. Keywords: Condensation, Multiphase Flows, Transient and Unsteady Heat Transfer.

Formulation of Two-Tube Model

A schematic of a two-tube horizontal condensing flow system undergoing complete condensation is depicted in Fig. 1. The flow distribution, heat flux, and cross-sectional geometry for each tube are allowed to be different, thus asymmetric. However, the tubes are of equal length, and the thermodynamic properties of the two-phase mixture are assumed to be the same in each tube, and evaluated at a mean condensing pressure.

Conservation of Mass; Two-Phase and Subcooled Liquid Regions. Referring to Fig. 1, the conservation-of-mass principle when applied to the two-phase region in each of the two tubes can be expressed as

$$\frac{d}{dt}\int_{z=0}^{\eta_1(t)} [\rho-(\rho-\rho')\alpha]A_{t,1}dz = m_{t,1}(z,\ t)_{z=0} - m^*_{t,1} \quad (1)$$

and

$$\frac{d}{dt}\int_{z=0}^{\eta_2(t)} [\rho-(\rho-\rho')\alpha]A_{t,2}dz = m_{t,2}(z,\ t)_{z=0} - m^*_{t,2} \quad (2)$$

where m^*_t represents the mass flow rate crossing the moving boundary $\eta(t)$, which is the effective point of complete condensation.

Similarly, for the subcooled liquid region, the conservation of mass principle yields for each of the two tubes

$$m^*_{t,1} = m_{t,1}(z,\ t)_{z=L} - \rho A_{t,1}\frac{d\eta_1(t)}{dt} \quad (3)$$

and

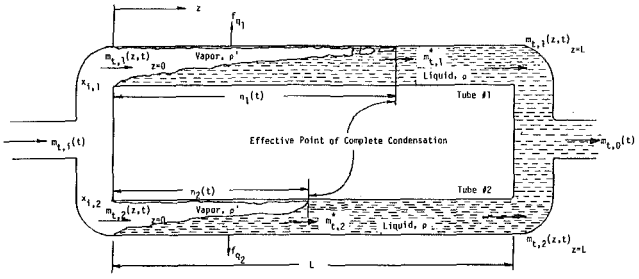

Fig. 1 Schematic of two-tube horizontal condensing flow system

$$m^*_{t,2} = m_{t,2}(z,\ t)_{z=L} - \rho A_{t,2}\frac{d\eta_2(t)}{dt} \tag{4}$$

Introducing the system mean void fraction $\bar{\alpha}$, and assuming it to be time invariant (Wedekind et al., 1978), equations (1), (3) and (2), (4) can each be combined to eliminate $m^*_{t,1}$ and $m^*_{t,2}$. The result for each of the tubes becomes

$$m_{t,1}(z,\ t)_{\ z=L} = m_{t,1}(z,\ t)_{z=0} + (\rho - \rho')\bar{\alpha}_1 A_{t,1}\frac{d\eta_1(t)}{dt} \tag{5}$$

and

$$m_{t,2}(z,\ t)_{\ z=L} = m_{t,2}(z,\ t)_{z=0} + (\rho - \rho')\bar{\alpha}_2 A_{t,2}\frac{d\eta_2(t)}{dt} \tag{6}$$

where the system mean void fraction $\bar{\alpha}$ for each individual tube is defined as

$$\bar{\alpha} \equiv \frac{1}{\eta(t)}\int_{z=0}^{\eta(t)} \alpha(z,\ t)dz \tag{7}$$

Therefore, the outlet liquid flow rate for each tube can be expressed in terms of the inlet vapor flow rate and the motion of the effective point of complete condensation $\eta(t)$ for each respective tube. This motion of the effective point of complete condensation can be determined by utilizing the unified system mean void fraction model (Wedekind et al. 1984), which has previously been developed for transient, two-phase flows, involving complete or incomplete vaporization or condensation in a single-tube.

System Mean Void Fraction Model. In its generalized form, the motion $\eta(t)$ of a representative propagating void α_0 is governed by the following differential equation (Wedekind et al., 1984):

$$\tau\frac{d\eta(t)}{dt} + \eta(t) = \frac{(h' - h)\ (x_o - x_i)}{\bar{f}_q P} m_t(z,\ t)_{z=0} \tag{8}$$

where

$$\tau = \frac{[\rho - (\rho - \rho')\ (1 - x_o)]\ (h' - h)\ (\alpha_a - \bar{\alpha})A_t}{\bar{f}_q P} \tag{9}$$

The above model represents the conservation of mass and energy principles, and incorporates the concept of a time-invariant system mean void fraction $\bar{\alpha}$.[1] For the special case of complete condensation, the representative propagating void is the effective point of complete condensation; thus, α_o = zero and the corresponding representative propagating flow quality x_o = zero. Also because condensation is taking place, the heat flux $\bar{f}_q$ is negative. Therefore, for each tube, the differential equation governing the motion of the effective point of com-

[1] A detailed discussion of the implications of time invariance of the system mean void fraction is given by Wedekind et al. (1978). However, in short, from a mathematical perspective, time invariance during a flow transient is guaranteed by the existence of a similarity relationship, which from a physical perspective requires that a specific redistribution of liquid and vapor within the two-phase region take place at a rate faster than that of the particular flow transient under consideration. This implies that, within the two-phase region, the *transient* form of the momentum principle is unnecessary; only the steady-state form is required. The validity of this conceptual simplication, for such extreme changes as a 25 percent step-change in inlet flow rate, is verified by the predictive capability of the model when compared to experimental measurements.

Nomenclature

A_t = total cross-sectional area of tube, m^2
d = inside diameter of tube, m
$\bar{f}_q$ = spatially averaged heat flux, W/m^2
h = enthalpy of saturated liquid, J/kg
L = total length of condenser, m
$m_t(z,\ t)$ = local instantaneous total mass flow rate of fluid, kg/s
m^*_t = instantaneous total mass flow rate of fluid leaving two-phase region relative to moving effective point of complete condensation, kg/s
$m_{t,i}$ = initial steady-state total mass flow rate at system inlet, kg/s
$m_{t,i}(t)$ = total time-dependent mass flow rate at system inlet, kg/s
$m_{t,f}$ = final steady-state total mass flow rate at system inlet, kg/s
$m_{t,0}(t)$ = total time-dependent mass flow rate at system outlet, kg/s
p = spatial mean system pressure, N/m^2
P = inside periphery of flow channel, m
x = flow quality; ratio of vapor mass flow rate to total mass flow rate
x_i = flow quality at system inlet
x_o = flow quality associated with representative propagating void, α_o
z = axial position coordinate, m
$\alpha(z,\ t)$ = local area mean void fraction
$\bar{\alpha}$ = system mean void fraction; see equation (7)
α_o = value of representative propagating void
β = thermal asymmetry parameter, see equations (23) and (24)
γ = flow distribution asymmetry parameter, see equation (17)
η = length of two-phase region in condenser tube (effective point of complete condensation), m
η_i = initial effective point of complete condensation, m
η_f = final effective point of complete condensation
ρ = density of saturated liquid, kg/m^3
τ = time constant for condensing flow in an individual tube, s
τ_m = time constant for inlet flow rate variation, s
τ_s = effective time constant for multitube condensing flow system, s

Subscripts and Superscripts

Primed (') symbols of quantities refer to saturated vapor. Numerical subscripts, unless otherwise indicated, refer to individual condenser tube number. Symbols of quantities generally refer to time-averaged quantities where the averaging time is small enough so as to just eliminate the inherent random fluctuations.

plete condensation becomes a special case of equations (8) and (9); thus

$$\tau_1 \frac{d\eta_1(t)}{dt} + \eta_1(t) = \frac{(h' - h)x_{i,1}}{\bar{f}_{q_1} P_1} m_{t,1}(z, t)_{z=0} \tag{10}$$

and

$$\tau_2 \frac{d\eta_2(t)}{dt} + \eta_2(t) = \frac{(h' - h)x_{i,2}}{\bar{f}_{q_2} P_2} m_{t,2}(z, t)_{z=0} \tag{11}$$

where τ_1 and τ_2 are the system time constants for the respective tubes, expressed as

$$\tau_1 = \frac{\rho' \bar{\alpha}_1 A_{t,1}}{\bar{f}_{q_1} P_1}(h' - h), \qquad \tau_2 = \frac{\rho' \bar{\alpha}_2 A_{t,2}}{\bar{f}_{q_2} P_2}(h' - h) \tag{12}$$

Two-Tube Model. Referring to the inlet and the outlet headers depicted in Fig. 1, the total inlet flow rate $m_{t,i}(t)$, and outlet flowrate $m_{t,o}(t)$, can be expressed respectively in terms of the sum of the inlet and outlet flow rates for each individual tube; thus

$$m_{t,i}(t) = m_{t,1}(z, t)_{z=0} + m_{t,2}(z, t)_{z=0} \tag{13}$$

and

$$m_{t,o}(t) = m_{t,1}(z, t)_{z=L} + m_{t,2}(z, t)_{z=L} \tag{14}$$

Substituting equations (10), (11), and (12) into equations (5) and (6), and using equations (13) and (14), the total outlet liquid flow rate from the two-tube system can be expressed in terms of the total inlet flow rate, and the motion of the effective point of complete condensation for each tube; thus

$$m_{t,0}(t) = \left\{1 + \left[\left(\frac{\rho}{\rho'}\right) - 1\right] x_i\right\} m_{t,i}(t) - \frac{\left[\left(\frac{\rho}{\rho'}\right) - 1\right]}{(h' - h)} \left\{\bar{f}_{q_1} P_1 \eta_1(t) + \bar{f}_{q_2} P_2 \eta_2(t)\right\} \tag{15}$$

where it is assumed that the inlet flow quality for each tube is the same; that is

$$x_{i,1} = x_{i,2} = x_i \tag{16}$$

A flow distribution parameter γ is introduced and defined such that it represents the fraction of total flow entering tube #1; therefore

$$m_{t,1}(z, t)_{z=0} = \gamma m_{t,i}(t) \tag{17}$$

and correspondingly for tube #2

$$m_{t,2}(z, t)_{z=0} = (1 - \gamma) m_{t,i}(t) \tag{18}$$

Consider the special case where the time varying total inlet flow rate $m_{t,i}(t)$ is an exponential function of the form

$$m_{t,i}(t) = m_{t,f} + (m_{t,i} - m_{t,f}) e^{-t/\tau_m} \tag{19}$$

where $m_{t,i}$ and $m_{t,f}$ are the initial and final total inlet flow rates, respectively, and τ_m is the time constant associated with the changing inlet flow rate.

Substituting equation (19) into equations (17) and (18), equation (17) into equation (10), and equation (18) into equation (11), the two differential equations governing the transient response of the effective point of complete condensation can be solved subject to the following initial conditions:

$$\eta_1(t)_{t=0} = \eta_{1,i} = \frac{(h' - h)}{\bar{f}_{q_1} P_1} x_i \gamma m_{t,i} \tag{20}$$

and

$$\eta_2(t)_{t=0} = \eta_{2,i} = \frac{(h' - h)}{\bar{f}_{q_2} P_2} x_i (1 - \gamma) m_{t,i} \tag{21}$$

When the solutions to equations (10) and (11) are substituted into equation (15), the result, after considerable rearrangement, can be expressed as

$$\frac{m_{t,0}(t) - m_{t,f}}{(m_{t,i} - m_{t,f})} = e^{-t/\tau_m} + \frac{\gamma\left(\frac{\tau_1}{\tau_m}\right)\left[\left(\frac{\rho}{\rho'}\right) - 1\right]}{\left[\left(\frac{\tau_1}{\tau_m}\right) - 1\right]} x_i \{e^{-t/\tau_m} - e^{-t/\tau_1}\} + (1 - \gamma) \frac{\beta\left(\frac{\tau_1}{\tau_m}\right)\left[\left(\frac{\rho}{\rho'}\right) - 1\right]}{\left[\beta\left(\frac{\tau_1}{\tau_m}\right) - 1\right]} x_i \{e^{-t/\tau_m} - e^{-t/\beta\tau_1}\} \tag{22}$$

where

$$\beta \equiv \tau_2/\tau_1 = \left(\frac{\bar{f}_{q_1}}{\bar{f}_{q_2}}\right)\left[\left(\frac{P_1}{P_2}\right)\left(\frac{A_{t,2}}{A_{t,1}}\right)\right] \tag{23}$$

The above expression describes the transient flow surge in the outlet liquid flowrate for a two-tube condensing flow system. The parameters γ and β respectively describe the flow distribution and thermal/geometric asymmetry associated with the two tubes. For example, $\gamma = 0.5$ means the flow distribution is symmetric. In general, however, $0 \leq \gamma \leq 1$. Also, $\beta = 1.0$ signifies thermal/geometric symmetry, while in general, $\beta \geq 0$. The parameter β is seen to be a product of the heat flux ratio between tube #1 and tube #2, and a geometric ratio between the two tubes. However, if the tubes are circular, the geometric ratio becomes the diameter ratio of the two tubes, d_2/d_1. Since for most applications the tube diameters would be equal, the parameter β would become a ratio of heat fluxes[2]; thus

$$\beta = \bar{f}_{q_1}/\bar{f}_{q_2} \tag{24}$$

Therefore, for the remainder of the paper, β will be considered to be a measure of *thermal* asymmetry.

In this phase of the development of the multitube model, the thermal and flow distribution parameters, β and γ, are considered system parameters in the classical sense. That is, they are assumed to be known, independent of each other, and thus arbitrarily specified. The purpose for this approach was initially to ascertain the primary physical mechanisms for, and the magnitude of, the influences of thermal and flow distribution asymmetry.

It is recognized that, from a physical perspective, the flow distribution within each tube will be governed by the momentum principle, and thus a function of the various flow resistances in the multitube system. This includes the flow resistances in the two-phase regions, which in turn can be effected by heat flux. Thus, the flow distribution parameter may even be coupled to the thermal distribution parameter, albeit weakly. Obviously then, the present scope of the model requires an independent determination of the thermal and flow distribution parameters, a limitation that can be addressed in future work.

Parametric Study of Two-Tube Model. The purpose of this section is to investigate the influence that flow distribution

[2]Theoretically, the model allows for the cross-sectional geometry of each tube to be different. Practically however, it would be rare to encounter different cross-sectional geometries in the same condenser system, although for the purposes of enhancing uniformity of flow distribution, some variation in tube cross-sectional areas or tube diameters might be encountered.

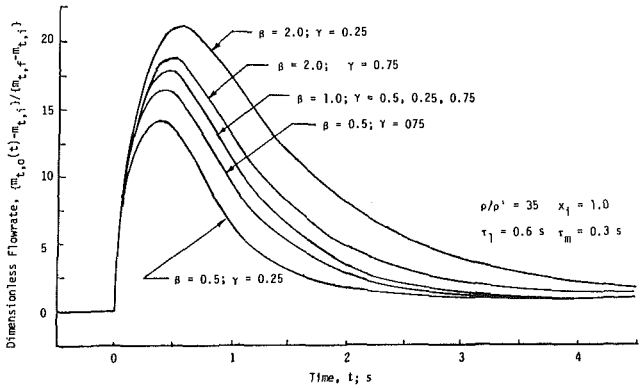

Fig. 2 Response of outlet liquid flow rate after an increase in inlet vapor flow rate; influence of thermal and flow distribution asymmetry for two-tube model

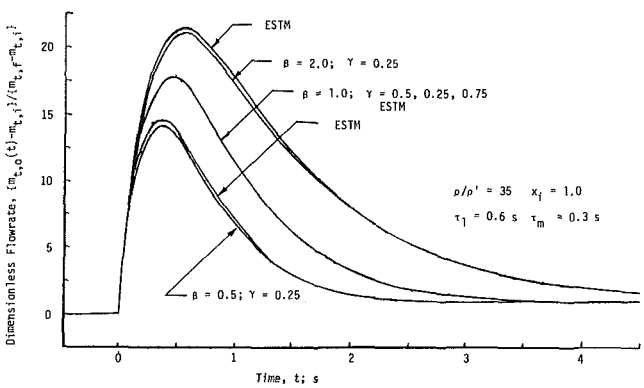

Fig. 3 Response of outlet liquid flow rate after an increase in inlet vapor flow rate; comparison of two-tube model with Equivalent Single-Tube Model (ESTM)

and thermal asymmetry have on the transient flow surges. This will be done by means of a parametric study involving the flow distribution and thermal parameters γ and β, respectively.

The response of the outlet liquid flow rate to an exponential increase in inlet vapor flow rate is depicted in Fig. 2 for various combinations of γ and β over a range of values most likely to be encountered. The time constant for the increase in inlet vapor flow rate τ_m, and the time constant[3] τ_1 for tube #1 were held constant for all of the plots with $\tau_m = 0.3$ s and $\tau_1 = 0.6$ s.

The symmetric case is when $\beta = 1.0$ and $\gamma = 0.5$. Therefore, it is clear from the figure that asymmetry can be very influential on the relative amplitude of the flow surge. For example, the peak of the flow surge is approximately 25 percent higher than that of the symmetric case when $\beta = 2.0$ and $\gamma = 0.25$, which would correspond to tube #2 having half the heat flux of tube #1, and 75 percent of the total flow rate. Also the peak of the flow surge is approximately 25 percent lower than that of the symmetric case when $\beta = 0.5$ and $\gamma = 0.25$, which corresponds to tube #2 having twice the heat flux of tube #1, and 75 percent of the total flow rate. It is also noteworthy that for thermal symmetry, $\beta = 1$, asymmetry in flow distribution has no relative influence on the peak amplitude of the flow surges.

A parametric study of the time constant τ_m for the inlet vapor flow rate indicates that as τ_m gets smaller, the relative spread between peak amplitudes for the two asymmetric parameters, γ and β, decreases; where in the limit as $\tau_m \to 0$ (a step change), the spread goes to zero with the peak being a simple function of the liquid-to-vapor density ratio, $[(\rho/\rho') - 1]$.

Equivalent Single-Tube Model

As a result of the insight obtained from the foregoing parametric study, a method is proposed for approximating the transient behavior of a multitube condensing flow system in terms of an equivalent single-tube model (ESTM), which includes the effects of flow distribution and other relevant thermal and geometric parameters associated with each individual tube in the multitube system. The approach will be first to establish the viability of an equivalent single-tube model for the two-tube model developed earlier in the paper, and then to generalize to an n-tube system.

Proposed Single-Tube Model for a Two-Tube System. Conceptually, the approach is quite simple. An equivalent single-system time constant $\tau_{s,2}$ for a two-tube system is defined as a weighted function of the time constants of each of the two individual tubes, where the weighting factors are the flow distribution parameters associated with each tube; thus

$$\tau_{s,2} = \gamma\tau_1 + (1-\gamma)\tau_2 \tag{25}$$

Therefore, the transient characteristics of a two-tube condensing flow system will be approximated by those of a single-tube system whose time constant is so defined. The thermally governed transient flow surges for a two-tube condenser system, as expressed by equation (22), will be approximated by the following Equivalent Single-Tube Model (ESTM):

$$\frac{m_{t,0}(t) - m_{t,f}}{(m_{t,i} - m_{t,f})} \cong e^{-t/\tau_m} + \frac{\left(\frac{\tau_s}{\tau_m}\right)\left[\left(\frac{\rho}{\rho'}\right) - 1\right]}{\left[\left(\frac{\tau_s}{\tau_m}\right) - 1\right]} x_i \{e^{-t/\tau_m} - e^{-t/\tau_s}\} \tag{26}$$

where equation (25) is used to determine the system time constant τ_s.

Theoretical Verification of Proposed Single-Tube Model. The validity of the equivalent single-tube model is established by comparing its predictive capability with that of the two-tube model as demonstrated in Fig. 3. As indicated, the ESTM converges identically with the two-tube model when $\beta = 1.0$ and $\gamma = 0.5$, which corresponds to a system with complete thermal and flow distribution symmetry. Also, as is demonstrated, the ESTM agrees very closely with the two-tube model for considerable thermal and flow distribution asymmetry. Experimental verification will be presented in a later section.

Generalization to an N-Tube Condensing Flow System. The generalization of the equivalent single-tube model (ESTM) from two-tubes to n-tubes can be developed by mathematical induction. The validity of the equivalent single-tube model to predict accurately the transient flow surges for a two-tube system was established in the previous section. Therefore, the approach will be first to extend the model to handle a three-tube system.

Consider a three-tube condensing flow system with individual tube time constant, τ_1, τ_2, and τ_3, and with flow distribution parameters, γ_1, γ_2, and γ_3, such that the inlet flow rate into each individual tube can be expressed in terms of the total inlet flow rate $m_{t,i}(t)$ as follows:

$$m_{t,1}(z, t)_{z=0} = \gamma_1 m_{t,i}(t) \tag{27}$$

[3] If the tube geometry, inlet quality, and condensing pressure do not change, then for a constant heat flux, the time constant τ_1 for tube #1 will remain constant.

$$m_{t,2}(z,t)_{z=0} = \gamma_2 m_{t,i}(t) \tag{28}$$

$$m_{t,3}(z,t)_{z=0} = \gamma_3 m_{t,i}(t) \tag{29}$$

where

$$\gamma_1 + \gamma_2 + \gamma_3 = 1 \tag{30}$$

The equivalent single-tube model for the first two tubes would have a system time constant $\tau_{s,2}$, as expressed by equation (25); thus

$$\tau_{s,2} = \gamma\tau_1 + (1-\gamma)\tau_2 \tag{31}$$

Now, considering only the first two tubes, the total inlet flow rate is $(\gamma_1+\gamma_2)m_{t,i}(t)$. Therefore, the distribution factor γ for the first tube would be

$$\gamma = \frac{\gamma_1 m_{t,i}(t)}{(\gamma_1+\gamma_2)m_{t,i}(t)} = \frac{\gamma_1}{(\gamma_1+\gamma_2)} \tag{32}$$

Similarly, for the second tube

$$(1-\gamma) = \frac{\gamma_2}{(\gamma_1+\gamma_2)} \tag{33}$$

Therefore, the equivalent single-tube time constant for the first two tubes $\tau_{s,2}$ can be obtained by substituting equations (32) and (33) into equation (31); thus

$$\tau_{s,2} = \frac{\gamma_1}{(\gamma_1+\gamma_2)}\tau_1 + \frac{\gamma_2}{(\gamma_1+\gamma_2)}\tau_2 \tag{34}$$

Now we repeat the process by treating the first two tubes as an equivalent single-tube, and combining it with tube #3 in a similar manner. The total inlet flowrate is $m_{t,i}(t)$, and the distribution factor γ for the equivalent single-tube would be

$$\gamma = \frac{(\gamma_1+\gamma_2)m_{t,i}(t)}{m_{t,i}(t)} = (\gamma_1+\gamma_2) \tag{35}$$

Similarly, for the third tube

$$(1-\gamma) = \gamma_3 \tag{36}$$

Therefore, the equivalent single-tube time constant for the three tubes, $\tau_{s,3}$, can be obtained by substituting equations (34), (35), and (36) into the equivalent of equation (31); thus

$$\tau_{s,3} = \gamma\tau_{s,2} + (1-\gamma)\tau_3 = \gamma_1\tau_1 + \gamma_2\tau_2 + \gamma_3\tau_3 \tag{37}$$

This readily suggests a recurrence relationship for any number of additional tubes. Therefore, the equivalent single-tube time constant for an n-tube condensing flow system can be expressed by

$$\tau_{s,n} = \gamma_{s,n-1}\tau_{s,n-1} + \gamma_n\tau_n = \sum_{i=1}^{n}\gamma_i\tau_i \tag{38}$$

which turns out to be simply a weighted average of the time constants for each of the individual tubes. The weighting factors are the corresponding flow distribution parameters.

Therefore, the thermally governed transient flow surges for an n-tube condensing flow system can be predicted by the equivalent single-tube model, as expressed by equation (26); where equation (38) is used to determine the multitube condensing flow system time constant τ_s.

Experimental Measurements: Two-Tube System

The experimental apparatus used in this research was similar to that described by Wedekind and Bhatt (1977), but modified to include two parallel, horizontal-tube condensers approximately 5 m long. The condenser test sections were copper, and of a concentric-tube configuration. Condensation of the flowing Refrigerant-12 took place inside an 8.0-mm inner tube, while cold water was circulated in the annulus of the two concentric tubes.

Flow distribution in each tube was measured with a turbine flowmeter, and was varied by slightly varying the flow resistance (ball-valve) between the inlet header and each tube. Variation in heat flux in each tube was controlled by controlling the combination of temperature and flow rate of cooling water circulating in the annulus of the concentric-tube condenser. Also, it was found that the actual measured transient inlet vapor flow rate could be approximated quite accurately as a simple exponential function of time of the same form as equation (19).

The thermal and flow distributions were established during an initial steady-state condition. The inlet flow transient was initiated by a control valve upstream of the header, and thermal and flow distribution parameters appeared to remain the same during the transient and on into the final steady-state configuration. Conceptually, the same experimental procedure could be used for a three-tube system.

Comparison of Theoretical Predictions With Experimental Measurements

The theoretical predictions of the transient flow surges in the outlet liquid flow rate for a two-tube condensing flow system are compared with experimental data for three different situations: complete thermal and flow distribution symmetry, thermal asymmetry, and flow distribution asymmetry. The theoretical predictions are those of the Equivalent Single-Tube Model (ESTM).

A comparison of the theoretical flow surge prediction with experimental measurements is shown in Fig. 4 for a two-tube condenser having complete thermal and flow distribution symmetry, that is, $\gamma = 1.0$, $\beta = 0.5$, respectively. The surge in the outlet liquid flow rate takes place in response to an increase in inlet vapor flow rate. A similar comparison is depicted in Fig. 5 but with thermal asymmetry and flow distribution symmetry; $\beta = 0.72$, $\gamma = 0.5$, respectively. Similarly, Fig. 6 shows a comparison for thermal symmetry and flow distribution asymmetry; $\beta = 1.0$, $\gamma = 0.38$, respectively.

The degree of agreement between the experimental data and the theoretical predictions of the Equivalent Single-Tube Model (ESTM) is very encouraging, especially when consideration is given to the complexity of the physical mechanisms involved, and the simplicity of the theoretical model, complete with its ability to predict the influence of thermal and flow distribution asymmetry.

It is interesting to note that in every case, the theoretical model predicted a peak in the flow-rate surge that was slightly greater than what was measured experimentally. Previous ex-

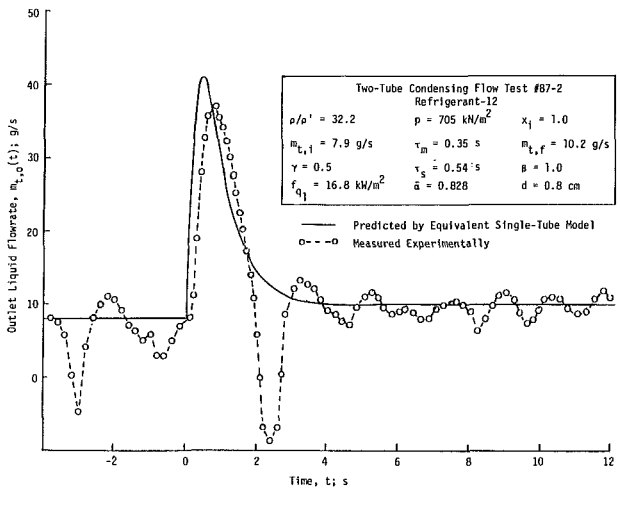

Fig. 4 Response of outlet liquid flow rate after an increase in inlet vapor flow rate for a two-tube condenser; thermal and flow distribution symmetry

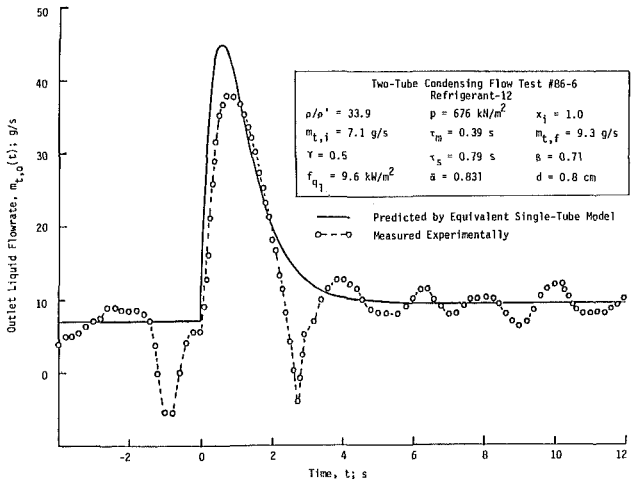

Fig. 5 Response of outlet liquid flow rate after an increase in inlet vapor flow rate for a two-tube condenser; thermal asymmetry and flow distribution symmetry

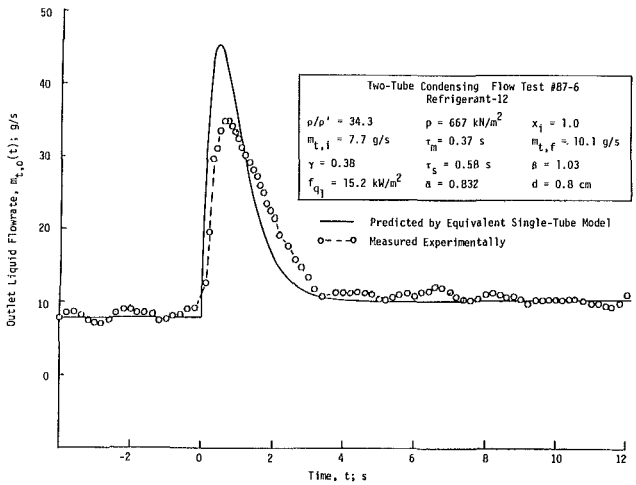

Fig. 6 Response of outlet liquid flow rate after an increase in inlet vapor flow rate for a two-tube condenser; thermal symmetry and flow distribution asymmetry

perimental uncertainty analyses on the transient flow measurements (Wedekind and Bhatt, 1977) indicate that the difference between theoretical and measured flow rates was not due to measurement errors. Therefore, it seems quite possible that an explanation for the surge attenuation in the experimental data was the existence of compressibility effects, effects not included in the present model. This would be consistent with previous observations (Bhatt and Wedekind, 1980a) for a single-tube condenser, and suggests that the influence of compressibility for multitube condensers should be the subject of future research. A further confirmation of this is that the magnitude of the parameters causing compressibility effects was highest for the data in Fig. 6, where the attenuation was greatest.

It is also significant to note that the experimental outlet flow-rate data depicted in Figs. 4 and 5 possess a tendency toward larger than normal oscillations, especially immediately following the flow surges. This was characteristic of a self-sustained oscillatory flow instability (Bhatt and Wedekind, 1980b) investigated earlier for a single-tube condenser. A cursory evaluation of the stability criteria developed in the above-referenced work suggests that the conditions present in the experimental data of Figs. 4 and 5 are nearer to the instability boundary than the conditions present in the experimental data of Fig. 6. This is confirmed by the obvious absence of larger flow oscillations in the latter data. Such evidence suggests a strong possibility of being able to develop further the equivalent single-tube model to the point where it will not only predict the flow instability, but the corresponding stability boundary for a multitube condensing flow system as well. This also will be the subject of future research.

Summary and Conclusions

An equivalent single-tube model has been proposed for predicting the thermally governed transient flow surges in multi-tube condensing flow systems undergoing complete condensation, and consisting of parallel tubes connected to common headers. The proposed multitube model, based upon a system mean void fraction model developed earlier, has the capability of predicting the influence of thermal and flow distribution asymmetry.

The multi-tube model was analytically verified by comparison with a two-tube model, and then extended to n-tubes by mathematical induction. The predictive capability of the model was also verified by comparison with experimental measurements for a two-tube configuration, with and without thermal and flow distribution asymmetry. Good agreement was found to exist, especially when consideration is given to the complexity of the physical mechanisms involved, and the relative simplicity of the model.

Although the results presented in this paper involved only thermal and flow distribution asymmetries, the model will readily handle asymmetries in tube geometries as well. The practical implications of the proposed model are exciting. For example, preliminary experimental observations indicate the potential for extending other previous work associated with single-tube condensing flow systems, such as the effects of compressibility, and the characteristics of the limit-cycle type of flow instability, to multitube condensing flow systems. Further research, including experimental verification of these various multitube implications, needs to be carried out.

Acknowledgments

The authors would like to acknowledge the National Science Foundation, Division of Chemical, Biochemical and Thermal Engineering, Thermal Systems and Engineering Program, for its part in the support of this research under Grant No. MEA-8314966.

References

Bhatt, B. L., and Wedekind, G. L., 1980, "Transient and Frequency Response Characteristics of Two-Phase Condensing Flows: With and Without Compressibility," ASME JOURNAL OF HEAT TRANSFER, Vol. 102, No. 3, pp. 495–500.

Bhatt, B. L., and Wedekind, G. L., 1980, "A Self-Sustained Oscillatory Flow Phenomenon in Two-Phase Condensing Flow Systems," ASME JOURNAL OF HEAT TRANSFER, Vol. 102, No. 4, pp. 649–700.

Wedekind, G. L., and Bhatt, B. L., 1977, "An Experimental and Theoretical Investigation Into Thermally Governed Transient Flow Surges in Two-Phase Condensing Flow," ASME JOURNAL OF HEAT TRANSFER, Vol. 99, pp. 561–567.

Wedekind, G. L., Bhatt, B. L., and Beck, B. T., 1978, "A System Mean Void Fraction Model for Predicting Various Transient Phenomena Associated With Two-Phase Evaporating and Condensing Flows," *International Journal of Multiphase Flow*, Vol. 4, pp. 97–114.

Wedekind, G. L., Beck, B. T., Bhatt, B. L., and Roslund, G. L., 1984, "A Unified System Mean Void Fraction Model for Predicting Transient Characteristics of Flow Quality, Void Fraction, Flowrate and Pressure Drop in Evaporating and Condensing Flows," *Two-Phase Flow and Heat Transfer; China–U.S. Progress*, Xue-jun Chen and T. N. Veziroglu, eds., Hemisphere Publishing Co., Washington, DC, pp. 633–646.

Forced Convection Condensation on a Horizontal Tube—Experiments With Vertical Downflow of Steam

A. G. Michael

J. W. Rose

Department of Mechanical Engineering,
Queen Mary College (University of London),
London E1 4NS United Kingdom

L. C. Daniels

Heat Transfer and Fluid
Flow Service (HTFS),
Thermal Hydraulics Division,
Harwell Laboratory,
Oxfordshire OX11 ORA United Kingdom

The paper reports an experimental investigation into the condensation of steam flowing vertically downward over a single horizontal tube. A limited number of experiments with steam-nitrogen mixtures are also reported. For the case of "pure" steam, data have been obtained at near atmospheric pressure for vapor approach velocities in the range 5 to 81 m/s and with superheats in the range 2 to 40 K. The results are compared with theory and earlier experimental data for steam and other fluids. The vapor-side heat transfer coefficients were found to increase with velocity. For vapor velocities in excess of 30 m/s, the rate of increase of the vapor-side coefficient was greater than predicted by laminar condensate flow theory. This behavior has also been observed by earlier workers for refrigerant-113 and ethylene glycol and may indicate onset of turbulence in the condensate film. Superheat had insignificant effect on the heat transfer coefficient for the condensate film. The results for steam-nitrogen mixtures were generally in good agreement with existing equations for the "gas-layer" resistance.

Introduction

In recent years considerable effort has been devoted to prediction of the shell-side performance of horizontal-tube condensers. The physical processes involved during condensation within a tube bundle are complex and as yet not well understood. Nonuniformity of both the vapor and condensate flows, inundation, and the possibility of condensate films being laminar on some tubes and turbulent on others, together with condensate–vapor interactions and the motion and accumulation of noncondensing gas, are the main problems still to be resolved.

Good progress has been made for the more tractable case of the single horizontal tube but even here, and when noncondensing gas effects are negligible, significant uncertainties remain; experimental data are widely scattered especially for the case of steam. The present single-tube investigation was undertaken to shed more light on the problem and to serve as a basis for comparison with data from proposed tube-bundle studies.

For an isothermal condensing surface and vertical vapor downflow over a single tube, the theoretical approach of Shekriladze and Gomelauri (1966), which used the asymptotic (infinite condensation rate) expression for the shear stress at the condensate surface, has been confirmed by Fujii et al. (1972) and the asymptotic shear stress approximation shown to hold for condensation rates typical of those found in practice. These approaches, which do not consider vapor boundary layer separation, are discussed in more detail by Lee and Rose (1982). For the case considered by Shekriladze and Gomelauri, it has been shown by Rose (1984) that the Nusselt number is represented to within 0.4 percent, for all values of the "two-phase" Reynolds number $\tilde{\mathrm{Re}}$ and the parameter $F (= \mu_L h_{fg} dg / u_\infty^2 k_L \Delta T)$, by

$$\mathrm{Nu}\tilde{\mathrm{Re}}^{-1/2} = \frac{0.9 + 0.728\,F^{1/2}}{(1 + 3.44\,F^{1/2} + F)^{1/4}} \qquad (1)$$

The validity of the assumption of uniform wall temperature has been questioned by Fujii et al. (1979) who gave a solution based on the alternative assumption of uniform heat flux. The validity of this approach was in turn questioned by Lee and Rose (1982). A "conjugate" (i.e., vapor-to-coolant) analysis has been given by Fujii and Honda (1984). A uniform coolant inside heat transfer coefficient was used when solving numerically for the temperature distribution in the condensate and tube wall.

Comparisons between experiment and theory are, however, as yet inconclusive.

Apparatus

The major components of the apparatus are shown in Fig. 1. Steam was supplied from the boiler house at an absolute pressure of approximately 8 bar and a temperature of about 175°C. After passing through the separator, where any liquid was removed, the steam flow was metered using an orifice plate. To cover the higher and lower flow-rate ranges, two orifice plates (of diameter 30 mm and 53.34 mm) were used. Steady conditions were maintained by pneumatically actuated flow and pressure controllers, which were set to automatic mode at the desired conditions.

Downstream of the controllers, a nitrogen supply line permitted the addition of nitrogen, if and when required, into the steam. The superheated steam (or steam–nitrogen mixture) then passed into the desuperheater where fine jets of demineralized water were sprayed into it. The amount of water sprayed was accurately controlled by the steam temperature (downstream of the desuperheater) controller and continuously monitored on a flow meter.

The steam (or steam–nitrogen mixture) was then passed via flow straighteners into the rectangular cross-sectional (180 mm × 80 mm) test section, where the internally cooled copper test condenser tube (exposed length = 141.5 mm, o.d. = 14 mm, i.d. = 9.88 mm) was located. The tube was well insulated from the walls of the test section by ptfe bushes. Its wall temperature was obtained as the arithmetic mean of the temperatures indicated by six thermocouples embedded in the tube wall and

Contributed by the Heat Transfer Division and presented at the National Heat Transfer Conference, Houston, Texas, July 24–27, 1988. Manuscript received by the Heat Transfer Division November 5, 1987. Keywords: Condensation, Multiphase Flows.

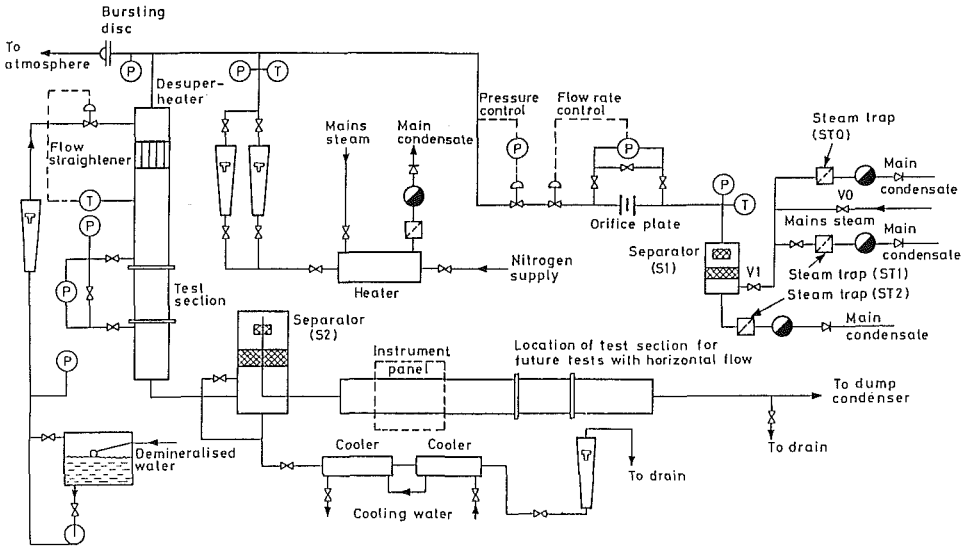

Fig. 1 Schematic diagram of the apparatus

evenly spaced around the circumference (see Fig. 2) with the junctions located midway along the length of the tube.

Downstream of the test section, any condensate present in the steam was removed by a second separator, and then passed through two coolers and a flow meter prior to discharging into a drain. The vapor (or vapor–gas mixture) was finally led to the "dump" condenser operating at atmospheric pressure and having an independent cooling system. A "vent" condenser could also be operated at high steam flow rates for additional condensing duty. The condensate was collected in a tank (fitted with a glass level-indicating tube) before being returned to the boiler house via a condensate manifold. Checks on the steam flow rate obtained from orifice plate calculations were made by condensate collection measurements. The two results were usually found to agree to within 5 percent and always to within 7 percent.

Demineralized water was used as coolant for the test condenser tube. The heat flux was obtained from the cooling water flow rate and the temperature rise. Measurements of the coolant inlet and exit temperatures were made after mixing sections. The coolant temperature rise was also obtained from a single-junction differential thermocouple. For the vast majority of runs the two methods agreed to within 0.1 K with a maximum discrepancy of 0.15 K. An additional check on the heat flux calculated from coolant measurements could be carried out by measuring the condensation rate on the tube by means of the collecting tray situated directly beneath it. Such checks were carried out only at the lowest vapor velocities since at high vapor velocities condensate was swept away by the steam and the amount collected was not a reliable measure of the amount condensed. Agreement was found to be better than 6 percent.

The test-section vapor pressure was measured using an absolute pressure gage, measuring to 0.5 mm Hg.

Procedure

Following startup, the pressure control valve was fully opened. The balancing valve (see Fig. 1) was adjusted so that

Nomenclature

a = constant, see equation (2)
d = tube outside diameter
D = diffusion coefficient
F = dimensionless parameter = $gd\mu_L h_{fg}/(k_L u_\infty^2 \overline{\Delta T})$
g = gravitational acceleration
G = dimensionless parameter = $k_L \overline{\Delta T}/\mu_L h_{fg}(\rho_L \mu_L/\rho_v \mu_v)^{1/2}$
h_{fg} = specific enthalpy of evaporation
k_L = thermal conductivity of condensate
M_g = molar mass of noncondensing gas, nitrogen
M_v = molar mass of vapor, steam
m_v = vapor mass flux at the vapor–condensate interface, condensation mass flux
n = constant, see equation (2)
Nu = Nusselt number = $\alpha d/k_L$
P_∞ = vapor or vapor–gas mixture pressure at bulk
$P_{sat}(T_i)$ = saturation pressure at the vapor–condensate interface temperature T_i
q = heat flux
r = molar mass ratio = M_v/M_g
r_{tc} = thermocouple location radius
Re = Reynolds number for vapor–gas mixture = $u_\infty \rho d/\mu$
$\tilde{\text{Re}}$ = two-phase Reynolds number = $u_\infty \rho_L d/\mu_L$
Sc = Schmidt number = $\mu/\rho D$
T_c = coolant mean temperature
T_∞ = vapor or vapor–gas mixture temperature at bulk
T_i = temperature at the vapor–condensate interface
$T_{sat}(P_\infty)$ = saturation temperature at the bulk pressure P_∞
$T_{w\phi}$ = wall outside surface temperature at angle ϕ
u_∞ = free-stream velocity
W_∞ = free-stream mass fraction of noncondensing gas
W_i = mass fraction of noncondensing gas at the vapor–condensate interface
α = heat transfer coefficient for the condensate film = $q/\overline{\Delta T}$
α_c = coolant heat transfer coefficient
$\overline{\Delta T}$ = average temperature difference across the condensate film
ΔT_ϕ = temperature difference across the condensate film at angle ϕ
μ = viscosity of vapor–gas mixture
μ_L = viscosity of condensate
μ_v = viscosity of vapor
ρ = density of vapor–gas mixture
ρ_L = density of condensate
ρ_v = density of vapor
ϕ = angle from forward stagnation point on tube

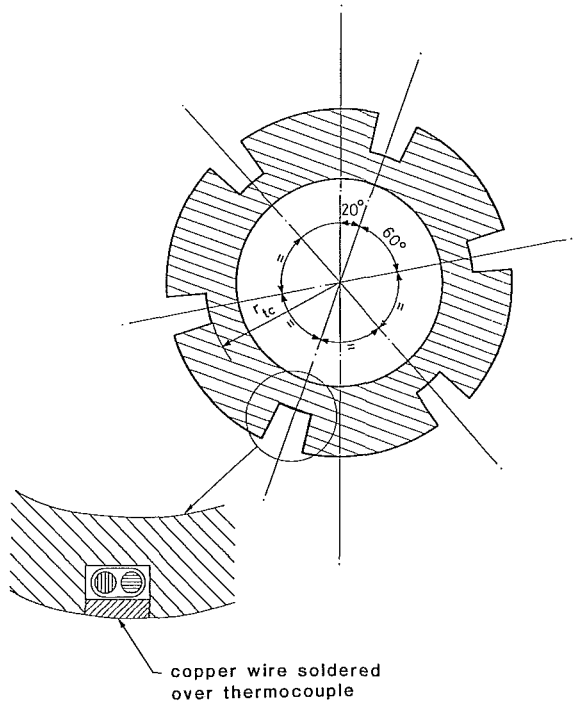

Fig. 2 Location of thermocouples in condenser tube

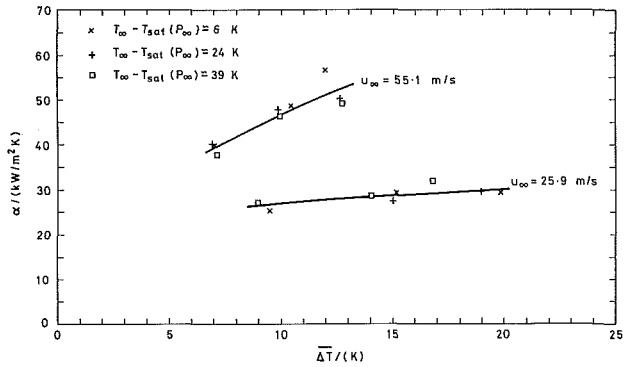

Fig. 3 Heat transfer coefficient against mean temperature drop across the condensate film; effect of steam superheat at two different steam velocities

condensate only was allowed to drain from the separator. The degree of superheat, the steam, nitrogen, and coolant flow rates were then set to the desired values. When steady conditions were established, pressures and flow rates were recorded and all thermocouple readings logged (with a resolution of 1 μV) using a microcomputer-controlled data logging system.

For a fixed degree of superheat and given steam and nitrogen flow rates, measurements were taken for three different cooling water flow rates. The whole procedure was then repeated for a range of steam and nitrogen flow rates and superheats.

It was generally found that the time required for equilibrium conditions to be established when changing the cooling water flow rate was only 2–3 min. Between 1 and 2 h had to be allowed when either the steam (or steam–nitrogen mixture) flow rate or superheat was adjusted to a new value.

Results and Discussion

Pure Steam. Figure 3 shows the dependence of the heat transfer coefficient for the condensate film, α, on the mean temperature drop across the condensate film, $\overline{\Delta T}$, for two steam velocities and three vapor superheats. As anticipated, vapor superheat has negligible effect on the data.

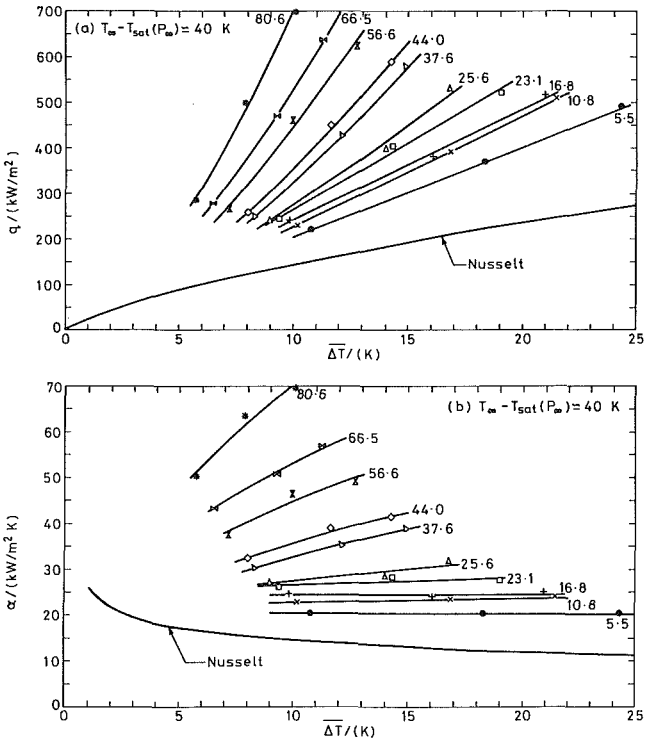

Fig. 4 Heat flux and heat transfer coefficient against mean temperature drop across the condensate film; effect of steam velocity (the numbers denote vapor velocity (m/s))

Figures 4(*a*) and 4(*b*) show the dependence of heat flux q and heat transfer coefficient α on the mean temperature drop for the whole range of vapor velocities used at one vapor superheat. The data are seen to be remarkably smooth and the interdependence of the different parameters clearly established. The heat transfer coefficient is markedly dependent on the vapor velocity. Moreover, the curvature of the q–$\overline{\Delta T}$ lines in Fig. 4(*a*) is opposite to that for natural convection condensation (Nusselt). Alternatively, except at the lowest vapor velocity, the heat transfer coefficient increases with increasing temperature difference.

The fact that α increases with $\overline{\Delta T}$ at the higher vapor velocities could be associated with suppression of vapor boundary layer separation with increasing "suction" and/or effects of turbulence in the condensate film (note that the shear stress at the condensate surface increases with increasing condensation rate, i.e., with increasing $\overline{\Delta T}$).

The lines drawn through the points in Figs. 4(*a*) and 4(*b*) are from "least-squares" fits of the data by equations of the form

$$q = a\,\overline{\Delta T}^{n} \tag{2}$$

The values of n varied from around unity at the lower vapor velocities up to around 1.5 at the highest vapor velocity. These may be compared with the laminar condensate flow models of Nusselt (gravity-controlled flow) where $n = 0.75$ and Shekriladze and Gomelauri (1966) (vapor-shear controlled) where $n = 1$.

In Fig. 5, the present results are compared with the earlier high-velocity, atmospheric-pressure steam data of Mandelzweig (1960). The scatter of these data was such that no dependence of α on $\overline{\Delta T}$ was discernable. The points representing the present results are mean values of α at the relevant vapor velocity with bars to indicate the highest and lowest values. It is evident that the two investigations are in broad general agreement.

The present data indicate that at lower velocities α varies approximately as $u_\infty^{0.12}$ and at high velocities as $u_\infty^{0.78}$. These

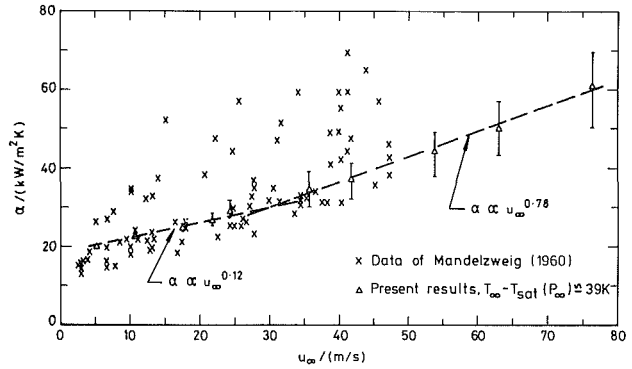

Fig. 5 Dependence of heat transfer coefficient on steam velocity; comparison of present results with the atmospheric-pressure steam data of Mandelzweig (1960)

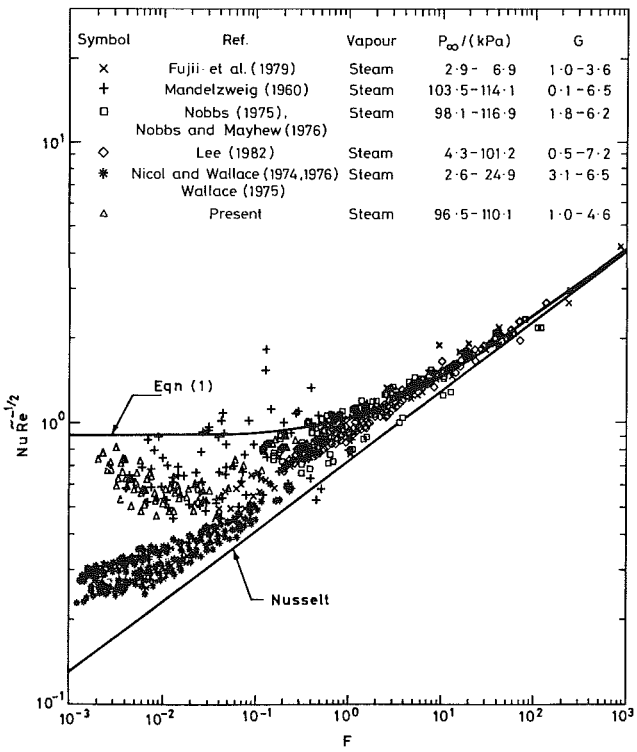

Fig. 6 Comparison of present results with other data for steam

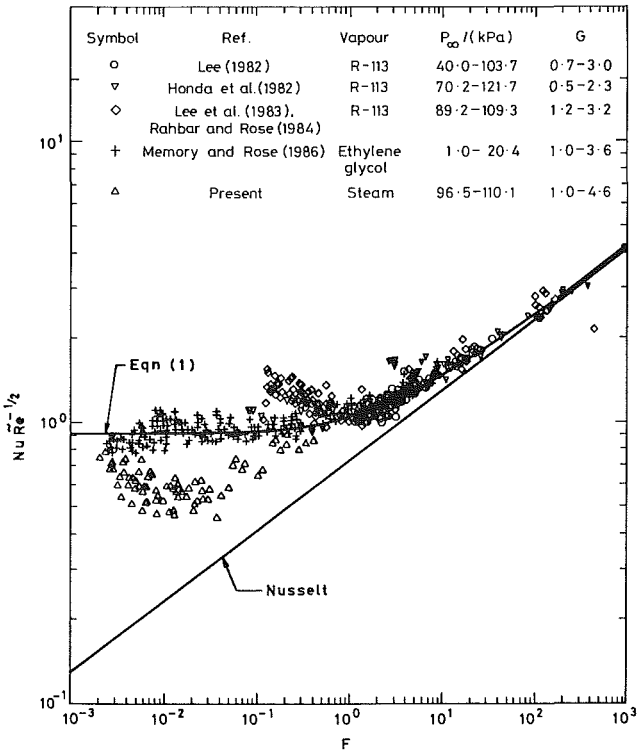

Fig. 7 Comparison of present results with data for other fluids

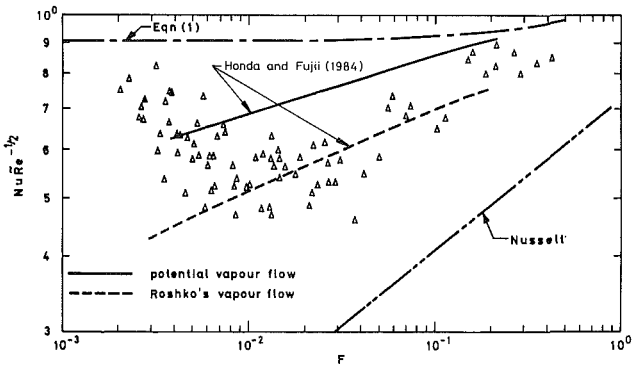

Fig. 8 Comparison of present results with theory

may be compared with the correlation of Fujii et al. (1979, 1980) for low-pressure steam where an index of 0.1 was reported. At high velocities, theory (Shekriladze and Gomelauri, 1966) would indicate a limiting value for the index of u_∞ in equation (2) of 0.5. The value of 0.78 found in the present results might suggest the presence of turbulence in the condensate film.

Figure 6 compares the present and earlier data for steam on a dimensionless basis. It is seen that, at moderate-to-low velocity (higher values of F), all data (Fujii et al., 1979; Mandelzweig, 1960; Nobbs, 1975; Nobbs and Mayhew, 1976; Lee, 1982) are in fair agreement with each other and with the laminar condensate flow theoretical result of Shekriladze and Gomelauri (1966). Of the three sets of data with high vapor velocity (values of F below 0.01) that of Nicol and Wallace (1974, 1976) and Wallace (1975) is significantly lower than the present results and those of Mandelzweig (1960). At the higher velocities the present values of $\mathrm{Nu}\tilde{\mathrm{R}}\mathrm{e}^{-1/2}$ dip significantly below the Shekriladze and Gomelauri (1966) theoretical line before rising again at the highest vapor velocity (lowest value of F). The minimum value of $\mathrm{Nu}\tilde{\mathrm{R}}\mathrm{e}^{-1/2}$ occurs at a value of F of about 0.014. The scatter of the data of Mandelzweig is such that a minimum value of $\mathrm{Nu}\tilde{\mathrm{R}}\mathrm{e}^{-1/2}$ cannot be discerned. In the case of Fujii et al. (1979), Mandelzweig (1960), Nobbs (1975), Nobbs and Mayhew (1976), and Lee (1982), the maximum vapor velocities are lower than those at which, on the basis of the present results, a minimum would be found.

In Fig. 7, the present data are compared with earlier measurements for other fluids. It may be seen that minimum values of $\mathrm{Nu}\tilde{\mathrm{R}}\mathrm{e}^{-1/2}$ have also been found for fluids other than steam. The data for refrigerant-113 (Lee, 1982; Honda et al., 1982; Lee et al., 1983; Rahbar and Rose, 1984) show minima (at values of F dependent on tube diameter) at values of F between 0.8 and 10 (relatively low velocities), while the data for ethylene glycol (Memory and Rose, 1986) show evidence of a shallow minimum in the neighborhood of $F = 0.06$. It has been suggested (Lee et al., 1983) that the upturn in $\mathrm{Nu}\tilde{\mathrm{R}}\mathrm{e}^{-1/2}$ at high vapor velocity (low values of F), indicating that α increases at a rate faster than $u_\infty^{1/2}$, might be due to onset of turbulence in the condensate film.

In Fig. 8 the present data are compared with the "conjugate" analysis of Honda and Fujii (1984). This treats the condensate

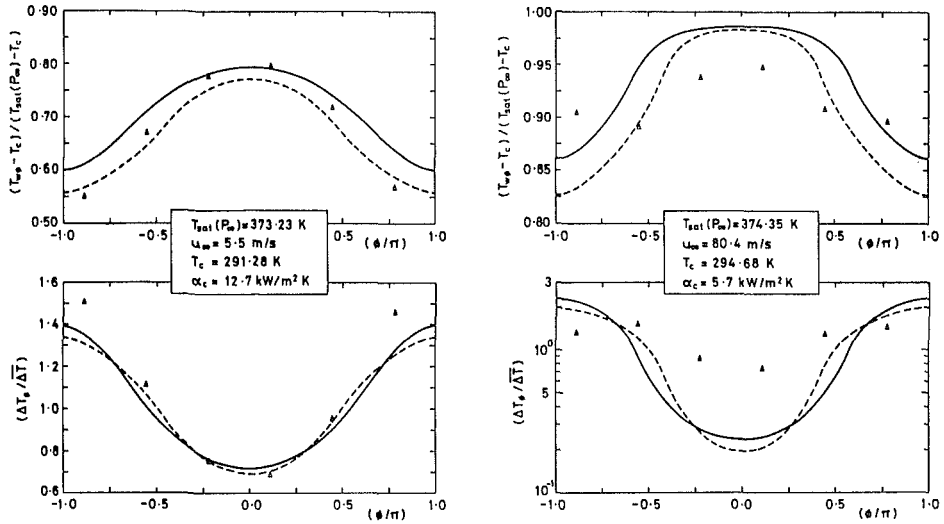

Fig. 9 Tube-wall temperature profiles: —— Honda and Fujii (1984), potential vapor flow; ---- Honda and Fujii (1984), Roshko's vapor flow; Δ present results

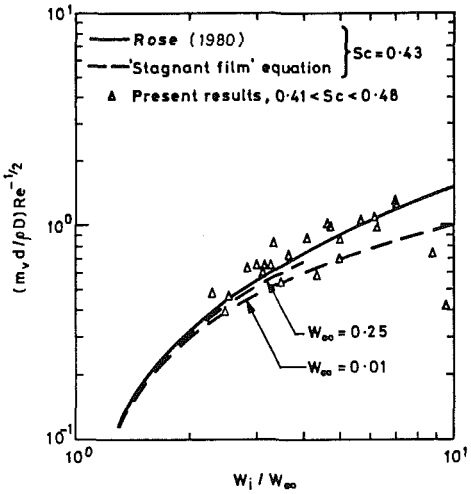

Fig. 10 Comparison of present steam-nitrogen results with the equation of Rose (1980) and the "stagnant-film" equation

film in much the same way as in the Shekriladze approach, except that the tube surface temperature is not assumed uniform. Numerical solutions are obtained with coolant- and vapor-side conditions as inputs, using a uniform coolant-side heat transfer coefficient and solving for the temperature distribution in the tube wall. Two kinds of distributions of vapor velocity around the tube at the "edge" of the vapor boundary layer are considered: (*a*) corresponding to potential flow—which leads to the highest velocities and hence to the highest values of shear stress at the condensate surface—and (*b*) corresponding to the pressure distribution measured by Roshko (1954), which, among the cases examined by Honda and Fujii (1984), gives the lowest velocities. The lines shown in Fig. 8 correspond to the present experimental conditions. It is seen that, except at the highest vapor velocities (lowest values of F), the results generally fall between the two theoretical lines. Comparisons of calculated and observed wall temperature distributions are given in Fig. 9 for low and high vapor velocities. It is seen that agreement with Honda and Fujii (1984) is good at low vapor velocity while at high vapor velocities the wall temperature is more uniform than predicted. The behavior of the data in relation to the theoretical calculations, in both Figs. 8 and 9, is consistent with the suggestion that the condensate film may be partially turbulent at the high vapor velocities.

Steam–Nitrogen Mixtures. The steam-nitrogen results are presented on a dimensionless basis in Fig. 10, where they are compared with theory (Rose, 1980; Colburn and Hougen, 1934). The nitrogen concentration at the interface W_i is obtained from the equilibrium condition

$$W_i = \frac{P_\infty - P_{sat}(T_i)}{P_\infty - (1-r)\,P_{sat}(T_i)} \tag{3}$$

and T_i is obtained from the observed heat flux and measured tube wall temperature using the equation for the condensate film

$$\mathrm{Nu}\tilde{\mathrm{R}}\mathrm{e}^{-1/2} = 1.11\,F^{0.19} \text{ for } F > 0.03 \tag{4}$$

or

$$\mathrm{Nu}\tilde{\mathrm{R}}\mathrm{e}^{-1/2} = 0.568 \qquad \text{for } 0.01 < F < 0.03 \tag{5}$$

Equations (4) and (5) represent the pure steam results discussed above to within ± 14 percent. As indicated by Lee and Rose (1983), the results of the "stagnant-film" model (Colburn and Hougen, 1934), and the theory of Rose (1980) may be expressed by

$$\frac{m_v d}{\rho D} = 0.57\,\mathrm{Re}^{1/2}\left\{(1 + rW_\infty - W_\infty) \times \mathrm{Sc}^{1/3} \ln\left[\frac{W_i}{W_\infty}\frac{(1+rW_\infty - W_\infty)}{(1+rW_i - W_i)}\right]\right\} \tag{6}$$

and

$$\frac{m_v d}{\rho D} = 0.5\,\mathrm{Re}^{1/2}\left\{\left[1 + 2.28\mathrm{Sc}^{1/3}\frac{(W_i - W_\infty)}{W_\infty}\right]^{1/2} - 1\right\} \tag{7}$$

respectively. It may be seen that quite good agreement between the present results and the equation of Rose (1980) is obtained while the "stagnant-film" model (two lines corresponding to the two extreme values of W_∞ in present experiments) gives somewhat more conservative predictions.

Conclusions

Experimental data for condensation of steam and steam-nitrogen mixtures at near atmospheric pressure on a single horizontal tube under conditions of high vapor shear have

been presented. Comparisons with theory and other experimental results lead to the following conclusions:

(*i*) steam superheats of up to 40 K have negligible effect on the heat transfer coefficient for the condensate film;

(*ii*) laminar condensate flow theories (Shekriladze and Gomelauri, 1966; Fujii et al., 1972) are accurate only at low vapor velocities (values of F greater than about 1);

(*iii*) Honda and Fujii's (1984) "conjugate" heat transfer analysis predicts the present results to within ± 18 percent down to a value of F of around 0.014;

(*iv*) for values of F below 0.014, the steam-side heat transfer coefficient increases at a rate faster than the square root of the vapor velocity (as indicated by laminar theory), possibly due to the onset of turbulence in the condensate film;

(*v*) the "gas-phase" resistance during condensation from a steam-nitrogen mixture is satisfactorily described by the equation of Rose (1980) and the "stagnant-film" model (Colburn and Hougen, 1934), the latter being somewhat conservative.

Acknowledgments

The present work was carried out under the research program of the Heat Transfer and Fluid Flow Service (HTFS), which receives funding from the UK Department of Trade and Industry.

References

Colburn, A. P., and Hougen, O. A., 1934, "Design of Cooler Condensers for Mixtures of Vapours With Non-condensing Gases," *Ind. Eng. Chem.*, Vol. 26, pp. 1178–1182.

Fujii, T., Honda, H., and Oda, K., 1979, "Condensation of Steam on a Horizontal Tube—the Influence of Oncoming Velocity and Thermal Condition at the Tube Wall," *Condensation Heat Transfer*, ASME, New York, pp. 35–43.

Fujii, T., Honda, H., and Oda, K., 1980, "Forced Convection Condensation on a Horizontal Tube—Experiments for Horizontal Flow of Low-Pressure Steam," *Trans. Jap. Soc. Mech. Engrs.*, Vol. 46, No. 401B, pp. 103–110.

Fujii, T., Uehara, H., and Kurata, C., 1972, "Laminar Filmwise Condensation of a Flowing Vapour on a Horizontal Cylinder," *Int. J. Heat Mass Transfer*, Vol. 15, pp. 235–246.

Honda, H., and Fujii, T., 1984, "Condensation of Flowing Vapour on a Horizontal Tube—Numerical Analysis as a Conjugate Heat Transfer Problem," ASME JOURNAL OF HEAT TRANSFER, Vol. 106, pp. 841–848.

Honda, H., Nozu, S., and Fujii, T., 1982, "Vapour-to-Coolant Heat Transfer During Condensation of Flowing Vapour on a Horizontal Tube," *Proc. 7th Int. Heat Transfer Conf.*, Munich, Vol. 5, pp. 77–82.

Lee, W. C., 1982, "Filmwise Condensation on a Horizontal Tube in the Presence of Forced Convection and Non-condensing Gas," PhD Thesis, Queen Mary College, University of London, United Kingdom.

Lee, W. C., Rahbar, S., and Rose, J. W., 1984, "Film Condensation of Refrigerant 113 and Ethanediol on a Horizontal Tube—Effect of Vapor Velocity," ASME JOURNAL OF HEAT TRANSFER, Vol. 106, pp. 524–530.

Lee, W. C., and Rose, J. W., 1982, "Film Condensation on a Horizontal Tube—Effect of Vapour Velocity," *Proc. 7th Int. Heat Transfer Conf.*, Munich, Vol. 5, pp. 101–106.

Lee, W. C., and Rose, J. W., 1983, "Comparison of Calculation Methods for Non-condensing Gas Effects in Condensation on a Horizontal Tube," *Inst. Chem. Eng. Symp. Ser.*, Vol. 75, pp. 342–355.

Mandelzweig, S. I., 1960, "The Effect of Vertically Downward Velocity on the Heat Transfer From a Steam-Nitrogen Mixture Condensing on a Horizontal Cylinder," MSc Thesis, Queen Mary College, University of London, United Kingdom.

Memory, S. B., and Rose, J. W., 1986, "Film Condensation of Ethylene Glycol on a Horizontal Tube at High Vapour Velocity," *Proc. 8th Int. Heat Transfer Conference*, San Francisco, CA, Vol. 4, pp. 1607–1612.

Nicol, A. A., and Wallace, D. J., 1974, "The Influence of Vapour Shear Force on Condensation on a Cylinder," *Inst. Chem. Eng. Symp. Ser.*, Vol. 38, pp. 1–19.

Nicol, A. A., and Wallace, D. J., 1976, "Condensation With Appreciable Vapour Velocity and Variable Wall Temperature," *Symp. on Steam Turbine Condensers*, NEL Report No 619, pp. 27–38.

Nobbs, D. W., 1975, "The Effect of Downward Vapour Velocity and Inundation on the Condensation Rates on Horizontal Tubes and Tube Banks," PhD Thesis, University of Bristol, United Kingdom.

Nobbs, D. W., and Mayhew, Y. R., 1976, "Effect of Downward Vapour Velocity and Inundation Rates on Horizontal Tube Banks," *Symp. on Steam Turbine Condensers*, NEL Report No 619, pp. 39–52.

Rahbar, S., and Rose, J. W., 1984, "New Measurements for Forced Convection Film Condensation," *1st UK Nat. Conf. on Heat Transfer*, Vol. 1, pp. 609–632.

Rose, J. W., 1980, "Approximate Equations for Forced Convection Condensation in the Presence of a Non-condensing Gas on a Flat Plate and Horizontal Tube," *Int. J. Heat Mass Transfer*, Vol. 23, pp. 539–546.

Rose, J. W., 1984, "Forced Convection Film Condensation on a Horizontal Tube—Effect of Pressure Variation in the Condensate Film," *Int. J. Heat Mass Transfer*, Vol. 27, pp. 39–47.

Roshko, A., 1954, "A New Hodograph for Free-Streamline Theory," NACA, TN 3168.

Shekriladze, I. G., and Gomelauri, V. I., 1966, "Theoretical Study of Laminar Film Condensation of a Flowing Vapour," *Int. J. Heat Mass Transfer*, Vol. 9, pp. 581–591.

Wallace, D. J., 1975, "A Study of the Influence of Vapour Velocity Upon Condensation on a Horizontal Tube," PhD Thesis, University of Strathclyde, Glasgow, United Kingdom.

The Measurement of Surface Heat Flux Using the Peltier Effect

E. C. Shewen
Pavement Management Systems Ltd., Cambridge, Ontario, Canada

K. G. T. Hollands

G. D. Raithby

Department of Mechanical Engineering, University of Waterloo, Waterloo, Ontario, Canada

Calorimetric methods for measuring surface heat flux use Joulean heating to keep the surface isothermal. This limits them to measuring the heat flux of surfaces that are hotter than their surroundings. Presented in this paper is a method whereby reversible Peltier effect heat transfer is used to maintain this isothermality, making it suitable for surfaces that are either hotter or colder than the surroundings. The paper outlines the theory for the method and describes physical models that have been constructed, calibrated, and tested. The tested physical models were found capable of measuring heat fluxes with an absolute accuracy of 1 percent over a wide range of temperature (5–50°C) and heat flux (15–500 W/m²), while maintaining isothermality to within 0.03 K. A drawback of the method is that it appears to be suited only for measuring the heat flux from thick metallic plates.

Introduction

As noted by Goldstein and Chiang (1985), steady-state devices for measuring the heat flux from a surface can be classified into two types: the thermal resistance type and the calorimetric type.[1] Both types have their limitations if the total surface, including both the measurement region and the region outside it (Fig. 1), is to remain isothermal. In the thermal resistance type, where measurement of a temperature drop gives an indication of the heat flux from Fourier's Law, some temperature difference is necessarily required, and this can prevent the desired degree of isothermality from being achieved. In the calorimetric type, where the heat flux is determined from a heat balance, a measured quantity of Joulean heating can produce the desired isothermality. However, this Joulean heating is only capable of producing isothermality if the heat flow is *out* of the surface (i.e., if q in Fig. 1 is positive). If the heat flows *into* the surface (i.e., q is negative), Joulean heating can only augment the temperature nonuniformity; some form of cooling is clearly required.

This paper describes a device in which the Peltier effect is used to provide the necessary energy transfer. Being reversible, the Peltier effect can provide either heating or cooling. The paper outlines the theory of this device, gives a method of calibration, and describes a physical model that has been constructed, calibrated, and validated.

Description of the Method

Thermoelectric Device. The thermoelectric device works on the principle, discovered by Peltier, that when a junction between two dissimilar materials experiences an electric current, heat is absorbed or liberated at the junction, the direction of this "Peltier heat flow" depending on the nature of the dissimilar materials and the direction of the current. The Peltier heat flow is jointly proportional to the current and the absolute temperature of the junction. The constant of proportionality, called the Seebeck coefficient σ, is a joint property of the two dissimilar materials. Figure 2 shows a single device in which P- and N-type semiconductors have been used as the main dissimilar materials, since this choice maximizes the Peltier effect. Heat sinks A and B are metal plates, heat sink B having a thin split (at C) to insulate the two halves electrically (but not thermally) from each other. As shown, for example by Angrist (1976), its input-output relations are

$$Q_A = \sigma T_A I + \frac{1}{2} R_e I^2 + (T_B - T_A)/R_t \quad (1)$$

$$Q_B = \sigma T_B I - \frac{1}{2} R_e I^2 + (T_B - T_A)/R_t \quad (2)$$

$$V = IR_e - \sigma(T_B - T_A) \quad (3)$$

where Q_A is the heat flow out of heat sink A and Q_B is the heat flow into heat sink B. T_A and T_B are the *absolute* temperatures of the heat sinks, σ is the Seebeck coefficient for the pair of semiconductors. R_e is the electrical resistance of

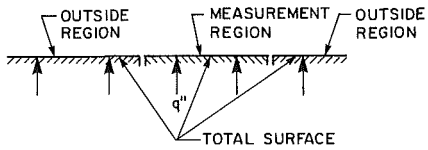

Fig. 1 Definition of regions for heat flux measurements

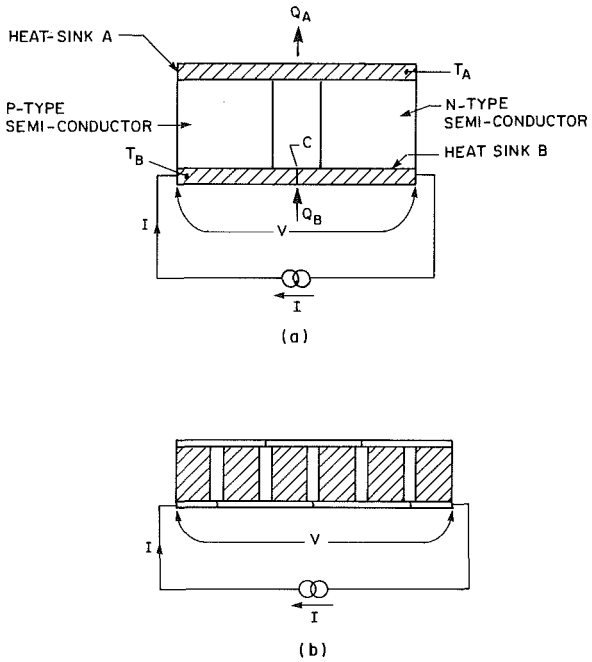

Fig. 2 Schematics of (a) a thermoelectric device, and (b) a thermoelectric module (TEM)

[1] Hollands (1973) has described a hybrid of the two types.

Contributed by the Heat Transfer Division and presented at the 24th National AIChE/ASME Heat Transfer Conference, Pittsburgh, Pennsylvania, August 9–12, 1987. Manuscript received by the Heat Transfer Division October 26, 1987. Keywords: Instrumentation, Measurement Techniques.

the two semiconductors in series, as seen from the external circuit, and R_t is the thermal resistance of the semiconductors in parallel. Equation (1) results from a heat balance on the heat sink A. The terms on the right-hand side may be interpreted as follows: $\sigma T_A I$ is the net of the two Peltier heat flows produced at the junctions of the plate with the P-type and N-type semiconductors; the sum of the other terms equals the heat conducted into the heat sink from the two semiconductors. This conducted heat is determined by solving the one-dimensional heat diffusion equation in the two semiconductor regions, allowing for the internal generation of Joulean heating, and assuming constant properties. (Under these conditions, one half of the total Joulean heating $R_e I^2$ is conducted into heat sink A, and one half into heat sink B.) An explanation similar to that just given for equation (1) applies to equation (2). Equation (3), on the other hand, results from treating the device as a thermocouple having an internal resistance and experiencing a current flow.

From these equations it is clear that provided σ, R_e, and R_t are known, then once I and V have been measured, either Q_A or Q_B can be determined, regardless of their respective signs. Moreover, by adjusting I until V is equal to IR_e, the device can be made isothermal. Thus the device has the potential to be an isothermal heat flux meter, capable of measuring heat flows in either direction.

Strictly equations (1)–(3) have only been shown to apply to a thermo-electric device in which the properties σ, R_e, and R_t are independent of temperature. If σ varies with temperature then the Thompson effect should be considered. Shewen (1986) has shown that provided σ is linear in T (which is generally close to the case) the Thompson effect is included in equations (1)–(3) if σ is evaluated at the average temperature $T_a = (T_A + T_B)/2$. Since in operation the device is made nearly isothermal, the assumption of temperature invariance would not appear to present any problems. However, in order to calibrate the device – a necessary step for finding σ and R_t – it will be necessary to cover a fair temperature range. This work will assume a linear temperature variation for σ, i.e., that

$$\sigma = \sigma_o + \sigma_1 (T_a - T_o) \tag{4}$$

where σ_o and σ_1 are constants for the device, T_o is a reference temperature.

Commercially purchased, these thermoelectric devices generally come in modules (called TEMs), containing say 30 devices connected electrically in series and thermally in parallel, as in Fig. 2(*b*). Equations (1)–(3) apply to the module taken as a whole, provided σ is interpreted as the sum of the σ's of each of the devices, and R_e and R_t are interpreted as the corresponding properties of the module as a whole.

Description of Meter. It is assumed that the surface whose heat flux is to be measured is a metallic plate (called here the main plate) sufficiently thick and heat conducting that one can machine into it a recess deep enough to receive both the TEM and an additional heat sink plate (called here the cap plate) without appreciably altering the main plate's isothermally (see

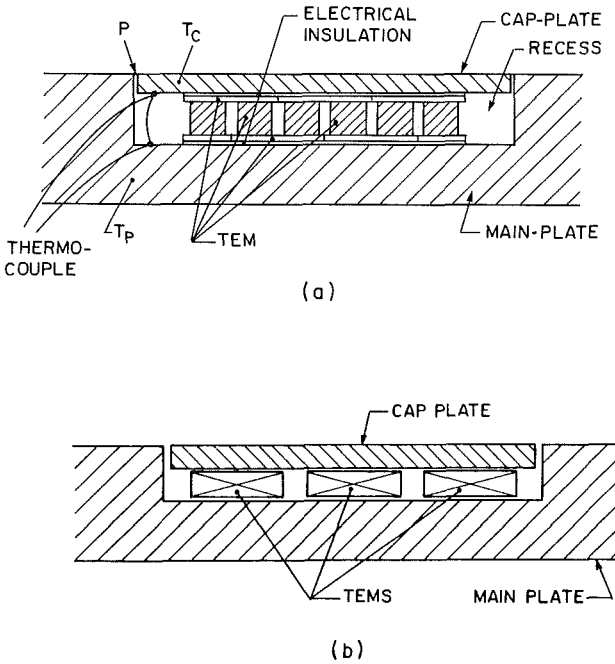

Fig. 3 Schematic of a Peltier heat flux meter (PHFM) (*a*) with a single TEM, (*b*) with an array of TEMs (three are shown)

Nomenclature

A = area of a cap plate
A_0, A_1 = constants in equation (12)
B_0 = constant in equation (12)
b = plate spacing
C_0, C_1 = constant in equation (13)
$c_1, \ldots, c_6$ = constants in equations (8) and (9)
D_0, D_1, D_2 = constants in equation (13)
E_0 = constant
I = current through thermoelectric module
Q = heat flow leaving cap plate at outside surface
$Q_A, (Q_B)$ = heat flow out of (into) heat sink A (B) in a thermoelectric device (see Fig. 2)
Q_p = quantity defined by equation (5*b*)
q = Q/A = average heat flux over cap-plate surface
R_e = electrical resistance of thermoelectric device, module, or array
R_i = thermal resistance betwen cap plate and the adjacent heat sink of the thermoelectric device or between the main plate and its adjacent heat sink
R_g = thermal resistance between cap plate and main plate in region outside of TEMs
R_t = thermal resistance of TEMs
T_A, T_B = temperature of heat sinks A and B
T_a = $(T_A + T_B)/2$
T_c = cap-plate temperature
T_m = $(T_c + T_p)/2$
T_o = reference temperature, taken as 0°C
T_p = main-plate temperature
T_r = room temperature
V = voltage across thermoelectric device module, or array
σ = Seebeck coefficient at temperature T_a
σ_0 = Seebeck coefficient at $T_a = T_o$
σ_1 = $d\sigma/dT_a$

Fig. 3*a*). It will usually be necessary to make the cross section of the recess wider than the TEM, for several reasons, one of which is to allow for the placement of electrical wires. Also, the surfaces of the TEMs tend to be less smooth and isothermal than would be desired. Thus the purpose of the cap plate is to fill in across the recess in such a way that, except for a very fine separation line (at P) between the cap plate and the main plate at the recess edge, the total plate presents an uninterrupted planar isothermal (or nearly isothermal) surface to the outside world. Temperature sensors should be placed on the cap plate and main plate to measure their respective temperatures T_p and T_c.

If one is interested in obtaining the heat flow over a broader area than that of a cap plate placed over a single TEM, several TEMs can be connected electrically in series and thermally in parallel, each sharing the same larger cap plate, forming a TEM *array* (Fig. 3*b*). Again equations (1)–(4) apply to the array, provided proper interpretations are given to σ, R_e, and R_t.

Thermal Analysis. Figure 4 shows the thermal circuit for the thermoelectric heat flux meter shown in Fig. 3. Nodes at temperatures T_c and T_p refer to the cap plate and main plate, respectively, while those at T_A and T_B refer to the TEM's heat sink plates. Resistance R_g is the thermal resistance between the cap plate and the main plate in the region outside the TEM(s). Thus it includes radiation and conduction across the air filling this region, including the fine separation line at P between the two plates, and conduction across any items (screws, etc.) securing the cap plate in position. Resistance R_i is the thermal resistance between the TEM's heat sink plate and the cap plate, or between the TEM's other heat sink plates and the main plate, these two resistances being assumed equal. The dominant component in this latter resistance will probably lie in the electrical insulation, which must be placed between the TEMs and the plates, to prevent electrical short-circuting through the plates. The quantity to be determined is Q, the heat flux at the cap-plate surface.

The thermal circuit may be subjected to an analysis, the primary purpose of which is to express Q as a function of the measured quantities T_p, T_c, I, and V, and the parameters σ, R_e, R_t, R_g, and R_i. The result is

$$Q=(1+2R_i/R_t)\sigma T_pI-\frac{1}{2}R_eI^2 - \left[\frac{1}{R_t}+\frac{1}{R_g}\left(1+\frac{2R_i}{R_t}\right)\right]\frac{1}{\sigma}(V-IR_e) + VI+\frac{R_i}{R_g}I(V-IR_e)-\sigma R_iQ_pI+\frac{\sigma}{R_g}(VI^2+2Q_pI)R_i^2 \quad (5a)$$

where

$$Q_p=\sigma T_pI-\frac{1}{2}R_eI^2-\frac{(V-IR_e)}{\sigma R_t}/(1+R_i\sigma I) \quad (5b)$$

In addition one can show from the circuit that

$$T_a=T_m+VIR_i/2$$

where $T_m = (T_c + T_p)/2$, so that, from equation (4)

$$\sigma=\sigma_o+\sigma_1(T_m-T_o)+\frac{\sigma_1R_i}{2}\cdot VI \quad (6)$$

Also derivable from the circuit is the useful equation

$$T_p-T_c=-\frac{1}{\sigma}\left(1+\frac{2R_i}{R_t}\right)(V-IR_c)+2\sigma R_iT_mI+\sigma R_i^2VI^2 \quad (7)$$

Calibration. While the manufacturers often provide estimates (± 10 percent) of the parameters σ, R_t, and R_e, these values are not sufficiently accurate for our purposes. Thus all the parameters σ, R_e, R_t, R_g, and R_i must be obtained by measurement, preferably in situ. The electrical resistance R_e can be measured as a function of T_a to a high accuracy using an AC Wheatstone bridge, in a situation where $Q \approx 0$, so that all nodes are nearly isothermal. (By using an a-c, rather than d-c, bridge, any slight contribution of the voltage V due to slight temperature variations is eliminated, as this voltage constitutes a d-c signal.) Having evaluated R_e once and for all, the quantity $V-IR_e$ can be treated as equivalent to a directly measured quantity in any subsequent regression analysis.

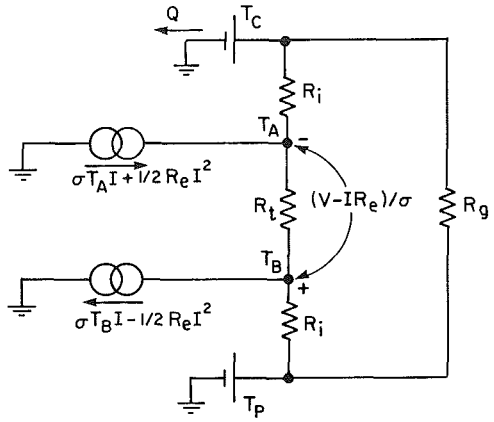

Fig. 4 Thermal circuit of a PHFM

The remaining variables can be determined in a calibration process. In this process the heat flow Q is measured independently by inserting a thin electrical heater immediately above the cap plate in Fig. 3, insulating it well at the top, and providing it with means for measuring its voltage and current. A wide three-dimensional matrix containing corresponding values of Q, I, and T_p is then covered, with the corresponding values of V, and $T_p - T_c$, as well as Q, I, and T_p, being measured at each setting. A multivariable regression analysis, having the form suggested by equations (5)–(7), will then yield values of the regression constants from which the parameters may be calculated.

In practice we have found that because of the large number of variables and parameters in the equations, this procedure is cumbersome and sometimes predicts unrealistic values for the parameters. Part of the problem is that R_t, R_g, and R_i are in fact temperature dependent, a factor ignored in equations (5)–(7). Including this dependence in the equations, however, would only compound their complexity.

Much simplification can be achieved if it can be shown that the resistance R_i is small. Through the use of grease or conductive paste and by providing a modest compressive force in the interfaces, it should be possible to minimize one part of this resistance. Nonetheless, R_i cannot be ignored without sound reasons. We suggest the following procedure for determining its significance. A regression analysis is entered into, using as forms equations (5)–(7), in which certain of the terms containing R_i are neglected, namely:

$$\left[Q-VI+\frac{1}{2}R_eI^2\right] = c_1\{T_pI\}+c_2\{T_pI(T_m-T_o)\}+c_3\{V-IR_e\} \quad (8)$$

$$[T_p-T_c]=c_4\{V-IR_e\}+c_5\{(V-IR_e)T_m\}+c_6\{T_mI\} \quad (9)$$

The quantities in square brackets are treated as the independent variables of the regresssion, while those in curly brackets are treated as the dependent variables. Having thus obtained values of $c_1, \ldots, c_6$, the values of the parameters are obtained by setting the multipliers in equations (8) and (9) equal to the corresponding terms in equations (5)–(7), as follows:

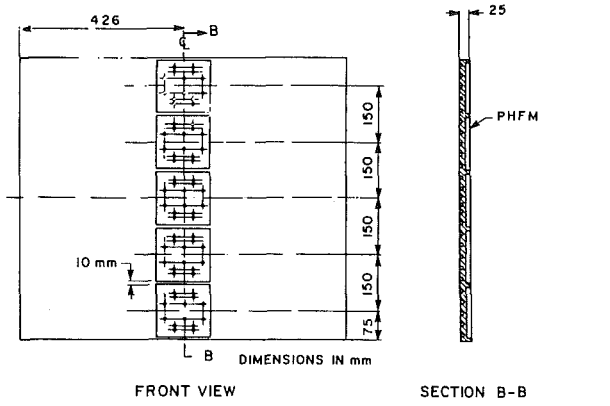

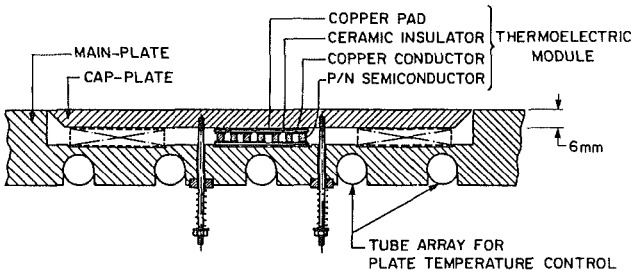

Fig. 5 Schematic of plate tested, detailing the PHFM

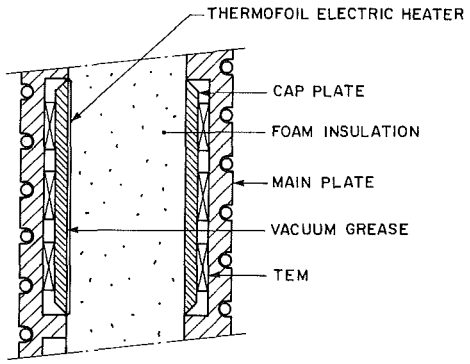

Fig. 6 Schematic of setup used for calibration, showing midsection of plates only

$$
\begin{aligned}
c_1 &= (1+2R_i/R_t)\sigma_o;\\
c_2 &= (1+2R_i/R_t)\sigma_1;\\
c_3 &= -\frac{1}{\sigma_o}\left(\frac{1}{R_t}+\frac{1}{R_g}\right)(1+2R_i/R_t);\\
c_4 &= -\frac{1}{\sigma_o}\,(1+2R_i/R_t);\\
c_5 &= \frac{\sigma_1}{\sigma_o^2}\,(1+2R_i/R_t);\\
c_6 &= 2\sigma_o R_i
\end{aligned}
\tag{10}
$$

These represent six equations in five unknowns (the equation for c_5 is redundant), so the parameters σ_o, σ_1, R_t, R_g, and R_i can be determined.

Once the parameters have been so estimated, an order-of-magnitude analysis of equations (5)–(7) can be carried out, from which it can be determined which terms may be safely dropped. Finally one can perform a regression analysis using as forms equations (5) and (6), in which insignificant terms have been dropped. With these equations, and a measure of the cap-plate area (to be divided into Q to obtain q), the Peltier Heat Flux Meter (PHFM) is ready for use. A final item, however, remains.

When making a measurement of Q, it is desirable to know the corresponding value of $(T_p - T_c)$, for it determines the degree of isothermality of the surface. If $|T_p - T_c|$ is excessive, I must be adjusted until $|T_p - T_c|$ is, indeed, within prescribed bounds. While $T_p - T_c$ can be directly meaured by the thermocouples, a much more accurate estimate can be made by equations (6) and (7), once the parameters have been established. Thus a final regression analysis on equations (6) and (7) is desirable before PHFM is put to use.

Construction, Calibration, and Testing of a PHFM

Construction. The ten PHFMs constructed and tested were part of two large aluminum main plates, which were designed for studies on natural convection heat transfer in an open cavity (Shewen, 1986). The objective was for the PHFMs to measure the heat flux, in the region along one of the long central axes of each main plate, for values up to 500 W/m^2 and with an accuracy of 1 percent, while maintaining an isothermality of ± 0.1 K over a plate temperature range of 5 to 50°C. Each 25 mm × 850 mm × 750 mm main plate was equipped with five PHFMs positioned at equal increments along the central axis, as shown in Fig. 5, with 10 mm spacings between recesses. Each PHFM contained nine TEMs positioned in a 3×3 array.

Figure 5 also shows a cross-sectional view of the recess of one PHFM. They each contained 31 Bi_2Te_3 P/N couples and measured 31.75 mm square by 5.334 ± 0.025 mm thick (see Acknowledgments). The modules were positioned in a 1.0 mm deep indentation, machined into the recess, with a flatness tolerance of ± 0.0025 at the indentation's bottom face. The 140 mm square copper cap plate and the main plate were in this way made flush to within ± 0.025 mm.

The thickness of 6 mm for the cap plate was decided upon based on a detailed thermal analysis of its temperature field under worst-case conditions (Shewen, 1986). These calculations indicated that for a cap-plate thickness of 6 mm, its maximum temperature variation should be less than ± 0.01 K for a uniform heat flux at the cap surface.

In securing the cap plates, emphasis was placed on minimizing R_g and R_i. Each cap plate was secured by ten 1.7-mm-dia stainless steel, threaded rods, which were epoxied to the cap plate, passed through holes in the main plate, and secured on the outside by a nut. A nylon insert prevented the rods from touching the plate, and a compression spring between the nut and the insert permitted a known compressive force of up to 100 kPa to be applied to the modules by tightening the nuts. The surfaces between the TEMs and the plates were coated with vacuum grease before assembly. A 45 deg chamfer was machined on the edge of the cap plate to mimimize R_g.

To measure $T_p - T_o$, five copper-constantan thermocouples were embedded in small holes drilled in the cap-plate underside (both in the TEM region and outside it) and connected to 0.127 mm insulated thermocouple wires, which ran in slots along the cap-plate underside before being connected, in thermopile, to similar thermocouples similarly attached to the main plate. Each main plate was maintained at uniform temperature by circulating, at a high capacity, water from a constant temperature bath through copper tubes thermally connected to the rear surfaces of the plates and spaced at 30 mm centers. Three copper-constant thermocouples were embedded in each plate, and these readings (which, under test conditions, were found to disagree by less than 0.07 K) were averaged to give T_p.

Calibration. First the electrical resistance R_e for each PHFM was measured for values of T_a ranging from 5°C to 50°C in 5°C steps, and the results fitted closely by

$$R_e = R_{e0} + R_{e1}(T_a - T_o)_g \tag{11}$$

T_o was taken as 0°C. Typical values of R_{e0} and R_{e1} were 2.3 Ω and 0.014 Ω/K. The overall uncertainty in predicting R_e from equation (11) was estimated as 0.014 Ω.

Next thermofoil electrical heaters, 12.3 mm square by 0.15 mm thick and having nominal resistance of 15 Ω, were attached to each of the five cap plates on one main plate, a thin layer of vacuum grease being applied to each surface before assembly (see Fig. 6). A 51 mm slab of polyisocynurate foam insulation was then sandwiched tightly between the two main plates, pressing the thermofoil heaters firmly against the cap plates. The thermal resistance between the heater and the cap plate was estimated as 0.01 K/W, while that between the heater and the opposite main plate was estimated at 120 K/W. Thus essentially all of the electrical heating Q_f went into the cap plate. However, to obtain Q, it was necessary first to correct Q_f for rear and side losses from the cap plate, which were estimated using an analytical steady heat conduction solution, taking into account the thermal conductivity of the foam insulation. To minimize these losses, the two main plates were kept at the same temperature, to within 0.1 K. The correction for rear and side losses never exceeded 0.015 W, whereas Q_f was typically 1–5 W.

Next, driven by a microcomputer, a calibration procedure stepped through a three-dimensional matrix in Q, I, and T_p covering the following values:

$0 \le Q \le 5.5$ W	in intervals of 1.1 W
$0 \le I \le 0.24$ A	in intervals of 0.04 A
$2 \le T_p \le 52$°C	in intervals of 10°C

All the variables (Q, I, T_p, V, and $(T_p - T_c)$) were measured at each setting. Typically V varied from -0.24 V to 1.2 V and $(T_p - T_c)$ from -2.5 K to 4 K.

The first regression analysis on equations (8) and (9) (with T_o = 0°C) gave the following (rough) values for the parameters: $\sigma_o = 0.06 \pm 0.1$ V/K; $\sigma_1 = 1.5 \times 10^{-4} \pm 0.3$ V/K^2; $R_t = 1.4 \pm 0.2$ K/W; $R_i = 0.05 \pm 0.005$ K/W, and R_g = 10 K/W. The ± variance given after each of these values is an indication of the variation found between the various PHFMs, not of the uncertainty in any one value. An order of magnitude analysis on equations (5)–(7) indicated that the last three terms in equation (5*a*) are less than 0.2 percent of the first term and therefore can probably be safely ignored. The middle of the three terms is the largest, being at least an order of magnitude larger than the other two. It was decided to retain this term. The last term in equation (6) was found to be insignificant, as was the last term in equation (7). With these guidelines, a second regression of the following forms was entered into for each PHFM:

$$[T_p - T_c] = (A_o - A_1(T_m - T_o))\{V - IR_e\} + B_o T_m I \tag{12}$$

$$[Q - VI + \frac{1}{2} R_e I^2 + \sigma_o R_i Q_p I] = (C_o + C_1(T_m - T_o))\{T_p I\}$$

$$+ (D_o + D_1(T_m - T_o) + D_2(T_m - T_o)^2)\{V - IR\} \tag{13}$$

The last term on the left-hand side of equation (13) was evaluated using equation 5(*b*) with the values of its parameters being given by the first regression analysis. Equation (13) allows for R_i, R_t, and R_g to vary with temperature, as well as σ. For the PHFMs at the plate edge, the term $E_o\{T_c - T_r\}$ was incorporated into the right-hand side of equation (13), T_r being the temperature of the room in which the calibration was performed. A sample set of values and their standard errors is given in Table 1.

Table 1 Sample values of constants in equations (12) and (13)

$A_0 = -14.7 \pm 0.05$ K/V
$B_0 = (10.53 \pm 0.02) \times 10^{-3}$ A^{-1}
$C_0 = 0.0643 \pm 0.0003$ W/AK
$C_1 = (1.97 \pm 0.01) \times 10^{-4}$ W/AK^2
$D_0 = -80.4 \pm 0.5$ W/V
$D_2 = 0.365 \pm 0.003$ W/VK
$D_2 = (-5.36 \pm 0.5) \times 10^{-4}$ W/VK
$E_0 = -(1.38 \pm 0.03) \times 10^{-3}$ W/VK^2

An error analysis on determining Q from equation (13), taking into account the standard errors in A_o, A_1, etc., as well as in the measured variables I, V, and T_p, indicated a constant error in the resultant heat flux q of ± 0.15 W/m^2. It also indicated that over the range $15 < q < 550$ W/m^2, the (95 percent confidence) random errors in q should be less than 1 percent.

Validation. As a first step in testing the method, the two plates (denoted X and Y) were spaced at a constant spacing of 10 mm and a temperature difference was established between them. The space between the plates was allowed to fill with atmospheric air and insulated at the edges. The heat fluxes of all ten PHFMs were measured and those over each main plate were then averaged, giving q_x and q_y, respectively. The experiment was carried out in both the horizontal and vertical plate positions, and for various plate temperatures, giving in all 15 independent measurements of q_x and q_y covering a heat flux range of $-70 < q_x < 150$ W/m^2 and $-150 < q_y < 75$ W/m^2. The resultant values of $|q_x|$ and $|q_y|$ were found to differ by no more than 1 percent over the full range. This test not only checked the internal consistency of the method but also established that the method can indeed measure heat flux in either direction, an item never actually tested in the calibration procedure.

In the second validation test, in which the thermal conductivity of dry air at 303 K was measured and compared to the literature value, the plates were set at 296 K and 310 K, respectively, and the values of $|q_x|$ and $|q_y|$ were measured and averaged, yielding $q = (|q_x| + |q_y|)/2$. The experiment was repeated for three values of the spacing b between the plates, in each case with dry atmospheric pressure air filling the space between the plates. The hotter of the two horizontal plates was on the top, so no natural convection currents were expected, and this was confirmed when a plot of q versus $1/b$ yielded a straight line with a regression coefficient of 0.99996. The thermal conductivity k of dry air, determined from the line's slope, gave a value for k of 0.0266 W/mK, which is within 0.5 percent of the value reported by Hilsenrath et al. (1960). During the measurement of each q, $|T_p - T_c|$, as determined by equation (12), was kept less than 0.03 K.

Conclusions

The Peltier heat flux meter described in this paper is a useful device for accurately measuring both positive and negative surface heat fluxes while maintaining a closely isothermal, smooth surface. The method requires that the surface in question be the surface of a thick metallic plate maintained at uniform temperature by some external means. The meters require calibration, but this is straightforward provided the thermal resistance between the thermoelectric module's surface

and that of the plate is small. A method of determining the significance of this resistance has been outlined.

Acknowledgments

The authors are indebted to the Natural Sciences and Engineering Research Council of Canada for providing supporting funds through an operating grant and a major equipment grant. We are also grateful to R. Kaptein and M. Van Reenan for their advice and assistance, and to Jo Brooks for her excellent typing of the manuscript.

The TEMs were manufactured by Cambridge Thermionic Corp., Cambridge, MA, and designated by that company as CAMBION 801-2001-02 (CAMBION is the company's registered trademark).

References

Angrist, S. W., 1976, *Direct Energy Conversion*, 3rd ed., Allyn and Bacon, Chapt. 4.

Goldstein, R. J., and Chiang, H. D., 1985, "Measurements of Temperature and Heat Transfer," in: *Handbook of Heat Transfer Applications*, McGraw-Hill, New York, pp. 12–80 to 12–82.

Hilsenrath, J., Beckett, C. W., Benedict, W. S., Fano, L., Masi, J. F., Nuttal, R. L., Touloukian, Y. S., and Wolley, H. W., 1960, *Tables of Thermodynamic and Transport Properties* (NBS Circular 564 – Tables of Thermal Properties of Gases), Pergamon Press, New York.

Hollands, K. G. T., 1973, "Natural Convection Heat Transfer in Thin-Walled Honeycomb Panels," ASME JOURNAL OF HEAT TRANSFER, Vol. 95, pp. 439–444.

Shewen, E. C., 1986, "A Peltier-Effect Technique for Natural Convection Heat Flux Measurement Applied to the Rectangular Open Cavity," Ph.D. Thesis, Department of Mechanical Engineering, University of Waterloo, Canada.

Journal of Heat Transfer

Technical Notes

This section contains shorter technical papers. These shorter papers will be subjected to the same review process as that for full papers.

On the Nondimensionalization of Constriction Resistance for Semi-infinite Heat Flux Tubes

K. J. Negus,[1] M. M. Yovanovich,[2] and J. V. Beck[3]

Nomenclature

a = radius of circular contact; half-width of square contact
A_c = contact area
A_t = cylinder cross-sectional area
b = radius of circular cylinder; half-width of square cylinder
I_0 = polar second moment of area
I_{RR} = radial second moment of area
$J_0(\cdot)$ = Bessel function of first kind of order zero
$J_1(\cdot)$ = Bessel function of first kind of order one
k = thermal conductivity
q = uniform heat flux on contact
Q = total heat flow rate through contact
r = polar coordinate
R_c = constriction resistance
$\bar{T}_c$ = average temperature across contact
$\bar{T}(z=0)$ = average temperature across top face of cylinder
x, y, z = Cartesian coordinates
γ_n = positive real roots of $J_1(\gamma_n)=0$
δ = characteristic dimension of length
ϵ = relative contact size $(\equiv\sqrt{A_c/A_t})$
ψ = dimensionless thermal constriction resistance parameter $(\equiv k\sqrt{A_c}R_c)$
ψ_∞ = constriction parameter for a contact on a half-space

Subscripts

a, c, e = denote respectively a solution type as approximate, correlated, or exact

Superscripts

c, s = denote respectively a circle or a square geometry

Introduction

The insulated semi-infinite cylinder with heat supplied uniformly through a coaxial contact area as shown in Fig. 1 is an important unit cell in the theory of contact resistance (Cooper et al., 1969). The three contact area/cylinder cross-sectional configurations shown in Fig. 2 are of interest not on-

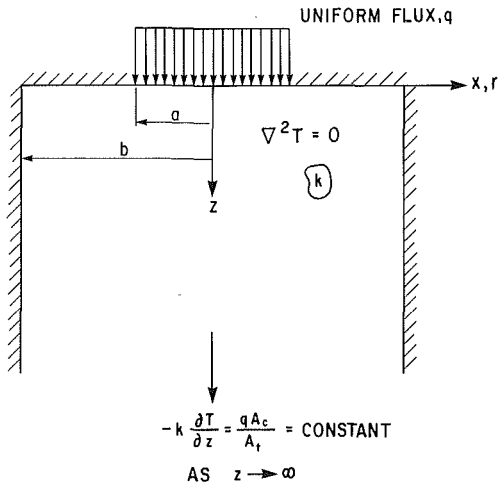

Fig. 1 Uniform heat flux on contact located centrally on a semi-infinite adiabatic cylinder

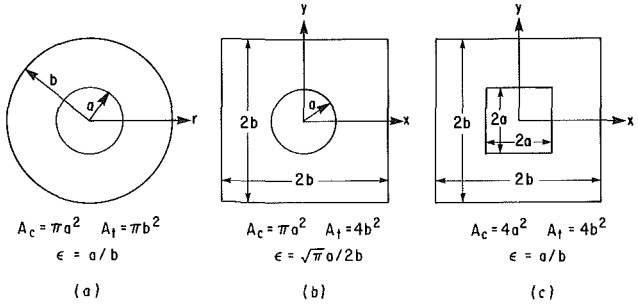

Fig. 2 Contact area/cylinder cross-sectional configurations under consideration

[1]Graduate Research Assistant, Thermal Engineering Group, Department of Mechanical Engineering, University of Waterloo, Waterloo, Ontario N2L 3G1, Canada.
[2]Professor, Thermal Engineering Group, Department of Mechanical Engineering, University of Waterloo, Waterloo, Ontario N2L 3G1, Canada: Fellow ASME.
[3]Professor, Heat Transfer Group, Department of Mechanical Engineering, Michigan State University, East Lansing, MI 48824; Mem. ASME.

Contributed by the Heat Transfer Division for publication in the JOURNAL OF HEAT TRANSFER. Manuscript received by the Heat Transfer Division March 5, 1986. Keywords: Conduction, Modeling and Scaling.

ly in contact resistance but also in electronic component cooling (Antonetti and Yovanovich, 1984) and storage of radioactive wastes (Schankula, 1985). Because of the similarities that will be demonstrated for these three important cases, estimation of the thermal resistance of other configurations is also possible.

In the past, several investigators have examined the problem of the thermal constriction resistance of a circular contact area on an insulated semi-infinite, coaxial circular cylinder as shown by Figs. 1 and 2(*a*). Recently the case shown in Fig. 2(*b*) of a circular contact on a square cylinder has been investigated for a small relative contact size by Beck (1979) and for any contact size by Negus and Yovanovich (1984). By using a new approximate technique developed by Beck (1979) and Negus and Yovanovich (1985), as well as double-infinite series solution to Laplace's equation in Cartesian coordinates (Mikic, 1966), the case of a square contact area on a square cylinder as shown in Fig. 2(*c*) can also be solved.

Previously the nondimensionalization technique employed for the results has varied with different configurations and researchers. However, the similarity of these three configurations in terms of their integrated parameter, the thermal constriction resistance, will only be seen when nondimensionalization is made using a characteristic dimension that best describes these geometries.

Nondimensionalization of Thermal Constriction Resistance

The thermal constriction resistance R_c for a finite contact area on a semi-infinite insulated cylinder is commonly defined as

$$R_c \equiv \frac{\bar{T}_c - \bar{T}(z=0)}{Q} \tag{1}$$

where $\bar{T}_c$ is the average temperature rise over the contact area, $\bar{T}(z=0)$ the average temperature rise of the cross section of the cylinder in the plane of the contact, and Q is the total heat flow rate across the contact area.

If heat is supplied to the cylinder for a sufficiently long time, R_c will reach a steady-state value. Nondimensionalization of R_c can be made by introducing a dimensionless thermal constriction parameter ψ defined as

$$\psi \equiv k\delta R_c \tag{2}$$

where k is the thermal conductivity of the cylinder and δ is any characteristic dimension with the units of length.

In the study of arbitrary single contacts on a half-space (Yovanovich et al., 1983, 1984), it was determined that for both steady-state and transient conditions, use of the square root of the contact area as the characteristic length gave similar results for many different geometries. Furthermore, Chow and Yovanovich (1982) have shown analytically that for single bodies or contacts in infinite or semi-infinite media, the constriction resistance R_c is inversely proportional to the square root of the contact area as a first approximation.

Although the problem considered in this work is not one of a single contact on a half-space, it will be demonstrated that the square root of the contact area is the characteristic dimension if the results for different cases are compared at a dimensionless contact size also based on the square root of the contact area. Thus the constriction parameter becomes

$$\psi \equiv k\sqrt{A_c}R_c \tag{3}$$

where A_c is the area of the contact through which a uniform heat flux is supplied.

For a given geometric configuration the constriction parameter is then a function only of the relative contact size. To compare results of different cases, a dimensionless relative contact size ϵ is defined as the square root of the ratio of contact area to cylinder cross-sectional area, or

$$\epsilon \equiv \sqrt{A_c/A_t} \tag{4}$$

where A_t is the area of the cylinder cross section as shown in Fig. 2.

Constriction Parameters

Case 1: Circle on Circle. For a circular contact area with uniform heat flux on a circular, insulated, semi-infinite, coaxial cylinder the constriction parameter is found analytically to be (Yovanovich, 1976a)

$$\psi_e^{cc} = \frac{16}{\pi\epsilon} \sum_{n=1}^{\infty} \frac{J_1^2(\gamma_n\epsilon)}{\gamma_n^3 J_0^2(\gamma_n)} \tag{5}$$

where the superscript *cc* indicates circle on circle, the subscript *e* indicates an exact solution, $J_0(\cdot)$ and $J_1(\cdot)$ are Bessel functions of the first kind of orders 0 and 1, and γ_n are the positive real roots of $J_1(\gamma_n) = 0$.

Equation (5) is not valid for the limiting case of $\epsilon = 0$ where (Yovanovich, 1976b)

$$\psi_e^{cc}(\epsilon = 0) = 8/3\pi^{3/2} \tag{6}$$

From the work of Roess (1950), an approximate analytical expression for ψ^{cc} can be derived for a small relative contact size ϵ to give

$$\psi_a^{cc} \approx 0.47890 - 0.62446\epsilon + 0.11239\epsilon^3 \tag{7}$$

where the subscript *a* indicates an approximate analytical solution.

Finally, a correlation to four decimal places for $0 \le \epsilon \le 0.9$ has been provided from the accurate optimized image results of Negus and Yovanovich (1984) giving

$$\psi_c^{cc} = 0.47890 - 0.62498\epsilon + 0.11789\epsilon^3 - 0.000071\epsilon^5 + 0.02582\epsilon^7 \tag{8}$$

where the subscript *c* indicates a correlation of results.

Case 2: Circle on Square. For a circular contact with uniform flux on a square insulated semi-infinite cylinder, an exact solution recently derived by Sadhal (1984) gives

$$\psi_e^{cs} = \frac{2}{\pi^2\epsilon}\left\{\sum_{n=1}^{\infty}\frac{J_1^2(2n\sqrt{\pi}\epsilon)}{n^3} + \sum_{m=1}^{\infty}\sum_{n=1}^{\infty}\frac{J_1^2[2\sqrt{\pi}\epsilon(m^2+n^2)^{1/2}]}{(m^2+n^2)^{3/2}}\right\} \tag{9}$$

where $\epsilon \equiv \sqrt{A_c/A_t} = \sqrt{\pi}a/2b$ for the circle on a square.

Although equation (9) is exact, the convergence of the double-infinite summation is extremely slow, especially for small ϵ. At the limiting case of $\epsilon = 0$, a circular contact on a half-space, $\psi_e^{cs}(\epsilon = 0) = 8/3\pi^{3/2}$ as given in equation (6).

For efficient calculation of the constriction parameter for the circle on a square configuration, a correlation for $0 \le \epsilon \le 0.8$ exists from the accurate optimized image results of Negus and Yovanovich (1984). Note that $\epsilon > \sqrt{\pi}/2 \approx 0.886$ is impossible for a circle on a square configuration. The correlation is

$$\psi_c^{cs} = 0.47890 - 0.62055\epsilon + 0.11593\epsilon^3 + 0.006688\epsilon^5 + 0.04015\epsilon^7 \tag{10}$$

Negus and Yovanovich (1985) have developed an approximate expression for an elliptical contact on a nominally rectangular flux tube. For the limiting case of a circle on a square, their expression reduces to

$$\psi_a^{cs} \approx 0.47890 - 0.62075\epsilon + 0.1144\epsilon^3 \tag{11}$$

Although it is derived by the assumption of small contact

Table 1 Dimensionless constriction resistance parameters for each contact/cylinder configuration as a function of relative contact size

ϵ	ψ_c^{cc} (circle/circle)	ψ_c^{cs} (circle/square)	ψ_e^{ss} (square/square)
0	0.4789	0.4789	0.4732
0.1	0.4165	0.4170	0.4112
0.2	0.3548	0.3557	0.3500
0.3	0.2946	0.2959	0.2902
0.4	0.2365	0.2382	0.2327
0.5	0.1813	0.1836	0.1782
0.6	0.1301	0.1333	0.1277
0.7	0.0840	0.0887	0.0823
0.8	0.0447	0.0524	0.0437
0.9	0.0147	–	0.0143

size, equation (11) is found to be accurate to 0.5 percent for $0 \le \epsilon \le 0.5$.

Case 3: Square on Square. For a square contact with uniform flux on a square insulated semi-infinite cylinder, an exact solution for the constriction parameter is (Mikic, 1966)

$$\psi_e^{ss} = \frac{2}{\pi^3 \epsilon}\left\{\sum_{m=1}^{\infty} \frac{\sin^2 m\pi\epsilon}{m^3} + \frac{1}{\pi^2\epsilon^2}\sum_{m=1}^{\infty}\sum_{n=1}^{\infty} \frac{\sin^2(m\pi\epsilon)\sin^2(n\pi\epsilon)}{m^2 n^2 \sqrt{m^2+n^2}}\right\} \tag{12}$$

As with the circle on square situation, the double-infinite summation in equation (12) converges quite slowly, especially for very small values of ϵ. At the limiting value of $\epsilon = 0$, or a square contact on a half-space, the exact value of the constriction parameter is (Carslaw and Jaeger, 1959),

$$\psi_e^{ss}(\epsilon = 0) = \frac{2}{\pi}\left\{\ln[1+\sqrt{2}] + \frac{1}{3}(1-\sqrt{2})\right\} \tag{13}$$

By using the methods of Beck (1979) and Negus and Yovanovich (1985), an approximate analytical expression for the constriction parameter for small ϵ has been developed in this work as

$$\psi_a^{ss} \approx 0.47320 - 0.62075\epsilon + 0.1198\epsilon^3 \tag{14}$$

This approximate expression is accurate to within 0.3 percent for $0 \le \epsilon \le 0.5$.

Comparison of Constriction Parameters

In Table 1 the values of the constriction resistance parameter, $\psi \equiv k\sqrt{A_c R_c}$, for each contact area/cylinder configuration are reported for relative contact sizes in the range $0 \le \epsilon \equiv \sqrt{A_c/A_t} \le 0.9$. For the square/square results the exact solution given by equation (12) was used. The correlations from optimized image results (equations (8) and (10)) were used to generate the values for the circle/circle and circle/square configurations. Comparison with exact solutions has shown these correlations to be accurate to the digits shown in Table 1.

Overall the constriction resistance parameters reported in Table 1 are very similar for each configuration at a given relative contact size, despite the fact that the actual temperature distributions can be quite different. At the limiting case of $\epsilon = 0$, a contact on a half-space, the constriction parameter of a circular contact is 1.2 percent higher than that of a square. For a relative contact size of $\epsilon = 0.5$, the constriction parameter for the circle/circle configuration differs from the circle/square by only 1.3 percent and the square/square by 1.7 percent. The circle/square and square/square results are 2.9 percent apart. Even at $\epsilon = 0.8$ where the actual temperature distributions are extremely different for the three different configurations, the maximum difference in their dimensionless constriction parameters is only 17 percent when the square root of contact area is chosen as the characteristic dimension. At the limiting case of $\epsilon = 1$, one-dimensional heat flow results, and thus the constriction resistance is zero.

For contact areas on a square cylinder, the approximate analysis of Negus and Yovanovich (1985) allows for some interesting generalizations. The approximate expression for ψ gives

$$\psi \approx \psi_\infty - 0.62075\epsilon + 1.4377\left(\frac{2I_0 - 3I_{RR}}{A_c^2}\right)\epsilon^3 \tag{15}$$

where $\psi \equiv k\sqrt{A_c}R_c$, $\epsilon \equiv \sqrt{A_c/A_t}$, ψ_∞ is the constriction parameter for the contact on a half-space, and I_0 and I_{RR} are second moments of area defined by Negus and Yovanovich (1985).

Equation (15) shows that if relative contact size ϵ is very small ($\epsilon << \epsilon^3$), the constriction parameter is given by the half-space result modified linearly by the relative contact size. Physically this linear term in ϵ represents the small perturbation to the temperature fields that is brought about by the placement of the adiabatic walls of the square cylinder in the vicinity of the contact area previously on a half-space. The next term in equation (15) is of order ϵ^3 and is a function of the contact shape. If ϵ is very large ($\epsilon \ge 0.6$) higher order terms in ϵ are required that cannot be easily evaluated by the approximate method of Negus and Yovanovich (1985). Note however that the two-term approximation $\psi \approx \psi_\infty - 0.62075\epsilon$ is accurate for engineering purposes to an ϵ of 0.3 where $\psi(\epsilon = 0.3)/\psi_\infty \approx 0.61$ and the three-term version (equation (15)) is accurate to an ϵ of 0.6 where $\psi(\epsilon = 0.6)/\psi_\infty \approx 0.27$.

Finally, simple observation of Table 1 leads to an engineering approximation for all three cases given as

$$\psi \approx 0.475 - 0.62\epsilon + 0.13\epsilon^3 \tag{16}$$

where the maximum error with respect to Table 1 is less than 2 percent for $0 \le \epsilon \le 0.5$ and 4 percent for $0 \le \epsilon \le 0.7$. The success of this simple formula over a fairly wide range in ϵ further reinforces the assertion made here that the optimum characteristic length dimension for problems of this type is the square root of the contact area.

Conclusions

From the observations made with three configurations of contact areas on insulated semi-infinite cylinders, nondimensionalization of constriction resistance by the square root of the contact area produces strikingly similar results for all configurations at any given relative contact size. Although analytical justification is not presently available as with the contact on a half-space, it seems apparent from the results obtained that the optimum characteristic length that describes conduction problems of this type is the square root of the contact area.

Acknowledgments

The authors acknowledge the financial support of the Natural Sciences and Engineering Research Council of Canada under operating grant No. A7455 for Dr. Yovanovich and from a Postgraduate Scholarship for Mr. Negus. The authors further acknowledge the financial support of the National Science Foundation under grant No. MEA81-21499 for Dr. Beck. The reviewers were very thorough in helping to find typographical errors in the many equations and the authors appreciate their contribution.

References

Antonetti, V. W., and Yovanovich, M. M., 1984, "Thermal Contact Resistance in Microelectronic Equipment," *The International Society for Hybrid Microelectronics*, Vol. 7, No. 3, pp. 44–50.

Beck, J. V., 1979, "Effects of Multiple Sources in the Contact Conductance Theory," ASME JOURNAL OF HEAT TRANSFER, Vol. 101, pp. 132–136.

Carslaw, H. S., and Jaeger, J. C., 1959, *Conduction of Heat in Solids*, Oxford, London.

Chow, Y. L., and Yovanovich, M. M., 1982, "The Shape Factor of the Capacitance of a Conductor," *J. of Applied Physics*, Vol. 53, No. 12, pp. 8470–8475.

Cooper, M., Mikic, B. B., and Yovanovich, M. M., 1969, "Thermal Contact Conductance," *Int. J. of Heat and Mass Transfer*, Vol. 12, pp. 279–300.

Mikic, B. B., 1966, Sc.D. Thesis, Massachusetts Institute of Technology, Cambridge, MA.

Negus, K. J., and Yovanovich, M. M., 1984, "Applications of the Method of Optimized Images to Steady Three-Dimensional Conduction Problems," ASME Paper No. 84-WA/HT-110.

Negus, K. J., Yovanovich, M. M., and DeVaal, J. W., 1985, "Development of Thermal Constriction Resistance for Anisotropic Rough Surfaces by the Method of Infinite Images," presented at the ASME-AIChE 23rd National Heat Transfer Conference, Denver, CO.

Roess, L. C., 1950, "Theory of Spreading Conductance," Beacon Laboratories of Texas Co., Beacon, NY, Appendix A (unpublished report).

Sadhal, S. S., 1984, "Exact Solutions for the Steady and Unsteady Diffusion Problems for a Rectangular Prism," ASME Paper No. 84-HT-83.

Schankula, M. H., 1985, Whiteshell Nuclear Research Establishment, Pinawa, Canada, Personal Communication.

Yovanovich, M. M., 1976a, "General Expressions for Circular Constriction Resistance for Arbitrary Flux Distributions," *Progress in Astronautics and Aeronautics: Radiative Transfer and Thermal Control*, Vol. 49, A. M. Smith, ed., AIAA, New York, pp. 381–396.

Yovanovich, M. M., 1976b, "Thermal Constriction Resistance of Contacts on a Half-Space: Integral Formulation," *AIAA Progress in Astronautics and Aeronautics: Radiative Transfer and Thermal Contact*, Vol. 49, A. M. Smith, ed., AIAA, New York, pp. 397–418.

Yovanovich, M. M., Thompson, J. C., and Negus, K. J., 1983, "Thermal Resistance of Arbitrarily Shaped Contacts," presented at the Third International Conference on Numerical Methods in Thermal Problems, Seattle, WA.

Yovanovich, M. M., Negus, K. J., and Thompson, J. C., 1984, "Transient Temperature Rise of Arbitrary Contacts With Uniform Flux by Surface Element Methods," AIAA Paper No. 84-0397.

Similarity Solution for Non-Darcy Free Convection From a Nonisothermal Curved Surface in a Fluid-Saturated Porous Medium

A. Nakayama,[1] H. Koyama,[1] and F. Kuwahara[1]

Nomenclature

- c = empirical constant associated with porous inertia
- f = dimensionless stream function
- g = acceleration due to gravity
- Gr = modified Grashof number, see equation (12*a*)
- K = permeability
- m = exponent associated with body shape
- n = exponent associated with wall temperature
- Nu_x = local Nusselt number
- r = function representing body shape
- Ra_x = local Rayleigh number, see equation (8*b*)
- T = temperature
- u, v = Darcian velocity components
- x, y = boundary layer coordinates
- z = vertical distance measured from the lower stagnation point
- α = equivalent thermal diffusivity
- β = coefficient of thermal expansion
- η = similarity variable, see equation (7*c*)
- θ = dimensionless temperature
- ν = kinematic viscosity
- ψ = stream function

Subscripts

- e = boundary layer edge
- r = reference
- w = wall

Introduction

Considerable attention has been directed to heat and fluid flow within fluid-saturated porous media because of its importance in geophysical and engineering applications such as geothermal energy conversion, thermal insulation of buildings, and packed-bed reactors. (Cheng, 1978). In most previous studies, either on free (e.g., Cheng and Minkowycz, 1977; Merkin, 1979; Nakayama and Koyama, 1987) or combined (e.g., Cheng, 1977; Minkowycz et al., 1985; Nakayama and Koyama, 1987) convection, boundary layer treatments based on Darcy's law were employed. It is, however, well known that the non-Darcy flow situation prevails when the Reynolds number based on the pore diameter and characteristic velocity becomes large (Forchheimer, 1901; Bear, 1972). Fand et al. (1986) experimentally showed deviations from the Darcy law. Forchheimer (1901) proposed a velocity square term in addition to the Darcy term to account for the inertia effects on the pressure drop, as the fluid makes its way through the porous media. This pioneering work was followed by many proposals for mathematically describing non-Darcy flows (e.g., Ergun, 1952; Ward, 1969).

An attempt to obtain a similarity solution for non-Darcian free convective flow over a vertical flat plate was first made by Plumb and Huenefeld (1981) using the model proposed by Ergun (1952). The same model was employed by Vasantha et al. (1986) for a vertical frustum of a cone and by Lai and Kulacki (1981) for a horizontal flat surface to investigate combined effects of the Darcy term and the inertia term. The limiting condition where the Darcy term is negligible, namely Forchheimer flow, was treated by Bejan and Poulikakos (1984) and Ingham (1986). So far, only a limited number of similarity solutions have been reported for simple flow configurations.

In this study, we shall investigate non-Darcy free convective flows using the Ergun model. It will be shown that there exists a certain family of body shape geometries and corresponding wall temperature distributions, which permit similarity solutions. The effects of inertia and geometric shape on the velocity and temperature fields are investigated and the corresponding heat transfer characteristics are discussed in detail.

Governing Equations and Transformation

Figure 1 depicts the physical model and its boundary layer coordinates (x, y). The coordinate z is the vertical distance measured from the lower stagnation point. The body under consideration is two dimensional and its geometry is described by r as a function of x (or z). The body surface may be nonisothermal, and its temperature $T_w(x)$ exceeds the ambient temperature T_e everywhere. Thus, there is an upward convective fluid movement as a result of buoyancy force.

The governing equations for non-Darcy free convective flow, namely, the continuity equation, the Forchheimer equation with the Boussinesq approximation, and the energy equation can be written by exploiting the usual boundary layer approximations as

[1]Department of Energy and Mechanical Engineering, Shizuoka University, Hamamatsu, 432 Japan.

Contributed by the Heat Transfer Division for publication in the JOURNAL OF HEAT TRANSFER. Manuscript received by the Heat Transfer Division January 29, 1988. Keywords: Geophysical Heat Transfer, Natural Convection, Porous Media.

Beck, J. V., 1979, "Effects of Multiple Sources in the Contact Conductance Theory," ASME JOURNAL OF HEAT TRANSFER, Vol. 101, pp. 132–136.

Carslaw, H. S., and Jaeger, J. C., 1959, *Conduction of Heat in Solids*, Oxford, London.

Chow, Y. L., and Yovanovich, M. M., 1982, "The Shape Factor of the Capacitance of a Conductor," *J. of Applied Physics*, Vol. 53, No. 12, pp. 8470–8475.

Cooper, M., Mikic, B. B., and Yovanovich, M. M., 1969, "Thermal Contact Conductance," *Int. J. of Heat and Mass Transfer*, Vol. 12, pp. 279–300.

Mikic, B. B., 1966, Sc.D. Thesis, Massachusetts Institute of Technology, Cambridge, MA.

Negus, K. J., and Yovanovich, M. M., 1984, "Applications of the Method of Optimized Images to Steady Three-Dimensional Conduction Problems," ASME Paper No. 84-WA/HT-110.

Negus, K. J., Yovanovich, M. M., and DeVaal, J. W., 1985, "Development of Thermal Constriction Resistance for Anisotropic Rough Surfaces by the Method of Infinite Images," presented at the ASME-AIChE 23rd National Heat Transfer Conference, Denver, CO.

Roess, L. C., 1950, "Theory of Spreading Conductance," Beacon Laboratories of Texas Co., Beacon, NY, Appendix A (unpublished report).

Sadhal, S. S., 1984, "Exact Solutions for the Steady and Unsteady Diffusion Problems for a Rectangular Prism," ASME Paper No. 84-HT-83.

Schankula, M. H., 1985, Whiteshell Nuclear Research Establishment, Pinawa, Canada, Personal Communication.

Yovanovich, M. M., 1976a, "General Expressions for Circular Constriction Resistance for Arbitrary Flux Distributions," *Progress in Astronautics and Aeronautics: Radiative Transfer and Thermal Control*, Vol. 49, A. M. Smith, ed., AIAA, New York, pp. 381–396.

Yovanovich, M. M., 1976b, "Thermal Constriction Resistance of Contacts on a Half-Space: Integral Formulation," *AIAA Progress in Astronautics and Aeronautics: Radiative Transfer and Thermal Contact*, Vol. 49, A. M. Smith, ed., AIAA, New York, pp. 397–418.

Yovanovich, M. M., Thompson, J. C., and Negus, K. J., 1983, "Thermal Resistance of Arbitrarily Shaped Contacts," presented at the Third International Conference on Numerical Methods in Thermal Problems, Seattle, WA.

Yovanovich, M. M., Negus, K. J., and Thompson, J. C., 1984, "Transient Temperature Rise of Arbitrary Contacts With Uniform Flux by Surface Element Methods," AIAA Paper No. 84-0397.

Similarity Solution for Non-Darcy Free Convection From a Nonisothermal Curved Surface in a Fluid-Saturated Porous Medium

A. Nakayama,[1] H. Koyama,[1] and F. Kuwahara[1]

Nomenclature

- c = empirical constant associated with porous inertia
- f = dimensionless stream function
- g = acceleration due to gravity
- Gr = modified Grashof number, see equation (12*a*)
- K = permeability
- m = exponent associated with body shape
- n = exponent associated with wall temperature
- Nu_x = local Nusselt number
- r = function representing body shape
- Ra_x = local Rayleigh number, see equation (8*b*)
- T = temperature
- u, v = Darcian velocity components
- x, y = boundary layer coordinates
- z = vertical distance measured from the lower stagnation point
- α = equivalent thermal diffusivity
- β = coefficient of thermal expansion
- η = similarity variable, see equation (7*c*)
- θ = dimensionless temperature
- ν = kinematic viscosity
- ψ = stream function

Subscripts

- e = boundary layer edge
- r = reference
- w = wall

Introduction

Considerable attention has been directed to heat and fluid flow within fluid-saturated porous media because of its importance in geophysical and engineering applications such as geothermal energy conversion, thermal insulation of buildings, and packed-bed reactors. (Cheng, 1978). In most previous studies, either on free (e.g., Cheng and Minkowycz, 1977; Merkin, 1979; Nakayama and Koyama, 1987) or combined (e.g., Cheng, 1977; Minkowycz et al., 1985; Nakayama and Koyama, 1987) convection, boundary layer treatments based on Darcy's law were employed. It is, however, well known that the non-Darcy flow situation prevails when the Reynolds number based on the pore diameter and characteristic velocity becomes large (Forchheimer, 1901; Bear, 1972). Fand et al. (1986) experimentally showed deviations from the Darcy law. Forchheimer (1901) proposed a velocity square term in addition to the Darcy term to account for the inertia effects on the pressure drop, as the fluid makes its way through the porous media. This pioneering work was followed by many proposals for mathematically describing non-Darcy flows (e.g., Ergun, 1952; Ward, 1969).

An attempt to obtain a similarity solution for non-Darcian free convective flow over a vertical flat plate was first made by Plumb and Huenefeld (1981) using the model proposed by Ergun (1952). The same model was employed by Vasantha et al. (1986) for a vertical frustum of a cone and by Lai and Kulacki (1981) for a horizontal flat surface to investigate combined effects of the Darcy term and the inertia term. The limiting condition where the Darcy term is negligible, namely Forchheimer flow, was treated by Bejan and Poulikakos (1984) and Ingham (1986). So far, only a limited number of similarity solutions have been reported for simple flow configurations.

In this study, we shall investigate non-Darcy free convective flows using the Ergun model. It will be shown that there exists a certain family of body shape geometries and corresponding wall temperature distributions, which permit similarity solutions. The effects of inertia and geometric shape on the velocity and temperature fields are investigated and the corresponding heat transfer characteristics are discussed in detail.

Governing Equations and Transformation

Figure 1 depicts the physical model and its boundary layer coordinates (x, y). The coordinate z is the vertical distance measured from the lower stagnation point. The body under consideration is two dimensional and its geometry is described by r as a function of x (or z). The body surface may be nonisothermal, and its temperature $T_w(x)$ exceeds the ambient temperature T_e everywhere. Thus, there is an upward convective fluid movement as a result of buoyancy force.

The governing equations for non-Darcy free convective flow, namely, the continuity equation, the Forchheimer equation with the Boussinesq approximation, and the energy equation can be written by exploiting the usual boundary layer approximations as

[1]Department of Energy and Mechanical Engineering, Shizuoka University, Hamamatsu, 432 Japan.

Contributed by the Heat Transfer Division for publication in the JOURNAL OF HEAT TRANSFER. Manuscript received by the Heat Transfer Division January 29, 1988. Keywords: Geophysical Heat Transfer, Natural Convection, Porous Media.

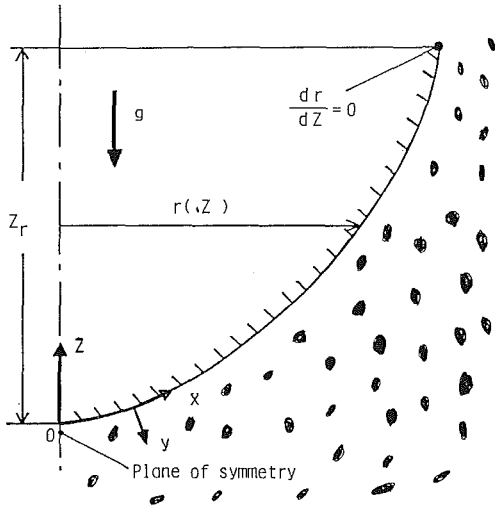

Fig. 1 Physical model and coordinate system

$$\frac{\partial u}{\partial x}+\frac{\partial v}{\partial y}=0 \tag{1}$$

$$u+\frac{c\sqrt{K}}{\nu}u^2=\frac{\beta K}{\nu}(T-T_e)g_x \tag{2}$$

$$u\frac{\partial T}{\partial x}+v\frac{\partial T}{\partial y}=\alpha\frac{\partial^2 T}{\partial y^2} \tag{3}$$

where

$$g_x=g\left(1-\left(\frac{dr}{dx}\right)^2\right)^{1/2} \tag{4}$$

and the boundary conditions are

$$y=0:\quad v=0,\quad T=T_w(x) \tag{5a, b}$$

$$y\to\infty:\quad u=0,\quad T=T_e \tag{5c, d}$$

The continuity equation (1) is satisfied by introducing the stream function ψ such that

$$u=\frac{\partial\psi}{\partial y} \tag{6a}$$

$$v=-\frac{\partial\psi}{\partial x} \tag{6b}$$

Introducing the following transformations

$$\psi=\alpha\mathrm{Ra}_x^{1/2}f(x,\eta) \tag{7a}$$

$$T-T_e=\Delta T_w\theta(x,\eta) \tag{7b}$$

$$\eta=\frac{y}{x}\mathrm{Ra}_x^{1/2} \tag{7c}$$

where

$$\Delta T_w=T_w-T_e \tag{8a}$$

and

$$\mathrm{Ra}_x=\frac{K\beta\Delta T_w g_x x}{\alpha\nu} \tag{8b}$$

into equations (2)–(6) yields

$$f'+\mathrm{Gr}(f')^2=\theta \tag{9a}$$

and

$$\theta''+\frac{1}{2}(1+m+n)f\theta'-nf'\theta=x\left(f'\frac{\partial\theta}{\partial x}-\theta'\frac{\partial f}{\partial x}\right) \tag{9b}$$

The boundary conditions are given by

$$\eta=0:\quad f=0,\quad \theta=1 \tag{10a, b}$$

$$\eta\to\infty:\quad f'=0,\quad \theta=0 \tag{10c, d}$$

where the primes in the above expressions denote differentiation with respect to η. The Darcian velocities are

$$u=\frac{\alpha}{x}\mathrm{Ra}_x f' \tag{11a}$$

and

$$v=-\frac{\alpha}{x}\mathrm{Ra}_x^{1/2}\left[\frac{1}{2}(1+m+n)f+x\frac{\partial f}{\partial x}+\frac{1}{2}(m+n-1)\eta f'\right] \tag{11b}$$

where

$$\mathrm{Gr}=CK^{3/2}\beta\Delta T_w g_x/\nu^2 \tag{12a}$$

$$m(x)=\frac{d\ln g_x}{d\ln x} \tag{12b}$$

and

$$n(x)=\frac{d\ln\Delta T_w}{d\ln x} \tag{12c}$$

Eliminating θ from equations (9a) and (9b) yields

$$f'''+\frac{1+m+n}{2}ff''-n(f')^2+\mathrm{Gr}\,[2f'f'''+2(f'')^2+(1+m+n)ff'f''-(m+2n)(f')^3]=x(1+2\mathrm{Gr}f')\left(f'\frac{\partial f'}{\partial x}-f''\frac{\partial f}{\partial x}\right) \tag{13}$$

For Darcy flows (i.e., $\mathrm{Gr}=0$), equation (13) reduces to

$$f'''+\frac{1+m+n}{2}ff''-n(f')^2=x\left(f'\frac{\partial f'}{\partial x}-f''\frac{\partial f}{\partial x}\right) \tag{14}$$

Thus, similarity solutions are possible when both m and n are constants, namely,

$$g_x\propto x^m \tag{15a}$$

$$\Delta T_w\propto x^n \tag{15b}$$

The preceding relation represents a certain class of possible similarity solutions for the Darcy flows. A more general similarity transformation has been reported by the authors (1987b).

For the non-Darcy flows considered here, $\mathrm{Gr}(\neq 0)$ must also be a constant. Hence, $m=-n$, and

$$g_x\propto x^m \tag{16a}$$

$$\Delta T_w\propto x^{-m} \tag{16b}$$

Under these conditions, the partial differential equation (13) reduces to a readily integrated ordinary differential equation, namely,

$$f'''+\frac{1}{2}ff''+m(f')^2+\mathrm{Gr}\,[2f'f'''+2(f'')^2+ff'f''+m(f')^3]=0 \tag{17}$$

The boundary conditions given by equations (10) become

$$\eta=0:\quad f=0,\quad f'=\frac{(1+4\mathrm{Gr})^{1/2}-1}{2\mathrm{Gr}} \tag{18a, b}$$

$$\eta\to\infty:\quad f'=0 \tag{18c}$$

Once the f distribution is found for a given set of values of Gr and m, the local Nusselt number can be evaluated from

$$\mathrm{Nu}_x\equiv-\frac{x}{\Delta T_w}\frac{\partial T}{\partial y}\bigg|_{y=0}=-\theta'(0)\mathrm{Ra}_x^{1/2}=-f''(0)(1+4\mathrm{Gr})^{1/2}\mathrm{Ra}_x^{1/2} \tag{19}$$

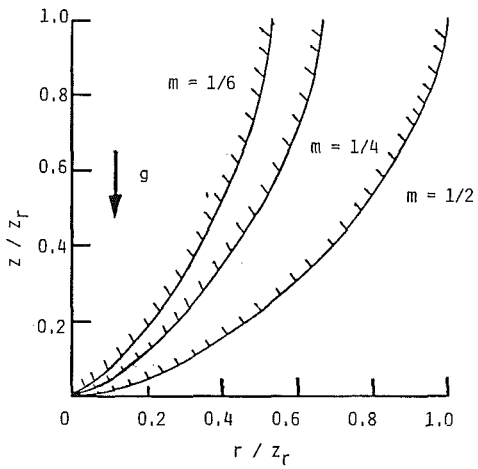

Fig. 2 Geometries that permit similarity solutions

Geometries for Similarity Solutions

The condition given by equations (16*a*) and (16*b*) must be satisfied for a similarity (exact) solution to exist. We shall seek the geometric shapes that permit similarity solutions. The geometric relations described by equations (16*a*) and (4) can be rewritten as

$$g_x/g = \frac{dz}{dx} = (x/x_r)^m \tag{20a}$$

and

$$r = \int_0^x (1-(g_x/g)^2)^{1/2} dx \tag{20b}$$

Equation (20*a*) indicates that the exponent m must be nonnegative for g_x to be finite at $x=0$. The equation can be integrated to give

$$z/z_r = (x/x_r)^{1+m} \tag{21a}$$

and

$$z_r = x_r/(1+m) \tag{21b}$$

where

$$\left.\frac{dr}{dz}\right|_{z=z_r} = 0 \quad \text{(see Fig. 1)} \tag{22a}$$

or equivalently,

$$\left.\frac{dr}{dx}\right|_{x=x_r} = 1 \tag{22b}$$

With the aid of equations (21*a*) and (21*b*), equation (20*b*) may be integrated to yield

$$r = \frac{1+m}{m} z_r \sum_0^\infty \binom{\frac{1}{2m}-1}{i} \frac{(-1)i}{2i+3} \left[1 - \left(1-(z/z_r)^{\frac{2m}{1+m}}\right)^{\frac{2i+3}{2}}\right] \tag{23}$$

The foregoing expression is valid for $0<m\le 1/2$. For example,

$$m=1/2 \quad (\Delta T_w \propto z^{-1/3}): \quad r/z_r = 1-(1-(z/z_r)^{2/3})^{3/2} \tag{24a}$$

$$m=1/4 \quad (\Delta T_w \propto z^{-1/5}): \quad r/z_r = \frac{2}{3} - \frac{5}{3}\left(1 - \left(\frac{z}{z_r}\right)^{2/5}\right)^{3/2} + \left(1-, \left(\frac{z}{z_r}\right)^{2/5}\right)^{5/2} \tag{24b}$$

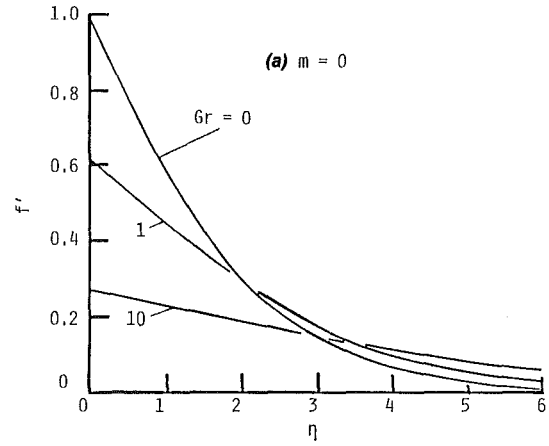

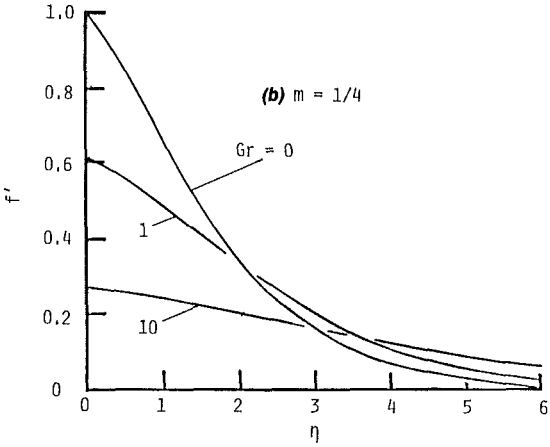

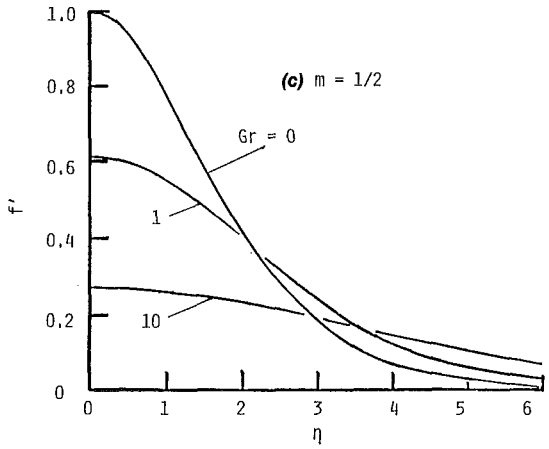

Fig. 3 Velocity profiles: (a) $m=0$, (b) $m=1/4$, (c) $m=1/2$

$$m=1/6 \quad (\Delta T_w \propto z^{-1/7}): \quad r/z_r = \frac{8}{15} - \frac{7}{3}\left(1 - \left(\frac{z}{z_r}\right)^{2/7}\right)^{3/2} + \frac{14}{5}\left(1-\left(\frac{z}{z_r}\right)^{2/7}\right)^{5/2} - \left(1-\left(\frac{z}{z_r}\right)^{2/7}\right)^{7/2} \tag{24c}$$

The geometries given by equations (24) are shown in Fig. 2. As m decreases the body becomes flatter, and transforms itself into a vertical flat plate as $m\to 0$.

Results and Discussion

Figures 3(*a*), 3(*b*), and 3(*c*) show the dimensionless velocity

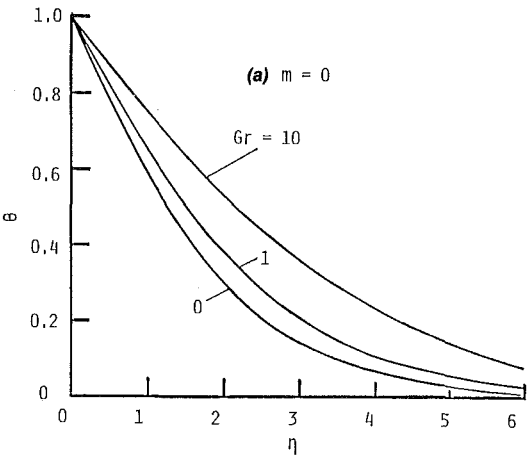

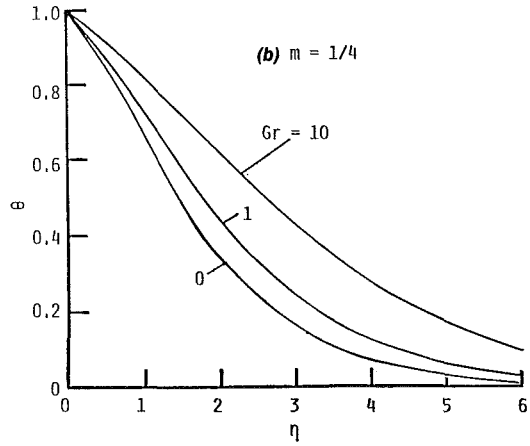

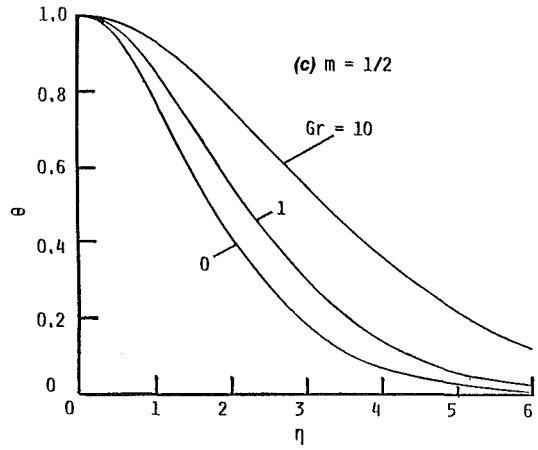

Fig. 4 Temperature profiles: (a) $m=0$, (b) $m=1/4$, (c) $m=1/2$

profiles for $m=0$, 1/4, and 1/2, respectively. Three different profiles obtained at $\mathrm{Gr}=0$ (Darcy flow), 1, and 10, are presented for each geometric configuration. The temperature profiles are also plotted in Figs. 4(*a*) to 4(*c*) in a similar fashion. The results for a vertical flat plate (Figs. 3(*a*) and 4(*a*)) are found to be in good agreement with those reported by Plumb and Huenefeld (1981) and Vasantha et al. (1986). As equation (18*b*) indicates, the porous media inertial resistance tends to decrease the velocity and create a more uniform velocity field. As a result, the boundary layer thickens as Gr grows. It is also interesting to note that the dimensionless velocity and temperature profiles overlap each other in the

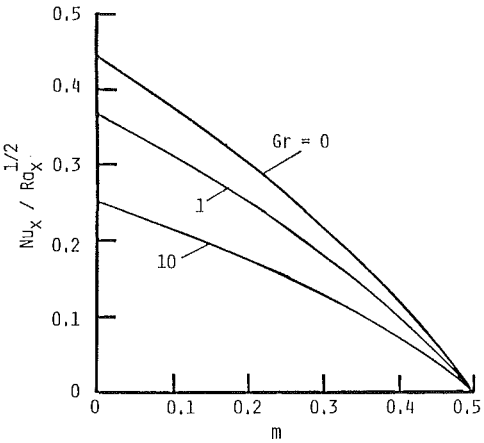

Fig. 5 Heat transfer results

region sufficiently away from the wall, since $\theta=f'+\mathrm{Gr}(f')^2\cong f'$ for small f'.

The parameter m associated with the body shape and its wall temperature variation has a pronounced effect on the gradients of the velocity and temperature profiles at the wall. As m increases from 0 to 1/2, the gradient at the wall, namely, $-\theta'(0)=-(1+4\ \mathrm{Gr})^{1/2}f''(0)$ becomes smaller, vanishes at $m=1/2$, and becomes negative (i.e., heat transfer from the fluid to the heated wall) for $m>1/2$. Since both $\theta(\eta)$ and $f'(\eta)$ must be nonnegative under the boundary layer treatment, only $0\leqq m\leqq 1/2$ (i.e., heat transfer from the heated wall to the fluid) is of physical interest. Let us note that the porous medium near the wall is heated by conduction from the hot wall as well as by convection of the hot fluid. In fact, streamwise convection can be quite significant if the wall temperature decreases rapidly in the streamwise direction as is the case for large m. Such streamwise convection tends to create a more uniform temperature profile yielding a negative second derivative at the wall. (As m exceeds 1/2, the streamwise convection dominates the conduction from the wall. Thus, heat transfer takes place from the hot fluid to the wall.)

Heat transfer results for $\mathrm{Gr}=0$, 1, and 10 are plotted in Fig. 5, where the heat transfer function $\mathrm{Nu}_x/\mathrm{Ra}_x^{1/2}$ is used as the ordinate variable, and the abscissa variable is chosen to be the exponent m associated with the wall geometry. As already seen from the temperature profiles in Figs. 4, additional flow resistance due to inertia thickens the boundary layer. Thus, the heat transfer rate for given Ra_x decreases with increasing Gr. All values of the heat transfer grouping $\mathrm{Nu}_x/\mathrm{Ra}_x^{1/2}$ monotonically decrease as the exponent m increases from 0 to 1/2, since the wall temperature gradient $-\theta'(0)$ has its maximum at $m=0$ and vanishes at $m=1/2$.

References

Bear, J., 1972, *Dynamics of Fluids in Porous Media*, Elsevier, New York.

Bejan, A., and Poulikakos, D., 1984, "The Non-Darcy Regime for Vertical Boundary Layer Natural Convection in a Porous Medium," *Int. J. Heat Mass Transfer*, Vol. 27, pp. 717–722.

Cheng, P., 1977, "Mixed Convection About a Horizontal Cylinder and a Sphere in a Fluid-Saturated Porous Medium," *Int. J. Heat Mass Transfer*, Vol. 25, pp. 1245–1247.

Cheng, P., 1978, "Heat Transfer in Geothermal Systems," *Advances in Heat Transfer*, Vol. 14, pp. 1–105.

Cheng, P., and Minkowycz, W. J., 1977, "Free Convection About a Vertical Flat Plate Embedded in a Saturated Porous Medium With Application to Heat Transfer From a Dike," *J. Geophysics Research*, Vol. 82, pp. 2040–2044.

Ergun, S., 1952, "Fluid Flow Through Packed Columns," *Chem. Engng. Prog.*, Vol. 48, pp. 89–94.

Forchheimer, P., 1901, "Wasserbewegung durch Boden," *Forschtlft Ver. D. Ing.*, Vol. 45, pp. 1782–1788.

Fand, R. M., Steinberger, T. E., and Cheng, P., 1986, "Natural Convection Heat Transfer From a Horizontal Cylinder Embedded in a Porous Medium," *Int. J. Heat Mass Transfer*, Vol. 29, pp. 119–133.

Ingham, D. B., 1986, "The Non-Darcy Free Convection Boundary Layer on Axisymmetric and Two-Dimensional Bodies of Arbitrary Shape," *Int. J. Heat Mass Transfer*, Vol. 29, pp. 1759-1763.

Lai, F. C., and Kulacki, F. A., 1987, "Non-Darcy Convection From Horizontal Impermeable Surfaces in Saturated Porous Media," *Int. J. Heat Mass Transfer*, Vol. 30, pp. 2189-2192.

Merkin, J. H., 1979, "Free Convection Boundary Layers on Axisymmetric and Two-Dimensional Bodies of Arbitrary Shape in a Saturated Porous Medium," *Int. J. Heat Mass Transfer*, Vol. 22, pp. 1461-1462.

Minkowycz, W. J., Cheng, P., and Chang, C. H., 1985, "Mixed Convection About a Non-isothermal Cylinder and Sphere in a Porous Medium," *Numerical Heat Transfer*, Vol. 8, pp. 349-359.

Nakayama, A., and Koyama, H., 1987a, "A General Similarity Transformation for Combined Free and Forced Convection Flows Within a Fluid Saturated Porous Medium," ASME JOURNAL OF HEAT TRANSFER, Vol. 109, pp. 1041-1045.

Nakayama, A., and Koyama, H., 1987b, "Free Convective Heat Transfer Over a Nonisothermal Body of Arbitrary Shape Embedded in a Fluid Saturated Porous Medium," ASME JOURNAL OF HEAT TRANSFER, Vol. 109, pp. 125-130.

Plumb, O. A., and Huenefeld, J. C., 1981, "Non-Darcy Natural Convection From Heated Surfaces in Saturated Porous Media," *Int. J. Heat Mass Transfer*, Vol. 24, pp. 765-768.

Vasantha, R., Pop, I., and Nath, G., 1986, "Non-Darcy Natural Convection Over a Slender Vertical Frustum of a Cone in a Saturated Porous Medium," *Int. J. Heat Mass Transfer*, Vol. 29, pp. 153-156.

Ward, J. C., 1969, "Turbulent Flow in Porous Medium," *Proc. Am. Soc. Civ. Engng.*, No. HY5, Vol. 90, pp. 1-12.

Geometric Mean Beam Lengths for the Space Between Two Coaxial Cylinders

K. M. Andersen[1] and S. Hadvig[1]

Introduction

Mean beam lengths are often a good tool in radiative heat transfer concerning gas bodies (Hottel and Sarofim, 1967). Geometric mean beam lengths are only valid for the optically thin limit. Analytical expressions are given for an infinite long gas body between two circular, coaxial cylinders.

Presentation of Mathematical Expressions

We first consider the general situation. Let F be some surface in space, P_o some point, and $\bar{e}$ some unit vector. It is supposed that F corresponds with a part E of the unit sphere K with center at P_o, when projected onto K from the center. The *geometric mean beam length* from P_o to F with respect to the direction given by $\bar{e}$ is defined as the following surface integral (see Fig. 1):

$$L_o = \frac{1}{\pi} \int_E |\overline{P_oP} \cdot \bar{e}| \, d\omega \tag{1}$$

Next we consider the situation in question, namely two infinite coaxial cylinders C_i and C_e with radii r and R, respectively, $r < R$. The point P_o lies on one of the cylinders, the vector $\bar{e}$ is normal to the cylinder in the point P_o and directed toward the other cylinder, and the surface F is that part of the cylinders that is "visible" from P_o (see Figs. 2, 3, and 4).

If P_o lies on C_e (case I), the surface F consists of two connected parts, namely a part A of C_i and a part B of C_e. If P_o lies on C_i (case II), the surface F is a part of C_e.

In order to calculate L_o in the two cases, a coordinate system XYZ is placed with starting point at P_o, with the x axis on the generator through P_o and the z axis in the direction given by $\bar{e}$.

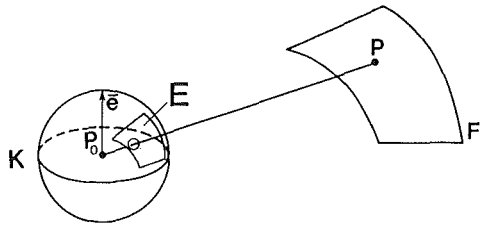

Fig. 1 Definitions

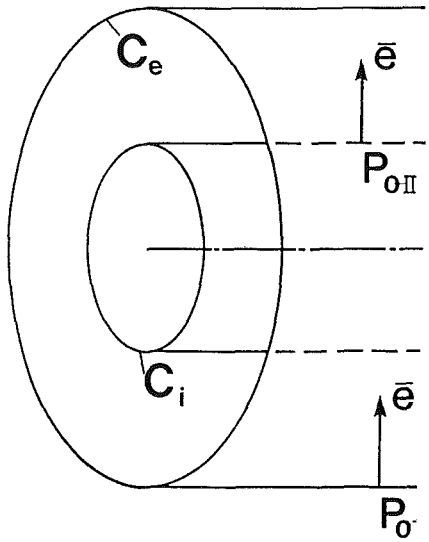

Fig. 2 Positions in question

Case I. Choosing the angles β and ψ as shown in Fig. 3, $0 \le \beta \le \pi$ and $0 \le \psi \le 2\pi$, the two contributions to L_o from parts A and B can be expressed, respectively, as follows:

$$L_o(A) = \frac{4}{\pi}(R^2 - r^2) \int_0^{\frac{\pi}{2}} \left[\int_0^{\frac{\pi}{2} - f(\psi)} \sin\beta \left[R + (r^2 - (R^2 - r^2)\tan^2\beta \sin^2\psi)^{1/2} \right]^{-1} d\beta \right] d\psi \tag{2}$$

and

$$L_o(B) = \frac{8}{\pi} R \int_o^{\frac{\pi}{2}} \left[\int_{\frac{\pi}{2} - f(\psi)}^{\frac{\pi}{2}} \sin\beta \left[1 + \tan^2\beta \sin^2\psi \right]^{-1} d\beta \right] d\psi \tag{3}$$

where $f(\psi)$ is the function given by

$$f(\psi) = \arctan\left[\frac{1}{r} (R^2 - r^2)^{1/2} \sin\psi \right]$$

Case II. Here E is a hemisphere with the equator in the XY plane. Choosing polar coordinates ρ and θ, where θ is measured from the x axis, in this plane, L_o can be expressed as follows:

$$L_o = \frac{4}{\pi}(R^2 - r^2) \int_o^{\frac{\pi}{2}} \left[\int_o^1 \rho \left[r(1-\rho^2)^{1/2} + (R^2(1 - \rho^2\cos^2\theta) - r^2\rho^2\sin^2\theta)^{1/2} \right]^{-1} d\rho \right] d\theta \tag{4}$$

The reductions of the surface integral, equation (1), to the double integrals, equations (2), (3), and (4), are of a purely geometric nature. It turns out to be possible to evaluate these three double integrals in terms of elementary functions. The calculations—based on successive substitutions—are somewhat tedious. The results are as follows:

[1]Associate Professor, The Mathematical Institute and The Laboratory of Heating and Air Conditioning, The Technical University of Denmark, Lyngby, Denmark.

Contributed by the Heat Transfer Division for publication in the JOURNAL OF HEAT TRANSFER. Manuscript received by the Heat Transfer Division January 5, 1988. Keywords: Furnaces and Combustors, Radiation, Radiation Interactions.

Ingham, D. B., 1986, "The Non-Darcy Free Convection Boundary Layer on Axisymmetric and Two-Dimensional Bodies of Arbitrary Shape," *Int. J. Heat Mass Transfer*, Vol. 29, pp. 1759-1763.

Lai, F. C., and Kulacki, F. A., 1987, "Non-Darcy Convection From Horizontal Impermeable Surfaces in Saturated Porous Media," *Int. J. Heat Mass Transfer*, Vol. 30, pp. 2189-2192.

Merkin, J. H., 1979, "Free Convection Boundary Layers on Axisymmetric and Two-Dimensional Bodies of Arbitrary Shape in a Saturated Porous Medium," *Int. J. Heat Mass Transfer*, Vol. 22, pp. 1461-1462.

Minkowycz, W. J., Cheng, P., and Chang, C. H., 1985, "Mixed Convection About a Non-isothermal Cylinder and Sphere in a Porous Medium," *Numerical Heat Transfer*, Vol. 8, pp. 349-359.

Nakayama, A., and Koyama, H., 1987a, "A General Similarity Transformation for Combined Free and Forced Convection Flows Within a Fluid Saturated Porous Medium," ASME JOURNAL OF HEAT TRANSFER, Vol. 109, pp. 1041-1045.

Nakayama, A., and Koyama, H., 1987b, "Free Convective Heat Transfer Over a Nonisothermal Body of Arbitrary Shape Embedded in a Fluid Saturated Porous Medium," ASME JOURNAL OF HEAT TRANSFER, Vol. 109, pp. 125-130.

Plumb, O. A., and Huenefeld, J. C., 1981, "Non-Darcy Natural Convection From Heated Surfaces in Saturated Porous Media," *Int. J. Heat Mass Transfer*, Vol. 24, pp. 765-768.

Vasantha, R., Pop, I., and Nath, G., 1986, "Non-Darcy Natural Convection Over a Slender Vertical Frustum of a Cone in a Saturated Porous Medium," *Int. J. Heat Mass Transfer*, Vol. 29, pp. 153-156.

Ward, J. C., 1969, "Turbulent Flow in Porous Medium," *Proc. Am. Soc. Civ. Engng.*, No. HY5, Vol. 90, pp. 1-12.

Geometric Mean Beam Lengths for the Space Between Two Coaxial Cylinders

K. M. Andersen[1] and S. Hadvig[1]

Introduction

Mean beam lengths are often a good tool in radiative heat transfer concerning gas bodies (Hottel and Sarofim, 1967). Geometric mean beam lengths are only valid for the optically thin limit. Analytical expressions are given for an infinite long gas body between two circular, coaxial cylinders.

Presentation of Mathematical Expressions

We first consider the general situation. Let F be some surface in space, P_o some point, and $\bar{e}$ some unit vector. It is supposed that F corresponds with a part E of the unit sphere K with center at P_o, when projected onto K from the center. The *geometric mean beam length* from P_o to F with respect to the direction given by $\bar{e}$ is defined as the following surface integral (see Fig. 1):

$$L_o = \frac{1}{\pi} \int_E |\overline{P_oP} \cdot \bar{e}| \, d\omega \tag{1}$$

Next we consider the situation in question, namely two infinite coaxial cylinders C_i and C_e with radii r and R, respectively, $r < R$. The point P_o lies on one of the cylinders, the vector $\bar{e}$ is normal to the cylinder in the point P_o and directed toward the other cylinder, and the surface F is that part of the cylinders that is "visible" from P_o (see Figs. 2, 3, and 4).

If P_o lies on C_e (case I), the surface F consists of two connected parts, namely a part A of C_i and a part B of C_e. If P_o lies on C_i (case II), the surface F is a part of C_e.

In order to calculate L_o in the two cases, a coordinate system XYZ is placed with starting point at P_o, with the x axis on the generator through P_o and the z axis in the direction given by $\bar{e}$.

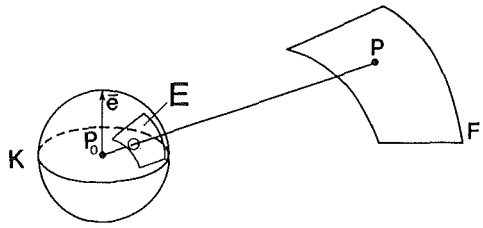

Fig. 1 Definitions

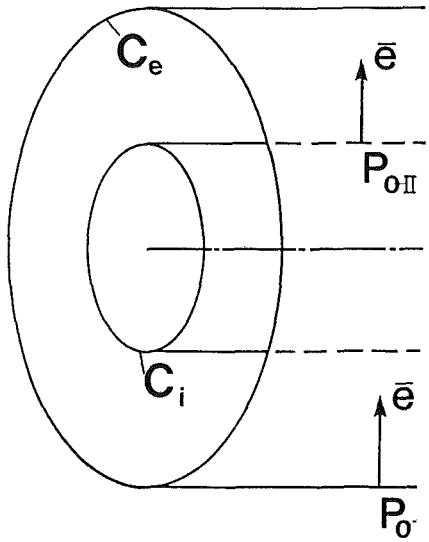

Fig. 2 Positions in question

Case I. Choosing the angles β and ψ as shown in Fig. 3, $0 \le \beta \le \pi$ and $0 \le \psi \le 2\pi$, the two contributions to L_o from parts A and B can be expressed, respectively, as follows:

$$L_o(A) = \frac{4}{\pi}(R^2 - r^2) \int_0^{\frac{\pi}{2}} \left[\int_0^{\frac{\pi}{2} - f(\psi)} \sin\beta \left[R + (r^2 - (R^2 - r^2)\tan^2\beta \sin^2\psi)^{1/2} \right]^{-1} d\beta \right] d\psi \tag{2}$$

and

$$L_o(B) = \frac{8}{\pi} R \int_o^{\frac{\pi}{2}} \left[\int_{\frac{\pi}{2} - f(\psi)}^{\frac{\pi}{2}} \sin\beta \left[1 + \tan^2\beta \sin^2\psi \right]^{-1} d\beta \right] d\psi \tag{3}$$

where $f(\psi)$ is the function given by

$$f(\psi) = \arctan\left[\frac{1}{r} (R^2 - r^2)^{1/2} \sin\psi \right]$$

Case II. Here E is a hemisphere with the equator in the XY plane. Choosing polar coordinates ρ and θ, where θ is measured from the x axis, in this plane, L_o can be expressed as follows:

$$L_o = \frac{4}{\pi}(R^2 - r^2) \int_o^{\frac{\pi}{2}} \left[\int_o^1 \rho \left[r(1-\rho^2)^{1/2} + (R^2(1 - \rho^2\cos^2\theta) - r^2\rho^2\sin^2\theta)^{1/2} \right]^{-1} d\rho \right] d\theta \tag{4}$$

The reductions of the surface integral, equation (1), to the double integrals, equations (2), (3), and (4), are of a purely geometric nature. It turns out to be possible to evaluate these three double integrals in terms of elementary functions. The calculations—based on successive substitutions—are somewhat tedious. The results are as follows:

[1]Associate Professor, The Mathematical Institute and The Laboratory of Heating and Air Conditioning, The Technical University of Denmark, Lyngby, Denmark.

Contributed by the Heat Transfer Division for publication in the JOURNAL OF HEAT TRANSFER. Manuscript received by the Heat Transfer Division January 5, 1988. Keywords: Furnaces and Combustors, Radiation, Radiation Interactions.

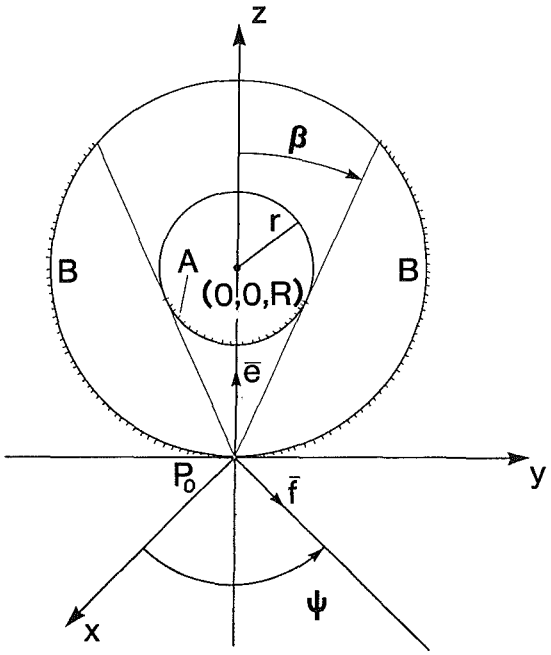

Fig. 3 Case I: $F = A + B$

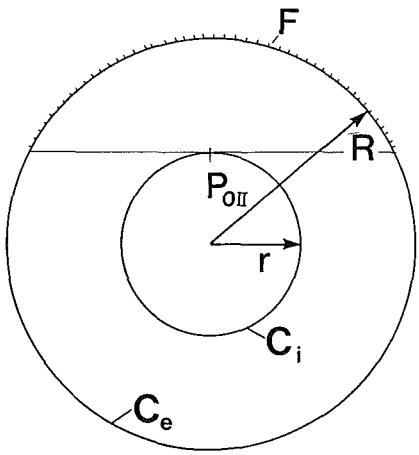

Fig. 4 Case II

Case I (Fig. 3)

$$L_o(A) = \frac{1}{R}(R^2 - r^2) + \frac{2}{\pi}\left[\frac{r}{R}(R^2 - r^2)^{1/2} - R \cdot \arctan\left(\frac{1}{r}(R^2 - r^2)^{1/2}\right)\right] \quad (5)$$

$$L_o(B) = \frac{4}{\pi}\left[R \cdot \arctan\left(\frac{1}{r}(R^2 - r^2)^{1/2}\right) - \frac{r}{R}(R^2 - r^2)^{1/2}\right] \quad (6)$$

hence

$$L_o = L_o(A) + L_o(B) = \frac{1}{R}(R^2 - r^2) + \frac{2}{\pi}\left[R \cdot \arctan\left(\frac{1}{r}(R^2 - r^2)^{1/2}\right) - \frac{r}{R}(R^2 - r^2)^{1/2}\right] \quad (7)$$

Note that $L_o \to 2R$ as $r \to 0$ (see Hottel and Sarofim, 1967). $L_o \to 0$ as $r \to R$.[2]

[2] A better limit for L_o as $r \to R$ is $2(R - r)$.

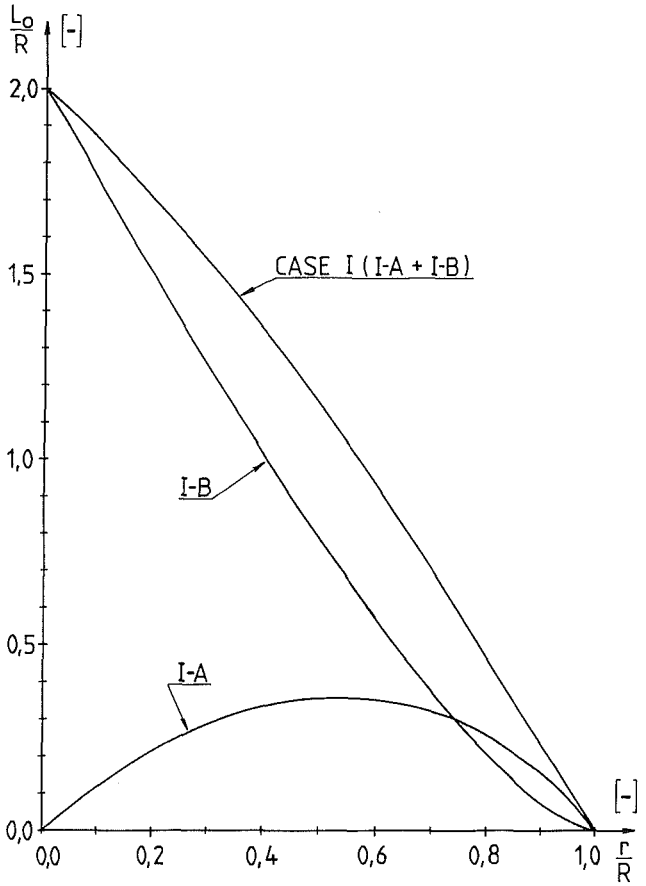

Fig. 5 Curves for Case I: The upper curve is equation (7*a*); the *A* and *B* curve from equations (5) and (6) in dimensionless form

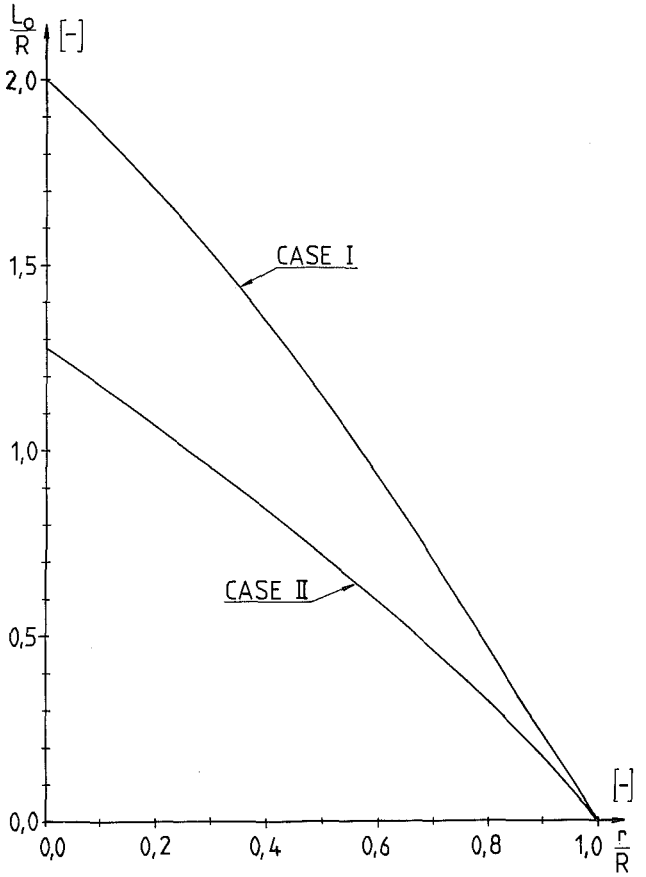

Fig. 6 Dimensionless curves for Cases I and II; the last is from equation (8*a*)

Case II (Fig. 4)

$$L_o = \frac{1}{r}(R^2 - r^2) - \frac{2}{\pi}\left[\frac{R^2}{r} \cdot \arctan\left(\frac{1}{r}(R^2-r^2)^{1/2}\right) - (R^2-r^2)^{1/2}\right]$$

Note that $L_o \to (4/\pi)\,R$ as $r \to 0$ in accordance with Hadvig (1985). $L_o \to 0$ as $r \to R$.[2] Introducing the ratio $\eta = r/R$, the two formulae can be written in dimensionless form:

Case I $(A + B)$

$$\frac{L_o}{R} = 1 - \eta^2 + \frac{2}{\pi}\left[\arctan\left(\frac{1}{\eta}\sqrt{1-\eta^2}\right) - \eta\sqrt{1-\eta^2}\right] \quad (7a)$$

Case II

$$\frac{L_o}{R} = \frac{2}{\pi}\left[\sqrt{1-\eta^2} + \frac{1}{\eta}\arctan\frac{\eta}{\sqrt{1-\eta^2}}\right] - \eta \quad (8a)$$

Curves are given in Figs. 5 and 6.

The well-known average mean beam length $L_{o,av}$ over all surfaces is

$$L_{o,av} = 2(R - r) \quad (9)$$

obtainable from 4 times the mean hydraulic radius. Equation (9) can be calculated by multiplying equations (7) and (8) by R and r, respectively, and adding the two new equations, giving the product $(R + r) \cdot L_{o,av}$.

We then get equation (9) valid for optically thin gas.

References

Hadvig, S., 1985, "Thermal Radiation for Engineers, Part II," Laboratory of Heating and Air Conditioning, Technical University of Denmark, Building 402, Lyngby, Denmark (in Danish), p. 306.

Hottel, H. C., and Sarofim, A. F., 1967, *Radiative Transfer*, McGraw-Hill, New York, p. 277.

A Dimensionless Number for the Contact Line Evaporative Heat Sink

P. C. Wayner, Jr.[1]

Nomenclature

- A = Hamaker constant
- $\bar{A}$ = $A/(6\,\pi)$
- h_{fg} = heat of vaporization
- P_l = "effective pressure" in liquid
- P_v = pressure in vapor
- Q = contact line heat sink per unit width of film
- Q^* = dimensionless contact line heat sink per unit width of film
- q = contact line heat flux
- V = average velocity
- Γ = mass flow rate per unit width of film
- δ = liquid film thickness
- δ' = slope of liquid–vapor interface
- ν = kinematic viscosity

[1]Professor of Chemical Engineering, Department of Chemical Engineering, Rensselaer Polytechnic Institute, Troy, NY 12180; Mem. ASME.

Contributed by the Heat Transfer Division for publication in the JOURNAL OF HEAT TRANSFER. Manuscript received by the Heat Transfer Division February 8, 1988; revised version submitted October 14, 1988. Keywords: Evaporation, Phase-Change Phenomena, Thin Film Flow.

Introduction

The van der Waals force per unit area associated with a spreading liquid film (zero contact angle system) of thickness δ on a horizontal substrate can be represented by $A/(6\,\pi\,\delta^3)$. In this equation, A is the Hamaker constant. The approximations associated with this equation are discussed by Dzyaloshinskii et al. (1959), Israelachvili (1985), and Truong and Wayner (1987). This force acts to give a film of uniform thickness on a horizontal plate when the dielectric properties of the intervening medium (liquid) are intermediate between the two interacting media (taken to be the vapor and substrate). If the film thickness is not constant (as presented in Fig. 1) fluid flows from the thicker portion of the film to the thinner portion of the film. The main driving force for flow in very thin films can be the gradient in the van der Waals force. This phenomenon was used by Wayner et al. (1976) to develop an equation for the interline heat transfer coefficient of an evaporating wetting film. Buried in this development is a dimensionless group that can enhance, when properly viewed, the understanding of the evaporation process in the contact line region where the film thickness becomes vanishingly thin. This process is crucial in systems that rely on heat transfer in ultrathin films such as evaporating drops on solid surfaces and evaporating menisci in heat pipes. Herein, we discuss the significance and use of this dimensionless contact line heat sink number.

Theoretical Background

First, we summarize the pertinent aspects of the development presented by Wayner et al. (1976). The thin film portion of a steady-state evaporating film in the contact line region consists of evaporating and nonevaporating regions as shown in Fig. 1. The film and substrate are at a temperature above the reference saturation temperature set by condensation in a region not shown in the figure. If the film is sufficiently thin, it is kept from evaporating by the van der Waals force acting between the solid and the liquid. For the spreading case, the liquid-solid interaction is stronger than the liquid-liquid interaction. In the limit, the film thickness can be of the order of a monolayer. If a section of the film is slightly tapered, portions of the film may be sufficiently thick to evaporate since the force of attraction between the solid and the surface molecules of the liquid decreases with an increase in liquid thickness. Fluid flows toward the thinner region as a result of the thickness gradient. Gradients in the temperature, composition, or curvature can either enhance or impede the flow. For convenience and clarity, these additional effects are neglected in this development. In addition, as an example it is possible to focus herein on a plane in the film where the thickness is approximately 10^{-8} m so that a continuum approach is acceptable.

For developed laminar flow in a slightly tapered thin liquid film, the mass flow rate per unit width of the film can be represented by

$$\Gamma = -\frac{\delta^3}{3\nu}\left(\frac{dP_l}{dx}\right) \quad (1)$$

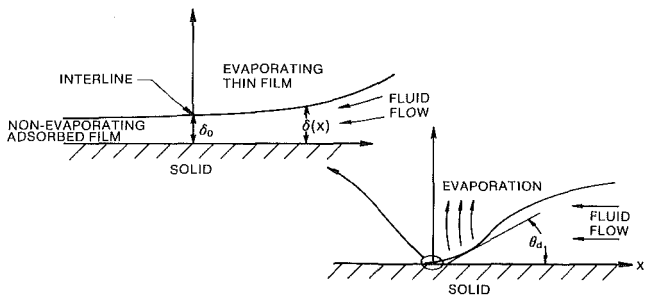

Fig. 1 Generic contact line region with evaporation (not drawn to scale)

Case II (Fig. 4)

$$L_o = \frac{1}{r}(R^2 - r^2) - \frac{2}{\pi}\left[\frac{R^2}{r} \cdot \arctan\left(\frac{1}{r}(R^2-r^2)^{1/2}\right) - (R^2-r^2)^{1/2}\right]$$

Note that $L_o \to (4/\pi)\,R$ as $r \to 0$ in accordance with Hadvig (1985). $L_o \to 0$ as $r \to R$.[2] Introducing the ratio $\eta = r/R$, the two formulae can be written in dimensionless form:

Case I $(A + B)$

$$\frac{L_o}{R} = 1 - \eta^2 + \frac{2}{\pi}\left[\arctan\left(\frac{1}{\eta}\sqrt{1-\eta^2}\right) - \eta\sqrt{1-\eta^2}\right] \quad (7a)$$

Case II

$$\frac{L_o}{R} = \frac{2}{\pi}\left[\sqrt{1-\eta^2} + \frac{1}{\eta}\arctan\frac{\eta}{\sqrt{1-\eta^2}}\right] - \eta \quad (8a)$$

Curves are given in Figs. 5 and 6.

The well-known average mean beam length $L_{o,av}$ over all surfaces is

$$L_{o,av} = 2(R - r) \quad (9)$$

obtainable from 4 times the mean hydraulic radius. Equation (9) can be calculated by multiplying equations (7) and (8) by R and r, respectively, and adding the two new equations, giving the product $(R + r) \cdot L_{o,av}$.

We then get equation (9) valid for optically thin gas.

References

Hadvig, S., 1985, "Thermal Radiation for Engineers, Part II," Laboratory of Heating and Air Conditioning, Technical University of Denmark, Building 402, Lyngby, Denmark (in Danish), p. 306.

Hottel, H. C., and Sarofim, A. F., 1967, *Radiative Transfer*, McGraw-Hill, New York, p. 277.

A Dimensionless Number for the Contact Line Evaporative Heat Sink

P. C. Wayner, Jr.[1]

Nomenclature

- A = Hamaker constant
- $\bar{A}$ = $A/(6\,\pi)$
- h_{fg} = heat of vaporization
- P_l = "effective pressure" in liquid
- P_v = pressure in vapor
- Q = contact line heat sink per unit width of film
- Q^* = dimensionless contact line heat sink per unit width of film
- q = contact line heat flux
- V = average velocity
- Γ = mass flow rate per unit width of film
- δ = liquid film thickness
- δ' = slope of liquid–vapor interface
- ν = kinematic viscosity

[1]Professor of Chemical Engineering, Department of Chemical Engineering, Rensselaer Polytechnic Institute, Troy, NY 12180; Mem. ASME.

Contributed by the Heat Transfer Division for publication in the JOURNAL OF HEAT TRANSFER. Manuscript received by the Heat Transfer Division February 8, 1988; revised version submitted October 14, 1988. Keywords: Evaporation, Phase-Change Phenomena, Thin Film Flow.

Introduction

The van der Waals force per unit area associated with a spreading liquid film (zero contact angle system) of thickness δ on a horizontal substrate can be represented by $A/(6\,\pi\,\delta^3)$. In this equation, A is the Hamaker constant. The approximations associated with this equation are discussed by Dzyaloshinskii et al. (1959), Israelachvili (1985), and Truong and Wayner (1987). This force acts to give a film of uniform thickness on a horizontal plate when the dielectric properties of the intervening medium (liquid) are intermediate between the two interacting media (taken to be the vapor and substrate). If the film thickness is not constant (as presented in Fig. 1) fluid flows from the thicker portion of the film to the thinner portion of the film. The main driving force for flow in very thin films can be the gradient in the van der Waals force. This phenomenon was used by Wayner et al. (1976) to develop an equation for the interline heat transfer coefficient of an evaporating wetting film. Buried in this development is a dimensionless group that can enhance, when properly viewed, the understanding of the evaporation process in the contact line region where the film thickness becomes vanishingly thin. This process is crucial in systems that rely on heat transfer in ultrathin films such as evaporating drops on solid surfaces and evaporating menisci in heat pipes. Herein, we discuss the significance and use of this dimensionless contact line heat sink number.

Theoretical Background

First, we summarize the pertinent aspects of the development presented by Wayner et al. (1976). The thin film portion of a steady-state evaporating film in the contact line region consists of evaporating and nonevaporating regions as shown in Fig. 1. The film and substrate are at a temperature above the reference saturation temperature set by condensation in a region not shown in the figure. If the film is sufficiently thin, it is kept from evaporating by the van der Waals force acting between the solid and the liquid. For the spreading case, the liquid-solid interaction is stronger than the liquid-liquid interaction. In the limit, the film thickness can be of the order of a monolayer. If a section of the film is slightly tapered, portions of the film may be sufficiently thick to evaporate since the force of attraction between the solid and the surface molecules of the liquid decreases with an increase in liquid thickness. Fluid flows toward the thinner region as a result of the thickness gradient. Gradients in the temperature, composition, or curvature can either enhance or impede the flow. For convenience and clarity, these additional effects are neglected in this development. In addition, as an example it is possible to focus herein on a plane in the film where the thickness is approximately 10^{-8} m so that a continuum approach is acceptable.

For developed laminar flow in a slightly tapered thin liquid film, the mass flow rate per unit width of the film can be represented by

$$\Gamma = -\frac{\delta^3}{3\nu}\left(\frac{dP_l}{dx}\right) \quad (1)$$

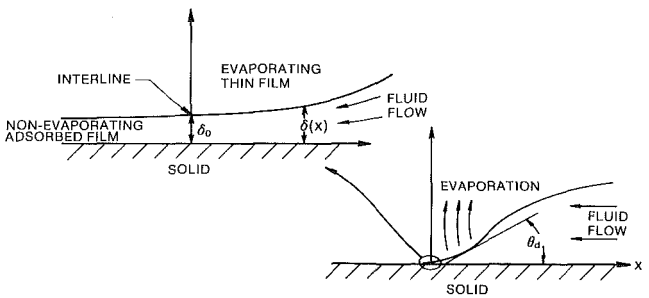

Fig. 1 Generic contact line region with evaporation (not drawn to scale)

As a result of the van der Waals forces between the molecules, an "effective pressure" in the liquid can be represented by

$$P_l = P_v + \frac{A}{6\,\Pi\,\delta^3} = P_v + \frac{\bar{A}}{\delta^3} \tag{2}$$

Since there is almost a random inconsistency in the sign convention used in the literature for this equation, we re-emphasize that we are analyzing spreading systems with $A < 0$. This is opposite the sign convention used in Wayner et al. (1976) but consistent with the Hamaker constant convention. In addition, the force concept is viewed two ways in the literature: Derjaguin pioneered the disjoining pressure concept (see, e.g., Derjaguin et al., 1965); an insight into the body force approach can be obtained from Huh and Scriven (1971), Miller and Ruckenstein (1974), or Lopez et al. (1976). Combining these two equations gives the mass flow rate per unit width at a given location "x," $\Gamma\ (x)$, in terms of the film geometry (thickness and thickness gradient) and a flow coefficient

$$\Gamma = \frac{\bar{A}\,\delta'}{\nu\,\delta} \tag{3}$$

In turn, the slope of the liquid–vapor interface is the dimensionless mass flow rate in the liquid film due to van der Waals forces. Assuming that all the liquid that flows through a plane perpendicular to the substrate at a given location evaporates in the thinner portion of the film, a contact line heat sink can be defined as

$$Q = -h_{fg}\,\Gamma = -\frac{h_{fg}\,\bar{A}\,\delta'}{\nu\,\delta} \tag{4}$$

In this case the slope is a dimensionless contact line heat sink

$$Q^* = \delta' = -\frac{Q}{\left(\frac{h_{fg}\,\bar{A}}{\nu\,\delta}\right)} \tag{5}$$

Using $\Gamma = -\rho\ V\ \delta$ in equation (3) leads to considerable insight:

$$\delta' = -\frac{\left(\frac{\mu\ V}{\delta}\right)}{\left(\frac{\bar{A}}{\delta^3}\right)} \tag{6}$$

The slope equals the ratio of a representative shear stress in the flow field to the van der Waals force per unit area causing the flow. At equilibrium the slope is zero. Therefore, the slope represents a measure of the departure from equilibrium at a given thickness. Viewing the dimensionless contact line heat sink defined in equation (5) in the same light, the product of δ' and the parameter $(h_{fg}\,\bar{A}/\nu\,\delta)$ gives the contact line heat sink.

Numerical Example

There is an extensive literature concerning the calculation of the van der Waals force. A recent book by Israelachvili (1985) allows relatively easy entry into this literature. In Table 1, we use the approximate values for the parameter $(h_{fg}\,\bar{A}/\nu)$ presented by Wayner (1978). In the third column, $\delta = 10^{-8}$ m. (Unfortunately, the approximation for Teflon in this reference was based on an incorrect source and is not used here.)

For an angle of 1 deg, the slope is 0.017. Therefore, the contact line heat sink in the region $\delta < 10^{-8}$ m for the octane–gold system discussed above is $Q = 4.5 \times 10^{-3}$ W/m when the slope is 0.017 at this thickness. This value might appear small but we would not expect a much larger value for most systems operating within these assumptions since this analysis represents the ideal limiting case of a stationary contact line with a steady-state low evaporation rate. At higher fluxes, the contact line is known to oscillate and "boiling" in the thin film is possible. In addition, a shear stress due to a composition gradient can enhance flow. The analysis illustrated above can also be used to approximate an upper limit to the heat flux in the region $\delta < 10^{-8}$ m. Assuming a triangle as an approximate (albeit poor) shape for the curved film, the minimum possible area under the film per unit width is δ/δ'. This is the solid substrate base of the triangle formed by the tangent to the curved meniscus shown in Fig. 1 and the vertical thickness δ at the point of contact of the tangent. Therefore the maximum possible evaporative flux in this example is estimated to be

Table 1 Approximate numerical values from Wayner (1978)

System	$-\frac{h_{fg}\,\bar{A}}{\nu}$ (W)	$-\frac{h_{fg}\,\bar{A}}{\nu\,\delta}$ (W/m)
Pentane–gold (293 K)	5.3×10^{-9}	5.3×10^{-1}
Octane–gold (293 K)	2.6×10^{-9}	2.6×10^{-1}
Octane–quartz (293 K)	0.42×10^{-9}	0.42×10^{-1}

$$q = -\left(\frac{h_{fg}\,\bar{A}}{\nu\,\delta}\right)\frac{(\delta')^2}{\delta} = 8 \times 10^3\ \text{W/m}^2 \tag{7}$$

A better estimate of the flux can be obtained, with more effort, using the more nearly exact profile given in Wayner et al. (1976).

It is interesting to note in conclusion that in this ideal example it is possible to start with one of the four distinct forces of nature (the electromagnetic force between molecules as represented by the Hamaker constant or by recently improved models) and derive a dimensionless number that represents the contact line heat sink of an evaporating pure thin film using simplified transport equations. The observed interfacial slope in the contact line region for a "spreading fluid" (zero contact angle system) is the dimensionless evaporation rate. A recent broad review of the details of the modeling of intermolecular forces that makes this possible is given by Israelachvili (1985). Experimental data in a recent thesis by Truong (1987) qualitatively confirm that the liquid–vapor interfacial slope is a function of the evaporation rate. However, quantitative confirmation of the above analysis has not yet been achieved because of the experimental difficulties associated with measurements in so small a region. At a much thicker location, the measured apparent contact was also found to be a function of the evaporation rate by Cook et al. (1981) and by Hirasawa and Hauptman (1986).

Acknowledgments

This material is based on work supported by the Aero Propulsion Laboratory, Air Force Wright Aeronautical Laboratory, Aeronautical Systems Division (AFSC), United States Air Force, Wright-Patterson AFB Ohio 45433-6563 under contract No. F33615-88-C-2821. The U.S. Government is authorized to reproduce and distribute reprints for governmental purposes notwithstanding any copyright notation. Any opinions, findings, and conclusions or recommendations expressed in this publication are those of the author and do not necessarily reflect the view of the U.S. Air Force.

References

Cook, R., Tung, C. Y., and Wayner, P. C., Jr., 1981, "Use of Scanning Microphotometer to Determine the Evaporative Heat Transfer Characteristics of the Contact Line Region," ASME JOURNAL OF HEAT TRANSFER, Vol. 103, pp. 325–330.

Derjaguin, B. V., Nerpin, S. V., and Churaev, N. V., 1965, "Effect of Film Transfer Upon Evaporation of Liquids From Capillaries," *Bull. R.I.L.E.M.*, Vol. 29, pp. 93–98.

Dzyaloshinskii, I. E., Lifshitz, E. M., and Pitaevskii, L. P., 1959, *Adv. Physics*, Vol. 10, pp. 165–209.

Hirasawa, S., and Hauptmann, E. G., 1986, "Dynamic Contact Angle of a Rivulet Flowing Down a Vertical Heated Wall," *Proceedings of Eighth International Heat Transfer Conference*, Vol. 4, pp. 1877–1882.

Huh, C., and Scriven, L. E., 1971, "Hydrodynamic Model of Steady Move-

ment of a Solid/Liquid/Fluid Contact Line," *J. Colloids and Interface Science*, Vol. 35, pp. 85–101.

Israelachvili, J. N., 1985, *Intermolecular and Surface Forces: With Applications to Colloidal and Biological Systems*, Academic Press, New York.

Lopez, J., Miller, C. A., and Ruckenstein, E., 1976, "Spreading Kinetics of Liquid Drops on Solids," *J. of Colloids and Interface Science*, Vol. 56, pp. 460–468.

Miller, C. A., and Ruckenstein, E., 1974, "The Origin of Flow During Wetting of Solids," *J. of Colloids and Interface Science*, Vol. 48, pp. 368–373.

Truong, J. G., 1987, "Ellipsometric and Interferometric Studies of Thin Films Wetting on Isothermal and Nonisothermal Surfaces," Ph.D. Thesis, Rensselaer Polytechnic Institute, Troy, NY.

Truong, J. G., and Wayner, P. C., Jr., 1987, "Effects of Capillary and van der Waals Dispersion Force on the Equilibrium Profile of a Wetting Liquid: Theory and Experiment," *J. Chem. Phys.*, Vol. 87, pp. 4180–4188.

Wayner, P. C., Jr., Kao, Y. K., and LaCroix, L. V., 1976, "The Interline Heat Transfer Coefficient of an Evaporating Wetting Film," *Int. J. Heat Mass Transfer*, Vol. 19, pp. 487–492.

Wayner, P. C., Jr., 1978, "The Effect of the London–van der Waals Dispersion Force on Interline Heat Transfer," ASME JOURNAL OF HEAT TRANSFER, Vol. 100, pp. 155–159.

An Upper Bound for the Critical Boiling Heat Flux

W. R. Gambill[1] and J. H. Lienhard[2]

Nomenclature

$\bar{c}$ = mean molecular velocity
h_{fg} = latent heat of vaporization
J = flux of molecules
k = Boltzmann constant (gas constant per molecular mass)
m = mass of a molecule
n = number density of molecules
p, p_c, p_r = pressure, critical pressure, reduced pressure
q_{max} = peak or "burnout" heat flux
$q_{max,max}$ = $\rho_g h_{fg}\sqrt{RT/2\pi}$ (theoretical upper bound for q_{max})
R = ideal gas constant on a unit mass basis
T_{sat} = saturation temperature
T_w = wall temperature of a heating (or cooling) surface
ΔT = $T_w - T_{sat}$
ρ_g = density of saturated vapor
ϕ = $q_{max}/q_{max,max}$

Introduction

The great value of boiling and condensation in process heat transfer is that they yield the highest known heat transfer coefficients. People who have to transfer a great deal of energy rapidly, under fairly low driving temperature differences, usually turn to these processes. We therefore constantly face the question, "What is the upper limit on these heat fluxes—how far can they be driven?"

Several investigators have taken particular pains to push the peak boiling heat flux q_{max} to its limits. For example, Gambill and Greene (1958) used inlet tangential-slot swirl-flow generators with water at pressures up to 7 MPa and at axial velocities up to 30 m/s. They obtained burnout heat fluxes as high as 172.8 MW/m^2. When this study was later extended to swirl flows induced by internal twisted tapes, Gambill et al. (1961) obtained q_{max} up to 117.8 MW/m^2 in water, and Gambill and Bundy (1963) obtained q_{max} up to 28.4 MW/m^2 in ethylene glycol.

Ornatskii and Vinyarskii (1965) have observed q_{max} in water flowing axially in small (0.5 mm i.d.) tubes at speeds up to 90 or 100 m/s, and attained a q_{max} of 224.5 MW/m^2.

Japanese investigators (see, e.g., Monde and Katto (1978) and Katto and Shimizu (1979)) have measured q_{max} in a different kind of system—a liquid jet impinging perpendicularly upon a heated disc. The set of experiments using water jets at atmospheric pressure yielded several values of q_{max} in excess of 10 MW/m^2. Monde and Katto's highest value was 18.26 MW/m^2. (Katto and Shimizu also did experiments using Freon-113 jets and Freon-12 jets under a wide range of elevated pressures, but burnout heat fluxes in these cases were not extremely high.)

The existing data strongly indicate that we should hold the hope of reaching far higher heat fluxes than we presently reach. Our present aim is to set a theoretical and/or practical limit on attainable heat fluxes, so we might henceforth aspire to reach that limit in practical design.

The Upper Limit for the Limiting Heat Flux

The highest heat flux that can conceivably be achieved in a phase-transition process—which we designate as $q_{max,max}$—was given by Schrage (1953), who made reference to antecedents of the idea extending back into the 19th century. Tien and Lienhard (1976, 1979) independently made this calculation in a simple approximate way, in reference to boiling burnout, in 1970. They noted that, if one could contrive to collect every vapor molecule that leaves a liquid-vapor interface without permitting any vapor molecules to return to the liquid, then

$$q_{max,max} = (mJ)h_{fg} \tag{1}$$

where m is the mass of a molecule and J is the flux of molecules in one direction. The kinetic theory gives $J = n\bar{c}/4$, where n is the number density of vapor molecules and $\bar{c}$ is the average molecular speed. They took the vapor leaving the liquid as having roughly the average speed of a Maxwellian gas, $\bar{c} = \sqrt{8RT/\pi}$. (This will be a reasonable approximation, even at pressures rather close to the critical pressure, because the average energy of molecules is little affected by the forces that give rise to nonideality in a gas.) The use of this $\bar{c}$ in the preceding equation gives

$$J \approx n\sqrt{kT/2\pi m} \tag{2}$$

We substitute equation (2) into (1) and obtain

$$q_{max,max} \equiv \rho_g h_{fg}\sqrt{RT/2\pi} \tag{3}$$

Schrage's more complete calculation took account of the distortion of the Maxwellian distribution when molecules are prevented from returning to the surface. He indicated that this would give rise to a hard-to-evaluate constant on the right side of equation (3), but that this constant would remain on the order of unity. Consequently the right side of equation (3) is not an exact upper bound, but rather a group that *characterizes* the upper limit correctly and gives its correct order of magnitude.

The arguments underlying this result would apply equally well in reverse—for vapor molecules condensing on an inter-

[1]Development Staff Member, Chemical Technology Division, Oak Ridge National Laboratory, Oak Ridge, TN 37831. The Oak Ridge National Laboratory is operated for the U.S. Department of Energy by Martin Marietta Energy Systems, Inc.

[2]Professor, Heat Transfer/Phase Change Laboratory, Mechanical Engineering and History Departments, University of Houston, Houston, TX 77204-4792; Fellow ASME.

Contributed by the Heat Transfer Division and presented at the 2nd ASME-JSME Thermal Engineering Joint Conference, Honolulu, Hawaii, March 1987. Manuscript received by the Heat Transfer Division October 27, 1986. Keywords: Augmentation and Enhancement, Boiling, Phase-Change Phenomena.

ment of a Solid/Liquid/Fluid Contact Line," *J. Colloids and Interface Science*, Vol. 35, pp. 85–101.

Israelachvili, J. N., 1985, *Intermolecular and Surface Forces: With Applications to Colloidal and Biological Systems*, Academic Press, New York.

Lopez, J., Miller, C. A., and Ruckenstein, E., 1976, "Spreading Kinetics of Liquid Drops on Solids," *J. of Colloids and Interface Science*, Vol. 56, pp. 460–468.

Miller, C. A., and Ruckenstein, E., 1974, "The Origin of Flow During Wetting of Solids," *J. of Colloids and Interface Science*, Vol. 48, pp. 368–373.

Truong, J. G., 1987, "Ellipsometric and Interferometric Studies of Thin Films Wetting on Isothermal and Nonisothermal Surfaces," Ph.D. Thesis, Rensselaer Polytechnic Institute, Troy, NY.

Truong, J. G., and Wayner, P. C., Jr., 1987, "Effects of Capillary and van der Waals Dispersion Force on the Equilibrium Profile of a Wetting Liquid: Theory and Experiment," *J. Chem. Phys.*, Vol. 87, pp. 4180–4188.

Wayner, P. C., Jr., Kao, Y. K., and LaCroix, L. V., 1976, "The Interline Heat Transfer Coefficient of an Evaporating Wetting Film," *Int. J. Heat Mass Transfer*, Vol. 19, pp. 487–492.

Wayner, P. C., Jr., 1978, "The Effect of the London–van der Waals Dispersion Force on Interline Heat Transfer," ASME JOURNAL OF HEAT TRANSFER, Vol. 100, pp. 155–159.

An Upper Bound for the Critical Boiling Heat Flux

W. R. Gambill[1] and J. H. Lienhard[2]

Nomenclature

$\bar{c}$ = mean molecular velocity
h_{fg} = latent heat of vaporization
J = flux of molecules
k = Boltzmann constant (gas constant per molecular mass)
m = mass of a molecule
n = number density of molecules
p, p_c, p_r = pressure, critical pressure, reduced pressure
q_{max} = peak or "burnout" heat flux
$q_{max,max}$ = $\rho_g h_{fg}\sqrt{RT/2\pi}$ (theoretical upper bound for q_{max})
R = ideal gas constant on a unit mass basis
T_{sat} = saturation temperature
T_w = wall temperature of a heating (or cooling) surface
ΔT = $T_w - T_{sat}$
ρ_g = density of saturated vapor
ϕ = $q_{max}/q_{max,max}$

Introduction

The great value of boiling and condensation in process heat transfer is that they yield the highest known heat transfer coefficients. People who have to transfer a great deal of energy rapidly, under fairly low driving temperature differences, usually turn to these processes. We therefore constantly face the question, "What is the upper limit on these heat fluxes—how far can they be driven?"

Several investigators have taken particular pains to push the peak boiling heat flux q_{max} to its limits. For example, Gambill and Greene (1958) used inlet tangential-slot swirl-flow generators with water at pressures up to 7 MPa and at axial velocities up to 30 m/s. They obtained burnout heat fluxes as high as 172.8 MW/m^2. When this study was later extended to swirl flows induced by internal twisted tapes, Gambill et al. (1961) obtained q_{max} up to 117.8 MW/m^2 in water, and Gambill and Bundy (1963) obtained q_{max} up to 28.4 MW/m^2 in ethylene glycol.

Ornatskii and Vinyarskii (1965) have observed q_{max} in water flowing axially in small (0.5 mm i.d.) tubes at speeds up to 90 or 100 m/s, and attained a q_{max} of 224.5 MW/m^2.

Japanese investigators (see, e.g., Monde and Katto (1978) and Katto and Shimizu (1979)) have measured q_{max} in a different kind of system—a liquid jet impinging perpendicularly upon a heated disc. The set of experiments using water jets at atmospheric pressure yielded several values of q_{max} in excess of 10 MW/m^2. Monde and Katto's highest value was 18.26 MW/m^2. (Katto and Shimizu also did experiments using Freon-113 jets and Freon-12 jets under a wide range of elevated pressures, but burnout heat fluxes in these cases were not extremely high.)

The existing data strongly indicate that we should hold the hope of reaching far higher heat fluxes than we presently reach. Our present aim is to set a theoretical and/or practical limit on attainable heat fluxes, so we might henceforth aspire to reach that limit in practical design.

The Upper Limit for the Limiting Heat Flux

The highest heat flux that can conceivably be achieved in a phase-transition process—which we designate as $q_{max,max}$—was given by Schrage (1953), who made reference to antecedents of the idea extending back into the 19th century. Tien and Lienhard (1976, 1979) independently made this calculation in a simple approximate way, in reference to boiling burnout, in 1970. They noted that, if one could contrive to collect every vapor molecule that leaves a liquid-vapor interface without permitting any vapor molecules to return to the liquid, then

$$q_{max,max} = (mJ)h_{fg} \tag{1}$$

where m is the mass of a molecule and J is the flux of molecules in one direction. The kinetic theory gives $J = n\bar{c}/4$, where n is the number density of vapor molecules and $\bar{c}$ is the average molecular speed. They took the vapor leaving the liquid as having roughly the average speed of a Maxwellian gas, $\bar{c} = \sqrt{8RT/\pi}$. (This will be a reasonable approximation, even at pressures rather close to the critical pressure, because the average energy of molecules is little affected by the forces that give rise to nonideality in a gas.) The use of this $\bar{c}$ in the preceding equation gives

$$J \approx n\sqrt{kT/2\pi m} \tag{2}$$

We substitute equation (2) into (1) and obtain

$$q_{max,max} \equiv \rho_g h_{fg}\sqrt{RT/2\pi} \tag{3}$$

Schrage's more complete calculation took account of the distortion of the Maxwellian distribution when molecules are prevented from returning to the surface. He indicated that this would give rise to a hard-to-evaluate constant on the right side of equation (3), but that this constant would remain on the order of unity. Consequently the right side of equation (3) is not an exact upper bound, but rather a group that *characterizes* the upper limit correctly and gives its correct order of magnitude.

The arguments underlying this result would apply equally well in reverse—for vapor molecules condensing on an inter-

[1]Development Staff Member, Chemical Technology Division, Oak Ridge National Laboratory, Oak Ridge, TN 37831. The Oak Ridge National Laboratory is operated for the U.S. Department of Energy by Martin Marietta Energy Systems, Inc.

[2]Professor, Heat Transfer/Phase Change Laboratory, Mechanical Engineering and History Departments, University of Houston, Houston, TX 77204-4792; Fellow ASME.

Contributed by the Heat Transfer Division and presented at the 2nd ASME-JSME Thermal Engineering Joint Conference, Honolulu, Hawaii, March 1987. Manuscript received by the Heat Transfer Division October 27, 1986. Keywords: Augmentation and Enhancement, Boiling, Phase-Change Phenomena.

face. Thus equation (3) provides an approximate upper bound for either boiling or condensation. (In this connection we do not include an accommodation coefficent in equation (3) because the preponderance of evidence (see, e.g., Mills, 1965) suggests that molecular accommodation is imperfect only when an interface is impure, and our interest is restricted to the kind of rapidly renewed interfaces that one encounters in intense nucleate boiling or condensation.)

Values of $q_{max,max}$ are plotted against reduced pressure, p/p_c, for some typical liquids in Fig. 1 to illustrate the astonishing heat fluxes that might seem to be attainable.

There are several reasons that this limit will be unattainable in practice. The most serious restriction is that many vapor molecules will inevitably be returned to the interface by molecular collisions. We can only hope to slow the return flow of vapor molecules, not to eliminate it.

Another problem lies in the premise that all the heat ultimately passes through a liquid-vapor interface. The problem in designing a process is to get the heat to flow through the liquid, up to an interface, and away from the interface on the vapor side. That is what the various investigators reviewed in the preceding section contrived to do with the help of swirl inserts, jets, high subcooling, high velocities, elevated pressure, and so forth. If a given strategy permits some of the heat to find a less efficient path to the liquid bulk, without involving phase change at a liquid-vapor interface, it will undoubtedly yield a lower heat flux.

Comparison of the Upper Bound With Data

Boiling Burnout. Table 1 and Fig. 2 display all of the highest experimental burnout heat fluxes we could locate, over a full range of pressures. We represent these data in the dimensionless form suggested by equation (3), as a function of reduced pressure

$$\phi \equiv \frac{q_{max}}{\rho_g h_{fg} \sqrt{RT/2\pi}} = f(p_r) \tag{4}$$

The data for the pressure range $0.004 < p_r < 0.10$ appear to be consistently bounded at $\phi = 0.1$. However, at higher pressures, the highest existing values of ϕ fall off roughly as $(p_r)^{-2}$. We see two possible reasons for this decrease:

As q approaches $q_{max,max}$ in any configuration in the lower pressure range, there will be a great deal of local boiling and of

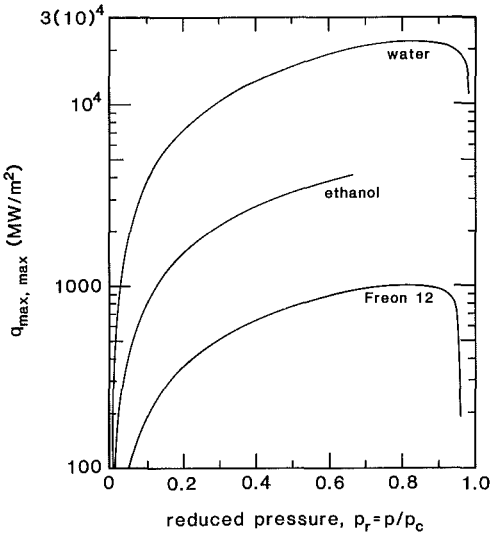

Fig. 1 Pressure dependence of $q_{max,max}$

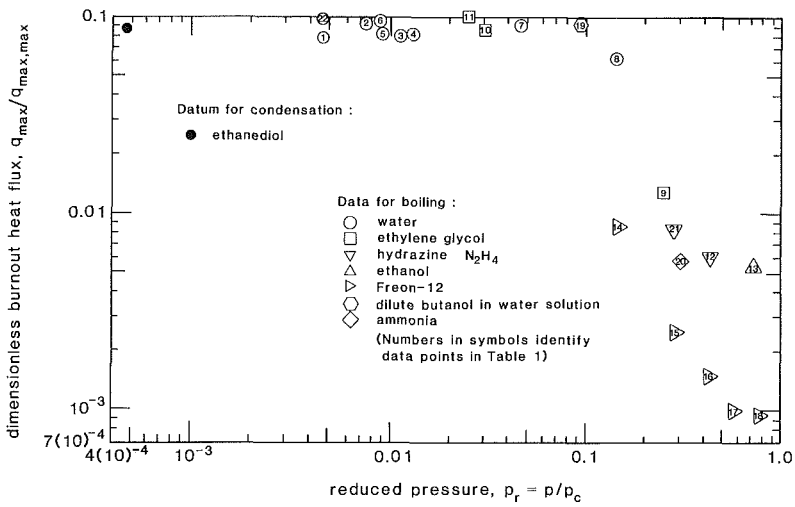

Fig. 2 Pressure dependence of the highest measured burnout heat fluxes

Table 1 List of extreme values of q_{max}

No.	Boiled liquid	$p_r = p/p_c$	ϕ	Source and configuration
1	water	0.0046	0.0815	Monde (1978) jet impinging on a disk
2	water	0.0074	0.0955	Gambill (1958) axial tube flow
3	water	0.0111	0.0809	" " inlet generated swirl
4	water	0.0130	0.0813	" " " " "
5	water	0.0090	0.0840	" (1961) twisted tape generated swirl
6	water	0.0091	0.0978	" " " " "
7	water	0.0459	0.0907	Ornatskii (1965a) axial flow, uniform q
8	water	0.1423	0.0625	" " axial flow, nonuniform q
9	ethylene glycol	0.2497	0.0128	Gambill (1963) twisted-tape swirl
10	ethylene glycol	0.0298	0.0863	" " " " "
11	ethylene glycol	0.0243	0.1033	" " " " "
12	hydrazine	0.4269	0.0060	Hines (1959) axial tube flow
13	ethanol	0.7137	0.0054	Kutateladze (1965) " " "
14	Freon-12	0.146	0.0087	Katto (1979) jet impinging on a disk
15	Freon-12	0.282	0.0025	" " " " " "
16	Freon-12	0.430	0.0015	" " " " " " "
17	Freon-12	0.571	0.0010	" " " " " " "
18	Freon-12	0.678	0.00095	" " " " " " "
19	water/3 percent butanol	0.0965	0.0961	Ornatskii (1965b) axial flow, nonuniform q
20	ammonia	0.3056	0.0058	Noel (1961b) axial tube flow
21	hydrazine	0.2791	0.0084	Noel (1961a) " " "
22	water	0.0047	0.0916	Weatherhead (1955) crossflow over a cylinder

interfacial structure near the surface. Not much of the heat *can* flow straight into the liquid without passing through an interface. At the higher pressures, however, $\rho_g h_{fg}$ increases, so less vapor volume is generated at a given heat flux. It is very probable that more of the heat finds a less efficient, direct convection path, at higher pressures.

Consider the Katto–Shimizu Freon data, for example. The Japanese visual observations (all made at low pressure), and observations of a cold-air-in-water analogy in support of Lienhard and Eichhorn's (1979) study of the jet-disk system, show that, at low pressure, burnout occurs at the outer edge of the disc. But even just before burnout, portions of the very thin sheet spreading over the disk are still intact at the outer edge of the disk. As the pressure increases and less vapor is generated, more and more of the sheet remains intact and more of the heat has to escape by direct conduction/convection through these portions. Thus, increased access to alternate flow paths is one reason that ϕ drops off with increased pressure.

The second reason becomes evident when we consider Fig. 1, where we read $q_{\max,\max}$ values for water in excess of 20,000 MW/m^2 at high pressures. It would require a temperature drop of about 4700 K to drive one-tenth of this heat flux through a 1-mm thickness of pure silver. At higher pressures it therefore becomes impossible to supply a heater surface with these heat fluxes (at steady state) by any known means. Gambill et al. (1960, 1961), for example, encountered the wall ΔT limit in a few of their early swirl-flow tests at $q > 94$ MW/m^2. Using 304 stainless steel tubes with a 0.89 mm wall thickness at these flux levels, they suffered tube failures initiated by melting of the external wall.

It is important to note that it was not the wall ΔT limitation that caused the high-pressure Katto–Shimizu measurements to be so low. The wall ΔT limitation and the inefficient-path limitation are independent of one another, with the wall ΔT limitation arising when $q_{\max,\max}$ becomes very high. The Katto–Shimizu data become limited by an inefficient heat transfer path long before the wall ΔT limitation is reached. Increasingly inventive strategies for configuring the convective flow are needed to beat the inefficient-path limitation as p_r is increased.

Effusion-Limited Burnout. The first motivation for looking at $q_{\max,\max}$ has been that of setting target levels for the heat transfer to which we may aspire in the design of boiling processes. From a practical standpoint, that limit appears to be about 0.1 $q_{\max,\max}$.

However, another very important use for the limit is immediately evident. If burnout consistently reaches one tenth of the limit, then burnout is occurring because molecular effusion fails to provide sufficient cooling. Molecular effusion is a hitherto unobserved burnout mechanism.

A very recent study of burnout is subcooled boiling by Elkassabgi and Lienhard (1988) shows that, at very high levels of liquid subcooling, the pool boiling $q_{\max}$ for horizontal cylinders becomes independent of subcooling. With reference to a prepublication version of this note, they show that highly subcooled burnout occurs in each of four different fluids at 0.01 $q_{\max,\max}$. That means that, even at fairly low heat fluxes, the breakdown in the boiling process occurs because molecular effusion fails to keep up with the heat supply. (We have subsequently discovered the same kind of a breakdown—at higher heat fluxes—during subcooled *flow* boiling over cylinders.)

Condensation. Condensation, like boiling, can occur in a "film" mode or a "nucleate" (more commonly called "dropwise") mode. Indeed, one can quite reasonably anticipate an approximate reflection of the boiling curve in the negative ΔT, negative heat transfer, portion of the boiling curve—a reflection that could rightly be called a "condensation" curve[2] (see Fig. 3).

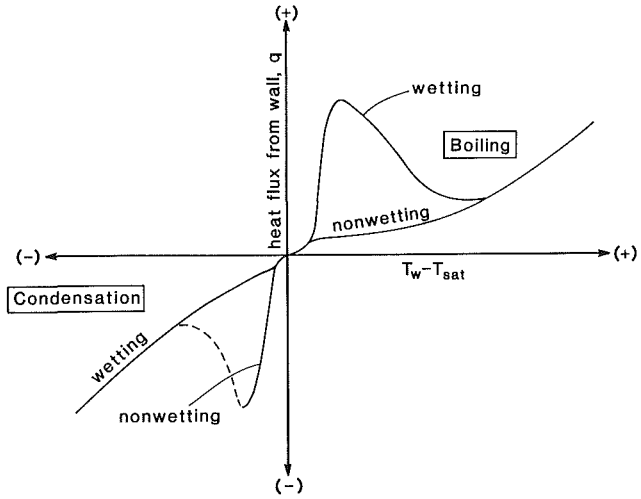

Fig. 3 Boiling and condensation curves viewed as approximate reflections of one another

A possible objection to such an analogy is that *either* dropwise or film condensation can exist at a given low ΔT. However, it is known that the same thing is true in pool boiling. Experiments conducted in completely nonwetting liquids have revealed that film boiling can be established in what would normally be the nucleate boiling range of temperature differences (see, e.g., Winterton, 1983). Thus either the boiling or condensation portion of the curve can exhibit hysteresis in the film or nucleate modes (Witte and Lienhard, 1982).

One would then look for a peak flux in condensation, analogous to that which occurs in boiling. Few investigators of dropwise condensation have pushed the heat flux to a maximum. Stylianou and Rose (1983) recently reviewed the history of extreme values of dropwise condensation measurements. They also developed an apparatus in which they subjected ethanediol (ethylene glycol) vapor to walls that could be brought to temperatures more than 80 K below saturation, at subatmospheric pressures. Their excellent photographs show clear evidence of hydrodynamic transitions from dropwise to filmwise condensation at maximum heat fluxes that range from 0.56 to 0.97 MW/m^2.

None of these measurements were obtained with serious augmentation; yet they reach values of ϕ that range from 0.09 at the lowest pressure of 3800 Pa, down to 0.02 at the highest pressure of 35,600 Pa. The clear implication is that very-low-pressure dropwise condensation also reaches the apparent practical limit of $\phi = 0.1$. Stylianou and Rose include some earlier data for aniline and nitrobenzene that they indicate are too crude to use quantitatively, but which verify these trends. (The aniline data range from $\phi \cong 0.14$ at low pressure down to 0.01 at higher pressure.) They report extreme condensing heat flux values reported by Tanasawa and Utaka (1979) for water at one atmosphere that yield ϕ values as high as 0.054. We include the limiting ethanediol value in Fig. 2.

Conclusions

1 The upper bound for heat flux by phase change, $q_{\max,\max}$, is given approximately by equation (3).

2 Boiling burnout can occur as the result of the failure of molecular effusion to keep up with a heat supply.

3 The practical limit to heat transfer by phase change is one

[2]This view was suggested to the second author by Prof. J. T. Kimbrell, Washington State University, ca. 1963.

tenth of $q_{max,max}$, at least at pressures less than about one tenth of the critical pressure.

4 At higher pressures, $q_{max,max}$ is such a large number that, for many liquids, we are not capable of supplying it.

5 If means exist for supplying $q_{max,max}$ at higher pressures, it then becomes increasingly difficult to capitalize on the enormous magnitude of $q_{max,max}$ because it is hard to design processes that prevent heat from finding non-phase-change flow paths.

6 The present ideas appear to apply to the limiting heat flux in dropwise condensation as well as to q_{max} in nucleate boiling. The few available observations of q_{max} in dropwise condensation appear to define the $\phi = 0.1$ limit, *without serious augmentation*, at low pressures.

References

Elkassabgi, Y., and Lienhard, J. H., 1988, "Influences of Subcooling on Burnout of Horizontal Cylindrical Heaters," ASME JOURNAL OF HEAT TRANSFER, Vol. 110, No. 2, pp. 479–486.

Gambill, W. R., and Greene, N. D., 1958, "Boiling Burnout With Water in Vortex Flow," *Chem. Engr. Prog.*, Vol. 54, No. 10, pp. 68–76.

Gambill, W. R., Bundy, R. D., and Wansbrough, R. W., 1960, "Heat Transfer, Burnout, and Pressure Drop for Water in Swirl Flow Through Tubes With Internal Twisted Tapes," Oak Ridge Nat'l. Lab. Rpt. ORNL-2911, Appendix 2, pp. 95–99.

Gambill, W. R., Bundy, R. D., and Wansbrough, R. W., 1961, "Heat Transfer, Burnout, and Pressure Drop for Water in Swirl Flow Through Tubes With Internal Twisted Tapes," *Chem. Engr. Prog. Symp. Series*, Vol. 57, No. 32, pp. 127–137.

Gambill, W. R., and Bundy, R. D., 1963, "High-Flux Heat-Transfer Characteristics of Pure Ethylene Glycol in Axial and Swirl Flow," *AIChE Journal*, Vol. 9, No. 1, pp. 55–59.

Hines, W. S., 1959, "Forced Convection and Peak Nucleate Boiling Heat Transfer Characteristics for Hydrazine Flowing Turbulently in a Round Tube at Pressures to 1000 psia," Rocketdyne Rept. R-2059.

Katto, Y., and Shimizu, M., 1979, "Upper Limit of the CHF in the Forced Convection Boiling on a Heated Disc With a Small Impinging Jet," ASME JOURNAL OF HEAT TRANSFER, Vol. 101, No. 2, pp. 265–269.

Kutateladze, S. S., 1965, "Criteria of Stability in Two-Phase Flow," *Symposium on Two-Phase Flow*, Vol. 1, Univ. of Exeter, United Kingdom, pp. 83–92.

Lienhard, J. H., and Eichhorn, R., 1979, "On Predicting Boiling Burnout for Heaters Cooled by Liquid Jets," *Int. J. Heat Mass Transfer*, Vol. 22, pp. 774–776.

Mills, A. F., 1965, "The Condensation of Steam at Low Pressures," Tech. Rpt. on NSF GP-2520, Series No. 6, Issue No. 39, Space Sciences Lab., Univ. of Calif. Berkeley.

Monde, M., and Katto, Y., 1978, "Burnout in High Heat-Flux Boiling System With an Impinging Jet," *Int. J. Heat Mass Transfer*, Vol. 21, pp. 295–305.

Noel, M. B., 1961a, "Experimental Investigation of Heat Transfer Characteristics of Hydrazine and a Mixture of 90 percent Hydrazine and 10 percent Ethylenediamine," JPL Technical Rept. No. 32-109.

Noel, M. B., 1961b, "Experimental Investigation of the Forced-Convection and Nucleate-Boiling Heat-Transfer Characteristics of Liquid Ammonia," JPL Technical Rept. No. 32-125.

Ornatskii, A. P., and Vinyarskii, L. S., 1965a, "Heat Transfer Crisis in a Forced Flow of Underheated [Subcooled] Water in Small-Bore Tubes," *High Temp.*, Vol. 3, No. 3, pp. 400–406.

Ornatskii, A. P., and Vinyarskii, L. S., 1965b, "Critical Heat Transfer in the Forced Motion of Underheated Water–Alcohol Mixtures in Tubes of Diameter 0.5 mm," *High Temp.*, Vol. 3, No. 6, pp. 881–882.

Schrage, R. W., 1953, *A Theoretical Study of Interphase Mass Transfer*," Columbia University Press, New York, Chap. II.

Stylianou, S. A., and Rose, J. W., 1983, "Drop-to-Filmwise Condensation Transition: Heat Transfer Measurements for Ethanediol," *Int. J. Heat Mass Transfer*, Vol. 26, No. 5, pp. 747–760.

Tanasawa, I., and Utaka, Y., 1979, "Measurement of Condensation Curves for Dropwise Condensation Heat Transfer," *Proc. 18th Nat'l. Heat Transfer Conf.*, ASME, p. 63.

Tien, C. L., and Lienhard, J. H., 1976, *Solutions Manual to Accompany Statistical Thermodynamics*, revised printing, Hemisphere, Washington, p. 13.

Tien, C. L., and Lienhard, J. H., 1979, *Statistical Thermodynamics*, revised printing, Hemisphere, Washington, p. 55, Problem 2.21.

Weatherhead, R. T., 1955, "Boiling Burnout Heat Flux for Wires in Water Crossflow at Atmospheric Pressure," Report NDA-9 (Boiling Burnout Progress No. 5).

Winterton, R. H. S., 1983, "Comments on 'On the Existence of Two 'Transition' Boiling Curves'," *Int. J. Heat Mass Transfer*, Vol. 26, No. 7, pp. 1103–1104.

Witte, L. C., and Lienhard, J. H., 1982, "On the Existence of Two 'Transition' Boiling Curves," *Int. J. Heat Mass Transfer*, Vol. 25, No. 6, pp. 771–779.

A New Interpolation Formula for Forced-Convection Condensation on a Horizontal Surface

J. W. Rose[1]

Nomenclature

$$G = \left(\frac{k\Delta T}{\mu h_{fg}}\right)\left(\frac{\rho\mu}{\rho_v\mu_v}\right)^{1/2}$$

h_{fg} = specific enthalpy of evaporation
k = thermal conductivity of condensate
Nu = local Nusselt number = $qx/k\Delta T$
Pr = Prandtl number of condensate
q = heat flux
$\tilde{\text{Re}}$ = local "two-phase" Reynolds number = $U_\infty \rho x/\mu$
U_∞ = free-stream vapor velocity
x = distance from leading edge of surface
ΔT = temperature difference across condensate film
μ = viscosity of condensate
μ_v = viscosity of vapor
ρ = density of condensate
ρ_v = density of vapor

The problem of forced-convection condensation, with (saturated) vapor flow parallel to a horizontal isothermal plane surface, has been considered in detail by Koh (1962). Solutions were obtained on the basis of the uniform-property boundary-layer equations for both condensate and vapor. It was shown that the surface heat transfer coefficient was expressible in terms of a relationship between four dimensionless parameters, thus

$$\text{Nu}\,\tilde{\text{Re}}^{-1/2} = \psi_1\left\{\frac{k\Delta T}{\mu h_{fg}},\ \text{Pr},\ \left(\frac{\rho\mu}{\rho_v\mu_v}\right)^{1/2}\right\} \tag{1}$$

or alternatively

$$\text{Nu}\,\tilde{\text{Re}}^{-1/2} = \Phi_1\left\{G,\ \text{Pr},\ \left(\frac{\rho\mu}{\rho_v\mu_v}\right)^{1/2}\right\} \tag{2}$$

where

$$G = \frac{k\Delta T}{\mu h_{fg}}\left(\frac{\rho\mu}{\rho_v\mu_v}\right)^{1/2} \tag{3}$$

However, in the range of practical interest, the Prandtl number dependence was weak, leading to

$$\text{Nu}\,\tilde{\text{Re}}^{-1/2} = \psi_2\left\{\frac{k\Delta T}{\mu h_{fg}},\ \left(\frac{\rho\mu}{\rho_v\mu_v}\right)^{1/2}\right\} \tag{4}$$

or

$$\text{Nu}\,\tilde{\text{Re}}^{-1/2} = \Phi_2\left\{G,\ \left(\frac{\rho\mu}{\rho_v\mu_v}\right)^{1/2}\right\} \tag{5}$$

Equations (4) and (5) relate to the case where the condensate film is treated on the basis of the Nusselt approximations, i.e., neglecting the inertia and convection terms in the conservation equations. The presence of $(\rho\mu/\rho_v\mu_v)^{1/2}$ arises from the conditions of continuity of velocity and shear stress at the vapor–liquid interface. The separate dependence on this parameter disappears in the limiting cases of zero and infinite condensation rate. In the former case Cess (1960) had earlier shown that

$$\text{Nu}\,\tilde{\text{Re}}^{-1/2} = 0.436G^{-1/3} \tag{6}$$

valid for $G \to 0$, while Shekriladze and Gomelauri (1966) had obtained, for infinite condensation rate,

[1]Department of Mechanical Engineering, Queen Mary College, University of London, London, United Kingdom.

Contributed by the Heat Transfer Division for publication in the JOURNAL OF HEAT TRANSFER. Manuscript received by the Heat Transfer Division July 5, 1988. Keywords: Condensation, Forced Convection, Phase-Change Phenomena.

tenth of $q_{max,max}$, at least at pressures less than about one tenth of the critical pressure.

4 At higher pressures, $q_{max,max}$ is such a large number that, for many liquids, we are not capable of supplying it.

5 If means exist for supplying $q_{max,max}$ at higher pressures, it then becomes increasingly difficult to capitalize on the enormous magnitude of $q_{max,max}$ because it is hard to design processes that prevent heat from finding non-phase-change flow paths.

6 The present ideas appear to apply to the limiting heat flux in dropwise condensation as well as to q_{max} in nucleate boiling. The few available observations of q_{max} in dropwise condensation appear to define the $\phi = 0.1$ limit, *without serious augmentation*, at low pressures.

References

Elkassabgi, Y., and Lienhard, J. H., 1988, "Influences of Subcooling on Burnout of Horizontal Cylindrical Heaters," ASME JOURNAL OF HEAT TRANSFER, Vol. 110, No. 2, pp. 479–486.

Gambill, W. R., and Greene, N. D., 1958, "Boiling Burnout With Water in Vortex Flow," *Chem. Engr. Prog.*, Vol. 54, No. 10, pp. 68–76.

Gambill, W. R., Bundy, R. D., and Wansbrough, R. W., 1960, "Heat Transfer, Burnout, and Pressure Drop for Water in Swirl Flow Through Tubes With Internal Twisted Tapes," Oak Ridge Nat'l. Lab. Rpt. ORNL-2911, Appendix 2, pp. 95–99.

Gambill, W. R., Bundy, R. D., and Wansbrough, R. W., 1961, "Heat Transfer, Burnout, and Pressure Drop for Water in Swirl Flow Through Tubes With Internal Twisted Tapes," *Chem. Engr. Prog. Symp. Series*, Vol. 57, No. 32, pp. 127–137.

Gambill, W. R., and Bundy, R. D., 1963, "High-Flux Heat-Transfer Characteristics of Pure Ethylene Glycol in Axial and Swirl Flow," *AIChE Journal*, Vol. 9, No. 1, pp. 55–59.

Hines, W. S., 1959, "Forced Convection and Peak Nucleate Boiling Heat Transfer Characteristics for Hydrazine Flowing Turbulently in a Round Tube at Pressures to 1000 psia," Rocketdyne Rept. R-2059.

Katto, Y., and Shimizu, M., 1979, "Upper Limit of the CHF in the Forced Convection Boiling on a Heated Disc With a Small Impinging Jet," ASME JOURNAL OF HEAT TRANSFER, Vol. 101, No. 2, pp. 265–269.

Kutateladze, S. S., 1965, "Criteria of Stability in Two-Phase Flow," *Symposium on Two-Phase Flow*, Vol. 1, Univ. of Exeter, United Kingdom, pp. 83–92.

Lienhard, J. H., and Eichhorn, R., 1979, "On Predicting Boiling Burnout for Heaters Cooled by Liquid Jets," *Int. J. Heat Mass Transfer*, Vol. 22, pp. 774–776.

Mills, A. F., 1965, "The Condensation of Steam at Low Pressures," Tech. Rpt. on NSF GP-2520, Series No. 6, Issue No. 39, Space Sciences Lab., Univ. of Calif. Berkeley.

Monde, M., and Katto, Y., 1978, "Burnout in High Heat-Flux Boiling System With an Impinging Jet," *Int. J. Heat Mass Transfer*, Vol. 21, pp. 295–305.

Noel, M. B., 1961a, "Experimental Investigation of Heat Transfer Characteristics of Hydrazine and a Mixture of 90 percent Hydrazine and 10 percent Ethylenediamine," JPL Technical Rept. No. 32-109.

Noel, M. B., 1961b, "Experimental Investigation of the Forced-Convection and Nucleate-Boiling Heat-Transfer Characteristics of Liquid Ammonia," JPL Technical Rept. No. 32-125.

Ornatskii, A. P., and Vinyarskii, L. S., 1965a, "Heat Transfer Crisis in a Forced Flow of Underheated [Subcooled] Water in Small-Bore Tubes," *High Temp.*, Vol. 3, No. 3, pp. 400–406.

Ornatskii, A. P., and Vinyarskii, L. S., 1965b, "Critical Heat Transfer in the Forced Motion of Underheated Water–Alcohol Mixtures in Tubes of Diameter 0.5 mm," *High Temp.*, Vol. 3, No. 6, pp. 881–882.

Schrage, R. W., 1953, *A Theoretical Study of Interphase Mass Transfer*," Columbia University Press, New York, Chap. II.

Stylianou, S. A., and Rose, J. W., 1983, "Drop-to-Filmwise Condensation Transition: Heat Transfer Measurements for Ethanediol," *Int. J. Heat Mass Transfer*, Vol. 26, No. 5, pp. 747–760.

Tanasawa, I., and Utaka, Y., 1979, "Measurement of Condensation Curves for Dropwise Condensation Heat Transfer," *Proc. 18th Nat'l. Heat Transfer Conf.*, ASME, p. 63.

Tien, C. L., and Lienhard, J. H., 1976, *Solutions Manual to Accompany Statistical Thermodynamics*, revised printing, Hemisphere, Washington, p. 13.

Tien, C. L., and Lienhard, J. H., 1979, *Statistical Thermodynamics*, revised printing, Hemisphere, Washington, p. 55, Problem 2.21.

Weatherhead, R. T., 1955, "Boiling Burnout Heat Flux for Wires in Water Crossflow at Atmospheric Pressure," Report NDA-9 (Boiling Burnout Progress No. 5).

Winterton, R. H. S., 1983, "Comments on 'On the Existence of Two 'Transition' Boiling Curves'," *Int. J. Heat Mass Transfer*, Vol. 26, No. 7, pp. 1103–1104.

Witte, L. C., and Lienhard, J. H., 1982, "On the Existence of Two 'Transition' Boiling Curves," *Int. J. Heat Mass Transfer*, Vol. 25, No. 6, pp. 771–779.

A New Interpolation Formula for Forced-Convection Condensation on a Horizontal Surface

J. W. Rose[1]

Nomenclature

$$G = \left(\frac{k\Delta T}{\mu h_{fg}}\right)\left(\frac{\rho\mu}{\rho_v\mu_v}\right)^{1/2}$$

h_{fg} = specific enthalpy of evaporation
k = thermal conductivity of condensate
Nu = local Nusselt number = $qx/k\Delta T$
Pr = Prandtl number of condensate
q = heat flux
$\tilde{\text{Re}}$ = local "two-phase" Reynolds number = $U_\infty \rho x/\mu$
U_∞ = free-stream vapor velocity
x = distance from leading edge of surface
ΔT = temperature difference across condensate film
μ = viscosity of condensate
μ_v = viscosity of vapor
ρ = density of condensate
ρ_v = density of vapor

The problem of forced-convection condensation, with (saturated) vapor flow parallel to a horizontal isothermal plane surface, has been considered in detail by Koh (1962). Solutions were obtained on the basis of the uniform-property boundary-layer equations for both condensate and vapor. It was shown that the surface heat transfer coefficient was expressible in terms of a relationship between four dimensionless parameters, thus

$$\text{Nu}\,\tilde{\text{Re}}^{-1/2} = \psi_1\left\{\frac{k\Delta T}{\mu h_{fg}},\ \text{Pr},\ \left(\frac{\rho\mu}{\rho_v\mu_v}\right)^{1/2}\right\} \tag{1}$$

or alternatively

$$\text{Nu}\,\tilde{\text{Re}}^{-1/2} = \Phi_1\left\{G,\ \text{Pr},\ \left(\frac{\rho\mu}{\rho_v\mu_v}\right)^{1/2}\right\} \tag{2}$$

where

$$G = \frac{k\Delta T}{\mu h_{fg}}\left(\frac{\rho\mu}{\rho_v\mu_v}\right)^{1/2} \tag{3}$$

However, in the range of practical interest, the Prandtl number dependence was weak, leading to

$$\text{Nu}\,\tilde{\text{Re}}^{-1/2} = \psi_2\left\{\frac{k\Delta T}{\mu h_{fg}},\ \left(\frac{\rho\mu}{\rho_v\mu_v}\right)^{1/2}\right\} \tag{4}$$

or

$$\text{Nu}\,\tilde{\text{Re}}^{-1/2} = \Phi_2\left\{G,\ \left(\frac{\rho\mu}{\rho_v\mu_v}\right)^{1/2}\right\} \tag{5}$$

Equations (4) and (5) relate to the case where the condensate film is treated on the basis of the Nusselt approximations, i.e., neglecting the inertia and convection terms in the conservation equations. The presence of $(\rho\mu/\rho_v\mu_v)^{1/2}$ arises from the conditions of continuity of velocity and shear stress at the vapor–liquid interface. The separate dependence on this parameter disappears in the limiting cases of zero and infinite condensation rate. In the former case Cess (1960) had earlier shown that

$$\text{Nu}\,\tilde{\text{Re}}^{-1/2} = 0.436G^{-1/3} \tag{6}$$

valid for $G \to 0$, while Shekriladze and Gomelauri (1966) had obtained, for infinite condensation rate,

[1]Department of Mechanical Engineering, Queen Mary College, University of London, London, United Kingdom.

Contributed by the Heat Transfer Division for publication in the JOURNAL OF HEAT TRANSFER. Manuscript received by the Heat Transfer Division July 5, 1988. Keywords: Condensation, Forced Convection, Phase-Change Phenomena.

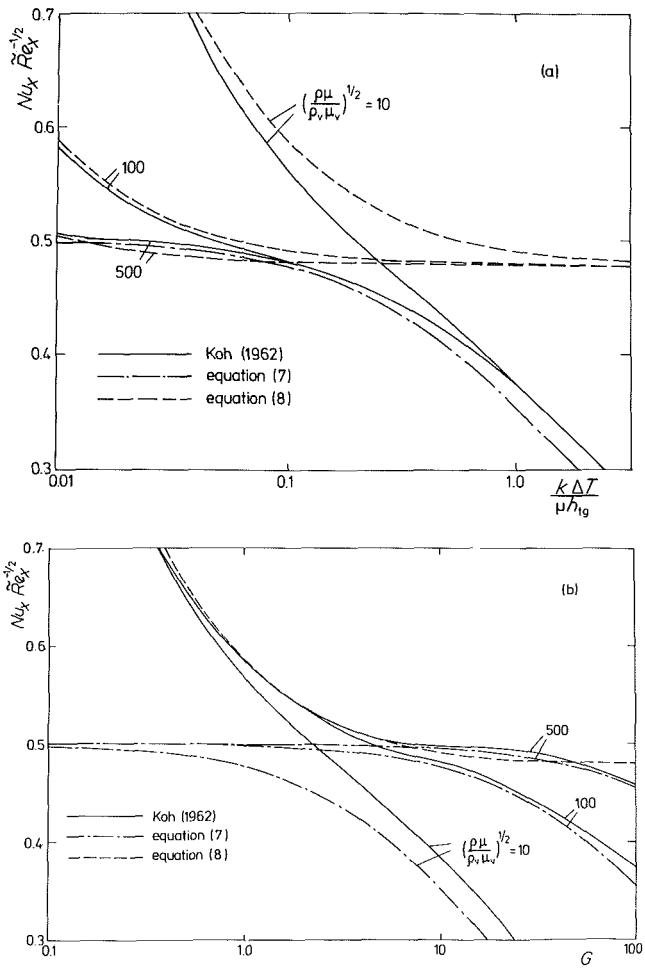

Fig. 1 Comparison of Shekriladze and Gomelauri (1966) solution, equation (7), and equation of Fujii and Uehara (1972), equation (8), with low-Pr numerical solutions of Koh (1962)

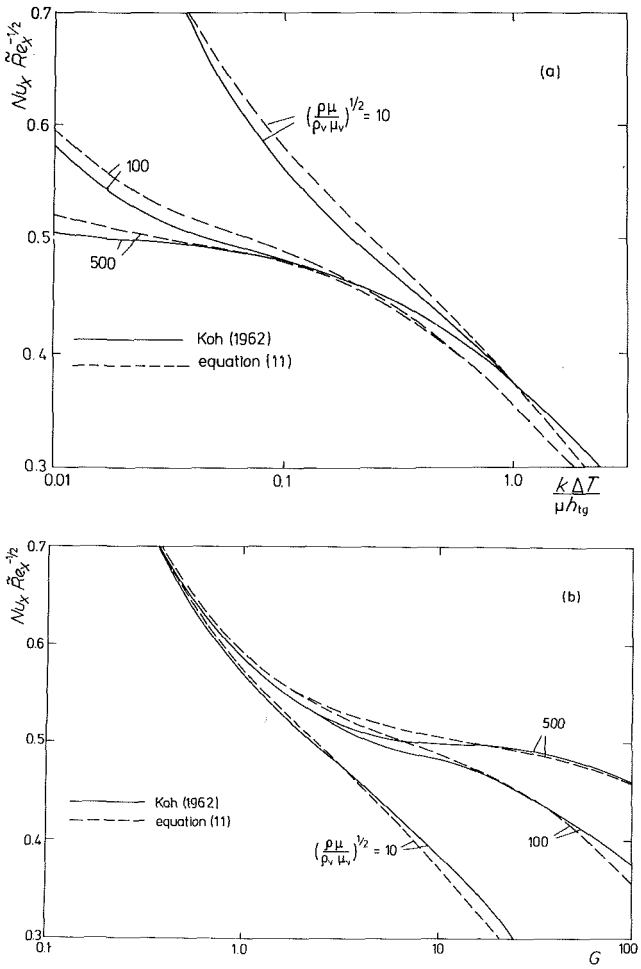

Fig. 2 Comparison of equation (11) with low-Pr numerical solutions of Koh (1962)

$$\mathrm{Nu}\,\tilde{\mathrm{R}}\mathrm{e}^{-1/2} = \frac{0.5}{\{1+(k\Delta T/\mu h_{fg})\}^{1/2}} \tag{7}$$

For the general case Fujii and Uehara (1972), on the basis of an approximate integral treatment of the vapor boundary layer, suggested

$$\mathrm{Nu}\,\tilde{\mathrm{R}}\mathrm{e}^{-1/2} = 0.45(1.2+G^{-1})^{1/3} \tag{8}$$

As may be seen, in the limiting case where $G\to 0$, equation (8) is in quite good agreement with the "exact" solution of Cess (1960), given in equation (6). At high condensation rates however ($G\to\infty$) equation (8) gives

$$\mathrm{Nu}\,\tilde{\mathrm{R}}\mathrm{e}^{-1/2} = 0.478 \tag{9}$$

which approximates the exact solution of Shekriladze and Gomelauri (1966), equation (7), only for small values of $k\Delta T/\mu h_{fg}$. Careful inspection of the solution of Fujii and Uehara (1972) reveals that the liquid surface velocity was implicitly considered small in comparison with the vapor free-stream velocity. In this case, and for the infinite condensation rate limit, one readily finds

$$\mathrm{Nu}\,\tilde{\mathrm{R}}\mathrm{e}^{-1/2} = 0.5 \tag{10}$$

i.e., in quite close agreement with equation (9).

As illustrated in Fig. 1, and anticipated in the light of the above discussion, equation (8) is generally in line with the numerical solutions of Koh (1962) for low $k\Delta T/\mu h_{fg}$ or low G, but approaches a constant value of $\mathrm{Nu}\tilde{\mathrm{R}}\mathrm{e}^{-1/2}$ at high $k\Delta T/\mu h_{fg}$ and G, where the Koh solutions fall with increasing values of these parameters. Equation (7), on the other hand, behaves correctly at high $k\Delta T/\mu h_{fg}$ and G, but approaches a constant value of $\mathrm{Nu}\tilde{\mathrm{R}}\mathrm{e}^{-1/2}$ at low values of these parameters. For values of $k\Delta T/\mu h_{fg}$ greater than about 0.1 the error in equation (8) becomes increasingly large, while for values of G less than about 5 equation (7) becomes increasingly inaccurate.

A new formula is now proposed that has the correct behavior in the limiting cases, i.e.,

$$\mathrm{Nu}\,\tilde{\mathrm{R}}\mathrm{e}^{-1/2} = 0.436\left\{\frac{1.508}{\left(1+\dfrac{k\Delta T}{\mu h_{fg}}\right)^{3/2}}+\frac{1}{G}\right\}^{1/3} \tag{11}$$

For the case of zero condensation rate where $k\Delta T/\mu h_{fg}$ and G approach zero, equation (11) reduces to the "exact" result of Cess, equation (6). At high condensation rate, $G\to\infty$, equation (11) virtually coincides with the analytical result of Shekriladze and Gomelauri (1966), equation (7). Figure 2 compares equation (11) with the numerical solutions of Koh (1962).

References

Cess, R. D., 1960, "Laminar-Film Condensation on a Flat Plate in the Absence of a Body Force," *Z. Angew, Math. Phys.*, Vol. 11, pp. 426-433.

Fujii, T., and Uehara, H., 1972, "Laminar Filmwise Condensation on a Vertical Surface," *Int. J. Heat Mass Transfer*, Vol. 15, pp. 217-233.

Koh, J. C. Y., 1962, "Film Condensation in a Forced-Convection Boundary-Layer Flow," *Int. J. Heat Mass Transfer*, Vol. 5, pp. 941-954.

Shekriladze, I. G., and Gomelauri, V. I., 1966, "Theoretical Study of Laminar Film Condensation of Flowing Vapour," *Int. J. Heat Mass Transfer*, Vol. 9, pp. 581-591.